Durham E-Theses

Synthetic, Spectroscopic, Structural and Computational Studies of Enyl and Ynyl Carbon-Rich Complexes

FARMER, JULIAN,DOMINIC

How to cite:

FARMER, JULIAN,DOMINIC (2009) *Synthetic, Spectroscopic, Structural and Computational Studies of Enyl and Ynyl Carbon-Rich Complexes*, Durham theses, Durham University. Available at Durham E-Theses Online: http://etheses.dur.ac.uk/162/

Use policy

The full-text may be used and/or reproduced, and given to third parties in any format or medium, without prior permission or charge, for personal research or study, educational, or not-for-profit purposes provided that:

- a full bibliographic reference is made to the original source
- a link is made to the metadata record in Durham E-Theses
- the full-text is not changed in any way

The full-text must not be sold in any format or medium without the formal permission of the copyright holders.

Please consult the full Durham E-Theses policy for further details.

Academic Support Office, Durham University, University Office, Old Elvet, Durham DH1 3HP
e-mail: e-theses.admin@dur.ac.uk Tel: +44 0191 334 6107
http://etheses.dur.ac.uk

Synthetic, Spectroscopic, Structural and Computational Studies of Enyl and Ynyl Carbon-Rich Complexes

Julian Dominic Farmer MChem (Dunelm)

Department of Chemistry

A Thesis submitted in part fulfilment of the requirements for the degree of Doctor of Philosophy at Durham University

2009

Statement of Copyright

The copyright of this thesis rests with the author. No quotation from it should be published in any form, including electronic and the internet, without the author's prior written consent and information derived from it should be acknowledged appropriately.

Declaration

The work described in this thesis was carried out at the University of Durham, Department of Chemistry, between October 2005 and December 2008. All the work is that of the author unless stated otherwise, and it has not been submitted for a degree at this or any other university.

Memorandum

Part of this work has been the subject of the following:

M.A. Fox, J.E. Harris, S.E. Heider, V. Perez-Gregorio, M.E. Zakrewska, J.D. Farmer, D.S. Yufit, J.A.K. Howard and P.J. Low, **A simple synthesis of *trans*-Ru(C≡CR)(dppe)$_2$ complexes and representative molecular structures**, *J. Organomet. Chem.,* 2009, **694**, 2350-2358.

M.A. Fox, J.D. Farmer, R.L. Roberts, M.G. Humphrey and P.J. Low, **Noninnocent Ligand Behaviour in Diruthenium Complexes Containing a 1,3- Diethynyl Bridge**, *Organometallics.,* 2009, **17**, 5266-5269.

And has been presented at:

- 6th Chianti Electrochemistry Meeting,

Certosa di Pontignano, Siena, Italy, 2008.

Lecture entitled: The Electronic Structure and Redox Properties of Tris(pyrazolyl)hydroborate ruthenium complexes featuring aryl vinyl ligands: a combined spectroelectrochemical and DFT study.

- XXII International Conference on Organometallic Chemistry

Zaragoza, Spain, 2006.

Poster entitled: Some Organometallic Chemistry of C≡N and CH=CH Containing Ligand Complexes.

- 5th Chianti Electrochemistry Meeting,

Certosa di Pontignano, Siena, Italy, 2006.

Poster entitled: Some Organometallic Chemistry of C≡N Containing Ligand Complexes.

Dedication

This thesis is dedicated to my late father Mr Derek Ward Farmer, whose personal achievements through his life, drive me on to greater and bigger things.

Abstract

This thesis describes the synthesis and analysis of organometallic complexes that feature either enyl or ynyl linkages. Chapter 1 introduces a general overview of electron transfer, classification of mixed-valence complexes and the modelling of mixed-valence complexes using density functional theory.

The synthesis of a range of *trans*-RuCl(C≡CC_6H_4R)$(dppe)_2$ complexes, in which R is either an electron donor (Me, OMe, C_5H_{11}) or acceptor (NO_2, CO_2Me), from the five-coordinate complex [RuCl$(dppe)_2$]OTf is described. This synthetic route represents an alternative to the long-standing methods based on *cis*-$RuCl_2(dppe)_2$. Improved synthetic routes to both [RuCl$(dppe)_2$]OTf and *cis*-$RuCl_2(dppe)_2$ are also given. These compounds were fully characterised spectroscopically and the molecular structures of [RuCl$(dppe)_2$]OTf, *trans*-RuCl(C≡CC_6H_4OMe)$(dppe)_2$, *trans*-RuCl(C≡CC_6H_4Me)$(dppe)_2$, and *trans*-RuCl(C≡C$C_6H_4CO_2$Me)$(dppe)_2$ determined and analysed. The structures conform with literature precedence.

The synthesis of ruthenium complexes based on RuCl$(dppe)_2$ and Ru(dppe)Cp* units, featuring 1,3-diethynylbenzene bridging ligands has been achieved. The electronic structures of 1,3-{*trans*-Cl$(dppe)_2$RuC≡C}$_2C_6H_4$, 1,3-{Cp*(dppe)RuC≡C}$_2C_6H_4$ and 1,3-{Cp*(dppe)RuC≡C}$_2$-5-(HC≡C)C_6H_3 have been investigated using a combination of UV-vis-NIR and IR spectroscopies and computational studies. In contrast to the case of closely related iron compounds, for the ruthenium complexes 1,3-{trans-Cl$(dppe)_2$RuC≡C}$_2C_6H_4$, 1,3-{Cp*(dppe)RuC≡C}$_2C_6H_4$ and 1,3-{Cp*(dppe)RuC≡C}$_2$-5-(HC≡C)C_6H_3 the bridging aryl moiety is heavily involved in the oxidation process, and consequently descriptions of the electronic structures and electronic transitions in terms of the language developed for mixed-valence systems with clearly identifiable metal oxidation states are not appropriate. The description of the low-energy absorption bands from the mixed-valence complexes are therefore better described as charge transfer transitions rather than IVCT transitions.

A range of mono vinyl Ru(CH=CHC$_6$H$_4$R-4)(CO)(PPh$_3$)Tp complexes have been obtained from the reaction of RuHCl(CO)(PPh$_3$)$_3$ with *para*- substituted ethynylphenylenes, and KTp. (R = NO$_2$, CO$_2$Me, CN, Me and OMe). These complexes have been fully characterised spectroscopically, with molecular structures for Ru(CH=CHC$_6$H$_4$NO$_2$-4)(CO)(PPh$_3$)Tp, Ru(CH=CHC$_6$H$_4$CN-4)(CO)(PPh$_3$)Tp, Ru(CH=CHC$_6$H$_4$CH$_3$)(CO)(PPh$_3$)Tp and Ru(CH=CHC$_6$H$_4$OMe-4)(CO)(PPh$_3$)Tp being determined and analysed. The electronic structures of these mono vinyl complexes have been also investigated using a combination of UV-vis-NIR and IR spectroscopies and computational studies, revealing the redox activity of the styrene-derived ligand. Hydroruthenation of 1,3-, 1,4- diethynylbenzene and 1,3,5-triethynylbenzene affords the di- and trimetalled vinyl complexes, which have been characterised spectroscopically. The bridging ligand is shown to be redox non-innocent.

A simple protocol that allows the preparation of either "symmetric" A$_3$ or "asymmetric" AB$_2$ triethynyl methanol derivatives through the reaction of acetylide anions with chloroethylformate, has been explored. This synthetic protocol is not only high yielding, but avoids the harsh conditions used in literature methods. The molecular structures of Me$_3$SiC≡C(COH)(C$_6$H$_4$I)$_2$ and HC≡C(COH)(C$_6$H$_4$I)$_2$ have been determined and analysed, with the packing motifs in the solid state arising from halogen interactions identified. The use of these ligands as branched core ligands has also been investigated, and whilst difficulties have been encountered synthetic work to resolve these has been initiated.

A selection of pro-ligands and both mono- and tris-metallated ligand complexes based on a triarylamine core have been prepared. The electronic and structural nature of Me$_3$SiC≡C(C$_6$H$_4$)NTol$_2$, Fe(C≡C(C$_6$H$_4$)NTol$_2$)(dppe)Cp and [{Fe(dppe)Cp}$_3$(μ-(C≡CC$_6$H$_4$)$_3$N)] have been investigated using a combination of UV-vis-NIR and IR spectroscopies and computational studies indicating electronic interactions between the remote metal centres in the case of [{Fe(dppe)Cp}$_3$(μ-(C≡CC$_6$H$_4$)$_3$N)]$^{n+}$ (n = 1, 2). The molecular structures of Me$_3$SiC≡C(C$_6$H$_4$)NTol$_2$, HC≡C(C$_6$H$_4$)NTol$_2$, Ru(C≡C(C$_6$H$_4$)NTol$_2$)(dppe)Cp* and Fe(C≡C(C$_6$H$_4$)NTol$_2$)(dppe)Cp have been determined and analysed.

Acknowledgements

Firstly, I would like to thank Dr Paul Low, very much for his supervision, help and support during the course of my Ph.D.

I would also like to thank the past and present members of the Lab 100, firstly for all of their friendship and secondly for keeping me sane through the Ph.D. I'd like to thank Dr Mark Fox, Dr Howard Spencer, Dr Mark Smith and Dr Rachel Roberts. I'd like to thank Mark especially for his invaluable synthetic and computational advice. I'd like to thank Dr Andy Beeby for the provision of the Gaussian fitting routine. Additionally I would like to thank the Durham Doctoral Fellowship Scheme for funding this PhD.

Thanks are also due to the technical staff at the Department of Chemistry, namely Dr Alan Kenwright, Mrs Catherine Heffernan and Mr Ian McKeag (NMR); Dr Mike Jones (Mass Spectrometry); Jarika Dostel and Judith Magee (Elemental analysis); Dr Horst Puschmann and Dr. Dimitri Yufit (X-ray crystallography);

Thanks are also extended to Prof. M. G. Humphrey and his group with whom some research, has been undertaken.

Finally, I would like to thank all of my friends and family, in particular my parents for their love and support.

Abbreviations

º	degrees
ºC	degrees Celsius
α	alpha
β	beta
δ	chemical shift
Δ	reflux / difference
ΔE	potential difference
ΔE_0	ground state energy difference
ε	molar extinction coefficient
λ	wavelength
λ_i	inner-sphere reorganisation energy
λ_o	outer-sphere reorganisation energy
Å	angstrom
A	acceptor
A	amperes
A_3	symmetric triethynylmethanol derivative
AB_2	asymmetric triethynylmethanol derivative
abs	absorbance
Ar	aryl
aver	average
B	bridge
$[BHpz_3]^-$	hydrido(tripyrazolyl)borate anion (Tp^-)
bpy	bipyridine
br	broad
Bu	butyl
^{t}Bu	tertiary butyl
B3LYP	Becke 3-parameter Lee-Yang-Parr
ca.	circa
CBP	4,4'-N,N'-dicarbozole-biphenyl
CE	counter electrode
CI	configuration interaction

clpz	chloropyrazine
cm	centimetres
cm^{-1}	wavenumbers (reciprocal centimetres)
CN	cyano
Cp	cyclopentadienyl
Cp*	pentamethylcyclopentadienyl
CV	cyclovoltammetry
d	doublet
D	donor
dba	dibenzylidene acetone
DBU	1,8-diazabicyclo[5.4.0]undec-7-ene
dd	doublet of doublets
DFT	Density Functional Theory
dmpz	dimethylpyrazine
DNA	deoxyribosenucleic acid
dHpe	1,2-diphosphinoethane
dppe	1,2-bis(diphenylphosphino)ethane
dppf	1,1'-bis(diphenylphoshino)ferrocene
E	potential
$E_{1/2}$	half-wave potential
E_a	anodic potential
E_c	cathodic potential
E_n	potential of the n^{th} redox process
E_{op}	optical transition energy
E^*_{th}	activation energy of thermal electron transfer
EC	electrochemical
EI	electron impact
EL	electroluminescence
equiv	equivalents
ES	electrospray
Et	ethyl
EtOH	ethanol
eV	electronvolts
F	Faraday constant

Fc	ferrocene
Fc*	pentamethylferrocene
h	hour(s)
H_{ab}	Hamiltonian coupling constant
HF	Hartree Fock
HK	Hohenberg Kohn
HOMO	highest occupied molecular orbital
HOSO	highest occupied spin orbital
HS	high spin
Hz	hertz
I	current
i_a	anodic peak current
i_c	cathodic peak current
irr.	irreversible
IR	infra-red
IVCT	intervalence charge transfer
K_c	comproportional constant
J	Joules
$^nJ_{AB}$	n bound coupling constant between nuclei A and B
L	generic 2 electron ligand
LANL2DZ	Los Alamos National Laboratory double-ζ
LDA	local density approximation
LF	ligand field
LMCT	ligand-to-metal charge transfer
LS	low spin
LSDA	local spin-density approximation
LUMO	lowest unoccupied molecular orbital
LUSO	lowest unoccupied spin orbital
m	medium
m	multiplet
M	metal / molarity
M	molecular ion
m/z	mass per unit charge
MALDI	Matrix-assisted laser desorption/ionisation

Me	methyl
MeCN	acetonitrile
MeOH	methanol
mg	milligrams
MHz	megahertz
min	minutes
mL	millilitres
MLCT	metal-to-ligand charge transfer
mmol	millimoles
MO	molecular orbital
MPW1K	modified Perdew-Wang 1-parameter model for kinetics
mpz	methylpyrazine
mV	millivolts
MV	mixed-valence
NBO	natural bond order
NBu_4BF_4	tetrabutylammonium tetrafluoroborate
NIR	near-infra-red
NLO	non-linear optics
nm	nanometres
NMR	nuclear magnetic resonance
NO_2	nitrile
OAc	acetoxy
occ	occupany
OLED	organic light emitting diodes
OMe	methoxy
OPE	oligo-phenylene ethynylene
OTf	triflate anion
Ph	phenyl
PhPy	phenylpyridine
PL	photoluminescence
PPh_3	triphenylphosphine
ppm	part per million
^{i}Pr	isopropyl
Py	pyridine

pz	pyrazine
q	quintet
QCA	quantum-dot cellular automata
R	general organic group
r_{ab}	effective charge transfer distance
rt	room temperature
s^{-1}	reciprocal seconds
s	singlet (NMR)
s	strong (IR)
SAM	self assembled monolayer
SCE	standard / saturated calomel electrode
sh	shoulder
$SiMe_3$	trimethylsilyl group
STM	scanning tunnelling microscopy
t	triplet
TCNQ	tetracyanoquinodimethane
TD DFT	Time Dependent Density Functional Theory
THF	tetrahydrofuran
TLC	thin layer chromatography
TMEDA	tetramethylethylenediamine
TMS	trimethylsilyl
TMSA	trimethylsilylacetylene
Tol	*para*- tolyl $C_6H_4CH_3$
Tp^-	hydrido(tripyrazolyl)borate anion
TTF	tetrathiafulvene
UV-vis-NIR	ultraviolet-visible-near infrared
V	volt(s)
w	weak
X	halide /substituents

Table of Contents

Chapter 1 : Introduction

In the mid-1960s, Gordon Moore, the co-founder of Intel, observed that the number of transistors on a chip had doubled approximately every two years. This observation has proven to be somewhat prophetic, and the original statement is now encompassed in Moore's Law which serves as a target for the semiconductor industry. [1] Over the last 40 years, technological advances in electronics have seen Moore's Law being largely obeyed, with silicon-based transistors becoming smaller and smaller in response to advances in both materials and processing methods. This approach in making silicon devices ever smaller, known as the 'top-down approach', has so far been successful, with some argument that the technology is ahead of Moore's Law. [2] However the question is no longer one of 'if?', but rather of 'when?', will significant obstacles to the miniaturisation of solid-state devices be reached. Two of the major limitations to the minimum size of silicon-based transistors are: the breakdown of the fundamental band structure of the solid materials used in the construction of these nano-scale devices; [3, 4] the monetary costs of both resources and equipment required to manufacture ever smaller devices on ever larger wafers. [3] As of this, Moore's Law based solid state technologies may reach failure point in the foreseeable future. [4]

The other approach to miniature size transistors is the 'bottom-up approach'. The nature of synthetic chemistry offers an alternative approach to the construction of functional materials through assembly with atomic precision. The ability to handle and manipulate the properties of molecules opens up the possibility to exploit molecular properties to our gain. The idea that a single molecule could provide an analogous function to that of an electrical device gained considerable momentum following the proposal in 1974 by Aviram and Ratner of a unimolecular rectifier (a p-n junction rectifier) based on a Donor-Acceptor (D-A) architecture (Figure **1**). [5] The Aviram-Ratner unimolecular rectifier, now considered a milestone in molecular electronics, [6] unsurprisingly received very little attention at the time as the requirements to synthesise such rectifying molecules and the subsequent fabrication of devices, that require vertical stacking of the molecules in organic monolayers of nanometre-scale thickness, sandwiched between two electrodes, are technically

challenging, even today. However, over the ensuing years great advances in both the synthesis of rectifying molecules and testing of electronic characteristics has advanced greatly, with numerous demonstrations of this concept having been reported. [7]

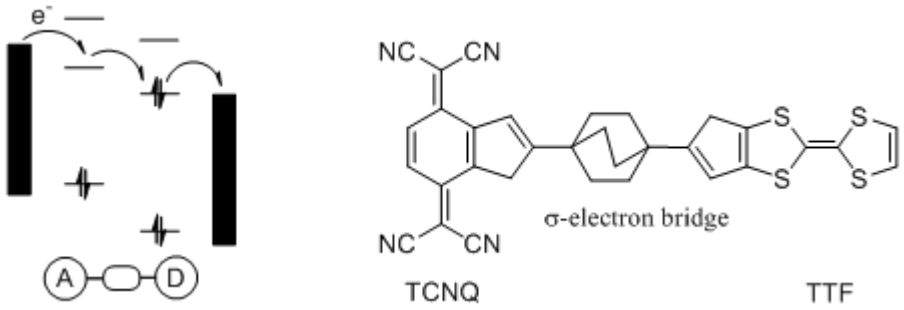

Figure **1** Band diagram for a A-bridge-D Aviram-Ratner rectifier, between two electrodes.

Recently the most widely investigated roles for the electronic properties of molecules within devices have returned to studies of simpler components, such as molecular wires, in which a molecule acts as a conduit for charge that is more effective than the transmission through space. [8] These 'molecular wires' are the fundamental building blocks of molecular electronic devices such as junctions, switches, transistors, logic gates, *etc*. There are a few basic requirements that molecules proposed to act as molecular wires must satisfy, such as conformational stability in the long term when exposed to a wide variety of conditions such as elevated temperature, oxidation or reduction. However, the most elementary requirement of a molecular wire is the capacity to conduct a hole or an electron, and hence carry a current. Therefore a 'molecular wire' provides a pathway between two sites and has been defined as a 'one dimensional molecule allowing a through-bridge exchange of an electron or hole, between its remote terminal groups, themselves able to exchange electrons with the outside world'. [9] In recent years, numerous types of molecules have been proposed as molecular wires, [10, 11] including conjugated carbon chains, [12] carbon nanotubes, [13, 14] polymers, [15] including DNA, [16] and porphyrin based complexes. [17] By decorating the basic linear molecular architecture with substituent groups the properties of the molecule as a whole, such

as solubility, electrode binding properties and redox potentials, can be tuned by the chemist to meet the requirements of the device.

In order to assess the conduction properties of a molecular wire, a potential has to be applied across the length of the molecule, just in the same way the conduction of a length of copper wire would be tested. Quantification of the conductance of a molecular wire has been approached in many different ways, which generally depend on the nature of the molecule being assessed. One technique that is used to obtain current-voltage characteristics is scanning tunnelling microscopy (STM). This often involves the formation of a self assembled monolayer (SAM) of alkane thiols adsorbed onto a gold substrate, of a known thickness, to give an insulating molecular layer on the surface. Exposure of a low concentration of the molecule wire to this SAM results in the insertion of the wire-like candidate into a grain boundary within the insulating supporting film. [8] In some cases the position of the wire-like candidate can be controlled via the application of a voltage pulse from the STM tip. [18] With the molecular wire aligned perpendicularly to the gold surface, the STM tip acts as the second electrode, completing the circuit. [19] This technique, the equivalent of contacting a molecule into a circuit by surface binding micro-crocodile clips, although popular in measuring the conductivity and length of molecular wires, is fraught with problems arising from, for example, defects in the monolayers, and the growth of metallic filaments between the STM tip and the underlying gold substrate. Numerous variations on the theme of contacting molecules between solid electrodes have been developed, and techniques continue to be devised. [20]

An alternative method arguably more suited to the study of a wider variety of molecules rests on the investigation of intramolecular electron transfer processes through spectroscopic techniques, with the conductivity of the wire assessed via relatively simple measurements in solution. The most basic model of a molecular wire consists of two molecular groups, which act as the source of electrons or holes, tethered together by a bridging ligand, which provides the conduit for efficient charge transfer (Figure **2**). [11]

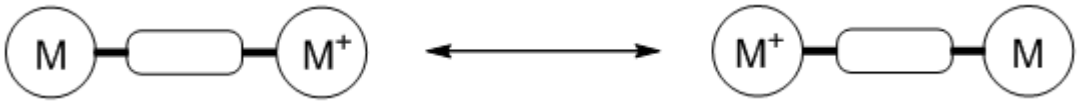

Figure **2** Basic model of a molecular wire consisting of two molecular groups tethered together by a bridging ligand.

The transfer of an electron from the electron rich centre (the donor) to the electron poor centre (the acceptor) can take place either thermally, or be initiated via photo-induced electron transfer (Figure **3**). [21, 22]

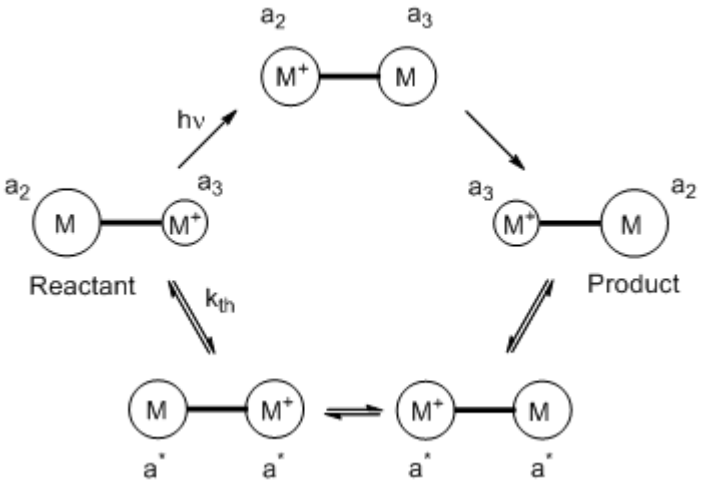

Figure **3** Thermal and optical electron transfer processes in a M-bridge-M binuclear mixed-valence complex.

Both thermal and photochemical electron-transfer are common processes in mixed valence materials. Consequently, studies of 'wire-like' behaviour in molecules in solution have been drawn to closely related studies of the characteristics of mixed valence complexes. [22-24] A mixed valence compound features an element in more than one formal oxidation state (e.g. the Creutz-Taube ion $[\{Ru(NH_3)_5\}_2(\mu\text{-pz})]^{5+}$, pz = pyrazine). [22] In the late 1960s Robin and Day [25] distinguished three broad classes of mixed-valence materials (Figure **4**):

- **Class I** the interaction between the M and M^+ centres is so weak, either because the M-M^+ separation is large, and/or the M and M^+ environments are extremely different, that the mixed-valence complex exhibits only the properties observed for isolated mononuclear M and M^+ complexes.

- **Class II** these complexes exhibit some interaction between the M and M^+ centres, to the extent that the complex M-M^+ exhibits some perturbation of M and M^+ characteristics. In this class the electron is vibrationally localised in one of the redox centres and an external or thermal stimulus is needed to promote electron transfer. In the case of photo-induced electron exchange between the two sites, the characteristic absorption band is usually termed the "Inter-Valence Charge Transfer" (IVCT) band, and is often found in the NIR region.

- **Class III** the interaction between the M and M^+ centres is so great that the properties of the isolated M and M^+ centres are absent, with new properties characteristic of $(M\text{-}M)^+$ being observed and the system essentially behaves as a unique species unrelated to either M or M^+.

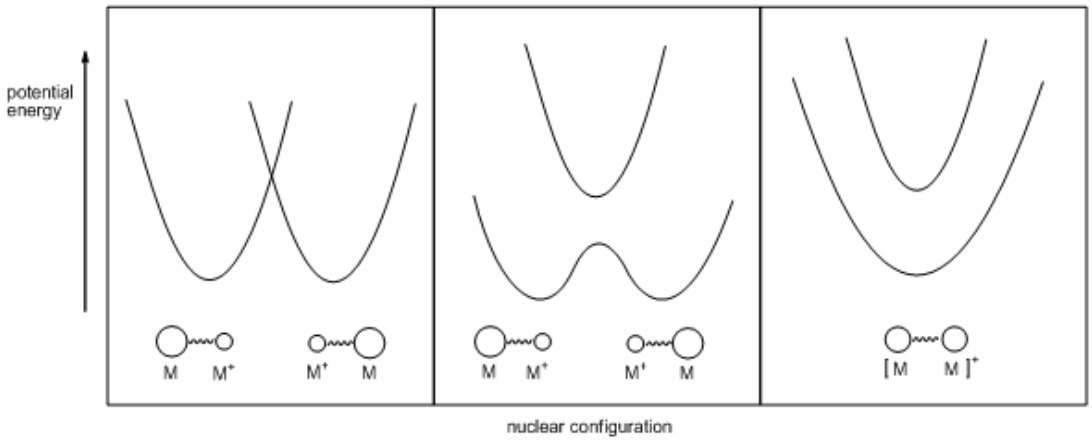

Figure **4** Potential energy curves associated with ligand bridged dinuclear mixed-valence complexes of: Class I (left); Class II (middle); and Class III (right). [25]

At the same time that Robin and Day proposed this classification of mixed-valence complexes, Hush proposed a theoretical model that linked the parameters of the

IVCT band to the activation energy for the electron transfer process, derived from Marcus theory [26, 27]

$$\nu_{max} = h\nu = \lambda_i + \lambda_o + \Delta E_0 + \Delta E'$$

where ν_{max} is the energy of the IVCT band, λ_i and λ_o are the inner- and outer-sphere re-organisation energies, ΔE_0 is the difference in ground state energy of the two states and $\Delta E'$ is the term that accounts for other energy terms, such as spin-orbit coupling and differences in the ligand field at each site. From the characteristics of these IVCT absorption bands, specifically their energy (ν_{max}), intensity (ε) and bandwidth at half-height ($\Delta\nu_{1/2}$), information into the fundamental factors governing the coupling of the two redox centres can be extracted. [28]

The frequency of the optical transition absorption E_{op} can be related to the activation energy of thermal electron transfer, E^*_{th},

$$E_{op} = 4\, E^*_{th}$$

From this relationship, Hush predicted that for the optical absorption band of a symmetric Class II species, the bandwidth at half intensity $\Delta\nu_{1/2}$ should be a function of the band maximum, ν_{max},

$$\Delta\nu_{1/2} = [2310\, \nu_{max}]^{1/2}\ cm^{-1}$$

The comparison of the calculated and experimental values of $\Delta\nu_{1/2}$ can be indicative of Class II or Class III behaviour. [22] In turn, the degree of electronic coupling between the two metal centres in a Class II system, which is related to the Hamiltonian H_{ab}, can be assessed from the relationship;

$$H_{ab} = 2.06 \times 10^{-2}\, [\{\nu_{max}\varepsilon_{max}\Delta\nu_{1/2}\}^{1/2}]/r_{ab}$$

where ν_{max} is the peak energy, ε_{max} is the molar extinction coefficient, $\Delta\nu_{1/2}$ is the bandwidth at half-height and r_{ab} is the effective charge transfer distance. [27]

Where the complex has three equivalent metal centres, with the assumption that all three sites behave independently, a modified Hush equation reported by Bonvoisin and Launay is used, with the two equations differing by a factor of √2, to take into account three equivalent redox centres; [29, 30]

$$H_{ab} = 2.06 \times 10^{-2} [\{\nu_{max}\varepsilon_{max}\Delta\nu_{1/2}\}^{1/2}]/[r_{ab}\sqrt{2}]$$

In keeping with the charge transfer nature of the IVCT process in a Class II mixed valence system, the IVCT band is typically solvatochromic. [28] Indeed, solvatochromism is often used as a diagnostic test to aid in the assignment of the IVCT band. [28]

However as Class III systems exhibit electron delocalisation, the rearrangement of the solvent spheres is not necessary, hence the analogous transition in Class III systems is solvent independent. The Hush relationship, derived for Class II systems, is not applicable to Class III systems, [22] and rather for a delocalised system H_{ab} is simply given by:

$$H_{ab} = \lambda/2$$

Recently, a new class of mixed-valence systems has been proposed in light of recent experimental experience. [24, 31, 32] This new class, Class II-III, named because of the systems exhibit intermediate localised-to-delocalised behaviour. [32, 33] Characteristic features which define Class II-III systems include electron localisation, solvent averaging and a residual barrier to electron transfer arising from intramolecular structural changes. [24] In essence, Class II-III defines a system in which electron exchange is faster than the time-scale of solvent reorganisation. [24]

However in reality there are no abrupt transitions between the different classes, with experimental studies revealing that there is a gradual change in behaviour from localised to delocalised limits. [24] Factors governing this change include the relative timescales for intramolecular electron transfer, with the picture complicated further

with the appearance of multiple IVCT absorptions, due the presence of multiple metal donor d-orbitals, spin-orbital coupling, and specific solvation. [34]

It has often been asserted that the extent of communication between metal centres of a molecular wire can be determined by cyclic voltammetry, an electrochemical technique. The thermodynamic stability of the mixed valence state $M\text{-}M^{+}$, with respect to M-M and $M\text{-}M^{2+}$, can be determined from the potential difference between $E_{0/1}$ and $E_{1/2}$. [35, 36] From the Nernst equation, the relationships below can be derived.

$$\Delta E = \Delta E^{o} - \{RT/nF\} \ln K_c$$

At equilibrium $\Delta E = 0$ and so

$$\Delta E^{o} = \{RT/nF\} \ln K_c$$

Therefore

$$K_c = \exp(\Delta EF/RT)$$

The argument runs that the more strongly delocalised the charge between the two sites M and M^{+}, the more stable the intermediate oxidation state should be relative to the two homovalent forms. In strongly coupled Class III systems the comproportionation constant K_c can be $>10^{13}$, whereas in Class I weakly coupled systems K_c can be as small as 4, which is the statistical limit. Whilst K_c has been used as a guide to the extent of electron delocalisation, technically no electronic structural information can be inferred from the value of K_c, as it is strictly a stability constant, [37] with;

$$K_c = \frac{[M\text{-}M^{+}]^2}{[M\text{-}M][M\text{-}M^{2+}]}$$

$$2\,[M\text{-}M^{+}] \overset{K_c}{\rightleftharpoons} [M\text{-}M] + [M\text{-}M^{2+}]$$

Figure **5** Equilibria between $[M\text{-}M^{+}]$, and [M-M] and $[M\text{-}M^{2+}]$.

Indeed, the thermodynamic stability of the mixed-valence state can be affected by many factors, including solvation, ion-pairing and different metal-ligand interactions (e.g. back-bonding) in the different formal oxidation states. [37] The situation becomes even more fraught when one considers the possibility of complexes containing redox non-innocent ligands.

Thus, the determination of the exact nature of the mixed-valence systems, despite the Hush analysis of IVCT processes and many claims of the role electrochemical data can play in the determination of Robin-Day class, is not always simple. In order to assess the electron transfer effects, a variety of spectroscopic techniques, on various timescales, have been used. [38] By way of recent examples Kubiak has used the ν(C≡O) band in a series of ligand bridged bis(ruthenium cluster) compounds, where upon the rate of electron-exchange between the two cluster redox sites was monitored as a function of the bridge structure, [31, 39] or solvation environment. [40] Another example of a study into electron transfer effects has been carried out by Winter, where compounds with the $RuCl(CO)(PR_3)_2$ (R = Ph, Me or ^{i}Pr) moieties, attached by a variety of carbon-rich bridges, have been investigated, using the ν(C≡O) band and the ν(C=O) band of the coligands, as probes of electron density changes at the metal and ligand sites respectively. [41, 42] The use of the ν(C≡C) and ν(B-H) bands as vibrational probes has also been investigated, by Low, with a selection of mono- and bi- metallic Ru(dppe)Cp* carborane (*p*-$C_2B_8H_8$ and *p*-$C_2B_{10}H_{10}$) acetylides. The mixed valence complexes of the bimetallic ethynylcarboranes exhibited spectroscopic properties consistent with the description of these species as valence-localised (Class II) mixed-valence compounds. [43] This point is addressed in greater detail in Chapters **3**, **4** and **6**.

Density functional theory (DFT) offers an alternative orbital picture of the electronic structure and through time dependent DFT (TD-DFT) a prediction of the nature of the electronic absorptions at a said oxidation state can be gained. This molecular orbital view of the electronic structure of mixed-valence complexes compliments and greatly advances the 'two-state' description encompassed in Hush theory. [44, 45] Quantum-chemical calculations either use approximations of individual electron wavefunctions or electron density methods to arrive at a description of the overall

molecular system, leading to *ab initio* and density-functional (DFT) techniques, respectively. Wavefunction–based *ab initio* methods, which employ the Hartree Fock approximation and subsequent configuration interaction (CI) treatment, are computationally very demanding and dependent on the number of atoms on the molecule. [45]

Although density functional theory has its conceptual routes in the Thomas-Fermi model, [46] the theoretical background relies on the two Hohenberg-Kohn theorems (HK). [47] The two HK theorems demonstrate that the ground state properties of a many-electron system are uniquely determined by an electron density that depends on only three spatial coordinates. The ability, through the use of functionals of electron density, to reduce the many-body problem of N electrons with 3N spatial coordinates to three spatial coordinates follows on from the two theorems. [47] The intractable many-body problem of interacting electrons in a static external potential, can be replaced with a tractable problem of non-interacting electrons moving in an effective potential, which includes external potentials and coulombic interactions between the electrons. [48] To simplify the problem, approximations are used, one such approximation is the local-density approximation (LDA), fitted to correlation energy for a uniform electron gas. [49]

One of the major problems with DFT is that the only exact functional for the exchange and correlation energies that is known is for the free electron gas. [49] To permit the calculation of physical properties approximations are needed, with one of the approximations being LDA, where the functional depends only on the density at the coordinate where the functional is evaluated, given by the relationship: [50]

$$E_{xc}[n] = \int \varepsilon_{xc}(n) n(\vec{r}) d^3r$$

The LDA functional can be modified to include the electron spin, to give the local spin-density approximation (LSDA): [50]

$$E_{xc}[n_\uparrow, n_\downarrow] = \int \varepsilon_{xc}(n_\uparrow, n_\downarrow) n(\vec{r}) d^3r$$

However one area where pure DFT functionals fail concerns charge-transfer excited states where the electron is excited from a donor orbital to an acceptor orbital, which is localised at a different part of the molecule. [45] This is due to pure DFT functionals not properly describing the long range electron hole separation. [45] As of this there is an overestimation on the stabilisation of the acceptor orbital, hence predicted lower in energy. With the inclusion of some HF character in the functional used, a better picture of the acceptor's energy can be determined, however with a trade-off with increased computational demand. [45]

Within this framework it is apparent that the wire-like properties of M-bridge-M systems depends critically on both the nature of the metal, the supporting ligands and the bridge, with the interaction between the M and bridge arguably dominating the electronic properties of the system. Within the vast array of bridging ligands that have been proposed and investigated, those based on carbon-rich structures have attracted particular attention. Homo- and hetero- bimetallic complexes of the simplest bridge, –C≡C– have been studied, with a wide range of metal end groups such as $ScCp^*_2$, [51] $Ti(PMe_3)Cp_2$, [52] $Ru(CO)_2Cp$ [53] and $Au(PR_3)$ (R = Ph, Tol) [54] to name just a few. The chain length of these bimetallic complexes has also been an area of extensive research, with the number of acetylenic –(C≡C)– repeat units being conceptually increased from one all the way up to twenty. [12, 55, 56] Bimetallic complexes where the carbon-rich bridge contains an odd-number of carbon atoms have also been investigated. [57] Related structures including polyacetylene, many of which have been studied by Jia (see Chapter **4**), and phenylene ethynylene (see Chapter **3**) have also been extensively studied.

This thesis attempts to address some of the issues arising from the challenging concept of linking more than two metal centres through a common carbon-rich bridging ligand. [58, 59] The introduction of a third metal, the metal-bridge-metal interaction picture increases in complication, with the possibility of $metal_A$-bridge-$metal_B$, $metal_A$-bridge-$metal_C$, and $metal_B$-bridge-$metal_C$ interactions. However, the problem can be simplified if all three metals are the same, in the same ligand coordination sphere and the same oxidation state (Figure **6**).

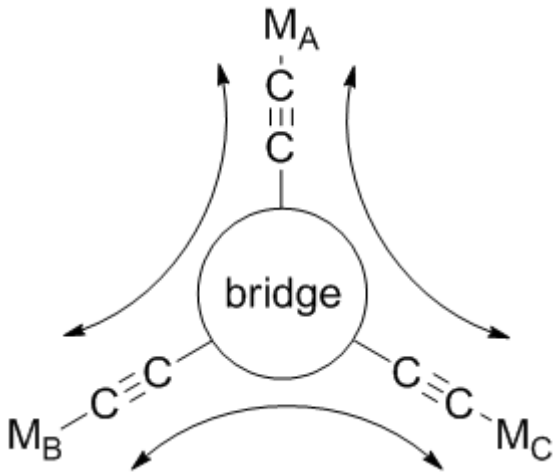

Figure **6** Representation of metal-bridge-metal interactions in a tris metallic complex with a common bridge core.

To be able to study and understand metal-bridge-metal interactions, it is required that first the metal-bridge interactions are understood. The best way to study these metal-bridge interactions is to study the analogous mono-metal bridge complexes. There is therefore a requirement for a straightforward synthetic method to obtain the mono- and polymetallic complexes in a good yield and high purity. The mono-metal complexes will be devoid of any metal-bridge-metal' interactions. Through comparison of the electrochemical and spectroscopic properties of the mono-metallic and polymetallic complexes, it is possible to separate the metal-bridge and metal-bridge-metal interactions from one another.

As metal-bridge-metal interactions in carbon rich complexes rely on the interaction between the metal centre and the bridge, the actual linkage between the metal centre and the bridge itself is important. An alternative metal bridge linker to the ynyl fragment, is the enyl –CH=CH–, which can be in either *cis* or *trans* conformation (Figure **7**).

Figure **7** Representations of mono-metallic bridge complexes with an; (left) ynyl linker, and (right) enyl linker (*trans*-).

As stated above, this thesis sets out to explore the challenges associated with the preparation and study of bridge-mediated charge transfer in systems containing more than two metal centres linked through a core bridging ligand (Figure **6**). In the Chapters that follow, the synthesis of mono- and polynuclear metal complexes are described, together with the concerted application of electrochemical, spectroscopic, spectroelectrochemical and computational methods to assess the electronic structure of these compounds in their various formal redox states. Each Chapter carries its own Introductory Section that more precisely defines the background to the particular area of study described.

Chapter 2 : *trans*-RuCl(C≡CR)(dppe)$_2$

2.1 Introduction

The chemistry of transition metal complexes *trans*-RuCl(C≡CR)(dppe)$_2$ and *trans*-Ru(C≡CR)$_2$(dppe)$_2$ is very well established, [60-69] with a considerable body of recent research demonstrating the utility of these moieties in the construction of multimetallic complexes, [70-74] and optical materials, [75-77] including those that exhibit a pH or redox-switchable NLO (Non-Linear Optical) response. [78-84] Other studies have focused on colourmetric [85] and fluorescent [86] sensing behaviour of suitably functionalised derivatives whilst the "wire-like" behaviour that arises from extensive d-π mixing along the Ru-C≡C fragment, [43, 87-95] and other characteristics including reversible redox properties, make these compounds potentially useful molecular electronic components. [65, 90-92, 96-99]

Organometallic complexes, particularly acetylide based systems, have been widely investigated as second- and third order NLO materials, in which the donor properties of the metal fragment can be tuned through both changes in molecular structure (i.e. by altering the nature of the supporting ligands) or redox state, or through reversible chemical reactions (e.g. protonation leading to acetylide / vinylidene equilibria). The acetylide complexes *trans*-RuCl(C≡CR)(dppe)$_2$ have proven to be particularly useful in this regard, offering: a site of protonation (the acetylide C$_\beta$ carbon); excellent redox stability in both the (formal) Ru(II) and Ru(III) states; [†] and the ability to construct bi- and polymetallic complexes through functionalisation of the acetylide ligand or the Ru-Cl moiety.

By way of example, the Samoc, Humphrey and Lapinte groups have collaborated to explore methods of switching cubic NLO properties through more than two states [79, 100] through redox control in the bimetallic complex [{Cp*(dppe)Fe}(μ-C≡C-1,4-C$_4$H$_4$C≡C){Ru(dppe)$_2$Cl}] (**1**), which can be switched through the three (formal) Fe(II)/Ru(II), Fe(III)/Ru(II) and Fe(III)/Ru(III) states (Figure **8**). [93]

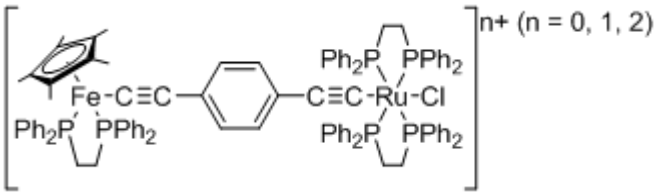

Figure **8** Bimetallic complex **1**.

All three states, **1** and the "mixed valence" $[\mathbf{1}]^{+}$ and $[\mathbf{1}]^{2+}$, are reversibly accessible under electrochemical control. Cubic NLO measurements at 790 nm show that progression through the redox series **1** to $[\mathbf{1}]^{+}$ to $[\mathbf{1}]^{2+}$, caused a dramatic change in the complex's NLO properties. The neutral form **1** of the complex exhibited negligible nonlinear absorption, the mixed-valence monocation form $[\mathbf{1}]^{+}$ was found to be an efficient two-photon absorber, and the dication $[\mathbf{1}]^{2+}$ a saturable absorber. Effectively **1** represents a complex in which its cubic NLO properties can be switched, by redox processes, through nonlinearity "off" to two forms of nonlinearity "on".

The facile replacement of the chloride ligand in complexes *trans*-$RuCl(C{\equiv}CR)(dppe)_2$ with a second alkynyl ligand either directly, from related vinylidenes or via *trans*-$[Ru(NH_3)(C{\equiv}CR)(dppe)_2]PF_6$, is well documented [60, 61, 63, 76, 92, 101-103] leading to the preparation of monometallic, oligomeric, polymeric and dendritic compounds featuring *trans*-$Ru(C{\equiv}CR)_2(dppe)_2$ fragments. [70, 72, 98, 104-111] One such study by Humphrey carried out in collaboration with the Low group has examined the third-order nonlinear optical properties of triphenylamine based dendrimers. [112]

The "wire-like" properties of a series of linear complexes based on the $Ru(dppe)_2$ fragment have been investigated by Fiedler, [91] using a series of phenylene ethynylene based bridging ligands, *trans*-$Ru(dppe)_2$ "connectors" and *trans*-$RuCl(dppe)_2$ end-caps. By comparing a selection of bi- and tri-metallic complexes based on purely organic bridges or those containing metal-fragments (Figure **9**), different factors influencing the efficacy of intramolecular electron transfer (ET), such as length of bridge, metal terminus and incorporated metal linker could be investigated (Figure **10**).

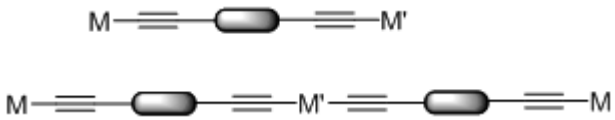

Figure **9** Schematic representation of the complexes used by Fiedler. [91]

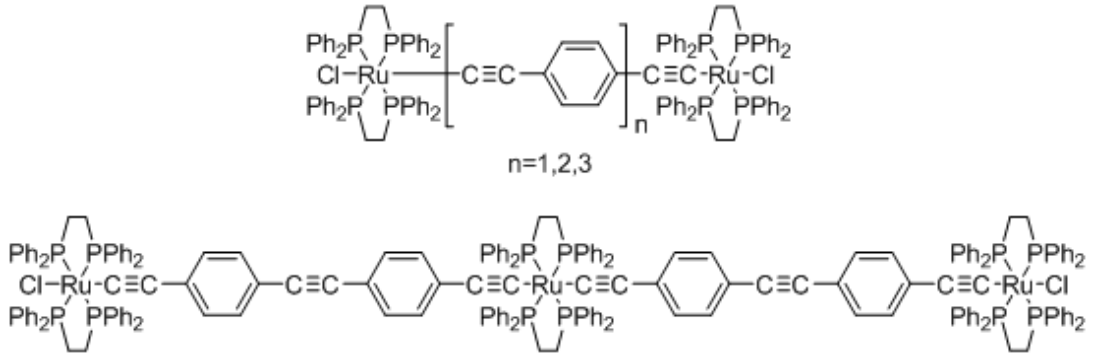

Figure **10** Some of the complexes prepared and studied in the Fiedler investigation of "wire-like" phenylene ethynylene bridging ligands. [91]

In the Fielder study the comproportionation constant, K_c [‡], was used as a measure of the extent of interaction between the remote metal sites. On this basis it was concluded that: elongation of the carbon chain past two phenylethynyl units ET vanished; and the introduction of a metal linker (whether that be $Ru(dppe)_2$, or $Pd(PBu_3)_2$) was conducive to electron transfer.

A more detailed study of the bonding and electronic nature of *trans*-$[RuCl(C{\equiv}CC_6H_4X)(dppe)_2]BF_4$ radical compounds has been reported recently. [113] Along with ESR work and spectroscopic and electrochemical spectroscopic studies, extensive DFT calculations have been performed on the radical models *trans*-$[RuCl(C{\equiv}CC_6H_4X)(dHpe)_2]^+$ as well as the corresponding neutral species. [113] Comparison of the experimental results with computational calculations on $[Ru(C{\equiv}CC_6H_4X)(dHpe)Cp^*]^{n+}$ (n = 0, 1) model compounds [113] allowed a better understanding of the similarities and differences exhibited by these isoelectronic and isolobal organometallic fragments. The DFT calculations found two conformational minima for both the neutral and cation model systems: one where the aryl plane and the ethane bridges of the dHpe ligands are parallel (||); and a second where the plane of the functional aryl ring bisected the dHpe ligands (⊥)

(Figure **11**). [113] The same conformers were found for the corresponding $[Ru(C{\equiv}CC_6H_4X)(dHpe)Cp^*]^{n+}$ (n = 0, 1) model compounds. [113] The (||) configuration for the *trans*-$[RuCl(C{\equiv}CC_6H_4X)(dHpe)_2]^+$ was found to be the lowest of the two minima, which is consistent with X-ray studies of compounds of the form *trans*-$[RuCl(C{\equiv}CC_6H_4X)(dppe)_2]$. [113]

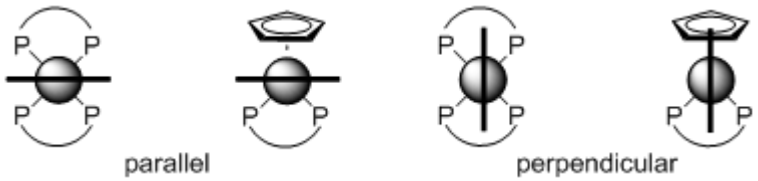

Figure **11** Schematic representations of the parallel and perpendicular arrangement of the aryl ring in $RuCl(C{\equiv}CC_6H_4X)(dppe)_2$ and $Ru(C{\equiv}CC_6H_4X)(dppe)Cp^*$.

Molecular orbital calculations on *trans*-$[RuCl(C{\equiv}CC_6H_4X)(dppe)_2]$ show that the HOMO and HOMO-1 are mainly metal and acetylide in character, whilst the LUMO is Ru-P antibonding. The HOMO-LUMO gap slightly decreases in energy going from electron withdrawing to electron donating substituents. [113] Upon oxidation to *trans*-$[RuCl(C{\equiv}CC_6H_4X)(dHpe)_2]^+$ the most stable conformer is found to be one where the plane of the aryl ring is located perpendicular to the dHpe ligands. Spin densities calculations indicate that more of the spin density is present on the arylacetylide than on the metal group. [113]

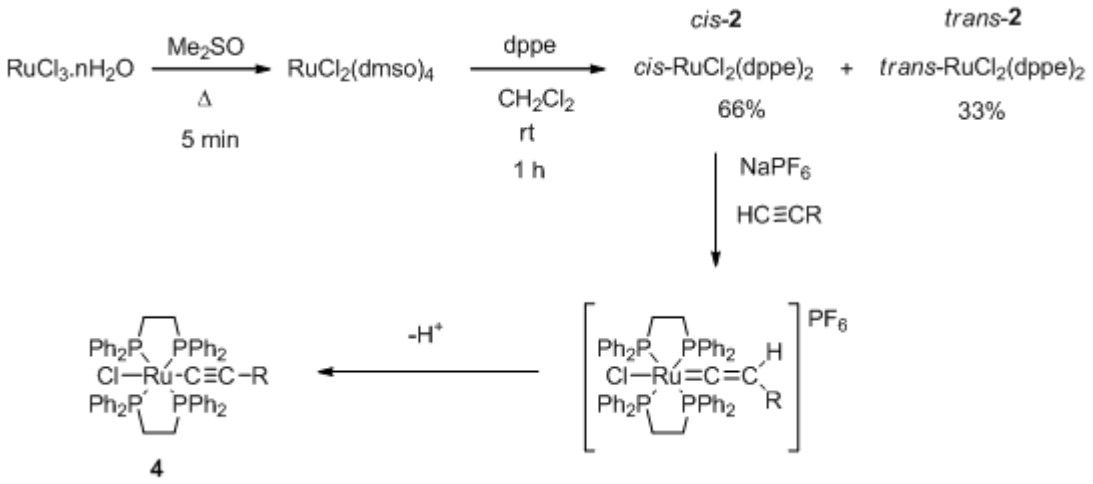

Scheme **1** The preparation of *trans*-RuCl(C≡CR)(dppe)$_2$ **4** from *cis*-RuCl$_2$(dppe)$_2$ *cis*-**2**.

Indeed all of the interesting physical phenomena associated with acetylide complexes of the Ru(dppe)$_2$ moiety are underpinned at the most elementary level by the extent of mixing of the metal d and alkynyl ligand π-orbitals. As part of a wider study of the electronic structure of metal acetylide complexes, [114-118] particularly those of ruthenium complexes that underpin the results in this thesis, ready access to a series of complexes *trans*-RuCl(C≡CR)(dppe)$_2$ was required. Complexes of the type *trans*-RuCl(C≡CR)(dppe)$_2$ are most often prepared from *cis*-RuCl$_2$(dppe)$_2$ (*cis*-**2**) using the method first reported by Dixneuf and colleagues (Scheme **1**). [60] Initial reaction between *cis*-**2** and NaPF$_6$ or similar salt in dichloromethane affords the five-coordinate species [RuCl(dppe)$_2$][PF$_6$] ([**3**][PF$_6$]), which in turn reacts with terminal alkynes HC≡CR to give the mono-chloro, mono-vinylidene species *trans*-[RuCl{C=C(H)R}(dppe)$_2$]PF$_6$. Subsequent deprotonation of the vinylidene affords the corresponding neutral acetylide *trans*-RuCl(C≡CR)(dppe)$_2$ **4** which can be isolated, or, in the presence of excess terminal alkyne, triethylamine and NaPF$_6$, undergo further reaction to give the *trans*-bis(acetylide) complexes *trans*-Ru(C≡CR)$_2$(dppe)$_2$ (**5**).

Conversion of the thermodynamically more stable isomer *trans*-**2** to acetylide complexes *trans*-RuCl(C≡CR)(dppe)$_2$ has been achieved following reaction of *trans*-**2** with trialkylstannyl alkynes, sometimes in the presence of a CuI catalyst. [64, 119] Prolonged (5 – 7 day) reaction of the *trans*-**2** with terminal alkynes in the

presence of $NaPF_6$ followed by deprotonation of the resulting vinylidene has also been shown to afford monoacetylide complexes *trans*-RuCl(C≡CR)(dppe)$_2$, [120] however the conversion of *trans*-**2** to the active 16-electron species $[RuCl(dppe)_2]^+$ $[\mathbf{3}]^+$ under these conditions is rather slow. [69, 121]

The use of isolated $[RuCl(dppe)_2]^+$ ($[\mathbf{3}]^+$) salts as an entry to acetylide complexes *trans*-RuCl(C≡CR)(dppe)$_2$ and related compounds has recently begun to attract attention. [71, 73, 86, 92, 93, 121, 122] This Chapter details a convenient preparation of acetylide complexes **4** from *trans*-**2** that takes advantage of the ready abstraction of a chloride ligand from *trans*-**2** by AgOTf in dichloromethane to give the key reagent [**3**]OTf. A facile synthesis of *cis*-**2** from [**3**]OTf is also described for completeness. The molecular structures of [**3**]OTf and three aryl acetylide complexes featuring representative electron donating (OMe, Me) and withdrawing (CO_2Me) groups have also been determined. Details of the electronic structure of *trans*-RuCl(C≡CR)(dppe)$_2$ complexes are given in Chapter **3**.

2.2 Results and Discussion

2.2.1 Syntheses

Many literature syntheses of complexes *trans*-RuCl(C≡CR)(dppe)$_2$ (**4**) utilise the reaction of *cis*-**2** with the appropriate terminal alkyne HC≡CR, a salt (typically $NaPF_6$) and a base (Scheme **1**). The key reagent *cis*-**2** is often cited as being prepared by the method originally described by Chaudret [123] for the preparation of *cis*-$RuCl_2(dppm)_2$. However, attempts to react $RuCl_2(dmso)_4$ [124] with two equivalents of the bis(phosphine) in toluene at 80 °C (the Chaudret conditions) produced only pure *trans*-**2**. [69] At ambient temperature in dichloromethane under normal laboratory lighting conditions, mixtures of *cis*-**2** and *trans*-**2** are obtained in ca. 3:1 ratio (estimated here from integration of ^{31}P NMR resonances) over the course of approximately 1 h. [64, 69, 97, 120, 125, 126] By lowering the temperature to 0 °C,

the ratio of *cis*-**2** : *trans*-**2** can be increased as high as 10 : 1, although the reaction becomes very slow, taking well over 24 h for complete conversion. Careful fractional crystallisation, best carried out in the dark (see below), results in separation of *cis*-**2** and *trans*-**2** from these mixtures.

In seeking to devise an alternative route to complexes **4**, the details of the reactions summarised in Scheme **1** were considered. Conversion of *cis*-**2** to the active five-coordinate species $[RuCl(dppe)_2]^+$ ($[\mathbf{3}]^+$) takes place readily upon reaction with alkali metal salts including $NaPF_6$ [62] and KPF_6, [70] and salts of $[\mathbf{3}]^+$ can be isolated from reaction of *cis*-**2** with $NaPF_6$, [101, 127] NaOTf or $NaBPh_4$. [128] The conversion of *trans*-**2** to salts of $[\mathbf{3}]^+$ has been implicated under similar conditions, although the reaction is considerably slower. [69, 127] In contrast, far more facile conversion of *trans*-**2** to $[\mathbf{3}]^+$ is achieved by halide abstraction with Ag(I) salts. [129, 130] Treatment of *trans*-**2** with two equivalents of AgOTf (dichloroethane, 50 °C) [129] or $AgBF_4$ (THF, room temperature or dichloromethane) [130] have been reported to yield [**3**]OTf or $[\mathbf{3}]BF_4$, respectively. The complex [**3**]OTf has also been isolated from reaction of mixtures of *cis*- and *trans*-**2** with the rather carcinogenic reagent MeOTf. [131]

With these precedents in mind, a simple, high-yielding, step-wise sequence of reactions can be constructed that results in conversion of $RuCl_3.nH_2O$ to the acetylide complexes **4** in good overall yield, via the readily prepared complexes *trans*-**2** and [**3**]OTf (Scheme **2**). The syntheses of *trans*-**2** [132] from $RuCl_3.nH_2O$ is most conveniently achieved by sequential reaction with PPh_3 in methanol to give $RuCl_2(PPh_3)_3$, [133, 134] followed by ligand exchange with dppe. [135, 136] Treatment of *trans*-**2** with 1 equiv. AgOTf in CH_2Cl_2 resulted in immediate colour change from yellow to red, with the precipitation of AgCl. Complete reaction was achieved within 1 h at room temperature. The product can be isolated as an air-stable solid by simple filtration and precipitation.

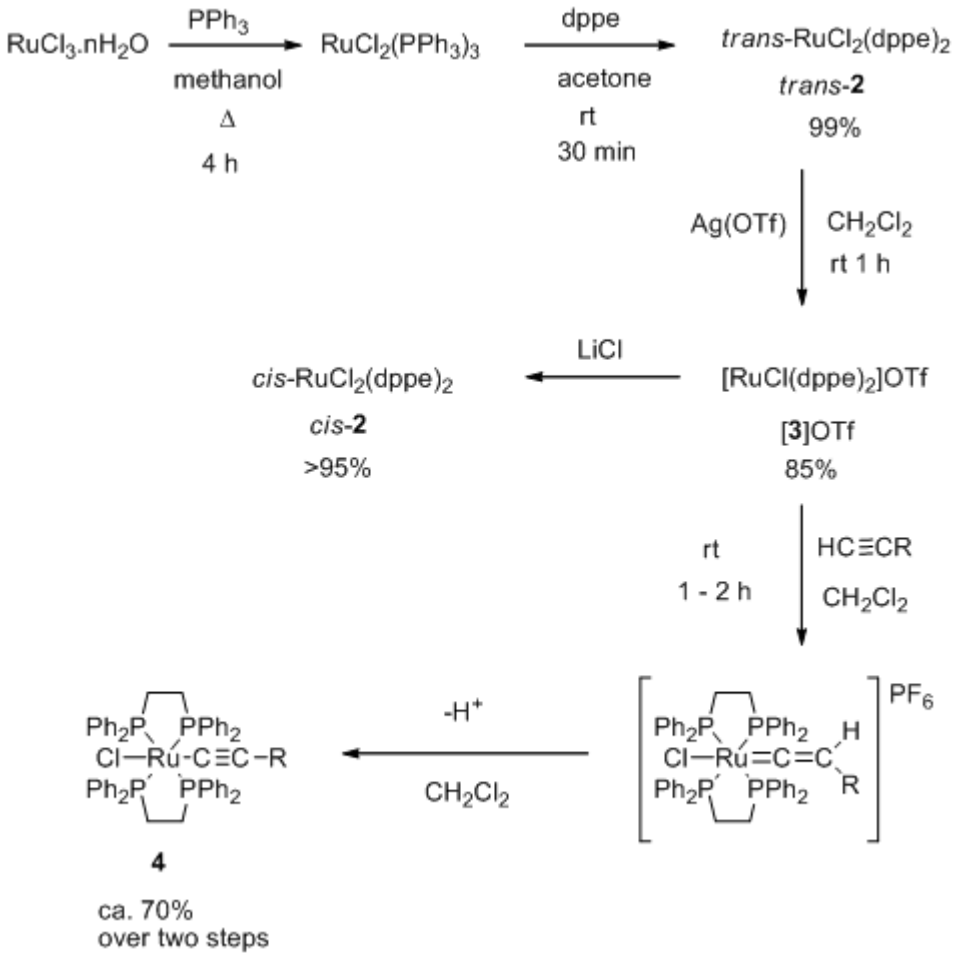

Scheme **2** The preparation of *trans*-RuCl(C≡CR)(dppe)$_2$ from *trans*-RuCl$_2$(dppe)$_2$.

The five-coordinate complex [**3**]OTf reacts rapidly with 1-alkynes in small volumes of CH_2Cl_2 at room temperature to give the corresponding vinylidene complexes. Simple washing of the crude vinylidene salts with further aliquots of hexane serves to remove any excess 1-alkyne, which is essential if formation of the bis(acetylide) complex is to be prevented during the next step. Formation and isolation of the desired acetylide complexes c.f. **4** is most conveniently performed by addition of a solution of KO^{t}Bu in methanol to a concentrated dichloromethane solution of the vinylidene. Under these conditions the acetylide precipitates essentially free of triflate salt by-products, and can be collected by filtration. The product obtained in this fashion is of high purity, with recrystallisation affording single crystals suitable for X-ray diffraction.

This reaction sequence was successfully applied in the preparation of a range of complexes *trans*-RuCl(C≡CR)(dppe)$_2$ [R = Ph (**6**), C_6H_4OMe-4 (**7**), C_6H_4Me-4 (**8**), $C_6H_4C_5H_{11}$-4 (**9**), $C_6H_4CO_2$Me-4 (**10**), $C_6H_4NO_2$-4 (**11**)] which were isolated in ca. 70-80% yield in each case. However, attempts to prepare *trans*-RuCl(C≡C$C_6H_4NH_2$-4)(dppe)$_2$ were hampered by the basicity of the aniline moiety, which deprotonated the intermediate vinylidene, leading to formation of the bis(acetylide) *trans*-Ru(C≡C$C_6H_4NH_2$-4)$_2$(dppe)$_2$. Reactions with 4-ethynylbenzonitrile were complicated by competitive coordination and chloride substitution reactions involving the nitrile moiety.

The acetylide complexes were characterised by the usual spectroscopic (IR, ^{1}H, ^{13}C, ^{31}P NMR, ES-MS) methods. The acetylide ν(C≡C) band was observed between 2050 - 2070 cm^{-1}, the lowest wavenumber bands being associated with **10** and **11**. The electrospray mass spectra (ES-MS) featured fragment ions formed from loss of chloride, the molecular ion not being observed. The observation of a singlet near δ 50 ppm, in the ^{31}P NMR spectra, confirmed the *trans* geometry of the complexes, whilst the ^{1}H (Table **1**) and ^{13}C (Table **2**) spectra featured characteristic resonances arising from both the dppe and aryl acetylide ligands. The acetylide C_α resonance, which was observed as a quintet ($^2J_{CP}$ ca. 15 Hz), proved to be sensitive to the electronic nature of the remote aryl substituent. The ^{1}H and ^{13}C NMR spectra could be fully assigned (see Figure **12** for NMR labelling scheme) through correlation spectroscopy, although the couplings of the methylene protons from the dppe ligands were not fully resolved.

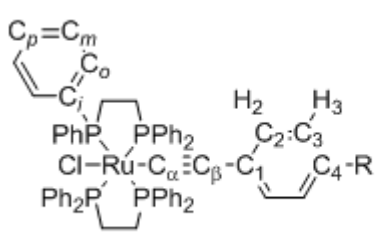

R	
H	**6**
OMe	**7**
Me	**8**
C_5H_{11}	**9**
CO_2Me	**10**
NO_2	**11**

Figure **12** NMR labelling scheme used in this work.

Table **1** ^{1}H NMR data from complexes **6** – **11**.

	7 R = OMe	**9** R = C_5H_{11}	**8** R = Me	**6** R = H	**10** R = CO_2Me	**11** R = NO_2
$H_{o/o'}$	7.57, 7.26 (2 × d, *J* = 7 Hz)	7.62, 7.20 (2 × d, unresolved)	7.58, 7.23 (2 × d, *J* = 7 Hz)	7.58, 7.25 (2 × d, *J* = 7 Hz)	7.42, 7.33 (2 × d, *J* = 7 Hz)	7.36, 7.34 (AB, *J* = 8 Hz)
$H_{m/m'}$	6.99, 6.97 (AB, *J* = 7 Hz)	6.94, 7.05 (unresolved)	6.99, 6.97 (AB) *J* = 7 Hz	6.99, 6.97 (dd) *J* = 7 Hz	7.01, 6.94 (dd) *J* = 7 Hz	7.03, 6.95 (dd) *J* = 8 Hz
$H_{p/p'}$	7.19 (t, *J* = 7 Hz)	7.20 (unresolved)	7.18 (t, *J* = 7 Hz)	7.18 (t, *J* = 7 Hz)	7.20, 7.18 (2 × t, *J* = 7 Hz)	7.21, 7.20 (2 × t, *J* = 8 Hz)
CH_2CH_2	2.65 (m)	2.66 (m)	2.65 (m)	2.68 (m)	2.69 (m)	2.69 (m)
H_2	6.64 (AB, *J* = 8 Hz)	6.65 (d, *J* = 8 Hz)	6.62 (d, *J* = 8 Hz)	6.70 (d, *J* = 8 Hz)	6.57 (d, *J* = 8 Hz)	6.44 (d, *J* = 8 Hz)
H_3	6.70 (AB, *J* = 8 Hz)	6.92 (d, *J* = 8 Hz)	6.93 (d, *J* = 8 Hz)	7.11 (d, *J* = 8 Hz)	7.77 (d, *J* = 8 Hz)	7.94 (d, *J* = 8 Hz)
R	3.80	0.92 (m), 1.35 (m), 1.61(m), 2.54(m)	2.30	7.11 (dd) *J* = 8Hz	3.89	-

Table **2** ^{13}C NMR spectroscopic data from complexes **6** – **11**.

	7 R = OMe	**9** R = C_5H_{11}	**8** R = Me	**6** R = H	**10** R = CO_2Me	**11** R = NO_2
C_α	119.2	121.2	121.5	124.1	136.7	148.4
C_β	112.7	113.7	113.6	113.9	114.9	116.8
C_1	123.5	127.8	127.8	130.6	135.1	137.2
C_2	131.0	129.9	130.0	130.2	129.9	130.0
C_3	113.1	127.6	128.4	127.6	129.1	123.5
C_4	155.8	137.5	132.4	123.0	123.6	142.4
$C_{i/i'}$	136.9 135.8	137.0 135.7	137.0 135.8	136.9 135.8	136.2 135.6	135.9 135.5
$C_{o/o'}$	134.5	134.6 134.5	134.6	134.6 134.6	134.5 134.2	134.5 134.1
$C_{m/m'}$	127.3 127.0	127.3 127.0	127.4 127.1	127.4 127.1	127.4 127.1	127.5 127.3
$C_{p/p'}$	129.0 128.8	128.9 128.8	129.0 128.9	129.1 129.0	129.0	129.2
CH_2CH_2	30.9	30.9	31.0	30.8	30.7	30.6
R	55.3	z 14.3 y 22.8 x 31.3 w 31.9 v 35.9	21.5	-	CO 167.7 Me 52.0	

The formation of *cis*-**2** from the reaction of [**3**]BF_4 with LiCl has been noted previously, although experimental conditions and isomeric purity were not reported.[127] The reaction of [**3**]OTf with LiCl in methanol at ambient temperature results in the formation of a yellow precipitate within a few minutes, which was collected by filtration and identified by ^{31}P and ^{1}H NMR spectroscopy to be pure *cis*-**2** (ca. 84% isolated yield). Whilst solutions of *cis*-**2** are stable in the dark, *cis*-**2** converts to *trans*-**2** under both normal laboratory and natural lighting. The conversion of *cis*-**2** to equilibrium mixtures of *cis*-**2** and *trans*-**2** was followed by ^{31}P NMR spectroscopy in both $CDCl_3$ (1:1, 24 hours) and dichloromethane (3:1, 48 hours). This facile conversion of *cis*-**2** to *trans*-**2** in solution at room temperature under ambient lighting conditions must be taken into account when trying to separate mixtures of *cis*-**2** and *trans*-**2** by fractional crystallisation.

2.2.2 Molecular Structure Analyses

Single crystals of [**3**]OTf, **7**, **8** (as both 0.5THF and $2CH_2Cl_2$ solvates) and **10** suitable for X-ray diffraction were obtained, those of **6**, [64] **11**, [120] and the related complexes *trans*-RuCl(C≡CC_6H_3-Me-2-NO_2-4)$(dppe)_2$, [120] *trans*-RuCl(C≡CC_6H_4CHO-4)$(dppe)_2$, [83] *trans*-RuCl(C≡CC_6H_4F-4)$(dppe)_2$, [76] *trans*-RuCl(C≡CC_6H_4F-3)$(dppe)_2$ [93] and *trans*-RuCl(C≡CC_6H_4CH=$CHC_6H_4NO_2$-4)$(dppe)_2$ [83] having been reported earlier. Crystallographic data and important bond lengths and angles are summarized in Table **3** and Table **4**, with plots of $[\mathbf{3}]^+$, **7**, **8** and **10** illustrated in Figure **15**, Figure **16**, Figure **17** and Figure **18**, respectively. There are no significant differences in the structures of the two different solvates of **8**.

The structures of salts containing five-coordinate ruthenium(II) cations of general form $[RuCl(PP)_2]X$ (where PP = chelating diphosphine ligand) have been reported on several previous occasions [PP = dppe, X = $[PF_6]^-$, [127] $[BF_4]^-$, [130] $[C_2B_9H_{12}]^-$; [137] PP = dppp, X = $[PF_6]^-$; [138] PP = dcpe, X = $[PF_6]^-$; [139] PP = $NH(CH_3)(PPh_2)_2$, X = $[SbF_6]^-$; [140] PP = bnpe, X = $[PF_2O_2]^-$. [141] The cation in [**3**]OTf is essentially identical to that in [**3**]PF_6 and [**3**]BF_4 with a similar degree of "Y"-shaped distortion of the equatorial plane from that in an idealised trigonal bipyramid. The two dppe ligands span axial and equatorial positions, with the equatorial plane defined by Cl(1), P(2) and P(4). Around the equatorial plane, the donor atoms define angles Cl(1)-Ru(1)-P(2, 4) 134.49(2), 130.35(2) ° and the rather small angle P(2)-Ru(1)-P(4) 95.16 ° to relieve degeneracy in the "e" type orbitals associated with a d^6 trigonal bipyramid. Theoretical studies on d^6-ML_5 complexes, have shown that there are many factors that determine the spatial arrangement of the ligands around the metal centre, one of the factors affecting the structure is the spin of the centre, with singlet states favouring square pyramidal structures [142] and triplet states favouring trigonal bi-pyramidal structures. [143] The electronic factors that underpin this distortion have been investigated by Rachidi and Eisenstein. [144] By varying the degree of "Y"-shaped distortion d^6-ML_5 16-electron complexes can span from square pyramid (L_2-M-L_3 α° = 180, A), through to square planar (α° = 30, C) via a distorted trigonal bipyramidal structure (α° = 80, B) (Figure **13**).

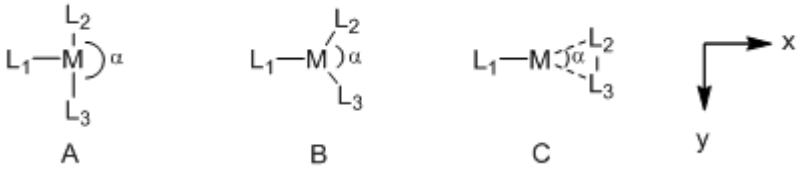

Figure **13** A schematic representation of the "Y" distortions in 5-coordinate complexes. L_4 and L_5, in the z-axis, have been removed for clarity.

The nature of the occupied d-orbitals has a correspondence to the total energy of the complex. The changing of the angle α does not affect the energy of the non-bonding e" set (d_{xz}, d_{yz}) as L_2 and L_3 are in the nodal planes of both orbitals, however structural distortion does strongly affect the energy of the e' ($d_{x^2-y^2}$, d_{xy}) set. Figure **14** shows the effect of varying α on the bonding interaction between $d_{x^2-y^2}$ and d_{xy} and L_2 and L_3.

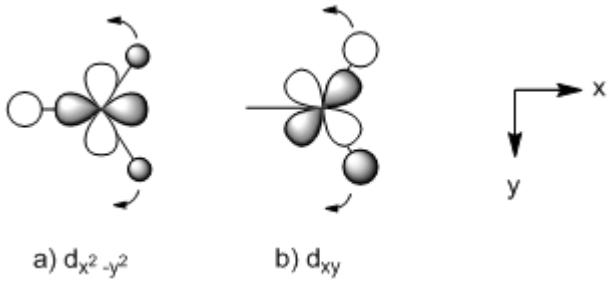

Figure **14** L_2 and L_3 bonding interaction with a) $d_{x^2-y^2}$ and b) d_{xy}.

On increasing α from 120 ° to 180 °, the interaction between the $d_{x^2-y^2}$ and L_2 and L_3 increases the energy of this orbital, whereas d_{xy} becomes fully non-bonding at 180 °, and hence d_{xy} is stabilised. The opposite effect occurs as α shifts from 120 ° to 30 °. Within this framework two minima can be identified, one at α = 180 ° (square based pyramid), and one at α = 80 ° (distorted trigonal bi-pyramid). Interconversion between the two minima via the TBP is symmetry forbidden due to the level crossing between occupied and empty orbitals.

The σ and π effects of the L_1 ligand can also affect the degree of "Y"-shaped distortion. Three of the four low-lying metal d-orbitals (d_{xz}, d_{yz}, d_{xy}) are unaffected by the effects of the σ-properties of L_1, as L_1 lies in one of their nodal planes. The

only orbital to be affected by L_1 is $d_{x^2-y^2}$. This orbital is metal-ligand antibonding in character, so with a strong σ-donor at L_1, the energy of the orbital goes up, independent of α. The opposite trend is seen for L_1 = σ-acceptor, where the $d_{x^2-y^2}$ orbital is lowered in energy. So in summary for the effects of σ-donor/acceptor properties;

Strong σ-donor L_1	Strong σ-acceptor L_1
favours opening	favours closing

All of the 16e$^-$ d^6-ML_5 complexes mentioned in this Chapter have Cl^- in the L_1 position, which in addition to being a strong σ-acceptor is also a double-faced π-donor ligand. The d_{z^2} and d_{yz} orbitals do not mix with any of the p-orbitals of L_1. The d_{xz} orbital is raised in energy by the σ-interaction with L_1. The $d_{x^2-y^2}$ orbital does not mix with any of the L_1 p-orbitals. However d_{xy} is raised in energy by interaction with p_y on L_1, consequently it is energetically favourable to fill $d_{x^2-y^2}$ before d_{xy}, which favours the trigonal bipyramid structure with a high degree of "Y"-shape distortion. [144, 145]

The cation of [**3**]OTf is more sterically crowded than other acetylide complexes described in this Chapter and as a result the planes of axial Ph-rings of the dppe ligands are almost parallel to each other.

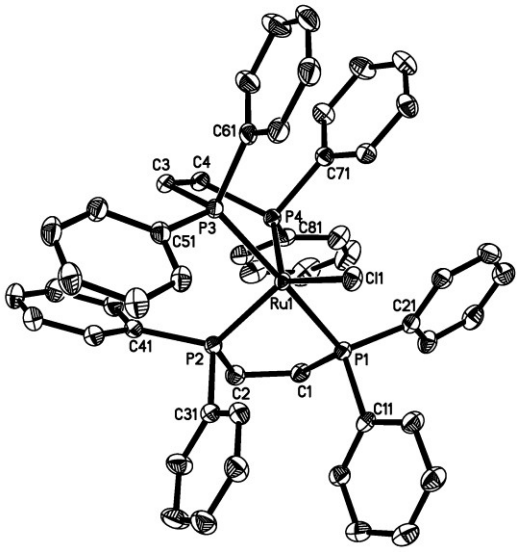

Figure **15** Plot of the cation in $[RuCl(dppe)_2]OTf$ ([**3**]OTf). In this and all subsequent plots, hydrogen atoms have been omitted for clarity, with thermal ellipsoids at 50%.

The structures of the acetylide complexes **7**, **8** and **10** illustrate the usual octahedral geometry around Ru, and linear Cl-Ru-C(1)-C(2)-C(3) chain. The C(1)-C(2) acetylide bond lengths fall in the range 1.188(5) – 1.202(5) Å, whilst the Ru-P bond lengths are insensitive to the electron donating (OMe) or withdrawing (CO_2Me) properties of the acetylide substituent. The Ru-C(1) [2.018(4) Å] and Ru-Cl [2.5118(9) Å] bond lengths in **7** are at the longer end of the range of values typically offered by complexes of general type **4** (Table **3**), possibly due to greater Cl 3p / Ru 3d / C≡C π filled orbital-filled orbital repulsive interactions along the linear back-bone. [146, 147]

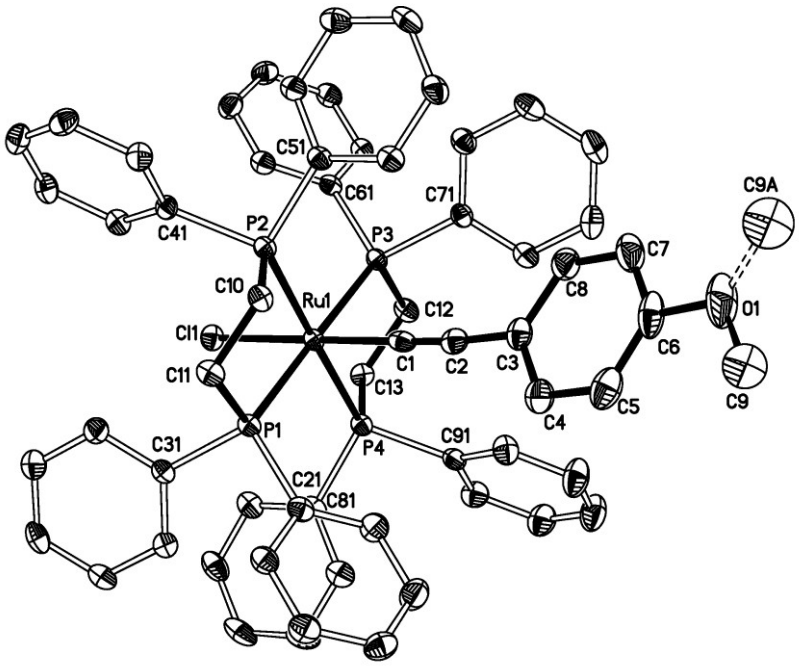

Figure **16** Plot of a molecule of *trans*-RuCl(C≡CC_6H_4OMe-4)$(dppe)_2$ **7**.

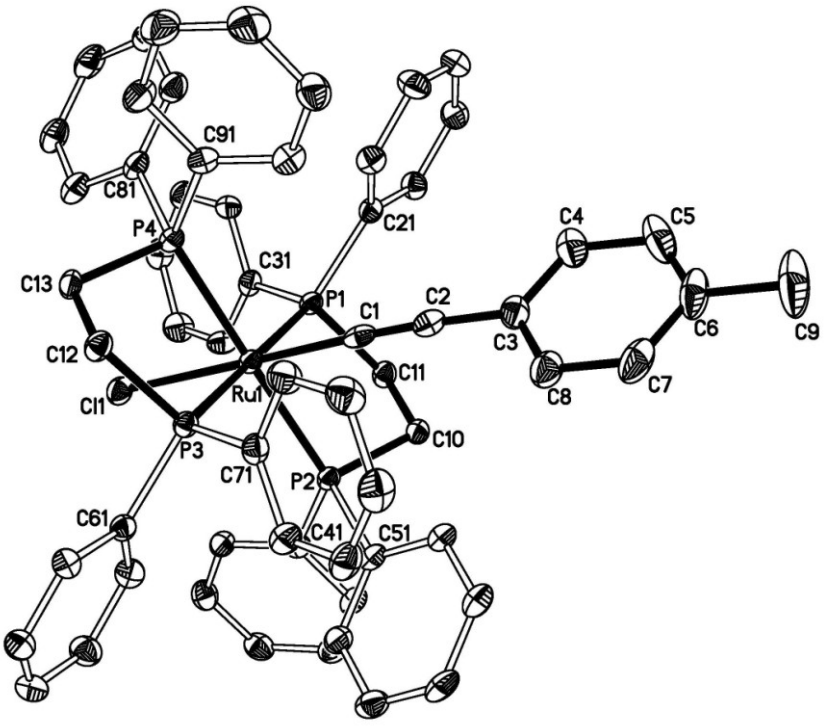

Figure **17** Plot of a molecule of *trans*-RuCl(C≡CC_6H_4Me-4)$(dppe)_2$ **8**.

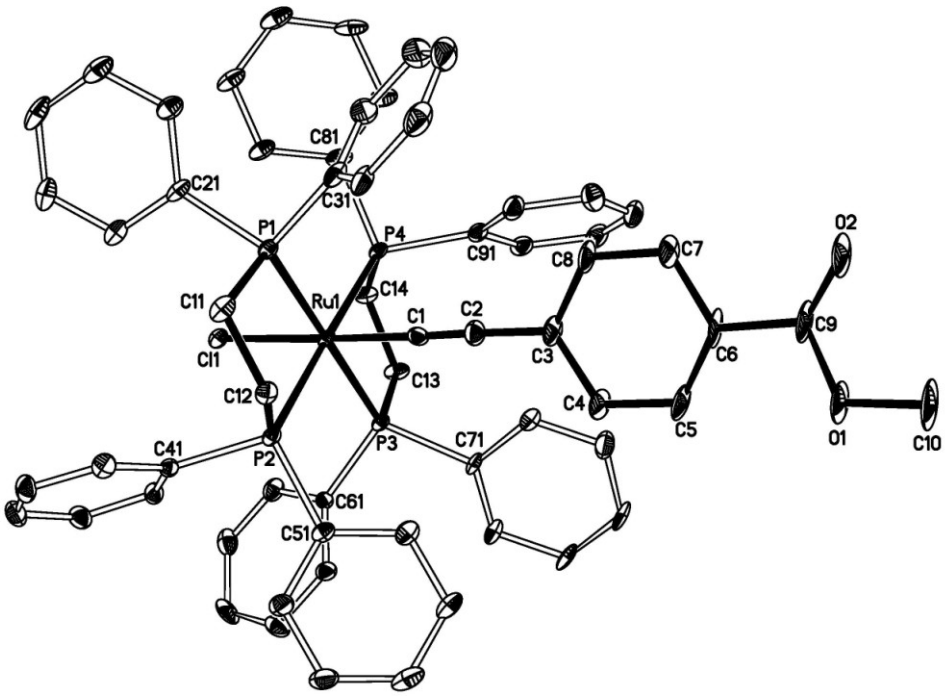

Figure **18** Plot of a molecule of *trans*-RuCl(C≡C$C_6H_4CO_2$Me-4)$(dppe)_2$ **10**.

As usual, in the absence of strong hydrogen bonds the packing of complexes in crystals is determined by a fine balance between a number of attractive intermolecular weak interactions of various nature (C-H…O, Cl, π; Cl…Cl, etc.). The presence and the nature of solvent molecules also significantly affects the crystal packing. For example, the metal complexes in isostructural crystals **7** and **8.CH_2Cl_2** form double layers perpendicular to the *b*-axis and disordered solvent molecules are located in channels between the layers, while ordered dichloromethane molecules are "trapped" in the voids of these layers. There are a number of weak C-H…π interactions in the structures. Hydrogen atoms of both methylene groups of dichloromethane molecules and aromatic rings take part in these interactions, while the methylene groups of the dppe ligands do not show any shortened contacts.

In the absence of solvent dichloromethane molecules in structure of **8.THF** the character of packing changes and complexes form chains along *c*-axis of the crystal. In this case the methylene groups of dppe ligands became stereochemically active and link the adjacent complexes by C-H…Cl contacts. These groups are also active

in the structure of **10** where they are involved in C-H…π interactions, while Cl atoms are linked with an aromatic hydrogen atom. Finally, the absence of stacking interactions between aromatic rings in these structures should be noted.

Table **3** Selected bond lengths (Å) and angles (°) for [**3**]OTf and complexes *trans*-RuCl(C≡CC_6H_4R-4)$(dppe)_2$ (**6**, **7**, **8**, **10** and **11**).

	[**3**]OTf	R = H **6.CH_2Cl_2** [64]	R = OMe **7.2CH_2Cl_2**	R = Me **8.0.5THF**	R = Me **8.2CH_2Cl_2**	R = CO_2Me **10.THF**	R = NO_2 **11.CH_2Cl_2** [122]
Ru-Cl	2.4061(5)	2.4786(13)	2.5118(9)	2.4907(12)	2.5096(8)	2.4806(13)	2.500(1)
Ru-P(1)	2.3786(5)	2.3680(14)	2.3526(9)	2.3792(12)	2.3539(8)	2.3753(14)	2.360(2)
Ru-P(2)	2.2449(5)	2.3524(14)	2.3824(9)	2.3642(11)	2.3827(8)	2.3552(14)	2.354(1)
Ru-P(3)	2.3639(5)	2.3917(14)	2.3610(9)	2.3433(11)	2.3627(8)	2.3768(13)	2.366(2)
Ru-P(4)	2.2434(5)	2.3734(14)	2.3812(9)	2.3549(11)	2.3781(8)	2.3679(14)	2.386(1)
Ru-C(1)		2.007(5)	2.018(4)	2.009(5)	2.007(4)	1.998(5)	1.986(5)
C(1)-C(2)		1.198(7)	1.188(5)	1.196(6)	1.202(5)	1.195(8)	1.206(7)
C(2)-C(3)		1.445(8)	1.437(5)	1.447(6)	1.432(5)	1.431(7)	1.442(7)
Cl-Ru-C(1)		175.72(14)	179.25(9)	176.41(12)	179.22(8)	178.54(15)	176.20(13)
Ru-C(1)-C(2)		174.1(5)	177.0(3)	175.6(4)	176.8(3)	178.4(5)	175.3(4)
C(1)-C(2)-C(3)		178.3	175.1(4)	175.5(5)	176.8(4)	171.1(6)	174.4(5)
P(1)-Ru-P(2)	79.39(2)	82.43(14)	81.83(3)	82.29(4)	81.97(3)	82.71(5)	83.23(6)
P(2)-Ru-P(3)	97.77(2)	97.78(5)	98.09(3)	98.38(4)	98.28(3)	96.43(5)	95.52(6)
P(3)-Ru-P(4)	80.02(2)	80.93(5)	81.57(3)	80.73(4)	81.54(3)	81.25(5)	82.58(6)
P(1)-Ru-P(4)	97.35(2)	98.48(5)	98.48(3)	98.54(4)	98.18(3)	99.62(5)	98.66(6)

Table **4** Crystal data and refinement details.

Complex	[**3**]OTf	**7**	**8**	**8**	**10**
Formula	$C_{53}H_{48}OF_3SClP_4Ru.2CHCl_3$	$C_{61}H_{55}OClP_4Ru.\ 2CH_2Cl_2$	$C_{61}H_{55}ClP_4Ru.\ 0.5C_4H_8O$	$C_{61}H_{55}ClP_4Ru.\ 2CH_2Cl_2$	$C_{62}H_{55}O_2ClP_4Ru.C_4H_8O$
Molecular weight ($g\ mol^{-1}$)	1321.11	1233.29	1084.50	1218.30	1128.51
Crystal system	Triclinic	Triclinic	Orthorhombic	Triclinic	Triclinic
Space group	$P\bar{1}$	$P\bar{1}$	$Pna2_1$	$P\bar{1}$	$P\bar{1}$
a (Å)	14.2259(2)	9.2242(3)	25.7427(6)	9.2375(5)	12.9760(4)
b (Å)	17.4740(3)	12.8045(4)	15.5668(4)	12.8488(7)	17.1779(5)
c (Å)	12.3513(3)	23.8399(7)	13.5683(3)	23.6105(12)	24.6946(7)
α (°)	72.08(1)	92.88(1)	90	92.97(1)	97.46(1)
β (°)	75.17(1)	94.63(1)	90	93.88(1)	90.47(1)
γ (°)	79.80(1)	99.13(1)	90	99.18(1)	104.20(1)
V ($Å^3$)	2807.86(9)	2765.35(15)	5437.2(2)	2754.5(3)	5286.6(3)
ρ_c ($g\ cm^{-3}$)	1.563	1.481	1.325	1.469	1.418
Z	2	2	4	2	4
$2\theta_{max}$ (°)	60	58	56	58	56
μ (Mo-K_α) (mm^{-1})	0.817	0.684	0.496	0.685	0.515
Crystal size (mm)	0.20 × 0.18 × 0.14	0.28 × 0.08 × 0.02	0.26 × 0.10 × 0.06	0.20 × 0.20 × 0.06	0.20 × 0.18 × 0.07
N_{Tot}	41337	34263	55975	26206	50880
N (R_{int})	16339 (0.0263)	14655 (0.0662)	12966 (0.0765)	14447 (0.0332)	25401 (0.0412)
R_1	0.0324	0.0481	0.0484	0.0528	0.0891
wR_2	0.0868	0.1265	0.1289	0.1640	0.2964
Goodness-of-fit on F^2	1.001	0.988	1.030	1.072	1.113

2.2.3 Cyclic Voltammetry

The cyclic voltammograms of the ruthenium bis-dppe complexes **6** – **11,** in dichloromethane, each exhibit two anodic processes, the first being fully reversible, the potential of which reflect the variation in the electronic properties of the aryl substituent (Table **5**). The nitro-substituted derivative **11** also contains a partially chemically reversible reduction with an anodic peak potential E_{px} –1.13 V (vs Fc/Fc^+), most likely localised on the nitroaromatic portion of the molecule. The sensitivity of the redox response to the nature of the remote substituent and the chemical reversibility of the first redox couple is consistent with the aryl acetylide character of the HOMO in *trans*-$RuCl(C{\equiv}CC_6H_4R)(dppe)_2$ complexes. This point is addressed in greater detail in Chapter **3**.

Table **5** Electrochemical data [a] from *trans*-$RuCl(C{\equiv}CC_6H_4R\text{-}4)(dppe)_2$ (**6** – **11)**.

R	E_1/**V**	E_2/**V**
OMe (**7**)	–0.10	+0.69[b]
C_5H_{11} (**9**)	–0.04	+0.83 [b]
Me (**8**)	–0.03	+0.85 [b]
H (**6**)	+0.01	+0.89 [b]
CO_2Me (**10**)	+0.10	+0.98 [b]
NO_2 (**11**)	+0.20	+1.07 [b]

[a] $E_{1/2}$ vs Fc/Fc^+ (CH_2Cl_2, 0.1 M NBu_4BF_4, Pt dot working electrode). Data are reported against an internal Fc^*/Fc^{*+} standard. Under these conditions Fc^*/Fc^{*+} = –0.53 V vs Fc/Fc^+.
[b] Irreversible, anodic peak potential E_{pa} reported.

2.3 Conclusions

Here a simple reaction protocol has been described that allows the preparation of acetylide complexes *trans*-$RuCl(C{\equiv}CR)(dppe)_2$ **4** from the five coordinate complex $[RuCl(dppe)_2]OTf$ ([**3**]OTf), which is obtained in three high yielding steps from

$RuCl_3.nH_2O$. The use of [**3**]OTf as an entry point to mono-acetylide complexes **4** is more convenient than the long-standing methods based on *cis*-$RuCl_2(dppe)_2$.

2.4 Experimental Details

2.4.1 General Condition

All reactions were carried out under an atmosphere of nitrogen using standard Schlenk techniques as a matter of routine, although no special precautions were taken to exclude air or moisture during work-up. Dichloromethane was purified and dried using an Innovative Technology SPS-400, and degassed before use. Diethyl ether, hexane and methanol were the best available commercial grade, and used without further purification. Reagents were purchased and used as received, with modifications to the literature procedures being used to prepare $RuCl_2(PPh_3)_3$, [134] *trans*-$RuCl_2(dppe)_2$, [135] and $[RuCl(dppe)_2]OTf$ [129] as detailed below.

NMR spectra were recorded on a Bruker Avance (^1H 400.13 MHz, ^{13}C 100.61 MHz, ^{31}P 161.98 MHz) spectrometer from $CDCl_3$ solutions and referenced against solvent resonances (^1H, ^{13}C) or external H_3PO_4 (^{31}P). IR spectra (CH_2Cl_2) were recorded using a Nicolet Avatar spectrometer from cells fitted with CaF_2 windows. Electrospray ionisation mass spectra were recorded using Thermo Quest Finnigan Trace MS-Trace GC or WATERS Micromass LCT spectrometers. Samples in dichloromethane (1 mg/mL) were 100 times diluted in either methanol or acetonitrile, and analysed with source and desolvation temperatures of 120 °C, with cone voltage of 30 V.

Cyclic voltammograms were recorded at v = 100 - 800 mV s^{-1} from solutions of approximately 10^{-4} M in analyte in dichloromethane containing 10^{-1} M NBu_4BF_4, using a gas tight single-compartment three-electrode cell equipped with platinum disk working, coiled platinum wire auxiliary, and platinum wire pseudo-reference electrodes. The working electrode surface was polished before scans with an

alumina paste. The cell was connected to a computer-controlled Autolab PGSTAT-30 potentiostat. All redox potentials are reported against the ferrocene/ferrocenium couple, and referenced against the decamethylferrocene/decamethylferrocenium (Fc^*/Fc^{*+} = –0.53 V) redox couple used as an internal reference system.

Single crystal X-ray data for all structures were collected on a Bruker SMART CCD 6000 diffractometer equipped with a Cryostream (Oxford Cryosystems) cooling device at 120K using λMoKα radiation. All the structures were solved by direct method and refined by full-matrix least squares on F^2 for all data using SHELXTL software. [148] All non-hydrogen atoms were refined with anisotropic displacement parameters, H-atoms were placed into calculated positions and refined in a "riding" mode.

2.4.2 Preparation of $RuCl_2(PPh_3)_3$

A suspension of $RuCl_3.nH_2O$ (1.00 g, 3.83 mmol for n = 3) and PPh_3 (6.00 g, 22.9 mmol) in methanol (50 ml) was heated for 4 h at reflux. The brown solid that precipitated was collected by filtration, washed with diethyl ether and dried in air to give $RuCl_2(PPh_3)_3$ as a dark brown powder (3.59 g, 98%). $^{31}P\{^1H\}$ NMR ($CDCl_3$, 81 MHz): δ 30.2 (s, PPh_3).

2.4.3 Preparation of *trans*-$RuCl_2(dppe)_2$ (*trans*-**2**)

A suspension of $RuCl_2(PPh_3)_3$ (3.59 g, 3.75 mmol) and dppe (3.14 g, 7.89 mmol) in acetone (40 ml) was stirred for 1 h at room temperature. The resulting yellow precipitate was collected by filtration, washed with acetone and dried in air to give *trans*-**2** as an orange-yellow powder (3.40 g, 99 %). ^1H NMR ($CDCl_3$): δ_H 2.70 (m, 8H, CH_2), 6.99 (dd, J_{HH} = 7 Hz, 16H, Ph H_m), 7.19 (t, J_{HH} = 7 Hz, 8H, Ph H_p), 7.26 (d, J_{HH} = 8 Hz, 16H, Ph H_o); $^{31}P\{^1H\}$ NMR ($CDCl_3$): δ 46.1 (s); ^{13}C NMR ($CDCl_3$): δ_C 28.8 (m, CH_2), 127.0 (m, C_m), 128.8 (m, C_p), 134.4 (m, C_o), 135.0 (m, C_i).

2.4.4 Preparation of [RuCl(dppe)$_2$][OTf] ([3]OTf)

A suspension of *trans*-**2** (3.40 g, 3.51 mmol) and AgOTf (0.90 g, 3.51 mmol) in dichloromethane (40 ml) was stirred for 1 h. The resulting dark red solution was filtered (Celite) to remove the precipitated AgCl, and the filtrate diluted with hexane. Careful removal of the CH_2Cl_2 on a rotary evaporator resulted in the precipitation of [**3**]OTf as well-formed red crystals, which were collected, washed with hexane and dried to give [**3**]OTf as a dark red solid, which is stable in air and chlorinated solvents (3.22 g, 85%). Crystals suitable for X-ray diffraction were obtained following recrystallisation from $CHCl_3$ / hexane. ^{1}H NMR ($CDCl_3$): δ_H 1.57 (m, 2H, CH_2), 2.44 (m, 4H, CH_2), 2.65 (m, 2H, CH_2), 6.71 (m, 4H, Ph H$_m$), 6.99 (m, 12H, Ph H), 7.19 (m, 16H, Ph H), 7.32 (t, J_{HH} = 7 Hz, 2H, Ph H$_p$), 7.52 (t, J_{HH} = 7 Hz, 2H, Ph H$_p$), 7.73 (m, 4H, Ph H$_m$). ^{31}P NMR ($CDCl_3$): δ 56.7 (dd, J_{PP} = 13 Hz, 2P), 84.0 (dd, J_{PP} = 13 Hz, 2P). ^{19}F NMR ($CDCl_3$, 188 MHz): δ -78.5 (s, $CF_3SO_3^-$); ^{13}C NMR ($CDCl_3$): δ_C 18.4 (m, CH_2), 30.1 (m, CH_2), 120.9 (q, J_{CF} = 321 Hz, CF_3), 127.5 (m), 128.0 (m), 128.7 (m), 129.3 (m, C$_p$), 129.4 (m, C$_i$ + other C), 130.4 (m, C$_i$), 131.1 (m, C$_p$ x 2), 131.7 (m), 132.0 (m, C$_i$), 132.1 (m), 132.3 (m, C$_p$), 132.7 (m), 133.1 (m, C$_i$), 133.7 (m). A mixture of *cis*-**2** and *trans*-**2** can also be used to give high yields of [**3**]OTf by this procedure.

2.4.5 Preparation of cis-RuCl$_2$(dppe)$_2$ (*cis*-2)

A solution of [**3**]OTf (198 mg, 0.182 mmol) in methanol (25 ml) was added to a stirred solution of LiCl (80 mg, 1.93 mmol) in methanol (4 ml). The yellow solid formed after 15 min was filtered, washed with 2 x 2 ml of methanol and dried *in vacuo*. This solid (148 mg, 0.152 mmol, 84%) was identified as pure *cis*-**2** by ^{31}P, ^{13}C and ^{1}H NMR spectroscopy. ^{1}H NMR ($CDCl_3$): δ_H 2.48 (m, 4H, CH_2), 2.55 (m, 2H, CH_2), 2.98 (m, 2H, CH_2), 6.73 (m, 8H), 6.78 (m, 8H), 6.84 (m, 4H), 6.93 (t, J_{HH} = 6 Hz, 2H, Ph H$_p$), 7.01 (m, 4H), 7.24 (t, J_{HH} = 6 Hz, 2H, Ph H$_p$), 7.26 (m, 4H), 7.54 (m, 4H), 8.22 (m, 4H). ^{31}P NMR ($CDCl_3$): δ 38.8 (dd, J_{PP} = 19 Hz, 2P) 53.6 (dd, J_{PP} = 19 Hz, 2P). ^{13}C NMR ($CDCl_3$): δ_C 24.6 (m, CH_2), 31.9 (m, CH_2), 126.6 (m), 127.2 (m), 127.5 (m), 127.7 (m, C$_p$), 128.0 (m), 128.5 (m, C$_p$), 128.7 (m, C$_p$),

128.9 (m, C_p), 131.2 (m), 131.5 (m), 133.9 (m), 134.3 (m, C_i), 134.7 (m), 135.2 (m, C_i), 137.9 (m, C_i), 139.7 (m, C_i).

2.4.6 Preparation of trans-RuCl(C≡CPh)(dppe)$_2$ (6)

A solution of [**3**]OTf (100 mg, 0.092 mmol) in CH_2Cl_2 (3 ml) was treated with phenylacetylene (10 μl, 0.09 mmol) and stirred at room temperature for 1 h. The solvent was removed *in vacuo* and the residue containing the crude vinylidene salt washed with hexane (2 × 10 ml) to remove any excess alkyne. The crude vinylidene salt was redissolved in dichloromethane (2 ml) and treated with a solution of KO^{t}Bu (35 mg) in methanol (5 ml), prompting the precipitation of a pale yellow solid, which was collected by filtration and dried to give **6** (72 mg, 75%). IR: ν(C≡C) 2072 cm^{-1}. ^{31}P NMR: δ 50.8 (s, PPh_2). ES-MS: *m/z* 1039 [M – Cl + K + H]$^+$.

2.4.7 Preparation of trans-RuCl(C≡CC$_6$H$_4$OMe-4)(dppe)$_2$ (7)

Prepared in a similar fashion to that described for **6** from [**3**]OTf (100 mg, 0.092 mmol), 1-ethynyl-4-methylbenzene (11 μl, 0.09 mmol), the vinylidene being formed after 2 h at room temperature. After deprotonation, yellow **7** was collected by filtration (42 mg, 43%). Crystals suitable for X-ray diffraction were obtained from CH_2Cl_2 / hexane. IR: ν(C≡C) 2070 cm^{-1}. ^{31}P NMR: δ 50.0 (s, dppe). ES-MS: *m/z* 1069 [M – Cl + K + H]$^+$.

2.4.8 Preparation of trans-RuCl(C≡CC$_6$H$_4$Me-4)(dppe)$_2$ (8)

Prepared in a similar fashion to that described for **6** from [**3**]OTf (100 mg, 0.092 mmol), 1-ethynyl-4-methylbenzene (11 μl, 0.09 mmol), the vinylidene being formed after 2 h at room temperature. After deprotonation, yellow **8** was isolated (75 mg, 78%). Crystals suitable for X-ray diffraction were obtained from CH_2Cl_2 / hexane and also THF / hexane. IR: ν(C≡C) 2073 cm^{-1}. ^{31}P NMR: δ 51.8 (s, PPh_2). ES-MS: *m/z* 1053, [M – Cl + K + H]$^+$.

2.4.2.9 Preparation of trans-RuCl(C≡CC$_6$H$_4$C$_5$H$_{11}$-4)(dppe)$_2$ (9)

Prepared in a similar fashion to that described for **6** from [**3**]OTf (100 mg, 0.092 mmol) and 4-pentyl phenylacetylene (18 μl, 0.09 mmol), the vinylidene being formed after 2 h at room temperature. After deprotonation **9** was obtained as a yellow powder (86 mg, 84%). IR: ν(C≡C) 2071 cm^{-1}. ^{31}P NMR: δ 51.5 (s, PPh$_2$). ES-MS: *m/z* 1069, [M – Cl]$^+$.

2.4.2.10 Preparation of trans-RuCl(C≡CC$_6$H$_4$CO$_2$Me-4)(dppe)$_2$ (10)

Prepared in a similar fashion to that described for **6** from [**3**]OTf (100 mg, 0.092 mmol) and methyl 4-ethynylbenzoate (15 mg, 0.09 mmol), the vinylidene being formed after 2 h at room temperature. After deprotonation, **10** was isolated as a yellow powder (66 mg, 66%). Crystals suitable for X-ray diffraction were obtained from THF / hexane. IR: ν(C≡C) 2065 cm^{-1}. ^{31}P NMR: δ 51.6 (s, PPh$_2$). ES-MS: *m/z* 1097, [M – Cl + K + H]$^+$.

2.4.2.11 Preparation of trans-RuCl(C≡CC$_6$H$_4$NO$_2$-4)(dppe)$_2$ (11)

Prepared in a similar fashion to that described for **6** from [**3**]OTf (100 mg, 0.092 mmol) and 4-nitro phenylacetylene (14 mg, 0.09 mmol) the vinylidene being formed after 6 h at room temperature. After deprotonation **11** was obtained a red powder (73 mg, 73%). IR: ν(C≡C) 2051 cm^{-1}. ^{31}P NMR: δ 48.4 (s, PPh$_2$). ES-MS: *m/z* 1084, [M – Cl + K + H]$^+$.

Chapter 3 : 1,3 Diethynyl Benzene Compounds

3.1 Introduction

Since the earliest work with the Creutz-Taube ion, the study of bridge-mediated electron-transfer in bimetallic complexes has centred on complexes featuring linear bridging moieties, with many early studies featuring bridging ligands with classical coordination properties, such as N-heterocycles. [22] With a view to the development of families of bridging ligands capable of allowing investigations of factors such as bridge length on the electron transfer process, attention has turned to bridge structures that are more readily amenable to simple, repetitive extension. The conceptually simple all-carbon oligo(yne)diyl ligands, $-(C\equiv C)_n-$, have allowed investigations free of potential complications arising from internal ligand rotational modes, [55] whilst the recognition of the remarkable conductivity of suitably doped polyacetylene that has led to the development of the plastic electronics industry has also spurred renewed interest in the "wire-like" properties of oligo(ene)s, oligo(phenylenevinylenes) and oligo(phenyleneethynylenes). [149-152] Of the various and numerous bridging ligands that have been considered, the "all-carbon" (e.g. buta-1,3-diyndiyl) [153-158] and "carbon-rich" (e.g. oligo(ene) [159-163] 1,4-phenylene, [164-167] 1,4-diethynyl benzene [72, 92, 93, 168, 169] and related oligo(phenylene ethynylene) [170-179]) have proven to be of particular interest in the last decade. [55, 155, 156, 180, 181]

The use of linear bridging ligands, B, permits investigation of electron-transfer processes in the classical $L_nM\text{-}B\text{-}ML_n$ structures, or linear metallo-oligomers $L_nM\{\text{-}B\text{-}ML_m\text{-}B\text{-}\}_xML_n$ by Wolf, [182-185] Lavastre [72, 103, 106, 186] and Rigaut, [71, 89, 92-94, 121, 187-189] to name but a few. However, very recently attention has begun to turn to more complex molecular structures with a view to developing more advanced architectures that could be suitable for use as, for example, QCA devices. [190, 191] The quantum-dot cellular automata (QCA) approach offers an alternative way in which binary information is encoded, with the original proposal of a QCA device consisting of islands of metal atoms on the corners of a square on a surface. [192, 193] Whereas in modern-day computers the binary information is stored in bits as on or

off signals which can in turn be considered as 0s and 1s, QCA devices realise functionality in ways which are well-suited to the properties of single molecules, not by using the molecules as switches but as structured charge containers. [190] The "dot" which refers to a unit of charge, can therefore be represented by a redox centre, whether that be metallic or organic, which essentially treats the information as electronic or magnetic states of a nanoscale island. [194] The attraction of using a metal centre is that the response of the centre can be modified dependent on pH, photoexcitation, electrochemical potential and by the metal centre's spatial environment. [195] By combining the QCA cells in different arrangements, molecular analogues of logic gates, such as AND and OR gates, can be constructed. [190, 196-199] Given the robust, chemically reversible redox processes associated with simple metal-ligand combinations, there is a great potential, and hence wide interest in, the synthesis of prototypical molecules, [200-203] such as the "Creutz-Taube square" [204] (Figure **19**) and the theoretical studies of electron transfer within such structures, for QCA-based molecular logic systems.

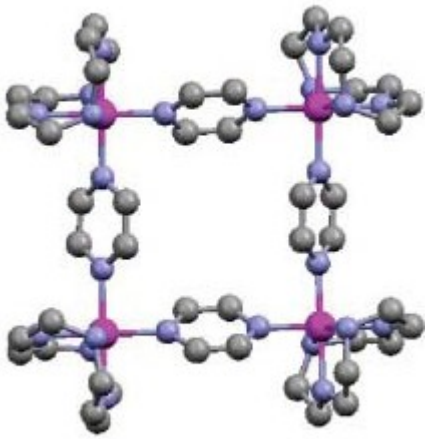

Figure **19** Long's $[(cyclen)_4Ru_4(pz)_4]^{9+}$ cation or "Creutz-Taube square". [204]

"Branched" carbon-rich systems, including those derived from 1,1,2,2-tetraethynylethene [58, 205, 206] and the 1,3,5-triethynylbenzene [207] motif have been recognized as offering a scaffold suitable for the assembly of polymetallic complexes, including metallodendrimers with interesting structural, [208] optical and non-linear optical properties. [104, 105, 109, 209-212] In many cases the extent of

interaction between metal centres at the periphery of these branched cores has been investigated using electrochemical methods. [59, 76, 213-220] More comprehensive studies by Lapinte [219] with weakly coupled mixed valence organoiron compounds based on 1,3-diethynyl- and 1,3,5-triethynyl-benzene ligands (Chart **1**) have also been conducted on both homo- and mixed-valence species. The interaction between the two or three Fe(dppe)Cp* centres in the bimetallic and trimetallic compounds based on **12** and **13** has been investigated by cyclic voltammetry, single crystal X-ray diffraction analysis and IR and UV-vis spectroscopy. These two neutral compounds were prepared from their respective silyl-protected pro-ligands ligands, 1,3-bis(trimethylsilylethynyl)- or 1,3,5-tris(trimethylsilylethynyl)-benzene, and FeCl(dppe)Cp* in the presence of methanol, potassium fluoride and potassium hexafluorophosphate (Scheme **3**).

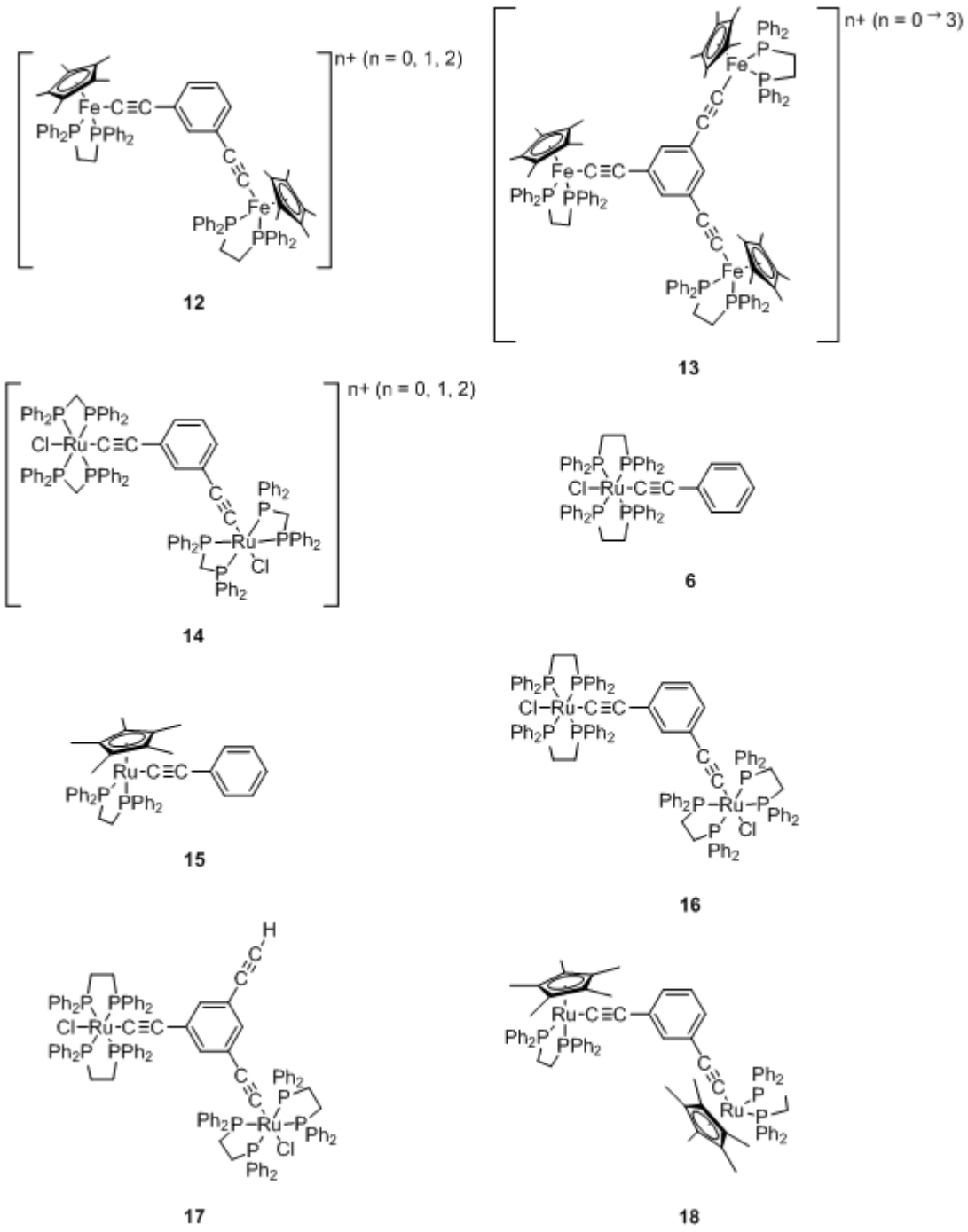

Chart **1** The complexes discussed in this Chapter (**6** and **12** - **18**).

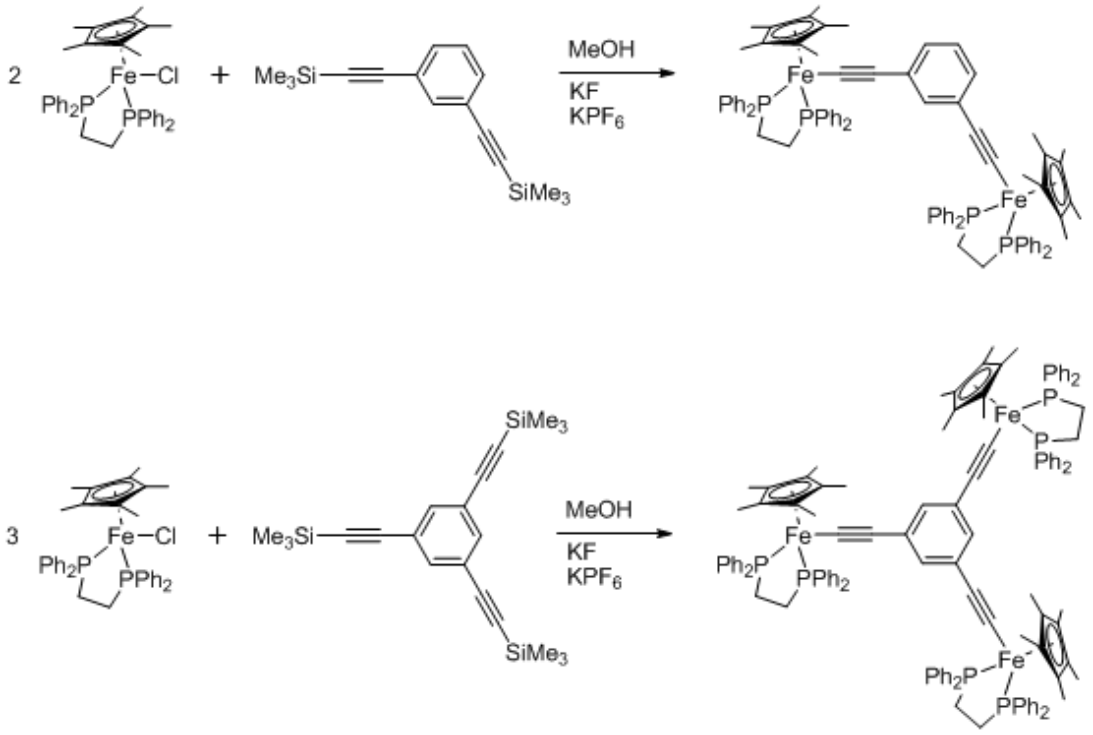

Scheme **3** Synthesis of bi- and tri iron acetylide complexes **12** and **13**. [219]

In room temperature solution **12** under goes two reversible one e^- oxidations and **13** undergoes three (Figure **20**). [219]

$$\underset{\mathbf{12}}{\text{Fe(II)-Fe(II)}} \overset{-e^-}{\rightleftharpoons} \underset{[\mathbf{12}]^+}{[\text{Fe(II)-Fe(III)}]^+} \overset{-e^-}{\rightleftharpoons} \underset{[\mathbf{12}]^{2+}}{[\text{Fe(III)-Fe(III)}]^{2+}}$$

Figure **20** Equilibria between **12**, $[\mathbf{12}]^+$ and $[\mathbf{12}]^{2+}$.

Comparison of the oxidation potentials of **12**, **13** and of the mononuclear iron complex [Fe(C≡CC_6H_5)(dppe)Cp*], shows that the first oxidation potential corresponding to the **13**/$[\mathbf{13}]^+$ couple is observed 40 mV lower than the **12**/$[\mathbf{12}]^+$ couple and 60 mV lower than that for the mononuclear iron complex Fe(C≡CPh)(dppe)Cp*. These electrochemical data are said to be indicative of weakly coupled mixed valence systems, [22] but care must be exercised in drawing conclusions about electronic structure from the electrochemical experiments (which provide thermodynamic data) alone. Nevertheless, the comproportionation constant

(K_c) values that can be derived from the electrochemical data indicate that the oxidised / mixed-valence species $[\mathbf{12}]^+$ and $[\mathbf{13}]^{+/2+}$ are stable enough to predominate in solution (K_c coincidently for all mixed-valence compounds ($[\mathbf{12}]^+$ and $[\mathbf{13}]^{+/2+}$) is; 1.3×10^2). [219]

Both compounds **12** and **13** have a characteristic ν(C≡C) band at 2050 cm^{-1} which provides a convenient spectroscopic probe through which to assess the effects of redox state change on the structure of the complex. The species $[\mathbf{12}]^{+/2+}$ and $[\mathbf{13}]^{+/2+/3+}$ can be obtained by oxidation of **12** and **13** respectively, by treatment with $[Cp_2Fe]PF_6$ and the IR spectroscopic data from the redox family are summarised in Table **6**.

Table **6** Infra-red data for **12** and **13** and their accessible redox states.

Compound	IR (cm^{-1}) (CH_2Cl_2)
12	2050
$[\mathbf{12}]^+$	2044 / 1998
$[\mathbf{12}]^{2+}$	2006
13	2050
$[\mathbf{13}]^+$	2044 / 1990
$[\mathbf{13}]^{2+}$	2041 / 2010
$[\mathbf{13}]^{3+}$	2011

The mixed-valence derivatives of **12** and **13** show two distinct ν(C≡C) bands, the higher frequencies corresponding to the Fe(II)–C≡C fragments and the lower corresponding to the Fe(III)–C≡C fragments. From the IR data it can be seen that there is a weak ground state interaction between the Cp*Fe–C≡C– building blocks through the arene connector. [219]

The UV-vis spectra of each of the binuclear and trinuclear compounds $[\mathbf{12}]^{n+}$ – $[\mathbf{13}]^{n+}$ have intense absorption bands in the range of 250-290 nm, which are attributed to π-π* ligand centred transitions. The red shift of these ligand centred bands following stepwise oxidation suggests that the site of oxidation is unlikely to be ligand centred. The UV spectra of the oxidised species $[\mathbf{12}]^{n+}$ and $[\mathbf{13}]^{n+}$ also

exhibit two weak bands above 550 nm which have been assigned to ligand to metal charge transfer (LMCT) transitions. [221] In the NIR region of $[\mathbf{12}]^{n+}$ and $[\mathbf{13}]^{n+}$, within the tail of the LMCT bands, very weak bands ($\varepsilon \approx 150$ $M^{-1}cm^{-1}$) corresponding to forbidden ligand field (LF) transitions specific to the Cp*(dppe)Fe(III) fragment and intervalence charge transfer (IVCT) transitions were observed. [221] From the characteristics of the IVCT band the coupling between the metal centres could be calculated using Hush theory, and in agreement with the other experimental data, the calculated coupling parameter H_{ab} ($[\mathbf{12}]^{+}$ 161 ± 2 cm^{-1}, $[\mathbf{13}]^{+}$ 143 ± 2 cm^{-1}, $[\mathbf{13}]^{2+}$ 117 ± 2 cm^{-1} and 71 ± 2 cm^{-1}) showed the organoiron compounds based on 1,3-diethynyl- and 1,3,5-triethynylbenzene to be weakly coupled Robin-Day Class II compounds. [219, 221, 222]

In earlier work by Friend and the Cambridge groups on analogous mixed-valence bimetallic ruthenium compounds based on the 1,3-diethynylbenzene bridging motif **14** (Chart **1**), detailed analyses were hindered by the weakness of the IVCT band. [220, 223] Thus, whilst the an intermediate oxidation state could be observed by voltammetric methods, the IVCT transition in the presumed Ru(II/III) mixed-valence state was not be observed. This weakness, or lack, of IVCT bands in mixed-valence bimetallic 1,3-diethynylbenzene compounds, was explained at the time by "*the fact that the 1,3-benzenediyl bridging ligand cannot form the quinoid mixed-valence structure*". [223] However, more recent studies demonstrating the ligand-centred oxidation behaviour of ruthenium-acetylide complexes, [115, 224] the observation of weak IVCT transitions in the iron analogues, the ongoing interest in electronic interactions between metal ethynyl moieties arranged in *meta*-positions around a benzene ring [116, 207, 225] and electron-transfer through branched ligands in general, coupled with the absence of detailed information about the IVCT band in even simple ruthenium complexes featuring this motif, has prompted a re-consideration the electronic structure of formally mixed-valence ruthenium (II/III) complexes of 1,3-diethynylbenzenes.

The concerted application of vibrational spectroscopy and DFT methods has proven useful in the analysis of the electronic structure of ruthenium(II) acetylide complexes such as *trans*-$RuCl(C{\equiv}CPh)(dppe)_2$ **6** and $Ru(C{\equiv}CPh)(dppe)Cp^*$ **15** (Chart **1**), [115] and also bimetallic derivatives, including those that might be regarded

as "mixed valence". [43, 88, 226] In this Chapter, studies of 1,3-{*trans*-$Cl(dppe)_2RuC{\equiv}C\}_2C_6H_4$ **16** and 1,3-$\{Cp^*(dppe)RuC{\equiv}C\}_2C_6H_4$ **17** and the related complex 1,3-{*trans*-$Cl(dppe)_2RuC{\equiv}C\}_2$-5-$(HC{\equiv}C)C_6H_3$ **18**, (Chart **1**) are described. Electrochemical oxidation of **16** and **17** results in the formation of stable "mixed valence" cation radicals, the electronic structures of which have been investigated using a suite of electrochemical, spectroscopic (UV-vis-NIR, IR) and computational methods.

3.2 Results and Discussion

Before discussing the electrochemical and spectroscopic properties of the dinuclear compounds, 1,3-{*trans*-$Cl(dppe)_2RuC{\equiv}C\}_2C_6H_4$ **16** and 1,3-$\{Cp^*(dppe)RuC{\equiv}C\}_2C_6H_4$ **17**, it is helpful to consider first the mononuclear model complexes **6** and **15** which have been studied in detail elsewhere. [81, 115, 224, 227] The HOMO of the mononuclear ruthenium acetylide complexes **6** and **15** features a considerable contribution from the alkynyl and phenyl π-orbitals (ca. 70%), mixed with ruthenium d character (ca. 20%). Each complex undergoes a one-electron oxidation event at moderate potentials. The orbital composition is largely retained upon oxidation, and the cation radical $[\mathbf{6}]^+$ and $[\mathbf{15}]^+$ could be described as metal-stabilised organic radical cations. The important involvement of the alkynyl ligand orbitals in the oxidation process is also evidenced by the large shift of ν(C≡C) (ca. –150 cm^{-1}) following oxidation of **6** or **15** in a spectroelectrochemical cell (Table **7**), a trend that is adequately reproduced in the calculated ν(C≡C) frequencies and geometries (Table **7**, Table **8**, Table **9**, Scheme **4**) of the appropriate computational models $[\mathbf{6\text{-}H}]^+$ and $[\mathbf{15\text{-}H}]^+$.

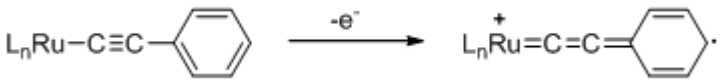

Scheme **4** A schematic representation of the redox products derived from a ruthenium acetylide.

Table **7** IR spectroelectrochemical data (0.1 M $[NBu_4][BF_4]$ / CH_2Cl_2) from compounds **6** – **18** (calculated values from related model systems in parentheses).

	0		+1		+2	
	v(C≡CRu)	*v*(C≡CH)	*v*(C≡CRu)	*v*(C≡CH)	*v*(C≡CRu)	*v*(C≡CH)
[**6**]	2075 (2072)	-	1910 (1912)	-	-	-
[**15**]	2072 (2075)	-	1929 (1905)	-	-	-
[**16**]	2063 (2073)	-	2049 (2024) 1905 (1935)	-	1909 (1858 HS, 1826 LS)	-
[**17**]	2063 (2075)	-	2060 (2032) 1934 (1944)	-	1938 (1886 HS, 1860 LS)	-
[**18**]	2059	[2059][a], 3303	2054	[2054][a], 3301	1908	2068, 3300

[a] C≡C band assumed to be present within the strong C≡CRu band observed.

Other structural variations that arise from the oxidation process include the elongation of Ru-P bond lengths and, in the case of $[\mathbf{6\text{-}H}]^{n+}$, contraction of the Ru-Cl bond. The optimised geometries of the computational model systems [*trans*-$RuCl(C{\equiv}CPh)(dHpe)_2]^{n+}$ ($[\mathbf{6\text{-}H}]^{n+}$) and $[Ru(C{\equiv}CPh)(PH_3)_2Cp]^{n+}$ ($[\mathbf{15\text{-}H}]^{n+}$) (Table **8**, Table **9**) and calculated spin densities (Table **10**) at the MPW1K/3-21G* level of theory are in agreement with the previous studies, [228, 229] and are presented here for purposes of comparison with results obtained from the bimetallic complexes at the same level. The atom-labelling scheme is illustrated in Scheme **5**.

Table **8** Selected bond lengths from the optimised geometries of [*trans*-RuCl(C≡CPh)(dHpe)$_2$]$^{n+}$ ([**6-H**]$^{n+}$) (n = 0, 1) and [1,3-{*trans*-Cl(dHpe)$_2$RuC≡C}$_2$C$_6$H$_4$]$^{n+}$ ([**16-H**]$^{n+}$) (n = 0, 1, 2).[a]

	Ru_1-P	Ru_1-$C_{\alpha1}$	$C_{\alpha1}$-$C_{\beta1}$	$C_{\beta1}$-C_1	C_1-C_2	C_2-C_3	C_3-C_4	C_4-C_5	C_5-C_6	C_6-C_1	C_3-$C_{\beta2}$	$C_{\beta2}$-$C_{\alpha2}$	$C_{\alpha2}$-Ru_2	Ru_2-P
6-H	2.300	2.007	1.216	1.419	1.395	1.380	1.384	1.384	1.380	1.395				
[**6-H**]$^+$	2.345	1.914	1.237	1.394	1.404	1.375	1.388	1.388	1.375	1.404				
16-H	2.299	2.009	1.216	1.420	1.392	1.392	1.395	1.380	1.380	1.395	1.420	1.215	2.009	2.299
[**16-H**]$^+$	2.331	1.919	1.241	1.382	1.403	1.384	1.414	1.385	1.374	1.416	1.405	1.220	1.991	2.308
[**16-H**]$^{2+}$ (LS)	2.340	1.908	1.245	1.378	1.390	1.390	1.433	1.377	1.376	1.433	1.378	1.245	1.908	2.340
[**16-H**]$^{2+}$ (HS)	2.357	1.936	1.230	1.405	1.396	1.396	1.404	1.380	1.380	1.404	1.405	1.230	1.936	2.357

also: **6-H** Ru-Cl 2.464; [**6-H**]$^+$ Ru-Cl 2.423; **16-H** Ru_1-Cl 2.464, Ru_2-Cl 2.464; [**16-H**]$^+$ Ru_1-Cl 2.436, Ru_2-Cl 2.459; [**16-H**]$^{2+}$ (LS) Ru_1-Cl 2.428, Ru_2-Cl 2.428; [**16-H**]$^{2+}$ (HS) Ru_1-Cl 2.399, Ru_2-Cl 2.399;

[a] See Scheme **5** for the atom labelling scheme.

Table **9** Selected bond lengths from the optimised geometries of [Ru(C≡CPh)(PH$_3$)$_2$Cp]$^{n+}$ ([**15-H**]$^{n+}$) (n = 0, 1) and [1,3-{Cp(PH$_3$)$_2$RuC≡C}$_2$C$_6$H$_4$]$^{n+}$ ([**17-H**]$^{n+}$) (n = 0, 1, 2).[a]

	Ru_1-P	Ru_1-$C_{\alpha1}$	$C_{\alpha1}$-$C_{\beta1}$	$C_{\beta1}$-C_1	C_1-C_2	C_2-C_3	C_3-C_4	C_4-C_5	C_5-C_6	C_6-C_1	C_3-$C_{\beta2}$	$C_{\beta2}$-$C_{\alpha2}$	$C_{\alpha2}$-Ru_2	Ru_2-P
15-H	2.253	2.003	1.215	1.418	1.395	1.380	1.384	1.384	1.380	1.395				
[**15-H**]$^+$	2.293	1.919	1.236	1.393	1.405	1.375	1.388	1.388	1.375	1.405				
17-H	2.253	2.003	1.215	1.419	1.391	1.392	1.395	1.381	1.380	1.395	1.419	1.215	2.004	2.252
[**17-H**]$^+$	2.285	1.920	1.237	1.385	1.401	1.385	1.411	1.385	1.374	1.414	1.406	1.219	1.990	2.261
[**17-H**]$^{2+}$ (LS)	2.285	1.918	1.240	1.382	1.389	1.390	1.428	1.376	1.377	1.429	1.382	1.239	1.923	2.281
[**17-H**]$^{2+}$ (HS)	2.306	1.930	1.232	1.402	1.396	1.397	1.404	1.380	1.380	1.405	1.402	1.231	1.937	2.299
[**17-H**]$^{2+}$ (HS, asym)	2.299	1.935	1.231	1.403	1.398	1.389	1.399	1.381	1.377	1.402	1.419	1.213	1.991	2.330

[a] See Scheme **5** for the atom labelling scheme.

Table **10** Calculated spin densities for the model systems [**6-H**]$^{+}$, [**15-H**]$^{+}$, [**16-H**]$^{+}$, HS-[**16-H**]$^{2+}$, [**17-H**]$^{+}$, HS-[**17-H**]$^{2+}$.[a]

	Ru_1	$C_{\alpha1}$	$C_{\beta1}$	C_1	C_2	C_3	C_4	C_5	C_6	$C_{\beta2}$	$C_{\alpha2}$	Ru_2
[**6-H**]$^{+}$	0.56	-0.06	0.37	–0.11	0.15	–0.11	0.19	–0.11	0.15			
[**15-H**]$^{+}$	0.51	–0.10	0.41	–0.17	0.22	–0.17	0.26	–0.17	0.22			
[**16-H**]$^{+}$	0.28	0.07	0.26	–0.07	0.04	–0.09	0.34	–0.17	0.30	0.06	0.00	0.04
[**16-H**]$^{2+}$	0.72	–0.19	0.41	–0.21	0.27	–0.21	0.26	–0.18	0.26	0.41	–0.19	0.72
[**17-H**]$^{+}$	0.36	0.02	0.31	–0.13	0.16	–0.18	0.37	–0.23	0.32	0.07	–0.06	0.00
[**17-H**]$^{2+}$	0.66	–0.26	0.49	–0.30	0.37	–0.30	0.35	–0.26	0.35	0.49	–0.25	0.65
[**17-H**]$^{2+}$ (asym)	0.63	–0.22	0.46	–0.22	0.25	–0.20	0.25	–0.19	0.24	0.16	–0.15	0.94

[a] See Scheme **5** for the atom labelling scheme.

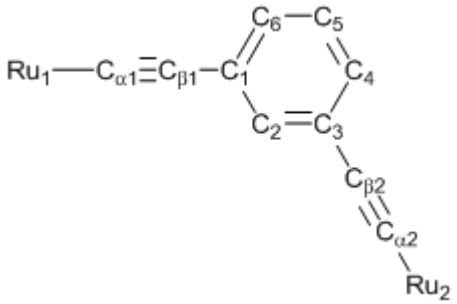

Scheme **5** The labelling scheme for the DFT calculations.

The UV-vis-NIR spectra of $[\mathbf{6}]^{n+}$ (n = 0, 1) are shown in Figure **23** for illustrative purposes, and data from $[\mathbf{6}]^{n+}$ and $[\mathbf{15}]^{n+}$ are summarised in Table **11**, together with assignments based on TD DFT calculations. [81, 115] The 18-electron, charge neutral (n = 0) complexes **6** and **15** each exhibit a broad absorption envelope in the UV region arising from transitions localised within the aryl groups of the phosphine ligands, and various approximately MLCT bands associated with both the phosphines and the acetylide ligand. The conventional "MLCT" description is used for convenience, although the mixed d/π character of the HOMO should be noted. These MLCT bands tail into the visible region, and are responsible for the yellow colour of the complexes. The oxidised compounds $[\mathbf{6}]^{+}$ and $[\mathbf{15}]^{+}$ feature a number of bands in the vis-NIR regions that can be broadly attributed to processes involving charge transfer from occupied orbitals with appreciable metal character to the β-LUSO, which is delocalised over the metal, acetylide and phenyl moieties. In the case of $[\mathbf{6}]^{+}$ a weak band near 9000 cm^{-1}, not resolved in a previous study, [81] is also apparent and attributed to charge transfer from the chloride ligand to the β-LUSO (i.e., approximately a chloride-to-metal LMCT transition) (Figure **21**, Table **11**). The NIR spectrum of $[\mathbf{15}]^{+}$ features a weak band near 8100 cm^{-1} (ε 600 $M^{-1}cm^{-1}$) that has been assigned to a transition between orbitals with significant phenylacetylide character. [115, 224, 227]

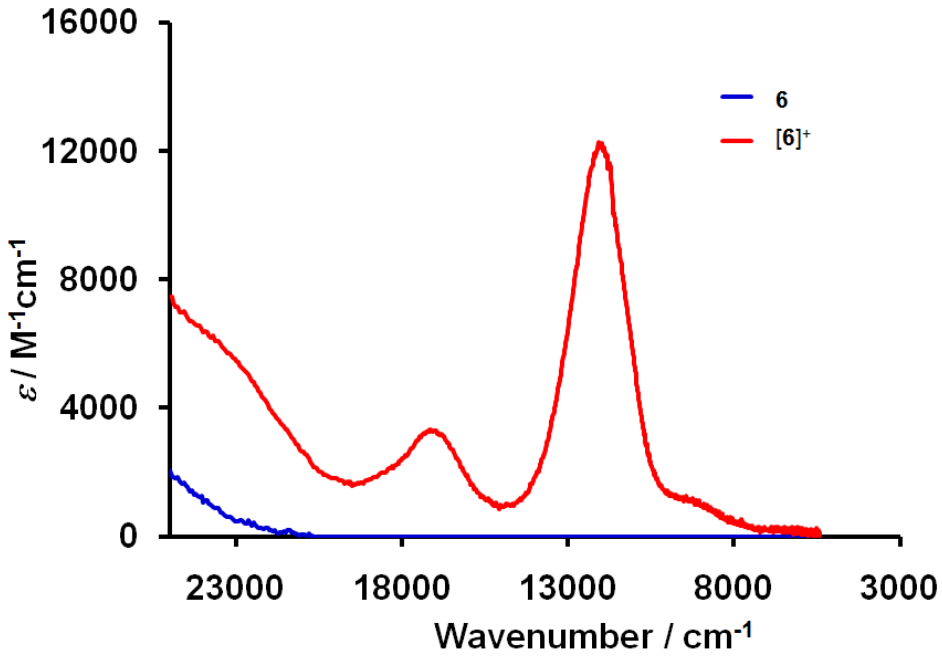

Figure **21** The UV-vis-NIR spectra of $[\mathbf{6}]^{n+}$ (n = 0, 1) (CH_2Cl_2 / 0.1 M $[NBu_4]BF_4$).

Table **11** Electronic transitions and assignments for [**6**]$^{n+}$, [**15**]$^{n+}$, [**16**]$^{n+}$, [**17**]$^{n+}$ and [**18**]$^{n+}$.

	wavenumber / cm^{-1} [ε / $M^{-1}cm^{-1}$]	wavenumber /cm^{-1} [f]	Assignment	Reference
6	31350 [23000]	31200 [0.0012]	Ru(d)→C_2Ph(π*), MLCT	[81]
	38480 [50000]	41700 [0.5389]	phenyl (π)→phenyl (π*)	
[**6**]$^+$	9080 [580]	4100 [0.0000]	Cl(p)→RuC_2 (dπ), LMCT	[81,a]
	12040 [10000]	13000 [0.2761]	ClRuC_2Ph (dπ)→RuC_2Ph (dπ)	
	16900 [1000]	15700 [0.0014]	ClRu →RuC_2Ph (dπ)	
15	29500 [9500]	31400 [0.0080]	RuC_2 (dπ)→Ru, MMCT	[115]
[**15**]$^+$	8100 [600]	7200 [0.0001]	phenyl (π)→RuC_2 (dπ)	[115]
	11200 [5100]	15500 [0.3131]	phenyl (π)→RuC_2, LMCT	
	21100 [4300]	27000 [0.0493]	phenyl (π)→RuCp, LMCT	
16	31350 [43500]	31000 [0.0013]	phenyl (π)→RuP_2	[a]
[**16**]$^+$	3750 [900]	5600 [0.0444]	dd ClRu → RuC_2Ph	[a]
	5800 [320]	6100 [0.1346]	IVCT RuC_2Ph → RuC_2Ph	
	9100 [1200]	12200 [0.0002]	ClRuC_2→RuC_2Ph(dπ)	
	12120 [7800]	14800 [0.2234]	RuP_2 →RuC_2Ph(dπ)	
	17300 [2800]	20400 [0.0082]	Cl(p) →RuC_2Ph(dπ), LMCT	
[**16**]$^{2+}$		*3200 [0.0000]*	*Dd*	[a]
		3300 [0.0000]	*Dd*	
	8800 [1800]	12200 [0.0001]	RuC_2Ph (dπ)→RuC_2Ph(dπ)	
	11900 [9400]	14700 [0.5242]	phenyl (π)→RuC_2Ph(dπ)	
	17000 [3400]	16000 [0.0494]	phenyl (π)→RuC_2Ph(dπ)	
17	31500 [13000]	31300 [0.0094]	Ru → phenyl (π*)	[a]
[**17**]$^+$	4800 [150]	5800 [0.1567]	IVCT RuC_2Ph (dπ)→RuC_2Ph(dπ)	[a]
	7750 [150]	8200 [0.0001]	dd RuCp →RuC_2Ph(dπ)	
	14000 [1000]	14900 [0.0084]	phenyl (π) →RuC_2Ph	
	17800 [500]	15800 [0.2716]	RuC_2→RuC_2Ph	
		21500 [0.0167]	RuC_2Ph (dπ)→ RuC_2Ph	
[**17**]$^{2+}$	4300 [90]	6600 [0.0003]	dd RuC_2 → RuC_2	[a]
	7500 [300]	6800 [0.0001]	dd RuCp → RuC_2	
	13500 [2300]	17200 [0.6145]	phenyl (π)→RuC_2Ph(dπ)	
	17400 [1300]	18600 [0.0636]	phenyl (π)→RuC_2Ph(dπ)	
18	29300 [13400]	-	Ru → phenyl (π*)	[a,b]
[**18**]$^+$	3780 [750]	-	IVCT RuC_2Ph (dπ)→RuC_2Ph(dπ)	[a,b]
	8550 [260]	-	dd RuCp →RuC_2Ph(dπ)	
	12000 [7100]	-	phenyl (π) →RuC_2Ph	
	16800 [2600]	-	Cl(p) →RuC_2Ph(dπ), LMCT	
	27000 [13300]	-	Ru → phenyl (π*)	
[**18**]$^{2+}$	8900 [1500]	-	RuC_2Ph (dπ)→RuC_2Ph(dπ)	[a,b]
	12000 [7600]	-	phenyl (π)→RuC_2Ph(dπ)	
	16600 [3000]	-	phenyl (π)→RuC_2Ph(dπ)	
	27700 [10500]	-	Ru → phenyl (π*)	

[a] assignments derived in this Chapter

[b] assignments for [**18**] and redox products made by analogy.

The compounds 1,3-{*trans*-Cl(dppe)$_2$RuC≡C}$_2$C$_6$H$_4$ **16** and 1,3-{Cp*(dppe)RuC≡C}$_2$C$_6$H$_4$ **17** were prepared from 1,3-diethynyl benzene via bis(vinylidene) intermediates, which were deprotonated *in situ* to afford the bis(acetylide) complexes as the sole isolated product in each case. Compound 1,3-{*trans*-Cl(dppe)$_2$RuC≡C}$_2$C$_6$H$_4$ **16** was also prepared from the [RuCl(dppe)$_2$]OTf [**3**]OTf salt and 1,3-diethynyl benzene resulting in a higher yield (82% versus 26%) than was obtained via the *cis*-RuCl$_2$(dppe)$_2$ procedure. Each compound undergoes two, essentially chemically reversible, one-electron oxidation events at potentials E_1 and E_2, giving rise to the redox series [**16**]$^{n+}$ and [**17**]$^{n+}$ (n = 0, 1, 2) (Table **12**). A chemically irreversible oxidation event can also be detected at higher potentials; this process has not been investigated further. The first oxidation potential E_1 from each of **16** and **17** is modestly more thermodynamically favourable than the first oxidation of the appropriate mononuclear model (Table **12**). The second oxidation in the bimetallic systems, which occurs at E_2, is some 160 – 200 mV more positive than E_1. This difference in first and second oxidation potential provides a measure of the stability of the mono-cation states, [**16**]$^+$ and [**17**]$^+$, with respect to disproportionation (K_c = 500 – 1600). [230]

Table **12** Oxidation potentials for complexes [**6**], [**15**], [**16**] and [**17**]. [a]

	E_1/V	E_2/V	E_3/V	ΔE_{1-2}/V	K_c
[**6**]	0.47	1.31[b]			
[**15**]	0.25	1.09[b]			
[**16**]	0.43	0.62	1.53[b]	0.19	1600
[**17**]	0.18	0.34	1.13[b]	0.16	500

[a] Data recorded from solutions in CH_2Cl_2 containing 0.1 M [NBu_4]BF_4 supporting electrolyte and referenced against decamethylferrocene/decamethylferrocenium Fc*H/Fc*H$^+$ couple at -0.07 V vs SCE scan rate 100 mV/s.

[b] Irreversible, anodic peak potential reported.

As noted in the introductory remarks, compounds such as 1,3-{*trans*-Cl(dppm)$_2$RuC≡C}$_2$-C$_6$H$_4$], [220, 223] 1,3-{*trans*-Cl(dppm)$_2$RuC≡C}$_2$-5-HC≡C-C$_6$H$_3$, [213] [1,3-{*trans*-Cl(dppe)$_2$RuC≡C}$_2$-5-HC≡C-C$_6$H$_3$ **18** [104, 105] and [1,3-{Cp(PPh$_3$)$_2$RuC≡C}$_2$-5-HC≡C-C$_6$H$_3$] [213] were also found to undergo two sequential and well separated oxidations in earlier studies. On the assumption that the

oxidation processes were metal centred, the intermediate mono-cation states were described as Ru(II/III) mixed-valence complexes. Furthermore, based on the electrochemical data, these mono-cations were taken as being examples of weakly coupled (i.e. Robin-Day Class II) systems. However, the thermodynamic stability of the mixed-valence state that is reflected in these electrochemical data is a sum of factors, including ion-pair interactions, intramolecular electrostatic factors, solvation energies, varying degrees of metal-ligand bond energies in the different metal oxidation states and the like, in addition to the "resonance", or delocalisation, term.[28, 231] Of these various factors, only the resonance term relates to the concept of electronic coupling between the remote sites. This resonance contribution to the stability of a mixed-valence compound cannot be easily extracted from a small set of electrochemical data in isolation of extensive work with closely related model systems, and various control experiments using different solvent and electrolyte combinations.

To more rigorously assess the electronic structures of the 1,3-diethynylbenzene bridged complexes $[\mathbf{16}]^{n+}$ and $[\mathbf{17}]^{n+}$, a combination of IR and UV-vis-NIR spectroelectrochemical methods and DFT calculations, was employed. The IR spectra of **16** and **17** are characterised by a single ν(C≡C) band, coincidently at 2063 cm^{-1} in each case, which do not differ significantly from the ν(C≡C) bands in the comparable mononuclear model complexes **6** and **15** (Table **7**). Unfortunately compound **16** was not very soluble in dichloromethane, so THF was also used as solvent for spectroelectrochemical studies of this species, which afforded somewhat better quality spectra (Figure **22**). The IR spectra of $[\mathbf{16}]^{+}$ and $[\mathbf{17}]^{+}$ each display two ν(C≡C) bands, which on the basis of comparison with the spectra of **6** and $[\mathbf{6}]^{+}$ or **15** and $[\mathbf{15}]^{+}$, as appropriate, can be approximately assigned to "Ru-C≡C" and "$[Ru\text{-}C{\equiv}C]^{+}$" moieties (Figure **22**, Table **7**).

Further oxidation of the bimetallic compounds to the dicationic state results in collapse of the characteristic two-band ν(C≡C) pattern, and only a slightly broadened ν(C≡C) band envelope is observed near 1900 cm^{-1} (Figure **22**, Table **7**). Clearly, the "mixed valence" bimetallic monocations $[\mathbf{16}]^{+}$ and $[\mathbf{17}]^{+}$ are localised on

the IR timescale, and electron density from the alkynyl moieties is involved in the oxidation process.

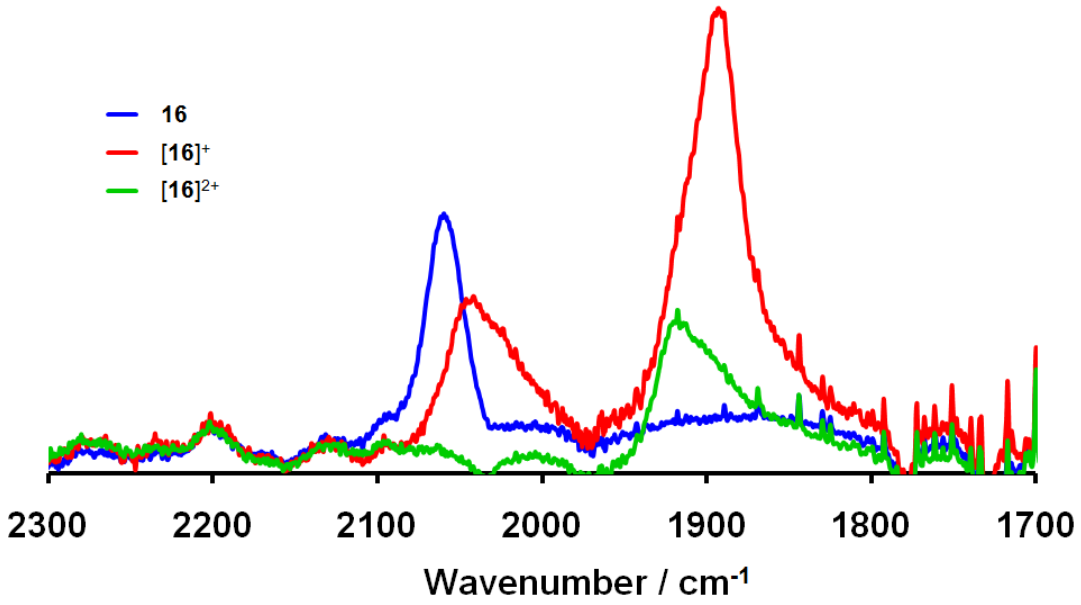

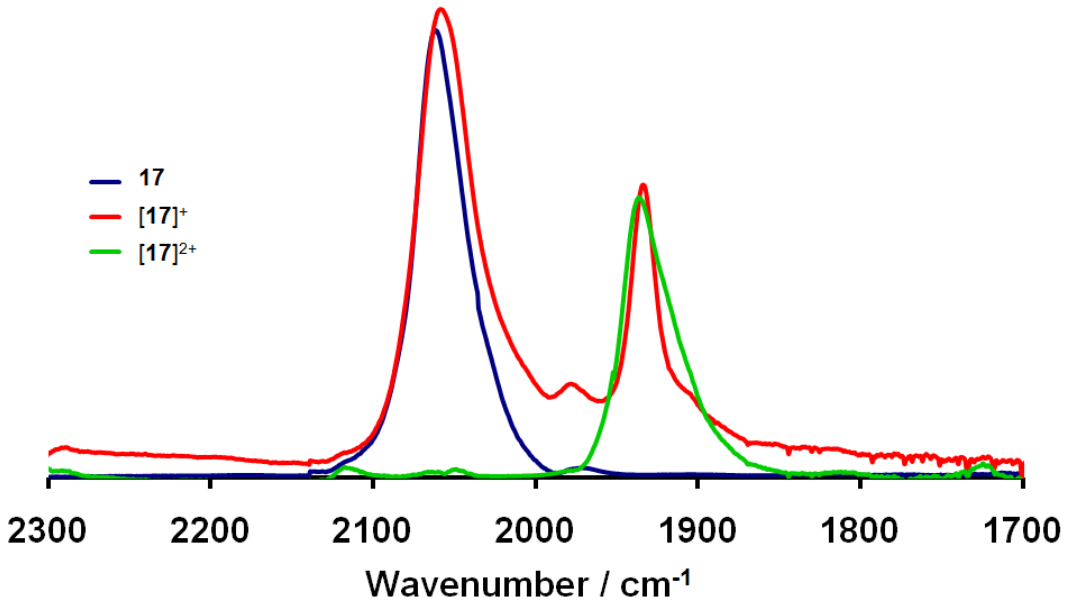

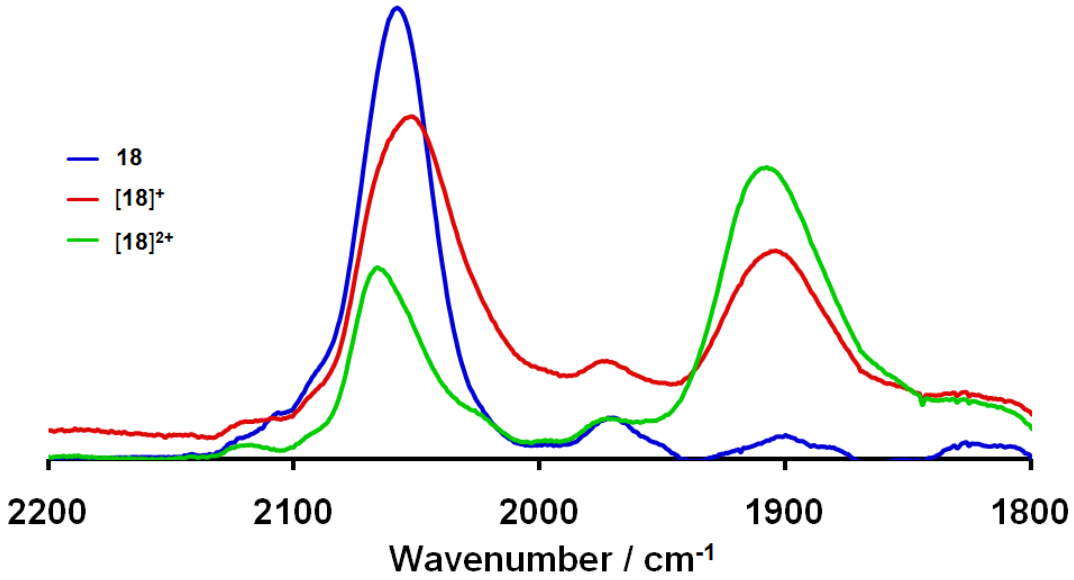

Figure **22** The IR spectra of $[\{1,3\text{-Cl(dppe)}_2\text{RuC}\equiv\text{C}\}_2\text{C}_6\text{H}_4]^{n+}$ (n = 0, 1, 2) $[\mathbf{16}]^{n+}$ (top, THF / 0.1 M $[\text{NBu}_4]\text{BF}_4$, room temperature), $[\{1,3\text{-Cp*(dppe)RuC}\equiv\text{C}\}_2\text{C}_6\text{H}_4]^{n+}$ (n = 0, 1, 2) $[\mathbf{17}]^{n+}$ (middle, CH_2Cl_2 / 0.1 M $[\text{NBu}_4]\text{BF}_4$, room temperature) and $[\{1,3\text{-Cl(dppe)}_2\text{RuC}\equiv\text{C}\}_2\text{-5-(HC}\equiv\text{C)C}_6\text{H}_3]^{n+}$ (n = 0, 1, 2) $[\mathbf{18}]^{n+}$ (bottom, CH_2Cl_2 / 0.1 M $[\text{NBu}_4]\text{BF}_4$, room temperature) collected from in situ oxidation in a spectroelectrochemical cell.

Geiger has proposed a method of estimating a "charge distribution parameter", $\Delta\rho$, for mixed valence compounds from IR spectroscopic data. [37, 232] The charge distribution parameter, which is a measure of the ground-state charge distribution between the two IR-active centres in the mixed valence case, is given by;

$$\Delta\rho = \frac{(\Delta\nu_{ox} + \Delta\nu_{red})}{2(\nu'_{ox} - \nu'_{red})}$$

where ν'_{ox} and ν'_{red} are the wavenumbers of signature vibrational bands associated with the complex in the fully oxidised and fully reduced states (i.e. the dication and neutral complexes in the present examples), and $\Delta\nu_{ox} = \nu'_{ox} - \nu_{ox(\text{obs})}$, $\Delta\nu_{red} = \nu'_{red} - \nu_{red(\text{obs})}$. The parameters $\nu_{ox(\text{obs})}$ and $\nu_{red(\text{obs})}$ refer to the observed vibrational bands associated with the "oxidised" and "reduced" centres in the mixed valence case.

From the data in Table **7**, $\Delta\rho$ = 0.06 and 0.03 for [**16**]$^{+}$ and [**17**]$^{+}$, respectively, consistent with the description of these compounds in terms of localised redox centres.

3.2.1 DFT Calculations

Electronic structure calculations (MPW1K/3-21G*, Gaussian 03) were carried out, using the model systems [1,3-{*trans*-Cl(dHpe)$_2$RuC≡C}$_2$C$_6$H$_4$]$^{n+}$ ([**16-H**]$^{n+}$) and [1,3-{Cp(PH$_3$)$_2$RuC≡C}$_2$C$_6$H$_4$]$^{n+}$ ([**17-H**]$^{n+}$) to reduce computational effort, but no symmetry constraints were applied. The atom-labelling scheme is illustrated in Scheme **5**, and results of the geometry optimizations are summarised in Table **8** and Table **9**, while calculated vibrational frequencies have been included in Table **7** to permit ready comparison with the available experimental data. Details of orbital energies and composition for selected orbitals from the frontier region of each of [**16-H**]$^{n+}$ and [**17-H**]$^{n+}$ are given in Table **13**.

Table **13** Decomposition of selected frontier MOs in [**6-H**]$^{n+}$, [**15-H**]$^{n+}$, [**16-H**]$^{n+}$ and [**17-H**]$^{n+}$.

6-H								
MO	occ	ε (eV)	%Cl	%PH_3	%Ru	%C_α	%C_β	%Ph
113	0	1.56	0	35	66	-1	0	1
112	0	1.50	0	24	50	4	0	21
111	0	1.41	0	28	71	0	0	1
110	0	1.35	6	52	42	0	0	0
109	0	1.21	1	55	44	0	0	0
108	0	0.91	0	10	19	10	3	58
107	2	-6.45	5	2	21	17	22	33
106	2	-6.94	21	2	42	9	24	2
105	2	-7.58	56	15	14	4	1	10
104	2	-7.86	46	24	1	12	15	2
103	2	-8.16	0	0	0	0	0	100

[**6-H**]$^{+}$								
MO	occ	ε (eV)	%Cl	%PH_3	%Ru	%C_α	%C_β	%Ph
110 β	0	-2.24	0	1	12	14	2	70
109 β	0	-2.46	9	39	48	3	0	1
110 α	0	-2.55	10	35	48	4	0	3
109 α	0	-2.75	0	3	7	19	5	66
108 β	0	-2.80	0	55	45	0	0	0
108 α	0	-3.01	0	56	44	0	0	0
107 β	0	-6.33	3	4	40	9	24	20
107 α	1	-10.53	1	3	9	15	14	57
106 β	1	-10.79	25	9	20	15	0	32
105 β	1	-11.02	17	3	38	11	29	3
106 α	1	-11.25	22	2	34	10	28	3
104 β	1	-11.41	0	0	0	0	0	100
105 α	1	-11.55	0	0	0	0	0	100
104 α	1	-11.68	68	23	9	0	0	1
103 β	1	-11.74	51	34	2	5	7	1

15-H								
MO	occ	ε (eV)	%Cp	%PH_3	%Ru	%C_α	%C_β	%Ph
90	0	1.70	0	0	0	0	0	100
89	0	1.52	0	11	84	1	0	4
88	0	1.45	16	18	59	6	1	0
87	0	1.03	2	3	9	13	3	69
86	0	0.91	1	10	89	0	0	0
85	0	0.79	22	28	49	0	0	1
84	2	–6.30	6	3	23	15	22	31
83	2	–7.11	13	5	55	8	17	1
82	2	–7.51	27	9	26	16	20	2
81	2	–8.06	27	8	25	6	0	34
80	2	–8.08	1	0	1	0	0	99

[**15-H**]$^+$								
MO	occ	ε (eV)	%Cp	%PH_3	%Ru	%C_α	%C_β	%Ph
86 β	0	-2.77	19	21	54	6	0	0
87 α	0	-2.92	20	20	52	8	0	0
86 α	0	-2.96	1	4	5	20	5	64
85 β	0	-3.46	26	26	47	0	0	0
85 α	0	-3.67	26	27	47	0	0	0
84 β	0	-6.44	7	4	35	10	23	21
84 α	1	-10.60	6	4	13	12	14	51
83 β	1	-11.21	9	4	22	15	0	49
82 β	1	-11.51	0	0	0	0	0	100
81 β	1	-11.51	5	2	36	18	36	4
83 α	1	-11.66	0	0	0	0	0	100
82 α	1	-11.71	53	10	26	8	3	1
81 α	1	-11.76	3	1	38	17	36	5

16-H													
MO	occ	eV	% Cl_1	% $PH_{3\ 1}$	% Ru_1	% $C_{\alpha 1}$	% $C_{\beta 1}$	% C_6H_4	% $C_{\beta 2}$	% $C_{\alpha 2}$	% Ru_2	% $PH_{3\ 2}$	% Cl_2
200	0	1.36	3	30	27	0	0	1	0	0	19	19	2
199	0	1.36	3	27	25	0	0	0	0	0	19	24	3
198	0	1.33	0	6	25	0	0	3	0	0	42	21	1
197	0	1.24	1	50	40	0	0	2	0	0	3	3	0
196	0	1.23	0	6	7	0	0	4	0	0	37	45	1
195	0	1.19	0	10	21	2	1	23	1	1	24	16	0
194	0	0.89	0	3	7	6	2	57	2	7	10	5	0
193	2	-6.23	2	1	10	10	11	39	9	9	8	1	2
192	2	-6.56	4	1	13	7	11	25	13	9	14	1	4
191	2	-6.86	8	1	17	5	11	2	15	6	23	1	11
190	2	-6.95	14	1	24	5	13	2	9	3	18	1	11
189	2	-7.49	37	9	11	3	0	8	0	1	6	5	20
188	2	-7.55	17	5	4	2	1	15	1	3	8	10	35
187	2	-7.79	26	13	1	7	8	1	6	6	1	10	21

[**16-H**]$^+$													
MO	occ	eV	% Cl_1	% $PH_{3\ 1}$	% Ru_1	% $C_{\alpha 1}$	% $C_{\beta 1}$	% C_6H_4	% $C_{\beta 2}$	% $C_{\alpha 2}$	% Ru_2	% $PH_{3\ 2}$	% Cl_2
197α	0	-1.70	10	38	50	2	0	0	0	0	0	0	0
196α	0	-1.73	0	1	3	2	1	78	1	8	4	1	0
195β	0	-1.93	0	2	10	12	2	69	0	3	1	0	0
194β	0	-1.95	0	55	45	0	0	0	0	0	0	0	0
195α	0	-2.06	0	55	45	0	0	0	0	0	0	0	0
194α	0	-2.66	0	1	4	15	2	70	0	5	1	0	0
193β	0	-6.25	1	3	21	13	19	34	3	4	2	0	0
192β	1	-8.53	1	1	8	1	6	16	23	11	26	3	6
193α	1	-9.11	0	0	0	0	0	19	23	10	32	2	13
191β	1	-9.19	0	0	0	0	0	1	21	6	46	2	23
192α	1	-9.23	0	0	0	0	0	1	21	6	45	2	25
190β	1	-9.79	1	0	2	0	1	6	2	5	10	17	56

LS-[**16-H**]$^{2+}$													
MO	occ	eV	% Cl_1	% $PH_{3\ 1}$	% Ru_1	% $C_{\alpha 1}$	% $C_{\beta 1}$	% C_6H_4	% $C_{\beta 2}$	% $C_{\alpha 2}$	% Ru_2	% $PH_{3\ 2}$	% Cl_2
199	0	-3.74	0	0	0	0	0	0	0	2	56	33	10
198	0	-3.95	10	32	55	3	0	0	0	0	0	0	0
197	0	-4.08	0	0	0	0	0	0	0	0	45	54	1
196	0	-4.29	0	55	45	0	0	0	0	0	0	0	0
195	0	-4.86	0	0	2	6	0	80	0	7	3	1	0
194	0	-5.54	0	1	3	10	0	73	0	9	3	1	0
193	0	-9.86	1	2	13	6	12	34	11	6	12	2	1
192	2	-11.48	3	2	18	3	14	13	15	3	21	3	4
191	2	-12.48	0	0	1	0	0	3	18	4	41	2	31
190	2	-12.75	35	2	38	3	16	2	0	0	1	1	2
189	2	-12.88	5	0	2	0	1	3	1	2	5	21	59
188	2	-13.03	52	21	5	2	1	3	1	0	1	7	7

HS-[**16-H**]$^{2+}$													
MO	occ	eV	% Cl_1	% $PH_{3\ 1}$	% Ru_1	% $C_{\alpha 1}$	% $C_{\beta 1}$	% C_6H_4	% $C_{\beta 2}$	% $C_{\alpha 2}$	% Ru_2	% $PH_{3\ 2}$	% Cl_2
195β	0	-4.51	0	1	1	0	0	0	0	0	44	52	0
194β	0	-4.51	1	52	44	0	0	0	0	0	1	1	1
196α	0	-4.77	0	11	8	0	0	2	0	0	34	44	0
195α	0	-4.77	0	45	35	0	0	0	0	0	9	11	0
194α	0	-4.79	0	1	3	11	1	67	1	11	3	1	0
193β	0	-7.76	2	2	24	2	10	17	10	2	24	2	2
192β	0	-7.91	3	2	27	2	12	9	12	2	27	2	3
191β	1	-12.37	13	6	7	11	1	26	1	11	7	6	13
193α	1	-12.28	0	2	4	8	9	53	9	8	4	2	0
190β	1	-12.61	15	8	5	8	3	20	3	8	5	8	15
189β	1	-12.67	10	2	17	6	13	4	13	6	17	2	10
188β	1	-12.76	13	1	19	4	12	2	12	4	19	1	13
192α	1	-12.79	1	3	6	7	11	44	11	7	6	3	1

17-H													
MO	occ	eV	% Cp_1	% $PH_{3\ 1}$	% Ru_1	% $C\alpha_1$	% $C_{\beta 1}$	% C_6H_4	% $C_{\beta 2}$	% $C_{\alpha 2}$	% $Ru_{\ 2}$	% $PH_{3\ 2}$	% $Cp_{\ 2}$
152	0	1.09	1	2	5	8	2	65	2	8	5	2	1
151	0	1.01	1	9	86	0	0	0	0	0	3	0	0
150	0	0.98	0	0	3	0	0	0	0	0	87	9	1
149	0	0.91	22	28	49	0	0	1	0	0	0	0	0
148	0	0.88	0	0	0	0	0	1	0	0	49	28	22
147	2	-6.00	3	1	11	9	10	37	9	8	9	1	2
146	2	-6.32	3	2	12	7	11	25	13	8	14	2	4
145	2	-6.95	6	3	36	7	15	2	7	4	16	1	3
144	2	-7.02	6	2	18	2	4	1	12	6	37	4	9
143	2	-7.35	19	7	18	10	12	2	4	4	10	4	11
142	2	-7.42	8	3	9	5	7	3	14	11	18	6	17

[**17-H**]$^+$													
MO	occ	eV	% Cp_1	% $PH_{3\ 1}$	% Ru_1	% $C\alpha_1$	% $C_{\beta 1}$	% C_6H_4	% $C_{\beta 2}$	% $C_{\alpha 2}$	% $Ru_{\ 2}$	% $PH_{3\ 2}$	% $Cp_{\ 2}$
150β	0	-1.98	3	2	10	13	2	67	0	2	0	0	0
149β	0	-2.03	18	19	57	6	0	0	0	0	0	0	0
150α	0	-2.13	19	19	55	7	0	0	0	0	0	0	0
148β	0	-2.70	26	26	48	0	0	0	0	0	0	0	0
149α	0	-2.73	3	2	6	16	3	64	0	4	1	0	0
148α	0	-2.83	24	27	46	1	0	2	0	0	0	0	0
147β	0	-6.20	5	3	23	13	20	32	1	2	2	0	0
146β	1	-8.47	1	1	5	0	4	15	22	9	29	4	9
147α	1	-8.83	0	0	0	0	0	17	23	8	34	6	12
145β	1	-9.31	0	0	0	0	0	0	9	5	56	8	22
146α	1	-9.31	0	0	0	0	0	0	8	4	55	8	24
144β	1	-9.70	0	0	0	0	0	2	25	14	31	6	21
145α	1	-9.73	0	0	0	0	0	2	26	14	32	5	20
144α	1	-10.07	10	5	20	10	16	37	0	0	0	0	1

LS-[**17-H**]$^{2+}$													
MO	occ	eV	% Cp_1	% $PH_{3\ 1}$	% Ru_1	% $C\alpha_1$	% $C_{\beta 1}$	% C_6H_4	% $C_{\beta 2}$	% $C_{\alpha 2}$	% $Ru_{\ 2}$	% $PH_{3\ 2}$	% $Cp_{\ 2}$
152	0	-4.64	0	0	0	0	0	1	0	0	48	27	24
151	0	-4.65	20	17	55	7	0	0	0	0	0	0	0
150	0	-4.72	1	1	1	4	1	78	1	9	3	1	0
149	0	-5.32	27	26	46	0	0	1	0	0	0	0	0
148	0	-5.42	1	2	4	12	1	71	0	6	2	0	0
147	0	-9.78	3	2	11	5	9	30	12	5	15	3	4
146	2	-11.25	6	4	18	3	14	13	12	2	18	4	7
145	2	-12.76	0	0	0	0	0	0	1	6	37	10	46
144	2	-12.9	0	0	0	0	0	3	35	13	39	2	7
143	2	-13.33	5	2	5	1	0	23	2	13	13	7	29
142	2	-13.52	50	10	29	7	3	0	0	0	0	0	0
141	2	-13.62	3	2	46	12	32	3	0	0	0	0	0
140	2	-13.87	28	7	11	12	2	28	2	2	2	1	6

HS-[**17-H**]$^{2+}$													
MO	occ	eV	% Cp_1	% $PH_{3\ 1}$	% Ru_1	% $C\alpha_1$	% $C_{\beta 1}$	% C_6H_4	% $C_{\beta 2}$	% $C_{\alpha 2}$	% $Ru_{\ 2}$	% $PH_{3\ 2}$	% $Cp_{\ 2}$
150α	0	-5.03	1	1	2	11	2	67	2	11	2	1	0
149β	0	-5.18	27	26	47	0	0	0	0	0	0	0	0
148β	0	-5.23	0	0	0	0	0	0	0	0	48	27	25
149α	0	-5.46	27	27	46	0	0	0	0	0	0	0	0
148α	0	-5.49	0	0	0	0	0	0	0	0	47	28	25
147β	0	-7.97	5	3	23	3	11	18	9	2	19	2	4
146β	0	-8.13	4	2	21	2	11	10	13	2	26	3	5
147α	1	-12.34	3	2	6	7	8	46	9	7	6	3	4
145β	1	-12.95	5	2	10	13	1	40	0	13	10	2	5
146α	1	-12.77	7	4	9	5	10	30	10	4	9	4	7
144β	1	-13.16	6	2	15	10	17	16	10	9	10	1	4

The important metric parameters of the neutral bimetallic systems **16-H** and **17-H** are indistinguishable from those of the comparable mononuclear models **6-H** and **15-H**. The calculated ν(C≡C) frequencies are in good agreement with the observed data (Table **7**), giving confidence in the accuracy of the structural models. Differences in energy arising from different orientations of the metal fragments with respect to the plane of the aromatic ring are negligible, as has been found in related studies of similar systems. [115, 233] In each case the HOMO is M-C_α anti-bonding, C_α-C_β bonding and C_β-C_6H_4 anti-bonding in character, and, as with the mononuclear analogues, contains considerable diethynylbenzene character (**16-H** 76%, **17-H** 73%) (Figure **23**, Table **13**).

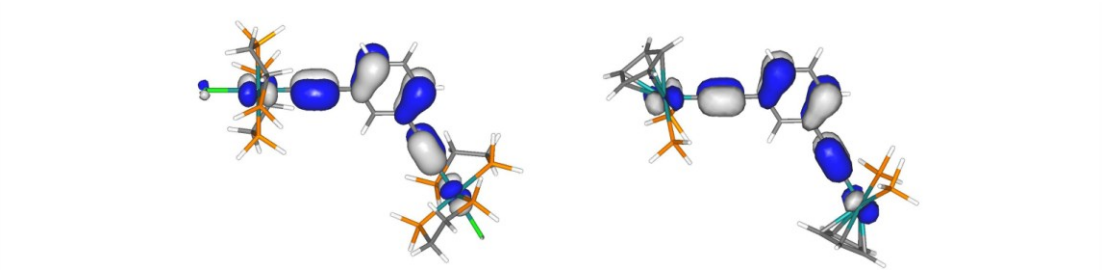

Figure **23** The HOMOs for the neutral bimetallic model systems **16-H** and **17-H**.

On the basis of the IR spectroscopic data (Table **7**), [**16**]$^+$ and [**17**]$^+$ offer distinct metal-acetylide environments, consistent with a localised "mixed valence" description. The distinction of the metal sites and associated ligands is reproduced in the optimised geometries of [**16-H**]$^+$ and [**17-H**]$^+$ and calculated electronic structures. When compared with the structures of the neutral, closed shell bimetallic models **16-H** and **17-H**, in each of the monocations [**16-H**]$^+$ and [**17-H**]$^+$ the local geometry around one of the metal ethynyl fragments (denoted Ru_1 for convenience, Scheme **5**) displays contracted Ru_1-$C_{\alpha1}$ and $C_{\beta1}$-C_1 bond lengths, and elongated $C_{\alpha1}$≡$C_{\beta1}$ and Ru_1-P bond lengths. The local geometries associated with the Ru_1 metal centre and the Ru_1-$C_{\alpha1}$≡$C_{\beta1}$ moieties in [**16-H**]$^+$ or [**17-H**]$^+$ are essentially identical to those calculated for the metal centre in [**6-H**]$^+$ or [**15-H**]$^+$ as appropriate. The Ru_2 site, and associated $C_{\alpha2}$≡$C_{\beta2}$ moiety, is less significantly affected by the loss of electron density from the molecule, and is closer in geometry to that calculated for **6-H** or **15-H**. The calculated vibrational frequencies from the

[**16-H**]$^+$ and [**17-H**]$^+$ computational models accurately reproduce the two ν(C≡C) bands observed in the spectroelectrochemical experiments (Table **7**). For example, whereas **16-H** gives rise to a single ν(C≡C) band at 2072 cm^{-1}, [**16-H**]$^+$ displays two distinct ν(C≡C) bands, both shifted to lower frequency relative to the single band **16-H**, with the smaller shift in one band (Δν(C≡C) 49 cm^{-1}) complemented by a much larger shift in the other (Δν(C≡C) 138 cm^{-1}). Similar shifts are also found for [**17-H**]$^+$ relative to **17-H**. Interestingly, there is some evidence for a degree of quinoidal character evolving in the aryl ring in conjugation with Ru_1-$C_{\alpha 1}$-$C_{\beta 1}$ in both [**16-H**]$^+$ (Table **8**) and [**17-H**]$^+$ (Table **9**).

The orbital structure of [**16-H**]$^+$ and [**17-H**]$^+$ is consistent with the valence localised (weakly coupled Class II mixed valence) description of these species (Table **13**). For both [**16-H**]$^+$ and [**17-H**]$^+$ the β-LUSO is delocalised over the Ru_1-$C_{\alpha 1}$≡$C_{\beta 1}$ and the C_4 and C_6 carbon atoms of the bridging phenylene ring, whilst the β-HOSO has significant Ru_2-$C_{\alpha 2}$≡$C_{\beta 2}$ and C_2 character. The distribution of spin densities in the various open-shell complexes [**6-H**]$^+$, [**15-H**]$^+$, [**16-H**]$^+$ and [**17-H**]$^+$ are particularly informative in deriving a description of the oxidation of ruthenium(II) compounds containing bridging ligands derived from 1,3-diethynylbenzene (Table **10**). The unpaired electron spin density in each of [**16-H**]$^+$ and [**17-H**]$^+$ is distributed over Ru_1, $C_{\alpha 1}$, $C_{\beta 1}$ and the aryl ring system. Within the aryl ring, the electron density is not evenly distributed, but rather is more concentrated at C_4 and C_6. The integrated electron density over the Ru_2-$C_{\alpha 2}$≡$C_{\beta 2}$ fragment in [**16-H**]$^+$ and [**17-H**]$^+$ is only ca. 0.1 – 0.01 e. Taken as a whole, the calculated geometry and spin density is consistent with the simple valence bond description shown in Scheme **6**, in which the phenylene ring plays an important role in the oxidation process.

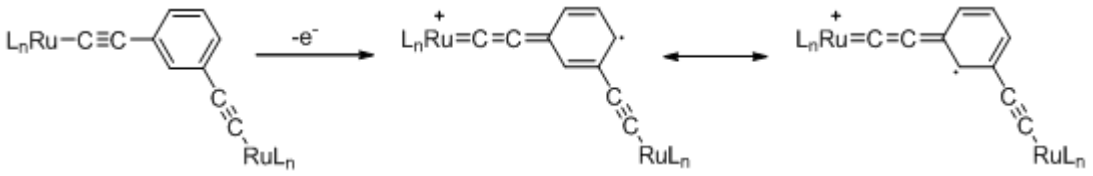

Scheme **6** The important role played by the phenylene ring in the oxidation process.

The pronounced electronic asymmetry calculated in [**16-H**]$^{+}$ using the MPW1K functional contrasts with the largely symmetrical distributions of electron density that arises from broken symmetry calculations on Class II mixed-valence iron systems. [221] In the case of the ruthenium systems, the thermodynamic stability of the valence-trapped mixed valence compounds [**16**]$^{+}$ and [**17**]$^{+}$ implied by the solution electrochemical data (i.e. the significant separation of E_1 and E_2 and associated calculated K_c values), and significant changes in the ν(C≡C) frequencies that are reproduced by calculations on simplified, gas-phase model systems, seems to be an inherent electronic feature associated with delocalisation of charge into the aromatic ring of the bridging ligand, and not just a consequence of external thermodynamic factors (e.g. ion pairing with the electrolyte), [37, 232] or through any significant charge-delocalisation between the metal centres (c.f. the negligible $\Delta\rho$ values).

The dicationic compound [**16-H**]$^{2+}$ offers both low spin (LS) and high spin (HS) electronic configurations. In their respective lowest energy conformations, the HS state, HS-[**16-H**]$^{2+}$, is more stable than the LS configuration, LS-[**16-H**]$^{2+}$, by some 35.5 kcal.mol^{-1}. Similar energetic preferences for the HS state have been found for [**17-H**]$^{2+}$ (36.4 kcal.mol^{-1}), and also in the case of closely related iron compounds. [222] Broadly, there is also a better agreement between the calculated vibrational features of the HS dications with those observed experimentally, and it is likely that the HS state dominates in solution (Table **7**).

The potential energy surface of HS-[**16-H**]$^{2+}$ features a large number of shallow energy minima differentiated by the orientation of the RuP_4 fragments relative to the plane of the bridging phenylene ring. However, the optimised geometries associated with these various local minima of HS-[**16-H**]$^{2+}$ are characterised by two common features: in contrast to the monocations, there is no significant structural distinction between the Ru_1-$C_{\alpha1}$≡$C_{\beta1}$ and Ru_2-$C_{\alpha2}$≡$C_{\beta2}$ fragments; the structure of the $Ru_{1,2}$-$C_{\alpha1,\alpha2}$≡$C_{\beta1,\beta2}$ fragments do not change greatly as the orientation of the $Ru(dHpe)_2Cl$ groups with respect to the bridging phenylene plane is systematically varied. Table **8** lists selected bond distances for the most stable form of HS-[**16-H**]$^{2+}$ in which the phenylene plane bisects the P-Ru-P angle at each metal centre.

The geometrical parameters for the Ru-C_α-C_β fragments are similar to those found in the monoruthenium cation [**6-H**]$^+$ (Table **8**), whilst the spin densities reflect the similarities between HS-[**16-H**]$^{2+}$ and [**6-H**]$^+$ (Table **10**).

In contrast, the nature of the Ru-C_α-C_β-C fragments in the optimised geometries of HS-[**17-H**]$^{2+}$ is sensitive to the orientation of the Ru$(PH_3)_2$Cp groups. When the Ru$(PH_3)_2$Cp moieties are in either a *cisoid* or *transoid* arrangement with the phenylene plane approximately perpendicular to the plane of the Cp rings, the geometry and spin distribution associated with the Ru_1-$C_{\alpha1}$-$C_{\beta2}$ and Ru_1-$C_{\alpha1}$-$C_{\beta2}$ fragments are similar to each other, and also to [**15-H**]$^+$ (Table **9**, Table **10**). Table **8** lists selected geometrical parameters for the most stable conformation, in which the phenylene ring approximately bisects the P-Ru-P angles for HS-[**17-H**]$^{2+}$ in a manner similar to that depicted for **17-H** in Figure **23**. Twisting one Ru$(PH_3)_2$Cp moiety in HS-[**17-H**]$^{2+}$ (nominally Ru_2) such that the phenylene plane is approximately parallel to the Cp ring ligated to Ru_2 prevents that metal dπ system from effectively conjugating with the phenylene bridge. The geometry of local minimum (ca. +2.5 kcal.mol^{-1}) associated with this conformation (denoted (HS, asym) in Table **9**) resembles [**15-H**]$^+$ substituted at C_3 by an oxidised Ru(C≡C)$(PH_3)_2$Cp fragment.

The redox products derived from 1,3-{*trans*-Cl$(dppe)_2$RuC≡C}$_2$-5-(HC≡C)C_6H_3 **18**, were also explored, which is a more soluble analogue of **16** that bears additional IR active [ν(C≡C), ν(C-H)] spectator groups. Compound **18** also undergoes two sequential one-electron oxidation processes, [104, 105] which, when monitored by IR spectroelectrochemistry, reveal the same pattern of behaviour for the metal-coordinated ν(C≡C) bands as described above for **16**. However, the spectator bands associated with the C≡CH moiety in the 5-position of the bridging phenylene ring in **18** are virtually unperturbed by the changes in redox state of the molecule, as would be reasonably expected for a probe group located *meta* to the redox-active substituent.

Electronic spectroscopy provides another view of the electronic structures of **16** and **17**, and their redox products. The UV-vis-NIR spectra of the homo-valent,

bimetallic complexes **16** and **17** are dominated by broad, relatively high-energy, absorption bands that are likely a combination of π-π* transitions associated with the diethynylbenzene moiety, and "MLCT" bands comparable to those observed in **6** and **15**. In the most general terms, the electronic spectra of localised mixed valence compounds $\{L_nM^+\}$-B-$\{ML_n\}$ such as $[\mathbf{16}]^+$ and $[\mathbf{17}]^+$ are expected to contain a unique intervalence charge transfer band which is not found in the spectra of the associated homovalent states, or mononuclear models of the constituent fragments.[22] In the case of mixed-valence $d\pi^5/d\pi^6$ complexes, Meyer has noted that the low energy region of the electronic spectrum can feature a five-band pattern arising from a combination of IVCT transitions and interconfigurational (dd) transitions, which gains in intensity in examples featuring low local symmetry and heavier metal centres.[23, 24]

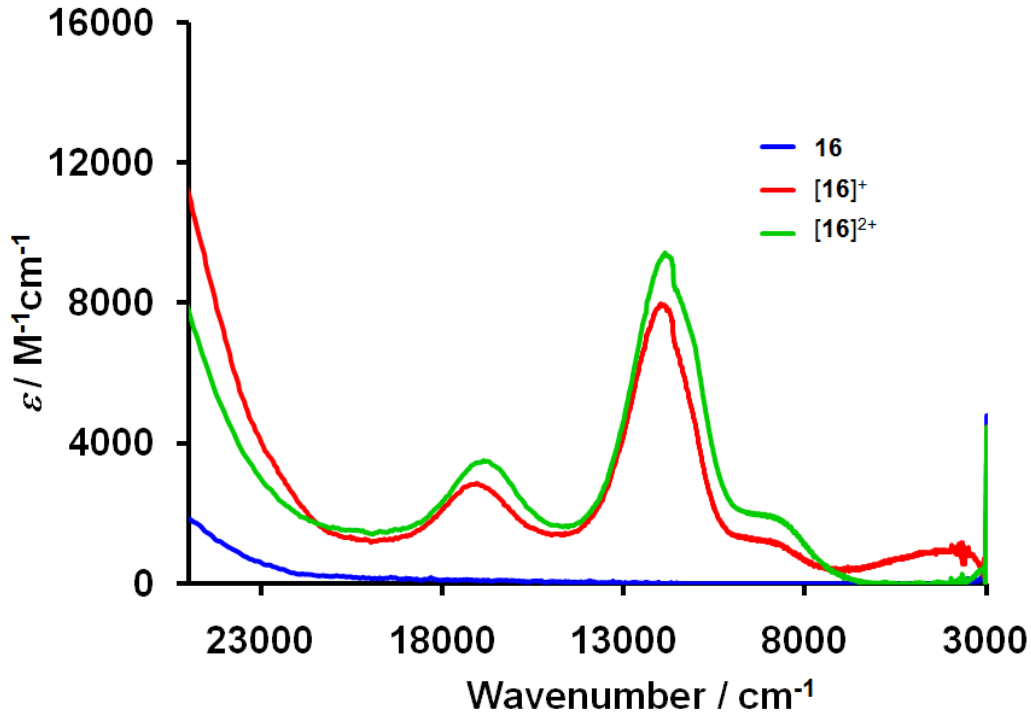

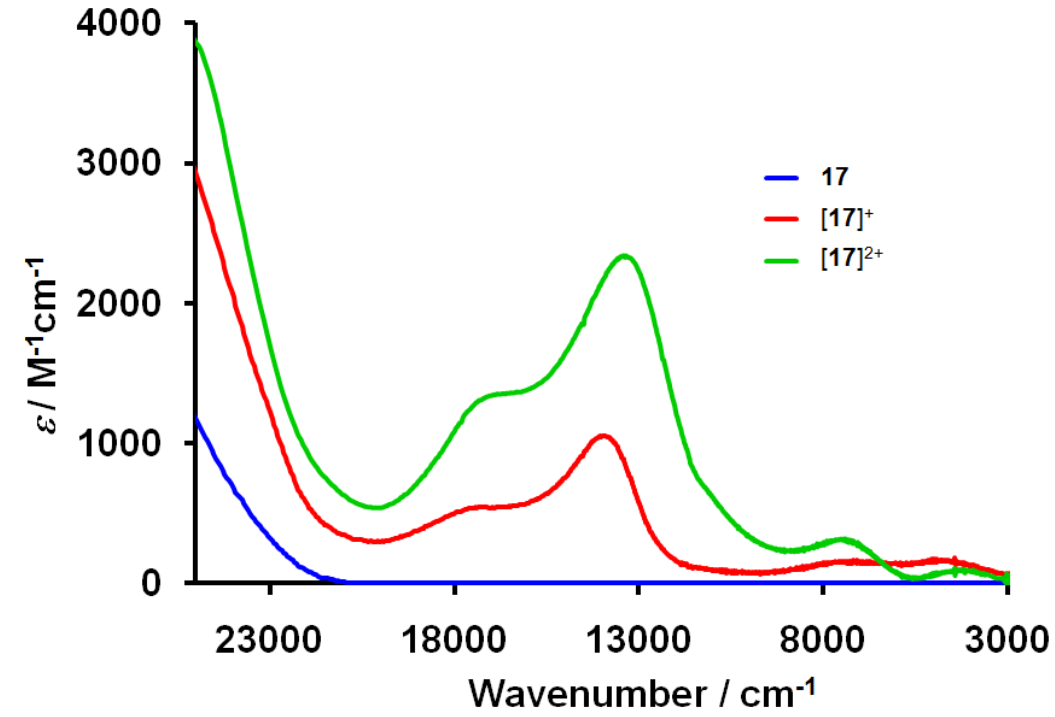

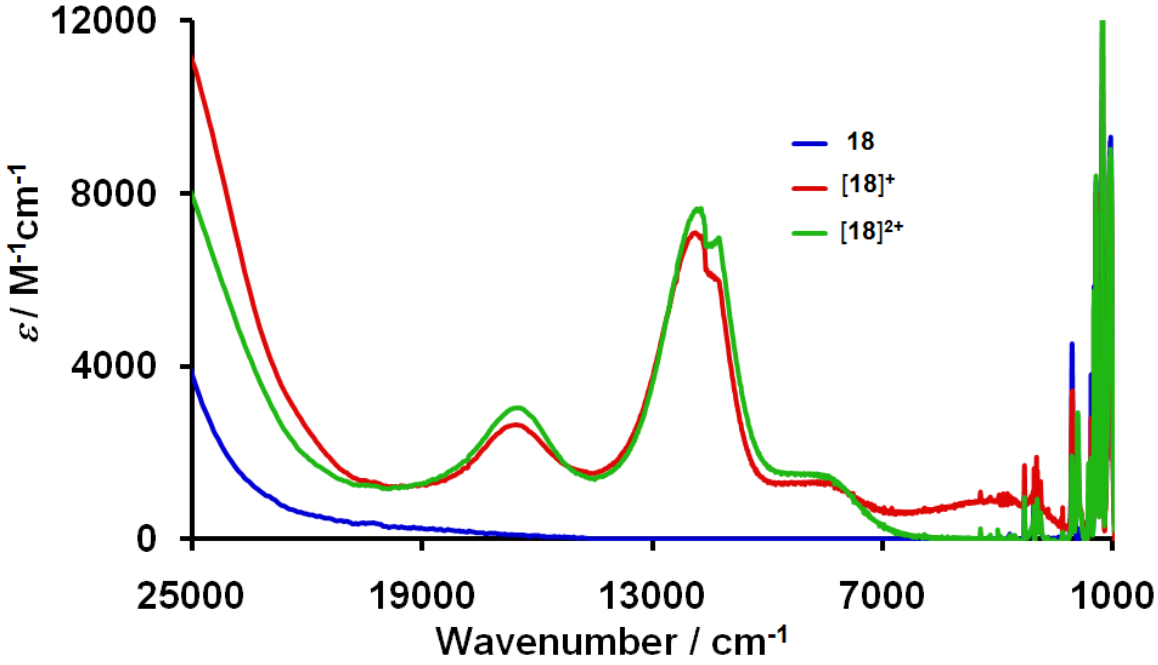

Figure **24** The UV-vis-NIR spectra of [**16**]$^{n+}$ (top, THF / 0.1 M [NBu_4]BF_4), [**17**]$^{n+}$ (middle, CH_2Cl_2 / 0.1 M [NBu_4]BF_4) and [**18**]$^{n+}$ (bottom, CH_2Cl_2 / 0.1 M [NBu_4]BF_4).

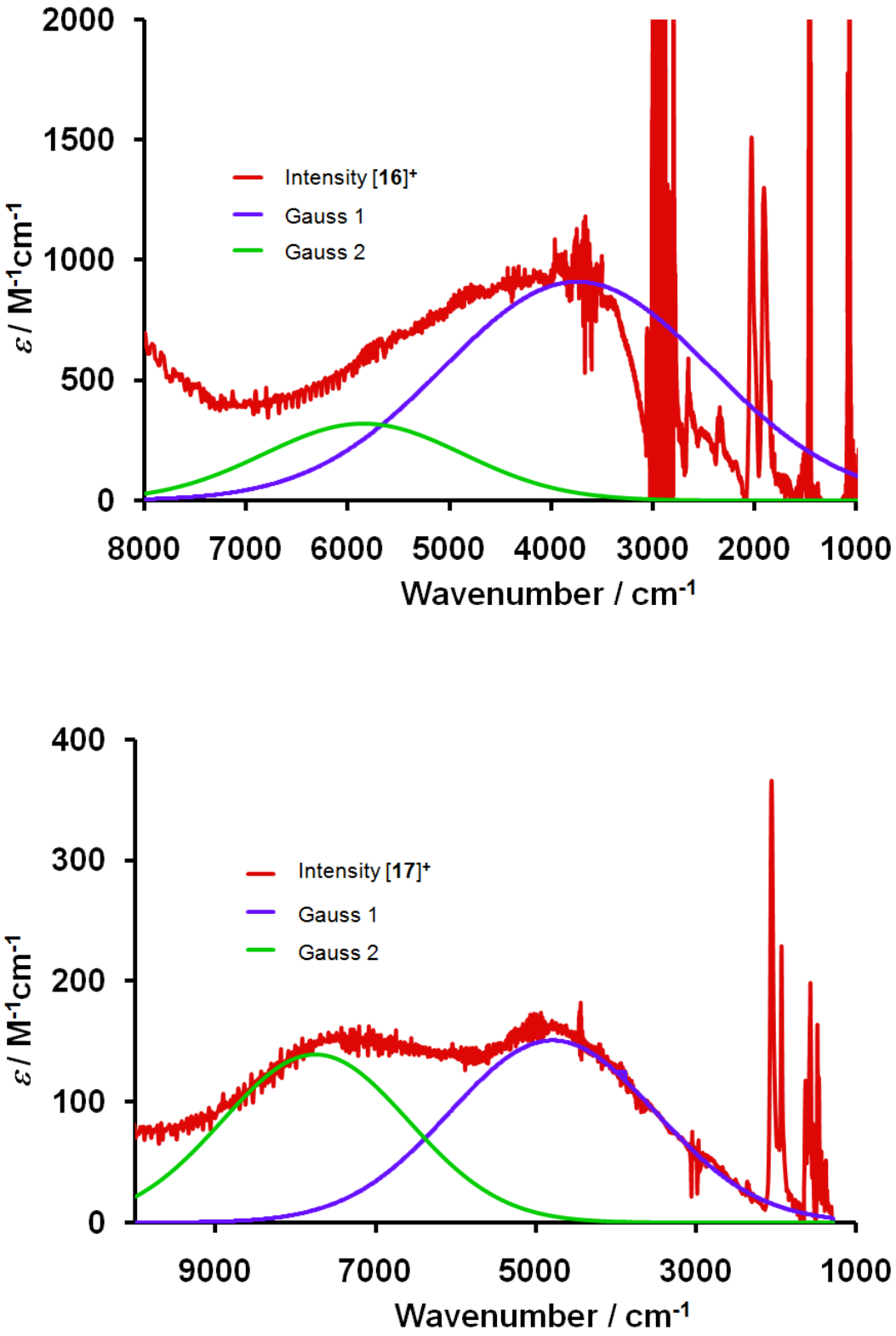

Figure **25** The NIR-IR region of $[\mathbf{16}]^+$ (top, THF / 0.1 M $[NBu_4]BF_4$) and $[\mathbf{17}]^+$ (bottom, CH_2Cl_2 / 0.1 M $[NBu_4]BF_4$, showing the deconvolution into a sum of two Gaussian- shaped absorption bands.

In the visible region, the spectra of the mixed-valence compound [**16**]$^{+}$, the dication [**16**]$^{2+}$ (

Figure **24**) and mono-nuclear [**6**]$^{+}$ (Figure **21**) are similar, each being composed of three main absorption bands (Table **11**). The NIR region of the mixed valence monocation [**16**]$^{+}$ also features a weak absorption envelope, which can be deconvoluted into two Gaussian shaped bands (Figure **25**, Table **11**). The lowest energy edge of the absorption envelope is partially obscured by IR (overtone) bands from the solvent and electrolyte. On the basis of TD-DFT calculations, the lower energy, more intense NIR band is assigned to the "primary" IVCT transition (Figure **25**), whilst the somewhat less intense band is assigned to a pseudo-dd transition. These NIR features collapse on further oxidation of the sample to [**16**]$^{2+}$. The dd bands in this more octahedral system are apparently too weak to be observed or masked by the more intense chloride-to-metal MLCT band. The more soluble compound 1,3-{*trans*-Cl(dppe)$_2$RuC≡C}$_2$-5-(HC≡C)C$_6$H$_3$ **18** was also examined by UV-vis-NIR spectroelectrochemistry, which revealed the same spectral patterns for the oxidised species.

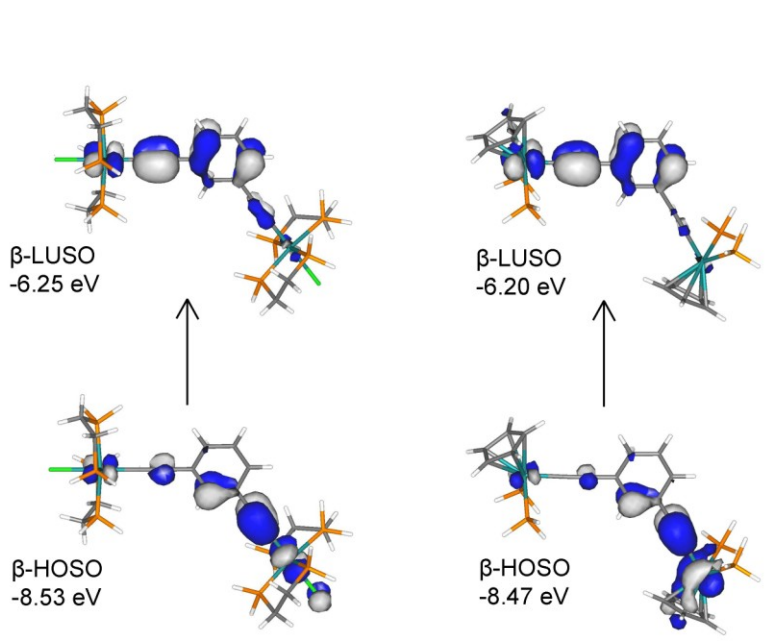

Figure **26** Frontier orbitals of mixed valence model systems [**16-H**]$^{+}$ (left) and [**17-H**]$^{+}$ (right) which are likely to be involved in the low-energy IVCT bands observed experimentally for [**16**]$^{+}$ and [**17**]$^{+}$, on the basis of TD-DFT computations.

The visible absorption spectrum of the half-sandwich complexes $[\mathbf{17}]^{+}$ and $[\mathbf{17}]^{2+}$ feature bands that are only slightly different to those observed for the related mononuclear system $[\mathbf{15}]^{+}$ and the closely related mononuclear complex $[Ru(C{\equiv}CC_6H_4Me\text{-}4)(dppe)Cp^*]^{+}$. [115] The NIR region of $[\mathbf{17}]^{+}$ features two absorption bands. The higher energy band is centred near 7750 cm^{-1} (ε 150 $M^{-1}cm^{-1}$), similar to the β-HOSO→β-LUSO transition in $[\mathbf{15}]^{+}$ [8100 cm^{-1} (ε 600 $M^{-1}cm^{-1}$)], and assigned to a similar pseudo-dd band associated with the formally d^5 metal centre. [115] The lower energy band is unique to the bimetallic mixed valence compound $[\mathbf{17}]^{+}$ and attributed to an IVCT process (
Figure **24**). Oxidation to the dication $[\mathbf{17}]^{2+}$ is accompanied by an increase in the intensity of the "dd" band near 7500 cm^{-1}, collapse of the IVCT band, and growth of a new, very weak transition at ca. 4300 cm^{-1} (ε 90 $M^{-1}cm^{-1}$). This new low energy band is tentatively assigned to a dd transition (which gains intensity as a consequence of the two formally d^5 centres in the dication) or an analogous MMCT transition between the d^5 centres.

The identification of the IVCT band associated with $[\mathbf{16}]^{+}$ and $[\mathbf{17}]^{+}$ permits estimation of the classical coupling parameter H_{ab} based on the relationships originally derived by Hush, provided the electron transfer distance, r_{ab}, is known, or can be estimated. In the absence of data from Stark spectroscopy, the metal-metal separation may be used as an upper limit estimate of r_{ab}. Using the through-space metal-metal distance in the optimised geometries of $[\mathbf{16\text{-}H}]^{+}$ (10.47 Å) and $[\mathbf{17\text{-}H}]^{+}$ (10.44 Å) as r_{ab}, values of H_{ab} for $[\mathbf{16}]^{+}$ and $[\mathbf{17}]^{+}$ are 180 cm^{-1} and 85 cm^{-1}, respectively. However, given the involvement of the bridge in the redox orbitals, the relevance of the two-state model to complexes $[\mathbf{16}]^{+}$ and $[\mathbf{17}]^{+}$ is limited. [234] The molecular orbital representations shown in Figure **26** and Table **13** offer an alternative interpretation of the systems.

3.3 Conclusions

The results described here clearly indicate that the connection of Ru(II) centres through the 1,3-diethynylbenzene core permits formation of thermodynamically stable mono-cations that might be described as valence trapped mixed-valence compounds for convenience. The electronic structures of $[\mathbf{16}]^+$ and $[\mathbf{17}]^+$ have been studied using spectroscopic and computational methods, with the MPW1K functional satisfactorily reproducing the electronic asymmetry observed in solution. The IVCT band has been located for both $[\mathbf{16}]^+$ and $[\mathbf{17}]^+$, with the coupling parameters extracted from a Hush-style analysis (H_{ab} = 180 cm^{-1} and 85 cm^{-1} for $[\mathbf{16}]^+$ and $[\mathbf{17}]^+$ respectively) consistent with the weak coupling indicated by Geiger's charge distribution parameter. However, as with related Ru(II) arylacetylide complexes, there is an important contribution from the ethynyl aromatic π-orbitals to the redox process, which necessitates caution when basing descriptions on concepts of well-defined metal oxidation states. Indeed, the stabilisation of the "mixed-valence" state seems to arise from the delocalisation of the unpaired electron in $[\mathbf{16}]^+$ and $[\mathbf{17}]^+$ between a formally Ru(III) centre, the acetylide moiety and the aromatic ring, rather than from delocalisation of the charge between the two metal centres. The mixing of metal d and acetylide π-type orbitals makes the ν(C≡C) bands a particularly useful diagnostic tool for assessing the degree of (de)localisation in polymetallic Ru(II) acetylide complexes.

3.4 Experimental Details

3.4.1 General Conditions

All reactions were carried out under an atmosphere of nitrogen using standard Schlenk techniques. Reaction solvents were purified and dried using an Innovative Technology SPS-400, and degassed before use. No special precautions were taken to exclude air or moisture during work-up. The compounds RuCl(dppe)Cp*, [234]

cis-$RuCl_2(dppe)_2$ *cis*-**2**, [235] $[RuCl(dppe)_2]OTf$ [**3**]OTf, [129] 1,3-diethynylbenzene, [236] *trans*-$RuCl(C{\equiv}CPh)(dppe)_2$ **6**, [61, 235] $Ru(C{\equiv}CPh)(dppe)Cp^*$ **15** [237] and 1,3-{*trans*-$Cl(dppe)_2RuC{\equiv}C\}_2$-5-$(HC{\equiv}C)C_6H_3$ **18** [105] were prepared by the literature methods. Other reagents were purchased and used as received. $[NBu_4]BF_4$ electrolyte was recrystallized twice and dried overnight under vacuum at 80 ºC before use.

Infrared spectra of the complexes were recorded using a Nicolet Avatar spectrometer from KBr discs. NMR spectra were obtained with Bruker Avance (^1H 400.13 MHz, ^{13}C 100.61 MHz, ^{31}P 161.98 MHz) or Varian Mercury (^{31}P 161.91 MHz) spectrometers from $CDCl_3$ solutions and referenced against solvent resonances (^1H, 7.26 ppm; ^{13}C. 77.0 ppm) or external H_3PO_4 (^{31}P). Mass spectra were recorded using Thermo Quest Finnigan Trace MS-Trace GC, Thermo Electron Finnigan LTQ FT mass spectrometers or Matrix-Assisted Laser Desorption/Ionisation-Time-of-Flight (Mass Spectrometry) (MALDI-TOF MS) ABI Voyager STR.

Cyclic voltammograms were recorded from solutions of approximately 10^{-4} M in analyte in dichloromethane containing 10^{-1} M $[NBu_4]BF_4$ at $\nu = 100$ mV s^{-1} in a gas-tight single-compartment three-electrode cell equipped with platinum disk working (apparent surface area of 0.42 mm^2), coiled platinum wire auxiliary, and platinum wire pseudo-reference electrodes. All redox potentials are reported against the SCE scale, with the decamethylferrocene/decamethylferrocenium (Fc^*H/Fc^*H^+) redox couple used as an internal reference system: –0.07 V vs SCE. [238] Data were collected using a computer-interfaced EcoChemie PGSTAT-30 potentiostat.

IR spectroelectrochemical experiments at room temperature were performed with an air-tight optically transparent thin-layer electrochemical (OTTLE) cell equipped with a Pt minigrid working electrode (32 wires cm^{-1}) and CaF_2 windows. [239] The cell was positioned in the sample compartment of a Nicolet Avatar FT-IR spectrometer (1 cm^{-1} spectral resolution, 16 scans). The controlled-potential electrolyses were carried out with a home-built potentiostat in THF **16** or CH_2Cl_2 (**6** - **18**) solutions that were 0.1 M in supporting electrolyte ($[NBu_4]BF_4$).

3.4.1.1 Preparation of 1,3-{trans-Cl(dppe)$_2$RuC≡C}$_2$C$_6$H$_4$ [16]

Method A

A mixture of *cis*-[RuCl$_2$(dppe)$_2$] *cis*-**2** (970 mg, 1.00 mmol), 1,3-diethynylbenzene (50.3 mg, 0.399 mmol) and $NaPF_6$ (180 mg, 1.07 mmol) in CH_2Cl_2 (40 mL) was stirred at room temperature overnight. The solvent volume was reduced and the mixture filtered into a large excess of rapidly stirred diethyl ether. The precipitated vinylidene complex was collected and dissolved in CH_2Cl_2. Triethylamine was added, and the solvent removed on the rotary evaporator. The residue was redissolved in CH_2Cl_2 and loaded on a pad of basic alumina. Elution with CH_2Cl_2 afforded a yellow fraction that was concentrated, and then filtered into rapidly stirred petrol, affording the product as a yellow powder, which was collected, washed with petrol, and dried. Yield 209 mg (26%).

Method B

A mixture of [RuCl(dppe)$_2$]OTf [**3**]OTf (388 mg, 0.36 mmol) and 1,3-diethynylbenzene (21 mg, 0.167 mmol) in CH_2Cl_2 (14 mL) was stirred at room temperature overnight. The solvent was removed *in vacuo* and the residue was washed with hexanes. The residual red solid was redissolved in CH_2Cl_2 (5 mL) and triethylamine (0.5 mL) was added, causing an immediate lightening of the solution to a yellow colour. The solvent was removed *in vacuo*, and the pale residue redissolved in $CHCl_3$ (4 mL). Addition of methanol (25 mL) gave a sandy yellow solid, which was collected by filtration, washed with hexanes and dried *in vacuo*. Yield 273 mg (82%).

IR(CH_2Cl_2 / cm^{-1}): ν(C≡C) 2063(s). ^{1}H NMR ($CDCl_3$, 400 MHz): δ_H 2.66 (m, 8H, CH_2), 2.76 (m, 8H, CH_2), 6.48 (d, 2H, $H_{4,6}$ of C_6H_4), 6.71 (s, 1H, H_2 of C_6H_4), 6.96 (t, 1H, H_5 of C_6H_4), 6.96 (m, 32H, CH dppe), 7.07 (m, 32H, CH dppe), 7.71 (m, 16H, Ph H_o). ^{31}P{^{1}H} NMR ($CDCl_3$, 81 MHz): δ 51.2 (s, dppe). ^{13}C{^{1}H} NMR ($CDCl_3$, 126 MHz): δ_C 30.9 (m, CH_2), 114.9 (s, C≡*C*C$_6$H$_4$), 126.8, 127.2 ($C_{m,m'}$ dppe); 128.5, 128.9 ($C_{p,p'}$ dppe); 134.1, 134.5 (dds, $J_{CP/CCP}$ ~ 5 Hz, $C_{o,o'}$); 135.2,

137.1 (m, $C_{i,i'}$). Other expected peaks were not observed due to poor solubility. ES(+)-MS (*m/z*): 1990, M^+.

3.4.1.2 Preparation of 1,3-{Cp*(dppe)RuC≡C}$_2$C$_6$H$_4$ [17]

A mixture of RuCl(dppe)Cp* (210 mg, 0.31 mmol) and NH_4PF_6 (75 mg, 0.45 mmol) was heated at reflux in dry degassed MeOH (15 ml) for 20 min to form an orange suspension. After cooling, 1,3-diethynylbenzene (22 μL, 0.15 mmol) was added to the reaction vessel and the solution stirred for 5 min. The reaction mixture was filtered under nitrogen and a solution of NaOMe (made from Na metal dissolved in MeOH) was added to the red solution. The yellow precipitate formed was filtered and washed with hexane. Yield (150 mg, 72 %). IR(CH_2Cl_2 / cm^{-1}): ν(C≡C) 2062(s). ^{1}H NMR ($CDCl_3$, 400 MHz): δ_H 1.54 (s, 30H, Cp*); 2.05 (m, 4H, CH_2); 2.70 (m, 4H, CH_2); 6.35 (dd, 2H, J_{HH} = 8 and 2 Hz, $H_{4,6}$ of C_6H_4), 6.67 (t, 1H, J_{HH} = 2 Hz, H_2 of C_6H_4), 6.70 (t, 1H, J_{HH} = 8 Hz, H_5 of C_6H_4), 7.17 (m, 8H, CH dppe), 7.27 (m, 24H, CH dppe), 7.75 (m, 8H, Ph H_o). ^{31}P{^{1}H} NMR ($CDCl_3$, 81 MHz): δ 82.1 (s, dppe). ^{13}C{^{1}H} NMR ($CDCl_3$, 126 MHz): δ_C 10.0 (s, $C_5\mathit{Me}_5$), 29.5 (m, CH_2), 92.4 (s, C_5Me_5), 109.8 (s, C≡$\mathit{C}C_6H_4$), 125.1 (t, J_{CP} = 23 Hz, RuC), 125.4 ($C_{4,6}$ of C_6H_4), 126.6 (C_5 of C_6H_4), 127.0, 127.3 ($C_{m,m'}$); 128.7 ($C_{p,p'}$); 130.4 ($C_{1,3}$ of C_6H_4); 131.9 (C_2 of C_6H_4); 133.0, 133.5 (dds, $J_{CP/CCP}$ ~ 5 Hz, $C_{o,o'}$); 137.0, 139.0 (m, $C_{i,i'}$). ES(+)-MS (*m/z*): 1394, $[M+H]^+$.

3.4.1.3 Preparation of 1,3-{Cp*(dppe)RuC≡C}$_2$-5-(HC≡C)C$_6$H$_3$ [18]

[**18**] was prepared by literature methods. [105]

^{1}H NMR ($CDCl_3$, 400 MHz): δ_H 2.65 (m, 8H, CH_2); 2.74 (m, 8H, CH_2); 3.02 (s, 1H, C≡CH), 6.44 (s, 2H, $H_{4,6}$ of C_6H_3), 6.58 (s, 1H, H_2 of C_6H_3), 6.94 (m, 32H, CH dppe), 7.11 (m, 32H, CH dppe), 7.59 (m, 16H, Ph H_o). ^{31}P{^{1}H2 NMR ($CDCl_3$, 81 MHz): δ 51.1 (s, dppe). ^{13}C{^{1}H} NMR ($CDCl_3$, 126 MHz): δ_C 30.7 (m, CH_2), 75.0 (C≡CH), 84.9 (C≡CH), 113.7 (RuC≡$\mathit{C}C_6H_3$), 120.3 (C_5 of C_6H_3), 124.0 (t, J_{CP} = 15 Hz, RuC), 126.8, 127.2 ($C_{m,m'}$ dppe); 128.6, 128.8 ($C_{p,p'}$ dppe); 129.6 ($C_{1,3}$ of C_6H_3), 129.6 (C_2 of C_6H_3), 129.9 ($C_{4,6}$ of C_6H_3), 134.2 ($C_{o,o'}$); 135.2, 136.8 (m, $C_{i,i'}$).

3.4.2 Computations

All *ab initio* computations were carried out with the Gaussian 03 package. [240] The model geometries of the mononuclear [**6-H**]$^{n+}$ and [**15-H**]$^{n+}$ (n = 0, 1), and dinuclear systems [**16-H**]$^{n+}$ and [**17-H**]$^{n+}$ (n = 0, 1, 2) discussed here were optimised using the MPW1K/3-21G* level of theory with no symmetry constraints. [228, 241-243] This MPW1K/3-21G* level of theory proved to be suitable for ruthenium complexes elsewhere. [43,229] The keywords used in Gaussian03 for the MPW1K functional [228, 241] here are MPWPW91 and iop(3/76=0472005280). Frequency calculations were computed on these optimised geometries at the corresponding levels and no imaginary frequencies were found in these geometries unless otherwise stated. A scaling factor of 0.89 was applied to the calculated frequencies, as it is known that DFT calculations over estimate the acetylide ν(C≡C) and acetylide ring substituent ν(C=C) frequencies. [244, 245] TD-DFT computations carried out on the model geometries gave complex data with heavily mixed transitions. However, the two lowest-energy transitions for the mixed valence cations [**16-H**]$^{+}$ and [**17-H**]$^{+}$ are clearly IVCT and dd transitions, attributable to a charge transfer process from a metal-acetylide donor to a metal-phenylacetylide acceptor. The MO diagrams and orbital contributions were generated with the aid of GaussView [246] and GaussSum [247] packages respectively.

Chapter 4 : Hydroruthenation – Mono and Multi-metallated Compounds

4.1 Introduction

In seeking to better understand the electronic structure of redox families derived from $[L_nM]$-bridge-$[ML_n]$ systems there is considerable advantage in the use of spectroscopic techniques that are sensitive to the formal redox state of the ML_n fragments and / or the electron density residing on the bridge. The use of IR spectroelectrochemical methods to follow the shift in ν(C≡C) bands in 1,3-{*trans*-$Cl(dppe)_2RuC{\equiv}C\}_2C_6H_4$ **16**, 1,3-{$Cp^*(dppe)RuC{\equiv}C\}_2C_6H_4$ **17** and 1,3-{*trans*-$Cl(dppe)_2RuC{\equiv}C\}_2$-5-$(HC{\equiv}C)C_6H_3$ **18** as a function of redox state illustrates this point (Chapter **3**). Since there is little back-bonding between the metal centre and the acetylide fragment, the large shifts in acetylide ν(C≡C) frequency upon oxidation of **16**, **17** and **18** clearly indicate that the oxidation event involves considerable acetylide ligand character.

The use of "spectator" vibrational groups to report on electronic structure within a redox family has developed rapidly over the last few years. [41-43, 59, 248-251] The fast time-scale of vibrational spectroscopy (ca. 10^{-13} s) permits study of all but the fastest of electron transfer events. In addition, since vibrational frequencies can be readily extracted from computational models, experimental vibrational data provide a convenient direct link between an optimized geometry and the experimental system, albeit with some need for empirical correction. [244, 245] For example, Kubiak has used the ν(C≡O) band in a series of ligand bridged bis(cluster) compounds $[\{Ru_3(\mu_3\text{-}O)(\mu\text{-}OAc)_6(CO)(L)\}_2(\mu\text{-}BL)]^-$ (L = 2-electron donor ligand, BL = bridging ligand, see Chart **2**) to follow the rate of electron-exchange between the cluster redox sites as a function of the bridge structure, [31, 39] or solvation environment. [40]

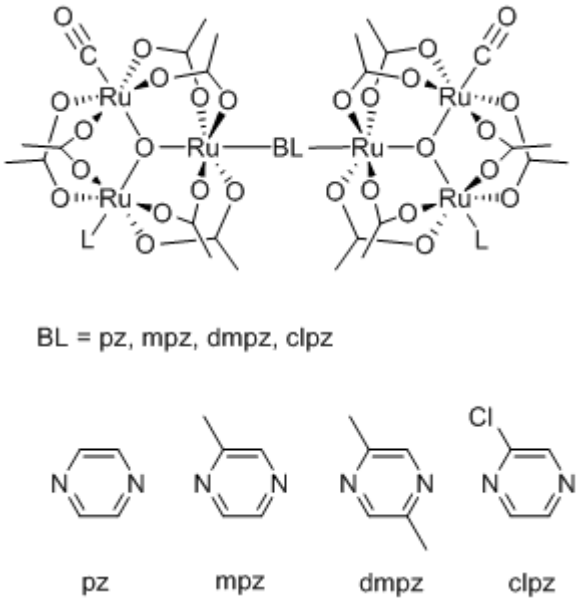

Chart **2** Kubiak bis(cluster) compounds. [31]

With many studies of bimetallic, acetylide-bridged metal complexes having been completed over the last 10 years or so, attention was directed to alternative ligand structures and metal fragments that directly incorporated an IR active reporting group. The assembly of ruthenium complexes featuring both a metal-bound carbonyl and a conjugated organic ligand can be conveniently achieved through the hydroruthenation of an alkyne with $RuHCl(CO)(PPh_3)_3$ (**19**). [252-257] The first step in this reaction is dissociation of a labile phosphine ligand due to a high *trans* effect of a hydride ligand, which leads to the formation of a five coordinate ruthenium hydride complex (Scheme **7**). The five coordinate species is susceptible to attack by the alkyne in a π-donor fashion and subsequently the C≡C bond is reduced by a regioselective addition of Ru-H. This five coordinate ruthenium vinyl species can then be isolated, [252, 253, 258, 259] or used *in situ* as a precursor to a wide range of complexes through ligand substitution reactions. [260-267]

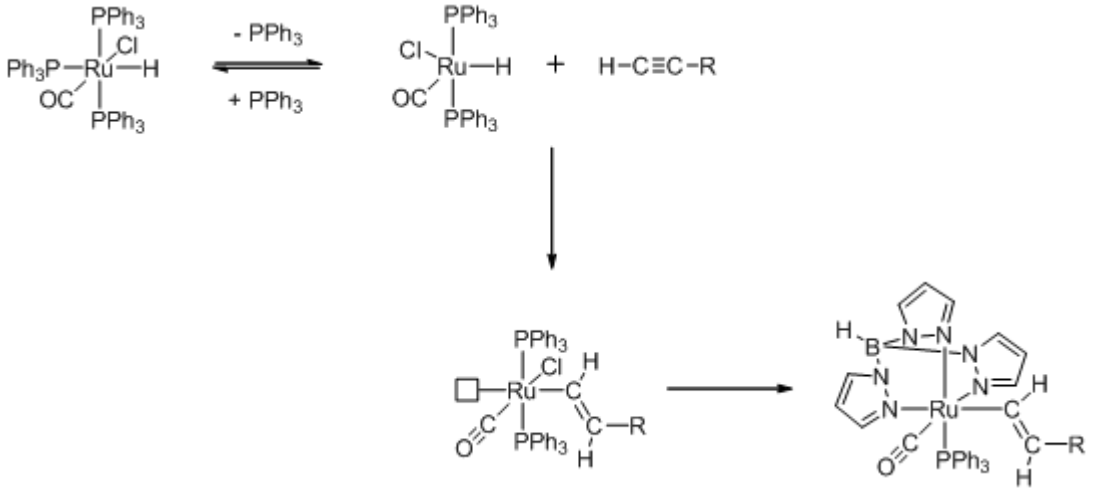

Scheme **7** Hydroruthenation reaction scheme.

However whilst the addition of M-H across a C≡C bond of a terminal alkyne is simple conceptually, there seems to be some detail lacking in the mechanism of this reaction. Some researchers have proposed that the reaction occurs by "addition of the alkyne to the metal centre, followed by rapid migration of the hydride from the metal to the carbon atom", [268] and also calling this reaction an "unexpected insertion".[269] However this reaction mechanism should also apply to alkenes, but these only form the metal adducts, rarely forming the alkyl product. [270, 271]

With the structure of the metal reactant being square pyramidal with an apical hydride, the LUMO is directed away from the hydride (Scheme **8**). Hence the adduct of any unsaturated ligand would be stereochemically unsuitable towards easy H transfer to the carbon. [272]

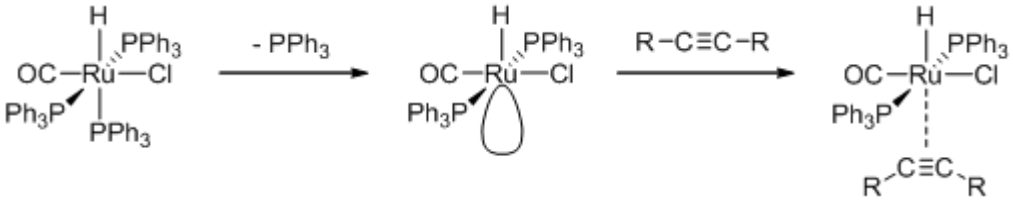

Scheme **8** One proposed model for the first steps of the hydroruthenation reaction. [272]

Alternative possible mechanisms have been proposed, [272, 273] including the formation of the vinyl product by bimolecular attack of the alkyne at the metal centre in the H-M-Cl quadrant (Scheme **9**). [272]

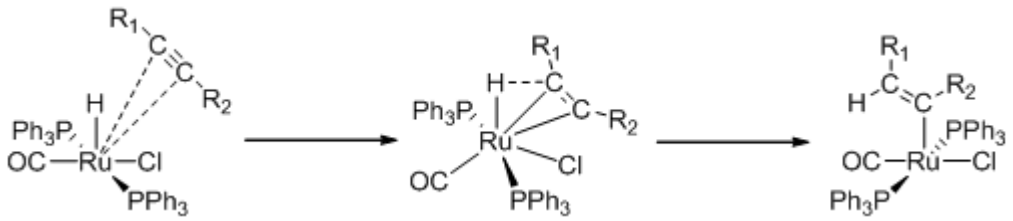

Scheme **9** Alkyne attack to the metal centre in the H-M-Cl quadrant. [272]

Regardless of the precise detail of the reaction mechanism, the hydroruthenation reaction is well suited to the conversion of alkynes to metal vinyl complexes. Jia has been very successful in building a series of metal-capped polyacetylene derivatives through the reaction of $RuHCl(CO)(PPh_3)_3$ with a series of bis(alkynes) $HC{\equiv}C(CH{=}CH)_nC{\equiv}CH$ (Scheme **10**). [159, 160, 162, 274] A rich variety of complexes are then accessible through facile ligand exchange reactions with the $Ru(vinyl)(CO)(PPh_3)_2$ fragment.

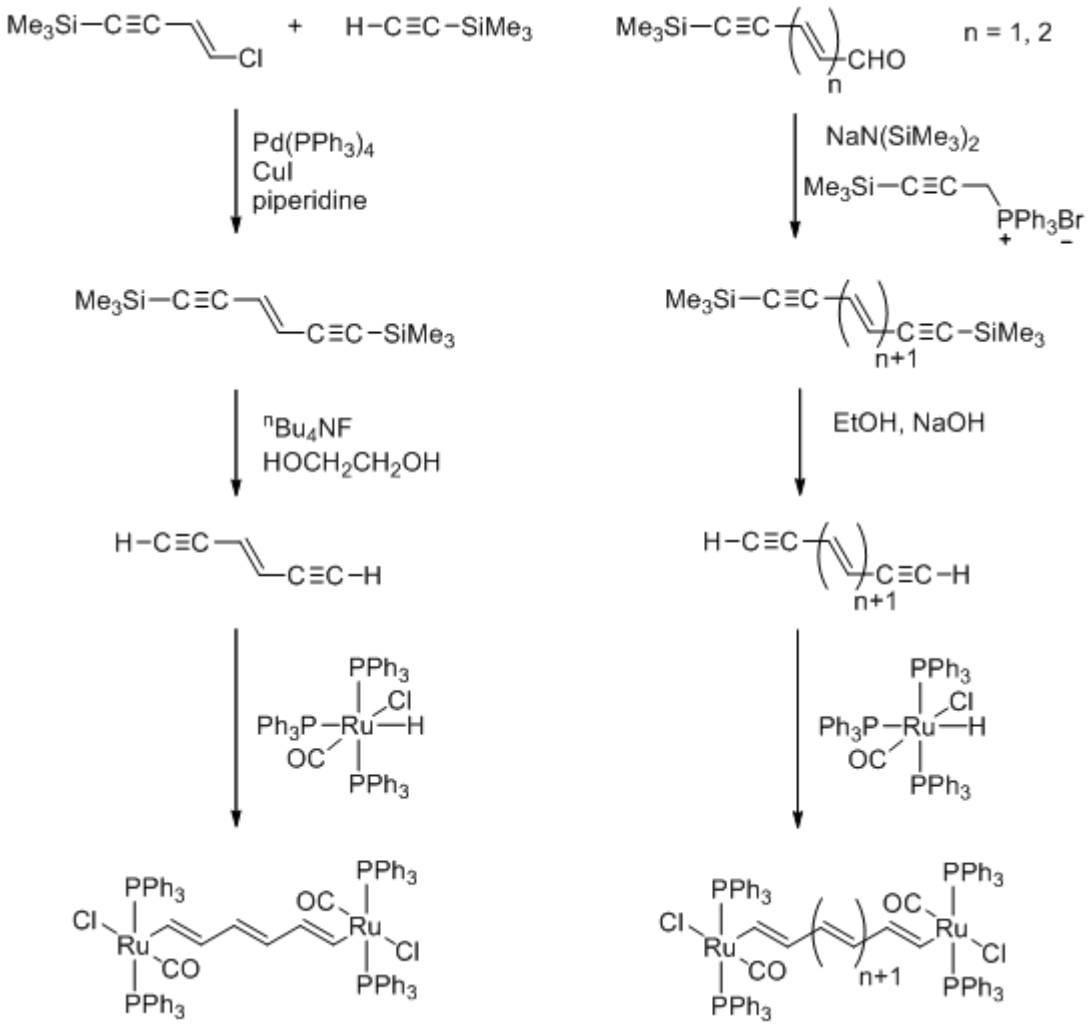

Scheme **10** Syntheses of a selection of bimetallated polyacetylene derivatives. [159, 160, 162, 274]

In a very clever variation, the polyacetylene chain has also been built through extension of the somewhat exotic Wittig reagent $[Ru(CH{=}CHCH_2PPh_3)(CO)(PPh_3)Tp]BF_4$ upon reaction with the hindered base $LiN(SiMe_3)_2$ and benzaldehyde (Scheme **11**). [161]

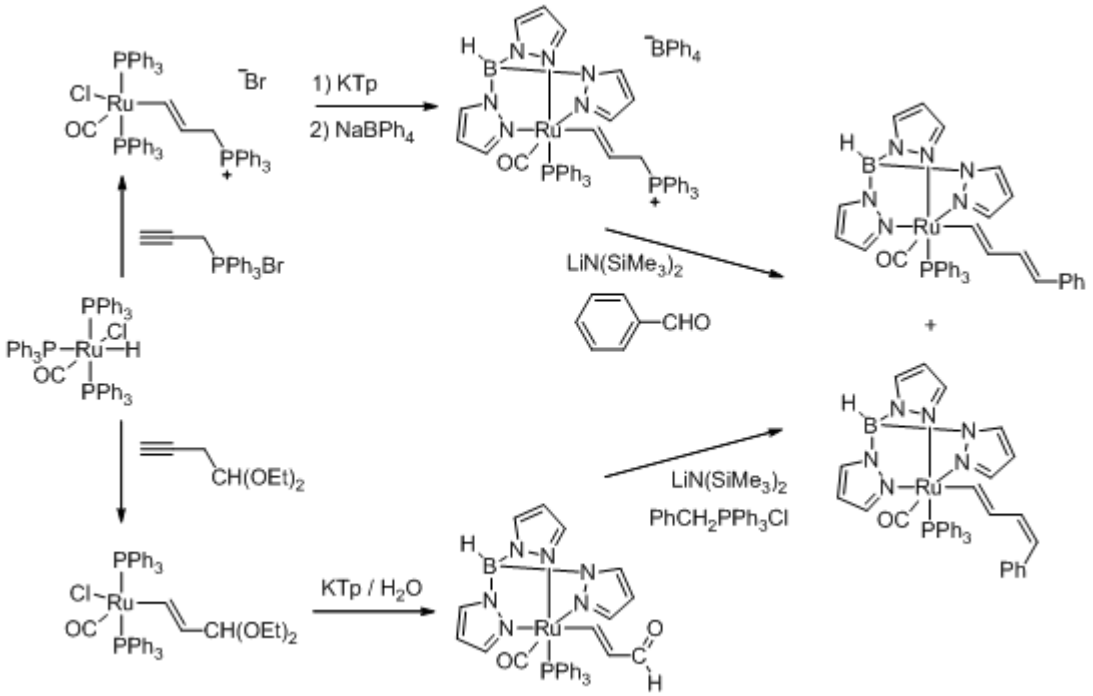

Scheme **11** Extension of the vinyl fragment, through the use of Wittig reactions. [161]

Similar strategies have also been used to prepare mixed ruthenium / ferrocene capped polyacetylene fragments (Scheme **12**). [163] However, detailed investigations of the electronic structure of these complexes and their redox products have not been forthcoming, with discussions largely limited to analyses of electrochemical data.

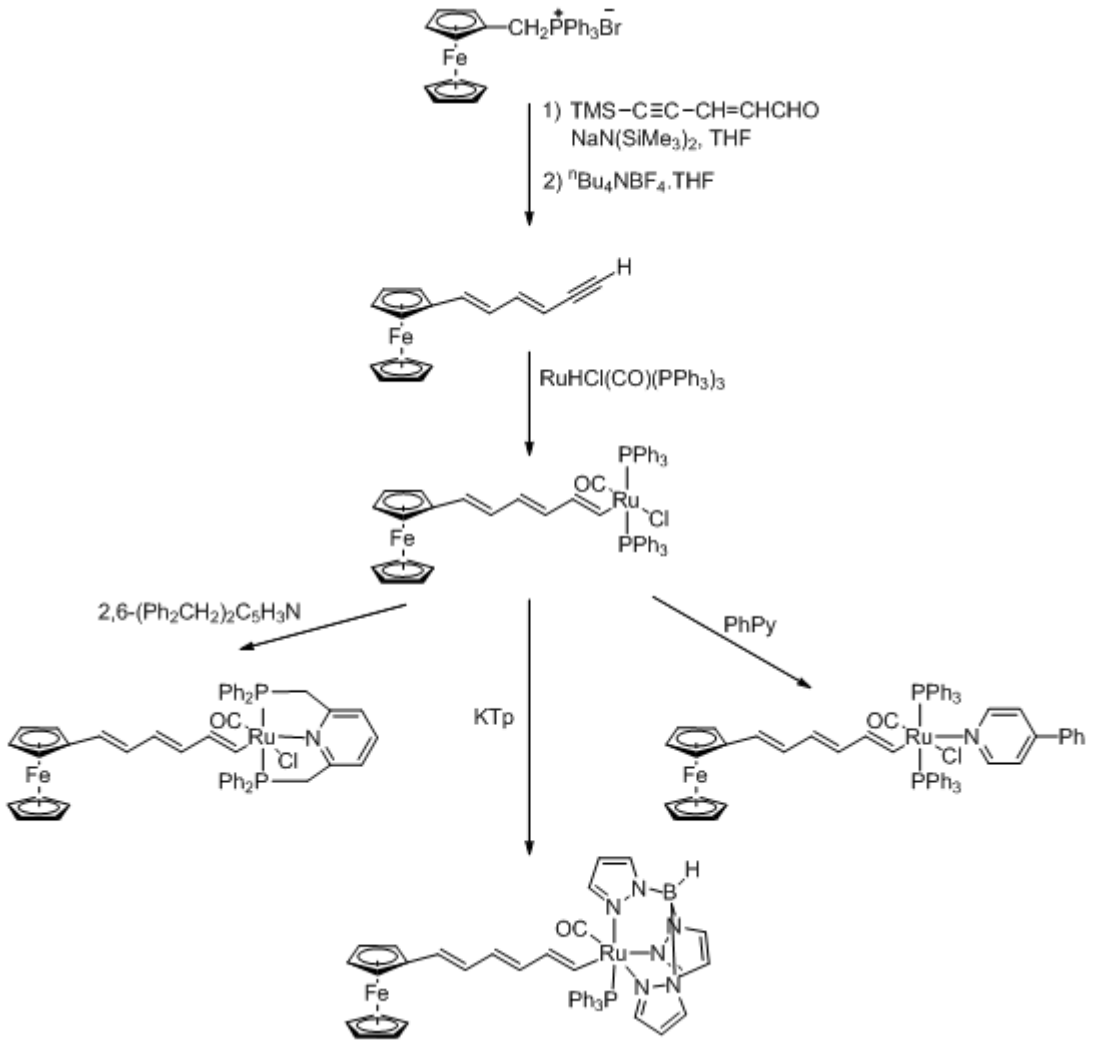

Scheme **12** Synthesis of Ruthenium / Ferrocene capped polyacetylene complexes. [163]

In a series of elegant studies reported during the course of the work that forms this thesis, Winter demonstrated the use of both metal carbonyl and supporting ligand vibrational bands in assessing the site of oxidation in bis(vinyl) complexes such as 1,4-[{RuCl(CO)(P^iPr_3)$_2$}$_2$(μ-CH=CHC_6H_4CH=CH)], 1,3-[{RuCl(CO)(P^iPr_3)$_2$}$_2$(μ-CH=CHC_6H_4CH=CH)], [42] and the ethyl isonicotinate adduct 1,4- and 1,3-[{RuCl(CO)(PPh_3)$_2$($NC_6H_4CO_2Et$)}$_2$(μ-CH=CHC_6H_4CH=CH)] (**20** and **21**) (Chart **3**). [41] In the Winter work , the small shifts in both ν(C≡O) (+13 cm^{-1} and +33 cm^{-1} for [**20**]$^+$ and [**20**]$^{2+}$, respectively) and ν(C=O, ester) (+2 cm^{-1} and +11 cm^{-1} for [**20**]$^+$ and [**20**]$^{2+}$, respectively), demonstrated the bridging ligand to be largely the redox active site in these molecules. Oxidation of **21**, gives very similar small shifts in both ν(C≡O) and ν(C=O, ester) to **20**, with the exception of the mixed-valence

[**21**]$^{+}$, where the ν(C≡O) splits, indicating a partial charge localisation on one of the styrylruthenium fragments.

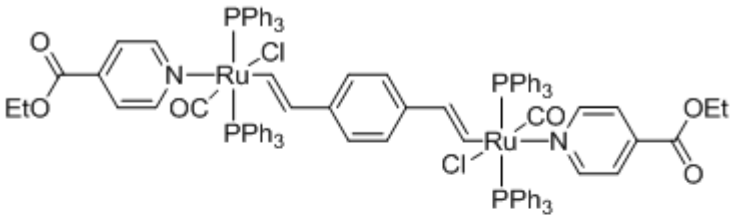

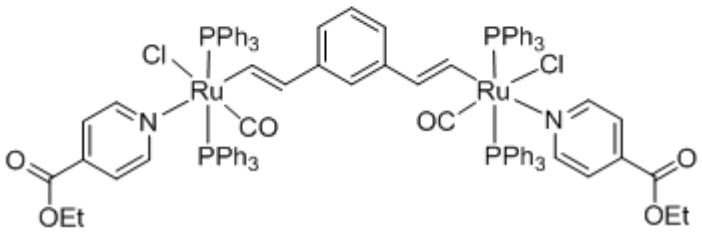

Chart **3** Isonicotinate ester capped 1,4- and 1,3-divinylbenzene complexes (**20** and **21**). [42]

Other spectroscopic methods, such as that from EPR spectroscopy, were consistent with these findings, although it is important to bear in mind that each spectroscopic method has a different timescale. [248-250] Extension of this work to the tetrametallic complex [{RuCl(CO)(P^iPr_3)$_2$}$_4${μ_4-(CH=CHC_6H_4)$_4$(CH=CH)}] (**22**) (Scheme **13**) has also been undertaken, with the tetraphenylethene core being shown to be the redox active portion of the molecule. [59]

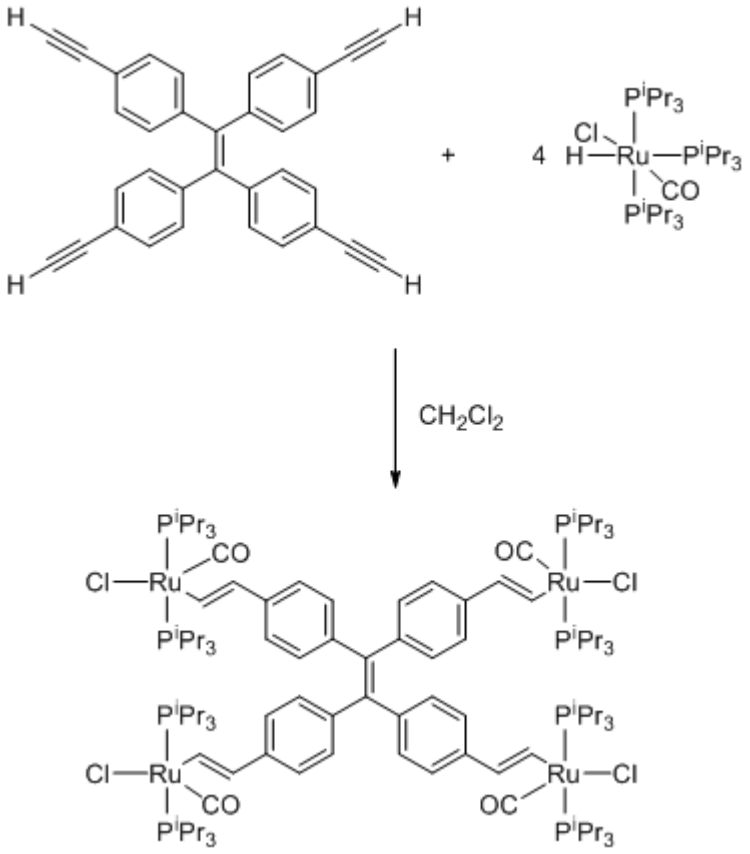

Scheme **13** Tetra- hydroruthenation of tetraphenylethene to form **22**. [59]

However, not all studies on related systems are so thorough. In the case of a series of complexes with general form 1,4-[{RuCl(CO)(PMe_3)$_3$}$_2$(μ-CH=CHC$_6$H$_2$R$_2$CH=CH)], electrochemical studies revealed two one electron oxidation waves, the separation of which was sensitive to the nature of the substituents on the aryl group of the bridging ligand. On the assumption that the redox events were metal centred, the authors interpreted their electrochemical data in terms of the degree of electronic interaction between the metal centres. If one considers that the first oxidation processes are likely to be rather more ligand in character, the flaws in reliance upon electrochemical data in isolation are obvious. [275]

In this Chapter the complexes [Ru(CH=CHC$_6$H$_4$R-4)(CO)(PPh_3)Tp] [Tp$^-$ = hydrido(trispyrazolyl)borate anion, [BHpz$_3$]$^-$] have been prepared and characterized. The electronic structure of [Ru(CH=CHC$_6$H$_4$R-4)(CO)(PPh_3)Tp]$^{n+}$ (n = 0, 1) have been studied by spectroelectrochemical methods supported by DFT calculations.

Extension of the work to ligands derived from 1,4-diethynyl, 1,3-diethynyl and 1,3,5-triethynyl benzene has allowed questions of ligand mediated electron transfer in bi- and tri-metallic di- and tri- vinyl bridged complexes to be investigated in detail.

The choice of the Tp^- ligand was inspired by the analogy with the anionic cyclopentadienyl ligand that has been used to support many half-sandwich ruthenium acetylide complexes. [276] The Cp^- and Tp^- ligands are isoelectronic, six electron donors, which are likely to coordinate in a tridentate manner, and lead to similar chemistry. [277, 278] For example, typical reactions in complexes such as $RuCl(PPh_3)_2Cp$ which contain the cyclopentadienyl ligand include phosphine dissociation, which occurs in non-polar solvents, and chloride ionisation and dissociation in polar solvents. [276] Similar characteristics are also prominent in the chemistry of $RuCl(PPh_3)_2Tp$. [279] KTp is a commercially available, air-stable solid. Consequently, [Ru(CR=CHR')(CO)(PPh_3)Tp] complexes are more readily available than the isoelectronic Cp analogues, [266] and were chosen as the entry point to studies of the electrochemical properties and electronic structure of ruthenium vinyl complexes.

The addition of Tp^- to five coordinate complexes of the form $MHCl(CO)(PR_3)_2$ (M = Ru / Os) has been shown to be a two step process where first, the incoming Tp^- ligand displaces the Cl^- ligand, with one further pyrazolyl ring coordinating to the vacant coordination site *trans*- to the hydride. The second step is the coordination of the third pyrazolyl ring which displaces one of the two phosphines. (Scheme **14**) Reaction conditions and other factors determine whether or not the η^2-Tp coordinated complexes can be isolated. [280, 281] Similar processes are likely in the substitution reactions of vinyl complexes described below.

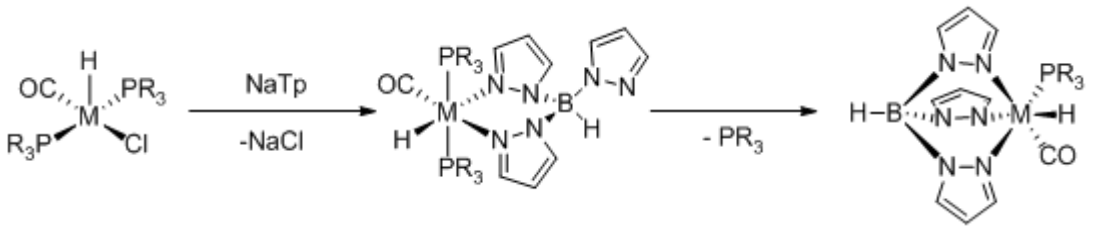

Scheme **14** Addition of Tp^- ligand to a metal hydride complex. [280]

4.2 Mono-Hydroruthenated Acetylene Complexes

4.2.1 Results and Discussion

On addition of each of the acetylenes $HC{\equiv}CC_6H_4R$-4 (R = CH_3, CN, NO_2, CO_2Me, OMe) to $RuHCl(CO)(PPh_3)_3$ in CH_2Cl_2, there is an instant colour change in the solution from a pale yellow to a deep red, with *in situ* monitoring of the reaction by IR or ^{31}P NMR spectroscopy indicating the rapid formation of $Ru(CH{=}CHC_6H_4R$-4$)Cl(CO)(PPh_3)_2$. The addition of KTp to these solutions of $Ru(CH{=}CHC_6H_4R$-4$)Cl(CO)(PPh_3)_2$ resulted in a slower ligand substitution reaction, evidenced by a slower colour change over 1 - 3 hours, the precise duration being dependent on the R group attached to the benzene ring, that ultimately afford $Ru(CH{=}CHC_6H_4R$-4$)(CO)(PPh_3)Tp$, [R = CH_3 (**23**) , CN (**24**), NO_2 (**25**), CO_2Me (**26**), OMe (**27**)] (Chart **4**).

For the most part, these reactions were straightforward and gave the vinyl products in moderate yield. Higher yields were obtained when an inert atmosphere was used and reactions performed in a glove box. Isolation of the product was achieved by first removal of precipitated KCl by filtration, followed by precipitation of the complex from CH_2Cl_2 with n-hexane. Purification of this series of complexes was achieved by recrystallisation (slow diffusion) in a suitable solvent system, as the complexes proved sensitive to common chromatography supports. Crystals of a suitable quality for single crystal X-ray diffraction were obtained for **23**, **24**, **25** and **26**.

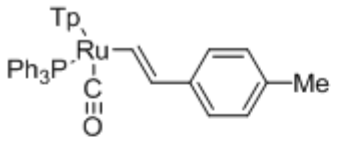

23

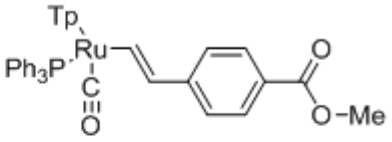

26

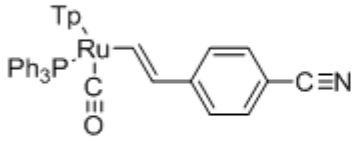

24

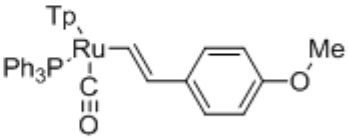

27

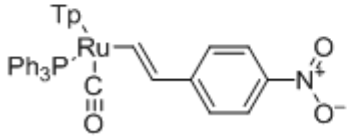

25

Chart **4** The monometallic vinyl complexes used in this study (**23** – **27**).

Curiously, the synthesis of **24** was difficult to reproduce, and the attempted preparation of $Ru(CH{=}CHC_6H_4NMe_2\text{-}4)(CO)(PPh_3)Tp$ was unsuccessful, with a complex mixture of products being observed in the final solution by ^{31}P NMR spectroscopy. In an attempt to elucidate the relative reaction timescales (hydroruthenation vs ligand substitution by Tp^-), but not a full kinetic profile, a 50 mg scale reaction between $RuHCl(CO)(PPh_3)_3$, $HC{\equiv}CC_6H_4NMe_2$ and KTp was followed by ^{31}P NMR spectroscopy. It was hoped that knowledge of the relative rates of the species formed, potentially a mixture of RuHCl(CO)Tp, $Ru(CH{=}CHC_6H_4R\text{-}4)Cl(CO)(PPh_3)_2$ and the desired complex $Ru(CH{=}CHC_6H_4NMe_2\text{-}4)(CO)(PPh_3)Tp$, the reaction conditions could be optimised. However, little could be deduced and this experiment merely provided the confirmation that the slowest step was the capping reaction that converts $Ru(CH{=}CHC_6H_4R\text{-}4)Cl(CO)(PPh_3)_2$ to $Ru(CH{=}CHC_6H_4R\text{-}4)(CO)(PPh_3)Tp$. However, isolation of $Ru(CH{=}CHC_6H_4NMe_2\text{-}4)(CO)(PPh_3)Tp$ from the reaction mixture was not successful.

The synthesis of **24** was only possible once but fortunately a crystal suitable for X-ray crystallographic work was obtained by crystallisation of the crude reaction mixture. However, attempts to repeat this experiment on a larger scale, in order to

complete the characterisation, were unsuccessful. In this particular experiment, the addition of 4-ethynylbenzonitrile to $RuHCl(CO)(PPh_3)_3$ led to the formation of a cloudy yellow suspension almost instantly. This is likely to be due to complications arising from competitive coordination leading to the formation of a polymer, whereby the lone pair on the nitrogen atom of the cyano group coordinates to the vacant site *trans* to the vinyl ligand (Scheme **15**).

On one occasion, addition of KTp to the cloudy suspension lead to the dissolution of the presumed polymer, and the formation of a clear green solution. This contained the "capped" six coordinate ruthenium vinyl complex **24**, which was isolated by crystallisation. The fact that this experiment could not be repeated led to the conclusion that the timescale of each step in the sequence and concentration of the reagents must be considered with the extent to which the formation of the suspected polymer or oligomeric by-products is allowed to take place, and the point in the polymer formation where KTp is added may be significant in determining whether the desired product is formed. However, the general time constraints prevented further examination of this reaction.

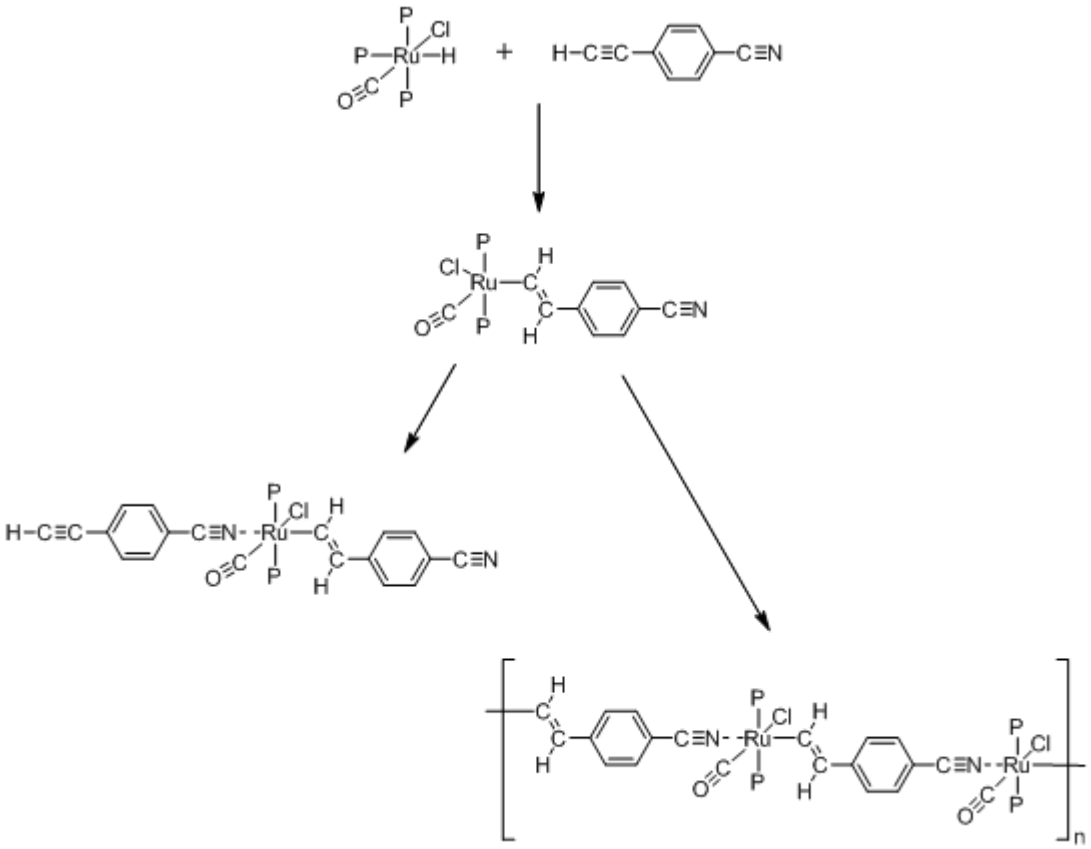

Scheme **15** A schematic showing possible diverse reaction pathways arising from CN coordination to the $RuCl(CO)(PPh_3)_2$ fragment.

The ruthenium centre in **23** - **27** is approximately octahedral, with the Tp ligand occupying three sites in a *fac* configuration with the remaining sites occupied by the vinyl, CO and PPh_3 ligands. The complexes are therefore chiral and both enantiomers (R and S), are formed in the reaction (Scheme **16**). The R and S enantiomeric forms give the same spectroscopic data hence can not be separated or distinguished spectroscopically. Both isomers are, of course, present in the single crystal and observed crystallographically.

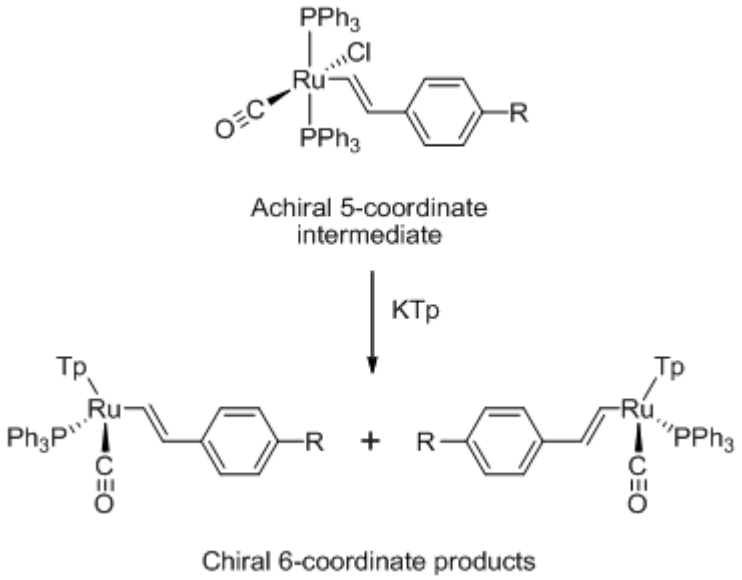

Scheme **16** A schematic showing the two possible enantiomers from the Tp capping step of the reaction.

The six-coordinate complexes **23** – **27** were characterised by the usual spectroscopic and spectrometric (IR, ^{1}H, ^{13}C, ^{31}P NMR, MALDI(+)-MS) methods along with $^{11}B\{^{1}H\}$ NMR. In the IR spectra, the carbonyl ν(C≡O) band was observed between 1940 and 1950 cm^{-1}, the lowest wavenumber bands being associated with **26** and **27**, and the borohydride ν(B-H) band was observed between 2470 and 2490 cm^{-1}, the lowest wavenumber band being associated with **27**. The MALDI (Matrix-Assisted Laser Desorption/Ionization) mass spectra (MALDI(+)-MS) featured the molecular ion. In the ^{31}P NMR spectra, the phosphine ligand gave rise to a single singlet near δ 50 ppm. In the ^{1}H NMR spectra of **23** - **27**, the aromatic protons were often observed as distinctive pseudo-doublet (AB pattern) resonance between δ_H 6.8 – 7.9 ppm.

The vinyl protons in **23 – 27** display the characteristic vinyl coupling patterns, with coupling between the alpha vinyl proton and the phosphorus centre of the phosphine ligand also apparent. The H_α resonance is therefore observed between δ_H 7.8 - 9.1 ppm as a doublet of doublets with coupling of $^{3}J_{HH}$ = 17 Hz and $^{3}J_{HP}$ = 2 Hz. The magnitude of the $^{3}J_{HH}$ coupling is diagnostic of *trans* vinyl Hs. The resonance for the H_β is observed as a doublet ($^{3}J_{HH}$ = 17 Hz), between δ_H 6.3 – 6.6 ppm. The chemical shifts of both of the vinyl proton resonances are sensitive to the electronic

nature of the remote *para*-substituent, the H_α resonances being the more sensitive of the two.

The NMR resonances of the pyrazolyl rings were assigned using the ^1H NMR spectra of potassium tris-pyrazolylhydroborate as reference, and correlation spectroscopy, although a few of the couplings from the aromatic ligands, especially those of the tris-pyrazolylhydroborate, were not fully resolved, with the assignments further aided by NMR simulation software. The free ligand Tp^- exhibits three sets of resonances, each with an integral of 3H. The same pattern is also observed for the Tp^- ligand in the complexes **23** – **27**. The first set of resonances for the coordinated Tp^- are observed at δ_H ~6 ppm, which from the pseudo-triplet arrangement ($^3J_{HH}$ = 2 Hz), are assigned as the 3 H_b protons on the three pyrazolyl rings. The second set are observed as doublets at δ_H ~7 ppm, and the third set of resonances are observed also as doublets at δ_H ~8 ppm. The second and third sets are assigned as the 3 H_c and 3 H_a protons respectively (Figure **27**). Within each set of resonances, there are two resonances close to each other and one a little further away. It is difficult to determine from which of the three pyrazolyl rings each of the three resonances in the sets arise.

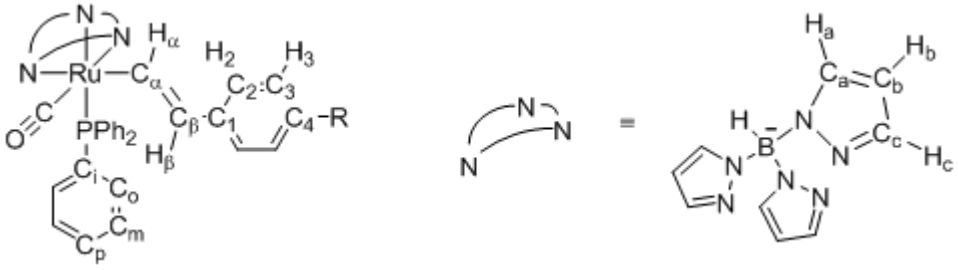

Figure **27** The NMR labelling scheme used in this Chapter.

The hydrido resonance of the Tp^- ligand is heavily broadened by coupling to the ^{11}B nucleus to the extent that it cannot be observed in routine ^1H NMR spectra. However, in a $^1H\{^{11}B\}$ NMR spectrum of **25** the boron-hydride resonance was observed at 4.64 ppm. In complementary fashion, the $^{11}B\{^1H\}$ NMR spectra of **25** shows one boron resonance at -3.8 ppm.

The ^{13}C NMR spectra of **23** – **27** all have a characteristic carbonyl resonance, which can be observed as a doublet ($^{2}J_{CP}$ = 16 Hz) at high frequency (δ_C 200 – 208 ppm), the precise position of which shows some sensitivity to the nature of the R-group, with compound **27** (R = OMe) having the lowest frequency carbonyl resonance (201 ppm). The chemical shift of the vinyl C_α resonances, which were observed as doublets ($^{2}J_{CP}$ ~ 13 Hz), proved to be sensitive to the electronic nature of the remote aryl substituent, varying between δ_C 158 and 180 ppm, where as the vinyl C_β resonances, which were also observed as doublets ($^{3}J_{CP}$ ~ 2 Hz), were located closely around δ_C 135 ppm.

The ^{13}C resonances of the Tp^- ligand were observed in three sets of three slightly different C environments, which are labelled in Figure **27** for clarity. From the NMR labelling scheme (Figure **27**) it can be seen that there are three different carbon environments on each pyrazolyl ring, however each pyrazolyl ring is in a slightly different electronic environment from the other two, i.e. $C_a \neq C_{a'} \neq C_{a''}$. These three sets of resonances, observed at δ_C ~106 ppm, δ_C 135 – 137 ppm and δ_C 142 – 145 ppm, are assigned to the $C_{b/b'/b''}$, the $C_{c/c'/c''}$ and the $C_{a/a'/a''}$ environments respectively. The $C_{c/c'/c''}$ environment set have been assigned to the set of resonances with the widest range of δ_C chemical shift due to the fact that there are closer to the ruthenium centre and hence more likely to be influenced by the electronic density changes at the ruthenium centre caused by the change in the electronic nature of the *para*-substituent. The chemical shifts within each set of resonances follow the same pattern as seen in the ^{1}H NMR spectra, with two resonances occurring at very similar chemical shifts whilst the third is found to slightly higher frequency.

4.2.2 Molecular Structure Analyses

The molecular structures of **23**, **24**, **25** and **26** have been determined by single crystal X-ray diffraction with plots of the molecules shown in Figure **28**, Figure **29**, Figure **30** and Figure **31**, respectively. Crystallographic data, selected bond lengths and angles are listed in Table **14**, Table **15** and Table **16**. The crystallographic work was carried out by Dr D.S. Yufit of Durham University, Chemistry Department.

Table **14** Crystal data and experimental parameters. The molecular structure of **26*** contains a molecule of CH_2Cl_2.

Empirical formula	$C_{37}H_{34}BN_6OPRu$	$C_{37}H_{31}BN_7OPRu$	$C_{36}H_{31}BN_7O_3PRu$	$C_{39}H_{36}Cl_2BN_6O_3PRu$
Complex number	**23**	**24**	**25**	**26***
Formula weight (g mol^{-1})	721.55	732.54	752.53	850.49
Temperature (K)	120(2)	120(2)	153(2)	120(2)
Wavelength (Å)	0.71073	0.71073	-	-
Crystal system	Monoclinic	Monoclinic	Monoclinic	Orthorhombic
Space group	P 2_1/n	P 2_1/n	P2_1/n	Pca2_1
a / (Å)	12.3553(4)	12.3271(4)	12.2388(2)	17.9655(9)
b / (Å)	17.5258(6)	17.7540(5)	17.7482(3)	13.7346(7)
c / (Å)	15.5575(5)	15.5549(4)	15.5664(3)	15.5579(9)
α / (°)	90.00	90.00	90.00	90.00
β / (°)	90.66(1)	90.19(1)	90.36(10)	90.00
γ / (°)	90.00	90.00	90.00	90.00
Volume ($Å^3$)	3368.54(19)	3404.25(17)	3381.21(10)	3838.9(4)
Z	4	4	4	4
Density (calculated) Mg/m^3	1.423	1.429	1.478	1.472
Absorption coefficient (mm^{-1})	0.553	0.549	0.559	0.635
F(000)	1480	1496	1536	1736
Crystal size (mm^3)	0.18 x 0.18 x 0.04	0.34 x 0.16 x 0.07	0.2 × 0.2 × 0.01	0.3 × 0.3 × 0.3
Theta range for data collection (°)	1.75 to 30.00	1.74 to 29.00	1.74 to 28.50	1.48 to 29.00

Index ranges	$-17 \le h \le 17$ $-24 \le k \le 24$ $-21 \le l \le 21$	$-16 \le h \le 16$ $-24 \le k \le 23$ $-21 \le l \le 21$	$-16 \le h \le 16$ $-23 \le k \le 23$ $-20 \le l \le 20$	$-21 \le h \le 24$ $-16 \le k \le 18,$ $-21 \le l \le 21$
Reflections collected	44956	38474	42882	30441
Independent reflections	9799 [R(int) = 0.0607]	8972 [R(int) = 0.0898]	8573[R(int) = 0.0727]	10183[R(int) = 0.0273]
Absorption correction	Numerical	None	-	-
Max. and min. Transmission	0.9796 and 0.8990	-	-	-
Refinement method	Full-matrix least-squares on F^2	Full-matrix least-squares on F^2	-	-
Data / restraints / parameters	9799 / 0 / 560	8972 / 0 / 437	8573/0/450	10183/1/483
Goodness of fit on F^2	1.026	0.976	0.986	1.047
Final R indices [$I>2\sigma(I)$]	$R_1 = 0.0324$ $wR_2 = 0.0745$	$R_1 = 0.0409$ $wR_2 = 0.0811$	$R_1 = 0.0334$ $wR_2 = 0.0754$	$R_1 = 0.0380$ $wR_2 = 0.1014$
R indices (all data)	$R_1 = 0.0493$ $wR_2 = 0.0820$	$R_1 = 0.0809$ $wR_2 = 0.0904$	$R_1 = 0.0574$ $wR_2 = 0.0847$	$R_1 = 0.0437$ $wR_2 = 0.1069$
Largest diff. peak and hole ($e.Å^{-3}$)	0.686/-0.438	0.558/-0.558	0.804/-0.478	1.327/-0.923

Table **15** Selected bond lengths (Å) for **23**, **24**, **25** and **26**.

	23 (R = CH_3)	**24** (R = CN)	**25** (R = NO_2)	**26*** (R = CO_2Me)
Ru(1) – C(1)	2.0582(19)	2.052(3)	2.044(2)	2.038(3)
Ru(1) – P(1)	2.3193(5)	2.3326(7)	2.3315(6)	2.3360(8)
Ru(1) – N(1) (*trans* to PPh3)	2.1407(16)	2.142(2)	2.1368(19)	2.121(2)
Ru(1) – N(3) (*trans* to CO)	2.1555(16)	2.155(2)	2.1504(19)	2.167(3)
Ru(1) – N(5) (*trans* to CHCH)	2.1952(15)	2.195(2)	2.1879(18)	2.179(2)
C(1) – C(2)	1.342(3)	1.334(4)	1.338(3)	1.352(4)
C(2) – C(3)	1.474(3)	1.473(4)	1.446(3)	1.472(4)
Ru(1) – C(9)	1.8273(19)	1.829(3)	1.829(2)	1.833(3)
C(9) – O(1)	1.153(2)	1.161(3)	1.154(3)	1.154(4)

* includes a molecule of CH_2Cl_2.

Table **16** Selected bond and dihedral angles (°) for **23**, **24**, **25** and **26**.

	23 (R = CH_3)	**24** (R = CN)	**25** (R = NO_2)	**26*** (R = CO_2Me)
C(9)-Ru(1)-C(1)	86.52 (8)	86.63 (11)	87.42 (10)	88.72 (12)
C(9)-Ru(1)-N(3)	172.72 (7)	173.01 (10)	173.36 (9)	174.54 (12)
C(1)-Ru(1)-N(5)	171.96 (7)	172.31 (9)	171.91 (8)	171.04 (10)
C(9)-Ru(1)-P(1)	92.75 (6)	92.39 (9)	92.32 (8)	93.37 (10)
C(1)-Ru(1)-P(1)	91.92 (5)	91.81 (7)	92.46 (6)	92.78 (8)
N(1)-Ru(1)-P(1)	177.27 (4)	177.16 (6)	176.85 (5)	174.19 (7)
C(2)-C(1)-Ru(1)	132.10 (15)	132.4 (2)	131.89 (19)	134.3 (2)
C(1)-C(2)-C(3)	127.02 (19)	127.7 (3)	126.9 (2)	125.2 (3)
C(9)-Ru(1)-C(1)-C(2)	-7.83	-3.85	7.89	5.52
Ru(1)-C(1)-C(2)-C(3)	173.57	175.44	176.61	176.29
C(1)-C(2)-C(3)-C(8)	19.6	15.0	18.3	2.3

* includes a molecule of CH_2Cl_2.

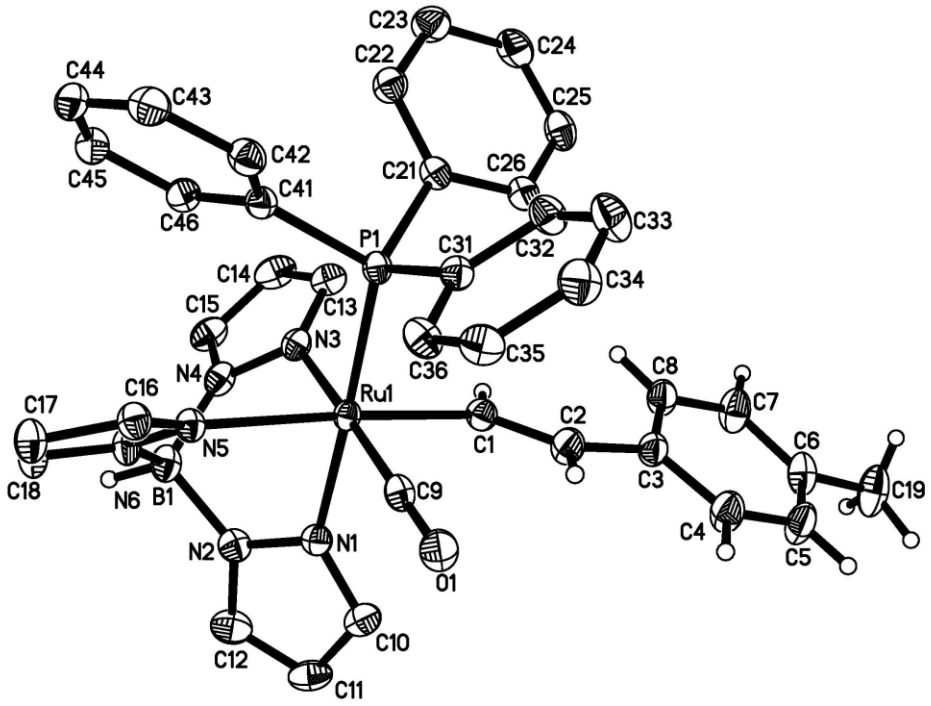

Figure **28** Molecular structure of **23**. In this and subsequent Figures, only a selection of the H atoms are shown for clarity.

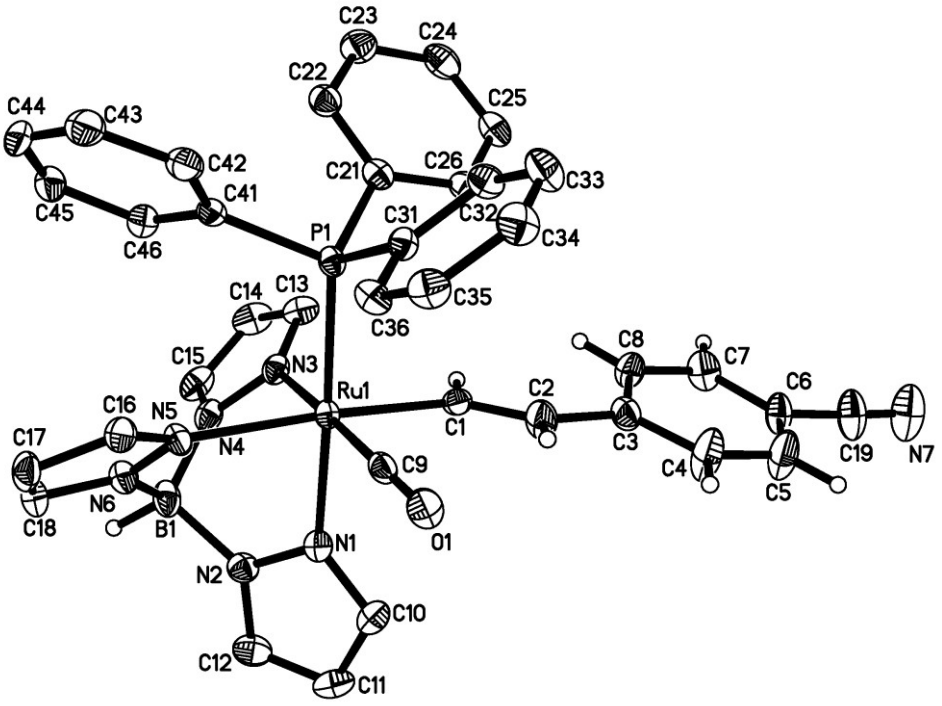

Figure **29** Molecular structure of **24**.

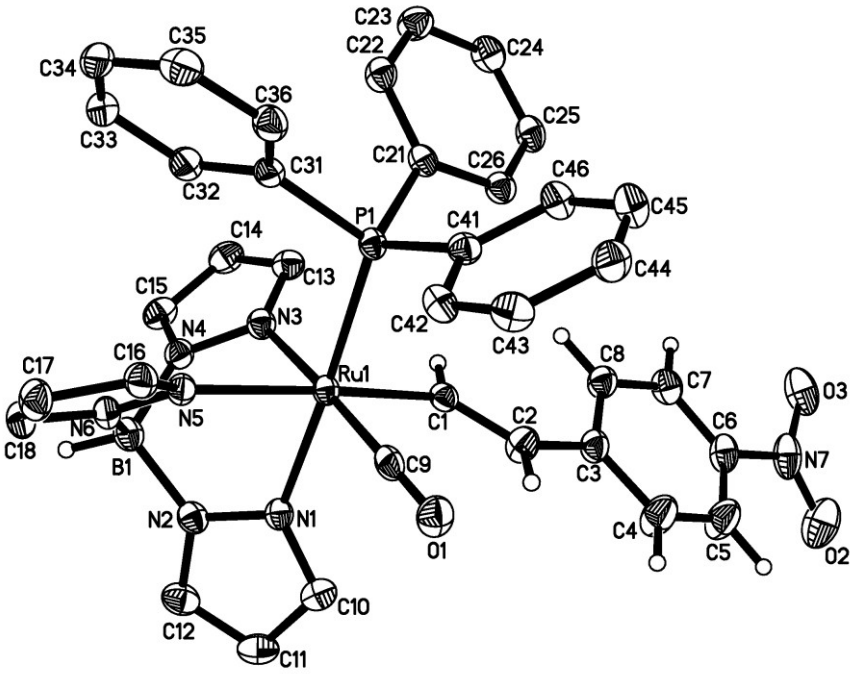

Figure **30** Molecular structure of **25**.

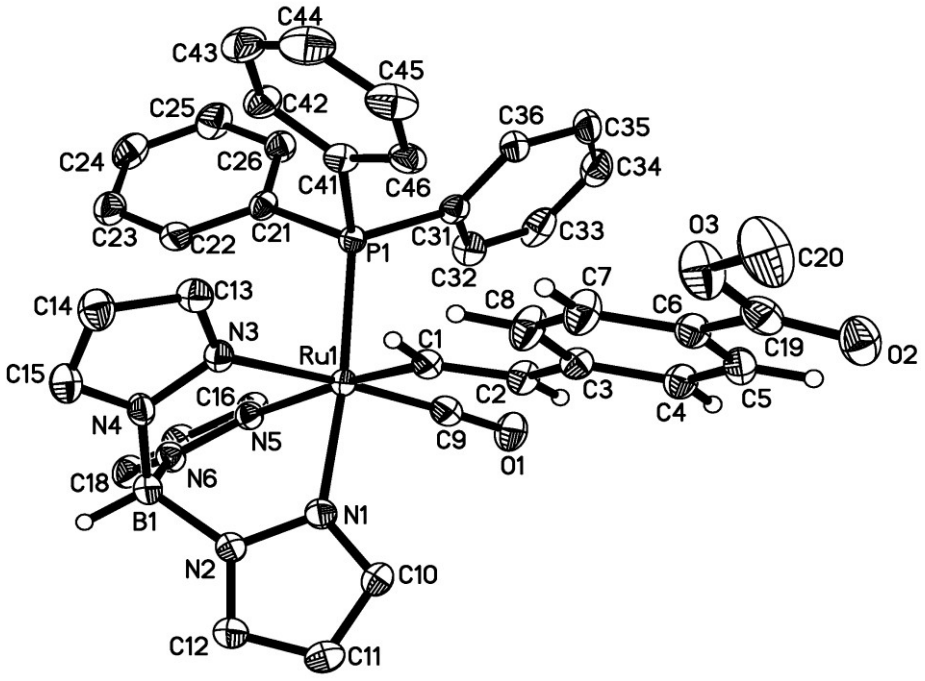

Figure **31** Molecular structure of **26**.

In each complex **23 – 26** the ruthenium centre exhibits a distorted octahedral geometry with the Tp^- anion acting as a facial tridentate ligand and occupying three

coordination sites. The Ru-vinyl-aromatic ring moiety is essentially planar [Ru(1)-C(1)-C(2)-C(3) dihedral angle 173.6 – 176.3 °], with a gentle curve in the molecular backbone, brought about by crystal packing. Within the series **23** – **26**, the Ru-C(9) [1.8273(19) – 1.833(3) Å], Ru-P [2.3193(5) – 2.3360(8) Å] and Ru-C(1) [2.038(3) – 2.0582(19) Å] bond lengths are comparable with those of related hydroruthenated compounds such as [Ru(CH=CHC$_3$H$_7$)Cl(CO)(PPh$_3$)$_2$(Me$_2$Hpz)] (**28**) [Ru-CO; 1.79(1) Å, Ru-P; 2.319(3) Å, and Ru-C$_\alpha$; 2.05(1) Å] [256] and [{RuCl(CO)(PPh$_3$)$_2$(Py)CH=CH}$_3$C$_6$H$_3$-1,3,5] (**29**) [Ru-CO; 1.809(10) Å, Ru-P; 2.397(2) Å, and Ru-C$_\alpha$; 2.050(8) Å]. [282] The three Ru-N bond lengths [Ru-N$_{PPh_3}$; 2.121(2) – 2.142(2) Å, Ru-N$_{vinyl}$; 2.179(2) – 2.1952(15) Å, Ru-N$_{CO}$; 2.1504(19) – 2.167(3) Å] are comparable with those of related tris(pyrazolyl)hydroborate capped ruthenium compounds, **30** [283] and **31**. [266]

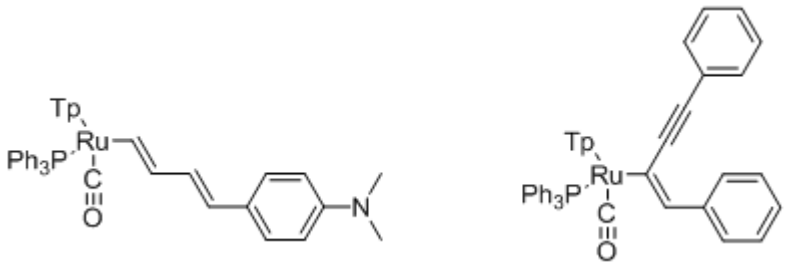

Chart **5** Tp capped mono-vinyl complexes **30** and **31**.

Table **17** Selected bond lengths comparison of complexes **23** – **26** with **30** and **31**.

	Range **23** – **26**	**30** [283]	**31** [266]
Ru-N$_{PPh3}$	2.121(2) – 2.142(2)	2.125(3)	2.117(11)
Ru-N$_{CO}$	2.1504(19) – 2.167(3)	2.154(3)	2.184(10)
Ru-N$_{vinyl}$	2.179(2) – 2.1952(15)	2.194(3)	2.17(1)
Ru – P	2.3193(5) – 2.3360(8)	2.3455(9)	2.341(4)
Ru – CO	1.8273(19) – 1.833(3)	1.817(5)	1.85(1)
Ru – C(1)	2.038(3) – 2.0582(19)	2.049(4)	2.090(12)
C(1) – C(2)	1.334(4) – 1.352(4)	1.209(2)	1.40(2)

There is little or no evidence for significant quinoidal character within the phenylene portion of the molecule, (Figure **32**).

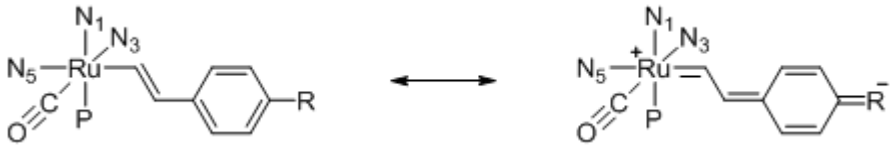

Figure **32** Possible resonance forms showing the evolution of quinoidal character in **23** – **26**.

The phenylene ring is almost perfectly in plane with the Ru-CH=CH moiety in the case of **26** (θ = 2.3 °) but significantly less conjugated with the metallovinyl portion of the molecule in the case of **23** – **25** (θ = 15.0 – 19.6 °) (Figure **33**). There are no obvious close contacts that might account for this geometric variation.

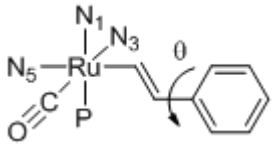

Figure **33** The torsion angle between C(1)-C(2) and C(3)-C(8).

In the compounds **23**, **24** and **25** the three respective distances between the ruthenium atom and the coordinating nitrogen atoms of the pyrazolyl rings, are essentially the same, within the limits of precision of the structure determination. The slight difference in ruthenium – pyrazolyl ring distances appears in the methyl-ester complex **26**, where all three Ru –N bonds are shorter in respect to the other compounds. This may be an electronic effect, with the electronic-withdrawing properties of the methyl-ester group being accentuated by the more planar arrangement of the metal vinyl and methylbenzoate fragments. Steric constraints associated with the PPh_3 supporting ligand and the tris(pyrazolyl)hydroborate capping ligand are like to restrict the close approach of the aromatic rings, and hence no π – π interactions between the phenyl rings occur. In each structure both chiral forms of the compounds are found, in a 1:1 ratio as expected.

Within any given complex, the strong *trans* influence of the vinyl ligand [284] can be observed in the longer Ru(1) – N(5) bonds when compared to Ru(1) – N(1) and Ru(1) – N(3). This difference in the three Ru-N bonds is due to the difference in *structural trans- effect* (STE) of each of the *trans* ligands; CO, vinyl and PPh_3. The *structural trans- effect* is the effect of a ligand on a bond length to a *trans* ligand. To fully understand the *trans*- effects of the many different coordinating ligands, both electronic effects such as polarisation, and σ- and π- bonding characteristics, and to a lesser extent the steric effects of the ligands, must be taken into consideration. Of the *trans*- ligands, in the mononuclear vinyl complexes, **23 – 26**, the vinyl moiety is a strong σ-donor, and both the CO and PPh_3 have σ-donor – π-acceptor properties, with the CO being a weak σ-donor and a strong π-acceptor and the PPh_3 being similar to CO but a stronger σ-donor and weaker π- acceptor. Consequently, the STE of these ligands follow the series in increasing STE: PPh_3 < CO < Vinyl. Hence the Ru-N bond length (Ru(1)-N(5) 2.179(2) – 2.1952(15) Å) *trans* to the vinyl moiety experiences a greater *trans*- effect, and therefore is longer than the other Ru-N bonds *trans* to the CO (Ru(1)-N(3) 2.1504(19) – 2.167(3) Å) and PPh_3 (Ru(1)-N(1) 2.121(2) – 2.142(2) Å). The electron withdrawing effect, and increased conjugation, of the CO_2Me substituent, in complex **26** may be causing the vinyl moiety to have less of a STE and hence a less significant increase in the Ru(1)-N(5) bond length (Ru(1)-N(5) 2.179(2) Å) in **26** compared to complex **23** (Ru(1)-N(5) 2.1952(15) Å), but this may also be due to packing constraints in the crystal, and conformational issues noted above.

The CO and vinyl moieties in all of the complexes **23** – **26** are essentially coplanar [C(9)-Ru(1)-C(1)-C(2): -7.8 ° (**23**), -7.9 ° (**25**)]. This coplanar arrangement of the vinyl group and CO is expected due to the strong π-interaction between CO and vinyl ligands with metal centres in an octahedral conformation. [285] A large proportion of the six-coordinate transition metal complexes that contain both a vinyl and a carbonyl ligand have a pseudo-octahedral structure. The two lowest energy configurations of the vinyl and *cis*- carbonyl ligands, where the degree of the planarity defined by the dihedral angle θ are shown in Figure **34**.

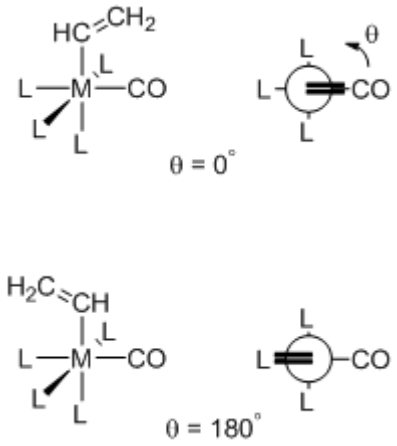

Figure **34** The two preferred configurations, along with the Newman projections (θ = 0 ° and 180 °).

It has been shown that with the use of orbital interaction models this coplanarity can be accounted for. In the case of most six-coordinate transition metal alkenyl complexes the metal centre satisfies the $18e^-$ rule with a full complement of filled t_{2g} orbitals (d_{xy}, d_{xz} and d_{yz}), which have π-symmetry with respect to the metal-ligand bond, (Figure **35**). Back-donation of electron density from these metal orbitals into the π* orbitals of the vinyl and carbonyl ligands is possible, favouring the coplanar arrangement of the two ligands. As there is competition between the π-acceptor ligands for back-donation, the relative orientation of the vinyl ligand with respect to the other π-acceptor ligands will affect the stability of the complex. Figure **35** shows the orientation of the π* orbitals of the vinyl and carbonyl ligands when *cis*- to one another. When d_{xz} interacts with the π* orbitals of the vinyl fragment, the remaining t_{2g} orbitals (d_{xy} and d_{yz}) can interact with the π* orbitals on the carbonyl. Therefore maximum back-donation and increased stability occurs when there is a coplanar configuration between the alkenyl and carbonyl ligands (θ = 0 and 180 °).

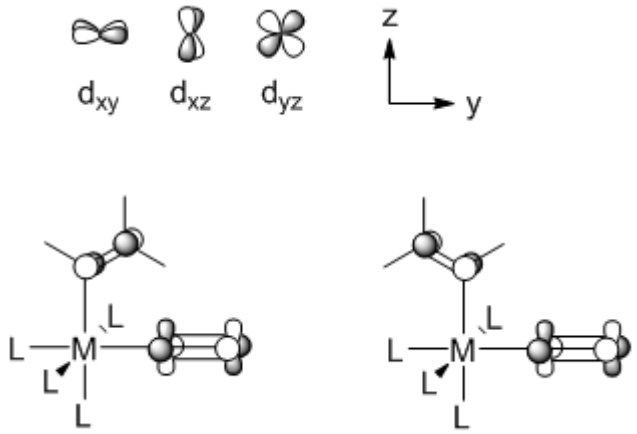

Figure **35** t_{2g} metal d-orbital and orientation of the π* orbitals of the alkenyl and carbonyl ligands.

This preferential bonding situation that arises from a coplanar orientation of the carbonyl and vinyl ligands results in a significant energy barrier to rotation about the metal alkenyl bond, up to 10 kcal.mol^{-1}, which is significantly higher than values found in simple organic alkene molecules, where rotation is often less than 2 kcal.mol^{-1}. [286, 287] Although this simple schematic MO description does not distinguish a preference for the θ = 0 ° vs θ = 180 ° conformations, detailed NBO analysis on suitable model systems suggests that the θ = 0 ° state is marginally (< 2 kcal.mol^{-1} more stable. [52]

4.2.3 Cyclic Voltammetry

The six coordinate Tp^- capped ruthenium vinyl complexes **23**, **25**, **26** and **27** all show a single reversible oxidation wave at potentials that reflect the electronic properties of the aryl substituent (Table **18**). Thus, **27** is easier to oxidise than **23**, **26** and **25** as might be expected given the strong electron donating properties of the OMe group. Compound **23** is also easier to oxidise than **26** and **25** because the methyl group is weakly electron donating in comparison to **26** and **25** which both bear electron with drawing groups. Complex **25** also has a reversible reduction wave, which can be readily assigned to the reduction of the nitrophenyl moiety.

The significant influence of the aryl ring substituent on the electrochemical potentials in the series of complexes **23**, **25**, **26** and **27** indicates that the aryl group is likely closely associated with the redox active orbitals.

Table **18** Cyclovoltammetry data of complexes **23**, **25**, **26** and **27**.

Complex	E_1/V	ΔE_{1-2}/mV	i_c/i_a
23	0.31	69	1.1
25 [b]	0.55	97	1.0
26	0.48	77	1.0
27	0.22	73	1.0

[a] Data recorded using a glassy carbon working electrode, platinum counter and pseudo reference electrodes, from solutions in MeCN containing 0.1 M NBu_4BF_4 supporting electrolyte and referenced against ferrocene/ferrocenium [FcH/FcH^+] couple = 0 V, scan rate 100 mV/s.

[b] Irreversible, anodic peak potential reported at -1.61 mV with a peak separation of 132 mV.

The electrochemical reversibility of the oxidation of the complexes **23**, **25**, **26** and **27** can be established from the linear dependence of the peak current with $\nu^{1/2}$ (Figure **36**) as expected from the Randles-Sevcik equation,

$$i_p = (2.69 \times 10^5) n^{3/2} A C D^{1/2} \nu^{1/2}$$

(where i_p is the peak current of the voltammetry wave, n is the number of electrons in the process, A is the area of the working electrode, C is the analyte concentration, D is the diffusion constant of the analyte, and ν is the scan rate), the unitary aniodic:cathodic current ratio and the peak-to-peak separation close to that of an internal ferrocene standard.

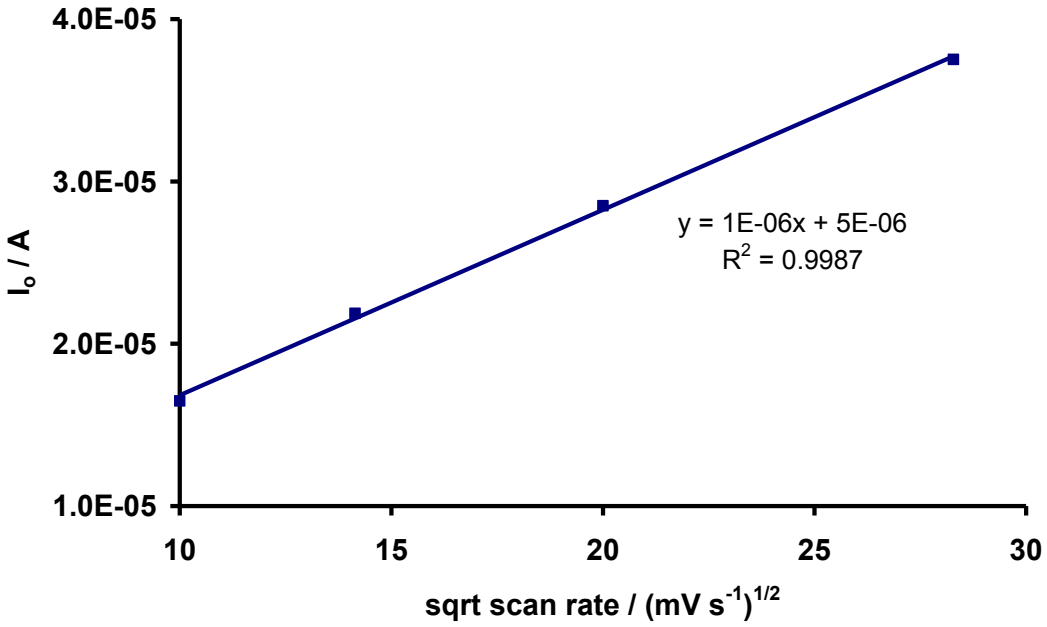

Figure **36** The linear relationship between peak current (A) and $\nu^{1/2}$ $(mVs^{-1})^{1/2}$ derived from the electrochemical response of **23**, illustrated for purposes of example.

4.2.4 IR Studies

The carbonyl ligand can act as a probe by which we can assess electron density at a metal centre, due to a synergistic interaction between the metal and the carbonyl ligand. This involves the forward donation of a lone pair from CO to the metal and subsequent π-backbonding from the metal d-orbitals to the CO ligand. In essence, greater electron density at the metal centre leads to a lower frequency CO stretching mode.

Table **19** IR stretching frequencies for **23**, **25**, **26** and **27** in CH_2Cl_2 solutions.

Complex	ν(C≡O) / cm^{-1}	ν(B-H) / cm^{-1}
23	1942	2481
25	1945	2485
26	1940	2483
27	1940	2486

It is clear from the data in Table **19** that the stretching frequencies of the carbonyl ligand do not differ significantly, despite the differing electron donating or withdrawing properties of the vinyl substituent. The effect of the R group in the stretching frequencies of the B-H bond is similarly limited, with these ν(B-H) data spanning only 5 cm^{-1}. When these IR data are considered alongside the structural and electrochemical data, it must be concluded that:

- the aryl ring is associated with the redox active orbitals of the complexes;
- the aryl ring substituent is not causing any significant electronic perturbation at the ruthenium metal centre.

To address this point in more detail, an '*in-situ*' spectroelectrochemical study was undertaken.

4.2.5 IR Spectroelectrochemical Studies

Spectroelectrochemistry combines the use of spectroscopic techniques in conjunction with electrochemical studies. As well known through textbook examples, and beautifully illustrated by the recent works of Kubiak [31, 39, 40] and Winter [59, 250], the presence of a carbonyl ligand in a complex provides a vibrational probe through which electron density at a metal can be assessed by relative changes in the ν(C≡O) stretching frequency. The monometallic capped ruthenium vinyl complexes **23 – 27** are ideal candidates for IR spectroelectrochemical studies with the shifts in ν(C≡O), ν(B-H) and ν(C=C) providing information about the site of oxidation. The complexes **23** and **25** were chosen as representative examples.

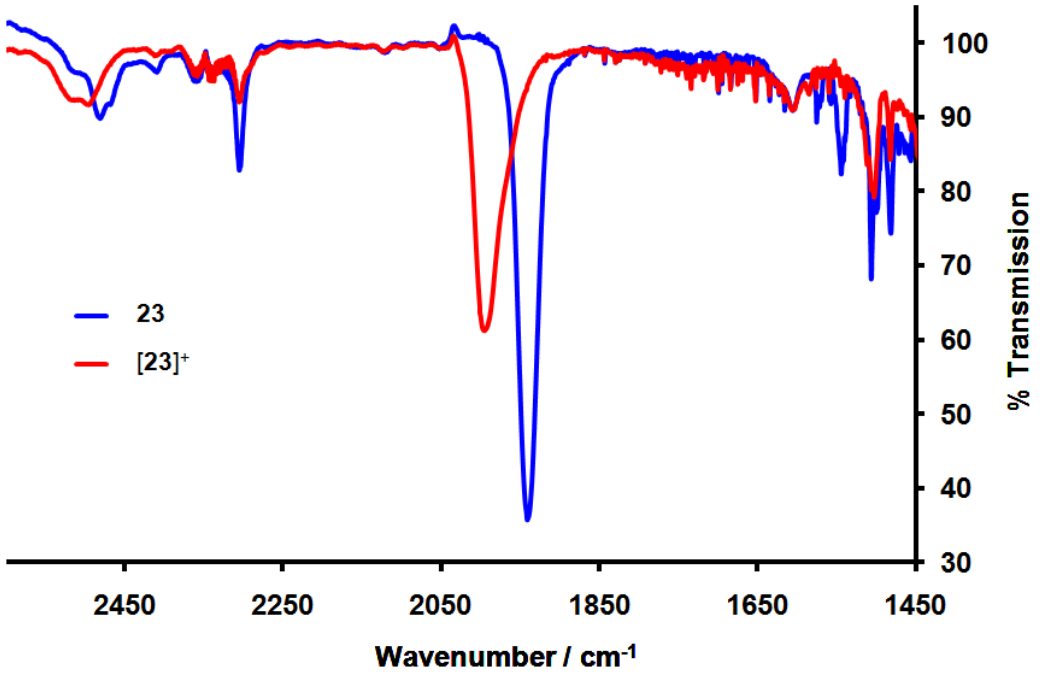

Figure **37** IR spectroelectrochemistry; first oxidation of **23** to $[\mathbf{23}]^+$ in CH_2Cl_2 0.1 M $[NBu_4][BF_4]$.

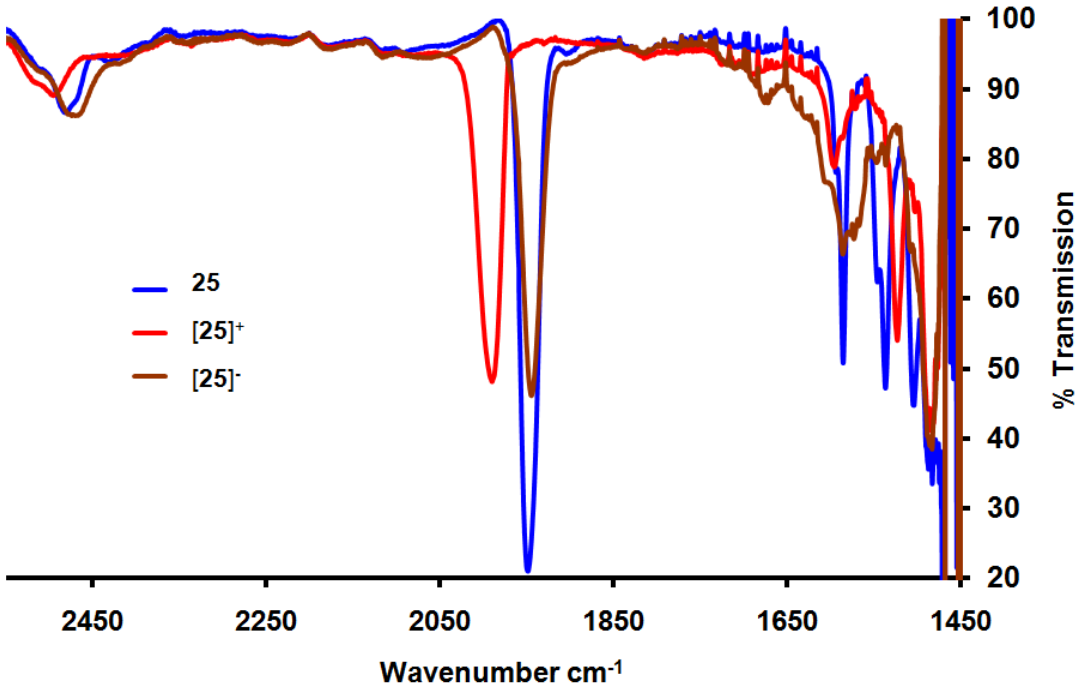

Figure **38** IR spectroelectrochemistry; oxidation and reduction of **25** in THF 0.1 M $[NBu_4][BF_4]$.

Table **20** IR spectroelectrochemical data for complexes [**23**], [**25**] and [**27**], recorded in (CH_2Cl_2, 0.1 M [NBu_4][BF_4]).

	Neutral / cm^{-1}		Cation / cm^{-1}		Anion / cm^{-1}	
	ν(C≡O)	ν(BH)	ν(C≡O)	ν(BH)	ν(C≡O)	ν(BH)
[**23**]	1942	2481	1999	2500	-	-
[**23**][a]	1946	2478	1991	2493	-	-
[**25**]	1945	2485	1997	2500	-	-
[**25**][a]	1947	2483	1991	2497	1946	2471
[**27**]	1941	2486	1996	2500	-	-

[a] Measurement taken in (THF , 0.1 M [NBu_4][BF_4])

On oxidation of **23** and **25** there is a shift in ν(C≡O) of ~ 50 cm^{-1} to lower wavenumbers. Metal based oxidations usually result in a shift in ν(C≡O) of ~ 100 cm^{-1}. [41] The small shift in ν(C≡O) of **23** and **25** therefore indicates a largely ligand based oxidation, and is comparable with the ca. 20 - 65 cm^{-1} shift that results from the oxidation of closely related systems [Ru(CH=CHAr)Cl(CO)(P^iPr_3)$_2$(L)] (Ar = Ph, pyrenyl; L = ethylisonicotinate, vacant coordination site) that have been shown to possess redox non-innocent vinyl ligands. [249] The small shift in ν(B-H) of ~ 15 cm^{-1} of **23** and **25** also shows that the Tp^- ligand is hardly affected by the oxidation process. The oxidation of **23** and **25** were carried out in CH_2Cl_2 as well as THF, to explore solvation effects on the oxidation process. However, Table **20** shows that there is little difference in these data.

4.2.6 UV-Vis Spectroelectrochemical Studies

The neutral and monocationic forms of **23** and **25** were further characterised by UV-vis-NIR spectroelectrochemical methods. These spectroscopic data are summarised in Table **21**, with assignments given based on results of the electronic structure and TD DFT calculations that are described in more detail below.

Table **21** Electronic transitions for [**23**]$^{n+}$ and [**25**]$^{n+}$ in both CH_2Cl_2 and THF with a supporting 0.1 M [NBu_4][BF_4] electrolyte.

	wavenumber / cm^{-1} [ε / $M^{-1}cm^{-1}$]	wavenumber / cm^{-1} [f]	Orbital Designation	Assignment
23	32900 [18570]	37600 [0.120]	HOMO → LUMO+4	ML-LCT
[**23**]$^{+}$	24390 [3270]	26020 [0.085]	α-HOSO → α-LUSO	ML-LCT
	13040 [1070]	13880 [0.178]	β-HOSO → β-LUSO	M-MLCT
23 [a]	33200 [10800]	37600 [0.120]	HOMO → LUMO+4	ML-LCT
[**23**]$^{+}$ [a]	22300 [1500]	26020 [0.085]	α-HOSO → α-LUSO	ML-LCT
	13900 [230]	13880 [0.178]	β-HOSO → β-LUSO	M-MLCT
25	22830 [28750]	29600 [0.688]	HOMO → LUMO	ML-LCT
[**25**]$^{+}$	16050 [4020]	24500 [0.105]	α-HOSO → α-LUSO	ML-LCT
	12800 [1070]	14700 [0.182]	β-HOSO → β-LUSO	M-MLCT
25 [a]	23300 [8400]	29600 [0.688]	HOMO → LUMO	ML-LCT
[**25**]$^{+}$ [a]	16500 [1800]	24500 [0.105]	α-HOSO → α-LUSO	ML-LCT
	12450 [350]	14700 [0.182]	β-HOSO → β-LUSO	M-MLCT

[a] Measurements taken in THF.

4.2.7 Electronic Structure Calculations

A theoretical investigation was conducted at the DFT level, initially on the model system Ru(CH=CHPh)(CO)(PPh_3)Tp, (**23-H**), which was used to mimic complex **23** and the corresponding radical cation [**23-H**]$^{+}$. Similar models for **24** – **27** (**24-H** – **27-H**) were constructed. The discussion which follows refers to results obtained from calculations at the MPW1K/LANL2DZ/3-21G* level of theory, where the ruthenium atom was modelled using LANL2DZ and the other atoms using 3-21G*, with no symmetry constraints (Table **22**). There is excellent agreement between the available crystallographically determined structures of **23 - 27** and the DFT optimised geometry determined here. The good agreement between observed and calculated ν(C≡O) and ν(B-H) frequencies gives further confidence in the accuracy of the optimised geometries (Table **23** and Table **24**). For illustrative purposes

selected bond lengths and bond angles of the optimised geometries of **23-H** and [**23-H**]$^{+}$ are shown in Table **25**, the structural changes upon oxidation of **24-H** – **27-H** follow a similar trend. Energies and composition of the frontier orbitals are summarised in Table **26**, Table **27** and Table **28**, while Figure **39** illustrates the labelling scheme.

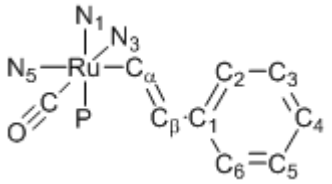

Figure **39** The labelling scheme used in the discussion of the DFT results.

The Ru-C_α, Ru-P, C_α=C_β, C≡O and C_β-C_1 bond lengths in the series of mono-nuclear vinyl compounds are similar, despite the change in nature of the vinyl substituent. At the level of theory employed, the aromatic ring and the vinyl bond lie in the same plane, with a dihedral angle C_β-C_α-Ru-CO of about -20 °.

Table **22** Selection of critical bond lengths from the crystallographically determined structures of **23**, **24**, **25** and **26**, and the corresponding bond lengths from the optimised geometries of the model systems and **23-H**, **24-H**, **25-H** and **26-H**.

	23	**23-H**[a]	**24**	**24-H**	**25**	**25-H**	**26**	**26-H**
Ru-CO	1.8273(19)	1.87266	1.829(3)	1.87404	1.829(2)	1.87482	1.833(3)	1.87358
C≡O	1.153(2)	1.16041	1.161(3)	1.15996	1.154(3)	1.15978	1.154(4)	1.16014
Ru-C_α	2.0582(19)	2.04711	2.051(3)	2.04338	2.044(2)	2.04054	2.038(3)	2.04424
C_α=C_β	1.342(3)	1.34203	1.334(4)	1.34434	1.338(3)	1.34590	1.352(4)	1.34390
C_β-Ph	1.474(3)	1.47031	1.473(4)	1.46415	1.466(3)	1.46089	1.472(4)	1.46524
Ru-P	2.3193(5)	2.32689	2.3326	2.33094	2.3315(6)	2.33309	2.3360(8)	2.32942
Ru-N_1 (*trans* phosphine)	2.1407(16)	2.08856	2.142(2)	2.08941	2.1368(19)	2.08934	2.121(2)	2.08905
Ru-N_3 (*trans* CO)	2.1555(16)	2.11614	2.155(2)	2.11416	2.1504(19)	2.11302	2.167(3)	2.11411
Ru-N_5 (*trans* vinyl)	2.1952(15)	2.15748	2.195(2)	2.15533	2.1879(18)	2.15487	2.179(2)	2.15682

[a] **23-H** has phenyl instead of tolyl.

Table **23** A comparison of the calculated optimised frequencies and experimental determined ν(C≡O) and ν(B-H) frequencies of **23**, **24**, **25**, **26** and **27**.

Neutral	ν(C≡O)		ν(B-H)	
	Expt	Calc	Expt	Calc
23	1942	1944 [a]	2481	2487[a]
24	-	1948	-	2490
25	1945	1948	2485	2491
26	1940	1946	2483	2489
27	1941	1944	2486	2486

[a] **23-H** has phenyl instead of tolyl

Table **24** A comparison of the calculated and experimentally determined ν(C≡O) and ν(B-H) frequencies of [**23**]$^+$, [**25**]$^+$ and [**27**]$^+$, and appropriate models.

Cation	ν(C≡O)		ν(B-H)	
	Expt	Calc	Expt	Calc
[**23**]$^+$	1999	1996 [a]	2500	2521
[**25**]$^+$	1997	2007	2500	2625
[**27**]$^+$	1996	1984	2500	2617

[a] **23-H** has phenyl instead of tolyl

Upon oxidation to the mono-oxidised species the vinyl-aromatic ring plane is rotated by only 2-3 °, and hence the gross structural features of the complexes are similar, regardless of oxidation state.

Table **25** Selected bond lengths (Å) of **23-H** and [**23-H**]$^+$, and the structural differences.

Bond Length	**23-H**	[**23-H**]$^+$	**Δ**
Ru-C_α	2.047	1.965	-0.082
Ru-CO	1.873	1.917	+0.044
Ru-P	2.327	2.400	+0.073
C≡O	1.160	1.150	-0.010
C_α=C_β	1.342	1.377	+0.035
C_β-C_1	1.470	1.442	-0.028
Ru-N_1 (*trans* to PPh3)	2.089	2.088	~ 0
Ru-N_3 (*trans* to CO)	2.116	2.087	-0.029
Ru-N_5 (*trans* to vinyl)	2.157	2.141	-0.016
C_1-$C_{2/6}$	1.398	1.405	+0.007
$C_{2/6}$-$C_{3/5}$	1.384	1.380	-0.004
$C_{3/5}$-C_4	1.387	1.390	+0.003

The model radical cation [**23-H**]$^+$ features a Ru-C_α bond somewhat shorter than **23-H** (Table **25**). The metal-phosphine bond lengths are sensitive to the net electron density available for π-back bonding and as such are elongated in [**23-H**]$^+$, relative to **23-H**. The elongation of the vinyl C_α-C_β bond in [**23-H**]$^+$ compared to the neutral model system **23-H** is consistent with a decrease in the net vinyl π-bonding character. Carbonyl bond lengths, and hence the ν(C≡O), are also sensitive to the net electron density at the metal centre. The CO bond length in the [**23-H**]$^+$ is modestly shorter than in **23-H**, leading to a higher ν(C≡O) frequency (**23-H**, 1944 cm^{-1}; [**23-H**]$^+$, 1997 cm^{-1}). The very slight contraction of the C_2-C_3 and C_5-C_6 bonds and elongation of the remaining C-C bonds in the phenyl substituent is consistent with only a small degree of cumulenic character in the radical cation. (Figure **40**)

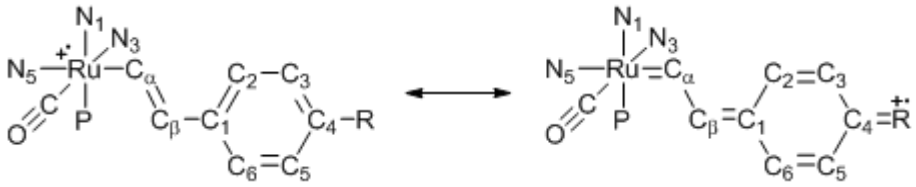

Figure **40** Possible resonance forms showing the evolution of quinoidal character in the radical cations [**23-H**]$^+$ - [**27-H**]$^+$.

Rotational barrier calculations were also carried out, using the same mixed basis set, for model complexes in both oxidation states by fixing the carbonyl-vinyl dihedral angle. This revealed a second minimum, 2 kcal.mol^{-1} higher in energy (1.5 kcal.mol^{-1} in the mono-oxidised species), where the vinyl-aromatic ring plane is bisecting the angle between two of the pyrazolyl rings, with a dihedral angle C_β-C_α-Ru-CO of ~135 ° (Figure **41**). As the ruthenium centre is chiral there are two distinct ways the vinyl-aromatic ring fragment can rotated around the Ru-C_α bond, clockwise and anticlockwise, therefore there are two rotation barriers. In both the neutral and mono-oxidised species the rotational barriers are considerable at ca 8-15 kcal.mol^{-1} (Figure **42**).

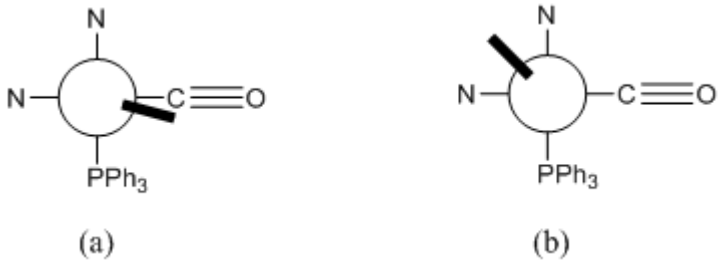

Figure **41** Schematic representation of the position of the vinyl bond relative to the carbonyl bond, looking down the C_α-Ru-N axis; (a) dihedral angle = -20 °, (b) dihedral angle = 135 °.

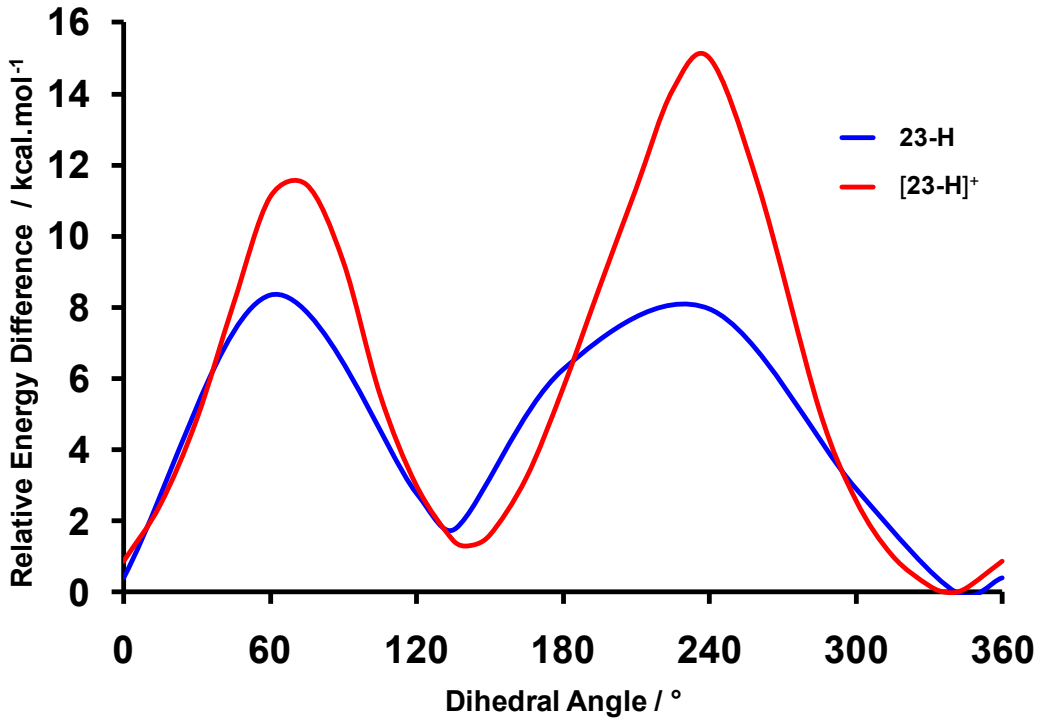

Figure **42** Rotational Barrier around Ru-C_α bond for [**23-H**]$^{n+}$ (n = 0, 1).

By fixing the vinyl-aryl dihedral angle in certain angles ranging from 0 ° to 180 °, rotational barrier calculations on the rotation around the C_β-C_1 bonds in the same model systems were also carried out (Figure **43**). The only minimum for the aryl rotation was, not unexpectedly, found to be when the vinyl and aryl ring are coplanar. The rotation barrier around the C_β-C_1 bond, in both the neutral and mono-oxidised species, is considerable, being 5 kcal.mol^{-1} and 10 kcal.mol^{-1} respectively (Figure **44**).

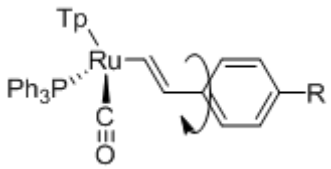

Figure **43** Showing the rotation around the C_β-C_1 bond.

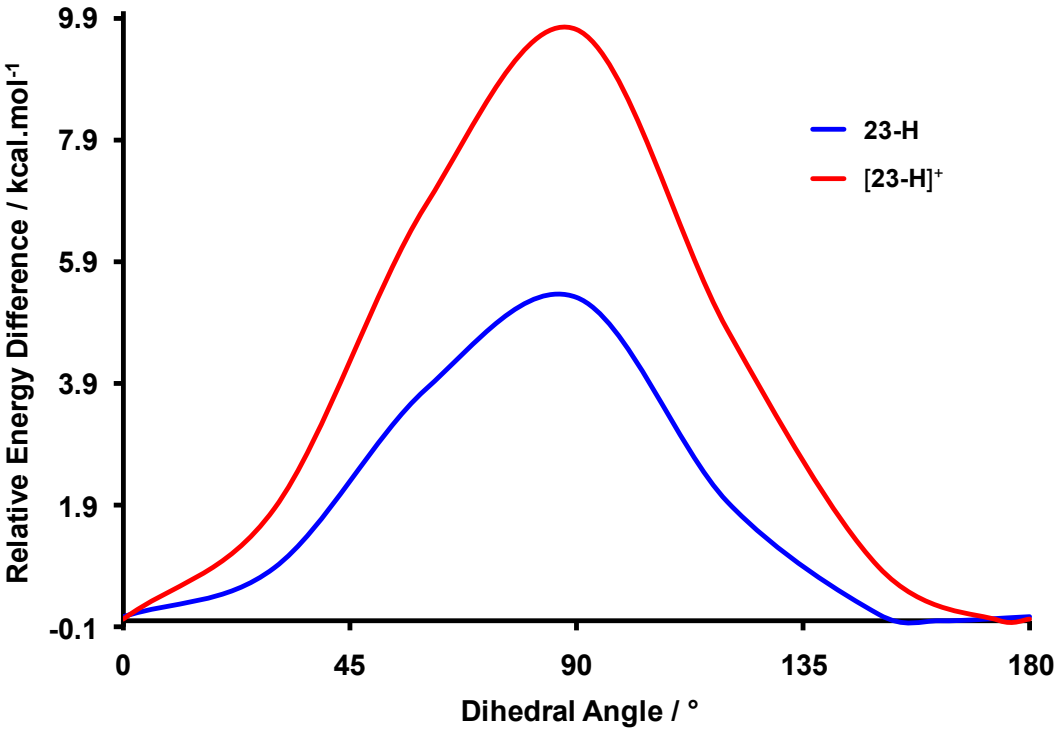

Figure **44** Rotational barrier around C_β-C_1 bond for [**23-H**]$^{n+}$ (n = 0, 1).

Table **26** Contributions of the frontier molecular orbitals of **23-H** and [**23-H**]$^{+}$.

23-H									
MO									
	LUMO+3	LUMO+2	LUMO+1	LUMO	HOMO	HOMO-1	HOMO-2	HOMO-3	HOMO-4
ε(eV)	0.43	0.23	0.14	-0.03	-5.76	-6.92	-7.06	-7.47	-7.54
Occ	0	0	0	0	2	2	2	2	2
%Ru	5	1	4	5	26	58	37	4	58
%Tp	5	1	2	4	4	28	30	1	14
%CO	2	0	1	1	0	6	3	0	4
%PPh_3	81	97	93	88	2	2	6	1	13
%C_α	2	0	0	1	16	4	6	1	1
%C_β	1	0	0	0	22	0	1	0	0
%Ph	4	0	0	1	30	0	17	94	9

[**23-H**]$^{+}$														
MO														
	170β	170α	169β	169α	168β	168α	167β	167α	166β	166α	165β	165α	164β	164α
	β-[LUSO+3]	α-[LUSO+2]	β-[LUSO+2]	α-[LUSO+1]	β-[LUSO+1]	α-[LUSO]	β-[LUSO]	α-[HOSO]	β-[HOSO]	α-[HOSO-1]	β-[HOSO-1]	α-[HOSO-2]	β-[HOSO-2]	α-[HOSO-3]
ε(eV)	-2.68	-2.74	-2.71	-2.95	-2.91	-3.16	-6.14	-9.61	-9.88	-10.35	-10.26	-10.35	-10.34	-10.42
Occ	0	0	0	0	0	0	0	1	1	1	1	1	1	1
%Ru	15	15	13	21	14	6	42	11	20	12	28	1	1	19
%Tp	12	15	14	8	5	3	6	5	26	40	59	88	92	46
%CO	6	32	31	3	8	4	0	0	0	1	3	0	0	1
%PPh_3	22	37	35	51	57	18	2	2	7	47	10	11	7	33
%C_α	13	0	2	6	5	26	8	15	16	0	1	0	0	1
%C_β	4	1	1	1	2	8	22	18	1	0	0	0	0	0
%Ph	28	0	3	9	9	34	19	49	30	0	0	0	0	0

Table **27** Contributions of the frontier molecular orbitals of **25-H** and [**25-H**]$^{+}$.

25-H									
MO									
	LUMO+3	LUMO+2	LUMO+1	LUMO	HOMO	HOMO-1	HOMO-2	HOMO-3	HOMO-4
ε(eV)	0.00	-0.07	-0.25	-1.41	-6.26	-7.25	-7.45	-7.83	-7.87
Occ	0	0	0	0	2	2	2	2	2
%Ru	1	4	6	1	31	56	33	8	32
%Tp	1	2	4	0	6	32	33	82	27
%CO	1	1	2	0	0	6	3	0	2
%PPh_3	97	93	85	0	2	2	8	9	37
%C_α	0	0	1	7	13	3	8	0	1
%C_β	0	0	0	0	23	0	3	0	0
%Aryl	0	0	0	32	23	0	12	0	1
%NO_2	0	0	0	58	3	0	1	0	0

[**25-H**]$^{+}$														
MO														
	181β	181α	180β	180α	179β	179α	178β	178α	177β	177α	176β	176α	175β	175α
	β-[LUSO+3]	α-[LUSO+2]	β-[LUSO+2]	α-[LUSO+1]	β-[LUSO+1]	α-[LUSO]	β-[LUSO]	α-[HOSO]	β-[HOSO]	α-[HOSO-1]	β-[HOSO-1]	α-[HOSO-2]	β-[HOSO-2]	α-[HOSO-3]
ε(eV)	-3.00	-3.04	-3.21	-3.31	-4.08	-4.23	-6.51	-10.11	-10.26	-10.58	-10.53	-10.60	-10.65	-10.70
Occ	0	0	0	0	0	0	0	1	1	1	1	1	1	1
%Ru	17	17	20	24	5	2	49	11	13	8	22	0	1	18
%Tp	16	17	6	7	2	1	8	6	26	28	55	83	91	60
%CO	37	40	9	6	0	0	1	0	0	0	2	0	0	1
%PPh_3	28	25	61	60	1	1	2	4	13	63	21	16	8	19
%C_α	0	0	1	1	10	14	4	14	18	0	1	0	0	1
%C_β	1	1	0	0	0	1	21	20	4	0	0	0	0	0
%Aryl	0	0	0	0	34	39	14	42	23	0	0	0	0	0
%NO_2	0	0	1	1	48	43	3	3	1	0	0	0	0	0

Table **28** Contributions of the frontier molecular orbitals of **27-H** and [**27-H**]$^{+}$.

27-H									
MO									
	LUMO+3	LUMO+2	LUMO+1	LUMO	HOMO	HOMO-1	HOMO-2	HOMO-3	HOMO-4
ε(eV)	0.46	0.26	0.17	0	-5.53	-6.85	-6.89	-7.43	-7.57
Occ	0	0	0	0	2	2	2	2	2
%Ru	4	1	4	5	18	42	58	56	10
%Tp	4	1	2	4	3	24	27	10	14
%CO	2	0	1	1	0	1	7	5	1
%PPh_3	87	97	93	88	1	4	1	5	14
%C_α	1	0	0	1	16	1	5	2	2
%C_β	1	0	0	0	18	1	1	3	1
%Aryl	1	0	0	0	36	20	1	15	57
%OMe	0	0	0	0	7	7	0	3	0

[**27-H**]$^{+}$														
MO														
	178β	178α	1777β	177α	176β	176α	175β	175α	174β	174α	173β	173α	172β	172α
	β-[LUSO+3]	α-[LUSO+2]	β-[LUSO+2]	α-[LUSO+1]	β-[LUSO+1]	α-[LUSO]	β-[LUSO]	α-[HOSO]	β-[HOSO]	α-[HOSO-1]	β-[HOSO-1]	α-[HOSO-2]	β-[HOSO-2]	α-[HOSO-3]
ε(eV)	-2.47	-2.49	-2.50	-2.72	-2.77	-3.08	-5.99	-9.11	-9.49	-10.15	-10.05	-10.18	-10.17	-10.22
Occ	0	0	0	0	0	0	0	1	1	1	1	1	1	1
%Ru	16	14	10	19	11	4	32	10	27	19	32	3	1	17
%Tp	14	14	10	7	5	3	4	3	20	58	57	85	90	35
%CO	14	23	11	3	5	2	0	0	0	2	3	0	0	1
%PPh_3	46	48	27	64	56	10	2	2	3	20	6	12	9	47
%C_α	3	0	12	3	7	29	11	13	9	1	1	0	0	0
%C_β	1	0	4	0	3	9	21	13	0	0	0	0	0	0
%Aryl	6	0	24	4	11	40	25	47	30	0	0	0	0	0
%OMe	0	0	2	0	1	3	4	12	10	0	0	0	0	0

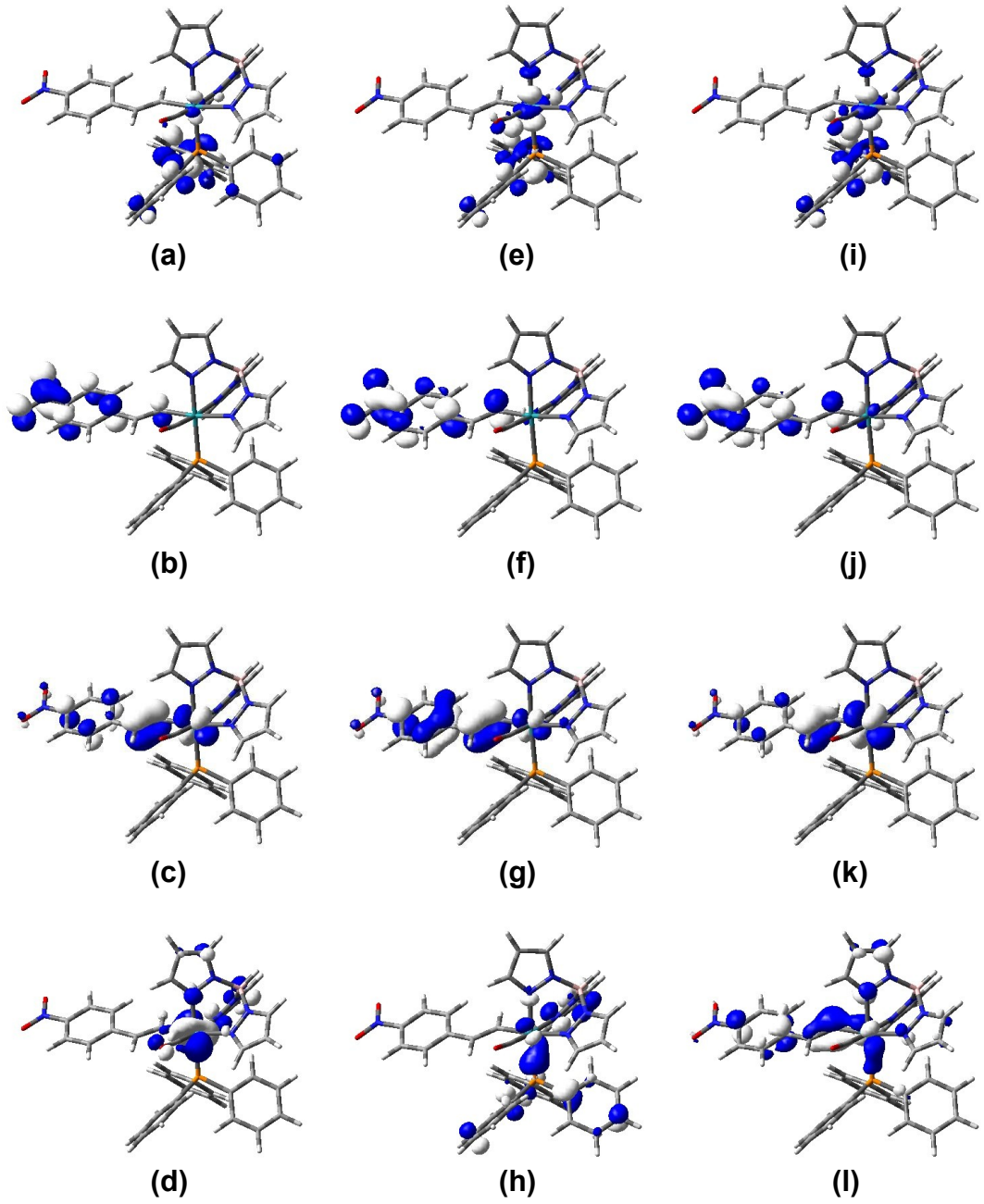

Chart **6** The (a) [LUMO+1] (b) LUMO (c) HOMO (d) [HOMO-1] of **25-H** together with (e) α-[LUSO+1] (f) α-LUSO (g) α-HOSO (h) α-[HOSO-1] and (i) β-[LUSO+2] (j) β-[LUSO+1] (k) β-LUSO (l) β-HOSO of [**25-H**]$^{+}$, plotted with contour values ±0.05 (e/bohr^{3})$^{1/2}$.

Table **29** Computed spin densities for the model radical cations [**23-H**]$^+$, [**24-H**]$^+$, [**25-H**]$^+$, [**26-H**]$^+$ and [**27-H**]$^+$.

	[**25-H**]$^{+a}$	[**25-H**]$^{+b}$	[**26-H**]$^{+a}$	[**24-H**]$^{+a}$	[**23-H**]$^{+a}$	[**23-H**]$^{+b}$	[**27-H**]$^{+a}$	[**27-H**]$^{+b}$
Ru	0.743	0.699	0.654	0.702	0.610	0.559	0.445	0.404
P	-0.030	-0.026	-0.025	-0.028	-0.022	-0.020	-0.015	-0.014
C (C≡O)	-0.016	-0.015	-0.015	-0.015	-0.014	-0.013	-0.011	-0.011
O (C≡O)	-0.011	-0.007	-0.011	-0.011	-0.011	-0.008	-0.010	-0.008
C_α	-0.224	-0.206	-0.173	-0.201	-0.136	-0.100	-0.007	0.034
C_β	0.439	0.451	0.446	0.439	0.439	0.438	0.366	0.352
$N_{trans\ PPh3}$	-0.010	-0.009	-0.008	-0.009	-0.007	-0.006	-0.003	-0.002
$N_{trans\ CO}$	-0.008	-0.009	-0.007	-0.008	-0.007	-0.007	-0.005	-0.004
$N_{trans\ vinyl}$	-0.004	-0.002	-0.005	-0.004	-0.005	-0.004	-0.005	-0.004
C_6H_4	0.067	0.074	0.109	0.089	0.130	0.140	0.180	0.188
R-group	0.011	0.012	0.005	0.009	-	-	0.058	0.060

[a] global minimum configuration, [b] local minimum configuration

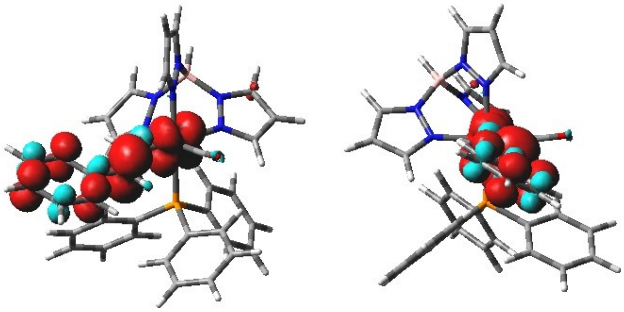

(**a**)

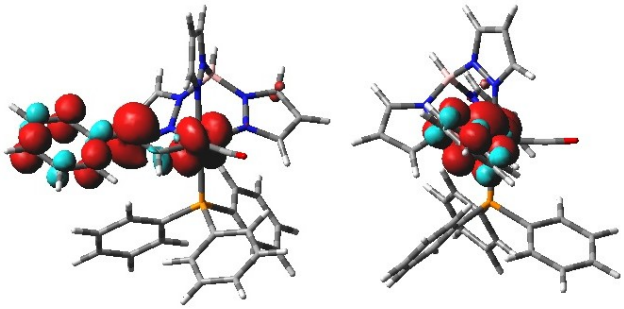

(**b**)

Chart **7** Showing the spin density distribution, plotted with contour values ±0.0024 (e/bohr^3) of [**23-H**]$^+$ in the two minima configurations;

(a) the global minimum, where the vinyl is coplanar with the carbonyl,

(b) a local minimum, where the vinyl is nestled between two of the pyrazolyl rings.

Table **26** - Table **28**, summarise the composition of the frontier orbitals of **23**, **25** and **27** and their mono-oxidised analogues, with representative contour plots of key orbitals from **25-H** and [**25-H**]$^+$ illustrated in Chart **6**. In the neutral systems, the metallic contribution to the HOMOs is sensitive to the nature of the substituent, with vinyl ligand contribution being more important as the donating strength of the substituent increases. Thus, the metal / vinyl contributions to the HOMO vary from 31 / 62 % (R = NO_2, **25**) to 18 / 77 % (R = OMe, **27**). Similarly significant contributions (67 – 84 %) of the vinyl ligand to the HOMOs in complexes [Ru(CH=CHAr)Cl(CO)(PMe_3)$_2$] (Ar = Ph, Py) have been computed by Winter and his team. [249] For both **23** and **27** the LUMO is essentially a phosphine σ*-orbital, with contributions from the metal centre, the vinyl π* system comprising the LUMO+4 and LUMO+8 for **23** and **27** respectively. Introduction of the strongly electron withdrawing NO_2 group causes this orbital to descend in energy, and comprises the LUMO in **25** (Table **27**, Chart **6**). These orbital characteristics are largely retained upon oxidation (Table **26** - Table **28**), although the metallic contribution to the β-LUSO is generally somewhat greater than in the HOMO of the corresponding neutral system. Clearly, the vinyl ligand is a significant component of the redox active orbitals in these vinyl complexes. The calculated ν(C≡O) frequencies are in good agreement with those observed from the spectroelectrochemical experiments, and the small increase in frequency of the ν(C≡O) band upon oxidation is consistent with the structure of the β-LUSO. Spin density calculations on the optimised geometries of [**23-H**]$^+$, [**24-H**]$^+$, [**25-H**]$^+$, [**26-H**]$^+$ and [**27-H**]$^+$ support the general conclusions, with the vinyl ligand supporting progressively more of the electron spin as the donating properties of the vinyl substituent increase (Table **29**). Unsurprisingly, the orientation of the vinyl ligand is also important and affects the net electron spin distribution (Table **29**, Chart **7**). Calculations with model systems at a local minimum in which the plane of the vinyl ligand and associated aryl ring are held approximately embraced by two of the pyrazine rings of the Tp^- ligand feature smaller spin density at the metal centre, and greater spin density on the vinyl ligand.

4.2.8 UV-vis-NIR Absorptions from TD DFT Calculations

To aid in the assignment of the electronic transitions, TD DFT calculations were carried out on the model systems $[Ru(CH=CHPh)(CO)(PPh_3)Tp]^{n+}$ $[\mathbf{23\text{-}H}]^{n+}$, $[Ru(CH=CHC_6H_4NO_2\text{-}4)(CO)(PPh_3)Tp]^{n+}$ $[\mathbf{25\text{-}H}]^{n+}$ and $[Ru(CH=CHC_6H_4OMe\text{-}4)(CO)(PPh_3)Tp]^{n+}$ $[\mathbf{27\text{-}H}]^{n+}$. Before discussing the TD DFT results from **23-H**, **25-H** and **27-H** it is helpful to re-cap a few pertinent points of the electronic structure of these compounds, and relevant data are summarised for ease of reference by the reader. In each case, the HOMO is predominately comprised of a Ru-CH=CH-Ar (Table **30**) π-type system and can be termed a "metal-ligand" (ML) orbital (Figure **45**, Figure **46** and Figure **47**). As a consequence of the significant aryl contribution to the HOMO, the energy of these orbitals are sensitive to the electronic nature of the R group being stabilised by the electron-withdrawing NO_2 group in the case of **25-H** and destabilised by the OMe group in **27-H** relative to **23-H**. The corresponding π* system with a node between the vinyl carbon atoms features an appreciably smaller metal contribution (Table **30**) and can be designated a "ligand" (L) orbital. The energy of this π* orbital is also sensitive to the electronic nature of the aryl substituent, and comprises the LUMO for **25-H**, LUMO+4 for **23-H** and LUMO+8 for **27-H**.

Table **30** Composition of selected frontier orbitals of **23-H**, **25-H** and **27-H**.

		ε(eV)	%Ru	%Tp	$\%PPh_3$	%CO	$\%C_\alpha$	$\%C_\beta$	%Aryl	%R-group
23-H	HOMO	-5.76	26	4	2	0	16	22	30	-
	LUMO+4	0.65	2	17	38	2	10	4	28	-
25-H	HOMO	-6.26	31	6	2	0	13	23	23	3
	LUMO	1.41	1	0	0	0	7	0	32	58
27-H	HOMO	-5.53	18	3	1	0	16	18	36	7
	LUMO+8	1.19	4	31	11	1	9	2	40	2

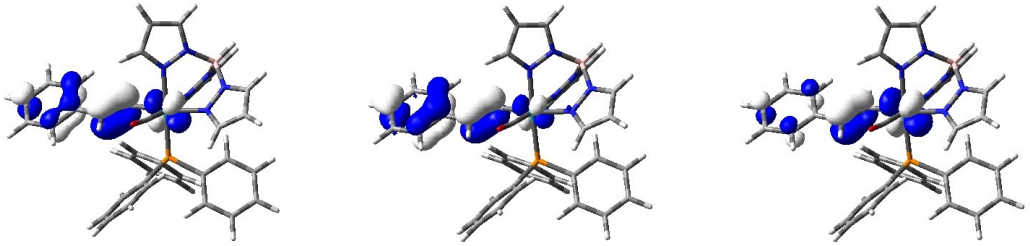

Figure **45** Contour plots: left; HOMO of **23-H**, centre; α-HOSO, right; β-LUSO of [**23-H**]$^{+}$.

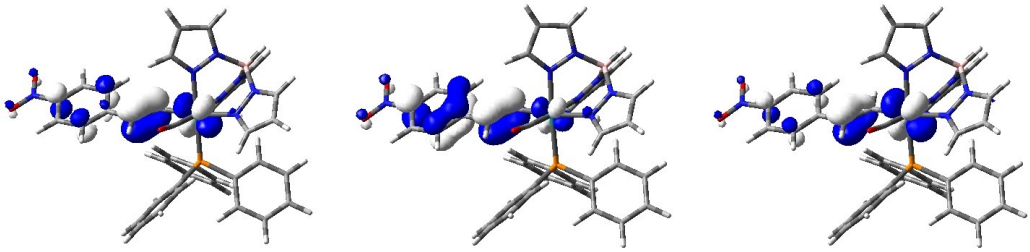

Figure **46** Contour plots: left; HOMO of **25-H**, centre; α-HOSO, right; β-LUSO of [**25-H**]$^{+}$.

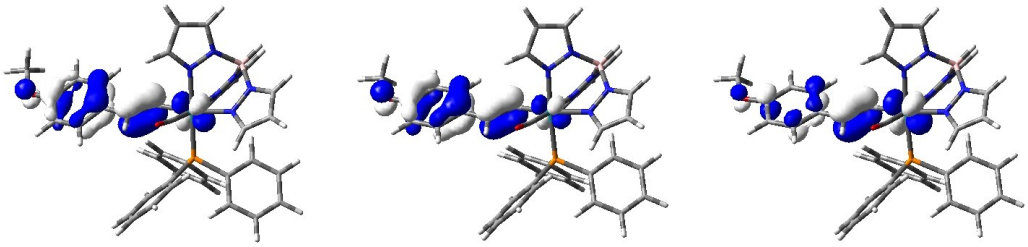

Figure **47** Contour plots: left; HOMO of **27-H**, centre; α-HOSO, right; β-LUSO of [**27-H**]$^{+}$.

For each of the neutral (18-electron, closed shell) systems **23-H**, **25-H** and **27-H** the most significant absorption band in the visible region is calculated to arise from transitions from the "ML" centred HOMO to the LUMO for **25-H**, LUMO+4 for **23-H** and LUMO+8 for **27-H**, and can hence be designated as an ML-LCT transition. Unsurprisingly, the transition energy is sensitive to the electronic nature of the *para*-substituent, with a bathochromic shift in evidence as the substituent becomes more and more electron withdrawing. The solvatochromism that is evidenced from the data presented in Table **31** is consistent with the degree of charge transfer associated with the transition.

Table **31** Electronic transitions for $[\mathbf{23}]^{n+}$ and $[\mathbf{25}]^{n+}$ in both CH_2Cl_2 and THF with a supporting 0.1 M $[NBu_4][BF_4]$ electrolyte.

	wavenumber / cm^{-1} [ε / $M^{-1}cm^{-1}$]	wavenumber / cm^{-1} [f]	Orbital Designation	Assignment
23	32900 [18570]	37600 [0.120]	HOMO → LUMO+4	ML-LCT
$[\mathbf{23}]^{+}$	24390 [3270]	26020 [0.085]	α-HOSO → α-LUSO	ML-LCT
	13040 [1070]	13880 [0.178]	β-HOSO → β-LUSO	M-MLCT
23 [a]	33200 [10800]	37600 [0.120]	HOMO → LUMO+4	ML-LCT
$[\mathbf{23}]^{+}$ [a]	22300 [1500]	26020 [0.085]	α-HOSO → α-LUSO	ML-LCT
	13900 [230]	13880 [0.178]	β-HOSO → β-LUSO	M-MLCT
25	22830 [28750]	29600 [0.688]	HOMO → LUMO	ML-LCT
$[\mathbf{25}]^{+}$	16050 [4020]	24500 [0.105]	α-HOSO → α-LUSO	ML-LCT
	12800 [1070]	14700 [0.182]	β-HOSO → β-LUSO	M-MLCT
25 [a]	23300 [8400]	29600 [0.688]	HOMO → LUMO	ML-LCT
$[\mathbf{25}]^{+}$ [a]	16500 [1800]	24500 [0.105]	α-HOSO → α-LUSO	ML-LCT
	12450 [350]	14700 [0.182]	β-HOSO → β-LUSO	M-MLCT

[a] Measurements taken in THF.

In the experimental studies, oxidation of **23** and **25** to $[\mathbf{23}]^{+}$ and $[\mathbf{25}]^{+}$ causes a collapse of the ML-LCT transition associated with the neutral species, with two smaller absorption bands growing into the spectrum at lower energy. On the basis of the TD DFT calculations, these lower energy bands can be assigned to the transitions from the α-HOSO to the α-LUSO and from the β-HOSO to the β-LUSO. The α-HOSO and β-LUSO of the monocations are both similar in composition to the HOMO (Figure **45**, Figure **46** and Figure **47**). The α-LUSO is similar in composition to the L orbitals described above (i.e. LUMO for **25-H**, LUMO+4 for **23-H** and LUMO+8 for **27-H**), whilst the β-HOSO is rather more metal in character (Figure **48**, Table **32**).

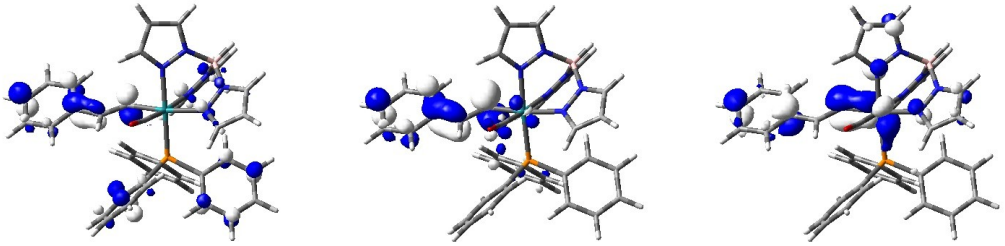

Figure **48** Contour plots of LUMO+4, α-LUSO and β-HOSO for **23-H**/[**23-H**]$^+$.

Table **32** Composition of the β-HOSO and α-LUSO of [**23-H**]$^+$, [**25-H**]$^+$ and [**27-H**]$^+$.

		ε(eV)	%Ru	%Tp	%PPh_3	%CO	%C_α	%C_β	%Aryl	%R-group
[**23-H**]$^+$	β-HOSO	-9.88	20	26	7	0	16	1	30	-
	α-LUSO	-3.16	6	3	18	4	26	8	34	-
[**25-H**]$^+$	β-HOSO	-10.26	13	26	13	0	18	4	23	1
	α-LUSO	-4.23	2	1	1	0	14	1	39	43
[**27-H**]$^+$	β-HOSO	-9.49	27	20	3	0	9	0	30	10
	α-LUSO	-3.08	4	3	10	2	29	9	40	3

On this basis, the α-HOSO - α-LUSO transition is also ML-LCT in character, while the β-HOSO - β-LUSO transition can be better described as M-MLCT in character.

4.2.9 Conclusions Drawn from the Electrochemical and Spectroelectrochemical Properties and Electronic Structures of Mono Hydroruthenated Acetylene Complexes

The studies described above have shown that the vinyl ligand in the complexes [Ru(CH=CHC_6H_4R-4)(CO)(PPh_3)Tp]$^{n+}$ (n = 0, 1) is significantly involved in both the HOMO of the neutral complexes and the β-LUSO of the monocations. Thus, as has been found in related systems studied by Winter, the vinyl ligand can be described as redox non-innocent. The involvement of the vinyl ligand in the redox-active orbitals is reflected in the relatively small positive shift of the ν(C≡O) frequencies that accompany oxidation of **23** – **27**, which is found in the

spectroelectrochemical studies, and reproduced in frequency calculations of $[\mathbf{23}]^+$, $[\mathbf{25}]^+$ and $[\mathbf{27}]^+$. Spin density calculations and analysis of the frontier molecular and spin orbitals are consistent with this description, with both the metal and vinyl ligand being involved in the HOMO of **23** – **27** and the β-LUSO of $[\mathbf{23}]^+$ - $[\mathbf{27}]^+$. The relative contributions of metal and vinyl are sensitive to the vinyl ligand substituent, permitting a degree of tuning of the electronic structure.

4.3 Bis- Hydroruthenated Linear and Branched Chain Acetylene Complexes

During the course of the studies that form this thesis, Winter *et al* reported the synthesis of some butadienyl [288] and divinylphenylene-bridged diruthenium complexes, [41, 42] and the analysis of their redox products by electrochemical, IR and UV-vis-NIR spectroelectrochemical means. The DFT studies of $[\{RuCl(CO)(PPh_3)_2\}_2(\mu\text{-}C_4H_4)]^{n+}$ (n = 0, 1, 2) (**32**) (Chart **8**) revealed that all three oxidation states, the ground state geometries are approximately symmetric with an inversion point passing through the midpoint of the central C-C bond of the butadienyl bridging ligand. The strong mixing between the ruthenium d-orbitals and ligand based π-orbitals in the HOMO (with 62% C_4H_4 character, 33% Ru_2) of all oxidation states lead to an extensive electron delocalisation and extended π-system makes the designation of redox events as metal or ligand centred processes tenuous, with the mixed valence mono-oxidised species being either intrinsically delocalised Class III in the Robin-Day classification, or nearly so. Investigations with 1,4- and 1,3-$[\{RuCl(CO)(P^iPr_3)_2\}_2(\mu\text{-}CH{=}CHC_6H_4CH{=}CH)]$ (**33**) and (**34**) (Chart **8**) have revealed that the oxidation processes are centred at the organic bridging ligand.

IR spectroelectrochemical studies on 1,4- and 1,3-$[\{RuCl(CO)(P^iPr_3)_2\}_2(\mu\text{-}CH{=}CHC_6H_4CH{=}CH)]$, **33** and **34**, showed that on oxidation of the neutral *para*-substituted complex **33**, the single ν(C≡O) band at 1910 cm^{-1} disappeared with a structured band appearing at 1932 cm^{-1} featuring high- and low- energy shoulders.

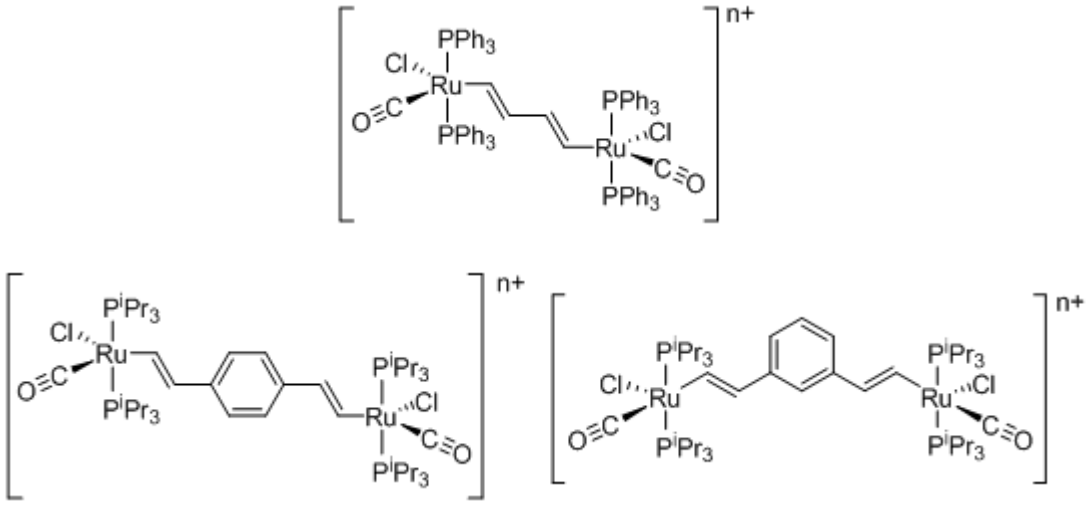

Chart **8** Bis-metallated bridging ligand complexes **32**, **33** and **34**.

On oxidation to the dication $[\mathbf{33}]^{2+}$ these ν(C≡O) bands collapsed to be replaced by one ν(C≡O) band at 1995 cm^{-1}. Oxidation of the neutral meta- substituted complex **34** to $[\mathbf{34}]^{+}$ resulted in the replacement of the neutral ν(C≡O) band at 1910 cm^{-1} by two equally intense bands at 1915 and 1971 cm^{-1}. On oxidation of $[\mathbf{34}]^{+}$ to the dication $[\mathbf{34}]^{2+}$ the two ν(C≡O) bands collapsed, being replaced by a single ν(C≡O) band at 1983 cm^{-1}. Computational studies on the two isomers, 1,4- and 1,3-$[\{RuCl(CO)(P^{i}Pr_3)_2\}_2(\mu\text{-}CH{=}CHC_6H_4CH{=}CH)]$, **33** and **34**, showed that, in the neutral states, they closely resemble each other with respect to the composition of the frontier orbitals that are relevant for their optical and electrochemical properties. The HOMO and the HOMO-1 for both complexes have a large contribution from the divinylphenylene interacting with the appropriate combinations of metal d-orbitals. In the *meta*- connected complex, the HOMO and HOMO-1 are nearly degenerate, whereas in the *para*- connected complex, there is an energy gap of nearly 1 eV. The LUMO and LUMO+1 of the two complexes are heavily centred on the metal end groups, admixed with some phosphine character. The computational models of $[\mathbf{33}]^{+}$ and $[\mathbf{34}]^{+}$ are symmetric, with the charge delocalised over the two metals and bridge. The authors note that the inherent asymmetry of the *meta* mono-cation $[\mathbf{34}]^{+}$ demonstrated by the experimental spectroscopic data is not adequately reproduced in the calculations. [42]

Interestingly the 1,4-di(butadienyl)benzene Tp^- capped diruthenium complex has been synthesised via Wittig-style chemistry (Scheme **17**). However, this compound has only been characterised by ^1H, ^{31}P NMR and elemental analysis, and details of the IR and UV-vis-NIR spectra, electrochemical properties, spectroelectrochemical properties, and electronic structure have not yet been reported. [161]

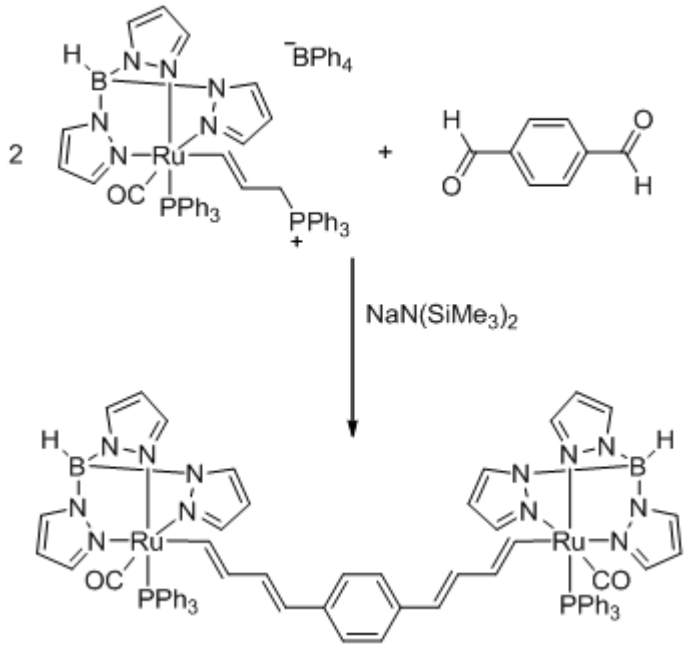

Scheme **17** Synthesis of bis-{Ru(CO)(PPh_3)Tp}-di-butadienyl-benzene. [161]

Extended chain complexes based on ruthenium vinyl building blocks have also been assembled. The use of 4-ethynyl-pyridine as the "6th ligand" in bimetallic 1,3 and 1,4- divinylbenzene complexes (Scheme **18**), introduces a reactive ethynyl moiety that can be further hydroruthenated to give tetrametallic, wire-like complexes. The tetra-oxidised tetraruthenium complexes are unique examples of organometallic complexes where the two different oxidised ligands are coordinated to the same metal atom. [248]

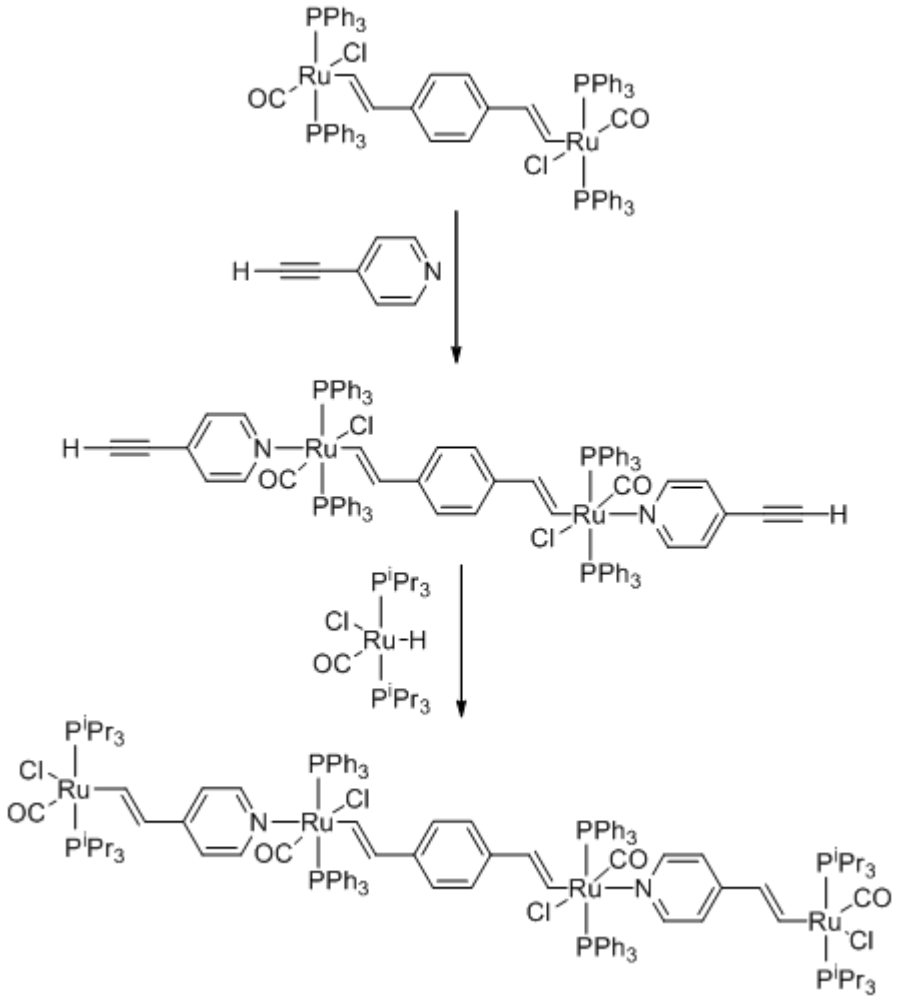

Scheme **18** Extension of diruthenium 1,4-divinylbenzene to a tetraruthenium bis(vinylpyridine) 1,4-divinylbenzene complex. [248]

The aim of this portion of the work was to synthesise purify and assess the electronic structures of some bimetallic ruthenium vinyl complexes featuring $Ru(CO)(PPh_3)Tp$ metal centres and a conjugated organic bridging ligand based on 1,4- and 1,3- phenylene cores.

4.3.1 Syntheses

The reaction of an excess of $RuHCl(CO)(PPh_3)_3$ with 1,4- or 1,3-diethynylbenzene in dichloromethane under nitrogen resulted in hydroruthenation of each ethynyl moiety. The progress of the hydroruthenation reaction was followed by IR spectroscopy, with the complete reaction being indicated by the disappearance of the

stretching frequencies of the C≡C and the C-H bonds of the alkyne. The subsequent capping of the metal end-caps in these five coordinate vinyl complexes by KTp gave 1,4-[{Ru(CO)(PPh_3)Tp}$_2$(CH=CHC_6H_4CH=CH)] (**35**) and 1,3-[{Ru(CO)(PPh_3)Tp}$_2$(μ-CH=CHC_6H_4CH=CH)] (**36**) respectively (Chart **9**), the reactions being adjudged complete when there were no further changes in the ν(C≡O) and ν(B-H) bands in the IR spectra of the crude reaction mixtures (ca. 2 h). Purification of **35** and **36** was achieved by extraction with hot ethanol and washing with hexane to remove liberated triphenylphosphine and the phosphine oxide formed by adventious oxidation in the sample, as indicated by ^{31}P NMR. However, accurate elemental analyses were not obtained, possibly due to traces of entrained triphenylphosphine or the phosphine oxide.

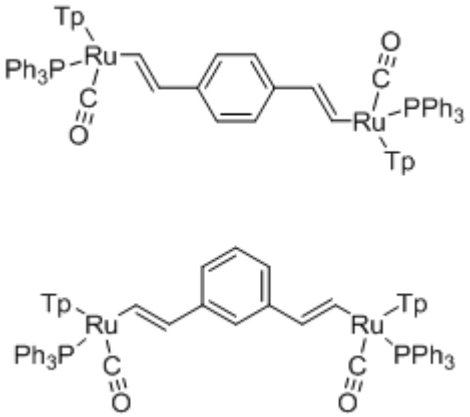

Chart **9** The bimetallic complexes **35** and **36** synthesised in this Chapter.

It is important to note at this point that each of the metal centres in **35** and **36** are chiral. As such, the bimetallic complexes **35** and **36** exist as pairs of diastereoisomers. However, the stereochemical problem is augmented by further complications from the relative disposition of the metal-vinyl fragments arising from rotation around the C_{Ar}-C_β bond, *and* rotation around the Ru-C_α bond (Figure **49**, Figure **50**), all of which lead to complex NMR spectra. Not surprisingly the ^{31}P NMR spectra were less sensitive to some of these complications, with only two resonances being observed arising from each pair of diastereoisomers (^{31}P δ **35** 51.1, 51.2 ppm; **36**, 50.7, 51.5 ppm). The ν(C≡O) and ν(B-H) are both insensitive to the stereochemistry of the metal centre, and the complexes were further characterised by MALDI mass spectrometry (**35**, *m/*z 1337.2 ; **36** *m*/*z* 1337.2).

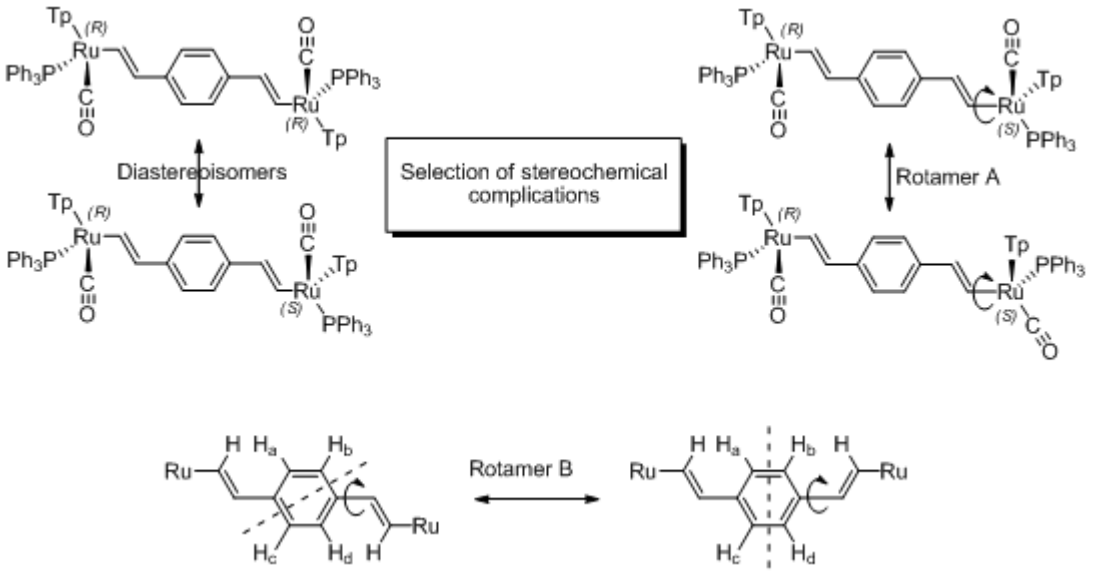

Figure **49** An illustration of some of the stereochemical complications associated with **35**.

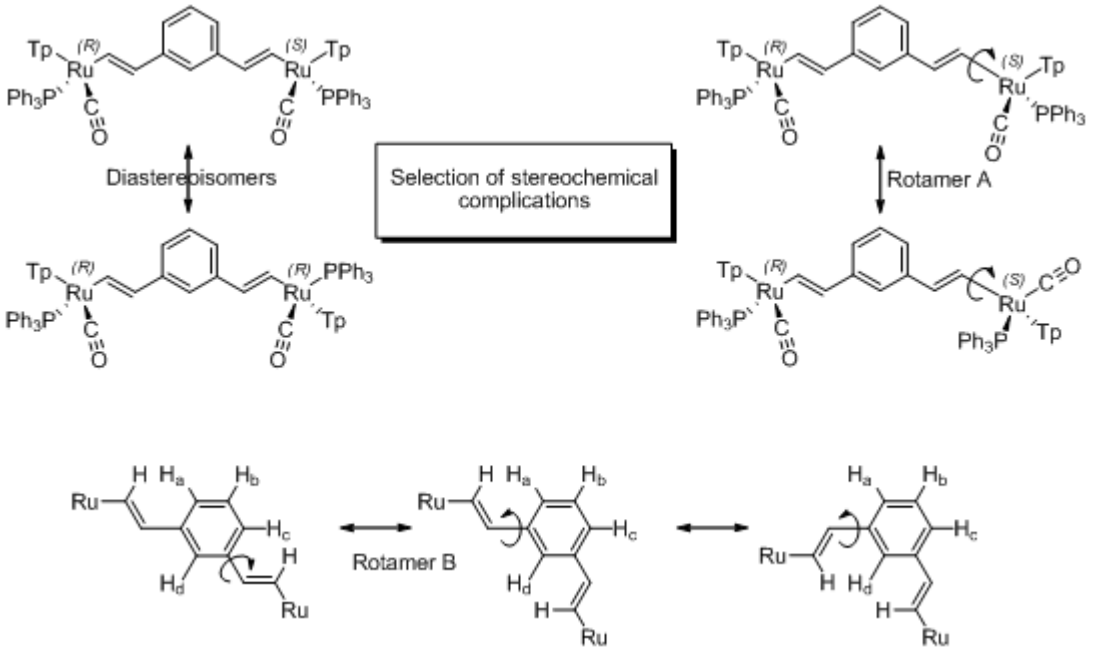

Figure **50** An illustration of some of the stereochemical complications associated with **36**.

4.3.2 Cyclic Voltammetry

Each of the complexes **35** and **36** exhibited two closely spaced one electron oxidation waves, which were only fully resolved in the case of **35** (Table **33**). [230] The separation of these redox waves reflects the relative thermodynamic stability of the intermediate mono-oxidised state compared with the neutral and dicationic forms. This relative stability can be expressed in terms of the comproportionation constant K_c, which is the equilibrium constant for the reaction

$$2\,[A^{+}] \overset{K_c}{\rightleftharpoons} [A] + [A^{2+}]$$

and can be extracted from the voltammetric data from the expression

$$K_c = \exp\{(\Delta E)F/RT\}$$

From the data in Table **33**, the comproportionation constants for $[\mathbf{35}]^{+}$ ($K_c = 2.5 \times 10^5$) and $[\mathbf{36}]^{+}$ ($K_c = 22$) can be calculated.

Table **33** Electrochemical data for **35** and **36** in MeCN 0.1 M $[NBu_4][BF_4]$.

Complex	$E_{0/+}$	$E_{+/2+}$	ΔE_p / mV [a]	i_c/i_a
35	0.02[b]	0.34[b]	114 / 124	1.0 / 1.0
36	0.28[c]	0.36[c]	Unresolved	unresolved

[a] ΔE_p is the peak-to-peak separation of the cathodic and anodic waves of the first / second redox process.

[b] Potentials are reported vs FcH/FcH^{+} = 0 V, using decamethylferrocene as an internal reference (Fc^*H/Fc^*H^{+} = -0.51 V vs FcH/FcH^{+}).

[c] Potentials are reported vs FcH/FcH^{+} = 0 V, using ferrocene as an internal reference. Potentials are estimated from two closely spaced waves.

Although the waves were not fully resolved in the case of **36**, the first oxidation is largely in agreement with the oxidation potentials observed for the analogous mononuclear vinyl complexes **23** ($E_{1/2}$ = 0.31 V) and the OMe bearing derivative **27** ($E_{1/2}$ = 0.22 V). In contrast, oxidation of the 1,4-substituted bimetallic complex **35**

is much more thermodynamically favourable than **36** and the related mononuclear compounds. Winter has observed similar patterns in studies of 1,4- and 1,3-[{RuCl(CO)(P^iPr_3)$_2$}$_2$(μ-CH=CHC$_6$H$_4$CH=CH)], **33** and **34** with the 1,4-isomer being considerable easier to oxidise than the 1,3-version. This observation was attributed to the mutual conjugation of two metal donors in the 1,4-isomer to the redox active phenylene vinylene redox centre. [42]

4.3.3 IR Studies

Each of the complexes **35** and **36** are characterised by ν(C≡O) bands near 1940 cm^{-1} and ν(BH) bands from the Tp ligand near 2480 cm^{-1} which are essentially identical to the mononuclear systems **23** – **27** described above.

Table **34** IR stretching frequencies for **35** and **36**, run in CH_2Cl_2.

Complex	ν(C≡O) / cm^{-1}	ν(B-H) / cm^{-1}
35	1942	2482
36	1941	2481

4.3.4 IR Spectroelectrochemical Studies

As with the mononuclear systems, spectroscopic data from the binuclear complexes **35** and **36** in their accessible oxidation states were obtained using spectroelectrochemical methods. In the case of **35**, which gave better resolved voltammetric response, and consequently larger K_c values for [**35**]$^+$, one-electron oxidation resulted in a shift of the single ν(C≡O) band in **35** from 1942 cm^{-1} to a single band at 1972 cm^{-1} in [**35**]$^+$ (Table **34**, Figure **51**). The observation of only a single ν(C≡O) band in the IR spectrum of [**35**]$^+$ clearly indicates that on the IR timescale, the metal centres in [**35**]$^+$ are identical. The shift of +30 cm^{-1} is

significantly smaller the ca. +50 cm^{-1} observed in the case of oxidation of mononuclear examples such as **23** (ν(C≡O) 1942 cm^{-1}) and [**23**]$^+$ (ν(C≡O) 1999 cm^{-1}), and very much smaller than might be expected for a purely metal centred oxidation.

Given the equivalence of the metal centres on the IR timescale, two extreme scenarios can be envisioned:

- the odd electron (or hole) may be in rapid (faster than 10^{13} s^{-1}) exchange between the metal centres;
- the odd electron (or hole) may be delocalised over the metal centres and the bridging ligand;

In the second scenario it is possible to debate the interpretation further, subject to the relative contributions of the metal centres and the bridging ligand to the redox-active orbital.

Table **35** IR spectroelectrochemical data for complexes **35** and **36** in CH_2Cl_2 0.1 M $[NBu_4][BF_4]$.

	ν(C≡O) / cm^{-1}		
Complex	Neutral	Cation	Dication
35	1942	1972	1996, 2071
36	1942	1972*	2005, 2072

*The pure monocation of **36** was not isolated.

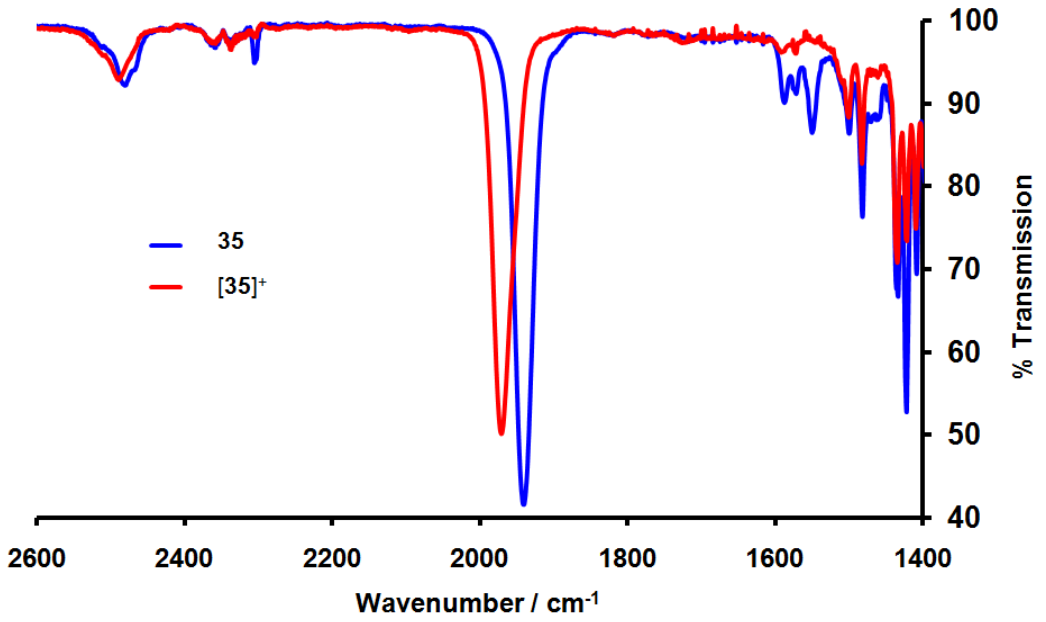

Figure **51** The change in ν(C≡O) as **35** is oxidised to $[\mathbf{35}]^+$ in CH_2Cl_2 0.1 M $[NBu_4][BF_4]$.

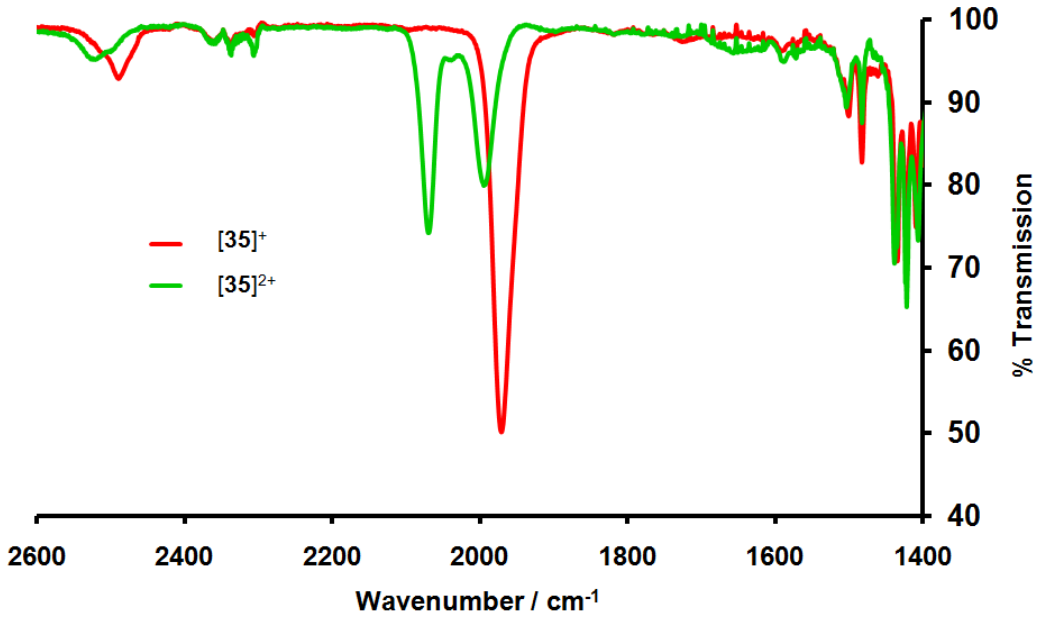

Figure **52** The change in ν(C≡O) as $[\mathbf{35}]^+$ is oxidised to $[\mathbf{35}]^{2+}$ in CH_2Cl_2, 0.1 M $[NBu_4][BF_4]$.

Further oxidation of $[\mathbf{35}]^+$ to $[\mathbf{35}]^{2+}$ causes the ν(C≡O) band to split into two higher frequency bands. The first, at 1996 cm^{-1}, is similar to that found in the case of the

monocations $[\mathbf{23}]^+$ and $[\mathbf{25}]^+$. The second peak is shifted by a much greater extent to 2070 cm^{-1} (Figure **52**). A large shift of ~ 130 cm^{-1} in the ν(C≡O) band is characteristic of a metal based oxidation, so to a first approximation it may be concluded that the first oxidation occurs on the vinyl aryl moiety (i.e. the ligand) with a modest contribution from the metal, whilst the second oxidation is more heavily based on one of the pendant metal centres (Figure **53**). Curiously, this behaviour of the dication differs from the Winter complex 1,4-$[\{RuCl(CO)(P^iPr_3)_2\}_2(\mu\text{-}CH{=}CHC_6H_4CH{=}CH)]^{2+}$ $[\mathbf{33}]^{2+}$ in which only a single ν(C≡O) band was observed.

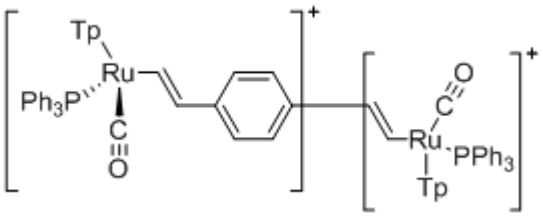

Figure **53** A schematic representation of $[\mathbf{35}]^{2+}$ showing an idealised representation of the charge distribution.

In the case of **36**, the small comproportionation constant associated with $[\mathbf{36}]^+$ made it impossible to obtain spectra of this species free of **36** and $[\mathbf{36}]^{2+}$. Nevertheless, from intermediate spectra collected during the oxidation of **36** to $[\mathbf{36}]^{2+}$, an intermediate with ν(C≡O) 1972 cm^{-1} could be observed, and assigned to $[\mathbf{36}]^+$. The data summarised in Table **35** clearly show the remarkable similarity of the ν(C≡O) frequencies of $[\mathbf{35}]^{n+}$ and $[\mathbf{36}]^{n+}$. Given the sensitivity of ν(C≡O) frequencies to metal charge density (oxidation state) it seems probable that the charge distribution in both families of complexes derived from **35** and **36** are similar as a function of overall complex oxidation state. The similar distribution of charge in the monocations $[\mathbf{35}]^+$ and $[\mathbf{36}]^+$ evidenced by the similar ν(C≡O) frequencies together with the small ν(CO) shifts upon change in redox state suggests strongly that these monocations be considered as being in fast exchange, rather than delocalised structures (Figure **54**).

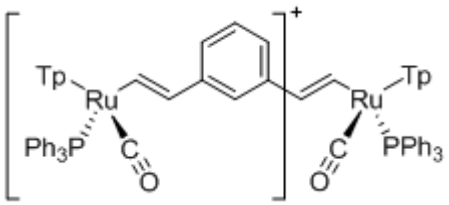

Figure **54** A schematic representation of [**36**]$^{+}$ showing an idealised representation of the localised charge distribution.

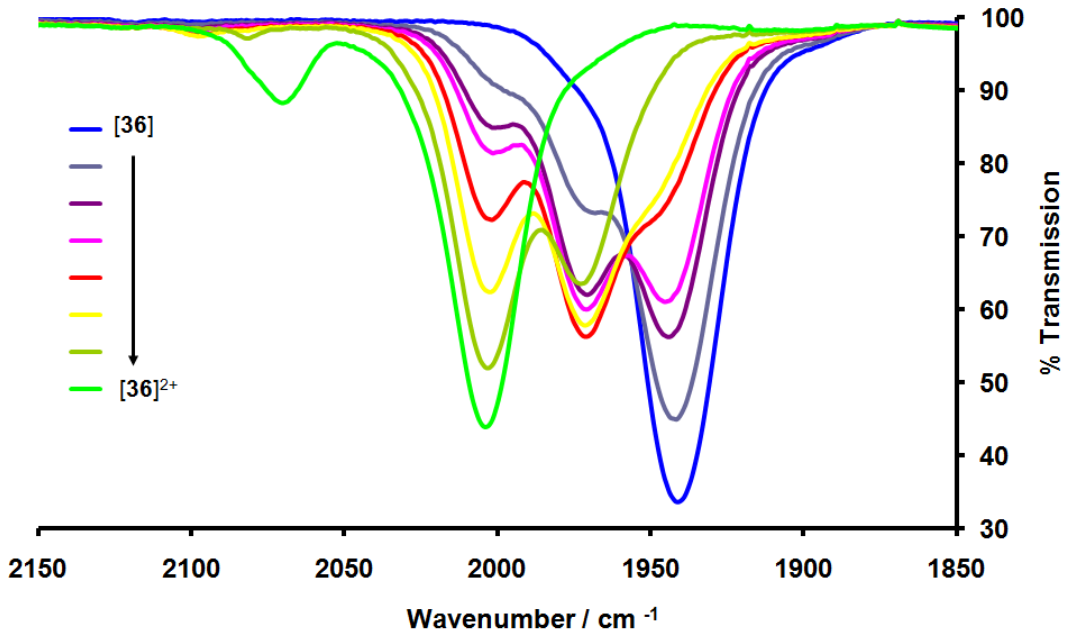

Figure **55** The change in ν(C≡O) as **36** is oxidised to [**36**]$^{2+}$ in CH_2Cl_2 0.1 M $[NBu_4][BF_4]$.

By assuming that the absorption bands in the IR spectra are Gaussian in profile, it is possible to attempt to deconvolute the experimental spectra of the oxidation of **36** to [**36**]$^{2+}$. The single ν(C≡O) band in the IR spectrum of **36** can be fitted to one Gaussian band at 1942 cm^{-1}. The two ν(C≡O) bands in the IR spectrum of the dication [**36**]$^{2+}$, can also be fitted, quite easily to two Gaussian bands. The first of these components at 2005 cm^{-1}, is similar to the ν(C≡O) band in the mono oxidised mono vinyl complexes ([**23**]$^{+}$ - [**27**]$^{+}$), the second at 2072 cm^{-1} is similar to that previously seen in the dicationic species [**35**]$^{2+}$, and has been assigned as the ν(C≡O) band of the "pendant" Ru-CO centre. A fourth Gaussian band can be deconvoluted from the intermediate IR spectra of the oxidation of **36** to [**36**]$^{2+}$, by varying the

amounts of the ν(C≡O) band corresponding to the neutral (1942 cm^{-1}) and the ν(C≡O) bands corresponding to the dication (2005 cm^{-1} and 2072 cm^{-1}). Figure **56** shows snap shots of the oxidation of **36** to $[\mathbf{36}]^{2+}$, with the deconvoluted Gaussian bands. The fourth Gaussian band at 1972 cm^{-1}, which is in a similar region as that of the symmetric $[\mathbf{35}]^{+}$, could be, without much persuasion, assigned to the ν(C≡O) frequency of the fast exchange $[\mathbf{36}]^{+}$ cation.

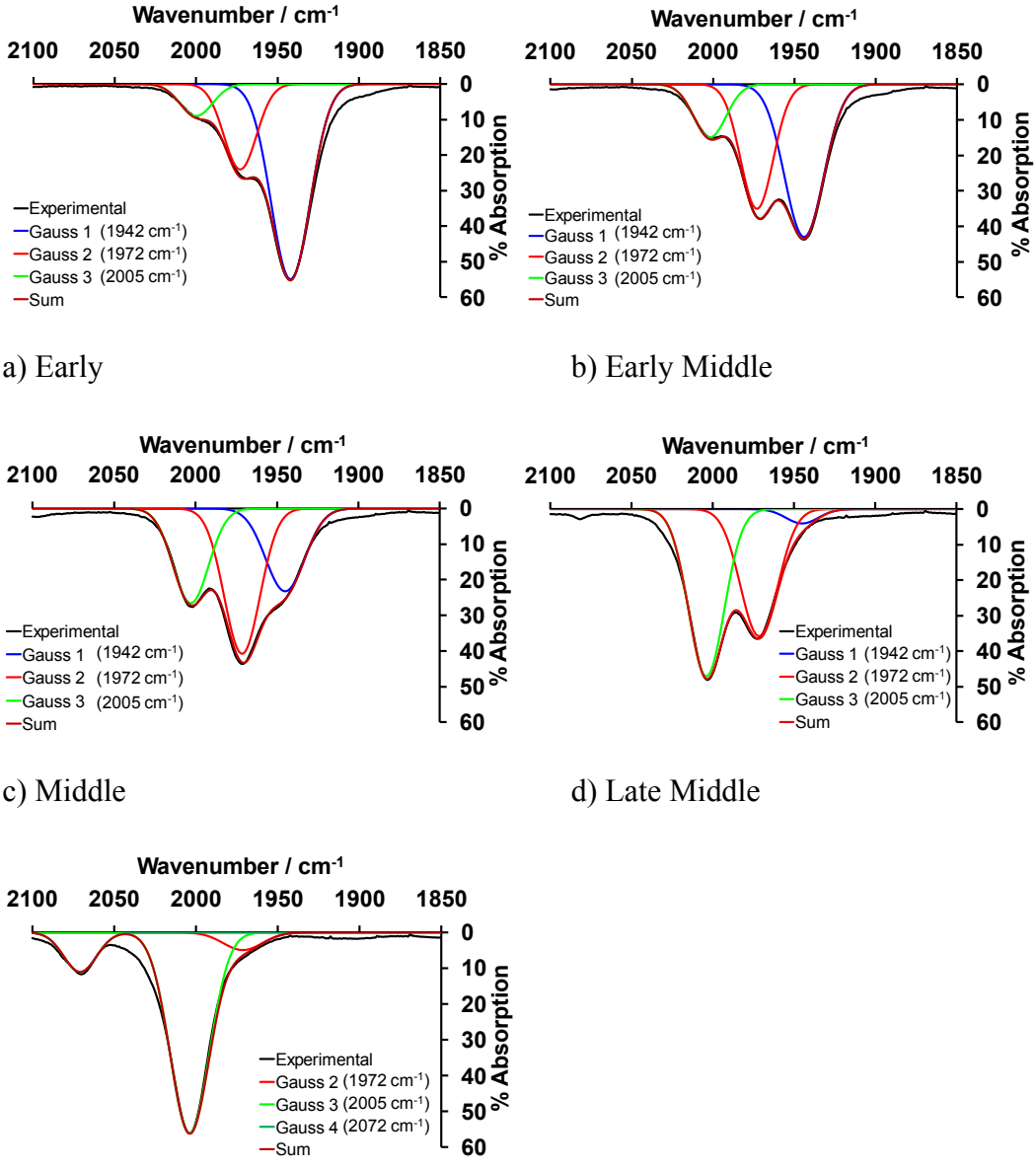

a) Early

b) Early Middle

c) Middle

d) Late Middle

e) End

Figure **56** Deconvolution of the IR spectra of the oxidation of **36** to $[\mathbf{36}]^{2+}$, into the four Gaussian shaped peaks, at 1942, 1972, 2005 and 2072 cm^{-1}. Examples a) – e) range from early in the oxidation to near completion of oxidation to $[\mathbf{36}]^{2+}$.

4.3.5 UV-Vis-NIR Spectroelectrochemical Studies

Due to the complications associated with disproportionation of the mono-oxidised $[\mathbf{36}]^{+}$ no further work on the characterising of **36** and its oxidised forms was undertaken. However, the neutral and oxidised forms of **35** were further characterised by UV-vis-NIR spectroelectrochemical methods (Figure **57**). These spectroscopic data are summarised in Table **36**, with assignments given based on results of the electronic structure and TD DFT calculations described in more detail below.

Table **36** UV-vis-NIR spectroscopic data for **35** in CH_2Cl_2 0.1 M $[NBu_4][BF_4]$. Some extinction coefficients were not reported due to broad indistinct peaks.

Complex	ν / cm^{-1}, (ε_{max} / $M^{-1}cm^{-1}$)
[**35**]	28990 (13110)
$[\mathbf{35}]^{+}$	12600 – 27100
$[\mathbf{35}]^{2+}$	12800 – 26800
	2750 – 3400

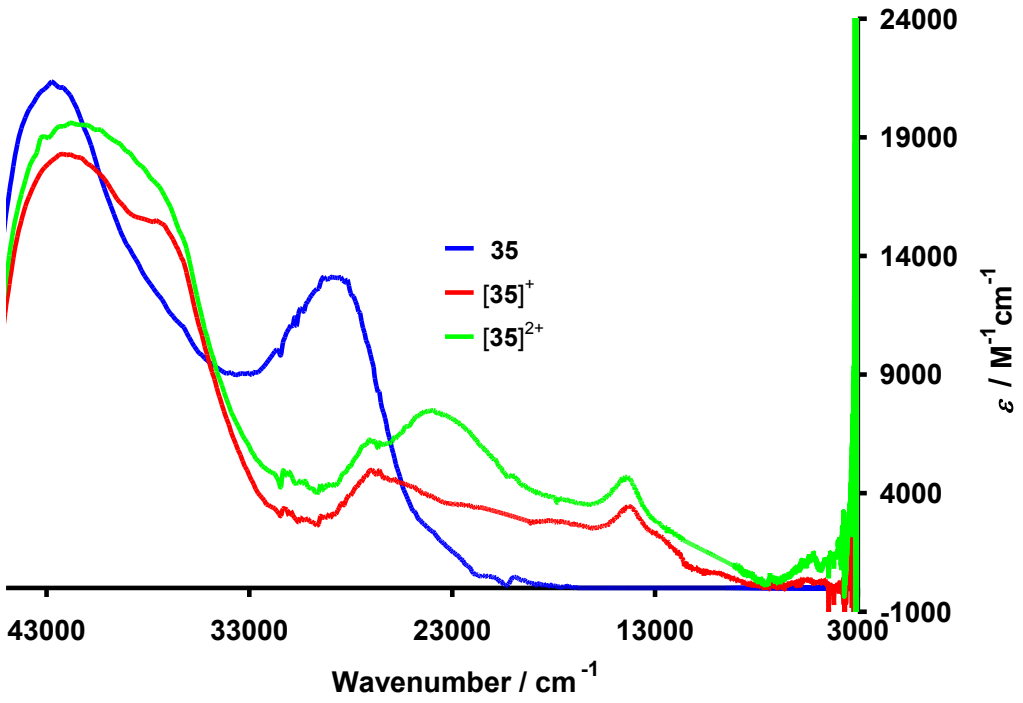

Figure **57** UV-vis-NIR spectra of $[\mathbf{35}]^{n+}$ (n = 0, 1, 2), CH_2Cl_2 0.1 M $[NBu_4][BF_4]$.

4.3.6 Electronic Structure Calculations

The theoretical investigation conducted at the DFT level, initially on the model system [Ru(CH=CHPh)(CO)(PPh_3)Tp], was extended to the bis- hydroruthenated compounds. Full structural model systems of 1,4-[{Ru(CO)(PPh_3)Tp}$_2$(μ-CH=CHC_6H_4CH=CH)] (**35-H**) and 1,3-[{Ru(CO)(PPh_3)Tp}$_2$(μ-CH=CHC_6H_4CH=CH)] (**36-H**) were used. Where isomers were possible only the isomer with the lowest computed energy was used in further calculations to minimise resource demands. The discussion which follows refers to results obtained from calculations at the MPW1K/LANL2DZ/3-21G* level of theory with no symmetry constraints.

The optimised geometries of the neutral forms of both **35-H** and **36-H** are symmetric, with **35-H** having a C_2 symmetry rotational axis normal to the plane of the benzene ring, whereas the C_2 symmetry axis in **36-H** lies in the plane. Important bond lengths are similar to those of **23** and other mono-metallic vinyl complexes described earlier in this Chapter (Table **37** and Table **38**, Figure **58**).

Table **37** Selected bond lengths (Å) of the optimised geometries of the neutral bimetallics **35-H** and **36-H** and **23-H**.

Bond Length	**35-H**	**36-H**	**23-H**
Ru-C_α	2.047	2.045	2.047
Ru-CO	1.871	1.870	1.873
Ru-P	2.333	2.333	2.327
C≡O	1.161	1.161	1.160
C_α=C_β	1.342	1.342	1.342
C_β-C_1	1.469	1.471	1.470
Ru-N_1 (*trans* to PPh3)	2.089	2.089	2.089
Ru-N_3 (*trans* to CO)	2.116	2.119	2.116
Ru-N_5 (*trans* to vinyl)	2.160	2.160	2.157

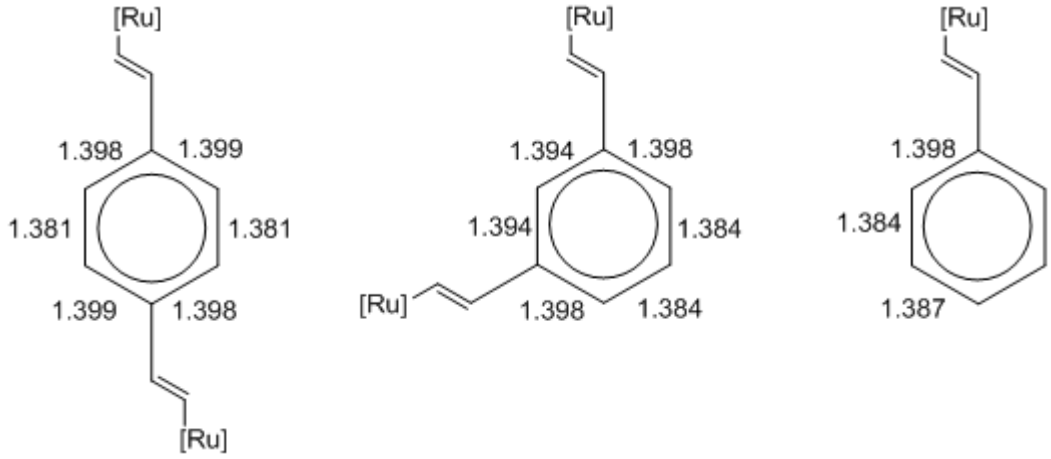

Figure **58** Bond lengths around the aromatic ring in **35-H**, **36-H** and **23-H**.

Table **38** Selected bond angles / dihedral angles table of the optimised geometries of the neutral bimetallics **35-H** and **36-H** and **23-H**.

	35-H [a]	**36-H** [a]	**23-H**
CO-Ru-C_α	89.21	89.25	89.00
CO-Ru-N_3	173.41	173.69	173.54
C_α-Ru-N_5	172.70	173.43	172.26
CO-Ru-P	94.17	94.31	94.09
C_α-Ru-P	88.26	87.25	89.68
N_1-Ru-P	174.75	173.73	175.29
C_β-C_α-Ru	131.04	130.39	130.70
C_α-C_β-C_1	126.41	126.42	126.18
CO-Ru-C_α-C_β	-16.81	-15.43	-18.87
Ru-C_α-C_β-C_1	-177.79	-176.61	178.72
C_α-C_β-C_1-C_2	-7.54	7.50	-17.21

[a] Neutral complexes **35-H** and **36-H** are geometrically symmetric

Table **39** shows good agreement of the calculated ν(C≡O) and observed ν(C≡O) frequencies, which gives further confidence in the accuracy of the optimised geometries.

Table **39** Comparison of the experimental ν(C≡O) of neutral **35** and **36**, with the calculated ν(C≡O) of **35-H** and **36-H**.

	ν(C≡O) / cm^{-1}
35 (**35-H**)	1942 (1941)
36 (**36-H**)	1942 (1940)

Table **40** and Table **41** summarise the composition of the frontier orbitals of **35-H** and **36-H**, with representative contour plots of key orbitals from **35-H** and **36-H**, illustrated in Figure **59** and Figure **60**. In the neutral system **35-H** the HOMO is mainly divinylphenylene in character, with a small metal contribution (79 / 16 %), and well removed from the other occupied and non-occupied orbitals. In the case of **36-H**, the HOMO is also heavily divinylphenylene in character (73 / 20 %) but now the HOMO-1 has risen in energy, resulting in the HOMO and HOMO-1 being close in energy, but well removed from the other orbitals. Figure **59** and Figure **60** show the HOMOs and HOMO-1 of **35-H** and **36-H**. Given the large contribution of the divinylphenylene ligand to these frontier orbitals, it seems more appropriate to discuss the structures in terms of organic redox systems, supported by electron-donating metal groups.

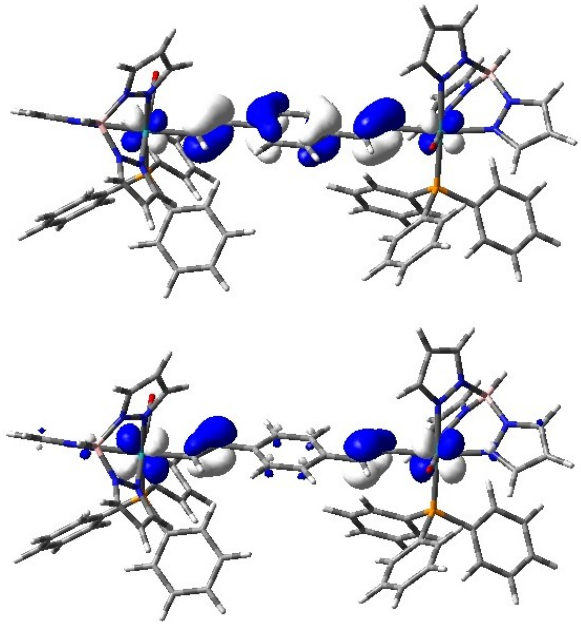

Figure **59** The HOMO (top) and HOMO-1 (bottom) of **35-H** plotted with contour values ±0.04 $(e/bohr^3)^{1/2}$.

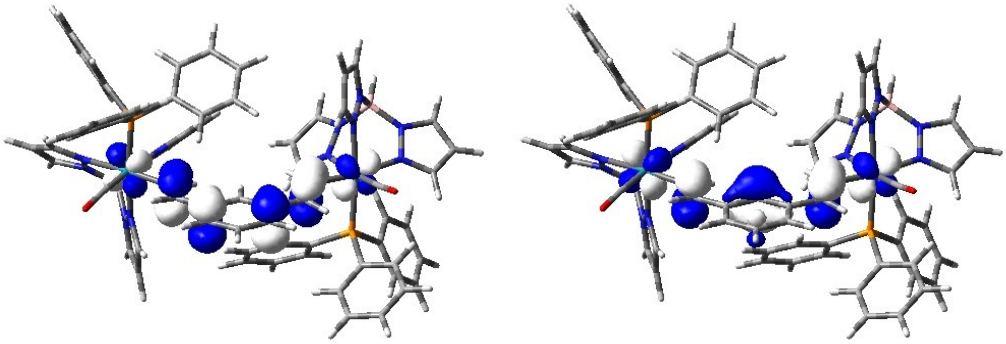

Figure **60** The HOMO (left) and [HOMO-1] (right) of **36-H** plotted with contour values ±0.04 $(e/bohr^3)^{1/2}$.

Not unlike the mononuclear systems, the LUMOs for the bimetallic **35-H** and **36-H** complexes, are phosphine σ*-orbital in character, with a small contribution from both of the metal centres, with the bridge π*- vinyl system comprising the LUMO+6 and the LUMO+8 for **35-H** and the LUMO+6 and the LUMO+10 for **36-H** (Table **40** and Table **41**).

Table **40** Contributions of the frontier molecular orbitals of **35-H**.

35-H												
MO												
	LUMO+7	LUMO+6	LUMO+3	LUMO+2	LUMO+1	LUMO	HOMO	HOMO-1	HOMO-2	HOMO-3	HOMO-4	HOMO-5
ε(eV)	0.52	0.45	0.22	0.21	0.06	0.05	-5.06	-6.20	-6.82	-6.82	-6.88	-7.17
Occ	0	0	0	0	0	0	2	2	2	2	2	2
%Ru	2, 2	3, 3	1, 1	1, 1	3, 3	3, 3	8, 8	24, 24	29, 29	29, 29	23, 23	0
%Tp	2, 2	4, 4	0, 0	1, 1	2, 2	2, 2	1, 1	6, 6	14, 14	14, 14	16, 16	0
%CO	1, 1	1, 1	0, 0	0, 0	1, 1	1, 1	0, 0	0, 0	3, 3	3, 3	1, 1	0
%PPh_3	31, 31	29, 29	48, 47	46, 46	45, 44	42, 43	1, 1	1, 1	1, 1	1, 1	3, 3	0
%C_α	0, 0	5, 5	0, 0	0, 0	0, 0	1, 1	12, 12	4, 4	2, 2	2, 2	2, 2	0
%C_β	0, 0	1, 1	0, 0	0, 0	0, 0	0, 0	10, 10	12, 12	3, 3	3, 3	0, 0	0
%Aryl	0, 0	14	1	2	0	2	35	7	0	0	9	100

Table **41** Contributions of the frontier molecular orbitals of **36-H**.

36-H												
MO												
	LUMO+7	LUMO+6	LUMO+4	LUMO+2	LUMO+1	LUMO	HOMO	HOMO-1	HOMO-2	HOMO-3	HOMO-4	HOMO-5
ε(eV)	0.71	0.53	0.37	0.23	0.11	0.10	-5.47	-5.79	-6.84	-6.84	-6.94	-6.98
Occ	0	0	0	0	0	0	2	2	2	2	2	2
%Ru	3, 3	3, 3	0, 0	2, 2	3, 3	3, 3	10, 10	15, 15	27, 31	32, 27	22, 22	18, 18
%Tp	29, 29	6, 6	0, 0	1, 1	2, 2	2, 2	2, 2	2, 2	12, 14	14, 12	15, 15	13, 13
%CO	7, 7	1, 1	0, 0	1, 1	1, 1	1, 1	0, 0	0, 0	3, 4	4, 3	1, 1	1, 1
%PPh_3	11, 11	33, 33	49, 46	47, 45	44, 44	44, 44	1, 1	1, 1	1, 1	1, 1	4, 4	3, 3
%C_α	0, 0	2, 2	0, 0	0, 0	0, 0	0, 0	9, 9	8, 8	2, 2	2, 2	2, 2	2, 2
%C_β	0, 0	1, 1	0, 0	0, 0	0, 0	0, 0	9, 9	13, 13	0, 0	0, 0	0, 0	0, 0
%Aryl	0	8	1	1	0	1	37	23	1	1	13	24

Upon oxidation of **35-H** to the mono-oxidised species [**35-H**]$^{+}$, in which both metal centres are in identical structural environments, the CO-Ru-C_α-C_β dihedral angle increases from -16.8 ° to -17.2 °, (similar to the increase, in the oxidation of **23-H** to [**23-H**]$^{+}$; 3 °). The vinyl-aromatic ring dihedral angle C_α-C_β-C_1-C_2 is also rotated by ~5 °, decreasing to result in a near planar arrangement of the *para*-substituted aromatic ring and the two vinyl moieties, probably driven by the increase in quinoidal character of the organic bridge. The gross structural features of [**35**]$^{n+}$ are therefore similar, regardless of oxidation state.

As described for the mono-metallic complexes [**23-H**]$^{+}$ **-** [**27-H**]$^{+}$, the bimetallic cation [**35-H**]$^{+}$ features a Ru-C_α bond somewhat shorter than the closed shell precursor **35-H** (Table **42**).

Table **42** Bond lengths (Å) of the optimised geometries of **35-H** and [**35-H**]$^{+}$ and differences with data from **23-H** and [**23-H**]$^{+}$ for comparison.

Bond Length	**35-H**	[**35-H**]$^{+}$	%Δ^a [**35-H**]$^{+}$	%Δ^b [**23-H**]$^{+}$
Ru-C_α	2.047	1.997	-2.44	-4.00
Ru-CO	1.871	1.885	+0.75	+2.35
Ru-P	2.333	2.355	+0.94	+3.14
C≡O	1.161	1.157	-0.34	-0.86
C_α=C_β	1.342	1.376	+2.53	+2.61
C_β-C_1	1.469	1.422	-3.20	-1.90
Ru-N_1 (*trans* to PPh3)	2.089	2.093	+0.20	~ 0
Ru-N_3 (*trans* to CO)	2.116	2.106	-0.47	-1.37
Ru-N_5 (*trans* to vinyl)	2.160	2.146	-0.65	-0.74

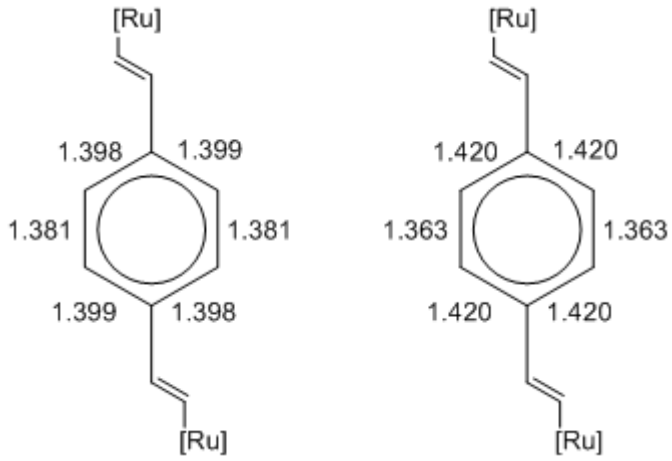

Figure **61** Aromatic bond lengths in: left; **35**, and right; cation $[\mathbf{35}]^+$.

There is a good agreement with the experimental IR spectra of $\mathbf{35}^+$ and $[\mathbf{35\text{-}H}]^+$, even though there may be an underestimation of the shift of the ν(C≡O) frequency (Table **43**).

Table **43** Comparison of the experimental and calculated ν(C≡O) frequencies of $[\mathbf{35}]^+$ and $[\mathbf{35\text{-}H}]^+$.

	$[\mathbf{35}]^+$	$[\mathbf{35\text{-}H}]^+$
ν(C≡O)	1972 cm^{-1}	1958 cm^{-1}
Δ ν(C≡O)	30 cm^{-1}	17 cm^{-1}

Structural changes upon oxidation are also evidenced in the elongation of the metal-phosphine bond lengths (Table **42**). Carbonyl bond lengths, and hence the ν(C≡O), are also sensitive to the net electron density at the metal centre. The CO bond length in the $[\mathbf{35\text{-}H}]^+$ is modestly shorter than in **35-H**, leading to a higher ν(C≡O) frequency [**35-H**, 1941 cm^{-1}; $[\mathbf{35\text{-}H}]^+$, 1958 cm^{-1}].

From Table **42** it can be seen that the percentage difference in the C≡O bond lengths of **35-H** and $[\mathbf{35\text{-}H}]^+$ is roughly half that of the mononuclear system [**23**] and $[\mathbf{23}]^+$ (-0.34 % and -0.86 %).

The molecule orbital calculations of **23-H – 27-H** showed the HOMO has significant vinyl character, which is also true of the bimetallic complexes **35-H** - **36-H**. Thus the effect of the oxidation, which is occurring mainly on the aromatic ring, is shared between the two metal centres in $[\mathbf{35}]^+$, consequently, the shift in ν(C≡O) in **35** and $[\mathbf{35}]^+$ is roughly half that found in **23-H** and $[\mathbf{23\text{-}H}]^+$ (17 cm^{-1} compared with 56 cm^{-1})

Table **44** summarises the composition of the frontier orbitals of $[\mathbf{35\text{-}H}]^+$ with representative contour plots of β-LUSO from $[\mathbf{35\text{-}H}]^+$ illustrated in Figure **62**. In $[\mathbf{35\text{-}H}]^+$, the α-HOSO and β-LUSO are similar in composition and mainly divinylphenylene in character, with a small metal contribution (70 / 22 %) and (75 / 20 %) respectively (Figure **62**). The α-LUSO is essentially the divinylbenzene π* system, whilst the β-HOSO is rather more metal in character (Table **44**).

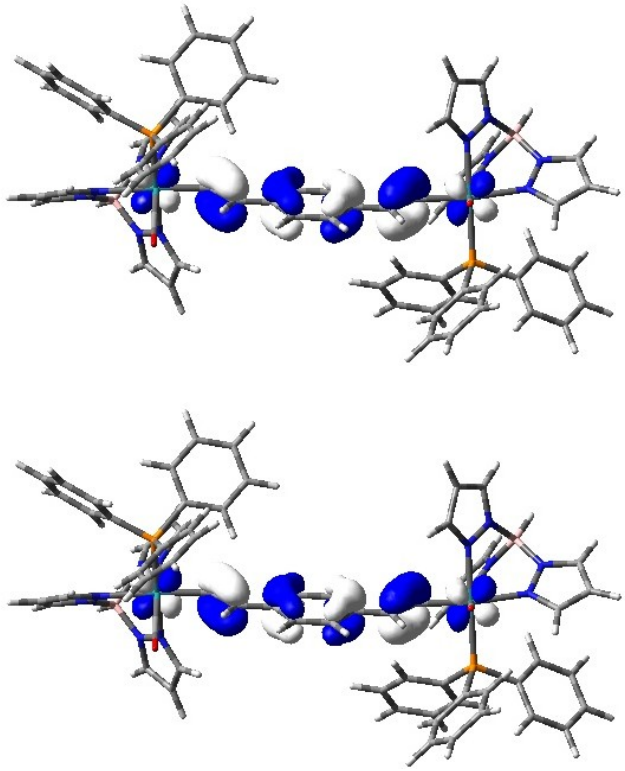

Figure **62** The β-LUSO (top) and the α-HOSO (bottom) of $[\mathbf{35\text{-}H}]^+$ plotted with contour values ±0.04 $(e/bohr^3)^{1/2}$.

Table **44** Molecular contributions for the frontier orbitals of [**35-H**]$^{+}$.

[**35-H**]$^{+}$														
MO														
	317β	317α	315β	315α	314β	314α	313β	313α	312β	312α	311β	311α	309β	309α
	β-[LUSO+4]	α-[LUSO+3]	β-[LUSO+2]	A-[LUSO+1]	β-[LUSO+1]	α-[LUSO]	β-[LUSO]	α-[HOSO]	β-[HOSO]	α-[HOSO-1]	β-[HOSO-1]	α-[HOSO-2]	β-[HOSO-3]	α-[HOSO-4]
ε(eV)	-1.72	-1.72	-1.99	-2.01	-2.41	-2.92	-5.47	-7.99	-8.14	-9.01	-9.08	-9.28	-9.22	-9.42
Occ	0	0	0	0	0	0	0	1	1	1	1	1	1	1
%Ru	3, 3	3, 3	5, 5	5, 5	4, 4	2, 2	10, 10	11, 11	23, 23	23, 23	19, 19	3, 40	27, 19	12, 12
%Tp	2, 2	2, 2	2, 2	2, 2	2, 2	1, 1	1, 1	2, 2	6, 6	16, 16	19, 20	4, 44	26, 18	24, 24
%CO	2, 2	2, 2	1, 1	1, 1	1, 1	0, 0	0, 0	0, 0	0, 0	0, 0	1, 1	0, 4	3, 2	1, 1
%PPh_3	45, 42	45, 42	41, 41	40, 40	6, 6	2, 2	1, 1	1, 1	1, 1	1, 1	3, 3	0, 2	1, 1	9, 9
%C_α	0, 0	0, 0	0, 0	1, 1	18, 18	17, 17	11, 11	11, 11	1, 1	1, 1	4, 4	0, 2	1, 1	2, 2
%C_β	0, 0	0, 0	0, 0	0, 0	1, 1	3, 3	10, 10	9, 9	12, 12	7, 7	0, 0	0, 0	0, 0	0, 0
%Aryl	0	0	1	1	38	49	33	30	13	5	9	0	0	5

Table **45** Spin Density Table [**35-H**]$^+$.

	[**35-H**]$^+$	
	Centre A	Centre B
Ru	0.113,	0.113,
P	-0.003,	-0.003,
C (CO)	-0.004	-0.004
C_α	0.213	0.213
C_β	0.059	0.059
N *trans* to CO	-0.001	-0.001
N *trans* to vinyl	-0.004	-0.004
N *trans* to PPh3	0.003	0.003
Aryl	0.278	

From the spin density calculations on [**35-H**]$^+$ it can be seen that the 82% of the spin is symmetrically delocalised on the divinylbenzene moiety (Table **45**).

From Table **46** it can be seen that the calculated geometry of [**36-H**]$^+$ is asymmetric with one of the metals in a similar spatial geometry to that of the neutral species **36**, and the other metal centre similar to the metal centres of the mono-oxidised mononuclear vinyl complexes. This geometry leads to a localised oxidation, heavily involving one of the metal centres and the bridging ligand. Hence the calculated IR gave two ν(C≡O) bands, one similar to the neutral system (1947 cm^{-1}) and another, at a shift of ~35 cm^{-1}, similar to the mono-oxidised mononuclear vinyl complexes (1982 cm^{-1}).

Table **46** Optimised geometries of **36-H** and [**36-H**]$^+$ and the bond length differences between the two oxidation states.

Bond Length / Å	**36-H**	[**36-H**]$^+$	Δ
Ru(A)-C_α	2.045	1.958	-0.087
Ru(A)-CO	1.870	1.902	+0.032
Ru(A)-P	2.333	2.396	+0.066
C≡O	1.161	1.153	-0.008
C_α=C_β	1.342	1.384	+0.042
C_β-C_1	1.471	1.433	-0.038
Ru(A)-N_1 (*trans* to PPh3)	2.089	2.089	~ 0
Ru(A)-N_3 (*trans* to CO)	2.119	2.095	-0.024
Ru(A)-N_5 (*trans* to vinyl)	2.160	2.149	-0.011
Ru(B)-$C_{\alpha'}$	2.045	2.042	-0.003
Ru(B)-CO	1.870	1.875	+0.005
Ru(B)-P	2.333	2.339	+0.006
C≡O	1.161	1.159	-0.002
$C_{\alpha'}$=$C_{\beta'}$	1.342	1.347	+0.005
$C_{\beta'}$-$C_{1'}$	1.471	1.464	-0.007
Ru(B)-$N_{1'}$ (*trans* to PPh3)	2.089	2.093	+0.004
Ru(B)-$N_{3'}$ (*trans* to CO)	2.119	2.113	-0.006
Ru(B)-$N_{5'}$ (*trans* to vinyl)	2.160	2.150	-0.010

The composition of the frontier orbitals of [**36-H**]$^+$ are summarised in Table **47** with representative contour plots of α-HOSO, α-LUSO, β-HOSO and β-LUSO illustrated in Figure **63**. The α-HOSO and β-LUSO of [**36-H**]$^+$ are both similar in composition, and again are mainly divinylphenylene in character, with a considerable metal contribution (49 / 39 %) and (59 / 30 %) respectively (Figure **63**). Again, the α-LUSO is essentially the divinylbenzene π* system, whilst the β-HOSO is rather more metal in character (Figure **63**, Table **47**).

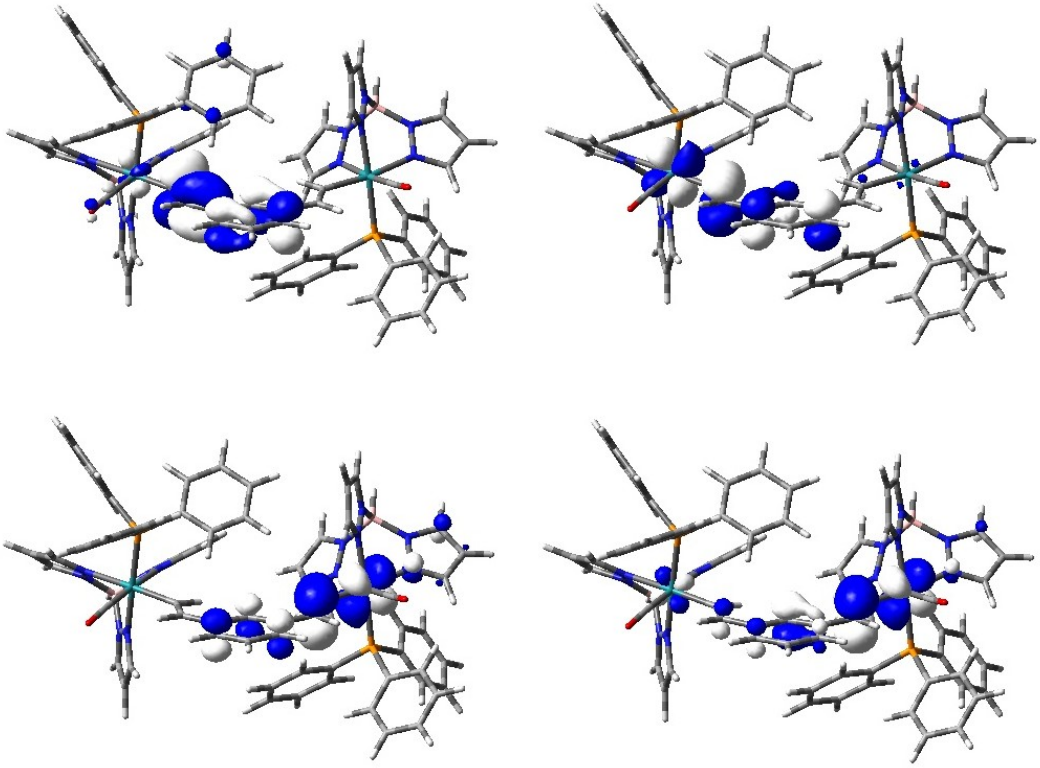

Figure **63** The α-LUSO (top left) the α-HOSO (bottom left), the β-LUSO (top right) and the β-HOSO (bottom right) of [**36-H**]$^{+}$ plotted with contour values ±0.04 $(e/bohr^3)^{1/2}$.

Table **47** Contributions of the frontier molecular orbitals of [**36-H**]$^{+}$.

[**36-H**]$^{+}$														
MO														
	316β	316α	315β	315α	314β	314α	313β	313α	312β	312α	311β	311α	310β	310α
	β-[LUSO+3]	α-[LUSO+2]	β-[LUSO+2]	α-[LUSO+1]	β-[LUSO+1]	α-[LUSO]	β-[LUSO]	α-[HOSO]	β-[HOSO]	α-[HOSO-1]	β-[HOSO-1]	α-[HOSO-2]	β-[HOSO-2]	α-[HOSO-3]
ε(eV)	-2.23	-2.27	-2.26	-2.47	-2.51	-2.80	-5.89	-8.14	-7.84	-8.91	-8.89	-9.09	-9.04	-9.19
Occ	0	0	0	0	0	0	0	1	1	1	1	1	1	1
%Ru (A)	13	12	12	19	12	5	30	0	5	0	0	8	2	8
%Tp (A)	9	13	13	7	5	3	4	0	1	0	0	2	1	3
%CO (A)	2	19	18	3	6	2	0	0	0	0	0	0	0	0
%PPh_3 (A)	29	54	56	62	56	12	2	0	0	0	0	1	0	1
%C_α (A)	13	0	0	3	6	28	11	0	0	0	0	7	0	6
%C_β (A)	4	0	0	0	3	8	21	0	3	0	0	9	0	11
%Aryl	28	0	0	5	11	40	27	18	16	1	1	26	9	23
%C_β (B)	0	0	0	0	0	0	1	22	22	1	1	1	3	4
%C_α (B)	0	0	0	0	0	1	2	9	10	4	2	4	7	3
%PPh_3 (B)	0	0	0	0	0	0	0	2	2	2	2	6	10	10
%CO (B)	0	0	0	0	0	0	0	0	0	7	7	1	2	2
%Tp (B)	0	0	0	0	0	0	0	10	7	32	32	17	32	13
%Ru (B)	0	0	0	0	0	0	1	39	33	54	54	16	32	15

The spin density calculations of [**36-H**]$^+$ (Table **48**), agree with the optimised geometry of [**36-H**]$^+$, with the charge being asymmetrically distributed.

Table **48** Spin Densities for [**36-H**]$^+$.

	[**36-H**]$^+$	
	Centre A	Centre B
Ru	0.460	0.003
P	-0.015	0
C (CO)	-0.012	0
C_α	-0.035	-0.055
C_β	0.403	0.050
N *trans* to CO	-0.004	0
N *trans* to vinyl	-0.005	0
N *trans* to PPh3	-0.004	0
Aryl	0.219	

The optimised geometries of both of the possible spin states, singlet (low spin) and triplet (high spin), of both [**35-H**]$^{2+}$ and [**36-H**]$^{2+}$, gave symmetric geometries. The DFT calculated ν(C≡O) frequencies for LS and HS [**35-H**]$^{2+}$, and LS and HS [**36-H**]$^{2+}$, gave poor agreement with the experimental result. Due to these geometry, frequency and spin issues, and given the limited computational resources available, the theoretical study of these rather large dicationic complexes was not pursued further.

4.3.7 UV-vis Absorptions from the TD DFT Calculations

To aid in the assignment of the electronic transitions observed in the experimental work (Section **4.3.5**) TD DFT calculations were carried out on the model system 1,4-[{Ru(CO)(PPh_3)Tp}(μ-CH=CHC_6H_4CH=CH)]$^{n+}$ ([**35-H**]$^{n+}$, n = 0, 1). Before discussing the TD DFT results from **35-H**, a few of the pertinent points of the electronic structure of this compound, will be summarised, to aid the reader. In a manner similar to that described for the mono-metallic compounds **23** – **27**, the

HOMO in **35** is predominately comprised of a Ru-CH=CH-Ar-CH=CH-Ru π-type system and can be termed a "metal-ligand" (ML) orbital (Table **49**, Figure **64**). The corresponding π* system (LUMO+6) with a node between the vinyl carbon atoms features an appreciably smaller metal contribution (Table **49**) and can be designated a "ligand" (L) orbital. The orbital composition of **35-H** compares most closely to that of **27-H** (Table **49**), suggesting that it is appropriate to consider the second metal centre as a good electron donor.

Table **49** Composition of selected frontier orbitals of **35-H** and **27-H**.

		ε(eV)	%Ru	%Tp	%PPh_3	%CO	%C_α	%C_β	%Aryl	%R-group
35-H	HOMO	-5.09	16	2	2	0	24	20	35	-
	LUMO+6	0.45	6	8	58	2	10	2	14	-
27-H	HOMO	-5.53	18	3	1	0	16	18	36	7
	LUMO+8	1.19	4	31	11	1	9	2	40	2

For the neutral (18-electron, closed shell) system **35-H** the most significant absorption band in the visible region is calculated to arise from transitions from the "ML" centred HOMO to the LUMO+6, and can hence be designated as an ML-LCT transition.

In the experimental studies, oxidation of **35** to $[\mathbf{35}]^+$ causes a collapse of the ML-LCT transition associated with the neutral species, with smaller absorption bands growing into the spectrum at lower energy. On the basis of the TD DFT calculations, and the TD DFT calculations of the mono-vinyl complexes **23** – **27**, these lower energy bands can be assigned to the transitions from the α-HOSO to the α-LUSO and from the β-HOSO to the β-LUSO. The α-HOSO and β-LUSO of $[\mathbf{35}]^+$ are both similar in composition to the HOMO (Figure **64**). The α-LUSO is similar in composition to the L orbitals described above (i.e. LUMO+6), whilst the β-HOSO is rather more metal in character (Figure **65**, Table **50**).

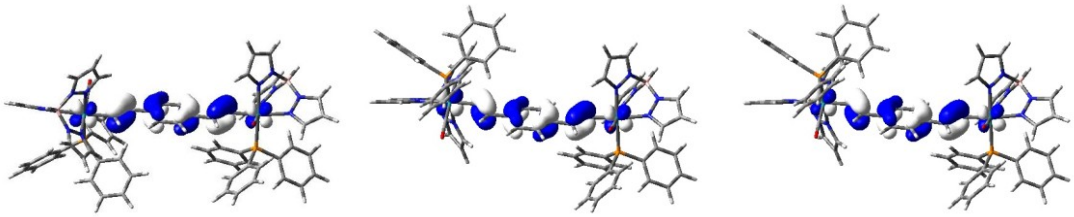

Figure **64** Contour plots: left; HOMO of **35-H**, centre; α-HOSO, right; β-LUSO of [**35-H**]$^+$.

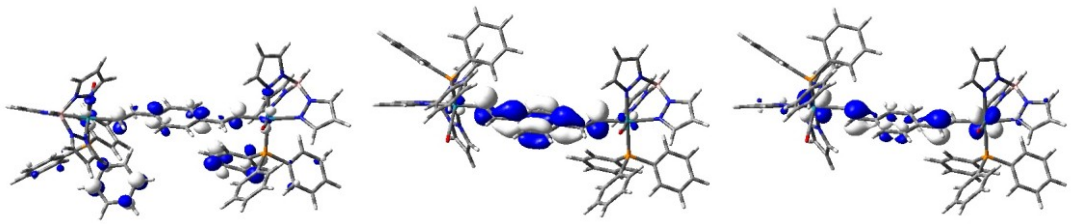

Figure **65** Contour plots: left; LUMO+6 of **35-H**, centre; α-LUSO, right; β-HOSO of [**35-H**]$^+$.

Table **50** Composition of the β-HOSO and α-LUSO of [**35-H**]$^+$, [**27-H**]$^+$ and [**23-H**]$^+$.

		ε(eV)	%Ru	%Tp	%PPh_3	%CO	%C_α	%C_β	%Aryl	%R-group
[**35-H**]$^+$	β-HOSO	-8.14	46	12	2	0	2	24	13	-
	α-LUSO	-7.99	22	4	2	0	22	18	30	-
[**27-H**]$^+$	β-HOSO	-9.49	27	20	3	0	9	0	30	10
	α-LUSO	-3.08	4	3	10	2	29	9	40	3
[**23-H**]$^+$	β-HOSO	-9.88	20	26	7	0	16	1	30	-
	α-LUSO	-3.16	6	3	18	4	26	8	34	-

On this basis, the α-HOSO - α-LUSO transition is also ML-LCT in character, while the β-HOSO - β-LUSO transition can be better described as M-MLCT in character.

As the DFT calculations were unable to successfully model the dication [**35**]$^{2+}$, the UV-vis absorptions assignments had to be done manually, hence the assignment of the band at roughly 24000 cm^{-1} is tentatively assigned as ML-LCT in character, akin to the higher energy absorption in the mono-vinyl complexes, and the band at lower energy band at roughly 13000 cm^{-1} as M-MLCT in character, similar to the

assignment of the band in the cationic species [**35**]$^+$. Any assignment of d-d or M-MCT bands in the NIR region, would be foolhardy as the quality of the data is poor and hence has not been attempted.

4.3.8 Conclusions Drawn from the Electrochemical and Spectroelectrochemical Properties and Electronic Structures of Bis Hydroruthenated Acetylene Complexes

Table **40** and Table **41**, Table **44** and Table **47** summarise the composition of the frontier orbitals of **35** and **36** and their mono-oxidised analogues, with representative contour plots of key orbitals from **35**, **36** and [**35**]$^+$ and [**36**]$^+$ illustrated in Figure **59** and Figure **60**. The HOMOs of both **35** and **36**, is the π-system of the metal vinyl aryl fragment, with metal / vinyl contributions of (16 / 79 %) and (20 / 73 %) for **35** and **36** respectively. For both **35** and **36** the LUMO is essentially a phosphine σ*-orbital, with contributions from the metal centre, the vinyl π* system comprising the LUMO+6 and the LUMO+6, for **35** and **36** respectively. Similarly significant contributions (69 – 71 %) of the vinyl ligand to the HOMOs in complexes 1,4- and 1,3- [{RuCl(CO)(P^iPr_3)$_2$}$_2$(μ-CH=CHC$_6$H$_4$CH=CH)], **33** and **34** have been computed by Winter and his team. [42] The orbital characteristics of **35** and **36** are largely retained upon oxidation (Table **44** and Table **47**), although the metallic contribution to the β-LUSO is generally somewhat greater than in the HOMO of the corresponding neutral system. The calculated ν(C≡O) frequencies for the bimetallic neutral species are in good agreement with those observed from the spectroelectrochemical experiments, with the small increase in frequency of the ν(C≡O) band upon oxidation to the monocation is consistent with the structure of the β-LUSO. However the optimised geometry and hence the calculated ν(C≡O) frequencies for the dications does not agree with the experimental data, with two distinct oxidation centres. Spin density calculations on the optimised geometry of [**35-H**]$^+$ agrees with that seen with the mono-vinyl complexes, with the vinyl ligand supporting progressively more of the electron spin as the donating properties of the vinyl substituent increase, where the second metal centre acts as a pseudo electron donor group (Table **45**). The optimised geometry of [**36-H**]$^+$ results in a localised

geometry with the oxidation being localised towards one side of the divinylbenzene fragment, with the calculated ν(C≡O) frequencies for [**36-H**]$^+$ resulting in two ν(C≡O) bands at positions similar to the calculated ν(C≡O) frequencies of **23-H** and [**23-H**]$^+$. The experimental observation of a single ν(C≡O) band in the 1,3-isomer [**36**]$^+$ may be described in terms of an average of the two rapidly exchanged cationic forms.

4.4 Tris- Hydroruthenated Complexes

In seeking to extend the structures further, attention was turned to the study of trivinyl complexes prepared from 1,3,5-triethynyl benzene. Over the past decades, 1,3,5-triethynyl benzene has often been used as a convenient ligand through which trimetallic complexes that exhibit a variety of properties ranging from reversible oxidation, [289, 290] luminescence, [213] photo- induced electron or energy transfer [291] and even liquid crystal behaviour can be assembled. [292] Some of Lang's recent work serves as an illustration of the some of these points. [207]

The incorporation of metal end groups around the periphery of the organic benzene ligand has given rise to homometallic iron-, iridium- chromium, gold and platinum complexes [208, 293-295] and heterometallic examples. [211, 296] Much of the recent work concerning heterometallic complexes featuring a 1,3,5-triethynylbenzene ligand has been carried out by Lang, with a variety of metal centres such as Ru(dppf)Cp, $Os(PPh_3)_2Cp$, $Re(^tBu_2bpy)(CO)_3$ and ferrocenyl units being incorporated into the extended π-system of the ligand. [207, 297]

Of particular relevance to the current studies are the tris(hydrometallated) compounds prepared by Jia. [282] Addition of three equivalents of the ruthenium complex $RuHCl(CO)(PPh_3)_3$, to 1,3,5-triethynylbenzene in CH_2Cl_2, gave the trimetallic five-coordinate complex $[\{RuCl(CO)(PPh_3)_2(CH=CH)\}_3C_6H_3]$ which can be either capped using a $2e^-$ nitrogen donor ligands [L = pyridine (Py) or 4-phenylpyridine (PhPy)] to give the six-coordinate

[{RuCl(CO)$(PPh_3)_2$L(CH=CH)}$_3C_6H_3$] (**29** and **37**) (Chart **10**), or treated with trimethylphospine (PMe_3), to give the six-coordinate [{RuCl(CO)$(PMe_3)_3$(CH=CH)}$_3C_6H_3$] complex, where the PMe_3 ligands are in a *mer*- configuration, indicated by the AM_2 pattern $^{31}P\{^1H\}$ NMR spectrum. X-ray studies of [{RuCl(CO)$(PPh_3)_2$Py(CH=CH)}$_3C_6H_3$] (**29**) showed that the three Ru centres are related by a pseudo-C_3 rotation axis. Interestingly the vinyl groups in **29** are not coplanar with the Ru-CO bond in contrast with other related mono and bimetallic ruthenium hydride compounds.

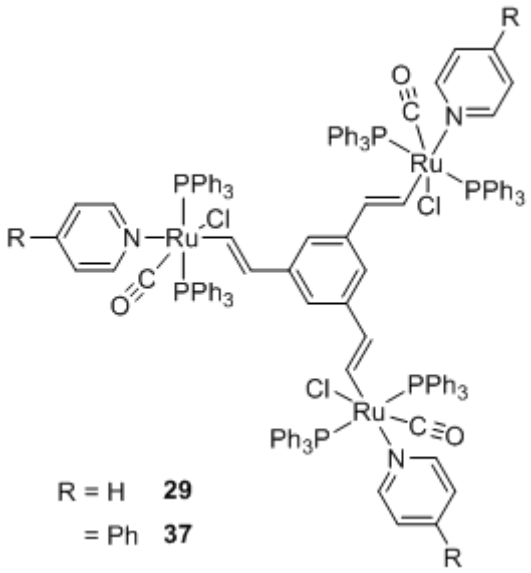

Chart **10** Six-coordinate tris-metallated 1,3,5-triethynylbenzene complexes **29** and **37**.

Attempts to metallate 1,3,5-triethynylbenzene using $OsHCl(CO)(PPh_3)_3$, afforded the bimetallated 1-HC≡C-3,5-[{$OsCl(CO)(PPh_3)_3$(CH=CH)}$_2C_6H_3$] which does not further metallate. On treatment with PMe_3 only the PPh_3 *trans* to the vinyl fragment was replaced.

Electrochemical analysis of the capped six-coordinated trimetallic compounds **29** and **37**, revealed three well resolved oxidation waves, (0.54, 0.92 and 1.19 V ; 0.54, 0.90 and 1.10 V, for **29** and **37** respectively, vs Ag/AgCl), which the authors have tentatively attributed to the formation of (Ru(II)/Ru(II)/Ru(III)), (Ru(II)/Ru(III)/Ru(III)) and (Ru(III)/Ru(III)/Ru(III)) and used the relatively large K_c

values as an indication of electronic interactions between the metal centres. However, the uncapped five-coordinate trimetallic parent complex and the PMe_3 treated complex showed both irreversible oxidation waves and unresolvable irreversible multiple oxidation waves.

The trimetallic complex 1,3,5-[{Ru(CO)(PPh_3)TpCH=CH}$_3$$C_6H_3$] **38** (Figure **66**) was prepared in a manner entirely analogous to that described for **35** and **36**, from KTp and [{RuCl(CO)(PPh_3)$_2$}$_3$(CH=CH)$_3$$C_6H_3$]. [282]

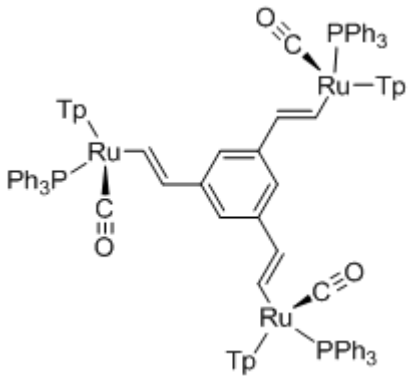

Figure **66** Tp^- capped trimetallic trivinylbenzene complex **38**.

With a linear molecule with three stereogenic centres, the number of stereoisomers is 8 (=2^3), resulting in four diastereoisomers, each a pair of two enantiomers. However with possible C_3 symmetry some of these stereoisomers are essentially the same, i.e. RRS ≡ SRR ≡ RSR. The arrangement of the three vinyl moieties also plays a part in the complication of the spectroscopic determination, as even restricting them to be planar with the aryl ring (in agreement with the crystal structures of the mono-metallic compounds), there are two arrangements that will give differing spectroscopic data (Figure **67**). This picture is further complicated by the fact that was shown earlier in the Chapter, in that there are two vinyl spatial arrangements with respect to the Ru-CO bond, one essentially coplanar to the carbonyl and the other (dihedral angle ~135 ˚ to the Ru-CO bond) nestled between two pyrazolyl rings.

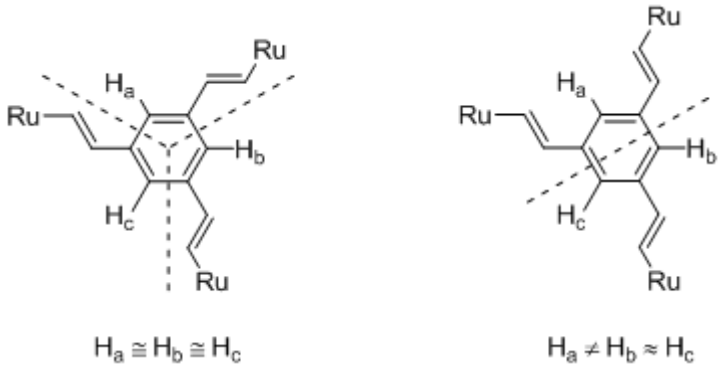

Figure **67** The two arrangements of the three vinyl moieties planar to the aryl ring.

Due to this, definitive assignment of the rather complex ^{1}H NMR spectrum is not possible and characterisation rests on the mass spectrometric data, ^{31}P NMR spectroscopy and IR spectroscopy. The ^{31}P NMR of **38** shows five peaks (50.5, 50.6, 50.7, 51.7, 52.6 ppm), the MALDI(+)-mass spectrometry featured the molecular ion; *m*/*z* 1966.4 amu. Cyclic voltammetry showed poorly resolved electrode events, and the resulting small K_c rendered it impossible to generate spectra of pure intermediate oxidation states.

The IR spectrum of the neutral complex **38** shows a single ν(C≡O) band at 1942 cm^{-1}, similar to both **35** and **36**. On oxidation to the fully oxidised species [**38**]$^{3+}$, the IR shows a low intensity ν(C≡O) band at 1997 cm^{-1} and a strong intensity ν(C≡O) band at 2072 cm^{-1}. The position of these two ν(C≡O) bands are in a similar region as the IR bands of the dications of **35** and **36**, (1996 cm^{-1} and 2071 cm^{-1}; and 2005 cm^{-1} and 2072 cm^{-1}; for [**35**]$^{2+}$ and [**36**]$^{2+}$ respectively), however, with the intensities of the peaks reversed.

This gives a picture which is consistent with the model proposed earlier for the dications of **35** and **36**, where in this instance, instead of having only one "fully oxidised" pendant arm, the trication of **38** ([**38**]$^{3+}$), has two (Figure **69**). The progression of the ν(C≡O) band(s), from neutral **38** to tricationic [**38**]$^{3+}$, is similar to that of the progression seen in **36** to [**36**]$^{2+}$. Upon oxidation of the neutral **38** species the initial ν(C≡O) band at 1942 cm^{-1}, collapses, with two new bands forming/shifting to roughly 1974 and 1997 cm^{-1}. As the oxidation progresses towards the fully oxidised trication [**38**]$^{3+}$ the band at 1974 cm^{-1} disappears, with a

new band at 2072 cm^{-1} emerging, whereby the intensity of this new band grows, as the band at 1997 cm^{-1}, decreases in intensity, until $[\mathbf{38}]^{3+}$ is fully formed (Figure **68**).

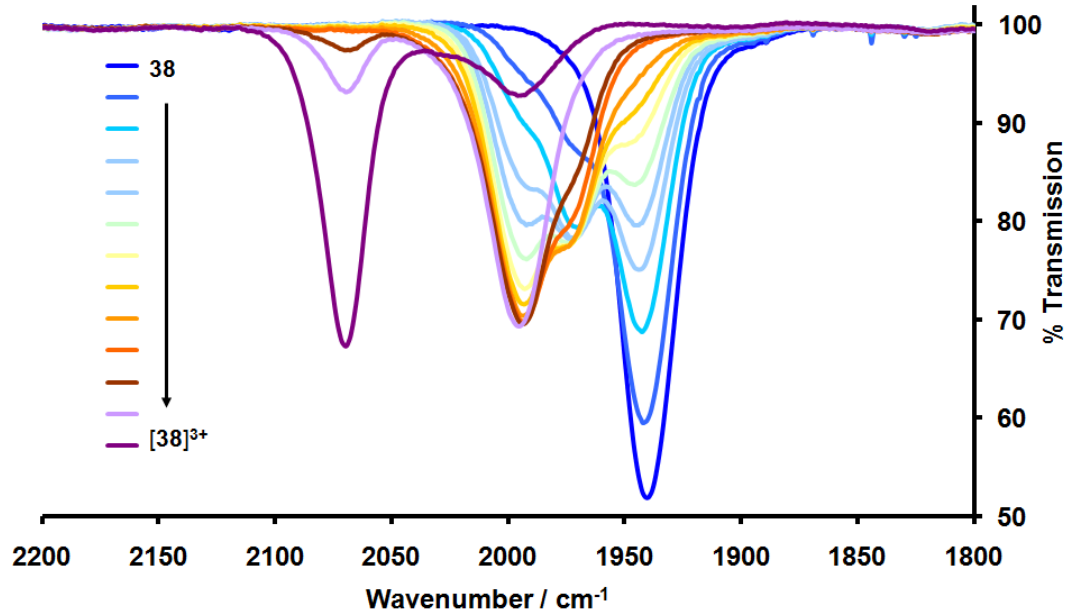

Figure **68** IR spectra of the progression of ν(C≡O) band(s) on the oxidation of **38** to $[\mathbf{38}]^{3+}$.

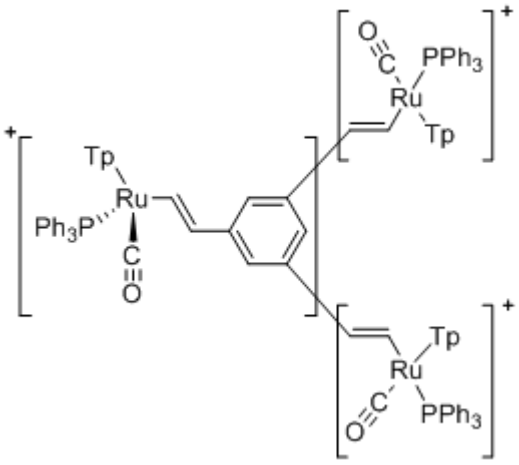

Figure **69** The proposed centres of oxidation in the trication $[\mathbf{38}]^{3+}$.

One interesting aside, is the *N*-trimethylborazine analogous compound where the benzene ring in **38** has been conceptually changed to the *N*-trimethylborazine, resulting in the trimetallic complex $[\{RuCl(CO)(PPh_3)_2(CH{=}CH)\}_3B_3N_3Me_3]$

(Figure **70**), which was synthesised from $RuHCl(CO)(PPh_3)_3$ and B-triethynyl-*N*-trimethylborazine. [298]

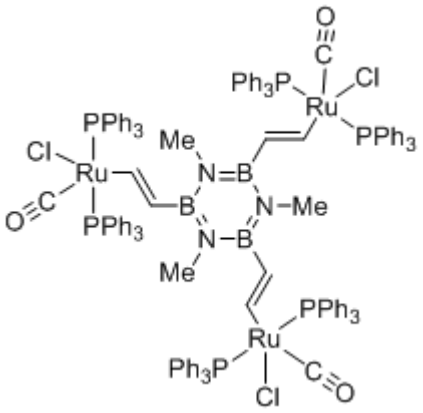

Figure **70** Tris-metallic trimethylborazine complex $[\{RuCl(CO)(PPh_3)_2(CH{=}CH)\}_3B_3N_3Me_3]$. [298]

The trimetallated Tp capped- hydroruthenated product of tri-(ethynylphenyl)amine was also synthesized **39** (Figure **71**), with the idea of conceptually adding a redox centre to the core of the molecule, that is *para*- to the metal vinyl end group on the benzene ring, which may benefit the communication/delocalisation of electron density from one metal centre to the others, but again due to the increased complications of the chirality, and other structural spatial arrangement, no electrochemical or spectroelectrochemical work was done on this complex. ^{1}H and ^{31}P spectroscopy, MALDI(+) mass spectroscopy and IR spectroscopy was employed to attempt characterisation of the compound **39**. Literature searches seem to suggest that this is the first trimetallated tris(vinylphenyl)amine complex synthesised.

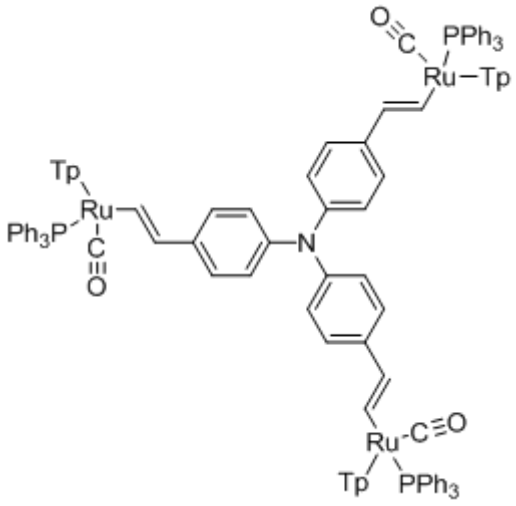

Figure **71** [{Ru(CO)(PPh_3)Tp}$_3$-(1,4-(CH=CH)(C_6H_4))$_3$N] (**39**).

In the ^{1}H NMR, even though the peaks were significantly broadened by overlapping resonances, it was possible to assign some of the characteristic features seen in this series of mono-, bi- and tri- metallic vinyl compounds. The H_α vinyl protons appear as a doublet of doublets with coupling of $^3J_{HH}$ = 17 Hz and $^3J_{HP}$ = 2 Hz, at δ 7.99 ppm, which is a similar chemical shift as found in the vinyl complex that bears an electron donating substituent, complex **27** (R = OMe). The H_β vinyl protons appear between δ 6.28 – 6.34 ppm, as a multiplet, again with a chemical shift as the H_β vinyl proton in **27**. There are also the characteristic three groups of peaks associated with the Tp^- protons, in the ranges δ 5.89 – 5.90 ppm, δ 6.08 – 6.79 ppm and δ 7.55 – 7.73 ppm. Peaks associated to the aromatic pseudo-AB protons and the phenyls of the three phosphines can all be accounted for, but definitive assignment is tentative.

The ^{31}P NMR showed three close peaks at δ 51.3 – 51.4 ppm. The MALDI(+)-mass spectroscopic data featured the molecular ion; *m*/*z* 2133.7. The IR of the neutral complex **39**, shows a single ν(C≡O) band at 1940 cm^{-1}, and a single ν(B-H) band at 2481 cm^{-1}, these are again similar to the mono- and bimetallic vinyl complexes.

4.5 Conclusions

The reaction of $RuHCl(CO)(PPh_3)_3$ with a number of acetylenes produced the five coordinate vinyl complexes $Ru(CH=CHC_6H_4R\text{-}4)Cl(CO)(PPh_3)_2$ which were not isolated but rather treated *in situ* with KTp, producing $[\{Ru(CO)(PPh_3)_2Tp\}(CH=CHC_6H_4R\text{-}4)]$. Molecular structures of **23**, **24**, **25** and **26** reveal that the complexes are pseudo-octahedral. There is no significant trend in ν(C≡O) as the R group is varied, and along with a small shift in ν(C≡O) on oxidation of the complex indicates that the aryl ligand plays a significant role in the oxidation of complex. The electrochemical reversibility of the first oxidation process suggests that the mono oxidised forms are easily accessible and so could used as a potentially redox terminal for a molecular wire. An electron acceptor group leads to a stabilisation of the HOMO and LUMO. On oxidation, these orbitals were stabilised further. With the aid of TD DFT the electronic transitions present in the neutral and cationic forms of **23** and **25** were assigned, with the main absorption in the neutral species being from the π-system of the Ru-vinyl-aryl to the π*-system, ML-LCT in character. The main absorptions in the cationic species arise from transitions from the β-HOSO to the β-LUSO and the α-HOSO to the α-LUSO, (M-MLCT and ML-LCT in character, respectively).

The reaction of $RuHCl(CO)(PPh_3)_3$ with 1,4- and 1,3-diethynylbenzene and the subsequent capping with KTp produced **35** and **36**. The monocation of **35** has typical attributes of Class III mixed valence systems. On further oxidation however, characteristics emerge which are typical of Class II mixed valence systems. Fundamentally, there is the development of an absorption band in the near infrared region. The monocation of **36** could not be isolated, but its neutral and dicationic forms are similar to that of **35**. More work is required to resolve the absorption spectrum of $[\mathbf{36}]^+$ fully.

The spectroscopic and structural nature of $[\mathbf{23\text{-}H}]^{n+}$ - $[\mathbf{36\text{-}H}]^{n+}$ (n = 0, 1) were satisfactorily reproduced with computational methods using the MPW1K functional. However the functional was not able to reproduced the spectroscopic characteristics of the dication of $[\mathbf{35\text{-}H}]^{2+}$ and $[\mathbf{36\text{-}H}]^{2+}$.

4.6 Experimental Details

4.6.1 General Conditions

All reactions were carried out using oven dried glassware, under an atmosphere of nitrogen using standard Schlenk techniques. Reagents purchased commercially were used without further purification. Starting materials were checked by using relevant spectroscopic techniques before use. $RuHCl(CO)(PPh_3)_3$ **19** was prepared using the literature method. [299] NMR spectroscopies were carried out a room temperature and referenced against $CDCl_3$ using the Varian Mercury-200 (^1H 199.99 MHz, ^{31}P 80.96 MHz), Bruker and Varian Mercury-400 (^1H 399.97 MHz, ^{31}P 161.10 MHz) or Varian Inova-500 (^1H 499.77 MHz, ^{13}C 125.67 MHz, ^{31}P (202.31 MHz). Chemical shifts are reported in δ / ppm and coupling constants, *J*, in Hz. The assignments are such that C_α is the vinyl carbon closest to the ruthenium, the carbons on the aromatic ring are labelled C_1 – C_4 where C_1 is closest to the ruthenium and the carbons on the triphenylphosphine rings are labelled C_i, C_o, C_m, C_p dependent on if they are in the ipso, ortho, meta and para positions. IR spectra were recorded using solution cells fitted with CaF_2 windows by the Nicolet Avatar FT IR spectrophotometer. Mass spectra were acquired using the Thermo- Finnigan LTQ FT spectrometer. Single crystal X-ray structure determinations were carried out by Dr DS Yufit of this department using a Bruker 3-circle diffractometer with a SMART 6K area detector, using graphite-monochromated sealed-tube Mo-K_α radiation. These data collections were performed at 120 K, and the temperature maintained using cryostream (Oxford cryosystem) open flow N_2 cryostats. Reflection intensities were integrated using the SAINT program. [300] The molecular structures were solved using direct-methods and refined by full matrix least-squares F^2 using SHELXTL software. [148] All non-hydrogen atoms were refined in anisotropic approximation. Hydrogen atoms were placed into calculated positions, and refined isotropically using a riding model. Electrochemical experiments were performed in an air tight one compartment cell, constructed by a carbon working electrode, a platinum pseudo reference electrode and a platinum counter electrode. These components were fixed into the system via a Teflon screw cap with a suitable fitting. Voltammetric data were acquired using Autolab PG-STAT 30 in either

CH_2Cl_2 or MeCN solutions containing 0.1 M electrolyte solutions of $[NBu_4][BF_4]$ at room temperature. Potentials are referenced to ferrocene or decamethylferrocene as appropriate.

4.6.2 Mono-Hydroruthenation Experimental

4.6.2.1 Preparation of [{Ru(CO)(PPh_3)Tp}(CH=CHC_6H_4Me-4)] (23)

To a suspension of $RuHCl(CO)(PPh_3)_3$ **19** (0.10 g, 0.105 mmol) in dichloromethane (10 ml) was added *p*-tolylacetylene (0.07 ml, 0.524 mmol). The solution immediately turned red and was stirred for 30 min. KTp (0.08 g, 0.315 mmol) was added and over the course of 1 hour, the solution turned green. The reaction mixture was filtered through celite and the solvent removed. The residual solid was re-dissolved in dichloromethane (2 ml), hexane was added (4 ml) and some solvent removed. A light green powder was collected by filtration and dried under vacuum (0.051 g, 64 %). Recrystallisation from dichloromethane and hexane (3:2) by slow diffusion gave yellow crystals. ^{1}H NMR (200 MHz, $CDCl_3$): δ_H 2.51 (s, 3H, CH_3), 5.94 (t, $^3J_{HH}$ = 2 Hz, 1H, Tp), 5.99 (t, $^3J_{HH}$ = 2 Hz, 1H, Tp), 6.12 (t, $^3J_{HH}$ = 2 Hz, 1H, Tp), 6.41 (d, $^3J_{HH}$ = 17 Hz, 1H, Ru-CH=C*H*), 6.79 (d, $^3J_{HH}$ = 2 Hz, 1H, Tp), 6.81 (d, $^3J_{HH}$ = 2 Hz, 1H, Tp), 6.87 (d, $^3J_{HH}$ = 2 Hz, 1H, Tp), 7.07 (dd, $^3J_{HH}$ = 11 Hz and $^3J_{HP}$ = 2 Hz, 2H, C_6H_4), 7.29 - 7.39 (m, 6H, Ph H_o), 7.42 - 7.51 (m, 8H, Ph H_m and C_6H_4), 7.57 - 7.64 (m, 3H, Ph H_p), 7.85 (t, $^3J_{HH}$ = 2 Hz, 1H, Tp), 7.95 (t, $^3J_{HH}$ = 2 Hz, 1H, Tp), 8.00 (d, $^3J_{HH}$ = 2 Hz, 1H, Tp), 8.33 (dd, $^3J_{HH}$ = 17 Hz and $^3J_{HP}$ = 2 Hz, 1H, RuC*H*=CH). ^{31}P NMR (200 MHz, $CDCl_3$): δ 50.6 (s). ^{13}C NMR (176 MHz, $CDCl_3$) δ_C 21.3 (s, CH_3), 105.3 (s, Tp), 105.4 (s, Tp), 105.5 (s, Tp), 124.6 (s, C_2), 128.2 (d, $^2J_{CP}$ = 10 Hz, $C_{m/m'}$), 129.1 (s, C_3), 130.0 (d, $^4J_{CP}$ = 2 Hz, $C_{p/p'}$), 133.2 (s, C_1), 133.3 (d, $^1J_{CP}$ = 44 Hz, $C_{i/i'}$), 134.4 (d, $^3J_{CP}$ = 10 Hz, $C_{o/o'}$), 134.7 (d, $^3J_{CP}$ = 2 Hz, C_β), 135.1 (s, Tp), 135.5 (s, Tp), 136.8 (s, Tp), 139.4 (s, C_4), 142.9 (s, Tp), 143.0 (s, Tp), 144.2 (s, Tp), 160.4 (d, $^2J_{CP}$ = 13 Hz, C_α), 207.1 (d, $^2J_{CP}$ = 16 Hz, CO). ES(+)-MS (*m/z*) 722.2 $[M + H]^+$. IR (CH_2Cl_2, cm^{-1}): ν(C≡O) 1942, ν(B-H) 2481. Elemental analysis: Calculated for $C_{37}H_{34}BN_6OPRu.0.25(CH_2Cl_2)$; C, 60.23; H, 4.68; N, 11.31. Found; C, 60.10; H, 4.79; N, 11.04.

4.6.2.2 Preparation of [{Ru(CO)(PPh_3)Tp}(CH=CHC_6H_4CN-4)] (24)

To a suspension of RuHCl(CO)(PPh_3)$_3$ **19** (0.10 g, 0.105 mmol) in dichloromethane (10 ml) was added 4-ethynylbenzonitrile (0.04 g, 0.315 mmol). A cloudy yellow suspension formed and was stirred for 3 h. KTp was added (0.08 g, 0.315 mmol) to the reaction mixture and left to stir overnight. The clear green solution was filtered through celite and the solvent removed. The residual solid was re-dissolved in dichloromethane (2 ml), hexane added (4 ml) and some solvent removed. A dull yellow powder was collected by filtration and dried under vacuum. Purification was achieved by dissolving the powder in a minimum amount of dichloromethane, and layering with hexane, to give a bright yellow powder (0.035 g, 45 %). Recrystallisation from dichloromethane and ethanol (3:2) by slow diffusion gave yellow crystals. ^{1}H NMR (200 MHz, $CDCl_3$): δ_H 5.92 (t, $^3J_{HH}$ = 2 Hz, 1H, Tp), 5.95 (t, $^3J_{HH}$ = 2 Hz, 1H, Tp), 6.08 (t, $^3J_{HH}$ = 2 Hz, 1H, Tp), 6.44 (d, $^3J_{HH}$ = 17 Hz, 1H, RuCH=C*H*), 6.80 (dd, $^3J_{HH}$ = 6 Hz and $^3J_{HH}$ = 2 Hz, 2H, C_6H_4), 7.01 (m, 18H + Tp), 7.32 – 7.33 (m, 1H, Tp), 7.35 – 7.36 (m, 1H, Tp), 7.42 – 7.46 (m, 1H, Tp), 7.56 – 7.60 (m, 2H, Tp), 7.70 (dd, $^3J_{HH}$ = 6 Hz and $^3J_{HH}$ = 2 Hz, 2H, C_6H_4), 8.78 (dd, $^3J_{HH}$ = 17 Hz and $^3J_{HP}$ = 2 Hz, 1H, RuC*H*=CH). ^{31}P NMR (200 MHz, $CDCl_3$) δ 50.9 (s).

4.6.2.3 Preparation of [{Ru(CO)(PPh_3)Tp}(CH=$CHC_6H_4NO_2$-4)] (25)

To a suspension of RuHCl(CO)(PPh_3)$_3$ **19** (0.30 g, 0.315 mmol) in dichloromethane (10 ml) was added 1-ethynyl-4-nitrobenzene (0.09 g, 0.630 mmol). The solution immediately turned dark green and was stirred for 30 min. KTp (0.05 g, 0.210 mmol) was added and over the course of 2 h, the solution turned red. The solution was filtered through celite and the reaction removed. The residual solid was re-dissolved in dichloromethane (5 ml), hexane added (8 ml) and some solvent removed. An orange powder was collected by filtration and dried under vacuum. Purification was achieved by dissolving the powder in a minimum amount of dichloromethane and layering with methanol, to give a bright orange powder (0.152 g, 64 %). Recrystallisation from dichloromethane and methanol by slow diffusion gave bright red crystals. ^{1}H NMR (400 MHz, $CDCl_3$) δ_H 5.93 (t, $^3J_{HH}$ = 2 Hz, 1H,

Tp), 5.96 (t, $^3J_{HH}$ = 2 Hz, 1H, Tp), 6.08 (t, $^3J_{HH}$ = 2 Hz, 1H, Tp), 6.54 (d, $^3J_{HH}$ = 17 Hz, 1H, Ru-CH=C*H*), 6.74 (s, 1H, Tp), 6.78 (d, $^3J_{HH}$ = 2 Hz, 1H, Tp), 6.80 (dd, $^3J_{HH}$ = 17 Hz and $^3J_{HP}$ = 2 Hz, 2H, C_6H_4), 6.82 (d, $^3J_{HH}$ = 2 Hz, 1H, Tp), 7.02 - 7.07 (d, $^3J_{HH}$ = 9 Hz, 2H, C_6H_4), 7.10 – 7.14 (m, 6H. Ph H$_o$), 7.19 – 7.23 (m, 6H. Ph H$_m$), 7.34 – 7.38 (m, 3H, Ph H$_p$), 7.58 (s, 1H, Tp), 7.70 (d, $^3J_{HH}$ = 2 Hz, 1H, Tp), 7.73 (d, $^3J_{HH}$ = 2 Hz, 1H, Tp), 8.05 (d, $^3J_{HH}$ = 9 Hz, 2H, C_6H_4), 9.03 (dd, $^3J_{HH}$ = 17 Hz and $^3J_{HP}$ = 2 Hz, 1H, RuC*H*=CH). ^{31}P NMR (200 MHz, $CDCl_3$) δ 50.7 (s). ^{13}C NMR ($CDCl_3$, 125 MHz) δ_C 105.6 (s, Tp), 105.7 (s, Tp), 105.8 (s, Tp), 124.3 (s, C_2), 124.5 (s, C_3), 128.4 (d, $^2J_{CP}$ = 10 Hz, C$_{m/m'}$), 130.03 (d, $^4J_{CP}$ = 2 Hz, C$_{p/p'}$), 132.7 (d, $^1J_{CP}$ = 44 Hz, C$_{i/i'}$), 134.2 (d, $^3J_{CP}$ = 10 Hz, C$_{o/o'}$), 135.1 (d, $^3J_{CP}$ = 2 Hz, C$_\beta$), 135.5 (s, Tp), 135.7 (s, Tp), 136.0 (s, Tp), 142.9 (s, Tp), 144.0 (s, Tp), 144.4 (s, Tp), 146.6 (s, C_4), 179.2 (d, $^2J_{CP}$ = 12 Hz, C$_\alpha$), 206.5 (d, $^2J_{CP}$ = 16 Hz, CO). *C_1 not observed. MALDI(+)-MS 753.10 $[M + H]^+$. IR (CH_2Cl_2, cm^{-1}): ν(C≡O) 1945, ν(B-H) 2485. Elemental analysis: Calculated for $C_{36}H_{31}BN_7O_3PRu.0.75(CH_2Cl_2)$; C, 54.08; H, 4.01; N, 12.01. Found; C, 54.20; H, 4.21; N, 11.66.

4.6.2.4 Preparation of [{Ru(CO)(PPh_3)Tp}(CH=CH$C_6H_4CO_2$Me-4)] (26)

To a suspension of RuHCl(CO)(PPh_3)$_3$ **19** (0.30 g, 0.315 mmol) in dichloromethane (10 ml) was added methyl 4-ethynylbenzoate (0.06 g, 0.400 mmol). The solution immediately turned brown and was stirred for 30 min. KTp was added (0.12 g, 0.476 mmol) and the solution turned green over the course of 3 h. The reaction mixture was filtered through celite and the solvent removed. The residual solid was re-dissolved in diethylether (6 ml) to which hexane was added (10 ml). The light green powder was collected by filtration and dried under vacuum (0.134 g, 56 %). Recrystallisation from dichloromethane and methanol by slow diffusion gave colourless crystals. ^{1}H NMR (400 MHz, $CDCl_3$): δ_H 3.95 (s, 3H, OCH_3), 5.91 (t, $^3J_{HH}$ = 2 Hz, 1H, Tp), 5.94 (t, $^3J_{HH}$ = 2 Hz, 1H, Tp), 6.07 (t, $^3J_{HH}$ = 2 Hz, 1H, Tp), 6.47 (d, $^3J_{HH}$ = 17 Hz, 1H, RuCH=C*H*), 6.78 (d, $^3J_{HH}$ = 2 Hz, 1H, Tp), 6.81 (d, $^3J_{HH}$ = 2 Hz, 1H, Tp), 7.04 – 7.09 (m, 7H, Ph H$_o$ + Tp), 7.13 (d, J = 8 Hz, 2H, C_6H_4), 7.18 – 7.23 (m, 6H, Ph H$_m$), 7.31 – 7.35 (m, 3H, Ph H$_p$), 7.52 – 7.62 (m, 1H, Tp), 7.60 – 7.71 (m, 1H, Tp), 7.69 (d, $^3J_{HH}$ = 2 Hz, Tp), 7.71 (d, $^3J_{HH}$ = 2 Hz, Tp), 7.86 (d, $^3J_{HH}$ = 8 Hz, 2H, C_6H_4), 8.68 (dd, $^3J_{HH}$ = 17 Hz and $^3J_{HP}$ = 2 Hz, 1H, RuCH=C*H*). ^{31}P

NMR (200 MHz, $CDCl_3$) δ 50.9 (s). ^{13}C NMR (176 MHz, $CDCl_3$) δ_C 52.0 (s, OMe), 105.5 (s, Tp), 105.6 (s, Tp), 105.7 (s, Tp), 124.2 (s, C_2), 125.0 (s, C_1), 128.3 (d, $^2J_{CP}$ = 10 Hz, $C_{m/m'}$), 130.1 (s, C_3), 130.2 (d, $^4J_{CP}$ = 2 Hz, $C_{p/p'}$), 133.0 (d, $^1J_{CP}$ = 43 Hz, $C_{i/i'}$), 134.3 (d, $^3J_{CP}$ = 10 Hz, $C_{o/o'}$), 134.9 (d, $^3J_{CP}$ = 2 Hz, C_β), 135.3 (s, Tp), 135.6 (s, Tp), 136.7 (s, Tp), 142.9 (s, Tp), 143.0 (s, Tp), 144.3 (s, Tp), 145.5 (s, C_4), 168.0 (s, CO of ligand), 171.3 (d, $^2J_{CP}$ = 13 Hz, C_α), 206.8 (d, $^2J_{CP}$ = 16 Hz, CO). MALDI(+)-MS 766.2 $[M + H]^+$. IR (CH_2Cl_2, cm^{-1}): ν(C≡O) 1940, ν(B-H) 2483. Elemental analysis: Calculated for $C_{38}H_{34}BN_6O_3PRu$; C, 59.62; H, 4.48; N, 10.98. Found; C, 58.74; H, 4.34; N 10.25.

4.6.2.5 Preparation of [{Ru(CO)(PPh_3)Tp}(CH=CHC_6H_4OMe-4)] (27)

To a suspension of $RuHCl(CO)(PPh_3)_3$ **19** (0.10 g, 0.105 mmol) in dichloromethane was added 1-ethynyl-4-methoxybenzene (0.03 ml, 0.210 mmol). The solution immediately turned dark red and was stirred for 30 min. KTp was added (0.05 g, 0.210 mmol) and the solution turned light yellow over the course of 2 h. The reaction mixture was filtered through celite and the solvent removed. The residual solid was re-dissolved in dichloromethane (3 ml) to which hexane was added (5 ml), and some solvent was removed. An off white powder was collected by filtration and dried under vacuum (0.036 g, 43 %). ^1H NMR (200 MHz, $CDCl_3$) δ_H 3.78 (s, 3H, OCH_3), 4.6 (br s, 1H, B-H), 5.89 (t, $^3J_{HH}$ = 2 Hz, 1H, Tp), 5.91 (t, $^3J_{HH}$ = 2 Hz, 1H, Tp), 6.05 (t, $^3J_{HH}$ = 2 Hz, 1H, Tp), 6.31 (d, $^3J_{HH}$ = 17 Hz, 1H, Ru-CH=C*H*), 6.35 (d, $^3J_{HH}$ = 2 Hz, 1H, Tp), 6.45 (d, $^3J_{HH}$ = 2 Hz, 1H, Tp), 6.77 (d, $^3J_{HH}$ = 2 Hz, 1H, Tp), 7.07 – 7.12 (m, 6H, Ph H_o and 2H C_6H_4), 7.18 – 7.23 (m, 6H, Ph H_m), 7.31 – 7.35 (m, 3H, Ph H_p), 7.55 (d, $^3J_{HH}$ = 1 Hz, 1H, Tp), 7.61 (d, $^3J_{HH}$ = 2 Hz, 1H, Tp), 7.66 – 7.70 (m, 1H, Tp and 2H C_6H_4), 7.97 (dd, $^3J_{HH}$ = 17 Hz and $^3J_{HP}$ = 2 Hz, 1H, RuC*H*=CH). ^{31}P NMR ($CDCl_3$, 200 MHz) δ 51.3 (s). ^{13}C NMR ($CDCl_3$, 126 MHz) δ_C 55.6 (s, OMe), 105.3 (s, Tp), 105.4 (s, Tp), 105.5 (s, Tp), 113.8 (s, C_3), 125.5 (s, C_2), 128.2 (d, $^3J_{CP}$ = 10 Hz, $C_{m/m'}$), 130.0 (d, $^4J_{CP}$ = 2 Hz, $C_{p/p'}$), 133.3 (d, $^1J_{CP}$ = 43 Hz, $C_{i/i'}$), 134.3 (d, $^2J_{CP}$ = 10 Hz, $C_{o/o'}$), 134.7 (d, $^3J_{CP}$ = 2 Hz, C_β), 135.1 (s, Tp), 135.5 (s, Tp), 135.6 (s, C_1), 136.0 (s, Tp), 142.9 (s, Tp), 143.0 (s, Tp), 144.2 (s, Tp), 156.7 (s, C_4), 158.5 (d, $^2J_{CP}$ = 13 Hz, C_α), 201.1 (d, $^2J_{CP}$ = 16 Hz, CO),. MALDI(+)-MS 738.2 $[M + H]^+$. IR (CH_2Cl_2, cm^{-1}): ν(C≡O) 1940, ν(B-H) 2479.

Elemental analysis: Calculated for $C_{37}H_{34}BN_6O_2PRu$; C, 60.25; H, 4.64; N, 11.39. Found; C, 54.11; H, 4.15; N, 9.16.

4.6.3 Multi-Hydroruthenation Experimental

4.6.3.1 Preparation of 1,4-[{Ru(CO)(PPh_3)Tp}$_2$(μ-CH=CHC_6H_4CH=CH)] (35)

To a suspension of RuHCl(CO)(PPh_3)$_3$ **19** (0.21 g, 0.218 mmol) in dichloromethane (10 ml) was added 1,4-diethynylbenzene (0.01 g, 0.087 mmol). The solution immediately turned red and was stirred for 2 h. KTp was added (0.09 g, 0.350 mmol) and the solution turned green over the course of a further two hours. The reaction mixture was reduced to dryness, re-dissolved in the minimum amount of dichloromethane and filtered through celite. Hexane was added (10 ml) to the filtrate and some solvent was removed. A green powder collected by filtration was subsequently heated in ethanol, and allowed to cool. This was filtered, washed with hexane, and dried under vacuum. (0.082 g, 70 %). ^{1}H NMR (500 MHz, $CDCl_3$): δ_H 5.94 – 5.95 (m, 4H, Tp), 6.09 (s, 2H, Tp), 6.38 (d, $^3J_{HH}$ = 17 Hz, 1H, RuCH=C*H*), 6.42 (d, $^3J_{HH}$ = 17 Hz, RuCH=C*H*), 6.80 (d, $^3J_{HH}$ = 7 Hz, 2H, C_6H_4), 6.84 (d, $^3J_{HH}$ = 7 Hz, 2H, C_6H_4), 6.98 – 7.00 (m, 2H, Tp), 7.06 – 7.11 (m, 2H, Tp), 7.15 – 7.21 (m, 12H, Ph H$_m$), 7.25 – 7.28 (m, 12H, Ph H$_o$), 7.34 – 7.40 (m, 6H, Ph H$_p$), 7.49 – 7.52 (m, 1H, Tp), 7.57 – 7.60 (s, 1H, Tp), 7.71 – 7.77 (m, 6H, Tp), 8.12 (unresolved dd, $^3J_{HH}$ = 17 Hz, 2H, RuC*H*=CH). ^{31}P NMR (161 MHz, $CDCl_3$): δ 51.1 (s) and 51.2 (s). ^{13}C NMR (126 MHz, $CDCl_3$): δ_C 105.7, 105.6 (6 Tp environments), 124.8 (s, C_2 and C_3), 124.8 (s, C_2 and C_3), 128.5 (d, $^2J_{CP}$ = 10 Hz, $C_{o/o'}$), 130.2 (s, $C_{p/p*}$), 130.2 (s, $C_{p/p'}$), 133.6 (d, $^1J_{CP}$ = 43 Hz, $C_{i/i*}$), 133.6 (d, $^1J_{CP}$ = 42 Hz, $C_{i/i'}$), 134.6 (d, $^3J_{CP}$ = 10 Hz, $C_{m/m'}$), 134.9 (unresolved doublet, C_β), 135.3 (s, Tp), 135.5 (s, Tp), 135.7 (s, Tp), 135.7 (s, Tp), 137.5 (s, Tp), 137.6 (s, Tp), 138.2 (s, C_1 and C_4), 143.2 (s, Tp), 143.3 (s, Tp), 143.4 (bs, 2 Tp environments), 144.4 (s, 2 Tp environments), 158.9 (d, $^2J_{CP}$ = 13 Hz, C_α), 159.0 (d, $^2J_{CP}$ = 12 Hz, C_α), 207.4 (d, $^2J_{CP}$ = 15 Hz, 2 CO environments). MALDI(+)-MS 1337.2 $[M + H]^+$. IR (CH_2Cl_2, cm^{-1}): ν(C≡O)

1942, ν(B-H) 2482 . Elemental analysis: Calculated for $C_{66}H_{58}B_2N_{12}O_2P_2Ru_2$; C, 59.29; H, 4.37; N, 12.57. Found; C, 51.91; H, 3.78; N, 8.74.

4.6.3.2 Preparation of 1,3-[{Ru(CO)(PPh_3)Tp}$_2$(μ-CH=CHC_6H_4CH=CH)] (36)

To a suspension of RuHCl(CO)(PPh_3)$_3$ **19** (0.240 g, 0.25 mmol) in dichloromethane (10 ml) was added 1, 3-diethynylbenzene (0.028 ml, 0.1 mmol). The solution immediately turned red and was stirred for 3 h. KTp was added (0.08 g, 0.158 mmol) and the solution turned dark green over the course of two hours. The reaction was reduced to dryness, re-dissolved in the minimum amount of dichloromethane and filtered through celite. Hexane was added (10 ml) to the filtrate and some solvent was removed. A light green powder collected by filtration was subsequently heated in ethanol, and allowed to cool. This was filtered, washed with hexane, and dried under vacuum (0.080 g, 60 %). ^{1}H NMR (500 MHz, $CDCl_3$) δ_H 5.97 (s, 1H, Tp), 6.02 (s, 3H, Tp), 6.18 (s, 2H, Tp), 6.44 (d, $^3J_{HH}$ = 17 Hz, 1H, RuCH=C*H*), 6.60 (d, $^3J_{HH}$ = 17 Hz, 1H, RuCH=C*H*), 6.75 (s, 1H, H_a), 6.90 (s, 1H, $H_{a'}$), 6.92 (unresolved doublet, 2H, H_b), 6.98 (unresolved doublet, 2H, $H_{b'}$), 6.98 – 7.02 (unresolved triplet, 2H, H_c), 7.06 – 7.07 (m, 2H, Tp), 7.18 – 7.20 (m, 1H, Tp), 7.18 – 7.25 (m, 12H, Ph H_m), 7.29 – 7.32 (m, 12H, Ph H_o), 7.35 – 7.45 (m, 6H, Ph H_p), 7.57 – 7.59 (m, 1H, Tp), 7.64 – 7.70 (m, 2H, Tp), 7.78 – 7.92 (m, 6H, Tp), 8.23 (dd, $^3J_{HH}$ = 17 Hz $^3J_{HP}$ = 2 Hz, 1H, RuC*H*=C*H*), 8.30 (dd, $^3J_{HH}$ = 17 Hz $^3J_{HP}$ = 2 Hz, 1H, RuC*H*=CH). ^{31}P NMR (161 MHz, $CDCl_3$) δ 50.7 (s) and 51.5 (s). ^{13}C NMR (126 MHz, $CDCl_3$) δ_C 105.2, 105.5 105.6 (6 Tp environments), 128.2 (d, $^2J_{CP}$ = 9 Hz, $C_{o/o*}$), 128.2 (d, $^2J_{CP}$ = 9 Hz, $C_{o/o'}$), 129.9 (s, C_p), 133.2 (d, $^1J_{CP}$ = 43 Hz, $C_{i/i*}$), 133.3 (d, $^1J_{CP}$ = 43 Hz, $C_{i/i'}$), 134.3 (d, $^3J_{CP}$ = 10 Hz, $C_{m/m'}$), 134.3 (d, $^3J_{CP}$ = 10 Hz, $C_{m/m'}$), 134.7 (s, C_β), 135.0 (s, Tp), 135.1 (s, Tp), 135.4 (s, Tp), 135.5 (s, Tp), 137.4 (s, Tp), 137.8 (s, Tp), 140.2 (broad, 2 C_1 environments and 2 C_3 environments), 141.4 (s, Tp), 141.6 (s, Tp), 142.6 (s, Tp), 143.1 (s, 2 C_2 environments), 143.2 (bs, Tp), 144.2 (s, Tp), 144.2 (s, Tp),207.2 (d, $^2J_{CP}$ = 15 Hz, CO), 159.9 (d, $^2J_{CP}$ = 12 Hz, $C_{\alpha'}$), 160.6 (d, $^2J_{CP}$ = 13 Hz, C_α), 207.1 (d, $^2J_{CP}$ = 13 Hz, CO), 124.5 – 120.4 (remaining aromatic environments). MALDI(+)-MS

1337.2 $[M + H]^+$. IR (CH_2Cl_2, cm^{-1}): ν(C≡O) 1941 ν(B-H) 2481. Elemental analysis: Calculated for $C_{66}H_{58}B_2N_{12}O_2P_2Ru_2$; C, 59.29; H, 4.37; N, 12.57. Found; C, 47.22; H, 3.50; N, 8.13

4.6.3.3 Preparation of 1,3,5-[{Ru(CO)(PPh$_3$)Tp(CH=CH)}$_3$C$_6$H$_3$] (38)

To a suspension of $RuHCl(CO)(PPh_3)_3$ **19** (0.36 g, 0.375 mmol) in dichloromethane (12 ml) was added 1, 3, 5 – triethynylbenzene (0.01 g, 0.093 mmol) in dichloromethane (3 ml). The solution immediately turned red and was stirred for 3 h. KTp was added (0.08 g, 0.315 mmol) and the solution turned dark green overnight. The reaction mixture was reduced to dryness, re-dissolved in the minimum amount of dichloromethane and filtered through celite. Hexane was added (10 ml) to the filtrate and some solvent was removed. A blue powder was collected by filtration, heated in ethanol, allowed to cool and filtered again. The powder was washed in hexane, and dried under vacuum (0.093 g, 51 %). Characterisation incomplete. ^{31}P NMR (126 MHz, $CDCl_3$) δ 50.5 (s), 50.6 (s), 50.7 (s), 51.7 (s), 52.6 (s). MALDI(+)-MS 1966.4. $[M + H]^+$. IR (CH_2Cl_2, cm^{-1}): ν(C≡O) 1942, ν(B-H) 2481. Elemental analysis: Calculated for $C_{96}H_{84}B_3N_{18}O_3P_3Ru_3$; C, 58.64; H, 4.30; N, 12.82. Found; C, 52.49; H, 3.89; N, 10.28.

4.6.3.4 Preparation of [{Ru(CO)(PPh$_3$)Tp}$_3$-(1,4-(CH=CH)(C$_6$H$_4$))$_3$N] (39)

To a suspension of $RuHCl(CO)(PPh_3)_3$ **19** (0.22 g, 0.228 mmol) in dichloromethane (10 ml) was added tris(4-ethynylphenyl)amine (0.02 g, 0.07 mmol) in dichloromethane (2 ml). The solution immediately turned red and was stirred for 3 h. KTp was added (0.06 g, 0.243 mmol) and the solution turned yellow over the course of two hours. The reaction mixture was reduced to dryness, re-dissolved in a minimum amount of dichloromethane and filtered through celite. Hexane was added (10 ml) to the filtrate and some solvent removed. A yellow powder was collected by filtration, heated in ethanol, allowed to cool, and filtered again. The

powder was washed in hexane and dried under vacuum (0.087 g, 58 %). ^{1}H NMR (400 MHz, $CDCl_3$): δ_H 5.89 – 5.90 (m, 9H, Tp), 6.08 – 6.09 (m, 3H, Tp), 6.28 – 6.34 (m, 3H, RuCH=C*H*), 6.77 – 6.79 (m, 6H, Tp), 6.95 – 7.02 (m, 6H, C_6H_4), 7.08 – 7.13 (m, 12H, Ph H_m), 7.20 – 7.24 (m, 12H, Ph H_o), 7.33 – 7.36 (m, 9H, Ph H_p), 7.55 – 7.56 (m, 3H, Tp), 7.67 – 7.69 (m, 3H, Tp), 7.73 (bs, 3H, Tp), 7.99 (dd, $^{3}J_{HH}$ = 17 Hz and $^{3}J_{HP}$ = 2 Hz, 3H, RuC*H*=CH). ^{31}P NMR (126 MHz, $CDCl_3$): δ 51.3 (s), 51.3 (s), 51.4 (s). MALDI(+)-MS 2133.7 $[M + H]^+$. IR (CH_2Cl_2, cm^{-1}): ν(C≡O) 1940, ν(B-H) 2481. Elemental analysis: Calculated for $C_{108}H_{93}B_3N_{19}O_3P_3Ru_3$; C, 60.78; H: 4.39; N, 12.47. Found; C, 57.10; H, 4.10; N, 10.09.

4.6.4 Computations

All *ab initio* computations were carried out with the Gaussian 03 package. [301] The model geometries of the mononuclear [**23-H**]$^{n+}$ to [**36-H**]$^{n+}$ (n = 0, 1), and dinuclear systems [**35-H**]$^{n+}$ and [**36-H**]$^{n+}$ (n = 0, 1, 2) discussed here were optimised using the MPW1K/LANL2DZ/3-21G* level of theory with no symmetry constraints. [228, 241-243] This MPW1K/3-21G* level of theory proved to be suitable for ruthenium complexes elsewhere. [43, 229] The keywords used in Gaussian03 for the MPW1K functional [228, 241] here are MPWPW91 and iop(3/76=0472005280). Frequency calculations were computed on these optimised geometries at the corresponding levels and no imaginary frequencies were found in these geometries unless otherwise stated. A scaling factor of 0.94 was applied to the calculated frequencies as it is known that DFT calculations over estimate the acetylide ν(C≡C) and acetylide ring substituent ν(C=C) frequencies. [244, 245] The MO diagrams and orbital contributions were generated with the aid of GaussView [246] and GaussSum [247] packages respectively.

Chapter 5 : Synthesis and Metallation of Triethynyl Methanols

5.1 Introduction

Organometallic complexes in which metal centres are linked by all carbon [55, 181] or carbon-rich, [302-304] ligands have been the subject of a considerable body of research in recent decades. Prominent within this work are studies of linear ligands capable of bridging two metal centres. The structurally simple examples derived from polyyndiyl ligands have proven to be particularly effective at promoting interactions between iron, ruthenium and rhenium based metal end-caps, and examples featuring all-carbon chains of truly impressive length have been structurally characterised in the case of platinum complexes. [94, 155, 156, 302, 305]

Equally, more synthetically accessible carbon rich ligands based on diethynyl aromatic scaffolds have also attracted considerable attention. Compounds featuring 1,4-diethynyl benzene based ligands have long been known, [72, 103, 169, 306-310] but surprisingly, detailed studies of the electronic structure, redox properties and magnetic characteristics of these almost prototypical examples of L_nM-B-ML_n systems have only recently been undertaken, [79, 92, 93, 178] and extended towards other aromatic cores, [289, 311] notably but not exclusively, thiophene based systems. [312-323] Current research is now largely directed towards the study of carbon-rich bridging ligands featuring extended π-conjugated systems, including oligomeric polyacetylenes, [159, 160, 162, 163, 324] (phenylene ethynylene)s [91, 178] and dendritic structures. [104, 108, 112, 325]

In recent times, consideration has been given to the role of branched all-carbon and carbon-rich ligands that may be suitable for the construction of mixed-valence compounds in which more than two metal centres are linked through a common core.[58, 59, 98, 111] Previous Chapters have shown that the *meta*-connection of Ru-based auxiliaries through the carbon-rich 1,3-diethynylbenzene fragment does not permit significant delocalisation between the metal centres. Similarly, the

conceptual extension of the 1,3-diethynylbenzene core to 1,3,5-triethynylbenzene does not provide access to "multi-centre" (i.e. >2) mixed valence systems with strong interactions between the remote metal centres. [116, 207, 214]

Both Winter and Akita have independently been drawn to tetraphenylethene based ligand systems. In the case of the Akita system **40** (Scheme **19**), the individual oxidation processes of the four iron centres were found to take place at very similar potentials, which was interpreted by those authors as evidence for only weak interactions between the metal sites. [58] However, as noted elsewhere in this thesis, conclusions drawn from the electrochemical data in isolation should be treated with care. Winter's tetra(vinyl) system **22** was shown by spectroelectrochemical methods to possess a redox active carbon-rich core, [59] and hence discussions of electron transfer between the metal centres are fraught with conceptual difficulty. In a similar vein, the preparation of trimetallic complexes using a cyclopropenium bridging ligand are also worthy of note (Figure **72**), [326, 327] but the preparation of mixed valence compounds from this system have not yet been achieved. The metal-carbon bonds have been shown to be essentially σ in nature. [328]

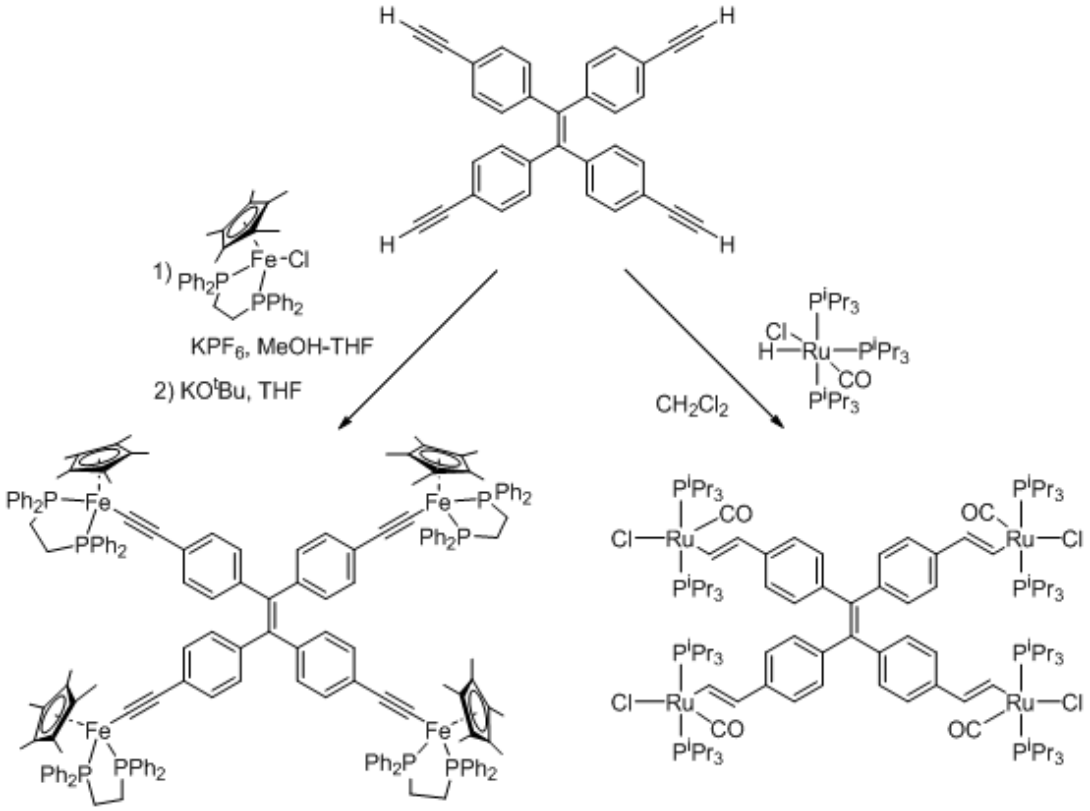

Scheme **19** Tetrametallated complexes **40** and **22** prepared from tetrakis(ethynylphenyl)ethene.

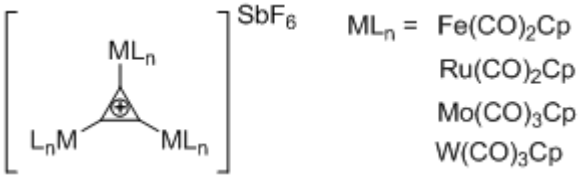

Figure **72** Trimetallatic cyclopropenium complexes.

With a view to the *de novo* design of a carbon fragment for the interconnection of multiple metal fragments, it is appropriate to consider the simplest possible fragment, namely the sp^2-hybridised carbon centre (Figure **73**).

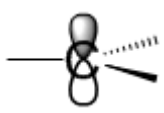

Figure **73** sp^2 hybrised C atom.

The D_{3h} sp^2 hybridised carbon centre offers a p-orbital of appropriate symmetry to interact with three π-donors, and it is possible to envision a carbon-rich "triethynylmethyl" radical or cation based bridging ligand that would allow delocalisation between three metal based dπ-systems (Figure **74**).

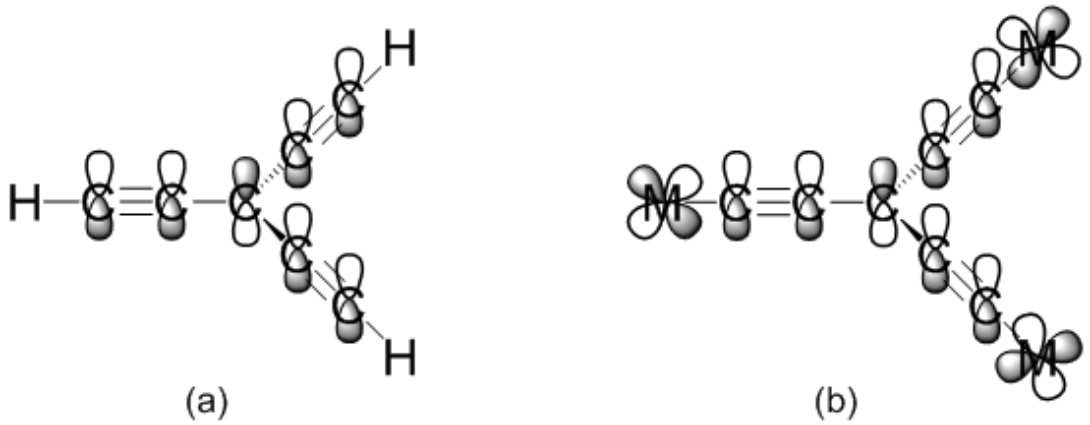

Figure **74** Delocalisation of the π-system over: (a) a C_7H_3 cationic fragment; (b) a metallated C_7M_3 fragment.

The trityl cation ($[CPh_3]^+$) is a textbook example of a stable cationic sp^2 carbon centre, and various metal complexes stabilising adjacent carbon cation cores have long been known. [329-332]

Triethynyl methyl cations which feature three ethynyl groups in conjugation with the carbocation (Figure **74**) are also known to be sufficiently stable to permit the recording of NMR spectra. [333-335] These triethynyl methyl cations can be considered as derivatives of propargyl cations, and consequently metal stabilised examples have also been isolated [336] and in one case crystallographically characterised (Figure **75**). [337]

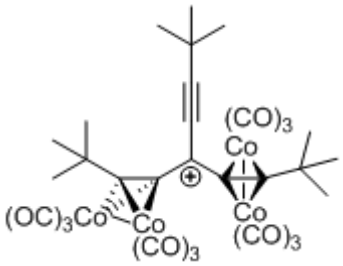

Figure **75** A triethynyl methyl cation stabilised by incorporation of cobalt clusters.

The use of a R_3C^+ carbocation based bridging ligand, was therefore considered to be a very interesting area of study. Triethynylmethanols provide a convenient entry to this chemistry through treatment with strong acids (Scheme **20**), [333-338] although many organometallic derivatives are likely to be incompatible with this approach.

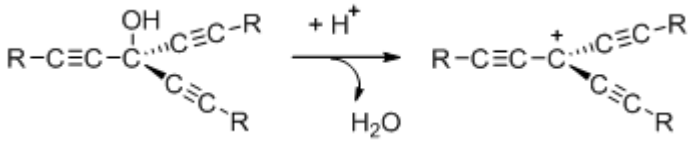

Scheme **20** Treatment of triethynylmethanols with strong acids to afford the triethynyl methane cation.

Curiously, despite the demonstrations of simple conversions of propargyl alcohols to allenylidenes by Selegue [339] (Scheme **21**) and the wide-spread adoption of this chemistry in the synthesis of carbon-rich metal complexes, [340-343] triethynyl methanol based systems have been essentially ignored as ligands and ligand precursors. Triethynyl methanols have, however, found considerable application as building blocks in the construction of carbon-rich molecules with unusual three dimensional structures, such as the expanded cubane [**41**] [344] (Scheme **22**), and a range of extended allenes. [345, 346]

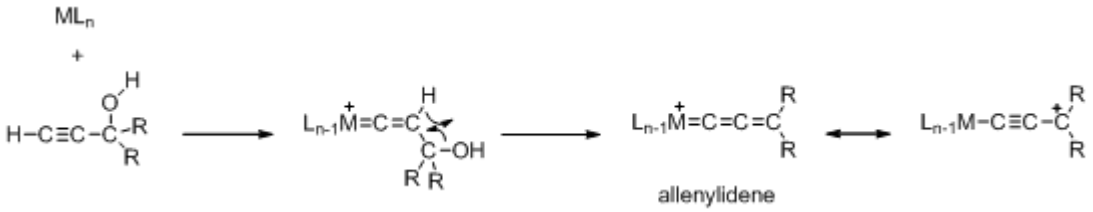

Scheme **21** Synthesis of an allenylidene complex from a propagylic alcohol.

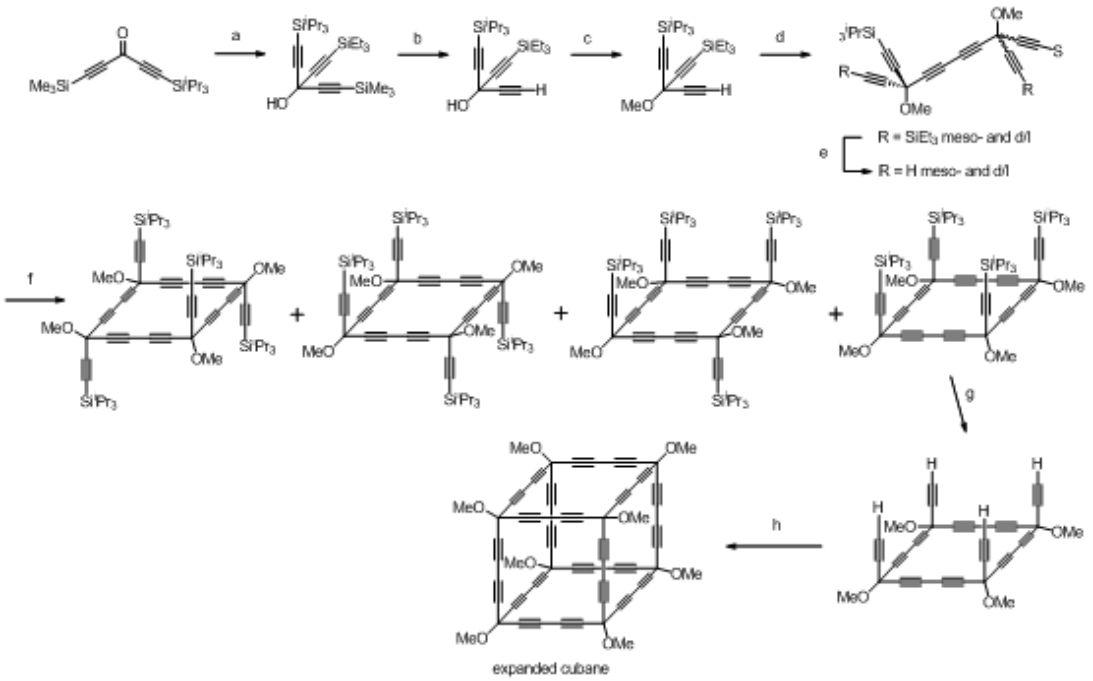

Scheme **22** Synthesis of the expanded cubane [**41**]; a) $Et_3SiC{\equiv}CH$, BuLi, THF, 0 °C, 3 h, 95%, b) 1 N NaOH, MeOH/THF (1/1), rt, 1 h, 86%, c) BuLi, THF, -78 °C, 10 min, then MeI, -78 °C rt, 16 h, 98%, d) CuCl, TMEDA, air, CH_2Cl_2, rt, 5 h 97%, e) K_2CO_3, MeOH/THF (1/1), rt, 3 h, 93%, f) CuCl, TMEDA, air, CH_2Cl_2, rt, 18 h, 8 / 18 / 36 / 10%, g) Bu_4NF, wet THF, -15 °C, 3 h, 87%, h) CuCl, TMEDA, air, CH_2Cl_2, rt, 3 h, 16%. [344]

The synthesis of triethynyl methanols is most commonly achieved via a sequence of transformations from diethyl carbonate [333, 334] or ethyl formate. [347-349] Interestingly, in one of the earliest preparations of triethynyl methanols, Gray and Marvel investigated the use of chloroethyl formate with $NaC{\equiv}C^tBu$ to successfully prepare $(^tBuC{\equiv}C)_3COH$, albeit in ca. 30% yield. [350] The use of this reagent in the preparation of related systems seems to have been overlooked.

The synthesis of the parent triethynylmethanol $(HC{\equiv}C)_3COH$ described by Alberts [347] serves to illustrate the general principles involved in the preparation of this class of compounds (Scheme **23**). Treatment of ethyl formate with $LiC{\equiv}CSiMe_3$ affords 1,5-bis(trimethylsilyl)-pentan-1,4-diyne-3-ol, after conventional workup. Oxidation of the secondary alcohol to the diethynyl ketone ($K_2Cr_2O_7$ or MnO_2) reintroduces an electrophilic carbonyl centre, which is subsequently treated with a third equivalent

of $LiC{\equiv}CSiMe_3$ to give $(Me_3SiC{\equiv}C)_3COH$. Desilylation affords the parent triethynyl methanol in good yield.

In the first step of the reaction, ethyl formate reacts with the acetylide anion to afford an intermediate ethynyl aldehyde. However, the reaction cannot be stopped at this point as the aldehyde reacts with the acetylide anion faster than the formate, leading exclusively to the diethynyl alcohol. Oxidation of the secondary alcohol gives a diethynyl ketone. The reaction of the diethynyl ketone with a differentially substituted acetylide is possible, leading to not only "A_3" substituted triethynyl methanols, but also "AB_2" derivatives. However, a significant disadvantage of the route as described rests on the use of the strongly oxidising reagents $K_2Cr_2O_7$ or MnO_2 in the conversion of the secondary alcohol to the diethynyl ketone, which prevents the use of acetylenic reagents bearing oxidatively sensitive substituents. Although the oxidation step can be avoided through the use of diethynyl carbonate as the initial building block, only A_3 systems can be prepared in this manner.

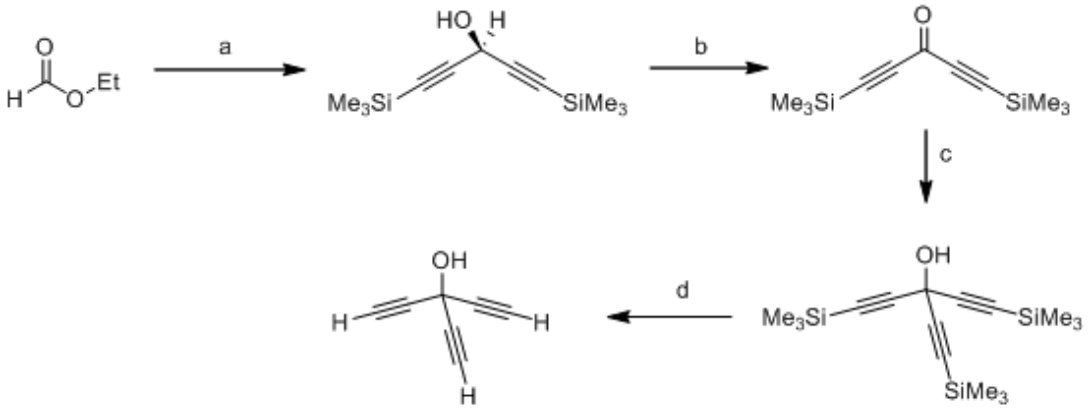

a) Trimethylsilylacetylene (TMSA) , ^{n}BuLi, b) $K_2Cr_2O_7$, c) TMSA, ^{n}BuLi, d) dil. NaOH-CH_2Cl_2

Scheme **23** The preparation of triethynyl methanols from ethyl formate. [347]

In this Chapter, a revised synthesis of triethynyl methanols is described. Through the use of chloroethylformate as a key building block not only are the strongly oxidising conditions avoided, but AB_2 systems can also be readily prepared. The use of triethynyl methanols as ligand precursors has also been investigated, although with less success.

5.2 Results and Discussion

5.2.1 Syntheses

The simplified synthetic method used is a modification of the Alberts method, [347] in which chloroethyl formate has been utilised as the key carbon building block rather than ethyl formate. For example, the addition of a three-fold excess of lithium trimethylsilylacetylide to chloroethyl formate affords the silyl-protected triethynylmethanol in good yield (Scheme **24**).

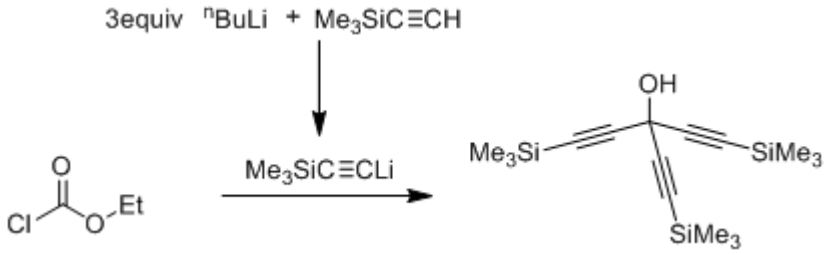

Scheme **24** The preparation of a triethynyl methanol from chloroethyl formate.

Given the order of reactivity of carbonyl carbons towards nucleophilic substitution [131] is

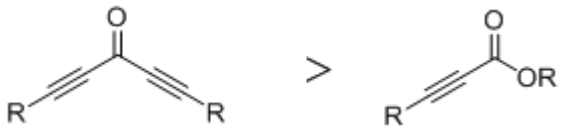

the addition of three ethynyl arms in the presence of excess lithiated acetylide is unavoidable.

However, in the case of ethyl chloroformate, reaction with strictly one equivalent of acetylide anion results exclusively in substitution of the chloride, providing very convenient entry to a range of ethynyl esters (Scheme **25**). The further reaction of these ethynyl esters with two equivalents of acetylide anions permits synthesis of not only symmetric A_3 triethynyl methanols, but also AB_2 systems rapidly and in high

yield (Table **51**, Chart **11**). Critically, this route avoids the use of the strongly oxidising reagents that underpin the established route.

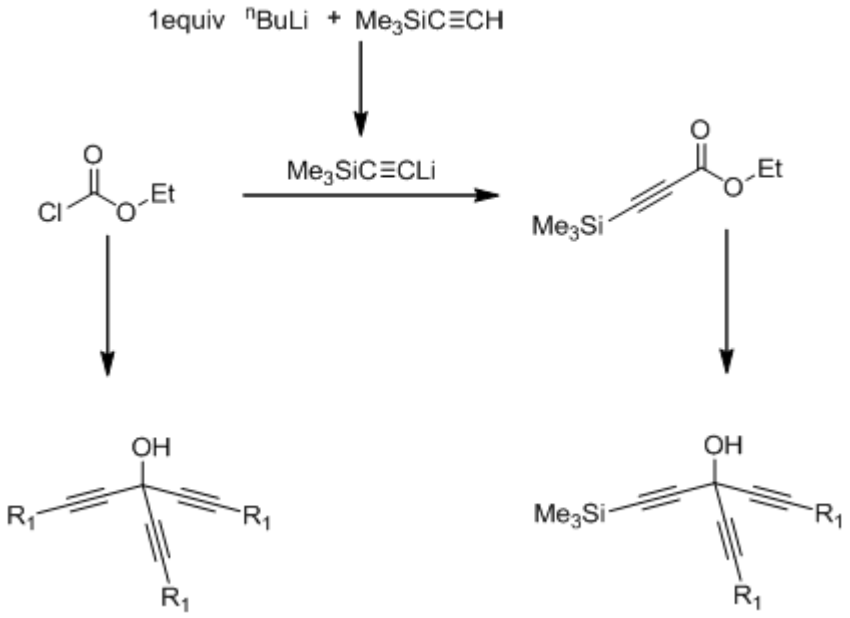

Scheme **25** The preparation of "A_3" and "AB_2" substituted triethynyl methanols from chloroethyl formate.

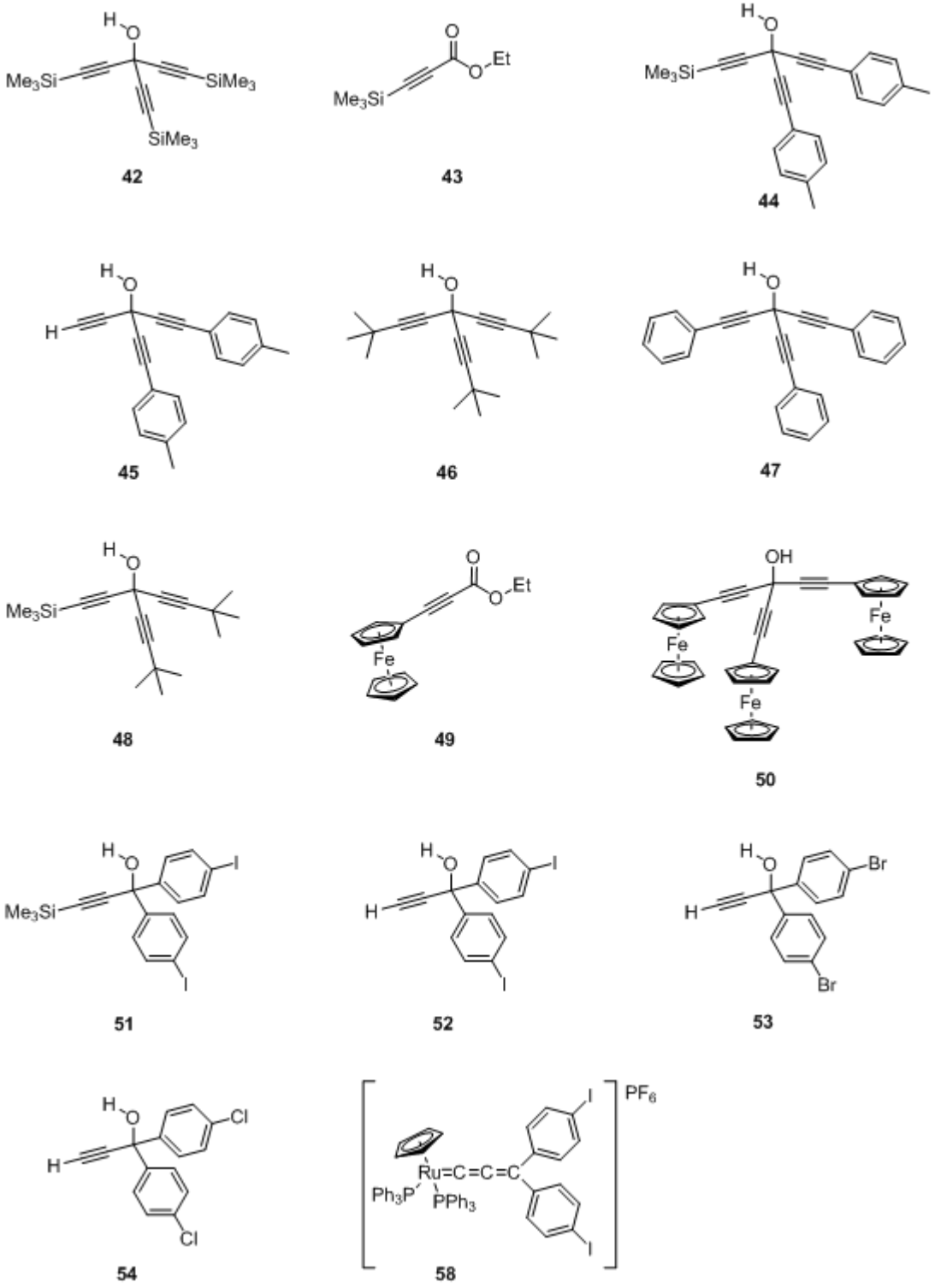

Chart **11** The acetylenic esters and triethynyl methanols prepared or discussed in this Chapter.

Table **51** The acetylenic esters and triethynyl methanols prepared in this work.

Compound	Yield %
$(Me_3SiC{\equiv}C)_3COH$ **42**	80
$Me_3SiC{\equiv}C(C{=}O)OEt$ **43**	82
$Me_3SiC{\equiv}C(COH)(C{\equiv}CC_6H_4CH_3)_2$ **44**	64
$HC{\equiv}C(COH)(C{\equiv}CC_6H_4CH_3)_2$ **45**	73
$(Me_3CC{\equiv}C)_3COH$ **46**	44
$(PhC{\equiv}C)_3COH$ **47**	70
$(PhC{\equiv}C)_3COH$ **47** (KO^tBu method)	47
$Me_3SiC{\equiv}C(COH)(C{\equiv}C^tBu)_2$ **48**	76
$\{Fe(C_5H_5)\}(C_5H_4)C{\equiv}C(C{=}O)OEt$ **49**	16
$(\{Fe(C_5H_5)\}(C_5H_4)C{\equiv}C)_3COH$ **50** (method A)	87
$(\{Fe(C_5H_5)\}(C_5H_4)C{\equiv}C)_3COH$ **50** (method B)	55
$Me_3SiC{\equiv}C(COH)(C_6H_4I)_2$ **51**	90
$HC{\equiv}C(COH)(C_6H_4I)_2$ **52**	69

A minor variation to this general synthetic method uses mixtures of the terminal acetylene and KO^tBu as a base in situ, instead of the pregeneration of $LiC{\equiv}CR$ from the alkyne and BuLi. Thus, the reaction of a terminal acetylene with ethyl chloroformate and potassium *t*-butoxide in refluxing methanol, affords the corresponding A_3 triethynylmethanol (Scheme **26**).

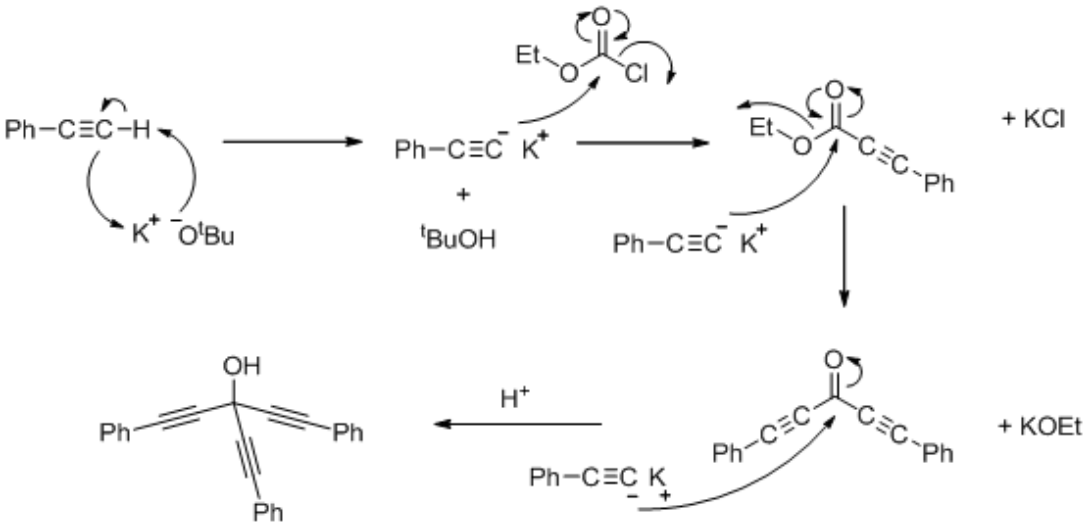

Scheme **26** Alternative synthetic method to form **47** using KO^{t}Bu.

With a range of triethynyl methanols in hand, attention was turned to the use of these systems in the construction of metal complexes. Trimethylsilylacetylenes $Me_3SiC{\equiv}CR$ have been shown to react with $RuCl(PPh_3)_2Cp$ and closely related systems in the presence of KF / NH_4PF_6 to give metal acetylide complexes $Ru(C{\equiv}CR)(PPh_3)_2Cp$. [351] However, the reaction of equimolar amounts $RuCl(PPh_3)_2Cp$, $(Me_3SiC{\equiv}C)_3COH$, NH_4PF_6 and catalytic KF in refluxing methanol gave purple solutions, from which only small amounts of an unidentified purple solid could be obtained (Scheme **27**).

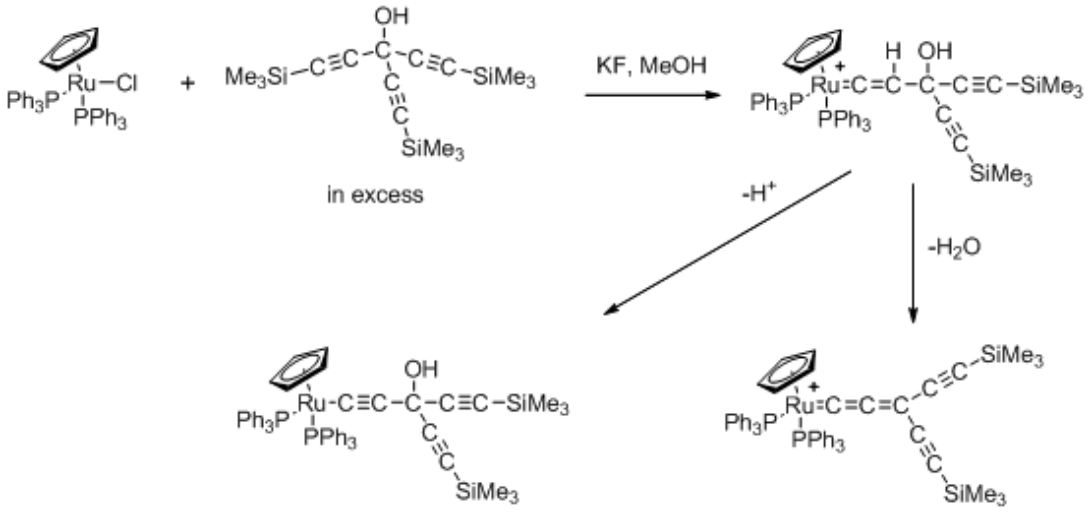

Scheme **27** The proposed desilylation / metallation reactions of $RuCl(PPh_3)_2Cp$ with a trimethylsilyl masked triethynyl methanol.

Terminal alkynes react with many metal systems to give vinylidene complexes, which can be easily deprotonated to afford the corresponding acetylide. [341] The silyl-protected compound **42** was converted to the parent triethynyl methanol by reaction with a solution of K_2CO_3 in methanol. [352] After reaction the compound was washed with H_2O/Et_2O, and extracted into diethylether. The literature suggests that this $(HC{\equiv}C)_3COH$ solution can be concentrated to give $(HC{\equiv}C)_3COH$ as a temperamental solid. [347] Rather than isolate a potentially hazardous material, an assumption was made that the desilylation step went 100% conversion and the diethylether extraction was used as a $(HC{\equiv}C)_3COH$ solution (Scheme **28**).

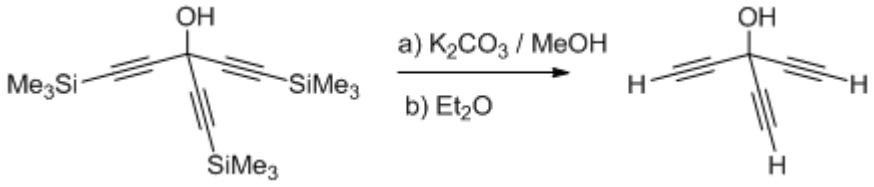

Scheme **28** The preparation of the parent triethynyl methanol $(HC{\equiv}C)_3COH$.

Attempts at metallation of $(HC{\equiv}C)_3COH$ with $RuCl(PPh_3)_2Cp$ using a large excess of the terminal tris(alkyne) in the presence of NH_4PF_6 in refluxing methanol were made. The characteristic purple colour of the ruthenium allenylidene compounds ($[Ru(=C=C=CR_2)(PPh_3)_2Cp]^+$) was observed but again any spectroscopic characterisation was hampered by the lack of compound obtained after work up.

In seeking to understand the complications encountered, we can consider the work of Phillip Zuber, a former project student in the Low group, with ferrocenyl substituted triethynyl methanols. [353] Dehydration of **55** by addition of $HBF_4.Et_2O$ results in a rearrangement of the triethynyl methanol core, and the generation of a carbonyl (Scheme **29**). Similar rearrangements have been reported elsewhere. [354, 355]

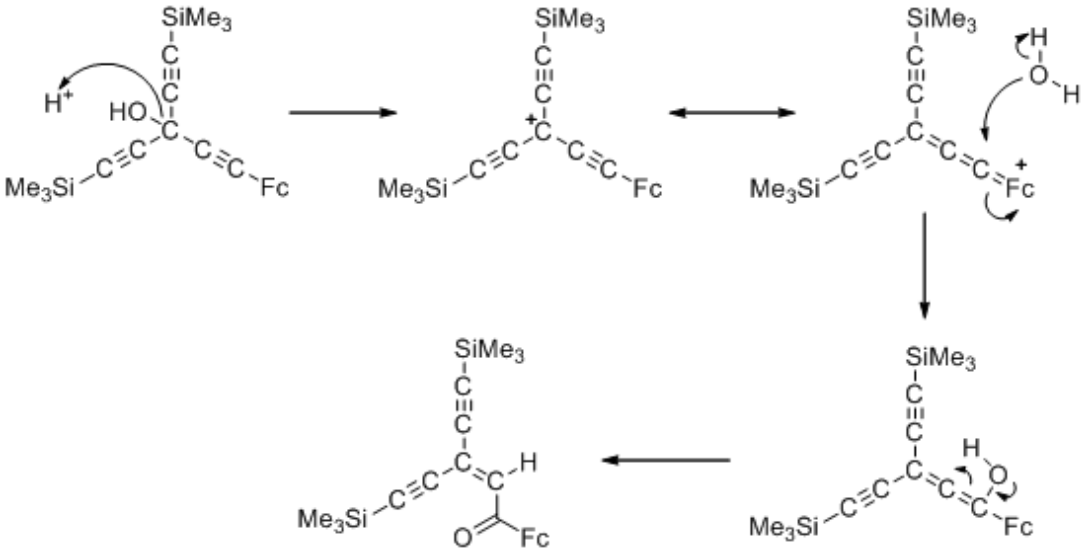

Scheme **29** Acid catalysed hydroxyl arrangement of **55**.

The ketone product was crystallographically characterised as the $Co_2(CO)_4$(dppm) derivative **56** following reaction with $Co_2(CO)_6$(dppm) (Scheme **30** and Figure **76**).

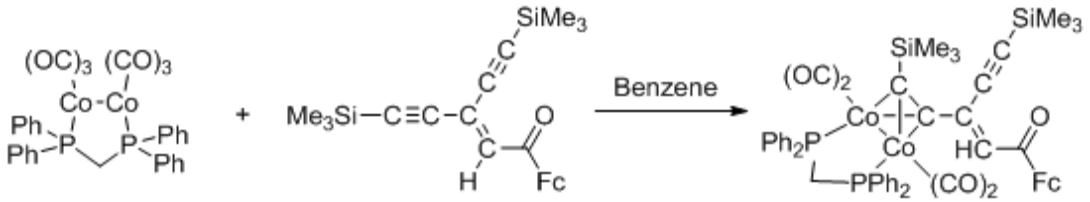

Scheme **30** Formation of the cobalt carbonyl cluster derivative **56**.

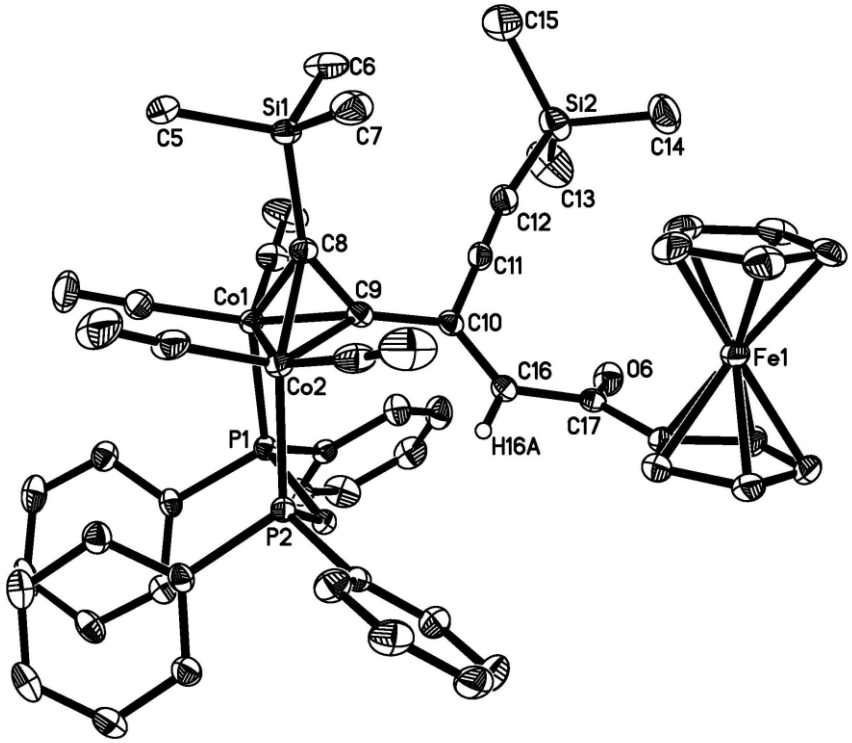

Figure **76** Molecular structure of **56**. Hydrogen atoms have been removed, except for the α–carbonyl hydrogen, for clarity.

It is possible that the ruthenium-mediated elimination of water from the triethynyl methanol could be complicated by similar water additions, but this remains speculative. Another source of complications could be from the possibility of attack of an alkyne, either inter- or intramolecularly, on a Grubbs-style intermediate (Scheme **31**).

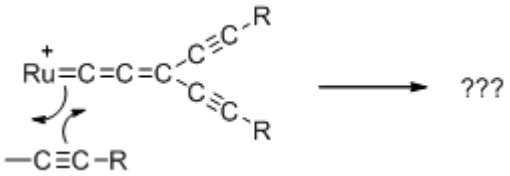

Scheme **31** Possible intermolecular alkyne attack

With the chemical complications associated with preparing metal complexes in which the triethynyl methyl cation was stabilised by σ-bonded metal moieties in

evidence, the ligand structure was altered in an effort to introduce greater inherent chemical stability. The trityl cation $[CPh_3]^+$ is sufficiently stable to be isolated as the $[PF_6]^-$ salt which can be handled in air for relatively long periods. The introduction of phenylene rings into the ligand structure was planned in the manner shown in Scheme **32**.

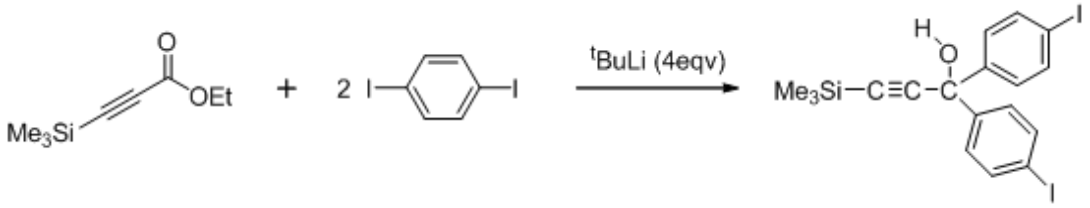

Scheme **32** Introduction of phenylene rings into the ligand structure.

The reaction of diiodobenzene with two equivalents of ^{t}BuLi affords lithio(iodo)benzene, butene and LiI. Trapping of the aryllithium by reaction with one half equivalent of $Me_3SiC{\equiv}C(C{=}O)OEt$ **43** proceeded smoothly to give **51** in 90% isolated yield (Scheme **32**). The trimethyl silyl group in **51** could be removed in the usual fashion (K_2CO_3 / MeOH) to give **52**.

The compounds **51** and **52** offer two complimentary routes to trimetallic complexes either through ligand expansion and subsequent metallation (Scheme **33**) or by initial coordination to form a functionalised allenylidene complex, which can be extended if required (Scheme **34**). Each of these methods represents an alternative to strategies employed by the Dixneuf group in the preparation of **57** (Scheme **35**). [71]

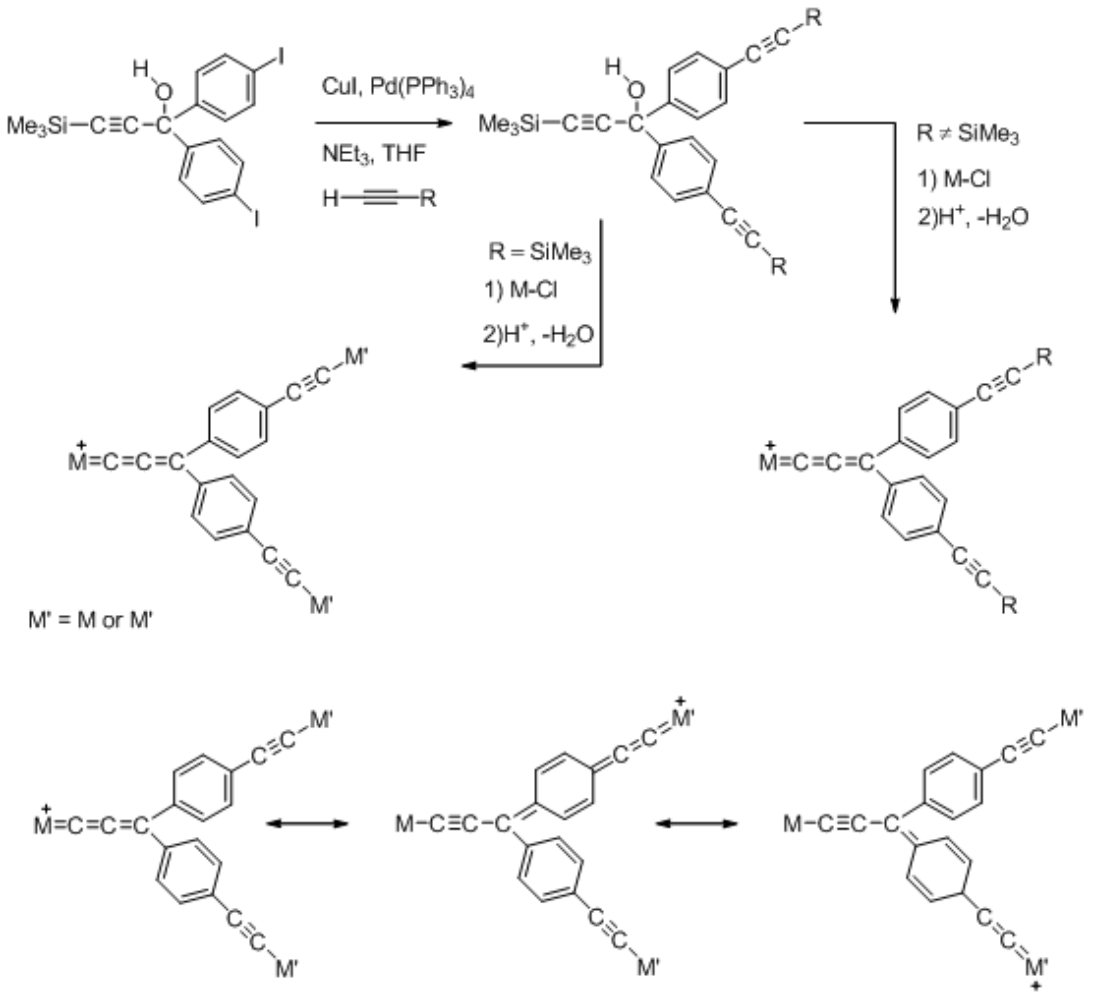

Scheme **33** Reaction scheme for **51**, and ligand extension and metallation, with some possible canonical structures.

Unfortunately, attempts to cross couple **51** with $HC{\equiv}CSiMe_3$ using established Sonogashira protocols were not successful, with multiple products being formed as evidenced by TLC, IR and ^{1}H NMR spectroscopies, and in light of time constraints, reaction conditions could not be investigated further. Reaction of **52** with $RuCl(PPh_3)_2Cp$ in the presence of NH_4PF_6 proceeded relatively smoothly to afford the diiodo allenylidene $[Ru(C{=}C{=}C(C_6H_4I\text{-}4)_2)(PPh_3)_2Cp]PF_6$ (**58,** ν(C=C=C) 1926 cm^{-1}). However, attempts to further cross-couple **58** with $HC{\equiv}CSiMe_3$ were unsuccessful, with a plethora of purple coloured compounds being observed by TLC analysis of the reaction mixture. In light of time constraints, this line of investigation was, with reluctance, abandoned.

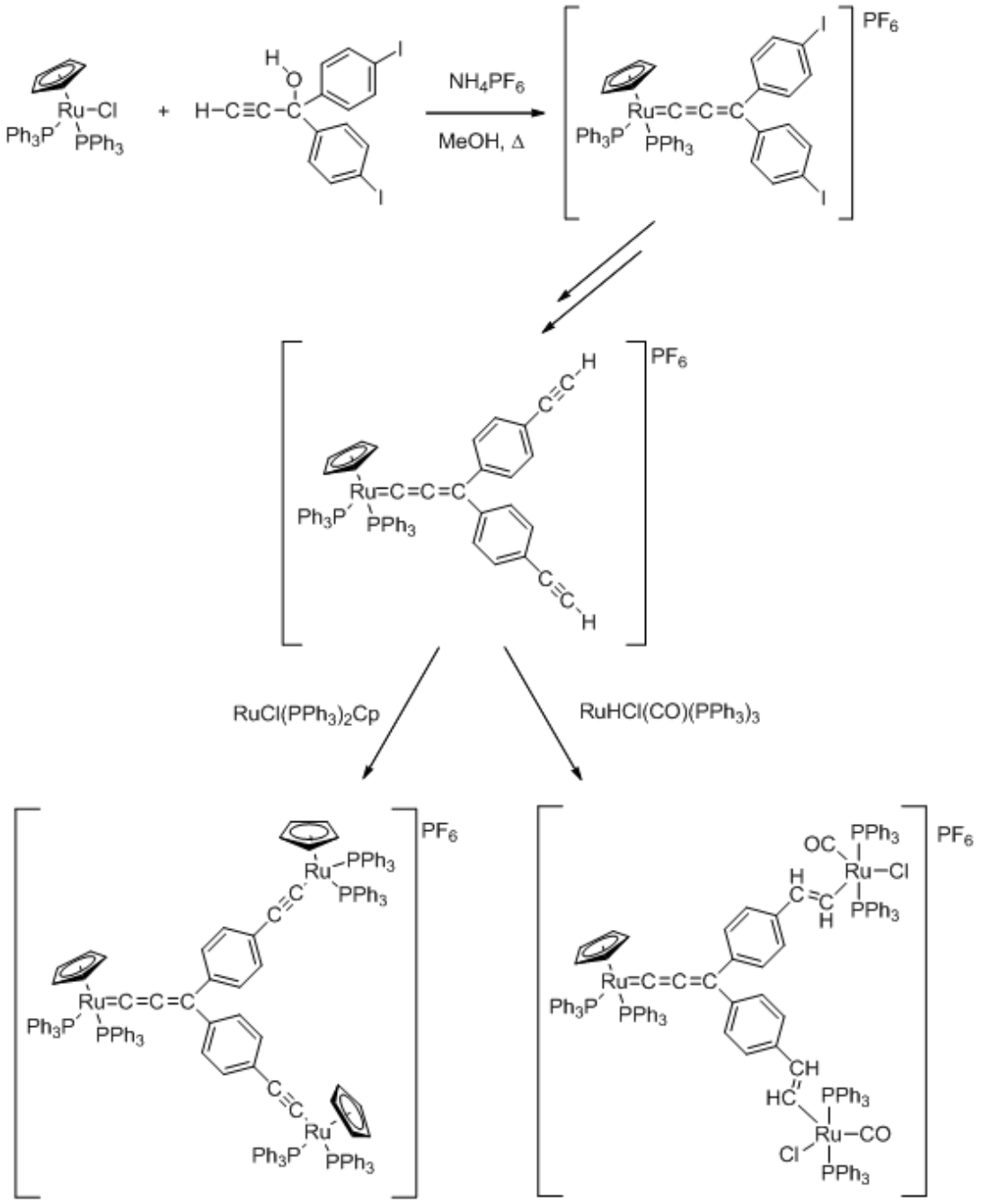

Scheme **34** Reaction scheme for **52**, initial metallation, then ligand extension and subsequent metallation

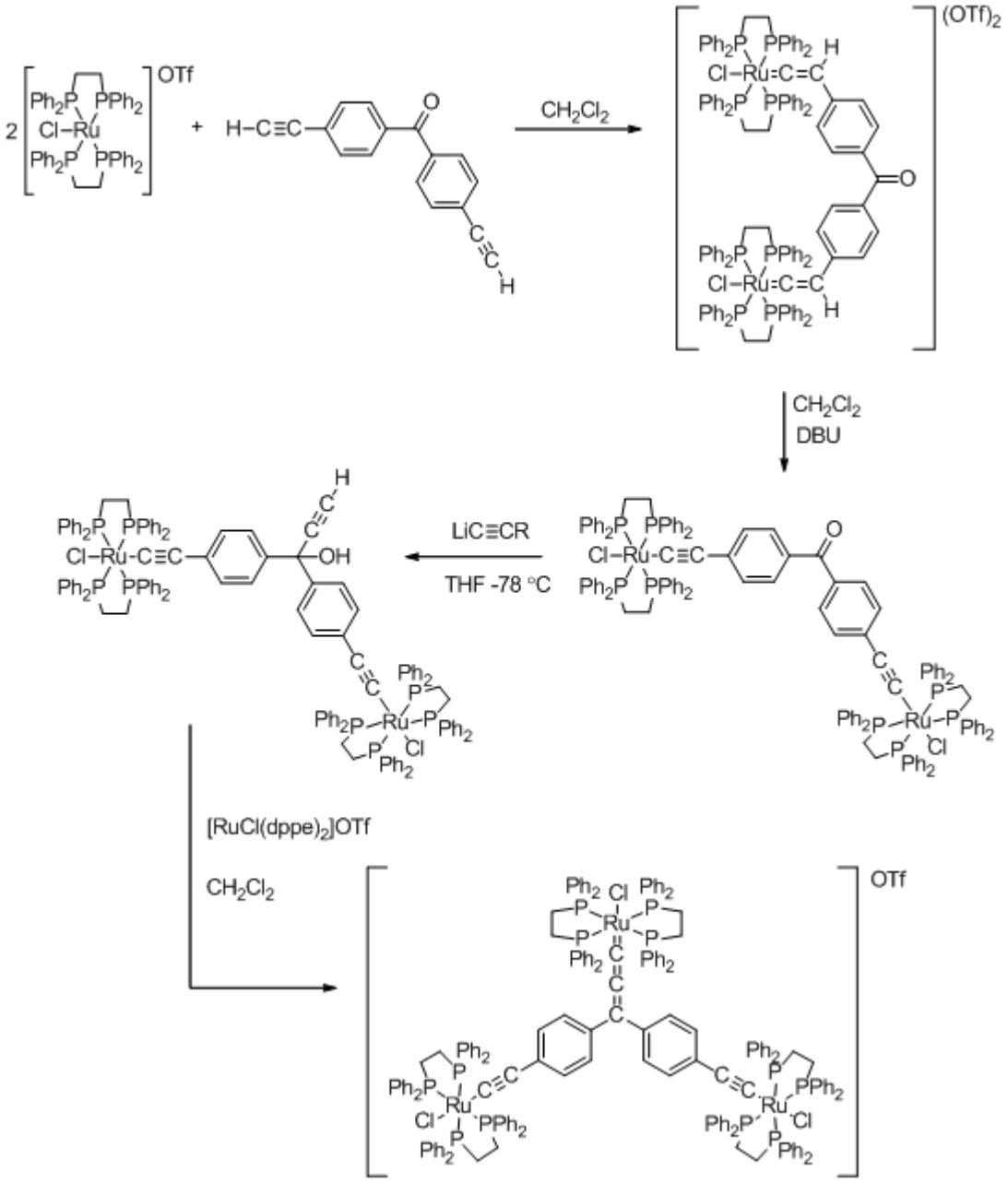

Scheme **35** The reaction scheme utilised by Dixneuf for the synthesis of **57**. [71]

5.2.2 Molecular Structure Analyses

Single crystals of **51** and **52** suitable for X-ray diffraction were obtained, the structures of related complexes $HC{\equiv}C(COH)(C_6H_4Br)_2$ **53** and $HC{\equiv}C(COH)(C_6H_4Cl)_2$ **54** having been reported earlier. [356] All four complexes discussed in this section are displayed in Chart **12**. Crystallographic data and

important bond lengths and angles are summarized in Table **52**, Table **53** and Table **54**, with plots of **51** and **52**, illustrated in Figure **79** to Figure **82**.

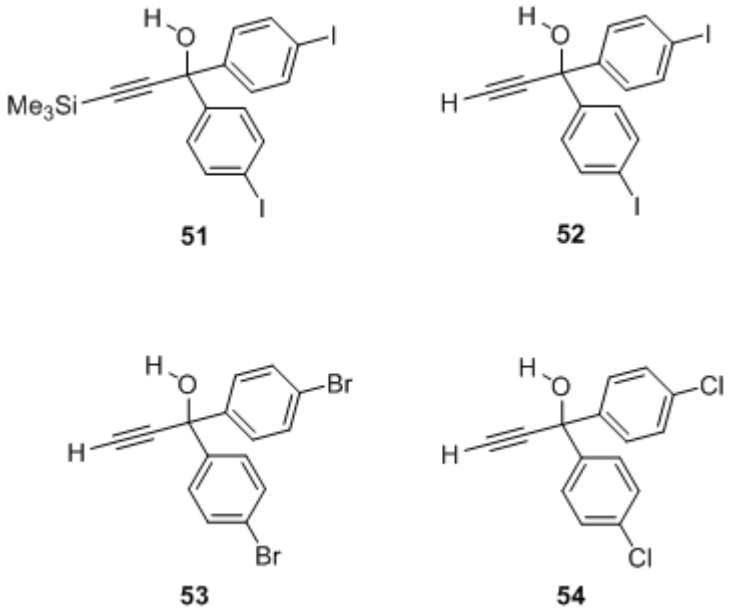

Chart **12** *p*-substituted aryl ethynyl methanols **51**, **52**, **53** and **54**.

All of the structures **51**, **52**, **53** and **54** are tetrahedral at the central C atom, in agreement with the sp^3 hybridised nature of this carbon.

In contrast to the silyl-protected derivative **51**, the three terminal acetylene derivatives **52**, **53** and **54** lack O–H · · ·O hydrogen bonding. This complete lack of expected O–H · · ·O hydrogen bonding in *gem*-alkynol complexes, has been accounted for by Allen and Bilton, [356] in terms of "*the OH group in gem-alkynols being sterically hindered by the ethynyl arm and the increased difficulty by the presence of the additional phenyl substituents at the gem-alkynol centre*". Instead the two most acidic protons of the molecule, O–H and C≡CH, participate in weak hydrogen bonding to π-acceptors.

All three of the terminal acetylene derivatives **52**, **53** and **54** all form dimers through the C≡CH · · ·π(arene) interactions (Figure **77**). Each molecule in this dimer, is further dimerised via a pair of weaker C(phenyl)–H · · ·O interactions to form stacks

along the *b* axis. These stacks are linked along the *a* axis by two weak interactions; O–H · · · π(arene) and C(phenyl)–H · · ·π(ethynyl).

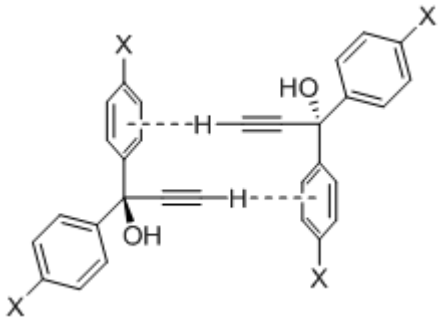

Figure **77** Schematic representation of the C≡CH · · ·π(arene) interactions in **52**, **53** and **54**.

These molecular stacks are further cross-linked along the *c* axis by halogen-halogen interactions (Figure **82**). Studies on the nature of halogen· · · halogen interactions by Desiraju has shown that carbon-bound halogens in a sufficiently electron-withdrawing environment cause an anisotropic charge distribution δ^+ forward of the halogen directly along the C-halogen bond vector, and δ^- perpendicular to the bond vector. [357] The halogen-halogen geometry in **52**, **53** and **54** is in almost perfect arrangement for type II halogen· · · halogen interactions (Figure **78**) described by Desiraju [357], with the Cl· · · Cl, Br· · · Br and I· · · I distances shorter than the appropriate van der Waals limits by 0.12, 0.20 and 0.20 Å, respectively. [358]

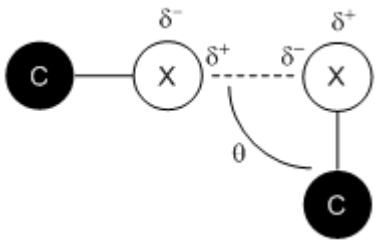

Figure **78** Type II halogen – halogen interaction geometry (θ = 90 °). [357]

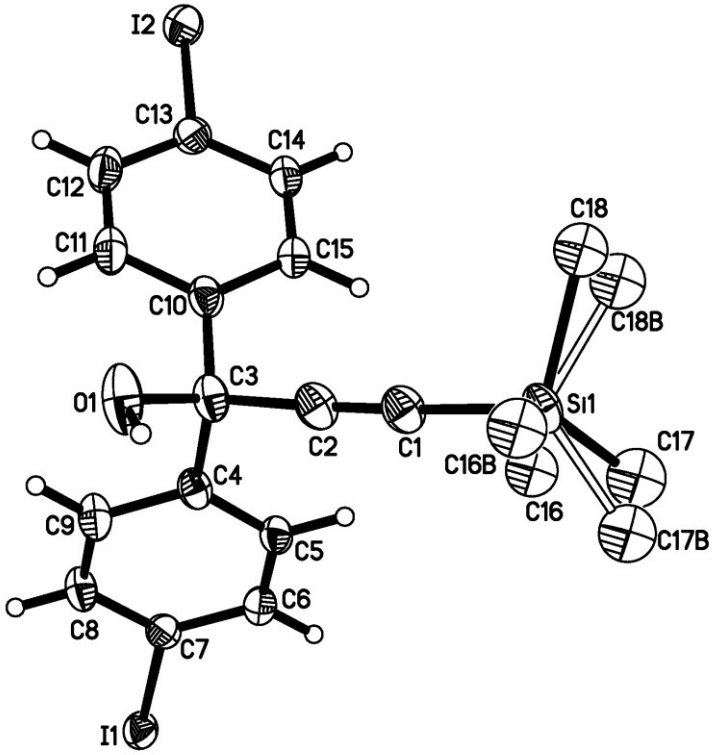

Figure **79** The molecular structure of **51** showing the atom labelling scheme.

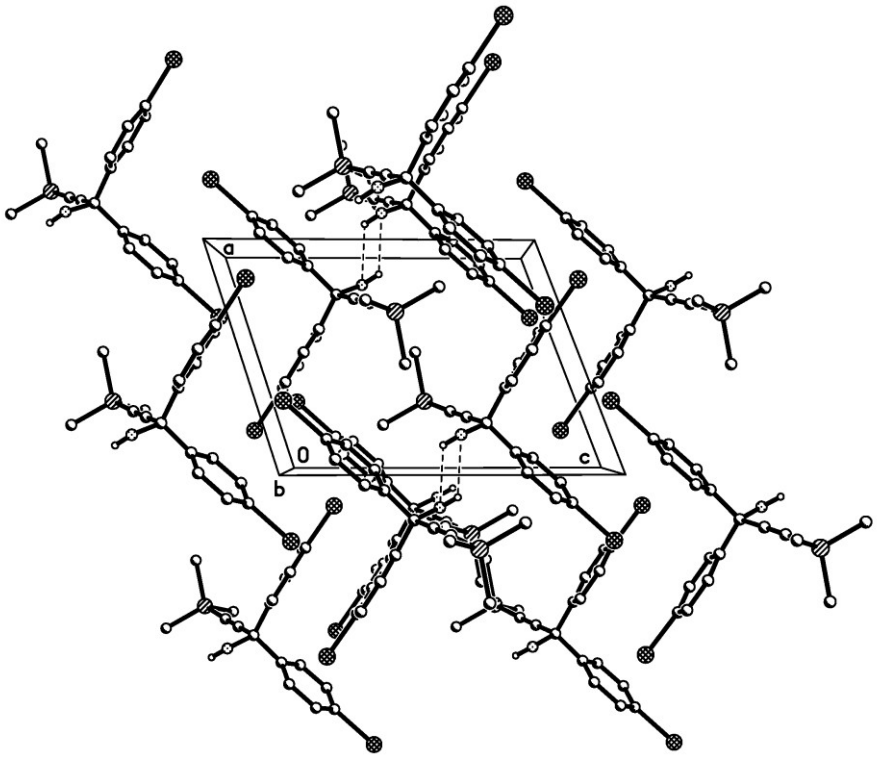

Figure **80** A plot showing the packing of **51** within the crystal lattice.

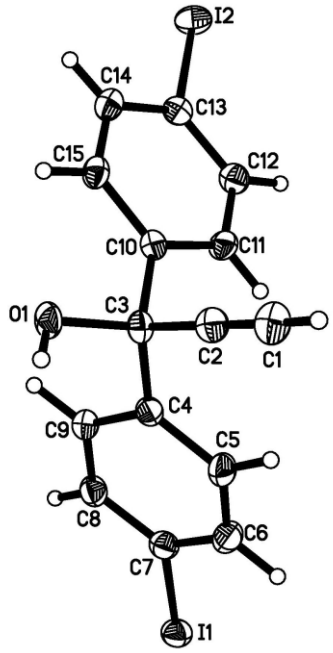

Figure **81** A plot of a molecule of **52** showing the atom labelling scheme.

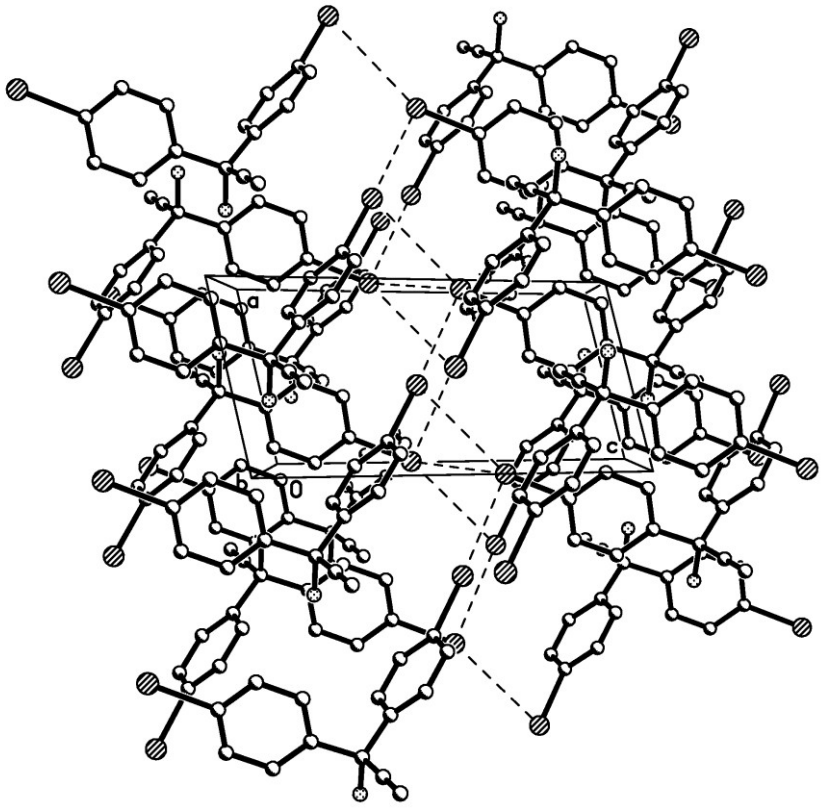

Figure **82** A plot showing the packing of **52** within the crystal lattice.

Table **52** Crystal data and experimental parameters of **51**, **52**, **53** and **54**.

	51	**52**	**53** [356]	**54** [356]
Empirical formula	$C_{18}H_{18}OSiI_2$	$C_{15}H_{10}OI_2$	$C_{15}H_{10}Br_2O$	$C_{15}H_{10}Cl_2O$
Formula weight	532.21	460.03	366.05	277.13
Temperature	120(2)	120(2)	150	150
Crystal system	Triclinic	Triclinic	Triclinic	Triclinic
Space group	P-1	P-1	P-1	P-1
Cell parameters / Å	a 9.5710(2), b 9.9895(2), c 11.8785(2)	a 5.8409(1), b 11.1705(3), c 12.5506(3)	a 5.7906(12), b 11.325(2), c 11.907(2)	a 5.7082(1), b 11.3645(2), c 11.5167(1)
Cell angles / °	α 93.0570(10) β 106.5880(10) γ 112.4320(10)	α 113.64 (1), β 98.85 (1), γ 98.44(1)	α 115.67(3), β 99.43 (3), γ 97.91(3)	α 117.268 (1), β 99.257 (1), γ 96.726(1)
Volume / $Å^3$	989.05(3)	721.34(4)	674.8(2)	639.734(17)
Z	2	2	2	2
ρ_{calc} mg/mm^3	1.787	2.118	1.801	1.439
μ/mm^{-1}	3.240	4.345	5.990	0.490
F(000)	508	428	998	500
Crystal size	0.31 × 0.18 × 0.06	0.34 × 0.2 × 0.16	0.4 × 0.3 × 0.2	0.5 × 0.4 × 0.4
Theta range for data collection	2.24 to 30.50 °	1.82 to 30.49 °	4.26 to 30.50 °	5.44 to 29.17 °
Index ranges	$-13 \le h \le 13$, $-14 \le k \le 14$, $-16 \le l \le 16$	$-8 \le h \le 8$, $-15 \le k \le 15$, $-17 \le l \le 17$	$-6 \le h \le 8$, $-15 \le k \le 12$, $-15 \le l \le 16$	$-6 \le h \le 7$, $-11 \le k \le 14$, $-14 \le l \le 12$
Reflections collected	14745	9930	5364	4371
Independent reflections	6022[R(int) = 0.0138]	4383[R(int) = 0.0158]	3456[R(int) = 0.0287]	2826[R(int) = 0.0425]
Data/restrains/ parameters	6022/1.0000P/203	4383/0.7000P/203	3456/-/203	2826/-/203
Goodness-of-fit on F^2	1.104	1.025	1.071	1.110
Final R indexes [$I>2\sigma(I)$]	$R_1 = 0.0234$, $wR_2 = 0.0543$	$R_1 = 0.0220$, $wR_2 = 0.0559$	$R_1 = 0.0276$, $wR_2 = 0.0718$	$R_1 = 0.0378$, $wR_2 = 0.1043$
Final R indexes [all data]	$R_1 = 0.0260$, $wR_2 = 0.0558$	$R_1 = 0.0259$, $wR_2 = 0.0582$	-	-
Largest diff. peak/hole	1.214/-1.090	1.166/-0.810	-	-

Table **53** Selected bond lengths (Å) of **51**, **52**, **53** and **54**.

Bond Lengths / Å	**51**	**52**	**53** [356]	**54** [356]
C1 ≡ C2	1.197(3)	1.190(3)	1.183(4)	1.183(2)
C1 – R	1.848(2)	0.90(3)	0.90(5)	0.90(3)
C2 – C3	1.485(3)	1.482(3)	1.483(3)	1.479(2)
C3 – O	1.434(2)	1.435(3)	1.438(3)	1.429(2)
C3 – C4/C10	1.533(3), 1.531(3)	1.534(3), 1.535(3)	1.538(3), 1.543(4)	1.534(3), 1.535(3)
Ar – X	2.0929(19), 2.098(2)	2.105(2), 2.100(2)	1.905(2), 1.906(3)	1.741(2), 1.740(2)
C4 – C5/9	1.377(3), 1.394(3) 1.392(3), 1.393(3)	1.395(3), 1.402(3) 1.385(3), 1.396(3)	1.384(2), 1.400(3) 1.393(3), 1.398(3)	1.389(2), 1.394(2) 1.389(2), 1.395(3)
C5/9 – C6/8	1.393(3),1.390(3) 1.385(3), 1.389(3)	1.397(3), 1.390(3) 1.390(3), 1.403(3)	1.400(3), 1.387(3) 1.393(4), 1.393(4)	1.381(3), 1.390(3) 1.385(3), 1.393(3)
C6/8 – C7	1.389(3), 1.387(3) 1.384(3), 1.391(3)	1.379(3), 1.399(3) 1.390(3), 1.388(3)	1.384(3), 1.390(2) 1.385(3), 1.391(3)	1.384(2), 1.387(3) 1.379(3), 1.389(2)

Table **54** Selected bond angles (°) of **51**, **52**, **53** and **54**.

Bond Angles / °	**51**	**52**	**53**	**54**
C1-C2-C3	177.5(2)	179.6(3)	179.4(3)	179.1(3)
C2-C3-C4/C10	111.95(17), 110.44(16)	111.30(18), 109.01(18)	111.31(17), 109.13(16)	111.25(16), 109.22(17)
C4-C3-C10	107.78(15)	108.97(17)	108.89(18)	108.87(16)

5.3 Conclusions

This Chapter has described a simple protocol that allows the preparation of either "symmetric" A_3 or "asymmetric" AB_2 triethynyl methanol derivatives through the reaction of acetylide anions with chloroethylformate. By adopting chloroethylformate as a key synthetic building block reactions that are both high

yielding and avoid the use of strongly oxidising conditions, which have previously limited the variety of substituents built into the triethynyl methanol framework to oxidatively non-sensitive substituents, have been devised. The introduction of phenylene units into the ligand structure to alleviate complications arising from suspected rearrangement processes, and help stabilise the possible carbocation, have commenced, although ligand extension via the use of ligand **51**, either before or after metallation to the allenylidene, had limited success. Although these two interesting synthetic avenues of chemistry were not fully investigated due to time restraints, they still merit further work.

5.4 Experimental Details

5.4.1 General Conditions

All reactions were carried out using oven dried glassware, under an atmosphere of nitrogen using standard Schlenk techniques. Reagents purchased commercially were used without further purification. Starting materials were checked by using relevant spectroscopic techniques before use. NMR spectroscopies were carried out a room temperature and referenced against $CDCl_3$ using the Varian Mercury-200 (^{1}H 199.99 MHz), Bruker and Varian Mercury-400 (^{1}H 399.97 MHz) or Varian Inova-500 (^{1}H 499.77 MHz, ^{13}C 125.67 MHz). Chemical shifts are reported in δ / ppm and coupling constants, *J*, in Hz. IR spectra were recorded using solution cells fitted with CaF_2 windows by the Nicolet Avatar FT IR spectrophotometer. Mass spectra were acquired using the Thermo- Finnigan LTQ FT spectrometer. Single crystal X-ray structure determinations were carried out by Dr DS Yufit of this department using a Bruker 3-circle diffractometer with a SMART 6K area detector, using graphite-monochromated sealed-tube Mo-K_α radiation. These data collections were performed at 120 K, and the temperature maintained using cryostream (Oxford cryosystem) open flow N_2 cryostats. Reflection intensities were integrated using the SAINT program. [300] The molecular structures were solved using direct-methods and refined by full matrix least-squares F^2 using

SHELXTL software. [148] All non-hydrogen atoms were refined in anisotropic approximation. Hydrogen atoms were placed into calculated positions, and refined isotropically using a riding model.

5.4.2 Preparation of $(Me_3SiC{\equiv}C)_3COH$ [42]

1,5-Bis-(trimethyl-silanyl)-3-(trimethyl-silanylethynyl)-penta-1,4-diyn-3-ol

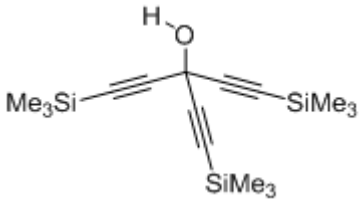

Ethyl chloroformate (1 mL, 10.50 mmol) in THF (5 mL) was added to a solution of lithium trimethylsilylacetylide [prepared by treating trimethylsilylacetylene (4.5 mL 31.70 mmol) in THF (10 mL) at –78 °C with ^{n}BuLi (20 mL, of a 1.6 M solution in hexane, 31.80 mmol)] at –78 °C and stirred for 30 min. The solution was then warmed to room temperature and became dark red in colour, which became dark brown on the addition of a sat. aqueous NH_4Cl (100 mL). The organic layer was separated and the aqueous phase was extracted with diethyl ether. The combined organic layers were dried over $MgSO_4$ and evaporated. The residue was purified by column chromatography (silica, CH_2Cl_2:Hexane 1:1), to afford **[42]** as pale yellow crystals (2.68 g, 80 %). IR (CH_2Cl_2): ν(C≡C) 2160m, ν(OH) 3544s cm^{-1}. ^{1}H NMR ($CDCl_3$): δ_H 0.21 (s, 27H, $SiMe_3$), 2.79 (s, 1H, OH). ^{13}C NMR ($CDCl_3$): δ_C -0.5 (s, $SiMe_3$), 54.7 (s, C-OH), 88.05, 101.4 (s, C≡C). ES-MS (*m/z*): 320, $[M]^+$; 303, $[M - OH]^+$; 288, $[M – OH- CH_3]^+$; 261, $[M – OH\text{-}3Me + 3H]^+$; 230, $[M – OH - SiMe_3]^+$; 215, $[M- OH- CH_3\text{-}SiMe_3]^+$, 191, $[M – OH – (C{\equiv}C)SiMe_3 – CH_3]^+$; 179, $[M – OH – (C{\equiv}C)SiMe_3 – 2Me + 3H]^+$; 133, $[M – OH – \{Me_3Si(C{\equiv}C)\} –Me_3Si]^+$; 121[M – OH – {$Me_3Si(C{\equiv}C)$ - Me_3SiC}]; 109, [M – OH – 2{$Me_3Si(C{\equiv}C)$].

5.4.3 Preparation of $Me_3SiC{\equiv}C(C{=}O)OEt$ [43]

Ethyl 3-(trimethylsilyl)propiolate

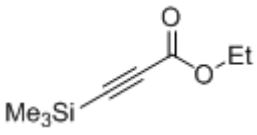

Ethyl chloroformate (1 mL, 10.50 mmol) in THF (5 mL) was added to a solution of lithium trimethylsilylacetylide [prepared by treating trimethylsilylacetylene (1.48 mL 10.50 mmol) in THF (10 mL) at –78 °C with ^{n}BuLi (6.5 mL, of a 1.6 M solution in hexane, 10.50 mmol)] at –78 °C and stirred for 30 min. The solution was then warmed to room temperature and became dark red in colour, which became dark brown on the addition of a sat. aqueous NH_4Cl (100 mL). The organic layer was separated and the aqueous phase was extracted with diethyl ether. The combined organic layers were dried over $MgSO_4$ and evaporated to afford a light brown oil. Fractional distillation of the light brown oil at 40 °C / 80 mmHg affords a clear oil. (Yield 1.46 g, 82 %). IR (CH_2Cl_2): ν(C≡C) 2185m, ν(C═O) 1713s, ν(O-Et) 3397m cm^{-1}. ^{1}H NMR ($CDCl_3$): δ_H 0.19 (s, 9H, $SiMe_3$), 1.26 (t, J_{HH} = 7 Hz, 3H, CH_3), 4.16 (q, J_{HH} = 7 Hz, 2H, CH_2). ^{13}C NMR ($CDCl_3$): δ_C -0.95 (s, $SiMe_3$), 13.9 (s, CH_3), 61.9 (s, CH_2), 93.6, 94.6 (s, C≡C), 153.0 (s, C=O). EI-MS (*m/z*): 229, $[M]^+$; 126.1, $[M\text{-}OEt]^+$; 98.0, $[M\text{-}SiMe_3]^+$.

5.4.4 Preparation of $Me_3SiC{\equiv}C(COH)(C{\equiv}CC_6H_4CH_3)_2$ [44]

1-(trimethylsilyl)-5-*p*-totyl-3-(2-*p*-tolylethynyl)penta-1,4-diyn-3-ol

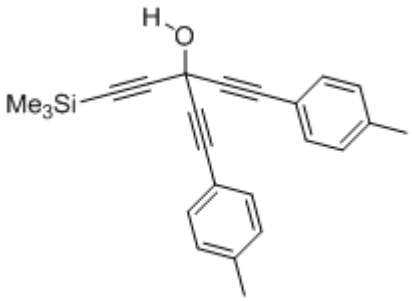

Ethyl 3-(trimethylsilyl)propiolate **43** (1 mL, 5.3 mmol) in THF (5mL) was added to a solution of lithium (*p*-tolylacetylide) [prepared by treating *p*-tolylacetylene (1.4 mL, 11 mmol) in THF (5 mL) at –78 °C with ^{n}BuLi (7 mL, of a 1.6 M solution in hexane, 11 mmol)] at –78 °C and stirred for 30 min. The solution was then warmed

to room temperature and became dark red in colour, which became dark brown on the addition of a sat. aqueous NH_4Cl (100 mL). The organic layer was separated and the aqueous layer was extracted with diethyl ether. The combined organic layers were dried over $MgSO_4$ and evaporated. The residue was purified by column chromatography (silica, CH_2Cl_2:Hexane 1:1), to afford **44** as an off-white powder (1.2 g, 64 %). IR (nujol): ν(C≡C-tolyl) 2228s, ν(C≡C-$SiMe_3$) 2190m, ν(O-H) 3512m, cm^{-1}. ^1H NMR ($CDCl_3$): δ_H 0.24 (s, 9H, $SiMe_3$), 2.36 (s, 6H, 2 p-CH_3), 2.99 (s, 1H, O-H), 7.14 (pseudo d, J_{HH} = 8 Hz, 4H, Ar C_6H_4), 7.41 (pseudo d, J_{HH} = 8 Hz, 4H, Ar C_6H_4). ^{13}C NMR ($CDCl_3$) δ_C -0.29 (s, $SiMe_3$), 21.6 (s, Me), 55.5 (s, C-OH), 83.2 (s, C≡*C*-tolyl), 86.0 (s, *C*≡C-tolyl), 88.2 (s, C≡*C*-$SiMe_3$), 101.8 (s *C*≡C-$SiMe_3$), 118.6 (s, C_i, tolyl), 129.1, 132.0 (2s, C_m , C_o, tolyl), 139.3 (s, C_p, tolyl). EI-MS (*m/z*): 356, $[M]^+$; 341.1, $[M\text{-}CH_3]^+$.

5.4.5 Preparation of $HC{\equiv}C(COH)(C{\equiv}CC_6H_4CH_3)_2$ [45]

1-*p*-tolyl-3-(2-*p*-tolylethynyl)penta-1,4-diyn-3-ol

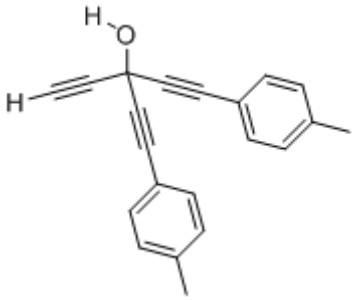

Desilylation of **44** (200 mg, 0.56 mmol) was carried out by treating a solution of **44** in MeOH (10 mL) with K_2CO_3 (940 mg, 6.8 mmol). After 1 h stirring, the organic phase was extracted using CH_2Cl_2 (3 x 10 mL). The combined organic layers were dried over $MgSO_4$ and evaporated, to afford an off-white solid (100 mg, 73 %). IR (CH_2Cl_2): ν(H-CC) 3294s, ν(C≡C-tolyl) 2224s, ν(C≡C-H) 2128m, ν(O-H) 3554m cm^{-1}. ^1H NMR ($CDCl_3$): δ_H 2.35 (s, 6H, 2 *p*-CH_3), 2.90 (s, 1H, O-H), 3.05 (s, 1H, H-C≡C), 7.14 (pseudo d, J_{HH} = 8Hz, 4H, AB C_6H_4), 7.41 (pseudo d, J_{HH} = 8Hz, 4H, AB C_6H_4). ^{13}C NMR ($CDCl_3$): δ_C 21.7 (s, Me), 55.1 (s, C-OH), 71.5 (s, C≡*C*H), 81.6 (s, *C*≡CH), 83.6 (s, C≡*C*-tolyl), 85.6 (s, *C*≡C-tolyl), 118.4 (s, C_i, tolyl), 129.2, 132.0 (2s, C_m , C_o, tolyl), 139.5 (s, C_p, tolyl). EI-MS (*m/z*): 308.9, $[M]^+$; 291.9 , $[M\text{-}OH]^+$; 218.0, $[M\text{-}C_6H_4CH_3]^+$

5.4.6 Preparation of $(Me_3CC{\equiv}C)_3COH$ [46]

5-(3,3-dimethyl-but-1-ynyl)-2,2,8,8-tetramethyl-nona-3,6-diyn-5-ol.

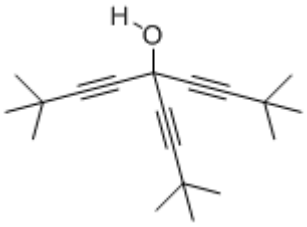

To 3,3-dimethyl-1-butyne (2.29 mL, 18.6 mmol) in THF (10 mL) at –78 °C, ^{n}BuLi (7.36 mL of a 2.5 M solution in hexane, 18.6 mmol) was added dropwise and the solution was allowed to stir (30 min) causing a colour change to pale yellow. Ethyl chloroformate was added dropwise (0.6 mL, 6.2 mmol) and the solution darkened in colour slightly. The reaction was allowed to warm to room temperature and left to stir (24 h). The reaction was quenched with (50 mL) of sat. aqueous NH_4Cl solution. The layers formed were separated, extracted with diethyl ether and the combined organic layers were dried with $MgSO_4$ and evaporated to give a pale yellow oil. The oil was recrystallised from hot hexane to give white crystals of **46** (0.74 g, 44 %). IR (nujol): ν(C≡C) 2246, ν(OH) 3560, cm^{-1}. ^{1}H NMR ($CDCl_3$): δ_H 1.2-1.3 (m, 27H, $(CMe_3)_3$), 2.6 (broad, OH). ^{13}C NMR ($CDCl_3$): δ_C 27.3 (s, $CMe_3)_3$), 30.5 (s, $CMe_3)_3$), 78.2, 90.6 (s, C≡C). ES(+)-MS (*m/z*): 272, $[M]^+$; 257, $[M\text{-}CH_3]^+$; 242, $[M\text{-}2Me]^+$; 227, [227, $[M\text{-}3Me]^+$; 215 $[M\text{-}CMe_3]^+$.

5.4.7 Preparation of $(PhC{\equiv}C)_3COH$ [47]

1,5-Diphenyl-3-phenylethynyl-penta-1,4-diyn-3-ol.

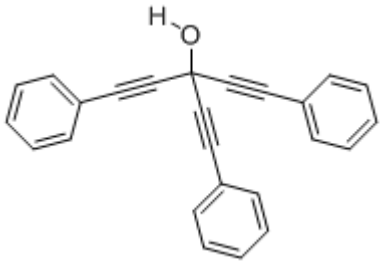

Method A

Ethyl chloroformate (0.59 mL, 6.17 mmol) in THF (5 mL) was added to a solution of PhC≡CLi [prepared from phenylacetylene (2.02 mL, 18.39 mmol) and ^{n}BuLi (7.37 mL, 2.5 M, 18.43 mmol) in dry THF (10 mL) at –78 °C] at –78 °C. The

solution was allowed to warm to room temperature and stirred for 18 h. The reaction was quenched with sat. aqueous NH_4Cl, the organic phase was separated and extracted with diethyl ether. The combined organic fractions were dried over $MgSO_4$ and evaporated to produce a red oil. This red oil was purified by chromatography (silica, CH_2Cl_2:hexane 1:1) and washed in hexane to afford creamy white powder (1.44 g, 70 %).

Method B

Potassium tert-butoxide (2.09 g, 18.6 mmol) was added to a Schlenk flask containing phenylacetylene (2.04 mL, 18.6 mmol) and ethyl chloroformate (0.6 mL, 6.2 mmol) in THF (20 mL) and then heated under reflux (3 h). After cooling, water (30 mL) and dichloromethane (30 mL) were added to the solution and separated. The organic phase was washed with water and the aqueous phase with dichloromethane. The organic fractions were combined, dried with $MgSO_4$ and evaporated to give a dark orange/brown oil. (3.6 g). The crude product was purified using column chromatography (silica, 1:1) (CH_2Cl_2:hexane) to give **5** as a pale yellow/white crystalline solid. Yield (0.97 g, 2.9 mmol, 47 %).

IR (CH_2Cl_2): ν(O-H) 3553s, ν(C≡C) 2228s cm^{-1}. ^{1}H-NMR ($CDCl_3$): δ_H 3.20 (s, 1H, OH), 7.36 (m, 3H, C_6H_5), 7.57 (dd, J_{HH} = 2 Hz, J_{HH} = 7 Hz, 2H, C_6H_5). ^{13}C-NMR ($CDCl_3$): δ_C 55.7 (s, C-OH), 83.1, 86.5 (2s, C≡C), 121.5 (s, C_i), 128.3 (s, $C_{o/m}$), 129.1 (s, C_p), 132.1 (s, $C_{o/m}$). EI-MS (*m/z*): 332, $[M]^+$; 315, $[M - OH]^+$; 255 $[M - C_6H_5]^+$; 230, $[M - H - C_6H_5C{\equiv}C]^+$; 178, $[M - 2\{C_6H_5\}]^+$.

5.4.8 Preparation of $Me_3SiC{\equiv}C(COH)(C{\equiv}C^tBu)_2$ [48]

2,2,8,8-tetramethyl-5-(2-(trimethylsilyl)ethynyl)nona-3,6-diyn-5-ol

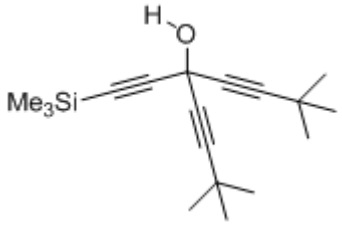

Ethyl 3-(trimethylsilyl)propiolate **43** (1 mL, 5.3 mmol) in THF (5 mL) was added to a solution of lithium (^{t}butylacetylide) [prepared by treating ^{t}butylacetylene (1.4 mL, 11.4 mmol) in THF (5 mL) at –78 °C with ^{n}BuLi (7.2 mL, of a 1.6 M solution in hexane, 11.5 mmol)] at –78 °C and stirred for 30 min. The solution was then warmed to room temperature and became dark red in colour, which became dark brown on the addition of a sat. aqueous NH_4Cl (100 mL). The organic layer was separated and the aqueous layer was extracted with diethyl ether. The combined organic layers were dried over $MgSO_4$ and evaporated, to afford a light brown waxy solid (1.15 g, 76 %). IR (CH_2Cl_2): ν(C≡C-^{t}Bu) 2241s, ν(C≡C-$SiMe_3$) 2167m, ν(O-H) 3554m cm^{-1}. ^{1}H NMR ($CDCl_3$): δ_H 0.18 (s, 9H, $SiMe_3$), 1.23 (s, 18H, 2 ^{t}Bu CH_3), 2.78 (s, 1H, O-H). ^{13}C NMR ($CDCl_3$): δ_C -0.4 (s, $SiMe_3$), 27.5 (s, *C*-Me_3), 30.5 (s, Me_3), 54.8 (s, C-OH), 86.6 (s, C≡*C*-$SiMe_3$), 91.4 (s C≡*C*-^{t}Bu), 101.7 (s *C*≡C-$SiMe_3$) 103.4 (s, *C*≡C-^{t}Bu). EI-MS (*m/z*): 288.2, $[M]^+$; 271.2 $[M\text{-}OH]^+$; 259.2 $[M\text{-}2Me]^+$; 229.1 $[M\text{-}4Me]^+$; 215.2, $[M\text{-}SiMe_3]^+$.

5.4.9 Preparation of $\{Fe(C_5H_5)\}(C_5H_4)C{\equiv}C(C{=}O)OEt$ [49]

Ethyl (Ferrocenyl)-propynoate.

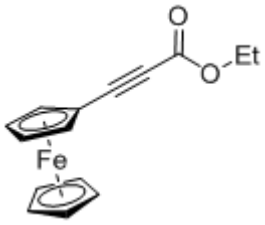

Ethyl chloroformate (0.10 mL, 1.05 mmol) in THF (5 mL) was added to a solution of FcC≡CLi [prepared from ethynylferrocene (220 mg, 1.05 mmol) and ^{n}BuLi (0.45 mL, 2.5 M, 1.05 mmol) in THF (10 mL) at –78 °C] at –78 °C. After stirring (30

min) at –78 °C sat. aqueous NH_4Cl solution (100 mL) was added and the organic phase separated and extracted with diethyl ether. Combined organic layers were dried over magnesium sulfate and evaporated. The residue was purified by preparative TLC, (silica plate, CH_2Cl_2:Hexane 60:40) to afford **49** as an orange-red solid (0.05 g, 16 %). R_f = 0.6 (CH_2Cl_2:hexane 60:40). IR (Nujol): ν(C=O) 1712w, 1691w, ν(C≡C), 2209w, 2249w cm^{-1}. ^1H NMR ($CDCl_3$): δ_H 1.36 (t, J_{HH} = 7 Hz, 3H CH_3), 4.27 (s, 5H C_5H_5), 4.28 (q, J_{HH} = 7 Hz, 2H CH_2), 4.34 (t, J_{HH} = 2 Hz, 2H C_5H_4), 4.60 (t, J_{HH} = 2 Hz, 2H C_5H_4). ^{13}C NMR ($CDCl_3$): δ_C 14.1 (s, CH_3), 61.8, (s, CH_2), 72.9 (s, C_5H_4, CH), 70.3 (s, C_5H_4, C_i), 70.3 (s, C_5H_4, CH), 70.3 (s, C_5H_4, C_5H_5), 78.1, 88.5 (2 × s, C≡C), 154.2 (s, CO_2Et). EI-MS (*m/z*): 282, M^+; 254, $[M - C_2H_4]^+$; 237, $[M - CO_2 - H]^+$; 210, $[M - C_2H_4 - CO_2]^+$.

5.4.10 Preparation of ({Fe(C_5H_5)}(C_5H_4)C≡C)$_3$COH [50]

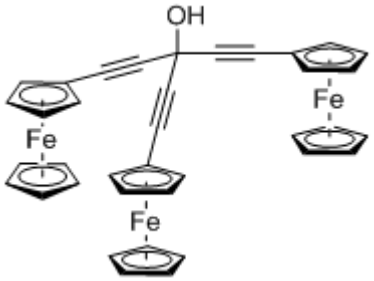

Method A

49 (0.062 g, 0.22 mmol) in THF (2 mL) was added to a solution of FcC≡CLi [prepared from ethynyl ferrocene (0.093 g, 0.44 mmol) and ^{n}BuLi (0.21 mL of a 2.5M solution in hexane, 0.53 mmol) in THF (2 mL) at –78 °C] at –78 °C. The solution was stirred at –78 °C for 35 min and then allowed to warm to room temperature and stirred for a further 90 min and then evaporated. The residue was washed successively (repeatedly) with hexane to afford **50** as an orange solid (0.126 g, 87 %).

Method B

To ethynylferrocene (0.210 g, 1.00 mmol) in THF (10 mL), at –78 °C, ^{n}BuLi (0.625 mL of a 1.6 M solution in hexane, 1.00 mmol) was added dropwise and the solution was allowed to stir (30 min) while warming to room temperature. To this ethyl chloroformate (0.034 g, 3.33 x 10^{-4} mol) in THF (5 mL) was added and stirred overnight at room temperature. The solvent was removed under reduced pressure and the crude product was dissolved in dichloromethane and washed twice with water. The solvent was removed and the dark brown solid was washed with hexane to yield the product. Yield (0.120 g, 0.183 mmol, 55 %). IR (Nujol): ν(C≡C) 2233s, 3566w cm^{-1}. ^{1}H NMR ($CDCl_3$): δ_H 2.92 (s, 1H OH), 4.24 (dd, J_{HH} 1.6 Hz, 6H, C_5H_5), 4.29 (m, 15H, C_5H_5), 4.54 (dd, J_{HH} = 1.6 Hz, 6H, C_5H_4). ^{13}C NMR ($CDCl_3$): δ_C 63.3 (s, C_5H_4), 69.0, (s, C_5H_4), 70.0 (s, C_5H_5), 71.7 (s, C_5H_4), 82.0 (s, C≡C), 83.7 (s, C≡C). EI-MS (*m/z*): 656 $[M]^+$; 446, $[M – FcC{\equiv}CH]^+$;

5.4.11 Preparation of $Me_3SiC{\equiv}C(COH)(C_6H_4I)_2$ [51]

1,1-bis(4-iodophenl)-3-(trimethylsilyl)prop-2-yn-1-ol

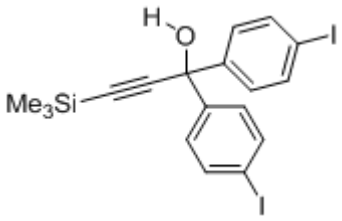

Ethyl 3-(trimethylsilyl)propiolate **43** (1 mL, 5.3 mmol) in THF (5 mL) was added to a solution [prepared by treating 1,4-diiodobenzene (3.5 g, 10.6 mmol) in diethyl ether (100 mL) at -78 °C with ^{t}BuLi (11.8 mL, of a 1.8 M solution in hexane, 21.2 mmol)] at –78 °C and stirred for 30 min. The solution was then warmed to room temperature and became pale yellow in colour, which became yellow on the addition of a sat. aqueous NH_4Cl (100 mL). The organic layer was separated and the aqueous layer was extracted with CH_2Cl_2. The combined organic layers were dried over $MgSO_4$ and evaporated, to afford a white semi-crystalline solid, (2.5 g, 90 %). Crystals were grown from CH_2Cl_2/Hexane. IR (CH_2Cl_2): ν(C≡C-$SiMe_3$) 2167m cm^{-1}. ^{1}H NMR ($CDCl_3$): δ_H 0.22 (s, 1H, $SiMe_3$), 2.74 (s, 1H, O-H), 7.30 (d, J_{HH} = 8.8 Hz, 2H, Ar H_o), 7.65 (d, J_{HH} = 8.8 Hz, 2H, Ar H_m). ^{13}C ($CDCl_3$): δ_C 0.09 (s, 9H,

$SiMe_3$), 74.1 (s, C-OH), 93.2 (s, C≡*C*-$SiMe_3$), 93.9 (s, C_p-I), 106.6 (s, *C*≡C-$SiMe_3$), 128.0 (s, C_o), 137.6 (s, C_m), 144.3 (s, C_i). EI-MS (*m/z*): 532.9, $[M]^+$; 459.9, $[M\text{-}SiMe_3]^+$; 406.0, $[M\text{-}I]^+$; 323.9, $[M\text{-}C_6H_4I]^+$;

5.4.12 Preparation of HC≡C(COH)(C_6H_4I)$_2$ [52]

1,1-bis(4-iodophenl)prop-2-yn-1-ol

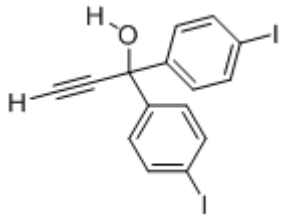

Desilylation of **51** (550 mg, 1.03 mmol) was carried out by treating a solution of **51** in MeOH (10 mL) with K_2CO_3 (570 mg, 4.1 mmol). After 1 h stirring, the organic phase was extracted using CH_2Cl_2 (3 x 10 mL). The combined organic layers were dried over $MgSO_4$ and evaporated, to afford an off-white solid (328 mg, 69 %). Crystals were grown from CH_2Cl_2/Hexane. IR (CH_2Cl_2): ν(C≡CH) 2120m cm^{-1}. ^1H NMR ($CDCl_3$): δ_H 3.06 (s, 1H, O-H), 3.46 (s, 1H, C≡C*H*), 7.31 (d, J_{HH} = 8 Hz, 2H, Ar H_o), 7.66 (d, J_{HH} = 8 Hz, 2H, Ar H_m). ^{13}C NMR ($CDCl_3$): δ_C 73.7 (s, C(OH)), 76.5 (s, C≡*C*H), 85.4 (s, *C*≡CH), 94.1 (s, C_p-I), 128.0 (s, C_o), 137.6 (s, C_m), 143.9 (s, C_i). EI-MS (*m/z*): 459.7, $[M]^+$; 332.8, $[M\text{-}I]^+$; 255.8, $[M\text{-}C_6H_4I]^+$; 205.9, $[M\text{-}2I]^+$

5.4.13 Preparation of Ru(C=C=C(C_6H_4I-4)$_2$)(PPh_3)$_2$Cp]PF_6 [58]

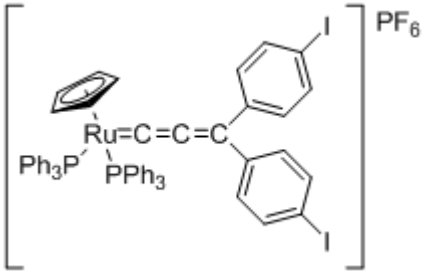

$RuCl(PPh_3)_2Cp$ (300 mg, 0.41 mmol) HC≡C(COH)(C_6H_4I)$_2$ **52** (203 mg, 0.44 mmol) and NH_4PF_6 (70 mg, 0.43 mmol) was stirred in MeOH (30 mL) for 2 h. The resulting purple solution was filtered and the solvent removed. The residue was taken up in the minimum of CH_2Cl_2 and precipitate into diethylether, and filtered,

yielding (265 mg, 60 %). IR (CH_2Cl_2): ν(C=C=C) 1926 cm^{-1}. ^1H NMR (400MHz): δ_H 5.12 (s, 5H, Cp), 7.00 (dd, 12H, $^3J_{HH}$ = 8 Hz, $^3J_{HP}$ = 2 H, H_o), 7.13 (t, 6H, $^3J_{HH}$ = 8Hz, H_m), 7.23 (pseudo d, 4H, Ar H), 7.34 (t, 6H, $^3J_{HH}$ = 8Hz, $H_{m'}$), 7.4-7.6 (m, 6H, H_p). ^{31}P NMR (161.9 MHz): δ 47.0 ^{13}C NMR (125.66 MHz): δ_C 94.3 (s, Cp), 100.1 (s, C_p-I), 142.8 (s, C_m-I), 155.5 (s, Ru=C=C=*C*), 214.6 (s, Ru=C=*C*), 294.3 (t, $^2J_{CP}$ = 17.6 Hz, Ru=*C*). ES(+)MS: 1132.8, $[M\text{-}PF_6]^+$; 1007.0, $[M\text{-}PF_6\text{-}I]^+$. ES(+)MS: 1132.8, $[M\text{-}PF_6]^+$; 1007.0, $[M\text{-}PF_6\text{-}I]^+$. Anal. Found: C 59.63; H, 3.73, Calc: C 59.31; H, 3.82

Chapter 6 : Aryl Amine Ligands and Metallated Complexes

6.1 Introduction

Triarylamines are remarkably stable organic one electron redox systems that have found use in a multitude of applications from hole-transport, [359] to photorefractive materials for optical data storage, [360] electrochromic polymers used in anti-glare mirrors, [361] and are commonly used as photoconductors in the Xerox® process in laser printers and photocopiers. [362, 363] Consequently there has been rapid development in the synthetic chemistry associated with the NAr_3 moiety. [364] With NAr_3 moieties readily available via synthetic protocols that are compatible with other functional groups, including acetylenes and vinyl groups, it is unsurprising that recent work has been undertaken that has hinted towards the possible use of NAr_3 systems as redox active bridging ligands. [98, 112, 325]

With a view to utilising approximately D_{3h} symmetric NAr_3 systems as a key component in a bridging ligand capable of linking more than two metal centres, we chose to examine complexes containing (phenylethynyl) amine ligands. Monometallic complexes derived from $HC{\equiv}CC_6H_4NTol_2$ have been used as models to help distinguish metal-ligand affects from genuine metal-metal interactions. It has been demonstrated in previous Chapters in this thesis and elsewhere, [87, 88, 115, 365] that ruthenium mixes strongly with the ethynyl bridge, resulting in bridge-centred redox properties. With iron, the metal orbitals are highly lying in energy, and consequently iron acetylide complexes feature more metal character in the redox orbitals than analogous ruthenium systems. [227, 233, 366] Therefore, in order to engineer systems more likely to display "true" mixed valence character, iron complexes were especially targeted in the work described in this Chapter.

Despite the vast body of metal acetylide chemistry, there are surprisingly few examples of transition metal complexes derived from mono-metallated mono-ethynyl aryl amines, in the literature; two organotin (tributyl and trimethyl), capped ethynylphenyl[bis(methoxyphenyl)]amines are also known. [367] Onitsuka has

synthesised two Ru(dppe)$_2$-ethynylphenyl bisphenylamines, **59** and **60** capped with either Cl or phenylacetylene (Chart **13**) from *cis*-RuCl$_2$(dppe)$_2$ using the chemistry summarised in Chapter **2**. [98]

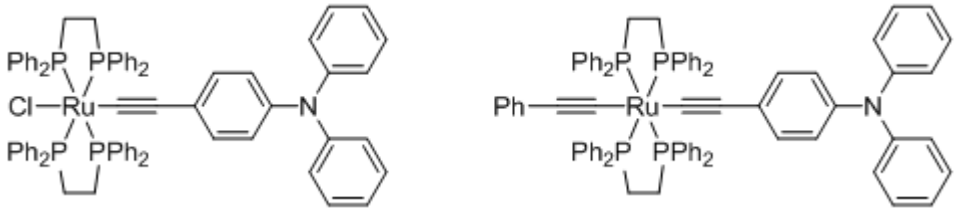

Chart **13** Ru(dppe)$_2$ ethynylphenyl bisphenylamine complexes **59** and **60**. [98]

The cyclic voltammogram of complex **59** showed two quasi-reversible waves at $E_{1/2}$ = –0.03 V and 0.48 V. The UV-vis spectra of **59** and **60** both contain an MLCT band at 349 nm, with compound **60** chosen for further study. Upon oxidation of **60** to [**60**]$^+$, the absorption band at 349 nm disappeared with a new band at 456 nm associated with [**60**]$^+$ being observed. With successive reduction and oxidation, the spectra are more or less reversibly obtained, but with a gradual decrease in the peak intensities indicating slow decomposition of the sample. The assignment of LMCT or MLCT character to the 456 nm transition in [**60**]$^+$ obviously depends on the correct assignment of the site of oxidation within [**60**]$^+$. The UV-vis spectrum of the dicationic species [**60**]$^{2+}$ was not investigated, nor were IR spectroelectrochemical studies carried out to confirm the site of oxidation. Thus, whilst the Onitsuka study clearly demonstrates that metal complexes of triaryl amines have potentially useful redox character, the system remains to be fully explored. The related tris ruthenium complexes are discussed later on in this section. [98]

One of the complexes in the class of luminescent gold(III) alkynyl complexes Vivian Yam and Hoi-Sing Kwok have recently investigated, and which demonstrate both electroluminescence properties and the ability to act as an emitter or dopant in organic light emitting diodes (OLEDs), is based on the organic ligand ethynylphenyl-diphenylamine **61**. Synthesis of **62** was achieved by reaction of Au(2,6-diphenylpyridine)Cl ([Au(CNC)]Cl) with **61**, in the presence of a catalytic

amount of copper(I) iodide in triethylamine and dichloromethane (Scheme **36**). It has been demonstrated that the incorporation of a strong σ-donating alkynyl ligand (such as ethynylaniline) onto the [Au(CNC)] moiety enriches the photoluminescence properties of gold acetylide complexes. [368] In solid-state thin films **62** displays a low-energy structureless emission band at about 570 nm, which has been assigned to the dimeric/oligomeric or excimeric emission arising from the π-π stacking of the planar CNC supporting ligand observed in the crystal packing. Utilising this photoluminescence (PL) property, organic light emitting diodes have been constructed using complex **62** as: a) the emitter layer, with the device producing an electroluminescence (EL) spectrum the same as the PL spectrum for **62**; and b) the dopant, into a host material of 4,4'-N,N'-dicarbozole-biphenyl (CBP), where, with varying the dopant level from 1 to 100 wt%, upon applying a voltage the EL maxima red-shifted from 500 to 580 nm. This red-shift has been attributed to a higher order and better packing of the molecules, and strong π-stacking of the CNC ligand, as the dopant concentration increases. [369]

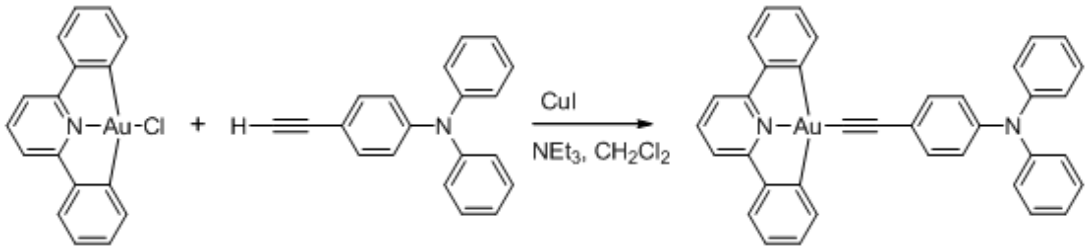

Scheme **36** Synthesis of **62**, from [Au(CNC)]Cl and **61** .[368]

The final example of a mono-metallic complex based on an ethynylphenyldiaryl amine known to date is the Pt-bridged bis-ethynylphenyldi(methoxyphenyl)amine **63**. This L–M–L complex was synthesis by reacting the terminal ethynyl ligand with *trans*-$PtCl_2(PEt_3)_2$, in $HNEt_2$ (Chart **14**). This complex has been used to assess the effect Pt has on the electronic delocalisation throughout the molecule. Crystallographic studies on the neutral species confirm that the two amine ligands are arranged *trans*- across a square planar Pt centre. The electronic spectrum **63** featured two strong transitions at 373 and 307 nm, and the luminescence spectrum showed a weak band at 405 nm assigned to $S_1 \rightarrow S_0$ relaxation and an intense $T_1 \rightarrow S_0$ transition at 494 nm. TDDFT calculations on the excited state of **63** revealed

that the T_1 and S_1 state originate from orbitals, delocalised over the molecule, with mixed triarylamine and ethynyl character. The MV species afforded by oxidation of **63** by $(p\text{-BrPh})_4NHSbF_6$ displays an IVCT band in the NIR region at 6450 cm^{-1}, along with peaks around 10000 - 15000 cm^{-1}, which have been assigned to Pt → N^+ charge transfer and triarylaminium excitation. Analysis of the IVCT band at 6450 cm^{-1} showed that the band to be broader than Hush model [27] predicts (4240 cm^{-1}), consistent with the MV species belonging to Class II (H_{ab} = 350 cm^{-1}) in the Robin-Day classification system. [25] The conclusions of this comparative study of Pt-bridged triarylamine and an all-organic structural analogue reported by Lambert, [370] is that electronic delocalisation in Pt-alkynyl π-conjugated systems is not substantially different when compared to all-organic oligo(phenylethynylenes). [371]

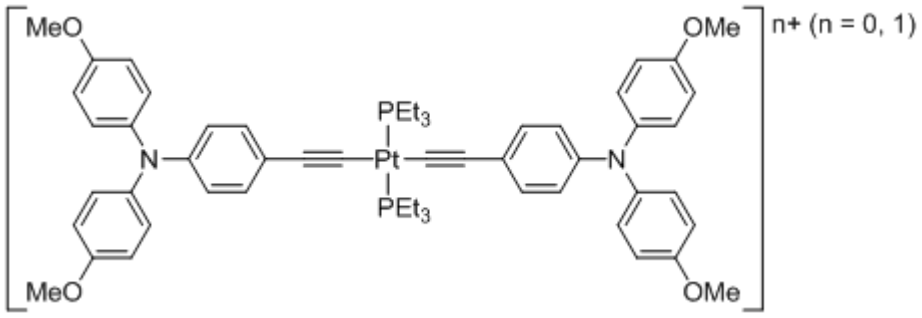

Chart **14** Platinum bridged bis-ethynylphenyldi(methoxyphenyl)amine **63**. [371]

Previous metallation reactions of the tris-ethynylphenyl amine ligand have centred mainly on the use of the *cis*-$RuCl_2(dppe)_2$ building block, to form the tris(*trans*-$RuCl(dppe)_2C{\equiv}CC_6H_4)_3N$ **64**, which can be reacted with HC≡CPh to give to the tris (ruthenium bis(acetylide)) complex **65** (Scheme **37**). [98]

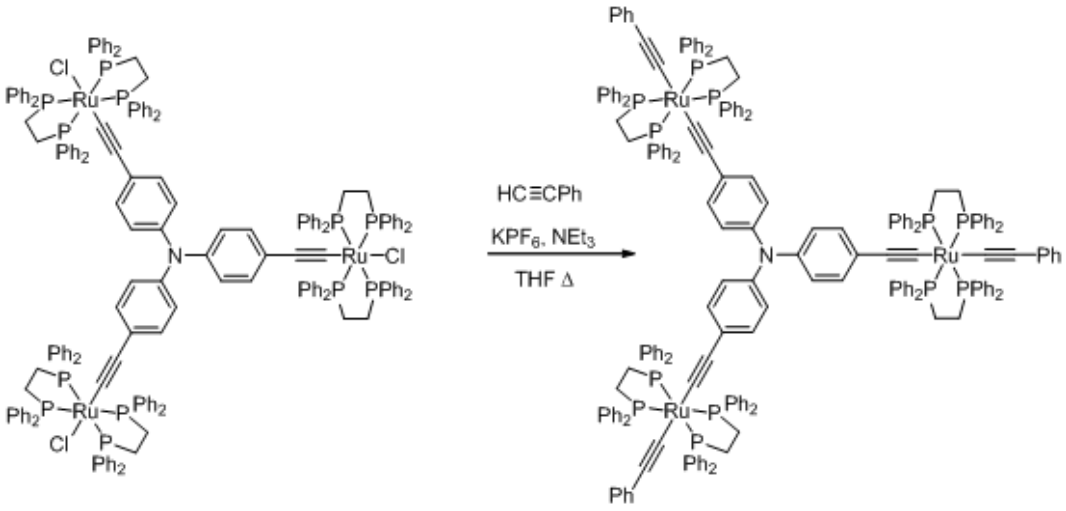

Scheme **37** Synthetic route from **64** to **65**. [98]

Electrochemical studies of **64** and **65** showed each complex exhibits four quasi-reversible waves, $E_{1/2}$ = -0.17, 0.11, 0.29 and 0.60 V **64**, and $E_{1/2}$ = -0.17, 0.10, 0.23 and 0.51 V **65** against Ag/AgCl reference. The first three redox events have been assigned to the stepwise Ru(II)-Ru(III) oxidation processes in each case, with the fourth wave assigned to the oxidation on the triphenylamine core, (c.f. the trimethylsilylated ligand precursor $E_{1/2}$ = 0.77 V). This cathodic shift of the stepped Ru(II)-Ru(III) oxidation events compared to the Ru(II)-Ru(III) couples in **59** ($E_{1/2}$ = -0.03 and 0.48 V), has been attributed to the strong electron-donating properties of the Ru(II) moieties with the separation of the waves taken as evidence for electronic interactions between the metal centres through the tri(*p*-ethynylphenyl)amine bridge.

NIR studies of [**65**]PF_6, obtained by chemical oxidation of **65**, showed a broad absorption at 4760 cm^{-1}, in a region where no absorptions were detected for the neutral species **65**. This absorption band was attributed to an IVCT process, with the calculated half-width ($\Delta\nu_{1/2}$) close to that of Class II mixed valence compounds. [25, 27] The authors have deduced that the structure of [**65**]$^+$ consists of one ruthenium allenylidene unit stabilised by the central nitrogen atom: the various valence forms can interconvert wither through thermal / ground state or photochemical (IVCT) processes (Scheme **38**). [98]

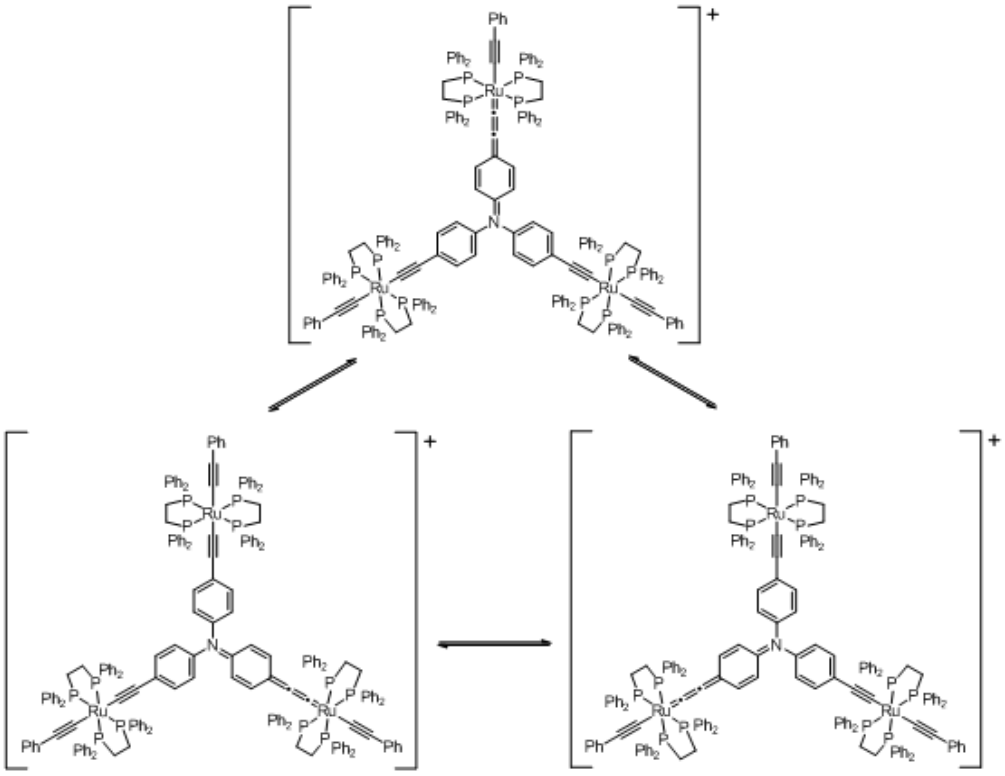

Scheme **38** Proposed IVCT processes in [**65**]$^{+}$. [98]

The failure of this incomplete body of work to fully take into account all possible interpretations of the available data, particularly the assignment of IVCT character to the NIR band and the assumption of metal centred redox character, means that the conclusions in this paper must be treated with a degree of caution. A more comprehensive study of this group of complexes is needed to provide greater confidence in the conclusions drawn from the results. [325]

Apart from the tris-trimethylstannyl capped triethynylphenyl amine complex, produced by first lithiating tris(4-ethynylphenyl)amine with ^{n}BuLi, and subsequent addition of trimethyltin chloride, which was used to prepare tris[4-(pyridin-4-ylethynyl)phenyl]amine (Chart **15**), [372] the only other metallated triethynylphenyl amine complexes synthesised have $Pt(PEt_3)_2$ fragments attached (Scheme **39**).

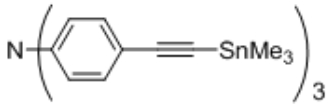

Chart **15** Tris((trimethylstannyl)-4-ethynylphenyl)amine. [372]

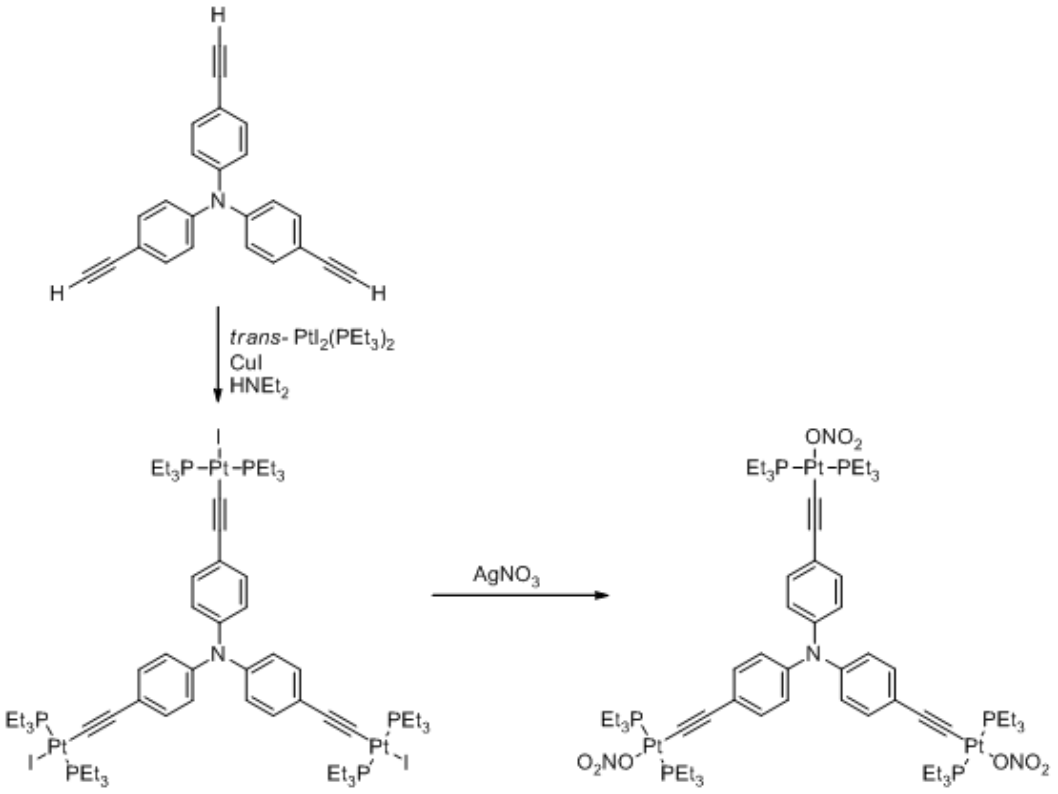

Scheme **39** Synthesis of **66** and **67**, from tris(*p*-ethynylphenyl)amine. [373]

Complex **67** has been used in an ingenious way to synthesis an organometallic version of bicyclo[2,2,2]octane, via a self-assembly reaction with three equivalents of a bidentate ligand, 1,3-bis(3-pyridyl)isophthalic amide, to two equivalents of the tris($Pt(PEt_3)_2ONO_2$) amine complex. [373]

As well as the directly coordinated tris metal complexes, mentioned above, ferrocene-based end groups have also been attached via a linker to the central triethynylphenyl amine core. The triferrocene triphenylamine complexes were synthesised by palladium catalysed cross-coupling reactions of ferrocenyl alkynes and 4,4',4''-triiodotriphenylamine (Scheme **40**). [374] These complexes are symmetric in nature in solution, for example in **68** there are three CH peaks at δ_H 4.21, 4.26 and 4.48 ppm; the first corresponding to the three unsubstituted Cp rings, the second two corresponding to the three alkyne substituted Cp rings. The pseudo-doublets seen in the *p*-substituted triphenylamines is also seen ~ δ_H 7 ppm. Electrochemical data of all of these complexes showed only one oxidation wave for the oxidation of ferrocene to the ferrocinium ion, possibly reflecting the absence of

electronic communication between the three ferrocene centres. [375, 376] The nature of the bridging has been proven crucial for efficient electronic communication between ferrocene centres, with benzene [376, 377] and ethynylbenzene [375] ferrocenyl derivatives not exhibiting any electronic communication, whereas with a cyclopropenium core, separate one electron oxidation steps were observed and ascribed to a strong interaction between the ferrocene centres. [378]

In this Chapter, a series of complexes derived from ethynyl derivatives of triaryl amines have been prepared, and studied using a combination of electrochemical, UV-vis-NIR and IR spectroelectrochemical methods, supported by computational investigations of electronic structure.

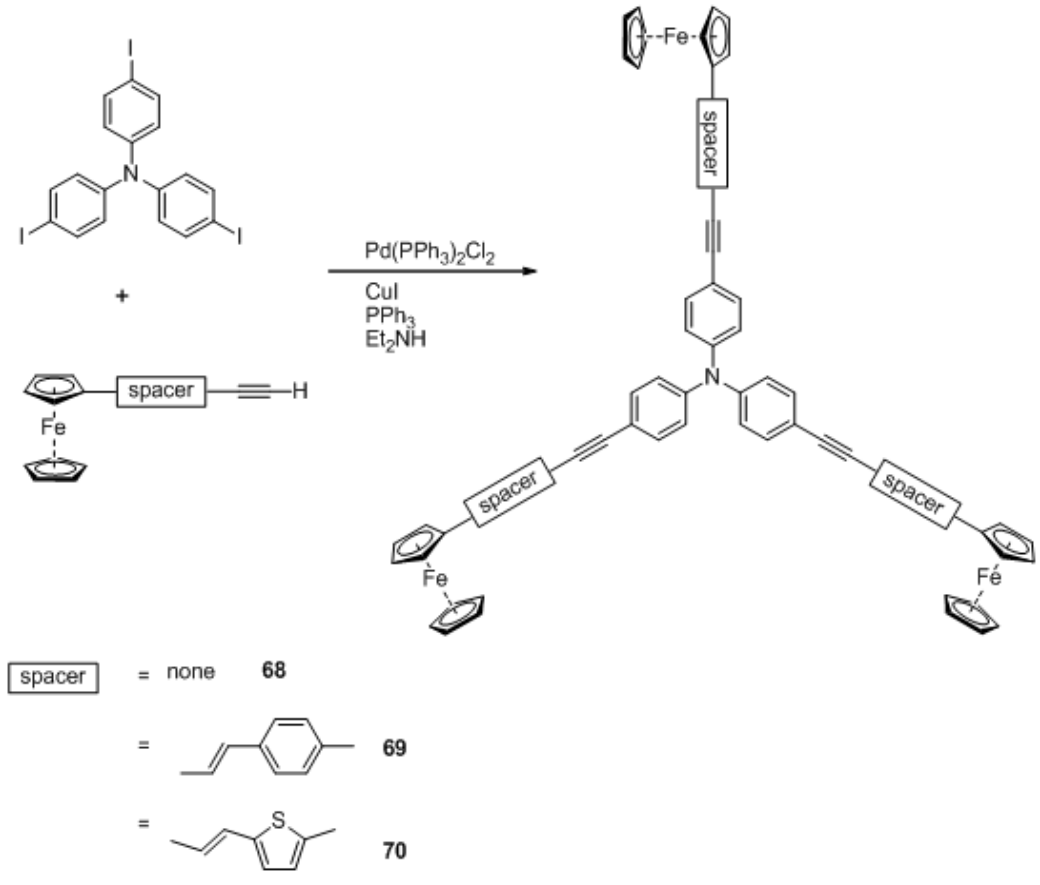

Scheme **40** Triferrocene triphenylamine complexes, **68**, **69** and **70**. [374]

6.2 Results and Discussion

The pro-ligands and precursors used in this Chapter are shown in Chart **16**.

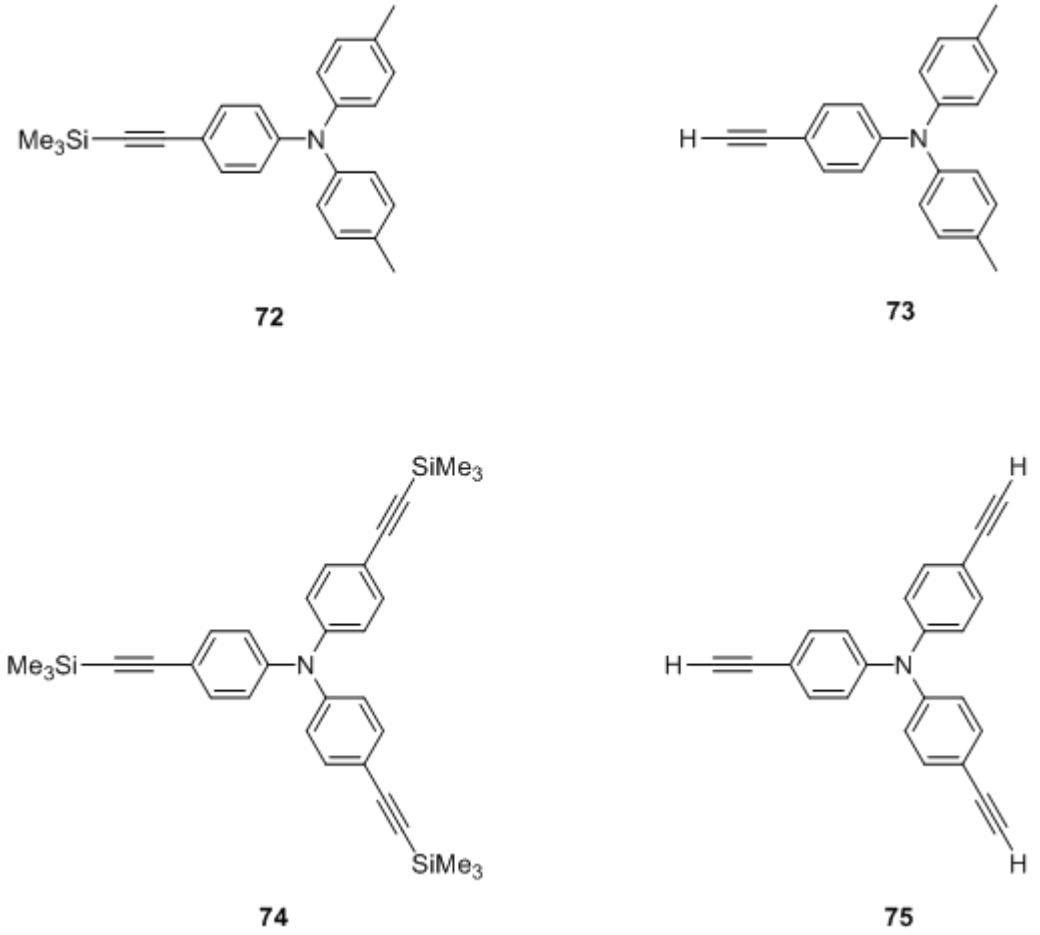

Chart **16** Pro-ligands used in this Chapter (**72** – **75**).

The decision to use ditolylamine over diphenylamine in the preparation of the amine ligands was taken to prevent any phenyl – phenyl coupling of the amine rings following oxidation (Scheme **41**). [379, 380]

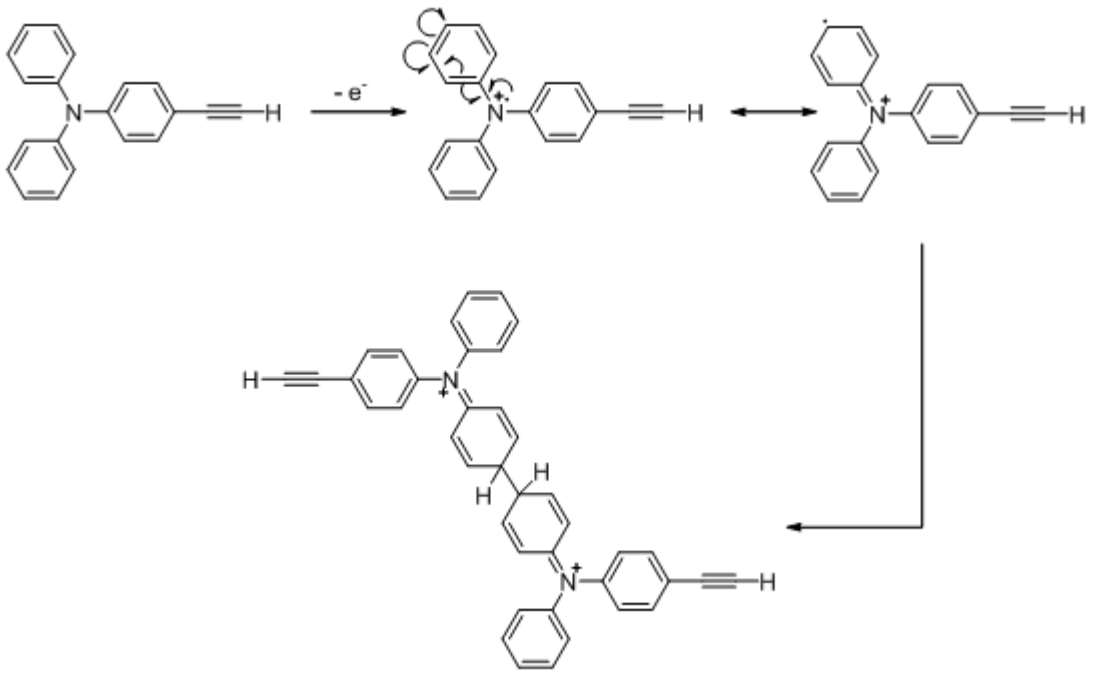

Scheme **41** Oxidative coupling of diphenyl ligands, based on the redox chemistry known for triphenylamine. [379, 380]

The synthesis of the mono-ethynyl compound HC≡C$C_6H_4NTol_2$ **73** is shown in Scheme **42**.

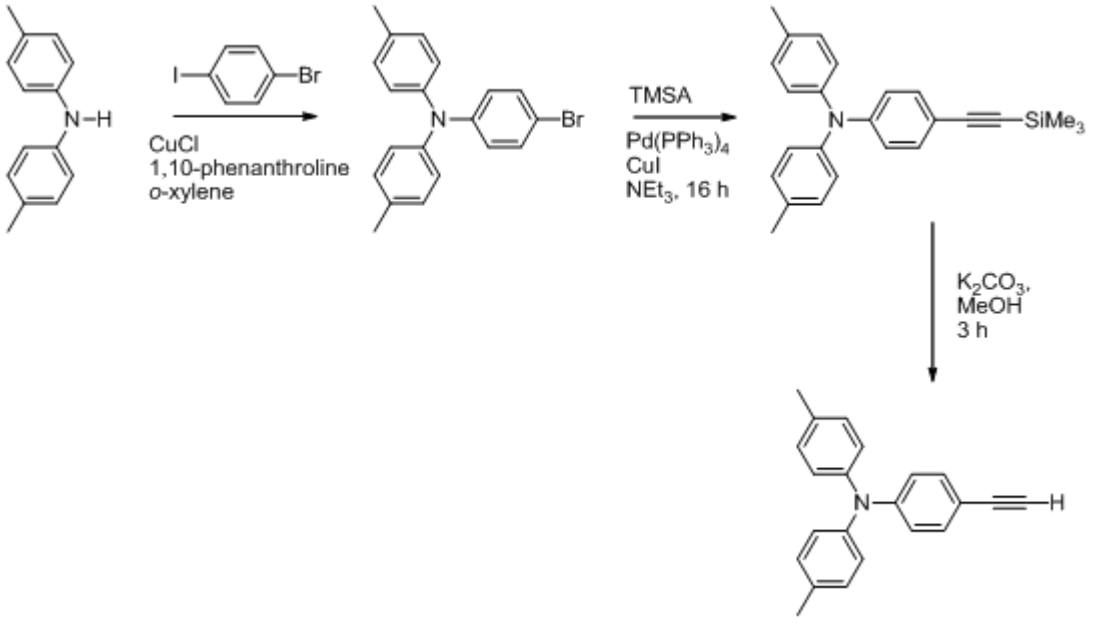

Scheme **42** The synthesis of HC≡C$C_6H_4NTol_2$ **73**.

The first step of the synthesis of **73** is an N-C bond forming reaction between 1-bromo-4-iodobenzene and ditolylamine (Scheme **42**). A N-C bond can be formed by many synthetic routes, with the Buchwald-Hartwig amination (Scheme **43**), in which an organic aryl halide is coupled to an amine in the presence of a base with the use of a palladium catalyst, being a modern method of choice. [364, 381-383] Along with a large variety of aryl halides, [364] the Buchwald-Hartwig protocol has been shown to work well with pseudohalides, such as triflates, [384] and both primary and secondary amines can be used to good effect in the cross-coupling reaction. [384, 385] The choice of Pd catalyst will depend on the requirements for the desired compound, for example chiral selectivity, and therefore a wide variety of Pd catalysts have been investigated. [364, 385] However, the Pd catalysts most commonly used with this reaction are $Pd(PPh_3)_4$, $PdCl_2(dppf)$ and $Pd_2(dba)_3$/phosphine.

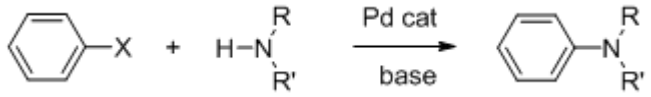

Scheme **43** The Buchwald-Hartwig N-C cross-coupling reaction.

If a Pd^{II} system is employed, the initial step in the reaction mechanism (Scheme **44**) is the reduction of the Pd^{II} catalyst (strictly a pre-catalyst), to an active Pd^0 species. The next step is the oxidative addition of the aryl halide to the Pd^0 catalyst, followed by the coordination of the amine through the nitrogen atom. The addition of a strong base abstracts the amine proton, which is followed by either reductive elimination to the desired aryl amine or the undesired β–hydride elimination to the arene and the imine. The β–hydride elimination can be prevented by selecting amine substituents that do not have β–hydride to eliminate, such as aryl rings and tertiary organic fragments, or the use of a bidentate chelating phosphine ligand on the palladium such as diphenylphosphinoferrocene (dppf).

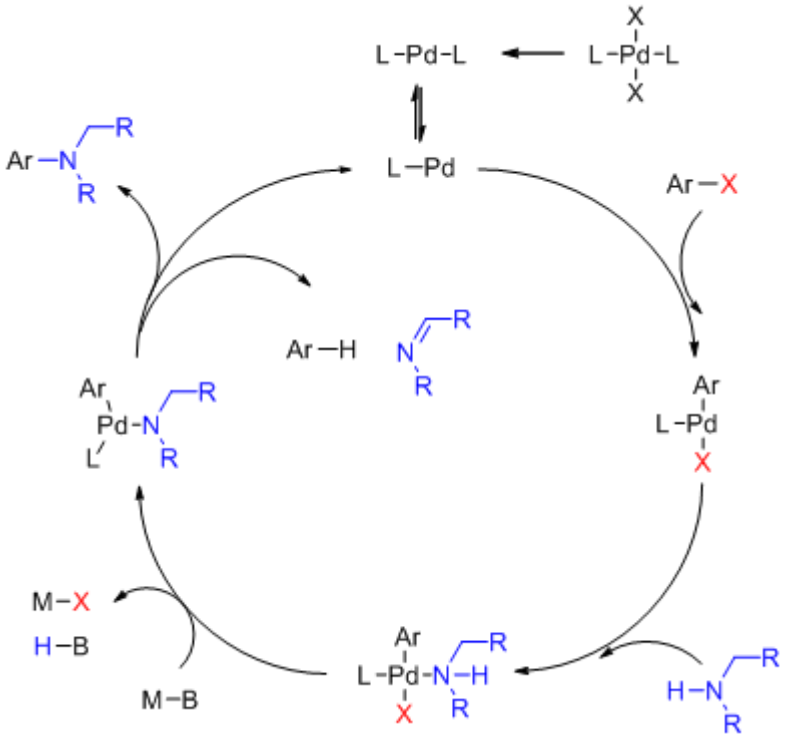

Scheme **44** The Buchwald-Hartwig reaction mechanism.

The use of a tertiary butoxide salt, e.g. NaO^{t}Bu, as the base in the Buchwald-Hartwig reaction can help to simplify the reaction work up, as the by-products of the deprotonation step are sodium chloride and ^{t}butanol.

The Ullmann-type reaction (Scheme **45**, Scheme **46**), another N-C bond forming reactions, is an older, but still valuable alternative to the Buchwald-Hartwig amination reaction, especially in the case of electron-rich aryl halides and aryl-iodides. [386]

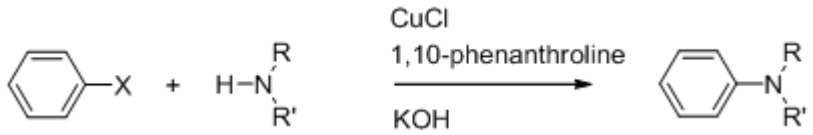

Scheme **45** The Ullmann-type coupling reaction route.

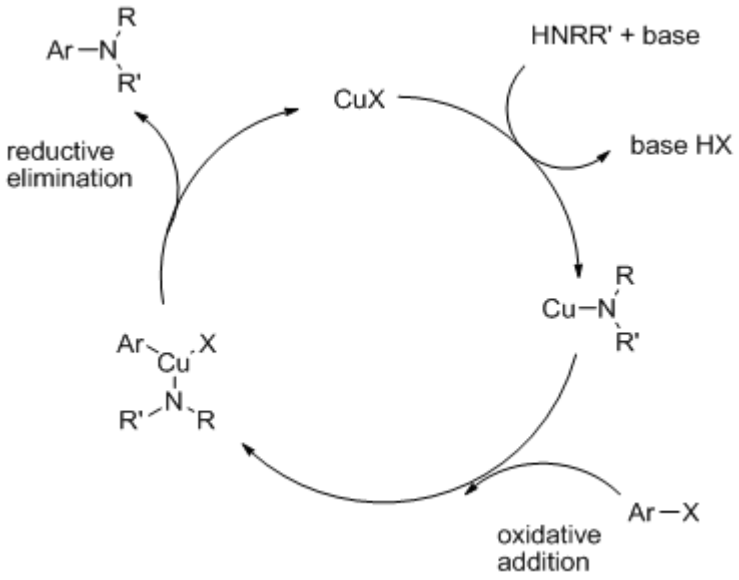

Scheme **46** The Ullmann-type reaction mechanism.

In this work, bromo-functionalised triaryl amines were prepared either by Ullmann-type coupling of 1-bromo-4-iodo-benzene with ditolylamine (Scheme **42**), or by bromination of triphenyl amine (see below). With bromo-functionalised triaryl amines in hand, ethynyl groups can be introduced through another cross-coupling sequence, this time directed towards C-C bond forming reactions, using the Sonogashira protocols (Scheme **47**). [387]

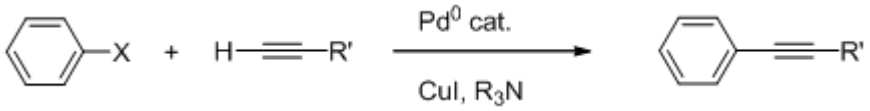

Scheme **47** The Sonogashira cross-coupling reaction.

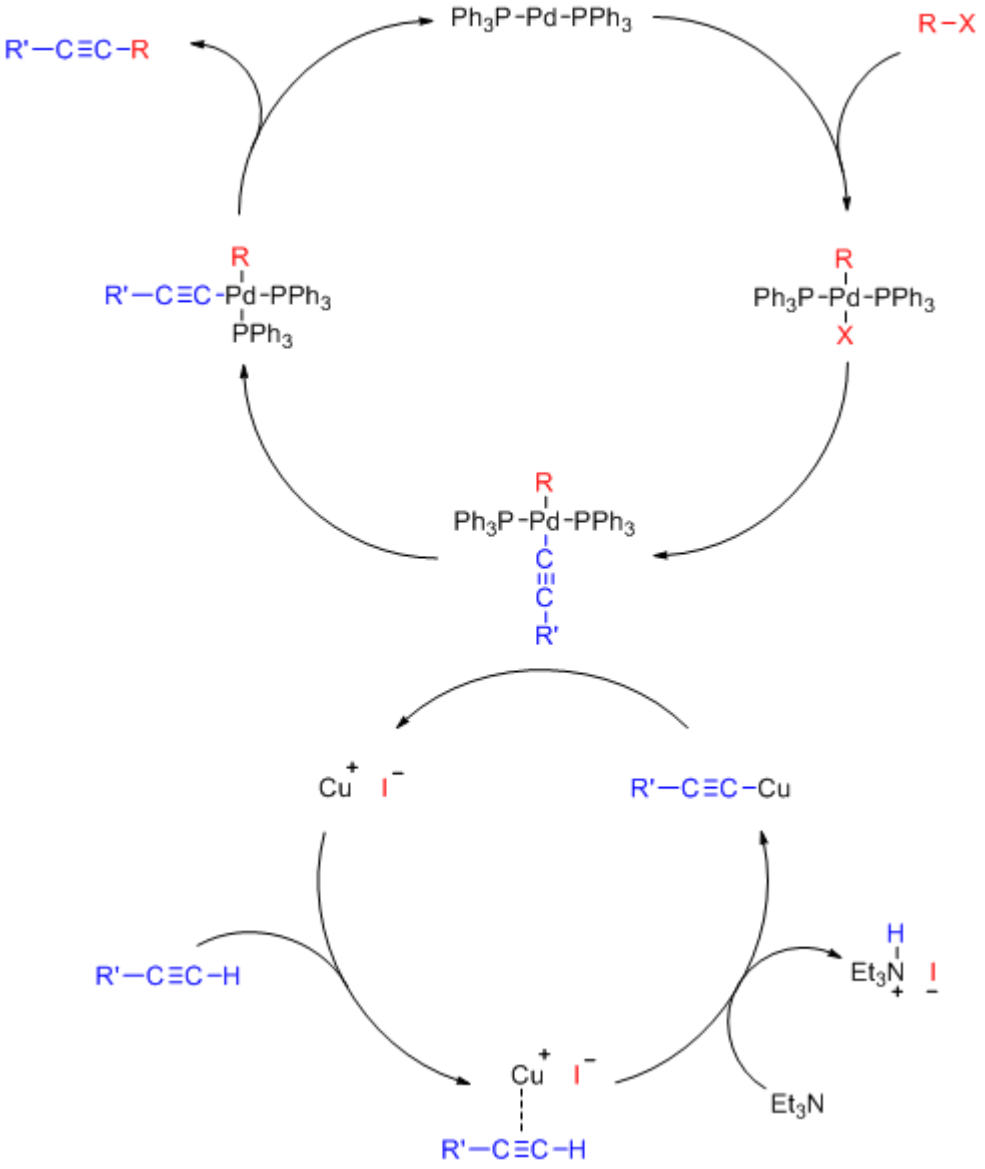

Scheme **48** The Sonogashira cross-coupling reaction mechanism.

On the most elementary level, the mechanism of the Sonogashira cross coupling reaction involves two cycles (Scheme **48**), one around palladium and another around copper. The initial step in the palladium cycle involves oxidative addition of an aryl halide to an active $14e^-$ palladium species Pd^0L_2 to form a Pd^{II} complex. The resulting $16e^-$ complex reacts in a rate limiting transmetallation step with the copper acetylide, produced in the copper cycle; to give the *trans*- square planar palladium acetylide, and expelling a copper halide in the process. *Trans-cis* isomerisation of the palladium acetylide is followed by a reductive elimination step which releases the final product and regenerates the Pd^0 catalyst. In the copper cycle, the copper

halide generates a copper acetylide, which reacts with the $Pd^{II}L_2RI$ in the transmetallation step, regenerating the copper halide. The precise details of the Sonogashira reaction and the underlying mechanism (or mechanisms, as there may be different mechanisms taking place under different conditions), have been thoroughly described elsewhere. [387]

Since the work described later in this Chapter necessitate the use of terminal acetylenes, it is simply worth noting at this point that trimethylsilyl acetylene has been used widely as the alkyne coupling partner in the Sonogashira work. The terminal alkynes can then be readily obtained in the final step, using K_2CO_3 in MeOH as a source of nucelophilic MeO^- (Scheme **49**). The preparation of tris(4-ethynylphenyl)amine is similar (Scheme **50**).

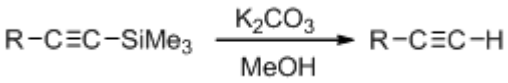

Scheme **49** Desilylation of a trimethylsilyl protected acetylene using potassium carbonate in methanol.

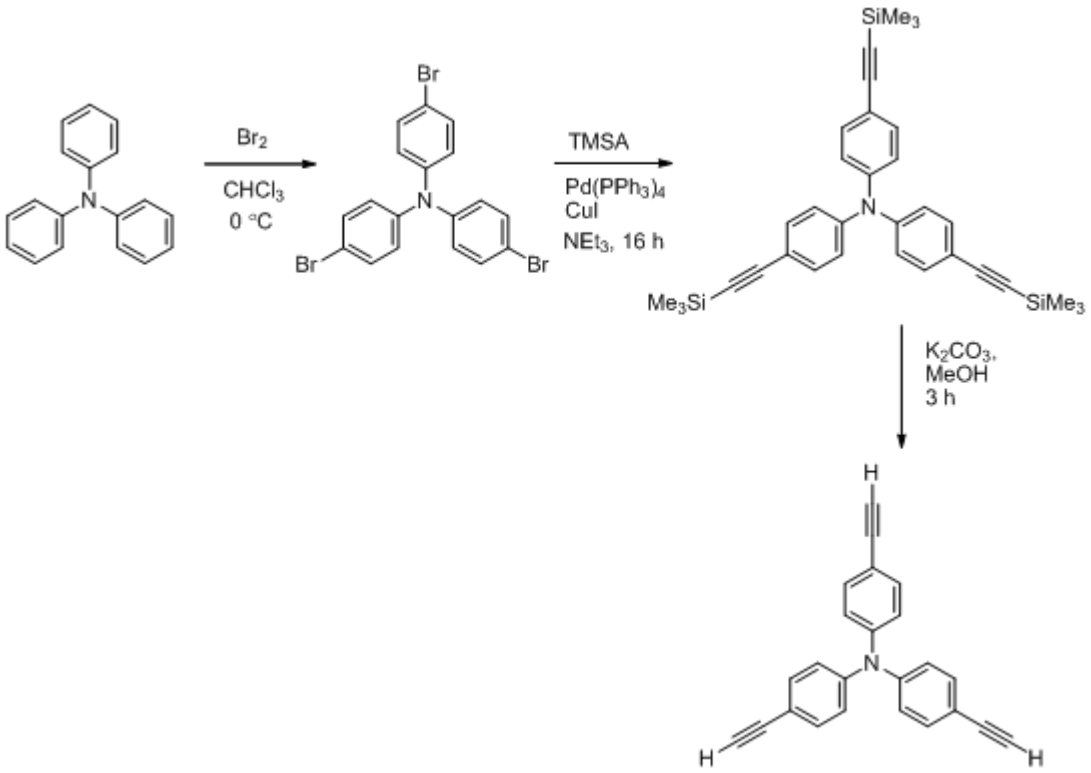

Scheme **50** Synthesis of tris(4-ethynylphenyl)amine **75**.

The amine substituent is both *ortho*- and *para*- directing to aryl halogenations, however, due to steric hindrance and the low temperature conditions employed in the bromination reaction, only the tris *para*-substituted compound is obtained (Scheme **51**).

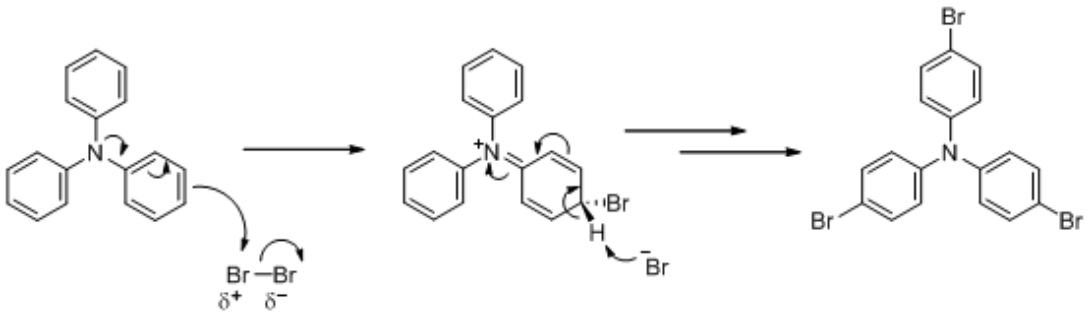

Scheme **51** Aryl halogenation of triphenylamine.

Three mono-metallic complexes were synthesised from the terminal alkyne **73** (Chart **17**): $Ru(C{\equiv}CC_6H_4NTol_2)(PPh_3)_2Cp$ (**76**); $Ru(C{\equiv}CC_6H_4NTol_2)(dppe)Cp^*$ (**77**); $Fe(C{\equiv}CC_6H_4NTol_2)(dppe)Cp$ (**78**).

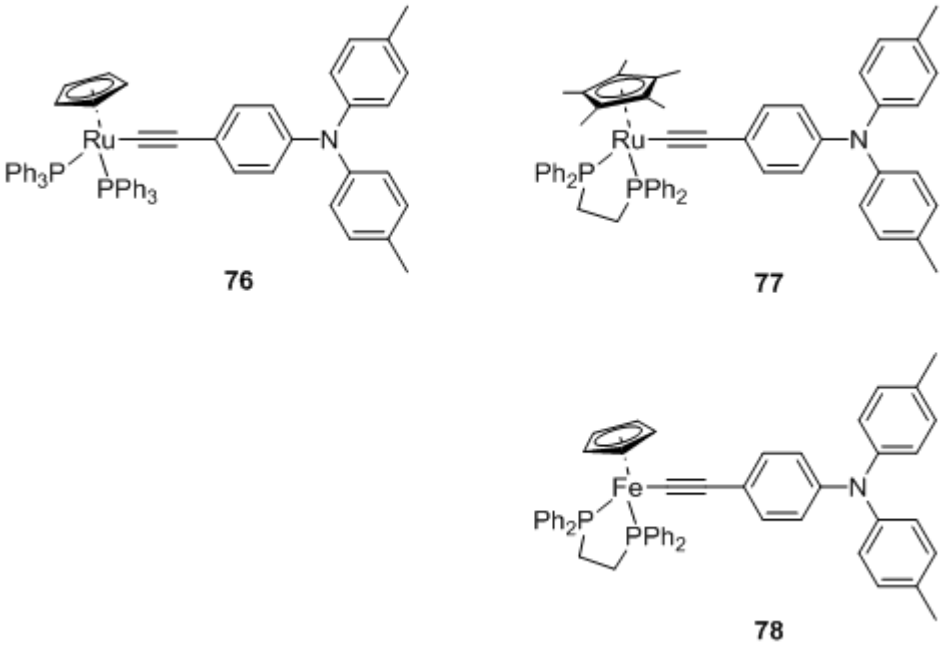

Chart **17** The mono-metallic complexes **76**, **77** and **78** synthesised in this Chapter.

The ruthenium complexes are prepared from $RuCl(PPh_3)_2Cp$ (for **76**) or $RuCl(dppe)Cp^*$ (for **77**), a slight excess of the alkyne **73**, and NH_4PF_6, in refluxing methanol. The resulting vinylidenes were not isolated, but rather deprotonated by addition of a suitable base (NaOMe) to give the acetylide complexes (Scheme **52**). The synthesis of **78** is essentially the same as the two ruthenium complexes, with the use of an '*in situ*' base for convenience (Scheme **53**), using established protocols. [388]

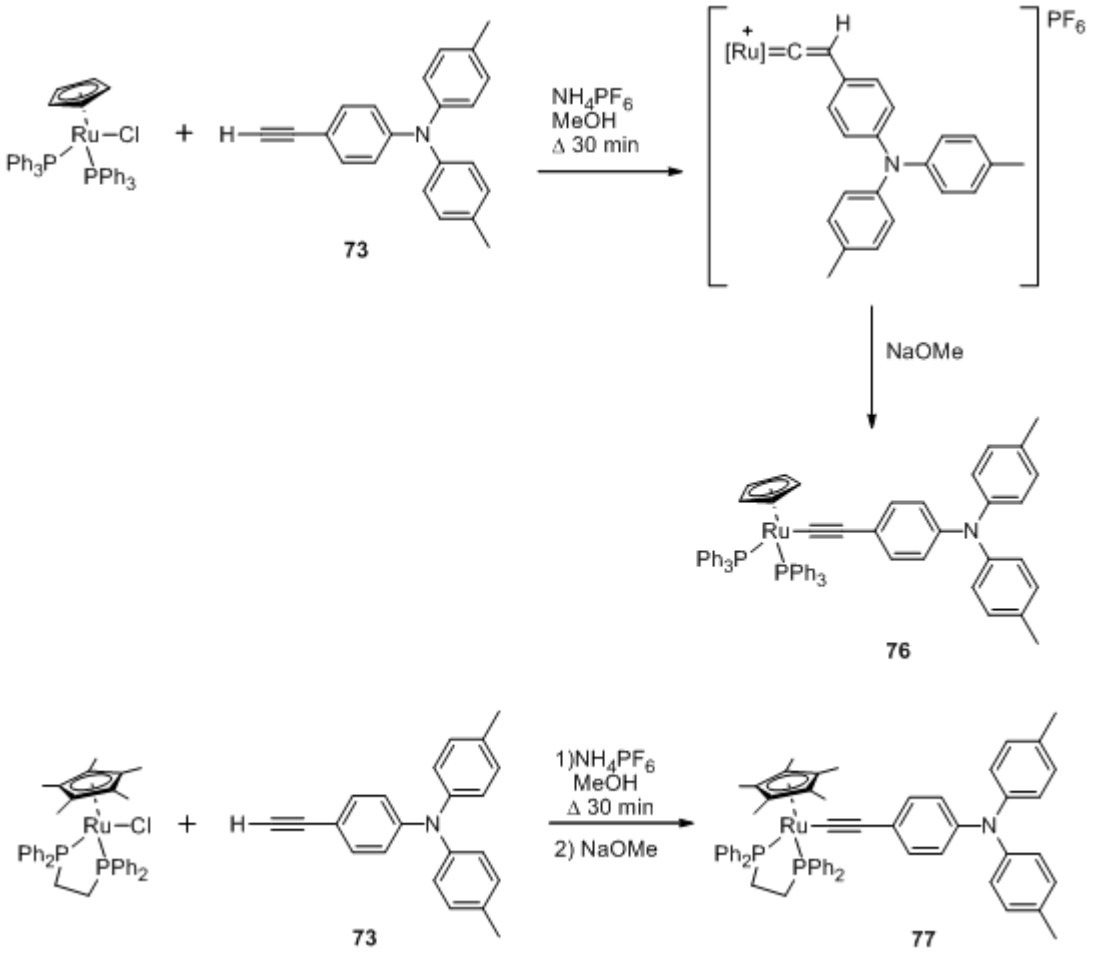

Scheme **52** Synthetic route for compounds **76** and **77** via the vinylidene complex.

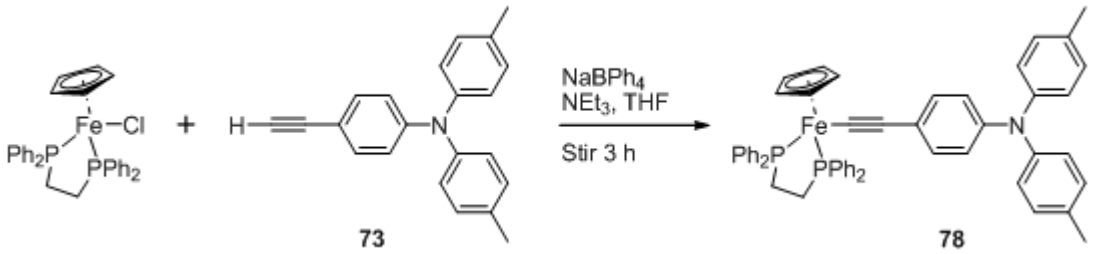

Scheme **53** Synthesis of **78**, with the use of an 'in situ' base.

The ^{31}P NMR spectra of all three mono-metallic complexes **76** – **78** gave a single peak corresponding to the supporting phosphine ligands, at δ_P 51.4 (PPh_3), 82.0 (dppe) and 108.2 (dppe) ppm, for **76**, **77** and **78** respectively, and a single Cp or Cp* ligand resonance in both the ^{1}H and ^{13}C NMR spectra in the usual regions (Cp_{Ru}: δ_H = 4.3 ppm; Cp^*_{Ru}: δ_H = 1.57 ppm; δ_C = 10.0 ppm ($C_5\mathit{Me}_5$) and 92.6 ppm (C_5Me_5); Cp_{Fe}: δ_H = 4.23 ppm; δ_C = 79.1 ppm). The characteristic set of two pseudo doublets

of the ligand aryl system, one with an integral of 4H, the other 8H, is also observed in the ^{1}H NMR spectra of all three complexes, in the range δ_H 6.2 – 7.2 ppm. The ES(+)-MS of the complexes **76** – **78** all feature the molecular ion (*m*/*z* 988.1 **76**, *m*/*z* 930.3 **77**, *m*/*z* 814.2 **78**). The IR spectra of the mono-metallic complexes exhibit ν(C≡C) bands at 2074 cm^{-1} **76**, 2069 cm^{-1} **77** or 2062 cm^{-1} **78**, somewhat lower in energy than that of the precursor alkyne **73** (2120 cm^{-1}).

The synthesis of **79** is similar to that described for **78**, with a slight excess of the metal chloride used to ensure complete metallation, in a 1:1 solution of triethylamine and THF (Scheme **54**). A small amount of KO^{t}Bu was also added to the final reaction mixture to make sure all of the vinylidene intermediate was deprotonated to the required metal acetylide complex.

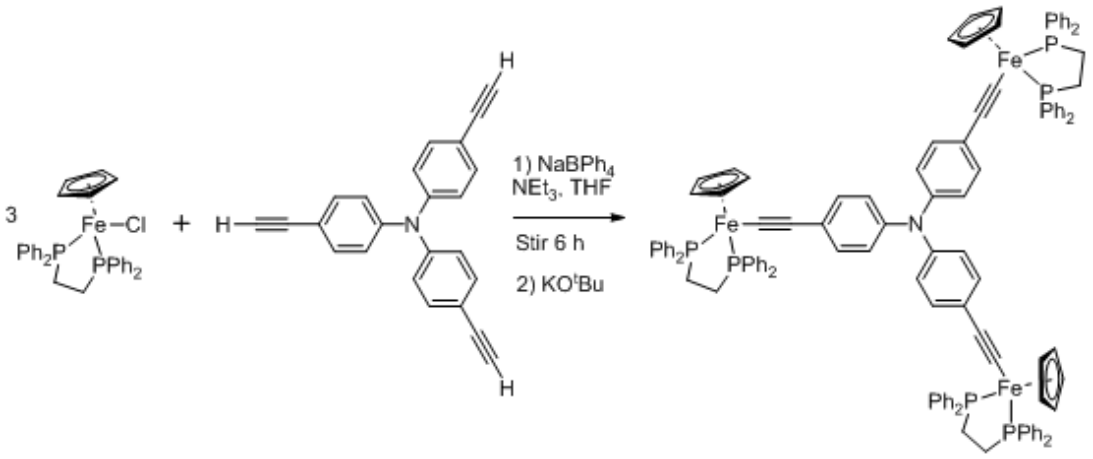

Scheme **54** Synthesis of **79** from FeCl(dppe)Cp and **75**.

The ^{31}P NMR spectrum of **79** gave a singlet at δ_P 108.4 ppm (dppe), and a singlet Cp ligand resonance in both the ^{1}H and ^{13}C NMR spectra was found (Cp_{Fe}: δ_H = 4.30 ppm; δ_C = 79.0 ppm); these are unsurprisingly very similar to mono-iron complex **78**. The ES(+)-MS (electrospray positive - mass spectrometry) of the complex **79** featured the molecular ion; (*m*/*z* 1872.0), along with the fragment ions at *m/z*; 1354.0, [M-[Fe]]$^{+}$, 835.3, [M-2[Fe]]$^{+}$, 677.7, [M-[Fe]]$^{2+}$, ([Fe] = Fe(dppe)Cp). The IR spectrum of the tris-metallic complex exhibits a ν(C≡C) band at 2062 cm^{-1} (c.f. ν(C≡C) **78** 2062 cm^{-1}, **73** 2120 cm^{-1}).

6.2.1 Molecular Structure Analyses of $Me_3SiC{\equiv}CC_6H_4NTol_2$ and $HC{\equiv}CC_6H_4NTol_2$

Single crystals of **72** and **73** suitable for X-ray diffraction were obtained from hexane, and the molecular structures determined by single crystal X-ray diffraction (Figure **84** and Figure **85**). Crystallographic data, selected bond lengths and angles are listed in Table **55** and Table **56**.

Crystals of **72** crystallised in the monoclinic space group (P 1 2_1/c 1) with four molecules of in the asymmetric unit, whilst **73** crystallised in the orthorhombic space group (Pna2_1) with four molecules in the asymmetric unit cell. The Si(1)-C(1)-C(2)-C(3) chain is essentially linear, in both the protected and deprotected ligands, with any slight bending due to the crystal packing forces. The N centre in both **72** and **73** is approximately trigonal planar, with the tolyl groups pushed back slightly causing the C(9)-N(1)-C(16) angle to decrease from the ideal trigonal planar geometry (120 °) to 117.13(10) ° and 117.64(12) ° for **72** and **73** respectively. To be perfectly sp^2 hybridised, the angles between the three N-C bonds should be 120 °, however, as can be seen in Table **56**, even though all three Aryl-N-Aryl bond angles sum to 360 °, there is some deviation from the perfect sp^2 arrangement. The planar nature of the N centre in triphenylamines is in contrast to the pyramidal nature associated with alkyl amines, and can be attributed to a degree of delocalisation between the nitrogen centre and the aryl rings, and steric constraints.

Due to the same steric constraints around the sp^2 hybridised nitrogen the three aromatic rings have to twist out of the plane. [389, 390] As both **72** and **73** can be considered as triaryl amines of general form $NAr(Ar')_2$, instead of having the same or equivalent pitch for each of the aromatic rings, two angles are observed, one corresponding to the Ar substituent and another set of pitches for the two Ar' substituents, which are the same or equivalent. [Pitch being the angle between the plane of the respective aromatic ring and the C(6)-C(9)-C(16) plane; Figure **83**]. This is the case with the TMS protected alkyne **72**, where the pitch for the aromatic ring with the alkyne moiety attached to it is ~22 °, and the pitch for the two tolyl rings are 50 ° and 51 °. In the deprotected form **73**, the acetylene substituted aromatic ring has a pitch of 25 °. However the two tolyl rings in **73** are not

equivalent (N(1)-C(16) bond length 1.4198(19) Å vs N(1)-C(9) 1.4341(19) Å), and the pitch of the two rings are 41 ° and 50 ° respectively. This increase in pitch is brought about by the increased packing in the solid state, and hence elongation of the N(1)-C(9) bond follows as the bond has more single bond character with less N(p)-aryl(π*) overlap.

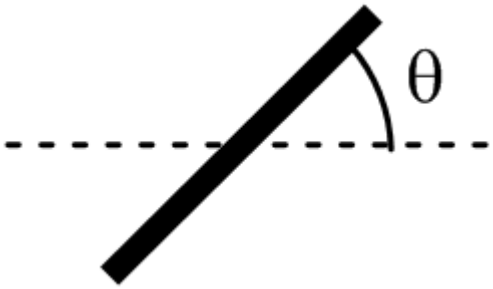

Figure **83** Schematic diagram of the angle between the plane of the phenyl ring (bold black line) and the plane of the three *ipso* C atoms [C(6)-C(9)-C(16)].

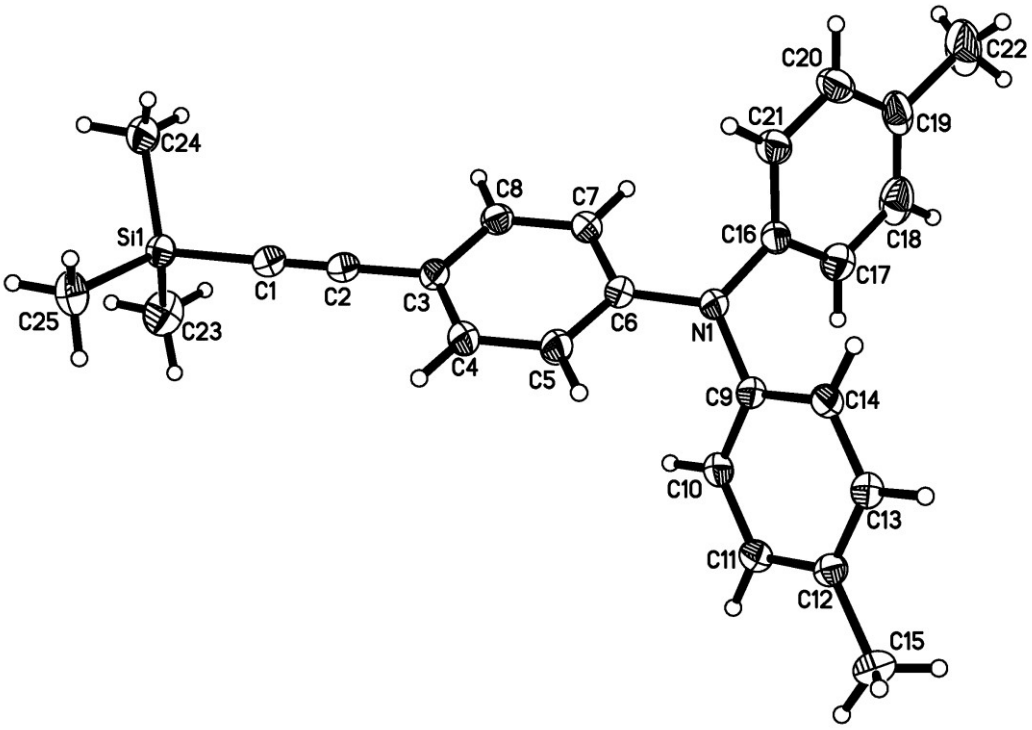

Figure **84** The molecular structure of the trimethylsilylated ligand **72**.

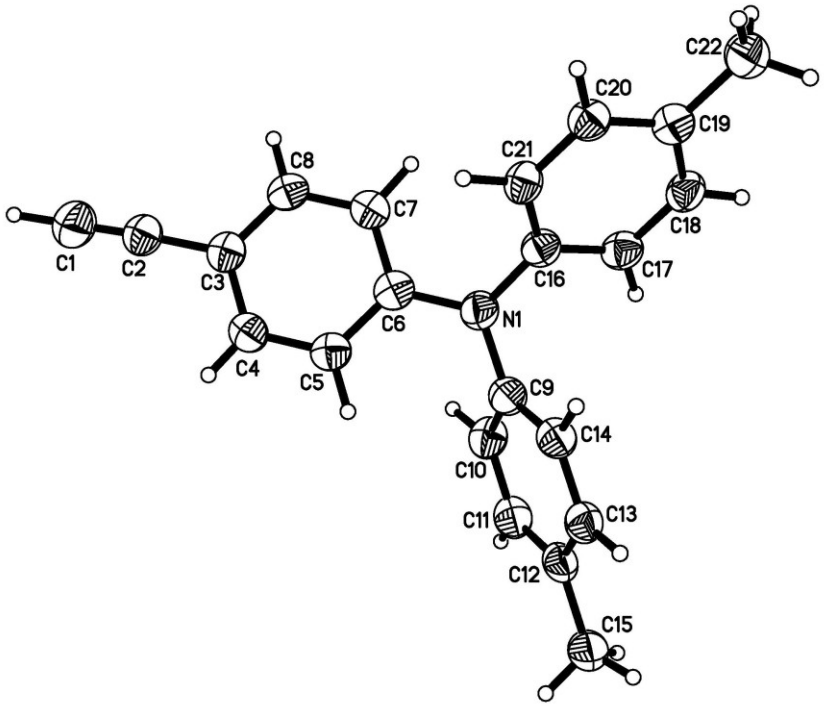

Figure **85** The molecular structure of the terminal alkyne ligand **73**.

Table **55** Crystal data and experimental parameters of aryl amine ligands **72** and **73**, with crystal data of NPh_3.

	72	**73**	NPh_3[391]
Empirical Formula	$C_{25}H_{27}NSi$	$C_{22}H_{19}N$	$C_{18}H_{15}N$
Formula Weight	369.57	297.39	245.2
Temperature (K)	120(2)	110(2)	297
Crystal System	Monoclinic	Orthorhombic	Monoclinic
Space Group	P 1 2_1/c 1	$Pna2_1$	Bb
a (Å)	12.3975(2)	10.1931(3)	15.655(5)
b (Å)	16.3669(3)	16.2072(5)	22.257(7)
c (Å)	10.8092(2)	10.3679(3)	15.807(5)
α (°)	90.00	90.003(3)	90.00
β (°)	98.325(10)	90.014(3)	90.00
γ (°)	90.00	89.997(3)	91.04(2)
Volume ($Å^3$)	2170.17(7)	1712.79(9)	5507(3)
Z	4	4	16
ρ_{calc} (mg/mm^3)	1.131	1.153	1.18
Abs Coeff (mm^{-1})	0.117	0.505	0.64
F (000)	792	632	2080
Crystal Size	0.32 × 0.25 × 0.22	0.4 × 0.3 × 0.08	0.32 × 0.39 × 0.50
θ Range for Data Collection	1.66 – 29.50 °	5.03 – 59.95 °	20 – 30 °
Index Ranges	$-17 \leq h \leq 17$, $-22 \leq k \leq 22$, $-14 \leq l \leq 14$	$-11 \leq h \leq 11$, $-18 \leq k \leq 18$, $-11 \leq l \leq 10$	$-16 \leq h \leq 16$, $0 \leq k \leq 26$, $0 \leq l \leq 16$
Reflections Collected	29442	15035	3582
Independent Reflections	6040	2445	
Data / Parameters	6040/352	2445/284	
Goodness-Of-Fit on F^2	1.055	1.105	
Final R indexes [I>2σ>(I)]	R1 = 0.0419, wR2 = 0.1065	R1 = 0.0269, wR2 = 0.0732	
Final R indexes [all data]	R1 = 0.0685, wR2 = 0.1164	R1 = 0.0277, wR2 = 0.0738	
Largest Diff Peak/Hole	0.322/-0.223	0.117/-0.110	

The molecules of **72** and **73**, illustrated in Figure **84** and Figure **85** to show the atom labelling scheme. Selected bond lengths and angles are summarised in Table **56**.

Table **56** Selected bond lengths (Å) and angles (º) for NPh_3 , **72**, **73** and **78**.

	NPh_3 [391]	**72**	**73**	**78**
N(1) – C(6)	1.416(7)	1.4055(16)	1.405(2)	1.435(3)
N(1) – C(9)	1.418(7)	1.4294(16)	1.4341(19)	1.420(3)
N(1) – C(16)	1.423(6)	1.4312(16)	1.4198(19)	1.421(3)
C(1) – C(2)	-	1.2050(18)	1.175(2)	1.218(3)
C(1) – R	-	1.8372(13)	1.070	1.900(2)
C(6) – N(1) – C(9)	118.6(4),	120.60(11)	120.09(11)	119.32(17)
C(6) – N(1) – C(16)	120.0(4),	120.75(11)	122.17(11)	118.49(18)
C(9) – N(1) – C(16)	120.4(4)	117.13(10)	117.64(12)	121.83(18)
Sum of C-N-C	359.0(12)	358.48(32)	359.90(34)	359.64(53)
Pitch A	44 (mean)	22	25	46
Pitch B		50	50	30
Pitch C		50	41	32

6.2.2 Molecular Structure Analyses of $Fe(C{\equiv}CC_6H_4NTol_2)(dppe)Cp$ and $Ru(C{\equiv}CC_6H_4NTol_2)(dppe)Cp^*$

Complex **78** crystallises in the orthorhombic crystal system (space group P $2_12_12_1$), with four molecules in the asymmetric unit cell (Table **57**). Whereas the monoclinic and triclinic crystal systems are more prevalent for both neutral and cationic piano-stool σ-organoiron complexes [227, 392, 393], the orthorhombic crystal system has been obtained only a handful of times, in such complexes as [Fe(C≡CAnth-CN-4)(dppe)Cp*] [394] and $[Fe(C{\equiv}CPh)(dppe)Cp^*]^+$. [227] The structure of the iron acetylide complex illustrates the usual piano stool geometry around the Fe, of related iron acetylide complexes. On the whole, the bond distances and angles are typical for piano-stool σ-organoiron(II) complexes. [9] The bending of the

Fe–C(1)-C(2)-C(3) chain from linear (158 °) is due to crystal packing constraints and a number of C-H … π, interactions between the tolyl rings on the ligand and the diphenyl phosphine (dppe) and C-H … C-H interactions between tolyl rings of neighbouring complex molecules. This bending masks the straightening effect on the C(1)-C(2)-C(3) axis by electron donating substituents, previously observed by Lapinte in similar iron acetylide complexes. [392] The phenyl ring is twisted, so that the phenyl plane is coplanar with one of the Fe-P bonds, which is typical of neutral complexes of the form Fe(C≡CR)(dppe)Cp*. [118, 393] The Fe-C(1) [1.900(2) Å], the C(1)-C(2) [1.218(3) Å] and C(2)-C(3) [1.442(3) Å] bond lengths in **78** (Table **58**) are comparable to other iron piano-stool complexes of the form Fe(C≡CC_6H_4R-4)(dppe)Cp*; ([Fe-C(1); 1.876(3) – 1.916(4) Å], [C(1) – C(2); 1.210(4) – 1.222(5) Å] and [C(2) – C(3); 1.419(4) – 1.440(5) Å]). [118, 392] The Fe-P bonds are a little shorter in **78** [2.1658(7), 2.1705(6) Å] compared with [2.1843(10), 2.1875(10) Å] that in **80** (Chart **18**) and other related Fe(dppe)Cp* acetylide complexes, [118, 392, 394] but this is more likely due to increased steric bulk of the Cp* ligand causing an elongation of the Fe-P bonds than any electronic influence. The Fe-$Cp_{centroid}$ in **78** is also shorter (1.710 Å) than in **80** [1.745 Å], this again is likely due to the differences in steric properties of the Cp and Cp* ligands than any underlying electronic effect.

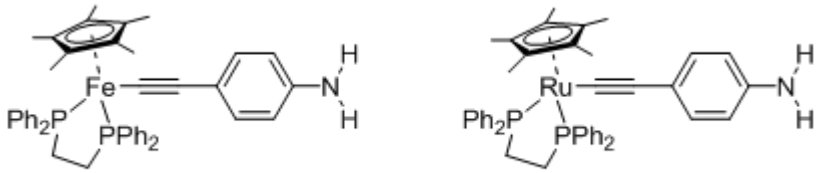

80 **81**

Chart **18** The crystallographically characterised complexes **80** and **81**, closely related to **77** and **78**.

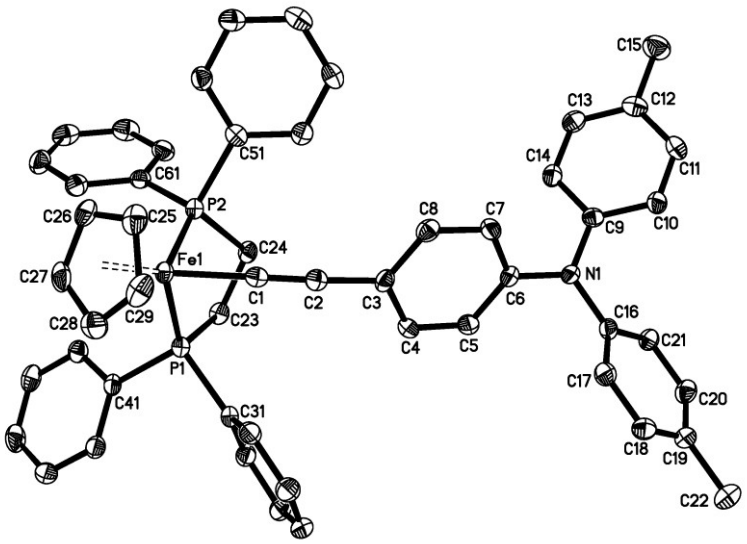

Figure **86** Plot of **78**. Hydrogen atoms have been omitted for clarity.

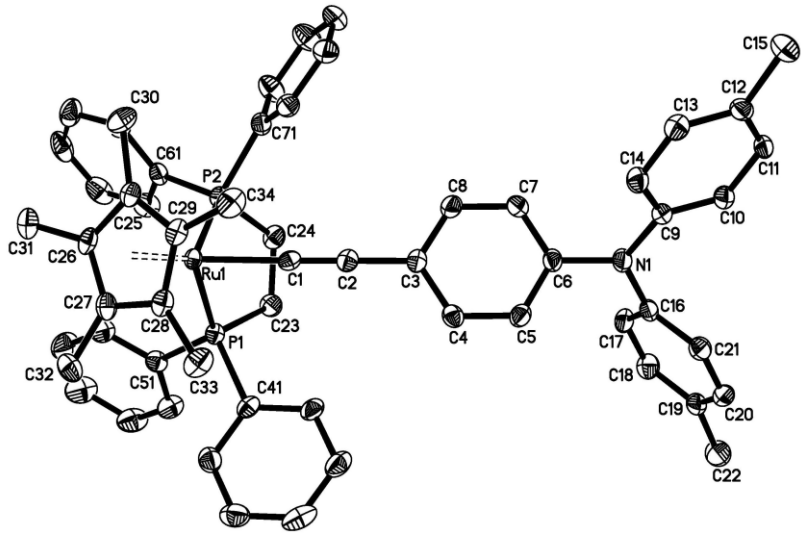

Figure **87** Plot of **77**. Hydrogen atoms have been omitted for clarity.

As with the ligands, the amine substituent part of the iron complex also has a propeller arrangment of the aromatic rings. The pitch of the phenyl ring attached to the metal fragment, to the C(6)-C(9)-C16) plane, has increased to 46 °, whereas the pitch of the two tolyl rings are 30 ° and 32 °. The C(6)-N(1) bond is comparable longer than in both the TMS protected- and deprotected- ligand (1.435(3) Å vs 1.4055(16) Å).

In comparison the N(1)-C(9) and N(1)-C(16) bond lengths in **72** and **78** are indistinguishable within the experimental error [N(1)-C(9) 1.4294(16) and 1.420(3) Å; N(1)-C(16) 1.4312(16) and 1.421(3) Å for **72** and **78** respectively]. The C(6)-N(1) bond distance, in **78** is slightly longer than usually observed for sp^2-hybridised amino substituents (1.435(3) Å vs 1.394 Å). [395]

Table **57** Crystal data and experimental parameters of **78** and **77**, with crystal data of related complexes **80** [118] and **81** [224].

	78	**80** [b]	**77**	**81**
Empirical Formula	$C_{53}H_{47}NP_2Fe$	$C_{44}H_{45}NP_2Fe$	$C_{58}H_{57}NP_2Ru$ 0.5 CH_2Cl_2	$C_{44}H_{45}NP_2Ru$
Formula Weight	815.71	705.60	973.52	750.82
Temperature (K)	120(2)	293(2)	120(2)	293(2)
Crystal System	Orthorhombic	Monoclinic	Monoclinic	Monoclinic
Space Group	P 2_1 2_1 2_1	$P2_1/c$	$P2_1/c$	$P2_1/c$
a (Å)	12.0416(5)	15.4172(4)	13.7897(6)	15.602(5)
b (Å)	16.2740(7)	11.0980(3)	33.1250(10)	11.132(5)
c (Å)	21.2001(9)	22.3218(7)	10.9205(4)	22.277(5)
α (°)	90.000(10)	90.00	90.00	90.00
β (°)	90.000(10)	107.535(1)	103.93(2)	108.800(5)
γ (°)	90.000(10)	90.00	90.00	90.00
Volume ($Å^3$)	4154.5(3)	3641.8(2)	4841.5(3)	3663(2)
Z	4	4	4	4
ρ_{calc} (mg/mm^3)	1.304	1.287	1.336	1.362
Abs Coeff (mm^{-1})	0.478	0.534	0.485	0.548
F (000)	1712	1488	2028	1560
Crystal Size	0.3 × 0.2 × 0.1	0.35 × 0.22 × 0.20	0.24 × 0.11 × 0.05	0.19 × 0.16 × 0.07
θ Range for Data Collection	1.92 – 29.50 °	2.00 – 27.53 °	2.02 – 28.50 °	2.65 – 27.54 °
Index Ranges	-16 ≤ h ≤ 16, -21 ≤ k ≤ 22, -29 ≤ l ≤ 29	0 ≤ h ≤ 20, 0 ≤ k ≤ 14, -28 ≤ l ≤ 27	-16 ≤ h ≤ 18, -44 ≤ k ≤ 44, -14 ≤ l ≤ 14	-20 ≤ h ≤ 20, -12 ≤ k ≤ 14, -26 ≤ l ≤ 28
Reflections Collected	38868	8371	36417	38712
Independent Reflections	11509	8371	12088	8338
Data / Parameters	11509/514	8371/440	12088/579	8338/434
Goodness-Of-Fit on F^2	1.045	1.005	1.037	1.035
Final R indexes [I>2σ>(I)]	R1 = 0.0429, wR2 = 0.0859	R1 = 0.055, wR2 = 0.140	R1 = 0.0498, wR2 = 0.1111	R1 = 0.039, wR2 = 0.084
Final R indexes [all data]	R1 = 0.0622, wR2 = 0.0925	R1 = 0.1175, wR2 = 0.1730	R1 = 0.0859, wR2 = 0.1289	R1 = 0.0733, wR2 = 0.0956
Largest Diff Peak/Hole	0.409/-0.314	0.618/-0.368	1.152/-1.422	0.441/-0.400

Table **58** Selected bond lengths (Å) and angles (º) for **72**, **78**, **80**, **77** and **81**.

	72	**78**	**80**	**77**	**81**
M – $Cp_{centroid}$	-	1.710	1.745[a]	1.895	1.901
M – P(1)	-	2.1658(7)	2.1843(10)	2.2531(9)	2.2622(11)
M – P(2)	-	2.1704(6)	2.1875(10)	2.2568(9)	2.2625(11)
M – C(1)	-	1.900(2)	1.916(4)	2.007(3)	2.026(3)
TMS – C(1)	1.8372(13)	-	-	-	-
C(1) – C(2)	1.2050(18)	1.218(3)	1.216(5)	1.206(4)	1.202(4)
C(2) – C(3)	1.4377(17)	1.442(3)	1.439(5)	1.436(4)	1.444(4)
C(6) – N(1)	1.4055(16)	1.435(3)	1.406(5)	1.439(4)	1.404(4)
N(1) – C(9)	1.4294(16)	1.420(3)	-	1.409(4)	-
N(1) – C(16)	1.4312(16)	1.421(3)	-	1.427(4)	-
P(1) – M – P(2)	-	86.58(3)	85.87(4)	82.99(3)	83.12(3)
C(9) – N(1) – C(16)	117.13(10)	121.83(18)	-	122.4(3)	-
P_1-Fe-C_3-C_4	-	-2.8	-118.1	-61.5	-25.5

[a] Cp* instead of Cp

Complex **77** crystallises in the monoclinic crystal system (space group P 2_1/c) with four molecules in the asymmetric unit cell (Table **57**). The structure of the ruthenium acetylide complex illustrates the usual piano stool geometry around the Ru, of related ruthenium acetylide complexes. [226, 396-400] One obvious difference in the structure of **77** and related Ru(C≡CC_6H_4R-4)(dppe)Cp* compared to the Cp analogues in the orientation of the aryl ring, with the plane of the ring in roughly perpendicular to the Ru-Cp*centroid, whereas with the Cp analogous complexes, the aryl plane is close to parallel. [398] Compared to complex **78**, the Ru-C(1)-C(2)-C(3) chain is essentially linear, as is the case in the closely related aniline complex Ru(C≡C$C_6H_4NH_2$)(dppe)Cp* **81**. [224] The Ru – C(1) [2.007(3) Å], C(1)-C(2) [1.206(4) Å] and C(2)-C(3) [1.436(4) Å] (Table **58**) bond lengths in **77** are comparable to other ruthenium piano-stool complexes of the form Ru(C≡CC_6H_4R-4) (dppe)Cp*; ([Ru-C(1); 2.004(6) – 2.026(3) Å], [C(1) – C(2); 1.195(7) – 1.225(8) Å]

and [C(2) – C(3); 1.431(5) – 1.445(4) Å]). [224] The P(1)-M-P(2) bond angle in **77** are understandably similar to that of **81**, (82.99(3) ° vs 83.12(3) °), [224] but, not surprisingly, smaller that the same angle in the **78** complex (86.58 (3) °).

The amine substituent part of the ruthenium complex also has a propeller arrangement of the aromatic rings. [389, 390] The pitch of the phenyl ring attached to the metal fragment to the C(6)-C(9)-C(16) plane has increased to 56 °, whereas the pitch of the two tolyl rings are 49 ° and 24 °. The N centre in **77** is planar, the angles between the aryl substituents on the amine adding to 360 °. Again the C(6)-N(1) bond is longer in the metallic complex **77** than in both the TMS protected **72** and deprotected **73** ligand (1.439(4) Å vs 1.4055(16) Å and 1.405(2) Å).

Within the asymmetric unit cell, the four molecules (Z = 4), are paired, with the organic fragments of the two paired molecules forming a cross when viewing the molecular pair side on. These pairs form lines of paired molecules along the c-axis, within which are number of C-H … π interactions between the tolyl rings on the ligand and the diphenyl phosphine (dppe), the phenyl ring on the amine substituent and the tolyl rings on a paired molecule. These crossed molecular stacks along the c-axis form layers of molecular stacks along the b-axis, with C-H … π interactions between the tolyl rings of one molecule and the aromatic Cp* of a molecule the layer below. There are also interactions between the dppe phenyl rings and the CH_2Cl_2 molecules within the crystal.

There are two other crystallographically studied mono-metallic ethynyl diphenylamine complexes, **62** and **63**. Both of these complexes show the same amine propeller arrangement with the two peripheral phenyl rings at a greater pitch to the plane of the carbon atoms adjacent to the nitrogen atom, than the phenyl ring attached to the metal. Table **59** shows that the M-C(1), C(1)-C(2), C(2)-C(3), and C(3)-N(1) bonds of both complexes **62** and **63** are comparative to that of the crystallographically determined complexes here. (**77** and **78**).

Table **59** Selected bond lengths (Å) of related ethynylphenyldiphenylamine complexes, **62** and **63**.

	62 [369]	**63** [371]
M – C(1)	1.977(9)	2.008(4)
C(1) – C(2)	1.18(1)	1.171(6)
C(2) – C(3)	1.44(1)	1.476(6)
C(6) – N(1)	1.41(1)	1.399(6)
N(1) – C(9)	1.41(1)	1.442(7)
N(1) – C(16)	1.452(8)	1.432(6)

6.2.3 Cyclic Voltammetry

Compound **73** undergoes one essentially chemically reversible, one-electron oxidation events at potential E_1 = +1.06 V, giving rise to $[\mathbf{73}]^+$. The iron complex **78** undergoes two one-electron oxidation events at potentials E_1 (-0.09 V) and E_2 (0.62 V), resulting in $[\mathbf{78}]^+$ and $[\mathbf{78}]^{2+}$ (Table **60**). The redox couples of the two oxidation events in **78** are very similar to those of $Fe(C{\equiv}CC_6H_4X)(dppe)Cp^*$, where X = NH_2 and NMe_2 (E_1 = -0.25 V, -0.25V and E_2 = 0.68 V, 0.53V, for X = NH_2 and NMe_2 respectively). [392] The first oxidation wave is assigned to the Fe(II)/Fe(III) oxidation, with the second occurring largely on the amine substituent. This assignment is supported by spectroelectrochemical and DFT studies described below.

Table **60** Oxidation potentials for complexes **73** and **78**. [a]

	$\mathbf{E_1}$ / V	$\mathbf{\Delta E_p}$ / V	$\mathbf{I_c/I_a}$ / V	$\mathbf{E_2}$ / V	$\mathbf{\Delta E_p}$ / V	$\mathbf{I_c/I_a}$ / V
73	1.06	0.12	0.9	-	-	-
78 [b]	-0.09	0.10	1	0.62	0.115	0.9

[a] Data recorded from solutions in CH_2Cl_2 containing 0.1 M $[NBu_4]BF_4$ supporting electrolyte and referenced against decamethylferrocene/decamethylferrocenium Fc^*H/Fc^*H^+ couple at -0.07 V vs SCE scan rate 100 mV/s.

[b] Fc/FcH used as the internal reference.

6.2.4 IR Spectroelectrochemical Studies

The chemical stability of $[HC{\equiv}CC_6H_4NTol_2]^+$ $[\mathbf{73}]^+$ under the conditions of cyclic voltammetry experiments prompted more thorough spectroscopic characterisation of the ligands, complexes and the various products derived from one-electron oxidation by spectroelectrochemical means. However as the timescale of the IR and UV spectroelectrochemical redox process is significantly longer than that of the voltammetric study, the oxidation of the (presumably) more stable trimethylsilyl protected analogue of **73**, **72** was monitored in both IR and UV-Vis-NIR spectroscopic regions. For this study and others in this Chapter, described in more detail below, an air-tight spectroelectrochemical cell fitted with CaF_2 windows to provide transparency across the spectroscopic region of interest was employed. [239]

On oxidation of **72** the intensity of the ν(C≡C) band at 2150 cm^{-1} decreased, being replaced by a new absorption at ~2110 cm^{-1}, with new bands in the aromatic ν(CC) region also observed. On back-reduction the original spectrum was fully recovered, confirming the assignment of the new bands to $[\mathbf{72}]^+$. The shift of the ν(C≡C) band by 40 cm^{-1} upon oxidation indicates a depopulation of an orbital with a small amount of C≡C bonding character.

In the neutral oxidation state **78** has a strong ν(C≡C) band at 2060 cm^{-1}, which is characteristic of the 18-electron iron acetylide, and is comparable to other iron aryl acetylides. [392, 401] On oxidation to $[\mathbf{78}]^+$ the intensity of the characteristic ν(C≡C) band decreased, being replaced by a new, more intense band at 1962 cm^{-1} (Table **61**, Figure **88**). In addition, new bands in the aromatic ν(CC) region were also observed. On back-reduction the original spectrum was fully recovered, which confirmed the assignment of the new bands to $[\mathbf{78}]^+$, and not to some product of an electro-chemical (EC) process. The position and shift of the new ν(C≡C) band of $[\mathbf{78}]^+$, is in agreement with other mono-oxidised iron aryl acetylides with electron donor groups *para* to the FeC≡C fragment. [392, 401] As the complex features two redox active groups (the metal fragment and the triaryl amine), a second one-electron oxidation can take place. The intensity of the ν(C≡C) band of the $[\mathbf{78}]^+$ species decreased on oxidation with a small new band appearing at 1860 cm^{-1}, as well as new bands in the aromatic ν(CC) region. The original spectrum of $[\mathbf{78}]^+$

was fully recovered on back-oxidation, confirming the assignment of the new bands to $[\mathbf{78}]^{2+}$. The shifts of the ν(C≡C) band by 98 cm^{-1} and 102 cm^{-1} upon oxidation (neutral to +1 and +1 to +2 respectively) indicates the appreciable depopulation of an orbital with C≡C bonding character, in both the neutral and mono-oxidised states. There is also an electronic absorption band rising into the NIR region in the spectrum of $[\mathbf{78}]^{+}$, which fully collapses on oxidation to $[\mathbf{78}]^{2+}$. This absorption band is either a forbidden dd band or the tail of an NIR band with LMCT character.

Table **61** IR data (cm^{-1}) for compounds **78** and **80** and the corresponding cations.

	Neutral		Cation		Dication	
	ν(C≡C)	ν(Aryl)	ν(C≡C)	ν(Aryl)	ν(C≡C)	ν(Aryl)
78 [a]	2060	1606	1962	1578	1860	1608
80 [b]	2060	-	1988 (sh), 1962	-	-	-

[a] data from CH_2Cl_2 solutions containing 0.1 M NBu_4BF_4 supporting electrolyte at ambient temperature

[b] data from Nujol mull of a solid state chemically oxidised

[c] complex [**80**][PF_6] obtained by chemically oxidisation of **80** using [FcH][PF_6]

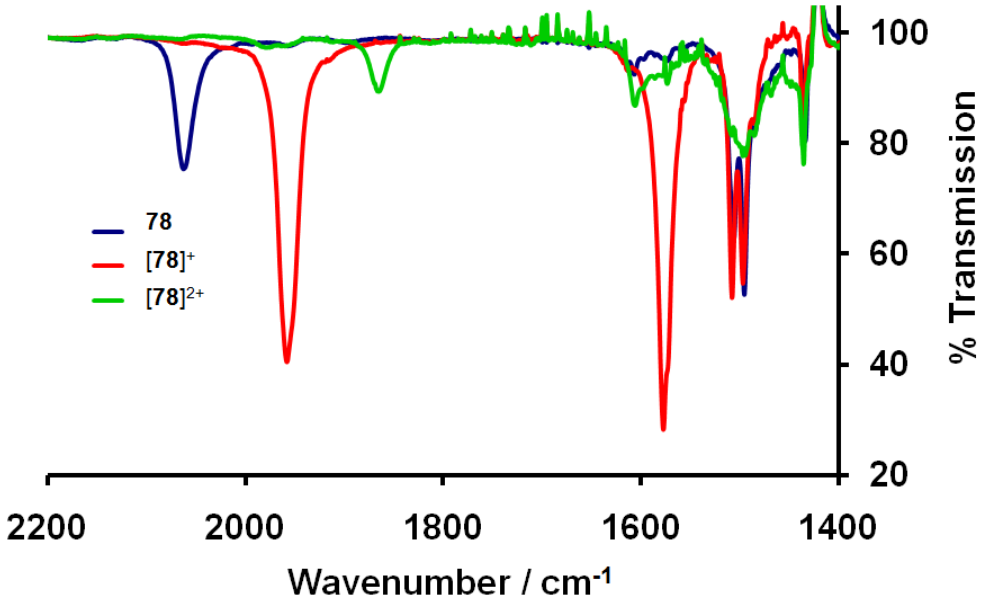

Figure **88** IR spectrum of $[\mathbf{78}]^{n+}$ (n = 0, 1, 2), in CH_2Cl_2 0.1 M NBu_4BF_4.

Since **78** behaved well under spectroelectrochemical conditions, spectroscopic characterisation of **79** and of the products derived from oxidation by spectroelectrochemical means, was also undertaken..

Like the mono-metallated complex **78**, in the neutral oxidation state **79** has a strong ν(C≡C) band at 2060 cm^{-1} (Table **62**, Figure **89**) which is also comparable to the tris-Fe(dppe)Cp*-1,3,5-benzene complex **13** (2050 cm^{-1}). [293] Upon the first oxidation the intensity of the characteristic ν(C≡C) band decreased about a third, with a slight shift to lower wavenumber, and a new ν(C≡C) band appeared at 1962 cm^{-1}. Akin to $[\mathbf{78}]^{n+}$, new bands in the aromatic ν(CC) region were also observed. Oxidation from $[\mathbf{79}]^{+}$ to $[\mathbf{79}]^{2+}$, resulted in another decrease in the intensity of the ν(C≡C) band around 2060 cm^{-1} and the ν(C≡C) band at 1960 cm^{-1} increased in intensity. On oxidation to the homovalent complex $[\mathbf{79}]^{3+}$, the band at 2060 cm^{-1} disappeared, with only one ν(C≡C) band in the spectrum (1962 cm^{-1}). The IR spectrum of $[\mathbf{79}]^{3+}$ is similar to that of $[\mathbf{78}]^{+}$. All told, the IR spectroelectrochemical results are consistent with sequential iron centred oxidations. The first three oxidations are all fully reversible, with the spectrum of the preceding oxidation state being recovered after back-reduction. As with **78**, oxidation can also occur on the triaryl amine centre in **79**, oxidation from $[\mathbf{79}]^{3+}$ to $[\mathbf{79}]^{4+}$ resulted in the single ν(C≡C) band (for the tris-oxidised species) at 1962 cm^{-1} disappearing with a small ν(C≡C) band at 1860 cm^{-1} appearing, similar to the IR spectrum of $[\mathbf{78}]^{2+}$.

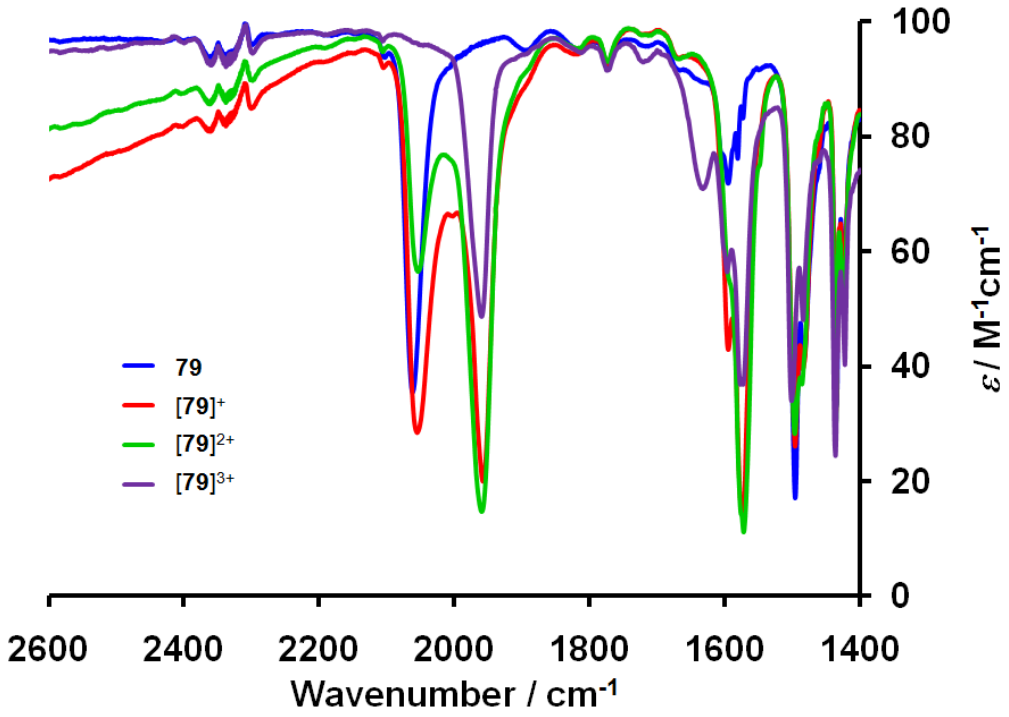

Figure **89** IR spectrum of **79**, $[\mathbf{79}]^{+}$, $[\mathbf{79}]^{2+}$ and $[\mathbf{79}]^{3+}$, in CH_2Cl_2 0.1 M NBu_4BF_4.

Table **62** IR data (cm^{-1}) for compound **79** and the corresponding cations [a]

	Neutral		Cation		Dication		Trication	
	ν(C≡C)	ν(Aryl)	ν(C≡C)	ν(Aryl)	ν(C≡C)	ν(Aryl)	ν(C≡C)	ν(Aryl)
79	2060	1594	2056, 1959[b]	1595, 1575	2056, 1961[b]	1595, 1575	1962	1632, 1575

[a] data from CH_2Cl_2 solutions containing 0.1 M NBu_4BF_4 supporting electrolyte at ambient temperature

[b] ν(C≡C) of the oxidised ethynyl arm

6.2.5 UV-Vis Spectroelectrochemical Studies

The neutral and monocation form of [**72**], [**78**] and [**79**], were further characterised by UV-vis-NIR spectroelectrochemical methods. The spectroscopic data are summarised in Table **63**. TD-DFT calculations that are summarised below support the conclusions drawn from the analysis of these data.

Table **63** UV-vis-NIR spectroscopic data for $[\mathbf{72}]^{x+}$, $[\mathbf{78}]^{y+}$ and $[\mathbf{79}]^{z+}$ (x = 0, 1; y = 0, 1, 2; z = 0, 1, 2, 3).

Complex	Wavenumber / cm^{-1} [ε / $M^{-1}cm^{-1}$]	Wavenumber / cm-1 [f]	Orbitals	Character
72	29500 [27000]	29000 [0.731]	HOMO → LUMO	π - π*
	33000 [20000]	32500 [0.252]	HOMO → LUMO+2	π - π*
$[\mathbf{72}]^{+}$	11000 [sh, 6000]	-	-	-
	14800 [16200]	12670 [0.338]	β-HOSO → β-LUSO	π - π*
	24000 [10000]	26150 [0.280]	α-HOSO → α-LUSO β-HOSO → β-LUSO+1	π - π* π - π*
	27000 [13900]	29500 [0.086]	α-HOSO → α-LUSO+1 α-HOSO → α-LUSO+2	π - π* π - π*
	36800 [14000]	37700 [0.144]	α-HOSO-1 → α-LUSO β-HOSO → β-LUSO+1	π - π* π - π*
78	28900 [31000]	28460 [0.194]	HOMO → LUMO+6 HOMO-1 → LUMO+6	MLCT MLCT
	32300 [25500]	37000 [0.097]	HOMO → LUMO+9	Fe – dppe (π - π*)
$[\mathbf{78}]^{+}$	10500 [21800]	10550 [0.380]	β-HOSO → β-LUSO	LMCT
	22730 [14200]	24000 [0.122]	a-HOSO → α-LUSO+4	C_2PhNTol π – C_2Ph π*
	33300 [24500]	31550 [0.118]	α-HOSO → α-LUSO+6	C_2PhNTol$_2$ – Fe-dppe (π - π*)
$[\mathbf{78}]^{2+}$	8800 [12700]	-	-	
	12900 [sh, 7200]	-	-	
	16600 [10900]	-	-	
	22100 [11700]	-	-	
	35000 [sh, 24000]	-	-	
79	26900 [38200]	26200 [0.903]	HOMO → LUMO+1	MLCT
$[\mathbf{79}]^{+}$	6640 [sh, 4000]	-	-	IVCT
	10600 [9100]	-	-	LMCT
	21900 [sh, 11900]	-	-	π - π*
	29000 [28700]	-	-	π - π*
$[\mathbf{79}]^{2+}$	6640 [3000]	-	-	IVCT
	10650 [14100]	16000 [0.258]	β-HOSO → β-LUSO *	LMCT
	21800 [13500]	-	-	π - π*
	29200 [28200]	-	-	π - π*
$[\mathbf{79}]^{3+}$	6640 [1000]	-	-	IVCT
	10700 [18500]	-	-	LMCT
	22400 [13900]	-	-	π - π*
	29600 [28300]	-	-	π - π*

* TD DFT Calculation run using MPW1K/6-31G*

The main absorption band in **72** (Figure **90**) at 31000 cm^{-1} is split into two discernable bands, one at 29500 cm^{-1} and one at 33000 cm^{-1} with the lower wavenumber component being the more intense of the two. This splitting of the main absorption band in neutral amine systems has been seen before, in asymmetric

tri(*p*-aryl)amines. [402] With neutral tri(*p*-aryl)amines of C_3 symmetry the main absorption band can be explained by one intense HOMO → LUMO ($S_0 \rightarrow S_1$) excitation into a degenerate (E) S_1 state. [402] However breaking the C_3 symmetry as in **72**, results in the splitting of the degenerate LUMO orbitals. [402] Hence two excitations are seen, one being the HOMO → LUMO and the other HOMO → LUMO+1 or higher. Upon oxidation to the cation species $[\mathbf{72}]^+$, the absorption at ~31000 cm^{-1}, is replaced by two medium intensity absorption bands, one around 27000 cm^{-1} and the second a much sharper absorption at 14800 cm^{-1}. There is also a broad shoulder at ~11000 cm^{-1}. This sharp absorption, seen before in asymmetric cationic tri(*p*-aryl)amines between 13000 cm^{-1} and 15000 cm^{-1}, with electron withdrawing groups such as chloro and methoxy substituents shifting the absorption maximum to lower wavenumbers, caused by the extension of the π-system. [403] This absorption has been shown to be a HOMO → SOMO, being π – π* in character. [402]

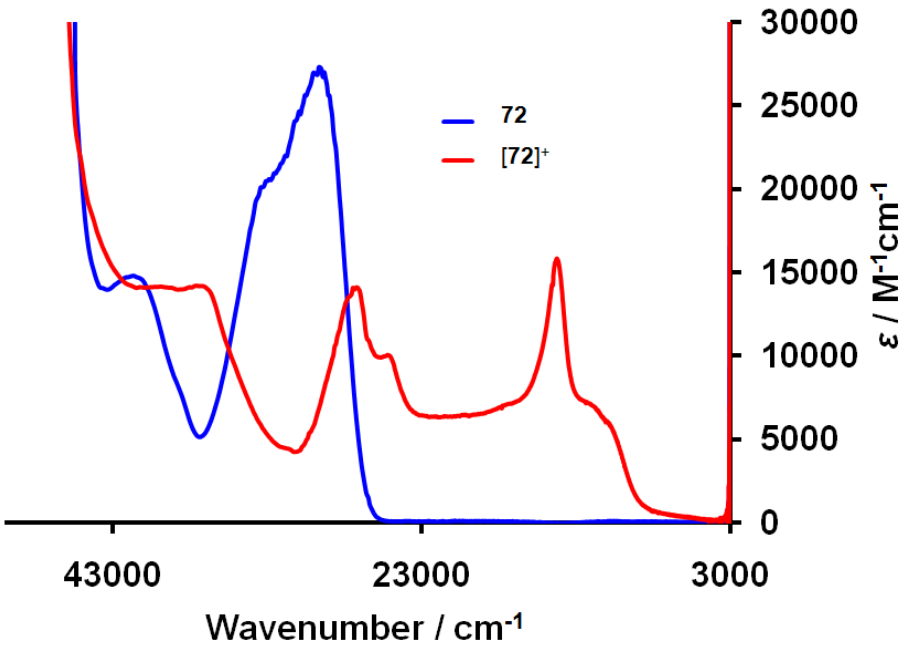

Figure **90** UV-vis-NIR spectra of $[\mathbf{72}]^{n+}$ (n = 0, 1), CH_2Cl_2, 0.1 M NBu_4BF_4.

The UV-vis-NIR spectrum of the neutral species **78** (Figure **91**) has two absorption bands, the band above 36000 cm^{-1}, can safely attributed to π – π* phosphine ligand centred transitions, with the broader, less intense transition, which has two discernable maxima at roughly 32300 and 28900 cm^{-1}, with the maxima at lower

wavenumber being the more intense of the two. This spectra of **78** resembles spectra of related Fe(II) acetylides previously reported. [404, 405] The broader, lower energy transition, which is the origin of the orange colour of the Fe(II) acetylides, [392] has been attributed as MLCT in character. The position of the MLCT band in Fe(II) acetylide has been shown to shift to higher energy with increasing electron donating nature of the *para*- substituent. [392] Even with a less electron rich metal centre (Fe(dppe)Cp), the position of the MLCT maxima in **78** is comparable to that of **80** [392] with the more electron rich [FeCp*] centre. (λ_{max} / nm: **78** 310 and 346; **80** 322).

Upon oxidation to the cation species [**78**]$^+$, the absorption band at about 30000 cm^{-1} is replaced by several absorptions that have been seen in related Fe(II) acetylides. [221, 319, 406] Two bands appear at 22720 cm^{-1} and 10530 cm^{-1}, which the lower energy band has previously been shown to shift bathochromically and grow in intensity as the *para*- substituent becomes more and more electron donating (λ_{max} / cm^{-1} ; Fe(C≡CC_6H_4R-4)(dppe)Cp*: R = NO_2 15400; H 15100; NH_2 12680; NMe_2 11185). [227] This shift indicates the band at 10530 cm^{-1} has LMCT in character.

In the NIR region of the cation [**78**]$^+$ there is a broad absorption band from 10000 cm^{-1} to 4000 cm^{-1}, with an intensity of roughly 1 × 10^3 M^{-1}cm^{-1}. In the related [Fe(C≡CC_6H_4R-4)dppe)Cp*]$^+$ complexes, an absorption band was observed in the NIR region that was sensitive to the electronic nature of the *para*- substituent, being hypsochromically shifted with increased electron donating property. The NIR absorption for the [**80**]$^+$ complex is observed at 6200 cm^{-1}. [227] This weak NIR absorption has been described as a forbidden metal centred ligand field (LF) electronic transition, as similar absorptions are also seen in [FeCl(dppe)Cp*]$^+$ and [FeH(dppe)Cp*]$^+$, which lack the acetylide ligand. [227]

Upon oxidation to the dication [**78**]$^{2+}$, the absorption peaks associated with the cation [**78**]$^+$ disappear, with new signatures at 22100 cm^{-1}, 16600 cm^{-1}, 12900 cm^{-1} and 8800 cm^{-1} appearing (Figure **91**). If the transition at 10500 cm^{-1} in [**78**]$^+$ is LMCT, the new absorption at 8800 cm^{-1} cannot be LMCT in character. The low intensity absorptions in the NIR region are shown in Figure **92**.

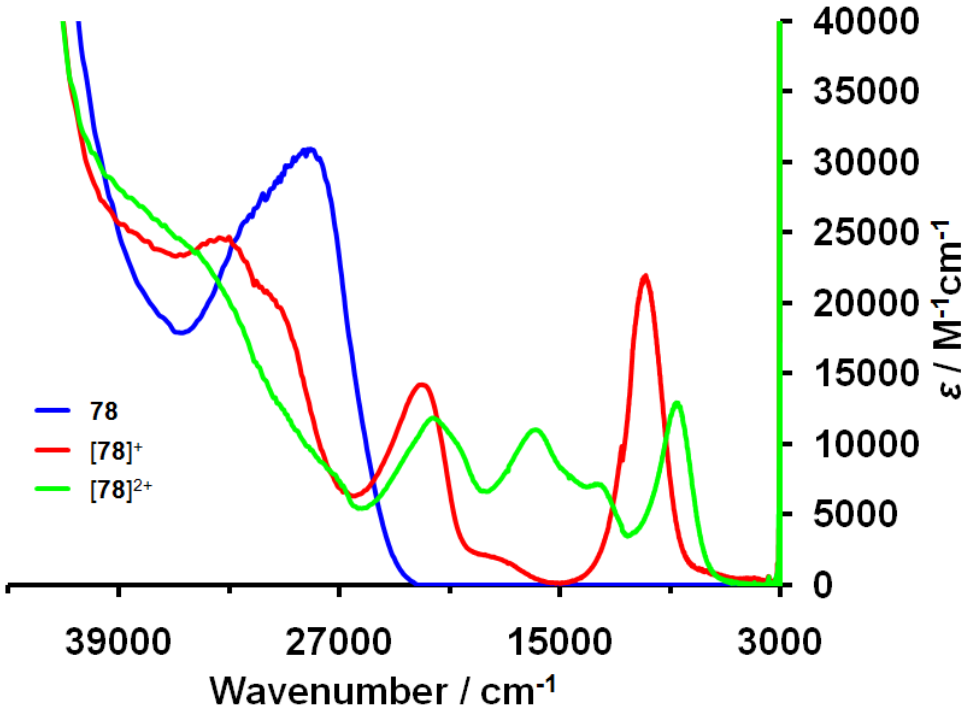

Figure **91** UV-vis-NIR spectra of [**78**]$^{n+}$ (n = 0, 1, 2), CH_2Cl_2, 0.1 M NBu_4BF_4

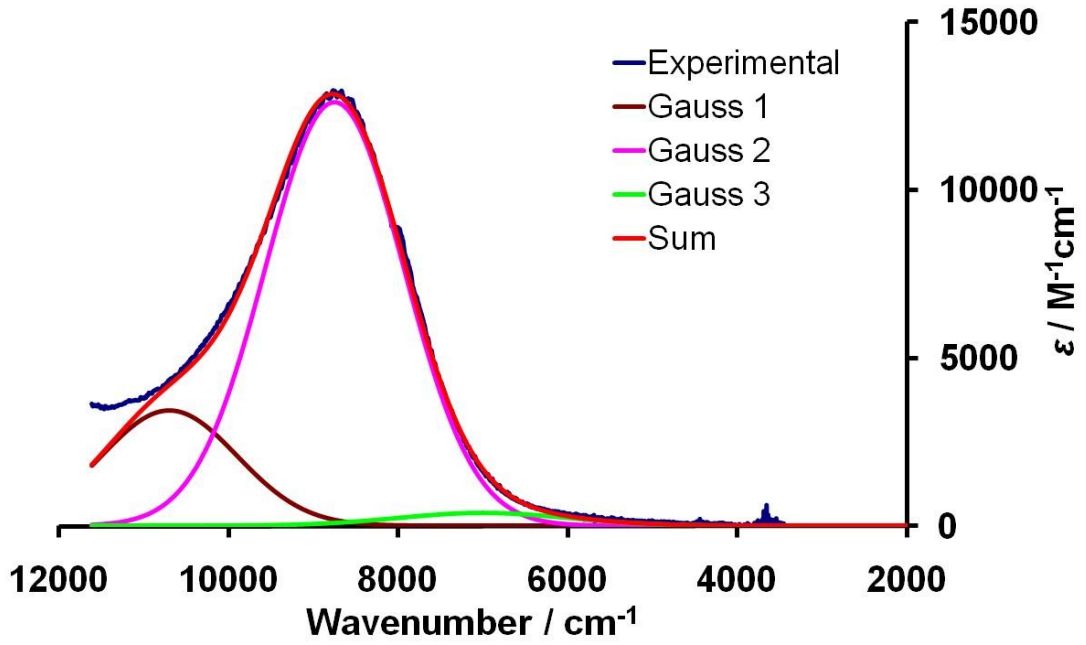

Figure **92** The deconvolution of the lower energy region of the electronic absorption spectrum of [**78**]$^{2+}$ into Gaussian components. The incomplete oxidation before decomposition of the sample is evidenced by the residual LMCT absorption at 10530 cm^{-1}.

The UV-vis-NIR spectrum of the neutral species **79** (Figure **93**), which is very similar to the UV-vis-NIR spectrum of **78**, also has two absorption bands, one band above 36000 cm^{-1}, and one at 26900 cm^{-1}, which like the mono iron complex is assigned to be MLCT in character. Upon oxidation to the monocation $[\mathbf{79}]^{+}$, the absorption band at 26900 cm^{-1}, shifts to higher wavenumbers and decreases in intensity. Two bands in similar regions to the $[\mathbf{78}]^{+}$ also grow in, 21900 cm^{-1} and 10600 cm^{-1} (compared to 22730 cm^{-1} and 10500 cm^{-1} $[\mathbf{78}]^{+}$). Further oxidation of the monocation $[\mathbf{79}]^{+}$ through the dication $[\mathbf{79}]^{2+}$ to the trication $[\mathbf{79}]^{3+}$, leads to the absorption band at 10600 cm^{-1}, growing in intensity, where it reaches a maximum at $[\mathbf{79}]^{3+}$ ($\varepsilon \sim 20000$ $M^{-1}cm^{-1}$), the two bands at 29600 cm^{-1} and 22400 cm^{-1} remain at the same wavenumber and intensity, but with a more distinct absorption profile. Unsurprisingly the UV-vis-NIR spectra of $[\mathbf{79}]^{3+}$, is very similar to the mono-oxidised $[\mathbf{78}]^{+}$, with both spectra showing three very similar relative intensities absorption bands; one at ~11000 cm^{-1}, one at ~21000 cm^{-1} and one ~ 33000 cm^{-1}. The band at 11000 cm^{-1} in $[\mathbf{79}]^{+/2+/3+}$ is assigned as LMCT in character, the same as in $[\mathbf{78}]^{+}$.

In the NIR region, below 10000 cm^{-1}, there is a reasonably sized shoulder absorption band ($\varepsilon \sim 4000$ $M^{-1}cm^{-1}$), that tails off into the IR region. This band is grows in intensity on oxidation from the neutral species **79** to the cationic $[\mathbf{79}]^{+}$. On oxidation to $[\mathbf{79}]^{2+}$ and further, this NIR band decreases in intensity, until it almost is non-existent in the trication $[\mathbf{79}]^{3+}$.

It is possible to fit Gaussian profiled bands to the NIR region of the UV-vis-NIR spectra of the oxidation of **79** to $[\mathbf{79}]^{3+}$. Figure **94** show the three deconvoluted absorption bands and the summed absorption of the lower energy region of the spectra of $[\mathbf{79}]^{n+}$ (n = 1, 2, 3). Within each oxidation state these NIR bands all have similar intensities ($[\mathbf{78}]^{+}$ $\varepsilon \sim 2500$ $M^{-1}cm^{-1}$) , with the greatest intensities in the mono oxidised cation $[\mathbf{78}]^{+}$, steadily decreasing to $\varepsilon \sim 200$ $M^{-1}cm^{-1}$ for the spectra of the trication $[\mathbf{79}]^{3+}$. Table **64** shows the position and intensities of the LMCT absorption band and the three NIR bands for $[\mathbf{79}]^{+/2+/3+}$.

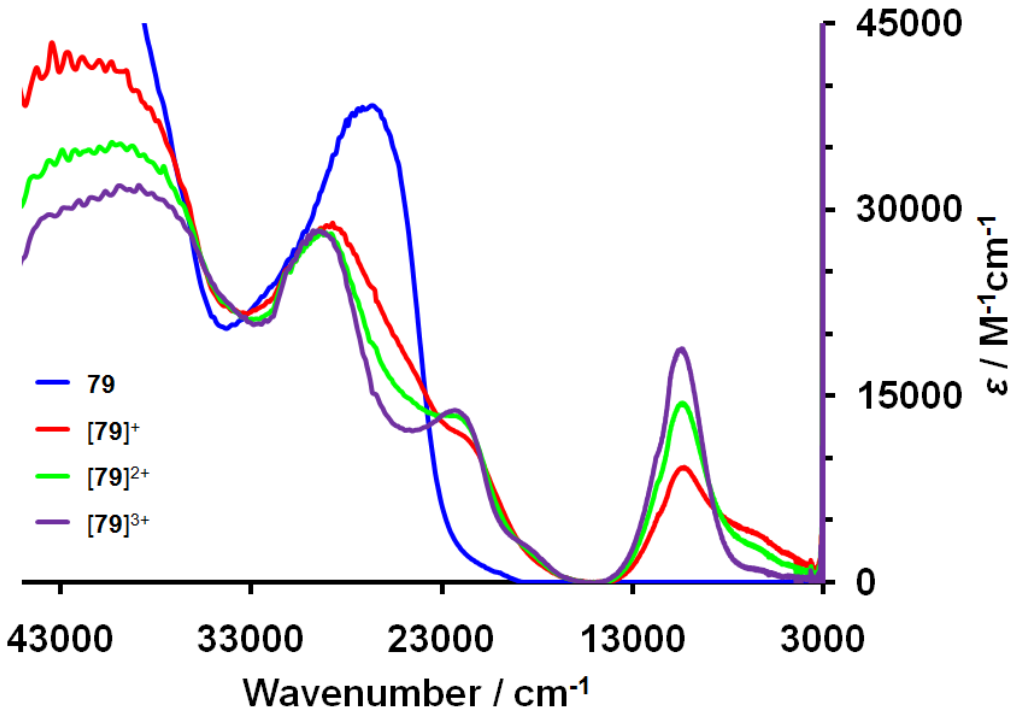

Figure **93** UV-vis-NIR spectra of $[\mathbf{79}]^{n+}$ (n = 0, 1, 2, 3), CH_2Cl_2, 0.1 M NBu_4BF_4.

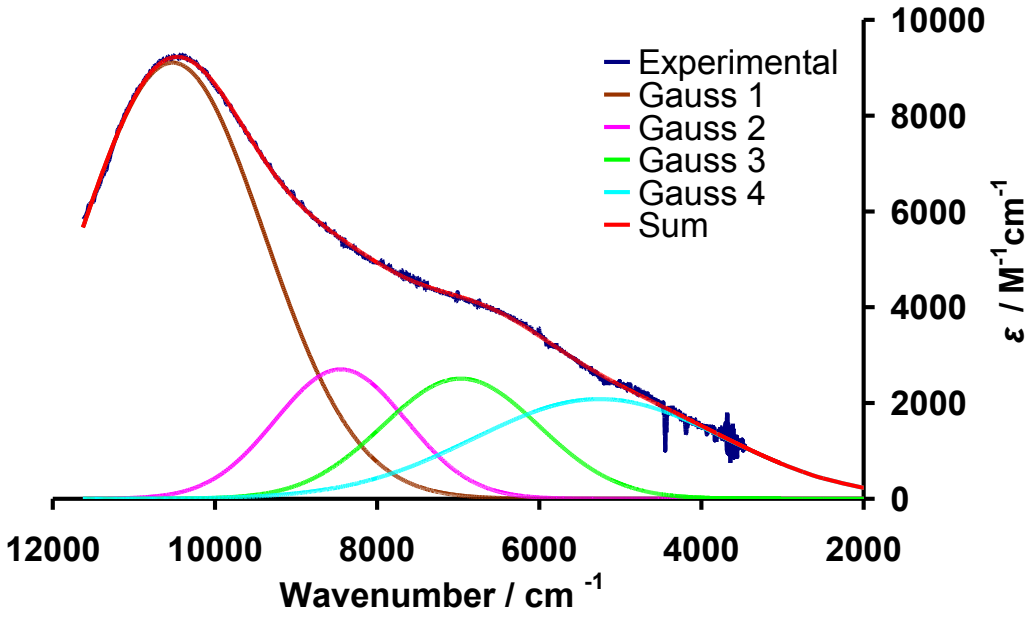

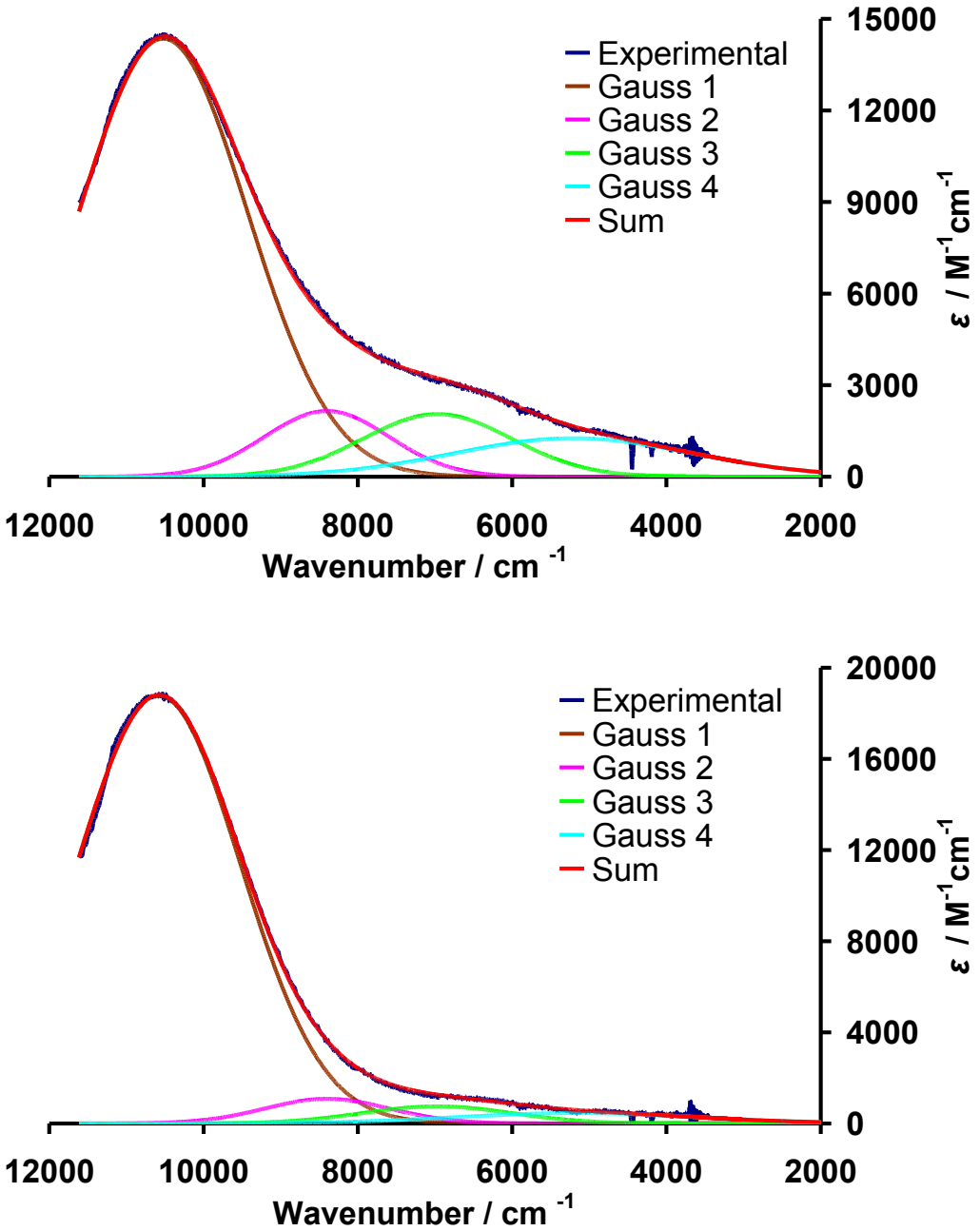

Figure **94** Gaussian Fitting of [**79**]$^{n+}$ (n = 1 (top), = 2 (middle), = 3 (bottom)).

Table **64** Position of LMCT and NIR bands from a Gaussian fitting of $[\mathbf{79}]^{n+}$ (n = 1, 2, 3). Intensities are in parentheses (ε / $M^{-1}cm^{-1}$).

	Assignment	$[\mathbf{79}]^{+}$	$[\mathbf{79}]^{2+}$	$[\mathbf{79}]^{3+}$
Gauss 1	LMCT	10520 (9100)	10520 (14400)	10580 (18800)
Gauss 2	$IVCT_3$	8450 (2700)	8400 (2150)	8400 (1050)
Gauss 3	$IVCT_2$	7000 (2500)	7000 (2000)	7000 (750)
Gauss 4	$IVCT_1$	5250 (2100)	5200 (1250)	5150 (450)

Multiple low energy transitions have been noted before in d^5/d^6 mixed valence compounds. In d^5/d^6 mixed valence compounds it has been noted that up to three IVCT transitions can occur in the NIR region. However these normally only gain appreciable intensity in heavy metal complexes in which spin orbit coupling serves to help break the selection rules. From the experimental data it can clearly be seen that the three NIR transitions in the spectra of **78** and **79** are associated with the intermediate oxidation states and are likely due to the three possible IVCT transitions in d^5/d^6 mixed valence systems. [24]

To help to understand the spectroelectrochemical data of the oxidation processes of $[\mathbf{72}]^{x+}$, $[\mathbf{78}]^{y+}$ and $[\mathbf{79}]^{z+}$ (x = 0, 1; y = 0, 1, 2; z = 0, 1, 2, 3), and to assist in the correct assignment of transitions, a theoretical study at DFT level was undertaken.

6.2.6 Electronic Structure Calculations

A theoretical investigation was conducted at the DFT level, initially on the model systems, $Me_3SiC{\equiv}CC_6H_4NTol_2$ **72-H** and $Fe(C{\equiv}CC_6H_4NPh_2)(PPh_2(CH_2)_2PPh_2)Cp$ **78-H** which were used to mimic complexes, **72** and **78**, and the corresponding radical cations $[\mathbf{72}]^{+}$ and $[\mathbf{78}]^{+/2+}$ at the B3LYP/6-31G* level which gave good agreement with the experimental data.

6.2.6.1 Ligand DFT Calculations

There is excellent agreement between the crystallographically determined structure of **72** and the DFT optimised geometry determined here (Table **65**). Important vibrational frequencies are summarised in Table **66**. Energies and composition of the frontier orbitals are summarised in Table **67** for **72-H** and [**72-H**]$^+$, whilst Scheme **55** illustrates the labelling scheme.

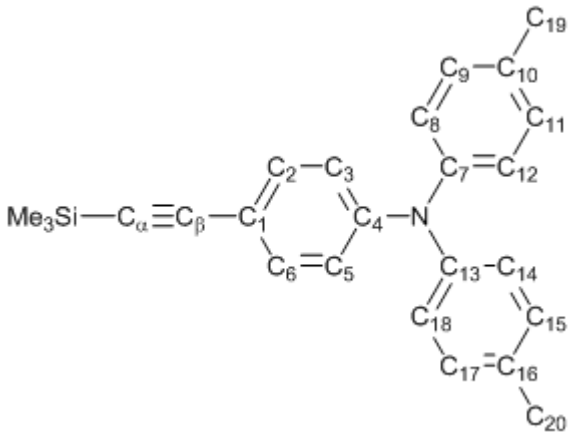

Scheme **55** The labelling scheme used in the discussion of the DFT results for the ligand **72-H** and [**72-H**]$^+$.

At the level of theory employed the optimised geometries for **72-H** and [**72-H**]$^+$ are very similar, (Table **65**), with some small contractions and elongations in specific areas of the molecular system. There is good agreement between the crystallographic determined geometry of **72** and the DFT optimised geometry of **72-H** (Table **65**). On oxidation to [**72-H**]$^+$ there is little structural change with some small contractions and elongations along the acetylene chain; with the $C_\alpha - C_\beta$ bond length increasing slightly (1.222 Å vs 1.225 Å), and the $Me_3Si - C_\alpha$ bond length also increasing slightly (1.837 Å vs 1.866 Å), and the C_β – C(1) bond length decreasing slightly (1.425 Å vs 1.412 Å). There is little evidence of evolution of quinoidal character along the ethynylphenyl in the optimised geometry of [**72-H**]$^+$. On oxidation there is some evidence of pertubance of the aryl amine part of the ligand, with a small decrease in the N – C bond lengths (~ 0.013 Å), and a decrease in the pitch of the propeller arrangement of the aryl rings (44 ° vs 41 °).

Table **65** Optimised bond lengths (Å) and angles (°) for **72**, **72-H** and [**72-H**]$^+$.

	72	**72-H**	[**72-H**]$^+$	**Δ** [a]
$Me_3Si – C_\alpha$	1.8372(13)	1.837	1.866	+0.029
Me – Si	1.8549(17)	1.891	1.885	-0.006
$C_\alpha – C_\beta$	1.2050(18)	1.222	1.225	+0.003
$C_\beta – C_1$	1.4377(17)	1.425	1.412	-0.013
$C_4 – N$	1.4055(16)	1.413	1.400	-0.013
$N – C_7$	1.4294(16)	1.425	1.419	-0.006
$N – C_{13}$	1.4312(16)	1.425	1.419	-0.006
$C_1 – C_{2,6}$	1.398	1.409	1.418	+0.009
$C_{2,6} – C_{3,5}$	1.383	1.388	1.380	-0.008
$C_{3,5} – C_4$	1.399	1.408	1.416	+0.008
$C_4 – N – C_7$ / °	120.6	120.4	120.4	-
$C_4 – N – C_{13}$ / °	120.8	120.4	120.4	-
$C_7 – N – C_{13}$ / °	117.2	119.2	119.2	-
Pitch A	22	35.4	34.1	-1.3
Pitch B	50	43.9	41.3	-2.6
Pitch C	51	44.1	41.3	-2.8

[a] **Δ** = [**72-H**]$^+$ **- 72-H**

The lack of elongation of the $C_\alpha \equiv C_\beta$ is supported by the small shift in the calculated ν(C≡C) frequencies of **72-H** (2141 cm^{-1}) and [**72-H**]$^+$ (2114 cm^{-1}), a shift of ~27 cm^{-1} (Figure **95**, Table **66**).

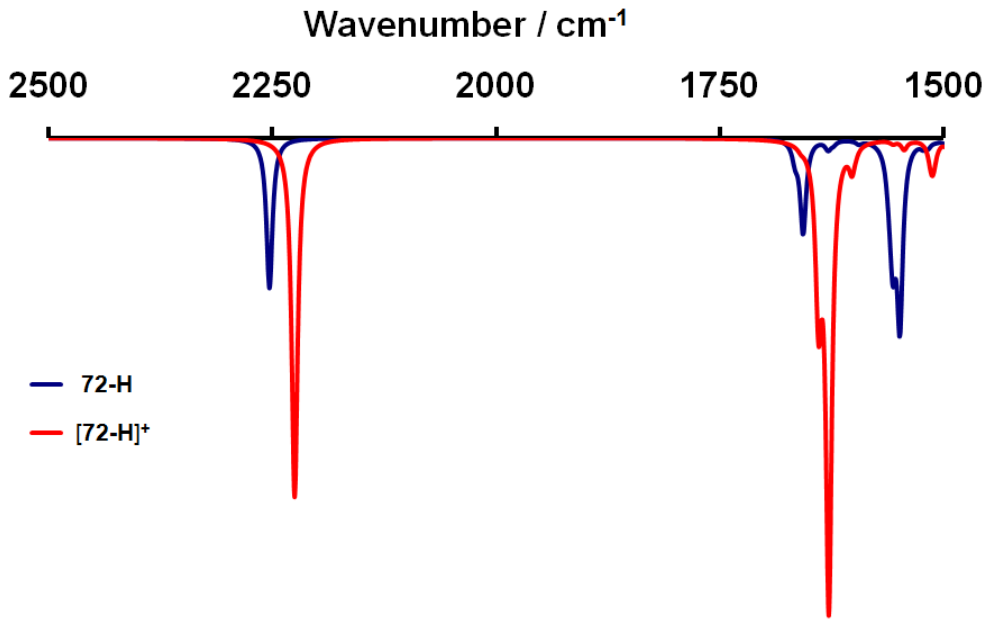

Figure **95** DFT Calculated IR spectra of [**72-H**]$^{n+}$, (n = 0, 1).

Table **66** Experimental and calculated ν(C≡C) frequencies for [**72**]$^{n+}$ and [**72-H**]$^{n+}$ (n = 0, 1).

	72 (**72-H**)	[**72**]$^{+}$ ([**72-H**]$^{+}$)
ν(C≡C) / cm^{-1}	2150 (2141)	2110 (2114)

The lack of elongation of the acetylide C≡C bond in [**72-H**]$^{+}$ when compared with the neutral model system **72-H** reflects the very small contribution of the C≡C character in the HOMO of **72-H** and the β-LUSO of [**72-H**]$^{+}$ (Chart **19**).

Table **67** Energy, occupancy and composition of frontier orbitals in the model complexes **72-H** and [**72-H**]$^+$ (B3LYP/6-31G*).

72-H										
MO										
	LUMO+4	LUMO+3	LUMO+2	LUMO+1	LUMO	HOMO	HOMO-1	HOMO-2	HOMO-3	HOMO-4
ε(eV)	0.19	0.17	-0.26	-0.37	-0.83	-4.87	-6.24	-6.65	-6.74	-6.85
Occ	0	0	0	0	0	2	2	2	2	2
%$SiMe_3$	0	0	0	0	6	1	5	0	1	0
%C_α	0	0	0	0	14	7	20	0	1	0
%C_β	0	0	0	0	6	1	12	0	1	0
%Ph	68	0	3	31	57	26	29	22	1	29
%N	0	0	1	0	1	24	2	0	0	0
%Tol_2	32	100	96	71	16	42	32	88	96	71

[**72-H**]$^+$														
MO														
	102β	102α	101β	101α	100β	100α	99β	99α	98β	98α	97β	97α	96β	96α
	β-[LUSO+3]	α-[LUSO+2]	β-[LUSO+2]	α-[LUSO+1]	β-[LUSO+1]	α-LUSO	β-LUSO	α-HOSO	β-HOSO	α-[HOSO-1]	β-[HOSO-1]	α-[HOSO-2]	β-[HOSO-2]	α-[HOSO-3]
ε(eV)	-3.65	-3.79	-3.75	-3.85	-4.19	-4.41	-7.24	-8.66	-9.24	-9.56	-9.74	-9.76	-9.89	-10.10
Occ	0	0	0	0	0	0	0	1	1	1	1	1	1	1
%$SiMe_3$	0	0	0	0	3	3	1	3	10	15	40	42	0	0
%C_α	0	0	0	0	14	12	8	11	19	16	25	24	0	0
%C_β	0	0	0	0	2	3	2	4	18	14	31	30	0	0
%Ph	3	18	41	30	59	65	26	27	25	16	4	4	4	7
%N	1	1	0	1	2	1	22	14	2	2	0	0	0	0
%Tol_2	96	82	59	70	20	16	40	40	26	36	0	0	95	93

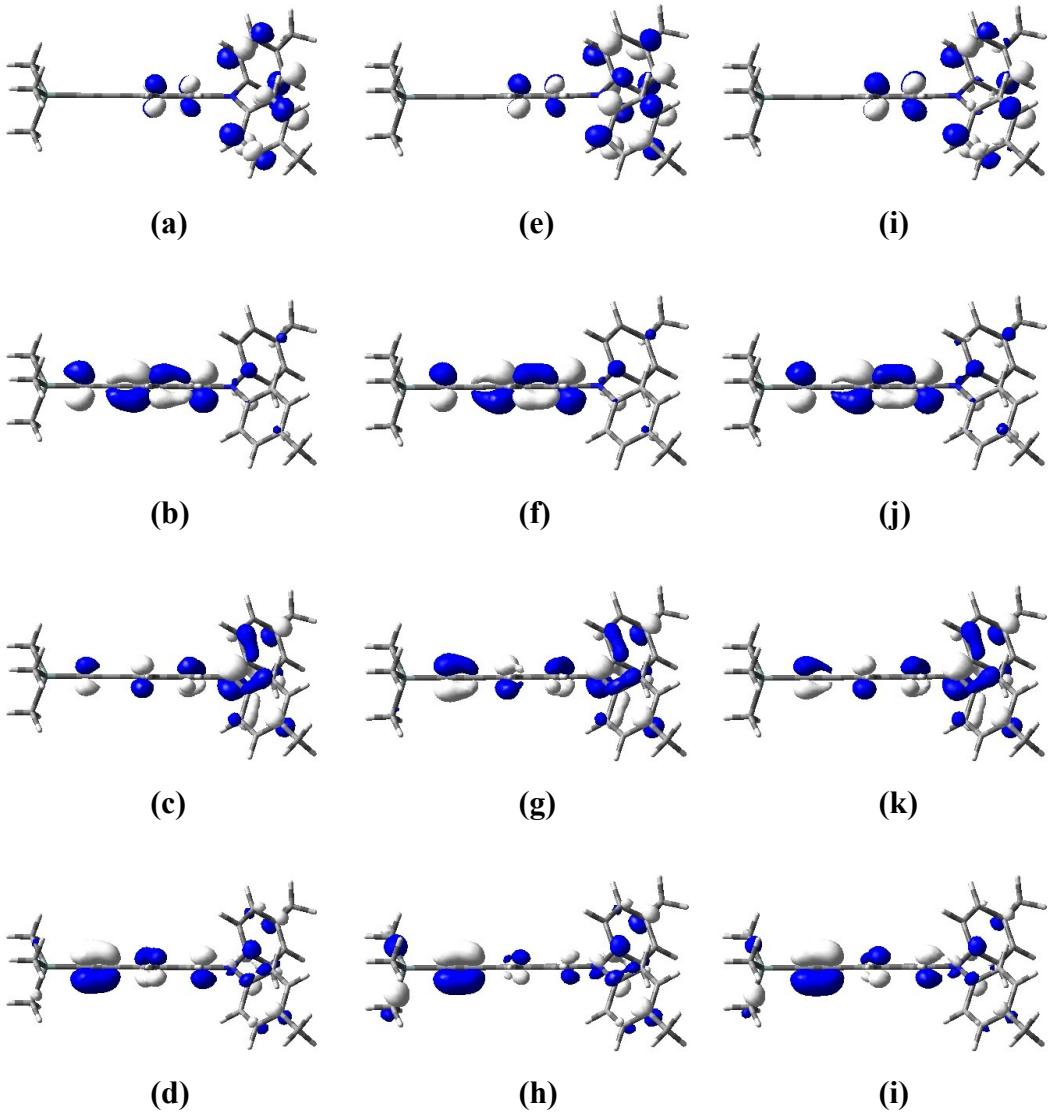

Chart **19** The (a) [LUMO+1], (b) LUMO, (c) HOMO, (d) [HOMO-1] of **72-H** together with (e) α-[LUSO+1], (f) α-LUSO, (g) α-HOSO, (h) α-[HOSO-1], and (i) β-[LUSO+2], (j) β- [LUSO+1], (k) β-LUSO, (l) β-HOSO of [**72-H**]$^{+}$ plotted with contour values of ±0.05 (e/bohr^{3})$^{1/2}$.

From Table **68**, it can be seen that 78 % of the charge in [**72-H**]$^{+}$ is localised over the triarylamine part of the ligand, with 40 % of that being localised on the nitrogen atom.

Table **68** Calculated spin densities of [**72-H**]$^{+}$.

	$SiMe_3$	C_α	C_β	C_6H_4	N	Tol $_1$	Tol $_2$
[**72-H**]$^{+}$	0.007	0.155	-0.06	0.107	0.319	0.176	0.176

6.2.6.2 UV-vis Absorptions from the TD DFT Calculations

To aid in the assignment of the electronic transitions observed in the experimental work (Section **6.2.5**) TD DFT calculations were carried out on the model ligand [**72**]$^{n+}$ (n = 0, 1). To recap the HOMO of the neutral compound **72-H** is based largely on the triarylamine fragment (92 %), with a small contribution from the acetylide (8 %), with the LUMO being predominately the phenyl π*-system and the LUMO+2 being the π*-system on the tolyl rings. The split absorption, at around 31000 cm^{-1}, in the spectrum of the neutral **72** is made up of HOMO → LUMO and HOMO → LUMO+2. Hence these transitions can be assigned as π-π* in character.

In the experimental studies, oxidation of **72** to [**72**]$^{+}$ causes the replacement of the π-π* band at 31000 cm^{-1} in the neutral species with two lower energy, structured absorptions bands growing in at 24000 to 29000 cm^{-1} and 13000 to 17000 cm^{-1}. On the basis of the TD DFT calculations the lower energy structured band can be assigned to be the transitions from the β-HOSO to β-LUSO and the β-HOSO-2 to β-LUSO, both π-π* in character, with the β-HOSO having similar composition to the HOMO. The structured absorption band at ~27000 cm^{-1} can be assigned to the transitions from the α-HOSO to α-LUSO and from the α-HOSO to α-LUSO+2.

6.2.6.3 Mono- and Tri-metallated Ligand Complex DFT Calculations

Following the theoretical study on [**72-H**]$^{n+}$ to model [**72**]$^{n+}$, the model [Fe(C≡C$C_6H_4NPh_2$)($PPh_2(CH_2)_2PPh_2$)Cp] (**78-H**) was used to mimic complex **78**, and the corresponding radical cations [**78**]$^{+/2+}$, which was done at the B3LYP/6-

31G* level, with no symmetry constraints. There is excellent agreement between the crystallographically determined structure of **78** and the DFT optimised geometry determined here (Table **69**). Figure **96** illustrates the labelling scheme, used in this section.

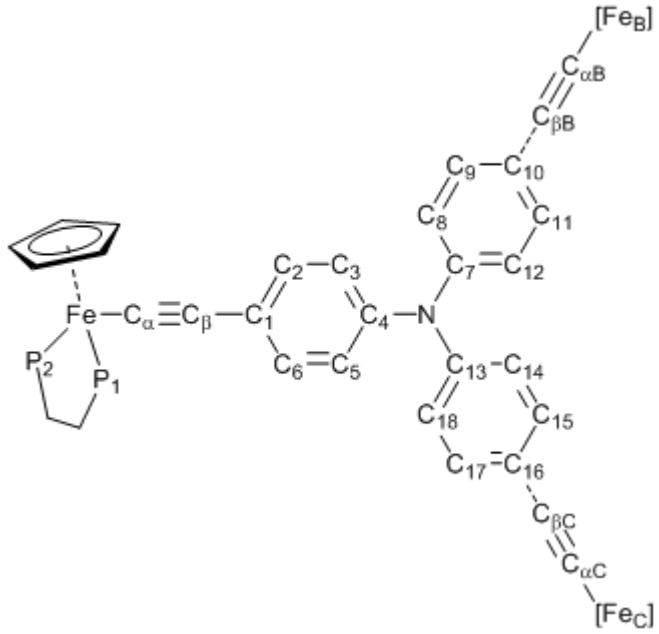

Figure **96** The labelling scheme used in the discussion of the DFT results.

Table **69** Bond lengths (Å) and bond angles (º) of crystallographically determined and optimised geometry of **78** and **78-H**.

	78	**78-H**	[**78-H**]$^+$	Δ
Fe-$Cp_{centroid}$	1.710	1.731	1.758	+0.027
Fe-$P_{1,2}$	2.1658(7)	2.213, 2.206	2.275, 2.277	+0.067
Fe-C_α	1.900(2)	1.909	1.851	-0.058
C_α-C_β	1.218(3)	1.222	1.240	+0.018
C_β-C_1	1.442(3)	1.422	1.410	-0.012
C_1-$C_{2,6}$	1.398(3) 1.411(3)	1.399	1.418	+0.019
$C_{2,6}$-$C_{3,5}$	1.383(3) 1.391(3)	1.381	1.382	~0
$C_{3,5}$-C_4	1.389(3) 1.389(3)	1.392	1.416	+0.024
C_4-N	1.435(3)	1.427	1.393	-0.034
N-C_7	1.420(3)	1.418	1.433	+0.015
N-C_{13}	1.421(3)	1.418	1.433	+0.015
P-Fe-P / °	86.58(3)	86.9	85.7	-1.2
C_4 – N – C_7 / °	119.32(17)	119.5	121.1	+1.6
C_4 – N – C_{13} / °	118.49(18)	119.6	121.2	+1.6
C_7 – N – C_{13} / °	121.83(18)	120.9	117.6	-3.3
Pitch A / °	44.0(3)	48.6	24.8	-23.8
Pitch B / °	27.1(3)	38.9	51.9	+13.0
Pitch C / °	29.2(3)	37.4	50.5	+13.1
P_1-Fe-C_1-C_6	-2.8	-21.0	35.0	+56.0

[a] Δ = [**78-H**]$^+$ - **78-H**

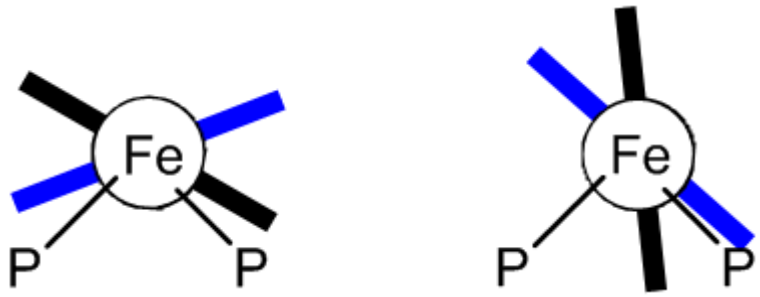

Figure **97** Schematic diagram the orientations of the phenyl plane (black line) and C_4-C_7-C_{13} plane (blue line) in the neutral **78-H** (left) and the cation [**78-H**]$^+$ (right) optimised geometries.

On oxidation to the mono-oxidised species [**78-H**]$^+$, there is an expansion of the coordination sphere of the iron centre, with the Fe-$Cp_{centroid}$ distance increasing (1.758 Å vs 1.731 Å), and the two Fe-P bond lengths increasing as well (2.276 Å vs 2.210 Å), (average length). This bond length increase leads to a decreased P-Fe-P bond angle. There is a slight increase in the acetylide $C_\alpha \equiv C_\beta$ bond length from 1.222 Å **78-H** to 1.240 Å in [**78-H**]$^+$. The Fe-C_α and C_β-C_1 bond lengths decrease on oxidation, by -0.058 and -0.012 Å respectively. There is evidence of evolution of quinoidal character in the calculated bond lengths of the cation [**78-H**]$^+$ along the metal-acetylide-phenyl ring-nitrogen skeleton (Figure **98**, Table **69**). These structural changes are consistent with oxidation of related metal acetylides. [227]

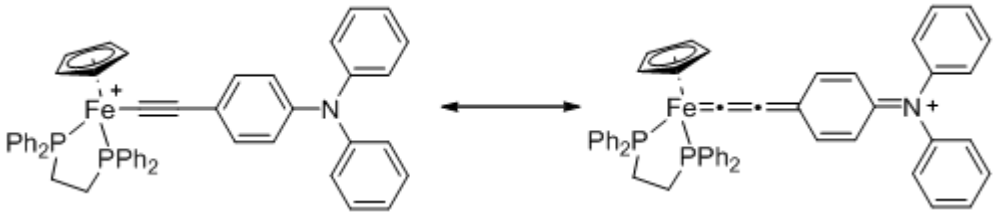

Figure **98** Possible resonance forms showing the evolution of quinoidal character in the cation [**78-H**]$^+$.

Other notable changes to the structure of the complex on oxidation occur within the arylamine fragment. On oxidation to [**78-H**]$^+$, the pitch of the *para*- substituted phenyl ring decrease from 48.6 ° to 28.4 °, probably to maximise delocalisation of the positive charge. This decrease in pitch pushes the tolyl rings on the amine

closer together (C_7-N-C_{13}: **78-H** 120.9 °, [**78-H**]$^+$ 117.6 °), which in turn causes the tolyl rings to twist further out of the (C_4-C_7-C_{13}) plane, hence an increased pitch (52 ° vs 39 °).

At the level of theory employed, the aromatic substituent in the neutral system **78-H** lie in the plane approximately parallel to one of the Fe-P bonds. In contrast, the aromatic substituent in the mono-oxidised species [**78-H**]$^+$ are found approximately bisecting the P-Fe-P angle. On oxidation to the dication [**78-H**]$^{2+}$, there are two possible spin configurations, a low spin singlet (LS) and high spin triplet (HS). Table **70** compares the two optimised geometries with that of [**78-H**]$^+$. Depending upon the spin, singlet or triplet, of the dication, the aromatic substituent can either lie bisecting the P-Fe-P angle, like the mono-oxidised species [**78-H**]$^+$, or lie in the plane approximately parallel to the Cp ring, like the neutral species **78-H**.

Table **70** Selected bond lengths (Å) and angles (°) of the optimised geometries of [**78-H**]$^{+}$, LS-[**78-H**]$^{2+}$ and HS-[**78-H**]$^{2+}$.

	[**78-H**]$^{+}$	LS-[**78-H**]$^{2+}$	Δ_1[a]	HS-[**78-H**]$^{2+}$	Δ_2[b]
Fe-$Cp_{centroid}$	1.758	1.754	-0.004	1.769	+0.011
Fe-$P_{1,2}$ (aver)	2.276	2.287	+0.011	2.313	+0.026
Fe-C_α	1.851	1.775	-0.076	1.882	+0.031
C_α-C_β	1.240	1.265	+0.025	1.236	-0.004
C_β-C_1	1.410	1.370	-0.040	1.410	~0
C_1-$C_{2,6}$	1.418	1.441	+0.021	1.421	+0.003
$C_{2,6}$-$C_{3,5}$	1.382	1.364	-0.018	1.379	-0.003
$C_{3,5}$-C_4	1.416	1.437	+0.021	1.418	+0.002
C_4-N	1.393	1.358	-0.035	1.394	~0
N-C_7	1.433	1.440	+0.007	1.424	-0.009
N-C_{13}	1.433	1.440	+0.007	1.424	-0.009
P-Fe-P / °	85.7	85.2	-0.5	85.0	-0.7
C_4 – N – C_7 / °	121.1	121.7	+0.6	120.6	-0.5
C_4 – N – C_{13} / °	121.2	121.7	+0.5	120.8	-0.4
C_7 – N – C_{13} / °	117.6	116.6	-1.0	118.6	+1.0
Pitch A / °	24.8	20.2	-4.6	31.2	+6.4
Pitch B / °	51.9	52.1	+0.2	43.8	-8.1
Pitch C / °	50.5	49.7	-0.8	42.3	-8.2
P_1-Fe-C_1-C_6	35.0	41.4	+6.4	-42.6	-77.6

[a] Δ_1 = LS-[**78-H**]$^{2+}$ - [**78-H**]$^{+}$.
[b] Δ_2 = HS-[**78-H**]$^{2+}$ - [**78-H**]$^{+}$.

Frequencies calculation were carried out at the same level of theory used in optimising the geometries of **78-H**, [**78-H**]$^{+}$, LS-[**78-H**]$^{2+}$ and HS-[**78-H**]$^{2+}$, with the calculated ν(C≡C) frequencies in Table **71**. There is very good agreement with the

experimental ν(C≡C) frequencies and the calculated ν(C≡C) frequencies for the neutral species **78-H** and the cationic species [**78-H**]$^{+}$. Of the two calculated ν(C≡C) frequencies for the dication [**78-H**]$^{2+}$, the ν(C≡C) frequencies calculated for the LS dication configuration provides a better fit to the experimental data (Figure **99**).

Table **71** Calculated ν(C≡C) frequencies of **78-H**, [**78-H**]$^{+}$, LS-[**78-H**]$^{2+}$ and HS-[**78-H**]$^{2+}$.

	78-H	[**78-H**]$^{+}$	LS-[**78-H**]$^{2+}$	HS-[**78-H**]$^{2+}$
ν(C≡C) / cm^{-1}	2065	1976	1895	1998

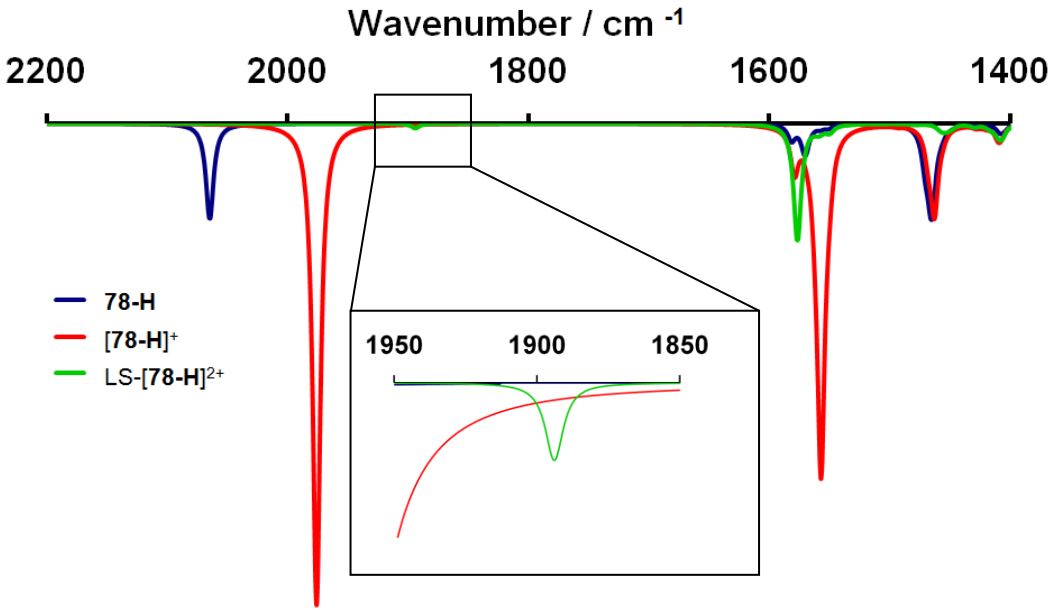

Figure **99** Calculated IR spectra of [**78-H**]$^{n+}$ (n = 0, 1, 2).

Table **72** Energy, occupancy and composition of frontier orbitals in the model complexes **78-H** and [**78-H**]$^+$ (B3LYP/6-31G*).

78-H										
MO										
	LUMO+6	LUMO+3	LUMO+2	LUMO+1	LUMO	HOMO	HOMO-1	HOMO-2	HOMO-3	HOMO-4
ε(eV)	-0.15	-0.49	-0.56	-0.64	-0.74	-4.23	-4.54	-4.93	-5.24	-6.06
Occ	0	0	0	0	0	2	2	2	2	2
%Fe	4	5	5	12	2	27	44	47	37	46
%Cp	0	2	1	5	1	3	6	8	9	6
%dppe	12	93	92	82	97	2	5	10	8	10
%C_α	10	0	0	0	0	9	7	0	6	12
%C_β	1	0	0	0	0	15	21	4	11	3
%Ph	53	0	2	0	0	21	6	4	6	14
%N	1	0	0	0	0	9	4	9	6	1
%Tol_2	19	0	0	0	0	14	8	18	16	8

[**78-H**]$^+$														
MO														
	209β	209α	208β	208α	207β	207α	206β	206α	205β	205α	204β	204α	203β	203α
	β-[LUSO+3]	α-[LUSO+2]	β-[LUSO+2]	α-[LUSO+1]	β-[LUSO+1]	α-LUSO	β-LUSO	α-HOSO	β-HOSO	α-[HOSO-1]	β-[HOSO-1]	α-[HOSO-2]	β-[HOSO-2]	α-[HOSO-3]
ε(eV)	-3.11	-3.13	-3.17	-3.35	-3.53	-3.83	-5.30	-7.02	-7.15	-8.17	-8.17	-8.42	-8.47	-8.66
Occ	0	0	0	0	0	0	0	1	1	1	1	1	1	1
%Fe	9	2	20	39	45	47	44	4	12	13	47	36	9	3
%Cp	3	1	6	15	16	19	7	1	2	5	2	2	1	2
%dppe	87	96	71	38	39	34	4	1	2	8	3	3	6	5
%C_α	1	0	1	5	0	0	3	9	4	8	13	17	15	0
%C_β	0	0	1	2	0	0	17	4	2	16	31	35	3	1
%Ph	0	1	0	1	0	0	17	32	23	13	3	4	19	1
%N	0	0	0	0	0	0	5	21	21	3	0	0	0	0
%Tol_2	0	0	0	0	0	0	4	29	34	34	0	2	47	87

Table **73** Energy, occupancy and composition of frontier orbitals in the model complexes LS-[**78-H**]$^{2+}$ and HS-[**78-H**]$^{2+}$ (B3LYP/6-31G*).

LS -[**78-H**]$^{2+}$										
MO										
	LUMO+4	LUMO+3	LUMO+2	LUMO+1	LUMO	HOMO	HOMO-1	HOMO-2	HOMO-3	HOMO-4
ε(eV)	-5.47	-5.72	-6.03	-6.18	-8.82	-10.50	-11.00	-11.05	-11.13	-11.15
Occ	0	0	0	0	0	2	2	2	2	2
%Fe	0	47	8	47	26	16	13	13	2	33
%Cp	0	18	2	19	4	4	6	2	2	2
%dppe	0	26	2	32	4	7	77	69	96	40
%C_α	0	5	14	0	6	1	1	3	0	5
%C_β	0	3	1	0	14	6	1	11	0	18
%Ph	78	0	57	1	26	14	1	1	0	2
%N	0	0	4	0	9	10	0	0	0	0
%Tol_2	21	0	12	0	10	41	2	0	0	2

HS-[**78-H**]$^{2+}$														
MO														
	209β	209α	208β	208α	207β	207α	206β	206α	205β	205α	204β	204α	203β	203α
	β-[LUSO+4]	α-[LUSO+2]	β-[LUSO+3]	α-[LUSO+1]	β-[LUSO+2]	α-LUSO	β-[LUSO+1]	α-HOSO	β-LUSO	α-[HOSO-1]	β-HOSO	α-[HOSO-2]	β-[HOSO-1]	α-[HOSO-3]
ε(eV)	-5.59	-5.83	-5.77	-6.27	-6.16	-6.77	-7.52	-10.04	-8.71	-10.93	-10.53	-11.04	-10.98	-11.19
Occ	0	0	0	0	0	0	0	1	0	1	1	1	1	1
%Fe	16	5	38	48	51	46	63	4	4	11	25	8	24	3
%Cp	6	2	12	21	19	23	11	1	0	12	2	3	8	1
%dppe	6	2	24	18	30	32	8	1	0	58	2	14	64	86
%C_α	11	12	6	8	0	0	1	10	7	4	9	10	2	2
%C_β	2	2	2	3	0	0	16	5	2	12	18	14	2	2
%Ph	44	61	13	2	0	0	1	29	27	2	18	14	0	86
%N	2	2	1	0	0	0	0	16	22	0	3	3	0	0
%Tol_2	14	14	4	0	0	0	0	36	38	2	24	35	0	4

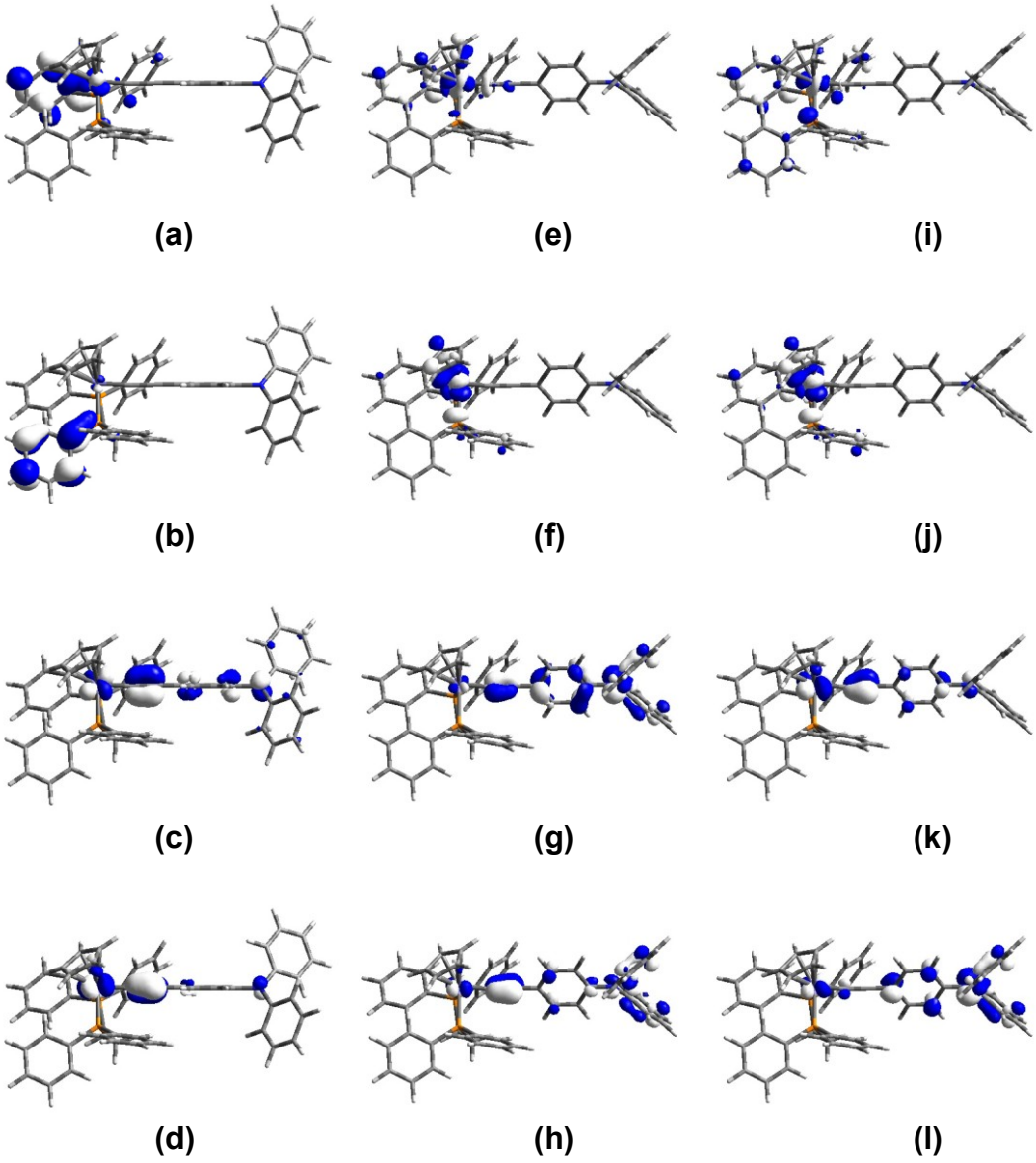

Chart **20** The (a) [LUMO+1], (b) LUMO, (c) HOMO, (d) [HOMO-1] of **78-H** together with (e) α-[LUSO+1], (f) α-LUSO, (g) α-HOSO, (h) α-[HOSO-1] and (i) β-[LUSO+2], (j) β-[LUSO+1], (k) β-LUSO, (l) β-HOSO of [**78-H**]$^{+}$ (B3LYP/6-31G*), plotted with contour values of ±0.05 $(e/bohr^3)^{1/2}$.

Table **72** and Table **73**, summarises the composition of the frontier orbitals of **78-H** and its oxidised forms [**78-H**]$^{+}$, LS- and HS-[**78-H**]$^{2+}$, with representative contour plots of key orbitals of **78-H** and [**78-H**]$^{+}$ illustrated in Chart **20**. In the neutral system, the HOMO and HOMO-1 are based mainly on the Fe-C≡C π system, with the HOMO-1 consisting to the Fe-C≡C π manifold parallel to the plane of the phenyl ring, and the HOMO the Fe-C≡C π manifold perpendicular to the phenyl ring, where

the π system includes both the phenyl and nitrogen atom. The LUMO and the LUMO+1 are largely phosphine π* and Fe – Cp antibonding in character, respectively. The phenyl π* system comprises the LUMO+6 (Figure **100**), 0.6 eV above the LUMO.

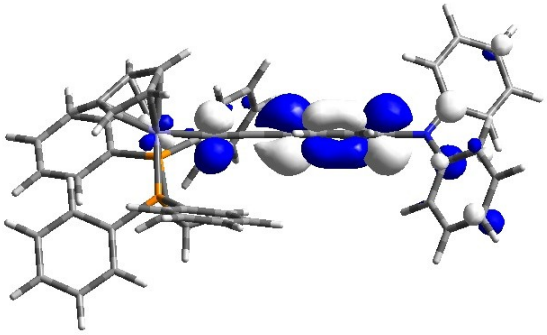

Figure **100** The LUMO+6 of **78-H** plotted with contour values of ± 0.04 $(e/bohr^3)^{1/2}$.

In the cation species [**78-H**]$^+$ the α-HOSO and the β-LUSO have similar orbital character ($FeC_2PhNTol_2$ π-system) to the HOMO of the neutral **78-H**, (Table **74**), but with the β-LUSO having more metal character and less $NTol_2$, than the HOMO. The opposite is true of the α-HOSO.

Table **74** Composition of the HOMO of **78-H** and the α-HOSO and β-LUSO of [**78-H**]$^+$.

		% Fe	% Cp	% dppe	% C_α	% C_β	% Ph	% N	% Tol_2
78-H	HOMO	27	3	2	9	15	21	9	14
[**78-H**]$^+$	α-HOSO	4	1	1	9	4	32	21	29
[**78-H**]$^+$	β-LUSO	44	7	4	3	17	17	5	4

The HOMO of the LS-[**78-H**]$^{2+}$ (Chart **21**) is located mainly on the $NTol_2$ portion of the complex, with some metal and phenyl character, with a node at the C_α. The LUMO of the LS-[**78-H**]$^{2+}$, has a similar composition to the β-LUSO of the [**78-H**]$^+$, but less metal character (26 % vs 44 %) and more phenyl ring character (26 % vs 17 %).

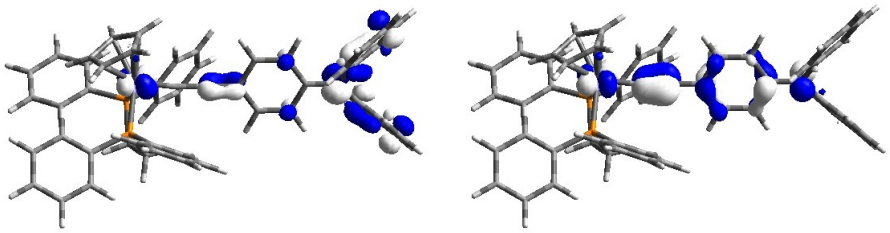

Chart **21** The HOMO (left) and LUMO (right) of LS-[**78-H**]$^{2+}$ plotted with contour values of ±0.05 (e/bohr^3)$^{1/2}$.

The spin density calculation on the optimised geometry of [**78-H**]$^+$ (Table **75**), compared to spin density calculations of the optimised [**72-H**]$^+$ supports the general conclusion that with the **78** complex, the first oxidation occurs on the metal centre and the second occurs on the arylamine substituent.

Table **75** Calculated spin densities of [**72-H**]$^+$, [**78-H**]$^+$ and using B3LYP / 6-31G*.

	Fe/Si	Cp	P_1	P_2	C_α	C_β	C_6H_4	N	Tol $_1$	Tol $_2$
[**72-H**]$^+$	-0.057	-	-	-	0.155	-0.061	0.228	0.319	0.176	0.176
[**78-H**]$^+$	0.830	-0.052	-0.032	-0.035	-0.091	0.206	0.081	0.056	0.012	0.012

From Table **65** and Table **69** it can be seen that B3LYP/6-31G* gave good agreement between the experimental and theoretical data, for both **72-H** and **78-H**. To facilitate the comparison of results between all three sets of model system, the same level of theory was used in the modelling the trimetallic complex **79-H**. However to make the DFT calculations for the tri-metallic complex manageable a simplified system [{Fe(C≡CC_6H_4-)($PH_2(CH_2)_2PH_2$)Cp}$_3$N]$^{n+}$ was used [**79-H**]$^{n+}$ (n = 0, 1, 2, 3). To help the reader, Figure **96** illustrates the labelling scheme used in this section.

The optimised geometry of the neutral tris- iron complex **79-H** has C_3 symmetry around the nitrogen atom at the centre of the complex. Table **76** contains selected bond lengths and angles of **79-H** compared to the mono metallic analogy **78-H**. The spatial geometry of each of the three [Fe]C≡CC_6H_4- arms is in a similar geometry to that of the mono metallic **78-H** complex, with any bond length differences due to the change of phosphine ligands from dppe to dHpe.

Frequency calculations on the symmetric **79-H** resulted in a single calculated ν(C≡C) frequency of 2071 cm^{-1}, which is similar to that of the neutral **78-H** 2065 cm^{-1}.

Table **76** Selected bond lengths (Å) and angles (°) of **78-H** and **79-H**.

	78-H	**79-H**
Fe-$Cp_{centroid}$	1.731	1.712
Fe-$P_{1,2}$ (aver.)	2.210	2.185
Fe-C_α	1.909	1.908
C_α-C_β	1.222	1.231
C_β-C_1	1.422	1.426
C_1-$C_{2,6}$	1.399	1.412
$C_{2,6}$-$C_{3,5}$	1.381	1.389
$C_{3,5}$-C_4	1.392	1.405
C_4-N	1.427	1.420
N-C_7	1.418	
N-C_{13}	1.418	
P-Fe-P / °	86.9	86.4
C_4 – N – C_7 / °	119.5	120.0
C_4 – N – C_{13} / °	119.6	
C_7 – N – C_{13} / °	120.9	
Pitch A / °	48.6	41.5
Pitch B / °	38.9	41.3
Pitch C / °	37.4	42.2
P_1-Fe-C_1-C_6	-21.0	-18.3

Table **77** summaries the occupancies, compositions and energies of the frontier orbital of **79-H**, with some representative molecular orbitals of **79-H** illustrated in Chart **22**. The HOMO is the π-system is delocalised evenly over the entire $\{[Fe]C{\equiv}CC_6H_4\}_3N$ skeleton. The LUMO is metal-dppe-Cp antibonding on one of the metal centres. The LUMO+1, and the near degenerate LUMO+2 are the π*-system, with the LUMO+1 on two of the $[Fe]C{\equiv}CC_6H_4$ arms, and the LUMO+2 based mainly on the other of the three arms.

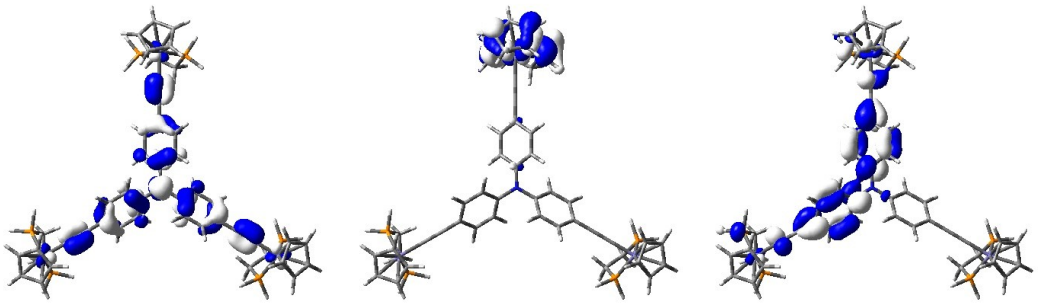

Chart **22** The HOMO (left), the LUMO (middle) and the LUMO+1 (right) of **79-H** plotted with contour values of ± 0.03 $(e/bohr^3)^{1/2}$, calculated using B3LYP/6-31G*.

On modelling the cationic species $[\mathbf{79\text{-}H}]^+$, the optimised geometry obtained was symmetric, with all three FeC_2Ph arms in the same spatial conformation, which is not in agreement with the localised state inferred by the IR results. DFT methods, even those using common hybrid functionals such as B3LYP, often fail to accurately model charge separated states. The origin of this can be traced to the failure of DFT methods to adequately model electron-hole correlations. [42, 45]

Given this failure at the B3LYP/6-31G* level, the modelling was attempted using an alternative functional with more Hartree Fock character (MPW1K/6-31G*). However to facilitate the comparison of the results of the mono-metallic **78-H** and the trimetallic **79-H**, it is required that the monometallic **78-H** be modelled using the same level. From Table **78** it can be seen that there is good agreement between the optimised geometries of **78-H** using both B3LYP/6-31G* and MPW1K/6-31G* and crystallographically determined geometry of **78**.

Table **77** Energy, occupancy and composition of frontier orbitals in the complexes **79-H**, using B3LYP/6-31G*.

79-H												
MO	LUMO+5	LUMO+4	LUMO+3	LUMO+2	LUMO+1	LUMO	HOMO	HOMO-1	HOMO-2	HOMO-3	HOMO-4	HOMO-5
ε(eV)	0.24	-0.05	-0.13	-0.16	-0.17	-0.18	-3.86	-4.46	-4.51	-4.66	-4.78	-4.83
Occ	0	0	0	0	0	0	2	2	2	2	2	2
%Fe (A)	23	0	0	2	8	52	4	1	21	17	8	25
%Cp (A)	2	0	0	0	2	18	0	0	3	3	1	3
%dppe (A)	16	0	0	2	6	24	0	0	2	1	1	2
%C_α (A)	0	0	0	2	5	0	5	0	6	2	2	7
%C_β (A)	1	0	0	0	1	0	3	0	12	9	4	15
%Ph (A)	1	0	0	10	30	3	15	1	9	1	2	7
%Fe (B)	17	0	55	2	5	0	5	14	18	10	18	19
%Cp (B)	1	0	20	0	0	0	0	2	3	2	2	2
%dppe (B)	13	0	23	2	5	0	0	1	1	1	1	1
%C_α (B)	0	0	0	2	5	0	5	3	3	1	4	4
%C_β (B)	1	0	0	1	1	0	3	7	9	5	9	9
%Ph (B)	2	0	1	13	29	1	15	5	4	1	4	4
%Fe (C)	9	56	0	6	0	0	5	32	5	22	22	1
%Cp (C)	1	20	0	0	0	0	0	5	1	3	2	0
%dppe (C)	8	24	0	6	0	0	0	2	0	2	2	0
%C_α (C)	0	0	0	7	0	0	5	5	1	4	4	0
%C_β (C)	1	0	0	2	0	0	3	16	2	11	10	0
%Ph (C)	3	0	0	42	1	0	16	7	1	4	5	0
%N	1	0	0	1	1	0	15	0	0	1	0	0

Table **78** Comparison of selected bond lengths (Å) and angles (°) of **78** and optimised geometry of **78-H** using B3LYP/6-31G* and MPW1K/6-31G*.

	78	**78-H**	**78-H**
		B3LYP/6-31G*	MPW1K/6-31G*
Fe-$Cp_{centroid}$	1.710	1.731	1.710
Fe-$P_{1,2}$	2.1658(7)	2.213, 2.206	2.213, 2.206
Fe-C_{α}	1.900(2)	1.909	1.909
C_{α}-C_{β}	1.218(3)	1.222	1.222
C_{β}-C_1	1.442(3)	1.422	1.422
C_1-$C_{2,6}$	1.398(3) 1.411(3)	1.399	1.399
$C_{2,6}$-$C_{3,5}$	1.383(3) 1.391(3)	1.381	1.381
$C_{3,5}$-C_4	1.389(3) 1.389(3)	1.392	1.391
C_4-N	1.435(3)	1.427	1.412
N-C_7	1.420(3)	1.418	1.403
N-C_{13}	1.421(3)	1.418	1.403
P-Fe-P / °	86.58(3)	86.9	86.3
C_4 – N – C_7 / °	119.32(17)	119.5	119.5
C_4 – N – C_{13} / °	118.49(18)	119.6	119.5
C_7 – N – C_{13} / °	121.83(18)	120.9	121.0
Pitch A / °	44.0(3)	48.6	48.6
Pitch B / °	27.1(3)	38.9	37.4
Pitch C / °	29.2(3)	37.4	36.6
P_1-Fe-C_1-C_6	-2.8	-21.0	-23.3

Table **79** Comparison of experimental and calculated ν(C≡C) frequencies of [**78**]$^{n+}$ and [**78-H**]$^{n+}$ (n = 0, 1, 2) modelled using B3LYP/6-31G* and MPW1K/6-31G*.

	78	**78-H** B3LYP/6-31G*	**78-H** MPW1K/6-31G*
Neutral	2060	2065	2065
Cation	1962	1976	2014
Dication	1860	LS(1895), HS(1998)	LS(1875), HS(2029)*

* includes a negative frequency.

Table **79** shows that there is good agreement between the experimental IR data and the calculated frequencies of [**78-H**]$^{n+}$ (n = 0, 1, 2) for both functional and basis sets used. The only exception is with the modelling of the cationic species of [**78-H**]$^{+}$, when using the MPW1K/6-31G* level, which calculates a ν(C≡C) frequency of (2014 cm^{-1}), which is high compared with the experimental data. However, there is generally good agreement between the two functional basis sets used and the experimental data, which is further seen in the similar energies and compositions of the frontier molecular orbitals of the neutral **78-H** and the LS[**78-H**]$^{2+}$ (Table **80** and Table **81** compared with Table **72** and Table **73**), and bodes well for the use of the MPW1K/6-31G* level to be used to model the [**79-H**]$^{n+}$ (n = 0 → 4).

Like with the B3LYP/6-31G*, the HOMO and HOMO-1 in the neutral system **78-H**, using MPW1K/6-31G* are based mainly on the Fe-C≡C π system, with the HOMO-1 consisting to the Fe-C≡C π manifold parallel to the plane of the phenyl ring, and the HOMO the Fe-C≡C π manifold perpendicular to the phenyl ring, where the π system includes both the phenyl and nitrogen atom. Both of the LUMO and the LUMO+1 are largely phosphine π* in character. The phenyl π* system comprises the LUMO+5 and LUMO+6, ~0.5 eV above the LUMO.

Table **80** Energy, occupancy and composition of frontier orbitals in the model complexes **78-H** using MPW1K/6-31G*.

78-H										
MO										
	LUMO+4	LUMO+3	LUMO+2	LUMO+1	LUMO	HOMO	HOMO-1	HOMO-2	HOMO-3	HOMO-4
ε(eV)	0.44	0.31	0.21	0.13	-0.02	-5.30	-5.89	-6.24	-6.51	-7.39
Occ	0	0	0	0	0	2	2	2	2	2
%Fe	4	6	2	3	2	9	38	36	33	8
%Cp	1	2	1	1	0	1	8	4	22	10
%dppe	93	92	95	93	98	1	8	5	14	58
$\%C_{\alpha}$	0	0	0	0	0	11	10	6	7	11
$\%C_{\beta}$	0	0	0	1	0	10	27	13	7	7
%Ph	1	0	2	2	0	28	3	6	6	5
%N	0	0	0	0	0	15	2	8	2	0
$\%Tol_2$	0	0	0	0	0	26	6	22	8	2

Table **81** Energy, occupancy and composition of frontier orbitals in the model complexes LS-[**78-H**]$^{2+}$ using MPW1K/6-31G*.

LS-[**78-H**]$^{2+}$										
MO										
	LUMO+4	LUMO+3	LUMO+2	LUMO+1	LUMO	HOMO	HOMO-1	HOMO-2	HOMO-3	HOMO-4
ε(eV)	-4.68	-4.79	-5.14	-5.37	-8.53	-11.40	-12.16	-12.22	-12.32	-12.33
Occ	0	0	0	0	0	2	2	2	2	2
%Fe	0	24	41	9	23	12	3	1	1	2
%Cp	0	9	17	1	4	3	4	2	1	0
%dppe	1	62	33	11	5	5	84	89	97	10
$\%C_{\alpha}$	0	2	1	13	7	1	1	1	0	0
$\%C_{\beta}$	0	3	0	1	16	6	1	1	0	0
%Ph	79	1	5	51	30	15	1	1	0	2
%N	0	0	0	4	8	10	0	0	0	0
$\%Tol_2$	20	0	2	10	8	47	6	4	0	84

There is good agreement between the two optimised geometries of **79-H** using B3LYP/6-31G* and MPW1K/6-31G* (Table **82**) and the calculated ν(C≡C) frequencies of **79-H** at these levels give good agreement with the experimental IR data (Table **83**).

Table **82** Selected bond lengths (Å) and angles (°) of **79-H** using B3LYP/6-31G* and MPW1K/6-31G*.

	79-H	**79-H**
	B3LYP/6-31G*	MPW1K/6-31G*
Fe-$Cp_{centroid}$	1.712	1.693
Fe-$P_{1,2}$ (aver)	2.185	2.185
Fe-C_{α}	1.908	1.909
C_{α}-C_{β}	1.231	1.221
C_{β}-C_1	1.426	1.423
C_1-$C_{2,6}$	1.411	1.398
$C_{2,6}$-$C_{3,5}$	1.389	1.380
$C_{3,5}$-C_4	1.405	1.394
C_4-N	1.420	1.405
Aryl-N-Aryl / °	120.0	120.0
Pitch A / °	41.0	40.3
Pitch B / °	41.7	40.8
Pitch C / °	40.8	39.3
P_1-Fe-C_1-C_6	-18.3	-20.6

Table **83** Experimental and calculated ν(C≡C) frequencies of **79** and **79-H**.

	Experimental	B3LYP/6-31G*	MPW1K/6-31G*
ν(C≡C) / cm^{-1}	2060	2071	2068

Table **84** MPW1K 6-31G* Molecular Contributions **79-H**.

79-H										
MO										
	LUMO+4	LUMO+3	LUMO+2	LUMO+1	LUMO	HOMO	HOMO-1	HOMO-2	HOMO-3	HOMO-4
ε(eV)	1.09	1.04	0.95	0.48	0.46	-4.85	-5.79	-5.83	-6.13	-6.22
Occ	0	0	0	0	0	2	2	2	2	2
%Fe (A)	4	14	0	1	3	2	6	12	28	11
%Cp (A)	0	0	0	0	0	0	1	2	5	1
%dppe (A)	4	12	0	2	4	0	1	1	3	1
%C_α (A)	0	0	0	2	6	5	4	7	8	5
%C_β (A)	0	1	0	1	2	2	6	11	20	9
%Ph (A)	0	2	33	13	34	18	7	11	3	3
%Fe (B)	29	20	0	1	3	2	2	13	7	15
%Cp (B)	1	0	0	0	0	0	0	2	1	3
%dppe (B)	25	19	0	2	4	0	0	2	1	2
%C_α (B)	0	0	0	2	6	5	2	9	2	6
%C_β (B)	0	1	0	1	2	2	3	13	5	12
%Ph (B)	2	1	33	12	34	18	3	15	1	3
%Fe (C)	19	14	0	4	0	3	18	0	6	12
%Cp (C)	0	0	0	0	0	0	3	0	1	2
%dppe (C)	16	13	0	5	0	0	2	0	1	1
%C_α (C)	0	0	0	8	0	5	10	0	1	4
%C_β (C)	0	1	0	2	0	2	16	0	4	9
%Ph (C)	1	2	33	45	1	18	16	1	1	2
% N	0	0	0	1	1	16	0	0	1	0

Table **85** summaries the occupancies, compositions and energies of the frontier orbitals of **79-H**, with some representative molecular orbitals of **79-H** illustrated in Chart **23** and Figure **101**. The HOMO of **79-H** computed using the MPW1K/6-31G* level of theory is very similar to that computed with B3LYP/6-31G*, where the π-system is delocalised evenly over the entire $\{[Fe]C{\equiv}CC_6H_4\}_3N$ skeleton. The LUMO and LUMO+1 are the π*-system, with the LUMO on two of the $[Fe]C{\equiv}CC_6H_4$ arms, and the LUMO+1 based mainly on the other of the three arms. Interestingly the LUMO+2 is comprised of just the π*-system of the three phenyl rings.

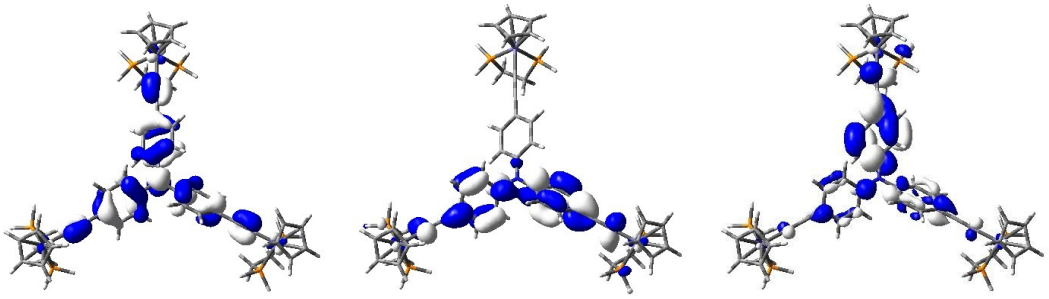

Chart **23** The HOMO (left), LUMO (middle), and the LUMO+1 (right) of **79-H** plotted with contour values of ± 0.03 $(e/bohr^3)^{1/2}$, calculated using MPW1K/6-31G*.

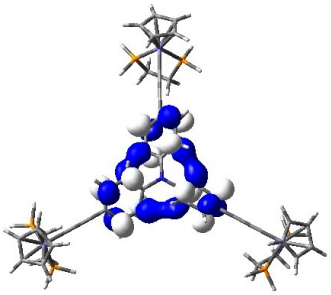

Figure **101** The LUMO+2 of **79-H**, plotted with contour values of ± 0.03 $(e/bohr^3)^{1/2}$.

However on modelling the cation $[\mathbf{79\text{-}H}]^+$ with MPW1K/6-31G*, the calculations fail to find a minimum. This is perhaps not surprising, since there were problems using this level of theory in modelling the monocation of the mono-iron complex $[\mathbf{78\text{-}H}]^+$. More success was gained on modelling the $[\mathbf{79\text{-}H}]^{2+}$ with the calculations

finding a preference for HS-[**79-H**]$^{2+}$. Calculations on the LS-[**79-H**]$^{2+}$ did not give rise to a stable minimum. On viewing the optimised geometry of HS-[**79-H**]$^{2+}$ (Table **85**), it can be seen that there are two different configurations of the three [Fe]C≡CC_6H_4 arms, most notable is the orientation of the phenyl rings with respect to the Fe-P_1 bonds.

Table **85** Selected computational determined bond lengths (Å) and angles (°) of **79-H** and HS-[**79-H**]$^{2+}$ using MPW1K/6-31G*.

	79-H	HS-[**79-H**]$^{2+}$		
		Arm A	Arm B	Arm C
Fe-$Cp_{centroid}$	1.693	1.696	1.716	1.717
Fe-$P_{1,2}$ (aver)	2.185	2.188	2.241	2.233
Fe-C_α	1.909	1.901	1.877	1.877
C_α-C_β	1.221	1.223	1.223	1.223
C_β-C_1	1.423	1.417	1.417	1.416
C_1-$C_{2,6}$	1.398	1.401	1.399	1.399
$C_{2,6}$-$C_{3,5}$	1.380	1.380	1.377	1.376
$C_{3,5}$-C_4	1.394	1.389	1.398	1.399
C_4-N	1.405	1.425	1.395	1.391
P-Fe-P / °	85.8	85.7	83.9	83.9
Pitch / °	40.3, 40.8, 39.3	61.4	33.1	30.3
P_1-Fe-C_1-C_6	-20.6	-25.2	37.2	29.1

Frequency calculations on the optimised geometry of the HS-[**79-H**]$^{2+}$, result in two sets of ν(C≡C) frequencies (Table **86**), one at 2060 cm^{-1}, corresponding to the C≡C bond of the [Fe]C≡CC_6H_4 arm in a similar configuration state as the neutral species **79-H**. The other calculated ν(C≡C) frequencies are at 2010 and 2018 cm^{-1}, comprising a broad band, are from the two oxidised arms.

Table **86** Experimental and calculated ν(C≡C) frequencies for [**79**]$^{0/2+}$ and HS[**79-H**]$^{0/2+}$.

	Experimental / cm^{-1}		Calculated / cm^{-1}	
	ν(C≡C)	$\nu(C\equiv C)^{+}$	ν(C≡C)	$\nu(C\equiv C)^{+}$
Neutral	2060	-	2068	-
Dication	2056	1962	2060	2010, 2018

Table **87** summarises the composition of the frontier orbitals of HS-[**79-H**]$^{2+}$, with a selection of key orbitals illustrated in Chart **24**. Both the α-HOSO and the β-HOSO have a similar composition, localised on the neutral iron acetylide aryl framework and are derived from the mixing of the metal d orbital and the acetylide π-system perpendicular to the phenyl ring. The α-HOSO-1 and the β-HOSO-1 are also similar to one another, but involve the acetylide π-system, on the neutral arm, parallel to the phenyl ring, and have more metal character than α-HOSO and β-HOSO, (37 % and 37 % compared to 30 % and 36 %). The α- and β-LUSOs and higher alternate in being localised on one of other of the metal centres of the oxidised arms, varying from consisting of either metal – Cp antibonding, metal – dHpe antibonding or the phenyl π*-system.

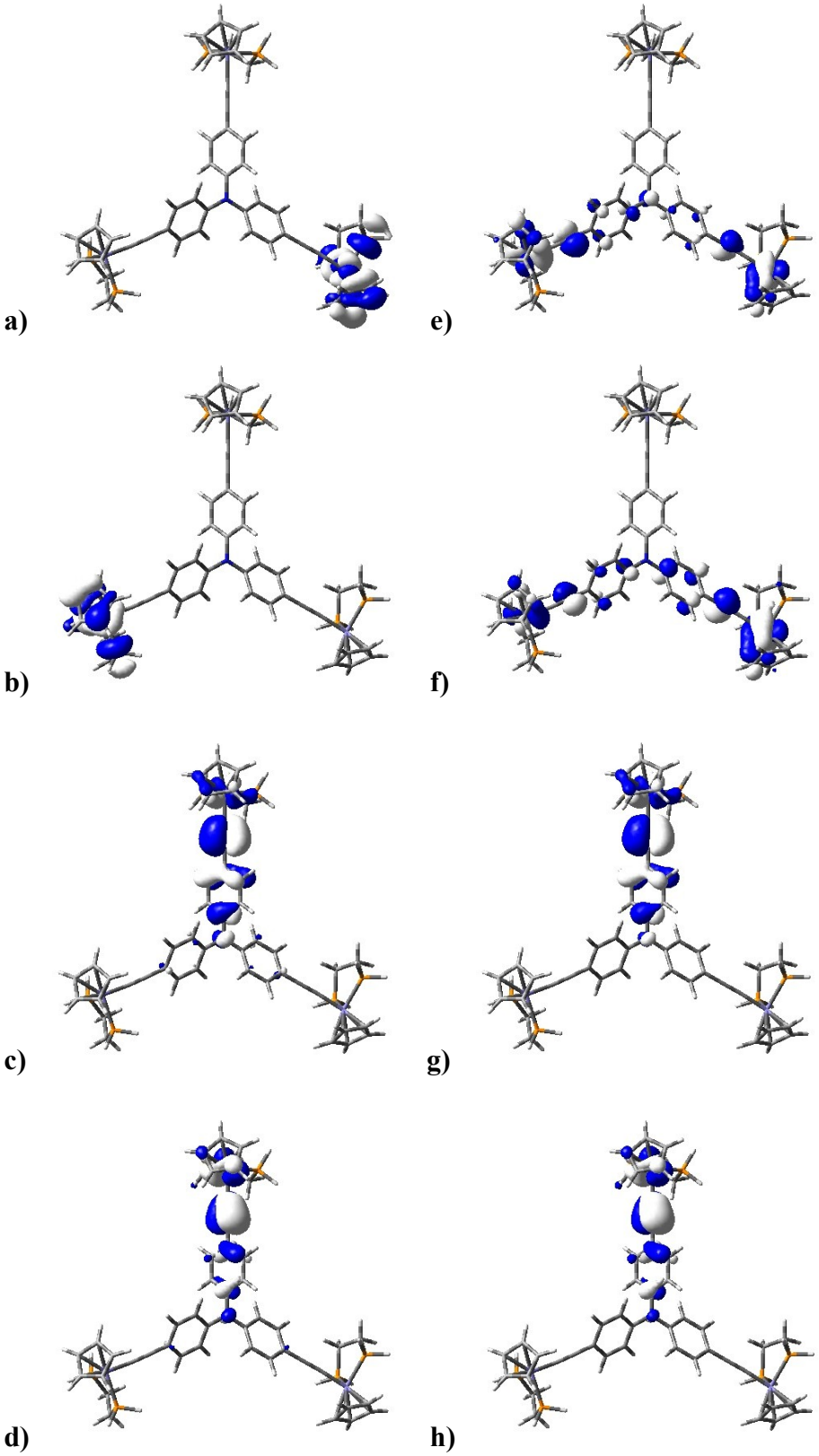

Chart **24** The a) α-[LUSO]+1, b) α-[LUSO], c) α-[HOSO] and d) α-[HOSO]-1, and e) β-[LUSO]+1, f) β-[LUSO], g) β-[HOSO] and h) β-[HOSO]-1, of $[\mathbf{79\text{-}H}]^{2+}$ plotted at contour values of ± 0.03 $(e/bohr^3)^{1/2}$, using MPW1K/6-31G*.

Table **87** Molecular Contribution of HS-[**79-H**]$^{2+}$ MPW1K 6-31G*.

HS- [**79-H**]$^{2+}$														
MO	251β	251α	250β	250α	249β	249α	248β	248α	247β	247α	246β	246α	245β	245α
	β-[LUSO+4]	α-[LUSO+2]	β-[LUSO+3]	α-[LUSO+1]	B-[LUSO+2]	α-[LUSO]	β-[LUSO+1]	α-[HOSO]	β-[LUSO]	α-[HOSO-1]	β-[HOSO]	α-[HOSO-2]	β-[HOSO-1]	α-[HOSO-3]
ε(eV)	-3.87	-4.47	4.14	-4.76	-4.22	-5.03	-5.65	-8.55	-5.98	-8.85	-8.49	-9.20	-8.82	-9.55
Occ	0	0	0	0	0	0	0	1	0	1	1	1	1	1
%Fe (A)	0	0	0	0	0	0	0	30	0	37	36	50	37	7
%Cp (A)	0	0	0	0	0	0	0	6	0	7	7	27	7	5
%dppe (A)	0	0	0	0	0	0	0	3	0	3	3	12	3	1
%C_α (A)	0	0	0	0	0	0	0	12	0	11	10	2	12	3
%C_β (A)	0	0	0	0	0	0	0	23	0	25	24	1	24	8
%Ph (A)	0	0	0	0	0	0	1	18	0	10	15	2	12	5
%Fe (B)	45	50	0	0	58	52	42	0	7	0	0	0	0	1
%Cp (B)	11	21	0	0	19	23	13	0	2	0	0	0	0	0
%dppe (B)	39	19	0	0	23	24	5	0	1	0	0	0	0	0
%C_α (B)	1	5	0	0	0	0	1	0	0	0	0	0	0	4
%C_β (B)	4	4	0	0	0	0	14	0	3	0	0	0	0	1
%Ph (B)	1	0	0	0	0	0	9	2	3	2	1	2	2	21
%Fe (C)	0	0	57	54	0	0	7	0	41	0	0	0	0	1
%Cp (C)	0	0	19	22	0	0	2	0	10	0	0	0	0	0
%dppe (C)	0	0	23	24	0	0	1	0	4	0	0	0	0	0
%C_α (C)	0	0	0	0	0	0	0	0	1	0	0	0	0	4
%C_β (C)	0	0	0	0	0	0	2	0	15	0	0	0	0	1
%Ph (C)	0	0	0	0	0	0	2	2	11	2	1	2	2	21
% N	0	0	0	0	0	0	2	2	1	2	1	1	1	15

Table **88** Calculated spin densities for [**78-H**]$^{+}$ and HS-[**79-H**]$^{2+}$ using MPW1K/6-31G*

[**78-H**]$^{+}$		HS-[**79-H**]$^{2+}$					
		Neutral Arm		Cation Arm		Cation Arm	
Fe	1.177	Fe (A)	0.000658	Fe (B)	1.156	Fe (C)	1.148
Cp	-0.107	Cp (A)	-0.000014	Cp (B)	-0.118	Cp (C)	-0.116
P_1	-0.056	P_1 (A)	-0.000061	P_1 (B)	-0.043	P_1 (C)	-0.043
P_2	-0.065	P_2 (A)	-0.000016	P_2 (B)	-0.048	P_2 (C)	-0.048
C_α	-0.214	C_α (A)	0.0046	C_α (B)	-0.202	C_α (C)	-0.202
C_β	0.231	C_β (A)	-0.003	C_β (B)	0.225	C_β (C)	0.224
Ar	0.026	Ar (A)	0.004	Ar (B)	0.034	Ar (C)	0.037
N	0.015	N	0.021				
Tol1	0.003						
Tol2	0.003						

Spin density calculations on the optimised geometry of HS-[**79-H**]$^{2+}$, shows that the spin density is localised on two iron centres (Table **88**). The iron centres with the localised charges are on the two metal ethynyl phenyl arms that are in a similar orientation/geometry of the monocation species [**78-H**]$^{+}$.

6.3 Conclusions

In this Chapter four pro-ligands **72**, **73**, **74**, and **75** have been synthesised and with the subsequent metallation, four mono and multi-metallic complexes have been made (**76** – **79**). The molecular structures of **72** and **73** reveal the usual propeller arrangement of the aryl rings around the amine core ubiquitous with triaryl amines.[389, 390] The molecular structures of the mono-metallic complexes **77** and **78** also show this triaryl amine propeller arrangement. The electrochemical data from the model ligand **73** and the iron metallated complex **78**, reveals that the first oxidation of **78** to [**78**]$^{+}$ occurs on the metal centre with the second oxidation event occurring

on the amine substituent *para*- to the metal centre. The spectroelectrochemical studies of the amine **72**, mono-metallic **78** and the trimetallic **79** agree with this conclusion. The spectroscopic and structural nature of $[\mathbf{72}]^{x+}$ and $[\mathbf{78}]^{y+}$ (x = 0, 1; y = 0, 1, 2) were satisfactorily reproduced with computational methods using the B3LYP functional at the 6-31G* level. The MPW1K functional at the 6-31G* level was also used to model $[\mathbf{78}]^{y+}$, which gave comparative reproduction of IR spectroscopic and structural results as using B3LYP/6-31G*. Computational effort to model the oxidation states of the trimetallic complex **79** above the neutral species, was fraught with difficulty, however the dication of $[\mathbf{79}]^{2+}$ was modelled with some success using the MPW1K/6-31G* level of theory. These results for the trimetallic complex **79** are the best obtained with the functionals available at the time. With the aid of TD DFT the electronic transitions present in the neutral and cationic forms of **72** were assigned, with the main absorption in the neutral species being from the π-system of the acetylene-substituented-triarylamine to the π*-system. The main absorptions in the cationic species $[\mathbf{72}]^{+}$ arise from the transitions from the β-HOSO to the β-LUSO and the α-HOSO to the α-LUSO, (also π-π* in character).

The electronic transitions from the oxidation states of [**78**] (**78**, $[\mathbf{78}]^{+}$ and $[\mathbf{78}]^{2+}$), were also assigned with the aid of TD DFT. In the neutral species **78** the main absorption, which has previously been seen in related complexes, [118, 221, 392] being from the Fe-C_2Ph π-system, (HOMO and the HOMO-1) to the C_2Ph π*-system, (LUMO+6), MLCT in character. The main absorptions in the cationic species originate from transitions from the β-HOSO to the β-LUSO and the a-HOSO to the a-LUSO+4, (LMCT and C_2PhNTol π – C_2Ph π* in character, respectively). The TD DFT for the dication $[\mathbf{78}]^{2+}$ did not give good agreement, however for the LS-$[\mathbf{78}]^{2+}$ the assignment of π – π*, for the absorption at ~9000 cm^{-1}, seems appropriate.

The UV-vis-NIR absorptions in the four oxidation states of the tris-metallic complex $[\mathbf{79}]^{0/+/2+/3+}$ are similar to the absorptions of **78** and $[\mathbf{78}]^{+}$. The main absorption in the neutral species **79** is from the HOMO, which is the $\{Fe\}_3N$ π-system to the π*-systems of the FeC≡CAr arms and to the metal-Cp antibonding centres. By analogy the absorption at ~11000 cm^{-1}, in the oxidised species $[\mathbf{79}]^{+/2+/3+}$, is LMCT in character.

The NIR transitions observed in [**79**]$^{+}$ and [**79**]$^{2+}$ likely have IVCT character. [**79**] therefore represents a well characterised case of a "three site" mixed-valence architecture.

6.4 Experimental Details

6.4.1 General Conditions

All reactions were carried out using oven dried glassware, under an atmosphere of nitrogen using standard Schlenk techniques. Reagents purchased commercially were used without further purification, but checked by using relevant spectroscopic techniques before use. The compounds **71**, [407] and **74** [98] were prepared by literature methods. NMR spectroscopies were carried out a room temperature and referenced against $CDCl_3$ using the Varian Mercury-200 (^{1}H 199.99 MHz), Bruker and Varian Mercury-400 (^{1}H 399.97 MHz) or Varian Inova-500 (^{1}H 499.77 MHz, ^{13}C 125.67 MHz). Chemical shifts are reported in δ / ppm and coupling constants, *J*, in Hz. IR spectra were recorded using solution cells fitted with CaF_2 windows by the Nicolet Avatar FT IR spectrophotometer. Mass spectra were acquired using the Thermo- Finnigan LTQ FT spectrometer. Single crystal X-ray structure determinations were carried out by Dr DS Yufit of this department using a Bruker 3-circle diffractometer with a SMART 6K area detector, using graphite-monochromated sealed-tube Mo-K_α radiation. These data collections were performed at 120 K, and the temperature maintained using cryostream (Oxford cryosystem) open flow N_2 cryostats. Reflection intensities were integrated using the SAINT program. [300] The molecular structures were solved using direct-methods and refined by full matrix least-squares F^2 using SHELXTL software. [148] All non-hydrogen atoms were refined in anisotropic approximation. Hydrogen atoms were placed into calculated positions, and refined isotropically using a riding model. Electrochemical experiments were performed in an air tight one compartment cell, constructed by a carbon working electrode, a platinum pseudo reference electrode and a platinum counter electrode. These components were fixed into the system via

a Teflon screw cap with a suitable fitting. Voltammetric data were acquired using Autolab PG-STAT 30 in CH_2Cl_2 solutions containing 0.1 M electrolyte solutions of NBu_4BF_4 at room temperature. Potentials are referenced to ferrocene or decamethylferrocene as appropriate.

6.4.2 Ligand Experimental

6.4.2.1 Preparation of *p*-bromophenylditolylamine [71] [407]

To an oven dried flask purged with nitrogen (equipped with an overhead mechanical stirrer and reflux condenser) is added the amine (9.60 g, 48.7 mmol), halide (21.50 g, 76.0 mmol), copper chloride (0.70 g, 7.10 mmol), 1,10-phenanthroline (0.91 g, 5.0 mmol) and *o*-xylene (ml). The system is stirred for about 30 minutes at 130-140 °C then KOH (45.0 g, 802.1 mmol) is added (as flakes or better as powder) and refluxed over night. The cooled mixture was neutralized with acetic acid (2M) filtered then washed with water (2 x 150 ml). The aqueous washes are extracted with CH_2Cl_2 (2 x 50 ml) and organic phases combined and again washed with water (2 x 150 ml) dried over $MgSO_4$ before removing solvent *in vacuo*. Product was isolated by column chromatography on silica eluted with hexane increasing polarity to 10:1 hexane:CH_2Cl_2 finally 4:1 hexane: CH_2Cl_2. The product was obtained as a white crystalline solid. (11.48 g, 67 %). ^{1}H NMR ($CDCl_3$): δ_H 2.31 (s, 6H, CH_3), 6.88 (pseudo d, 2H, J = 9 Hz, Ar AB), 6.96 (pseudo d, 4H, J = 8 Hz, Ar AB), 7.06 (pseudo d, 4H, J = 8 Hz, Ar AB), 7.27 (pseudo d, 2H, J = 9 Hz, Ar AB). ^{13}C NMR ($CDCl_3$): δ_C 20.8 (s, 2 x CH_3, tol), 113.6 (s, C_p-Br), 123.9 (s, C_o), 124.7 (s, $C_{m'}$), 130.0 (s, $C_{o'}$), 131.9 (s, C_m), 132.9 (s, 2 x $C_{p'}$), 145.0 (s, 2 x $C_{i'}$), 147.5 (s, C_i-Br). MS (MALDI): 353 (15%), 273 (100%).

6.4.2.2 Preparation of (4-((trimethylsilyl)ethynyl)phenyl)ditolylamine [72]

Degassed triethyl amine (150 ml), *p*-bromophenylditolylamine **71** (1.76 g, 5.00 mmol), trimethylsilyl acetylene (0.85 ml, 6.00 mmol), copper(I) iodide (0.024 g, 0.125 mmol) and palladium tetrakis(triphenylphosphine) (0.175 g, 0.250 mmol) were added to the amine and the pale yellow suspension refluxed overnight. After 18 hours the solvent was filtered from the black solid and removed under vacuo with gentle warming. The residue was washed with water and extracted with hexane. The organic fractions were combined, dried over $MgSO_4$ and condensed to isolate a yellow powder. (1.09 g, 59%). IR (CH_2Cl_2): 2150 cm^{-1}. ^1H NMR ($CDCl_3$): δ_H 7.27 (d, 2H, J = 9 Hz), 7.07 (d, 4H, J = 9 Hz), 6.99 (d, 4H, J = 9 Hz), 6.89 (d, 2H, J = 9 Hz), 2.39 (s, 6H, CH_3), 0.24 (s, 9H, $SiMe_3$). ^{13}C NMR ($CDCl_3$): δ_C 148.4 (s, C_i), 144.6 (s, 2 x $C_{i'}$), 133.2 (s, 2 x $C_{p'}$), 132.7 (s, C_m), 129.9 (s, $C_{o'}$), 125.2 (s, $C_{m'}$), 120.7 (s, C_o), 118.4 (s, C_p), 105.6 (s, *C*≡C-$SiMe_3$), 92.5 (s, C≡*C*-$SiMe_3$), 20.7 (s, 2 x CH_3, tol), 0.0 (s, $SiMe_3$). MS (GC EI): 369 (100%), 354 (45%);

6.4.2.3 Preparation of 4-Ethynylphenyl-ditolylamine [73]

Methanol (50 ml) was added to a THF solution (10 ml) of **72** (1.0 g, 2.73 mmol). Excess potassium carbonate (0.38 g, 10.9 mmol) was added and the reaction monitored by TLC. After 2 h. the mixture was poured into water and the precipitated product extracted with CH_2Cl_2 (3 x 30 ml). The combined organic extracts were washed with water (3 x 20 ml) and dried over $MgSO_4$ before removing the solvent *in vacuo*. The product was purified by passing through a silica column eluting with hexane to obtain a pale yellow solid. (0.68 g, 84%). IR (CH_2Cl_2): 2120 cm^{-1}. ^1H NMR ($CDCl_3$): δ_H 7.30 (d, 2H, J = 9 Hz), 7.09 (d, 4H, J = 9 Hz), 7.00 (d, 4H, J = 9 Hz), 6.91 (d, 2H, J = 9 Hz), 3.01 (s, 1H, C≡C*H*), 2.32 (s, 6H, 2 x CH_3). ^{13}C NMR ($CDCl_3$): δ_C 148.8 (s, C_i), 144.6 (s, 2 x $C_{i'}$), 133.4 (s, 2 x $C_{p'}$), 132.9 (s, C_m), 130.0 (s, 2 x $C_{o'}$), 125.3 (s, 2 x $C_{m'}$), 120.8 (s, C_o), 113.7 (s, C_p), 84.2 (s, *C*≡C-H), 75.8 (s, C≡*C*-H), 20.9 (2 x CH_3, tol). MS (GC EI): 297 (100%).

6.4.2.4 Preparation of Tris(4-((trimethylsilyl)ethynyl)phenyl)amine [74].

Triethyl amine (250 ml) was degassed by freeze-pump-thaw method in an oven dried flask. Tris(*p*-bromophenyl)amine (12.10 g, 25.0 mmol), trimethylsilyl acetylene (53.4 ml, 375 mmol), copper(I) iodide (0.12 g, 0.625 mmol) and palladium tetrakis(triphenylphosphine) (0.72 g, 0.625 mmol) were added to the amine and the pale yellow suspension refluxed overnight. After 18 h. the amine was removed from the black mixture (containing a heavy grey precipitate) using vacuum with gentle warming. The crude product was passed through a silica column eluted with hexane then 10:1 hexane:CH_2Cl_2. The product was isolated as a pale yellow solid. (12.73 g, 95%). IR (CH_2Cl_2): 2160 cm^{-1}. ^1H NMR ($CDCl_3$): δ_H 7.35 (d, 6H, J = 9 Hz, H_m), 6.96 (6H, d, J = 9 Hz, H_o), 0.24 (s, 18H, $SiMe_3$). ^{13}C NMR ($CDCl_3$): δ_C 146.8 (s, C_i), 133.2 (s, C_m), 123.8 (s, C_o), 117.8 (s, C_p), 104.9 (s, *C*≡C-$SiMe_3$), 94.0 (s, C≡*C*-$SiMe_3$), 0.0 (s, $SiMe_3$). MS (GC EI): 553 (100%), 518 (25%).

6.4.2.5 Preparation of Tris(4-ethynylphenyl)amine [75].

Methanol (150 ml) was added to a THF solution (30 ml) of **74** (3.00 g, 5.62 mmol). Excess potassium carbonate (11.70 g, 84.30 mmol) was added and the reaction monitored by TLC. After 2 h. the mixture was poured into water and the precipitated product extracted with CH_2Cl_2 (3 x 75 ml). The combined organic extracts were washed with water (3 x 50 ml) and dried over $MgSO_4$ before removing the solvent *in vacuo*. The product was purified by passing through a silica column eluting with hexane to obtain a pale yellow solid. (1.57 g, 88%). IR (CH_2Cl_2): 2125 cm^{-1}. ^1H NMR ($CDCl_3$): δ_H 7.39 (d, 6H, J = 9 Hz, H_m), 7.01 (d, 6H, J = 9 Hz, H_o), 3.06 (s, 3H, C≡C*H*). ^{13}C NMR ($CDCl_3$): δ_C 147.0 (s, C_i), 133.4 (s, C_m), 123.9 (s, C_o), 116.9 (s, C_p), 83.4 (s, *C*≡C-H), 77.0 (s, C≡*C*-H). MS (MALDI): 317 (100%).

6.4.3 Metallated Aryl Amine Experimental

6.4.3.1 Preparation of $Ru(C{\equiv}CC_6H_4NTol_2)(PPh_3)_2Cp$ [76]

$RuCl(PPh_3)_2Cp$ (100 mg, 0.138 mmol), $HC{\equiv}CC_6H_4NTol_2$ **73** (45 mg, 0.16 mmol) and NH_4PF_6 (45 mg, 0.28 mmol) were added to dry, degassed methanol (10 ml). Refluxed for 30 min, reaction mixture turned from orange suspension to red solution. Addition of NaOMe (2-3 drops) gave a yellow precipitate which was collected and washed with hexane. The yellow solid obtained was dried *in vacuo*, (70 mg, 52 %). IR (CH_2Cl_2): ν(C≡C) 2074m cm^{-1}. ^1H NMR ($CDCl_3$): δ_H 2.30 (s, 6H, 2 PhMe), 4.30 (s, 5H, Cp), 6.85 (d, 2H, *J* = 8 Hz, AB Ar H), 7.10 (d, 4H, *J* = 8 Hz, AB Ar), 7.17 (d, 4H, *J* = 8 Hz, AB Ar), 7.19 (d, 2H, *J* = 8 Hz, AB Ar). 6.90 – 7.50 (m, 30H, Ph). ^{31}P NMR: δ 51.4 (PPh_3). ES(+)-MS (m/z): 987.6, $[M]^+$; 765.6, $[M\text{-}PPh_3{+}K]^+$; 726.2, $[M\text{-}PPh_3]^+$.

6.4.3.2 Preparation of $Ru(C{\equiv}CC_6H_4NTol_2)(dppe)Cp$ [77]

$RuCl(dppe)Cp^*$ (100 mg, 0.15 mmol), $HC{\equiv}CC_6H_4NTol_2$ **73** (50 mg, 0.17 mmol) and NH_4PF_6 (49 mg, 0.3 mmol) were added to dry, degassed methanol (10ml). Refluxed for 20 min, reaction mixture turned from orange suspension to red solution. Addition of ^{t}BuOK / MeOH (2-3 drops) gave a yellow precipitate which was collected, washed with hexane and dried *in vacuo*, 74 mg, 58 %. IR (CH_2Cl_2): ν(C≡C) 2069m cm^{-1}. ^1H NMR (CD_2Cl_2): δ_H 1.57 (s, 15H, Cp*), 2.28 (s, 6H, 2 Me), 2.0-2.8 (2m, 4H, dppe), 6.64 (pseudo d, 2H, *J* = 8 Hz, AB Ar H), 6.75 (pseudo d, 2H, *J* = 8 Hz, AB Ar), 6.92 (pseudo d, 4H, *J* = 8 Hz, AB Ar), 7.00 (pseudo d, 4H, *J* = 8 Hz, AB Ar), 7.20 – 7.90 (m, 20H, Ph). ^{31}P NMR: δ 82.0 (dppe). ^{13}C NMR (CD_2Cl_2): δ_C 10.0 (s, Me Cp*), 20.6 (s, Me), 29.4 (s, dppe), 92.6 (s, Cp*), 109.2 (s, C_β), 110.6 (s, C_1), 123.7 (s, tolC_2), 124.0 (s, C_3), 126.1 (s(br), C_α), 127.4, 127.7 (s, C_m, $C_{m'}$, PPh), 129.1 (s, C_p, PPh), 129.8 (s, tolC_3), 130.8 (s, C_2), 131.7 (s, tolC_4), 133.3, 134.0 (s, C_o, $C_{o'}$, PPh), 137.0 (s, C_i, PPh), 139.2 (s, $C_{i'}$, PPh), 145.9 (s, tolC_1), 149.6 (s, C_4). ES(+)-MS (m/z): 932.6, $[M]^+$.

6.4.3.3 Preparation of Fe(C≡CC$_6$H$_4$NTol$_2$)(dppe)Cp [78]

FeCl(dppe)Cp (100 mg, 0.18 mmol), HC≡CC$_6$H$_4$NTol$_2$ **73** (62 mg, 0.21 mmol) and NaBPh$_4$ (72 mg, 0.21 mmol) were added to dry, degassed NEt$_3$ (6 ml) and THF (6 ml). Stirred for 3 h, reaction mixture turned from bright red solution to brown solution with orange precipitate. After evaporation of the solvent, the residue was extracted with diethyl ether. The extract was concentrated. Purification done by preparative thin layer chromatography (PTLC) using 90:10 hexane:acetone. An orange band was collected to afford an orange solid. Yield (50 mg, 40 %). IR (CH_2Cl_2): ν(C≡C) 2062m cm^{-1}. ^{1}H NMR ($CDCl_3$): δ_H 2.20 (m, 2H dppe), 2.30 (s, 6H, 2 × Me), 2.55 (m, 2H, dppe), 4.23 (s, 5H, Cp), 6.20 (pseudo d, 2H, *J* = 9 Hz, AB Ar H), 6.65 (pseudo d, 2H, *J* = 9 Hz, AB Ar H), 6.80 (pseudo d, 4H, *J* = 9 Hz, AB Ar), 6.95 (pseudo d, 4H, *J* = 9 Hz, AB Ar), 7.10 - 7.90 (m, 20H, Ar). ^{31}P NMR: δ 108.2 (dppe). ^{13}C NMR ($CDCl_3$): δ_C 20.7 (s, 2 Me), 28.1 (m, dppe), 79.1 (s, Cp), 118.3 (s, C$_\beta$), 123.2, 123.7, (2s, C$_3$ + tolC$_2$), 127.5, 127.9 (s, C$_m$ + C$_{m'}$, PPh), 128.7 (s, C$_p$, PPh), 129.1 (s, C$_{p'}$, PPh), 129.5, (2s, ArC$_2$ + tolC$_3$), 131.4, (s, tolC$_4$), 131.7, (s, C$_o$, PPh), 132.4 (s(br), C$_\alpha$), 133.8 (s, C$_{o'}$, PPh), 137.9 (s, C$_i$, PPh), 143.3 (s, C$_{i'}$, PPh), 145.5, (s, tolC$_1$), 148.7, (s, ArC$_4$). ES(+)-MS (m/z): 816.3, [M]$^+$. Elemental analysis for $C_{53}H_{47}NP_2Fe$: C, 78.01; H, 5.81; N, 1.72. Found: C, 78.31; H, 5.90; N, 1.68.

6.4.3.4 Preparation of [{Fe(dppe)Cp}$_3$(μ-(C≡CC$_6$H$_4$)$_3$N)] [79].

FeCl(dppe)Cp (400 mg, 0.72 mmol), (HC≡CC$_6$H$_4$)$_3$N **75** (124 mg, 0.24 mmol) and NaBPh$_4$ (144 mg, 0.76 mmol) were added to dry, degassed NEt$_3$ (20 ml) and THF (30 ml). Stirred for 4 h. reaction mixture turned from bright red solution to brown solution with orange precipitate. After evaporation of the solvent, the residue was extracted with diethyl ether. The extract was concentrated. A dark orange powder was obtained by triturating with hexane, (134 mg, 30 %). IR (CH_2Cl_2): ν(C≡C) 2062m cm^{-1}. ^{1}H NMR ($CDCl_3$): δ_H 2.0-2.8 (2m, 12H, dppe), 4.20 (s, 15H, Cp), 6.80 (pseudo d, 6H, *J* = 9 Hz, AB Ar), 6.95 (pseudo d, 6H, *J* = 9 Hz, AB Ar), 7.10 - 7.90 (m, 20H, PPh). ^{31}P NMR ($CDCl_3$): δ 107.4 (dppe). ^{13}C NMR ($CDCl_3$): δ_C 28.3 (m,

dppe), 79.0 (s, Cp), 118.2 (s, C_β), 123.2 (s, C_3), 127.5, 127.9 (2s, C_m + $C_{m'}$, PPh), 128.7 (s, C_p, PPh), 129.1 (s, $C_{p'}$, PPh), 129.8, (s, C_2), 131.8, (s, C_o, PPh), 132.3 (s, C_α), 134.0 (s, $C_{o'}$, PPh), 137.7 (s, C_i, PPh), 143.2 (s, $C_{i'}$, PPh), 148.7, (s, C_4). ES(+)-MS (m/z): 1872, $[M]^+$, 1354.0, $[M-[Fe]]^+$, 835.3, $[M-2[Fe]]^+$, 677.7, $[M-[Fe]]^{2+}$.

6.4.4 Computations

All *ab initio* computations were carried out with the Gaussian 03 package. [301] The model geometries of the ligand [**72-H**]$^{x+}$ and mono-metallic iron complex [**78-H**]$^{y+}$ (x = 0, 1, and y = 0, 1, 2), discussed here were optimised using the B3LYP/6-31G* level of theory with no symmetry constraints. [241, 243, 408] The mono-metallic iron complex [**78-H**]$^{y+}$ and trimetallic iron complex [**79-H**]$^{z+}$ (y = 0, 1, 2, and z = 0, 1, 2) discussed here were also optimised using the MPW1K/6-31G* level of theory. The keywords used in Gaussian03 for the MPW1K functional [228, 241] here are MPWPW91 and iop(3/76=0472005280). Frequency calculations were computed on these optimised geometries at the corresponding levels and no imaginary frequencies were found in these geometries unless otherwise stated. A scaling factor of 0.95 was applied to the calculated frequencies calculated using the B3LYP/6-31G* level of theory, whereas a scaling factor of 0.91 was applied when MPW1K/6-31G* was used, as it is known that DFT calculations over estimate the acetylide ν(C≡C) and acetylide ring substituent ν(C=C) frequencies. [244, 245] The MO diagrams and orbital contributions were generated with the aid of GaussView [246] and GaussSum [247] packages respectively.

Summary

This thesis has addressed some of the issues surrounding the design of complexes containing two or more metal centres linked through a common carbon-rich bridging ligand, and the study of bridge-mediated charge transfer in these systems.

An improved synthetic route to *trans*-RuCl(C≡CR)$(dppe)_2$ acetylide complexes from the five coordinate complex [RuCl$(dppe)_2$]OTf was devised, which is more convenient that the long-standing methods based on *cis*-$RuCl_2(dppe)_2$. Metal acetylide complexes based on the 1,3-diethynylbenzene core and *trans*-RuCl(C≡CR)$(dppe)_2$ and the similar half-sandwich Ru(dppe)Cp* centre have been shown to form thermodynamically stable mono-cations, which have been described as valence trapped mixed-valence compounds. The stabilisation of the mixed-valence state seems to arise from the delocalisation of the unpaired electron between the formally oxidised metal centre and the arylacetylide fragment.

A series of mono, bi- and tri-metallic ruthenium vinyl complexes were prepared via the *trans*- addition of the Ru-H bond in RuHCl(CO)$(PPh_3)_3$ across a ethynyl C≡CH bond. The monometallic complexes possess redox-non-innocent vinyl ligands, similar in many respects to acetylide analogues. The bimetallic complexes showed interesting oxidation properties, with the first oxidation occurring on the divinylaryl ligand and the second occurring on a pendant metal centre. The trimetallic vinyl complexes exhibit similar electronic structures on stepwise oxidation.

Two alternative "Y-shaped" ligand systems based on triethynyl methanol and tris(4-ethynylphenyl)amine have been investigated. An improved method to triethynylmethanol carbon skeleton that uses chloroethylformate as the key synthetic building block has been developed. Although metallation attempts were not successful, complexes derived from triethynyl methanols provide an interesting area of chemistry that should be further investigated. The mono- and tri-metallic triaryl acetylide complexes showed metal centred oxidation, with the possibility to sequentially oxidise the three iron centres in the trimetallic complex, leading to one of the first trimetallic mixed-valence compounds.

References

† Note that the mixing of acetylide and metal based orbitals makes the assignment of a formal metal oxidation state tenuous. The oxidation states are assigned here based on conventional electron counting protocols as is commonly found in the literature. For a more detailed discussion on elements of the problem, see Chapter **3**.

‡ K_c is a measure of the position of the comproportionation equilibrium, and therefore can be influenced by factors such as solvation and ion-pairing energies. Whilst K_c has been widely used in the literature as a measure of the magnitude of "electronic interactions", such data should be treated judiciously.

1. http://www.intel.com/technology/mooreslaw/index.htm.
2. http://www.intel.com/technology/architecture-silicon/32nm/index.htm.
3. J. M. Tour, *Acc. Chem. Res.*, 2000, **33**, 791-804.
4. L. B. Kish, *Phys. Lett. A.*, 2002, **305**, 144-149.
5. A. Aviram and M. A. Ratner, *Chem. Phys. Lett.*, 1974, **29**, 277-283.
6. E. Hitt, *P. Natl. Acad. Sci. USA.*, 2004, **101**, 7213-7214.
7. R. M. Metzger, *Chem. Rev.*, 2003, **103**, 3803-3834.
8. L. A. Bumm, J. J. Arnold, M. T. Cygan, T. D. Dunbar, T. P. Burgin, L. Jones, D. L. Allara, J. M. Tour and P. S. Weiss, *Science*, 1996, **271**, 1705-1707.
9. F. Paul and C. Lapinte, *Coordin. Chem. Rev.*, 1998, **180**, 431-509.
10. N. Robertson and C. A. McGowan, *Chem. Soc. Rev.*, 2003, **32**, 96-103.
11. M. D. Ward, *J. Chem. Educ.*, 2001, **78**, 321-328.
12. R. Dembinski, T. Bartik, B. Bartik, M. Jaeger and J. A. Gladysz, *J. Am. Chem. Soc.*, 2000, **122**, 810-822.
13. P. Avouris, *Acc. Chem. Res.*, 2002, **35**, 1026-1034.
14. G. Seifert, T. Kohler and T. Frauenheim, *Appl. Phys. Lett.*, 2000, **77**, 1313-1315.
15. A. J. Heeger, *J. Phys. Chem. B*, 2001, **105**, 8475-8491.
16. F. C. Grozema, Y. A. Berlin and L. D. A. Siebbeles, *J. Am. Chem. Soc.*, 2000, **122**, 10903-10909.
17. M. J. Crossley and P. L. Burn, *J. Chem. Soc. Chem. Commun.*, 1991, 1569-1571.
18. J. Chen, M. A. Reed, C. L. Asplund, A. M. Cassell, M. L. Myrick, A. M. Rawlett, J. M. Tour and P. G. Van Patten, *Appl. Phys. Lett.*, 1999, **75**, 624-626.
19. J. D. Monnell, J. J. Stapleton, S. M. Dirk, W. A. Reinerth, J. M. Tour, D. L. Allara and P. S. Weiss, *J. Phys. Chem. B*, 2005, **109**, 20343-20349.
20. D. K. James and J. M. Tour, *Chem. Mater.*, 2004, **16**, 4423-4435.
21. F. Barigelletti and L. Flamigni, *Chem. Soc. Rev.*, 2000, **29**, 1-12.
22. C. Creutz, *Prog. Inorg. Chem.*, 1983, **30**, 1-73.

23. J. J. Concepcion, D. M. Dattelbaum, T. J. Meyer and R. C. Rocha, *Philos. Trans. Soc. A*, 2008, **366**, 163-175.
24. K. D. Demadis, C. M. Hartshorn and T. J. Meyer, *Chem. Rev.*, 2001, **101**, 2655-2685.
25. M. B. Robin and P. Day, *Adv. Inorg. Chem. Radiochem.*, 1967, **10**, 247-422.
26. G. C. Allen and N. Hush, *Prog. Inorg. Chem.*, 1967, **8**, 357-390.
27. N. Hush, *Prog. Inorg. Chem.*, 1967, **8**, 391-444.
28. D. M. D'Alessandro and F. R. Keene, *Chem. Soc. Rev.*, 2006, **35**, 424-440.
29. J. Bonvoisin, J. P. Launay, M. Vanderauweraer and F. C. Deschryver, *J. Phys. Chem.*, 1994, **98**, 5052-5057.
30. J. Bonvoisin, J. P. Launay, W. Verbouwe, M. VanderAuweraer and F. C. DeSchryver, *J. Phys. Chem.*, 1996, **100**, 17079-17082.
31. J. C. Salsman, S. Ronco, C. H. Londergan and C. P. Kubiak, *Inorg. Chem.*, 2006, **45**, 547-554.
32. B. S. Brunschwig, C. Creutz and N. Sutin, *Chem. Soc. Rev.*, 2002, **31**, 168-184.
33. D. M. D'Alessandro, A. C. Topley, M. S. Davies and F. R. Keene, *Chem. Eur. J.*, 2006, **12**, 4873-4884.
34. P. Y. Chen and T. J. Meyer, *Chem. Rev.*, 1998, **98**, 1439-1477.
35. F. Coat, M. A. Guillevic, L. Toupet, F. Paul and C. Lapinte, *Organometallics*, 1997, **16**, 5988-5998.
36. W. Kaim and B. Sarkar, *Coordin. Chem. Rev.*, 2007, **251**, 584-594.
37. C. G. Atwood and W. E. Geiger, *J. Am. Chem. Soc.*, 2000, **122**, 5477-5485.
38. J. P. Launay, *Chem. Soc. Rev.*, 2001, **30**, 386-397.
39. C. H. Londergan, J. C. Salsman, S. Ronco, L. M. Dolkas and C. P. Kubiak, *J. Am. Chem. Soc.*, 2002, **124**, 6236-6237.
40. B. J. Lear, S. D. Glover, J. C. Salsman, C. H. Londergan and C. P. Kubiak, *J. Am. Chem. Soc.*, 2007, **129**, 12772-12779.
41. J. Maurer, R. F. Winter, B. Sarkar, J. Fiedler and S. Zalis, *Chem. Commun.*, 2004, 1900-1901.
42. J. Maurer, B. Sarkar, B. Schwederski, W. Kaim, R. F. Winter and S. Zalis, *Organometallics*, 2006, **25**, 3701-3712.
43. M. A. Fox, R. L. Roberts, T. E. Baines, B. Le Guennic, J. F. Halet, F. Hartl, D. S. Yufit, D. Albesa-Jove, J. A. K. Howard and P. J. Low, *J. Am. Chem. Soc.*, 2008, **130**, 3566-3578.
44. N. S. Hush and J. R. Reimers, *Chem. Rev.*, 2000, **100**, 775-786.
45. A. Vlcek and S. Zalis, *Coordin. Chem. Rev.*, 2007, **251**, 258-287.
46. L. H. Thomas, *Proc. Cambridge Phil. Soc.*, 1927, **23**, 542-548.
47. P. Hohenberg and W. Kohn, *Phys. Rev.*, 1964, **B136**, 864-872.
48. W. Kohn and L. J. Sham, *Phys. Rev.*, 1965, **140**, 1133-1138.
49. L. Pollack and J. P. Perdew, *J. Phys. Condens. Mat.*, 2000, **12**, 1239-1252.
50. J. P. Perdew, A. Ruzsinszky, J. M. Tao, V. N. Staroverov, G. E. Scuseria and G. I. Csonka, *J. Chem. Phys.*, 2005, **123**.
51. M. StClair, W. P. Schaefer and J. E. Bercaw, *Organometallics*, 1991, **10**, 525-527.
52. P. Binger, P. Muller, P. Philipps, B. Gabor, R. Mynott, A. T. Herrmann, F. Langhauser and C. Kruger, *Chem. Ber. Recl.*, 1992, **125**, 2209-2212.
53. G. A. Koutsantonis and J. P. Selegue, *J. Am. Chem. Soc.*, 1991, **113**, 2316-2317.
54. R. J. Cross and M. F. Davidson, *J. Chem. Soc. Dalton Trans.*, 1986, 411-414.

55. M. I. Bruce and P. J. Low, *Adv. Organomet. Chem.*, 2004, **50**, 179-444.
56. M. Brady, W. Q. Weng, Y. L. Zhou, J. W. Seyler, A. J. Amoroso, A. M. Arif, M. Bohme, G. Frenking and J. A. Gladysz, *J. Am. Chem. Soc.*, 1997, **119**, 775-788.
57. T. Bartik, W. Q. Weng, J. A. Ramsden, S. Szafert, S. B. Falloon, A. M. Arif and J. A. Gladysz, *J. Am. Chem. Soc.*, 1998, **120**, 11071-11081.
58. Y. Tanaka, T. Ozawa, A. Inagaki and M. Akita, *Dalton Trans.*, 2007, 928-933.
59. M. Linseis, R. F. Winter, B. Sarkar, W. Kaim and S. Zalis, *Organometallics*, 2008, **27**, 3321-3324.
60. D. Touchard, C. Morice, V. Cadierno, P. Haquette, L. Toupet and P. H. Dixneuf, *J. Chem. Soc. Chem. Commun.*, 1994, 859-860.
61. D. Touchard, P. Haquette, S. Guesmi, L. LePichon, A. Daridor, L. Toupet and P. H. Dixneuf, *Organometallics*, 1997, **16**, 3640-3648.
62. P. Haquette, D. Touchard, L. Toupet and P. Dixneuf, *J. Organomet. Chem.*, 1998, **565**, 63-73.
63. C. Lebreton, D. Touchard, L. Le Pichon, A. Daridor, L. Toupet and P. H. Dixneuf, *Inorg. Chim. Acta.*, 1998, **272**, 188-196.
64. C. W. Faulkner, S. L. Ingham, M. S. Khan, J. Lewis, N. J. Long and P. R. Raithby, *J. Organomet. Chem.*, 1994, **482**, 139-145.
65. S. Rigaut, J. Perruchon, L. Le Pichon, D. Touchard and P. H. Dixneuf, *J. Organomet. Chem.*, 2003, **670**, 37-44.
66. S. Rigaut, F. Monnier, F. Mousset, D. Touchard and P. H. Dixneuf, *Organometallics*, 2002, **21**, 2654-2661.
67. B. Gomez-Lor, A. Santos, M. Ruiz and A. M. Echavarren, *Eur. J. Inorg. Chem.*, 2001, 2305-2310.
68. D. Touchard, P. Haquette, A. Daridor, L. Toupet and P. H. Dixneuf, *J. Am. Chem. Soc.*, 1994, **116**, 11157-11158.
69. R. F. Winter, K. W. Klinkhammer and S. Zalis, *Organometallics*, 2001, **20**, 1317-1333.
70. M. Uno and P. H. Dixneuf, *Angew. Chem. Int. Ed.*, 1998, **37**, 1714-1717.
71. S. Rigaut, J. Perruchon, S. Guesmi, C. Fave, D. Touchard and P. H. Dixneuf, *Eur. J. Inorg. Chem.*, 2005, 447-460.
72. O. Lavastre, J. Plass, P. Bachmann, S. Guesmi, C. Moinet and P. H. Dixneuf, *Organometallics*, 1997, **16**, 184-189.
73. J. L. Fillaut, N. N. Dua, F. Geneste, L. Toupet and S. Sinbandhit, *J. Organomet. Chem.*, 2006, **691**, 5610-5618.
74. S. K. Hurst, N. T. Lucas, M. G. Humphrey, T. Isoshima, K. Wostyn, I. Asselberghs, K. Clays, A. Persoons, M. Samoc and B. Luther-Davies, *Inorg. Chim. Acta.*, 2003, **350**, 62-76.
75. S. K. Hurst, M. P. Cifuentes, A. M. McDonagh, M. G. Humphrey, M. Samoc, B. Luther-Davies, I. Asselberghs and A. Persoons, *J. Organomet. Chem.*, 2002, **642**, 259-267.
76. J. P. L. Morrall, M. P. Cifuentes, M. G. Humphrey, R. Kellens, E. Robijns, I. Asselberghs, K. Clays, A. Persoons, M. Samoc and A. C. Willis, *Inorg. Chim. Acta.*, 2006, **359**, 998-1005.
77. S. K. Hurst, M. G. Humphrey, T. Isoshima, K. Wostyn, I. Asselberghs, K. Clays, A. Persoons, M. Samoc and B. Luther-Davies, *Organometallics*, 2002, **21**, 2024-2026.

78. S. K. Hurst, M. G. Humphrey, J. P. Morrall, M. P. Cifuentes, M. Samoc, B. Luther-Davies, G. A. Heath and A. C. Willis, *J. Organomet. Chem.*, 2003, **670**, 56-65.
79. M. Samoc, N. Gauthier, M. P. Cifuentes, F. Paul, C. Lapinte and M. G. Humphrey, *Angew. Chem. Int. Ed.*, 2006, **45**, 7376-7379.
80. G. T. Dalton, M. P. Cifuentes, S. Petrie, R. Stranger, M. G. Humphrey and M. Samoc, *J. Am. Chem. Soc.*, 2007, **129**, 11882-11883.
81. C. E. Powell, M. P. Cifuentes, J. P. Morrall, R. Stranger, M. G. Humphrey, M. Samoc, B. Luther-Davies and G. A. Heath, *J. Am. Chem. Soc.*, 2003, **125**, 602-610.
82. M. P. Cifuentes, C. E. Powell, J. P. Morrall, A. M. McDonagh, N. T. Lucas, M. G. Humphrey, M. Samoc, S. Houbrechts, I. Asselberghs, K. Clays, A. Persoons and T. Isoshima, *J. Am. Chem. Soc.*, 2006, **128**, 10819-10832.
83. S. K. Hurst, M. P. Cifuentes, J. P. L. Morrall, N. T. Lucas, I. R. Whittall, M. G. Humphrey, I. Asselberghs, A. Persoons, M. Samoc, B. Luther-Davies and A. C. Willis, *Organometallics*, 2001, **20**, 4664-4675.
84. M. P. Cifuentes, C. E. Powell, M. G. Humphrey, G. A. Heath, M. Samoc and B. Luther-Davies, *J. Phys. Chem. A*, 2001, **105**, 9625-9627.
85. J. L. Fillaut, J. Andries, J. Perruchon, J. P. Desvergne, L. Toupet, L. Fadel, B. Zouchoune and J. Y. Saillard, *Inorg. Chem.*, 2007, **46**, 5922-5932.
86. J. L. Fillaut, J. Andries, R. D. Marwaha, P. H. Lanoe, O. Lohio, L. Toupet and J. A. G. Williams, *J. Organomet. Chem.*, 2008, **693**, 228-234.
87. O. F. Koentjoro, R. Rousseau and P. J. Low, *Organometallics*, 2001, **20**, 4502-4509.
88. M. I. Bruce, P. J. Low, K. Costuas, J. F. Halet, S. P. Best and G. A. Heath, *J. Am. Chem. Soc.*, 2000, **122**, 1949-1962.
89. B. Kim, J. M. Beebe, C. Olivier, S. Rigaut, D. Touchard, J. G. Kushmerick, X. Y. Zhu and C. D. Frisbie, *J. Phys. Chem. C.*, 2007, **111**, 7521-7526.
90. N. Gauthier, G. Argouarch, F. Paul, M. G. Humphrey, L. Toupet, S. Ababou-Girard, H. Sabbah, P. Hapiot and B. Fabre, *Adv. Mater.*, 2008, **20**, 1952.
91. A. Klein, O. Lavastre and J. Fiedler, *Organometallics*, 2006, **25**, 635-643.
92. C. Olivier, B. Kim, D. Touchard and S. Rigaut, *Organometallics*, 2008, **27**, 509-518.
93. N. Gauthier, C. Olivier, S. Rigaut, D. Touchard, T. Roisnel, M. G. Humphrey and F. Paul, *Organometallics*, 2008, **27**, 1063-1072.
94. S. Rigaut, C. Olivier, K. Costuas, S. Choua, O. Fadhel, J. Massue, P. Turek, J. Y. Saillard, P. H. Dixneuf and D. Touchard, *J. Am. Chem. Soc.*, 2006, **128**, 5859-5876.
95. S. Rigaut, L. Le Pichon, J. C. Daran, D. Touchard and P. H. Dixneuf, *Chem. Commun.*, 2001, 1206-1207.
96. Z. Q. Wei, S. Guo and S. A. Kandel, *J. Phys. Chem. B*, 2006, **110**, 21846-21849.
97. H. Qi, A. Gupta, B. C. Noll, G. L. Snider, Y. H. Lu, C. Lent and T. P. Fehlner, *J. Am. Chem. Soc.*, 2005, **127**, 15218-15227.
98. K. Onitsuka, N. Ohara, F. Takei and S. Takahashi, *Dalton Trans.*, 2006, 3693-3698.
99. Q. Y. Hu, W. X. Lu, H. D. Tang, H. H. Y. Sung, T. B. Wen, I. D. Williams, G. K. L. Wong, Z. Y. Lin and G. C. Jia, *Organometallics*, 2005, **24**, 3966-3973.

100. M. Samoc, N. Gauthier, M. P. Cifuentes, F. Paul, C. Lapinte, M. G. Humphrey and G. T. Dalton, *Angew. Chem. Int. Ed.*, 2008, **47**, 629-629.
101. S. Guesmi, D. Touchard and P. H. Dixneuf, *Chem. Commun.*, 1996, 2773-2774.
102. D. Touchard, P. Haquette, A. Daridor, A. Romero and P. H. Dixneuf, *Organometallics*, 1998, **17**, 3844-3852.
103. O. Lavastre, M. Even, P. H. Dixneuf, A. Pacreau and J. P. Vairon, *Organometallics*, 1996, **15**, 1530-1531.
104. C. E. Powell, S. K. Hurst, J. P. Morrall, M. P. Cifuentes, R. L. Roberts, M. Samoc and M. G. Humphrey, *Organometallics*, 2007, **26**, 4456-4463.
105. S. K. Hurst, M. P. Cifuentes and M. G. Humphrey, *Organometallics*, 2002, **21**, 2353-2355.
106. N. Matsumi, Y. Chujo, O. Lavastre and P. H. Dixneuf, *Organometallics*, 2001, **20**, 2425-2427.
107. G. R. Whittell and I. Manners, *Adv. Mater.*, 2007, **19**, 3439-3468.
108. M. Samoc, J. P. Morrall, G. T. Dalton, M. P. Cifuentes and M. G. Humphrey, *Angew. Chem. Int. Ed.*, 2007, **46**, 731-733.
109. C. E. Powell, J. P. Morrall, S. A. Ward, M. P. Cifuentes, E. G. A. Notaras, M. Samoc and M. G. Humphrey, *J. Am. Chem. Soc.*, 2004, **126**, 12234-12235.
110. A. M. McDonagh, M. G. Humphrey, M. Samoc and B. Luther-Davies, *Organometallics*, 1999, **18**, 5195-5197.
111. A. M. McDonagh, C. E. Powell, J. P. Morrall, M. P. Cifuentes and M. G. Humphrey, *Organometallics*, 2003, **22**, 1402-1413.
112. R. L. Roberts, T. Schwich, T. C. Corkery, M. P. Cifuentes, K. A. Green, J. D. Farmer, P. J. Low, T. B. Marder, M. Samoc and M. G. Humphrey, *Adv. Mater.*, 2009, **21**, 2318-2322.
113. N. Gauthier, N. Tchouar, F. Justaud, G. Argouarch, M. P. Cifuentes, L. Toupet, D. Touchard, J. F. Halet, S. Rigaut, M. G. Humphrey, K. Costuas and F. Paul, *Organometallics*, 2009, **28**, 2253-2266.
114. M. A. Fox, J. D. Farmer, R. L. Roberts, M. G. Humphrey and P. J. Low, *Organometallics*, 2009, **28**, 5266-5269.
115. M. A. Fox, R. L. Roberts, W. M. Khairul, F. Hartl and P. J. Low, *J. Organomet. Chem.*, 2007, **692**, 3277-3290.
116. R. Packheiser, M. Lohan, B. Brauer, F. Justaud, C. Lapinte and H. Lang, *J. Organomet. Chem.*, 2008, **693**, 2898-2902.
117. Y. Liao, J. K. Feng, L. Yang, A. M. Ren and H. X. Zhang, *Organometallics*, 2005, **24**, 385-394.
118. K. Costuas, F. Paul, L. Toupet, J. F. O. Halet and C. Lapinte, *Organometallics*, 2004, **23**, 2053-2068.
119. Z. Atherton, C. W. Faulkner, S. L. Ingham, A. K. Kakkar, M. S. Khan, J. Lewis, N. J. Long and P. R. Raithby, *J. Organomet. Chem.*, 1993, **462**, 265-270.
120. M. Younus, N. J. Long, P. R. Raithby, J. Lewis, N. A. Page, A. J. P. White, D. J. Williams, M. C. B. Colbert, A. J. Hodge, M. S. Khan and D. G. Parker, *J. Organomet. Chem.*, 1999, **578**, 198-209.
121. Y. F. Liu, C. Lagrost, K. Costuas, N. Tchouar, H. Le Bozec and S. Rigaut, *Chem. Commun.*, 2008, 6117-6119.
122. D. Weiss and P. H. Dixneuf, *Organometallics*, 2003, **22**, 2209-2216.

123. B. Chaudret, G. Commenges and R. Poilblanc, *J. Chem. Soc. Dalton Trans.*, 1984, 1635-1639.
124. I. P. Evans, A. Spencer and G. Wilkinson, *J. Chem. Soc. Dalton Trans.*, 1973, 204-209.
125. M. T. Bautista, E. P. Cappellani, S. D. Drouin, R. H. Morris, C. T. Schweitzer, A. Sella and J. Zubkowski, *J. Am. Chem. Soc.*, 1991, **113**, 4876-4887.
126. L. Russo, J. Figueira, J. Rodrigues and K. Rissanen, *Acta. Cryst.*, 2006, **E62**, M1154-M1155.
127. B. Chin, A. J. Lough, R. H. Morris, C. T. Schweitzer and C. Dagostino, *Inorg. Chem.*, 1994, **33**, 6278-6288.
128. Y. Nishibayashi, S. Takemoto, S. Iwai and M. Hidai, *Inorg. Chem.*, 2000, **39**, 5946-5957.
129. S. J. Higgins, A. La Pensee, C. A. Stuart and J. M. Charnock, *J. Chem. Soc. Dalton Trans.*, 2001, 902-910.
130. J. R. Polam and L. C. Porter, *J. Coord. Chem.*, 1993, **29**, 109-119.
131. N. Mantovani, M. Brugnati, L. Gonsalvi, E. Grigiotti, F. Laschi, L. Marvelli, M. Peruzzini, G. Reginato, R. Rossi and P. Zanello, *Organometallics*, 2005, **24**, 405-418.
132. J. Chatt and R. G. Hayter, *J. Chem. Soc.*, 1961, 896-904.
133. T. A. Stephenson and G. Wilkinson, *J. Inorg. Nucl. Chem.*, 1966, **28**, 2285-2291.
134. P. S. Hallman, T. A. Stephenson and G. Wilkinson, *Inorg. Synth.*, 1970, **12**, 237.
135. R. Mason, D. W. Meek and G. R. Scollary, *Inorg. Chim. Acta.*, 1976, **16**, L11-L12.
136. M. Rohr, M. Gunther, F. Jutz, J. D. Grunwaldt, H. Emerich, W. van Beek and A. Baiker, *Appl. Catal. A-Gen.*, 2005, **296**, 238-250.
137. D. N. Cheredilin, F. M. Dolgushin, E. V. Balagurova, I. A. Godovikov and I. T. Chizhevsky, *Russ. Chem. B+*. 2004, **53**, 2086-2089.
138. A. A. Batista, L. A. C. Cordeiro and G. Oliva, *Inorg. Chim. Acta.*, 1993, **203**, 185-191.
139. A. Mezzetti, A. Delzotto, P. Rigo and N. B. Pahor, *J. Chem. Soc. Dalton Trans.*, 1989, 1045-1052.
140. J. Diez, M. P. Gamasa, J. Gimeno, Y. Rodriguez and S. Garcia-Granda, *Eur. J. Inorg. Chem.*, 2004, 2078-2085.
141. R. M. Stoop, C. Bauer, P. Setz, M. Worle, T. Y. H. Wong and A. Mezzetti, *Organometallics*, 1999, **18**, 5691-5700.
142. J. K. Burdett, M. A. Graham, R. N. Perutz, M. Poliakoff, A. J. Rest, J. J. Turner and R. F. Turner, *J. Am. Chem. Soc.*, 1975, **97**, 4805-4808.
143. P. J. Hay, *J. Am. Chem. Soc.*, 1978, **100**, 2411-2417.
144. I. E. Rachidi, O. Eisenstein and Y. Jean, *New. J. Chem.*, 1990, **14**, 671-677.
145. D. L. Thorn and R. Hoffmann, *Nouv. J. Chim.*, 1979, **3**, 39-45.
146. J. E. McGrady, T. Lovell, R. Stranger and M. G. Humphrey, *Organometallics*, 1997, **16**, 4004-4011.
147. C. D. Delfs, R. Stranger, M. G. Humphrey and A. M. McDonagh, *J. Organomet. Chem.*, 2000, **607**, 208-212.
148. SHELXTL, version 6.14, Bruker, AXS, Madison, Wisconsin, USA, 2000
149. W. A. Chalifoux and R. R. Tykwinski, *C.R. Chim.*, 2009, **12**, 341-358.

150. W. Y. Kim, Y. C. Choi, S. K. Min, Y. Cho and K. S. Kim, *Chem. Soc. Rev.*, 2009, **38**, 2319-2333.
151. R. Mas-Balleste, O. Castillo, P. J. S. Miguel, D. Olea, J. Gomez-Herrero and F. Zamora, *Eur. J. Inorg. Chem.*, 2009, 2885-2896.
152. D. Mihailovic, *Prog. Mater. Sci*, 2009, **54**, 309-350.
153. M. I. Bruce, M. Z. Ke and P. J. Low, *Chem. Commun.*, 1996, 2405-2406.
154. M. I. Bruce, L. I. Denisovich, P. J. Low, S. M. Peregudova and N. A. Ustynuk, *Mendeleev Commun.*, 1996, 200-201.
155. S. Szafert and J. A. Gladysz, *Chem. Rev.*, 2003, **103**, 4175-4205.
156. S. Szafert and J. A. Gladysz, *Chem. Rev.*, 2006, **106**, PR1-PR33.
157. M. I. Bruce, B. G. Ellis, M. Gaudio, C. Lapinte, G. Melino, F. Paul, B. W. Skelton, M. E. Smith, L. Toupet and A. H. White, *Dalton Trans*, 2004, 1601-1609.
158. F. Coat, F. Paul, C. Lapinte, L. Toupet, K. Costuas and J. F. Halet, *J. Organomet. Chem.*, 2003, **683**, 368-378.
159. S. H. Liu, Y. H. Chen, K. L. Wan, T. B. Wen, Z. Y. Zhou, M. F. Lo, I. D. Williams and G. C. Jia, *Organometallics*, 2002, **21**, 4984-4992.
160. S. H. Liu, H. P. Xia, T. B. Wen, Z. Y. Zhou and G. C. Jia, *Organometallics*, 2003, **22**, 737-743.
161. S. H. Liu, H. P. Xia, K. L. Wan, R. C. Y. Yeung, Q. Y. Hu and G. C. Jia, *J. Organomet. Chem.*, 2003, **683**, 331-336.
162. S. H. Liu, Q. Y. Hu, P. Xue, T. B. Wen, I. D. Williams and G. C. Jia, *Organometallics*, 2005, **24**, 769-772.
163. P. Yuan, S. H. Liu, W. C. Xiong, J. Yin, G. A. Yu, H. Y. Sung, I. D. Williams and G. C. Jia, *Organometallics*, 2005, **24**, 1452-1457.
164. S. Ibn Ghazala, F. Paul, L. Toupet, T. Roisnel, P. Hapiot and C. Lapinte, *J. Am. Chem. Soc.*, 2006, **128**, 2463-2476.
165. L. Droz, M. A. Fox, D. Hnyk, P. J. Low, J. A. H. MacBride and V. Vsetecka, *Collect. Czech, Chem. C.*, 2009, **74**, 131-146.
166. S. Kim, A. Oehlhof, B. Beile and H. Meier, *Helv. Chim. Acta.*, 2009, **92**, 1023-1033.
167. H. Meier, *Angew. Chem. Int. Ed.*, 2005, **44**, 2482-2506.
168. N. Lenarvor and C. Lapinte, *Organometallics*, 1995, **14**, 634-639.
169. M. I. Bruce, B. C. Hall, P. J. Low, B. W. Skelton and A. H. White, *J. Organomet. Chem.*, 1999, **592**, 74-83.
170. J. N. Wilson, P. M. Windscheif, U. Evans, M. L. Myrick and U. H. F. Bunz, *Macromolecules.*, 2002, **35**, 8681-8683.
171. Y. Q. Wang, B. Erdogan, J. N. Wilson and U. H. F. Bunz, *Chem. Commun.*, 2003, 1624-1625.
172. S. Shotwell, P. M. Windscheif, M. D. Smith and U. H. F. Bunz, *Org. Lett.*, 2004, **6**, 4151-4154.
173. B. C. Englert, M. D. Smith, K. I. Hardcastle and U. H. F. Bunz, *Macromolecules.*, 2004, **37**, 8212-8221.
174. C. D. Zangmeister, S. W. Robey, R. D. van Zee, Y. X. Yao and J. M. Tour, *J. Am. Chem. Soc.*, 2004, **126**, 3420-3421.
175. C. Risko, C. D. Zangmeister, Y. Yao, T. J. Marks, J. M. Tour, M. A. Ratner and R. D. van Zee, *J. Phys. Chem. C.*, 2008, **112**, 13215-13225.
176. F. R. F. Fan, R. Y. Lai, J. Cornil, Y. Karzazi, J. L. Bredas, L. T. Cai, L. Cheng, Y. X. Yao, D. W. Price, S. M. Dirk, J. M. Tour and A. J. Bard, *J. Am. Chem. Soc.*, 2004, **126**, 2568-2573.

177. A. Funston, J. P. Kirby, J. R. Miller, L. Pospisil, J. Fiedler, M. Hromadova, M. Gal, J. Pecka, M. Valasek, Z. Zawada, P. Rempala and J. Michl, *J. Phys. Chem. A*, 2005, **109**, 10862-10869.
178. G. T. Dalton, M. P. Cifuentes, L. A. Watson, S. Petrie, R. Stranger, M. Samoc and M. G. Humphrey, *Inorg. Chem.*, 2009, **48**, 6534-6547.
179. B. Babgi, L. Rigamonti, M. P. Cifuentes, T. C. Corkery, M. D. Randles, T. Schwich, S. Petrie, R. Stranger, A. Teshome, I. Asselberghs, K. Clays, M. Samoc and M. G. Humphrey, *J. Am. Chem. Soc.*, 2009, **131**, 10293-10307.
180. T. L. Stott and M. O. Wolf, *Coordin. Chem. Rev.*, 2003, **246**, 89-101.
181. P. J. Low and M. I. Bruce, *Adv. Organomet. Chem.*, 2001, **48**, 71-288.
182. Y. B. Zhu and M. O. Wolf, *J. Am. Chem. Soc.*, 2000, **122**, 10121-10125.
183. Y. B. Zhu, D. B. Millet, M. O. Wolf and S. J. Rettig, *Organometallics*, 1999, **18**, 1930-1938.
184. N. D. Jones, M. O. Wolf and D. M. Giaquinta, *Organometallics*, 1997, **16**, 1352-1354.
185. Y. B. Zhu, O. Clot, M. O. Wolf and G. P. A. Yap, *J. Am. Chem. Soc.*, 1998, **120**, 1812-1821.
186. J. Sedlacek, J. Vohlidal, N. Patev, M. Pacovska, S. Cabioch, O. Lavastre, P. H. Dixneuf, H. Balcar and P. Matejka, *Macromol. Chem. Physic.*, 1999, **200**, 972-976.
187. C. Olivier, S. Choua, P. Turek, D. Touchard and S. Rigaut, *Chem. Commun.*, 2007, 3100-3102.
188. S. Rigaut, J. Massue, D. Touchard, J. L. Fillaut, S. Golhen and P. H. Dixneuf, *Angew. Chem. Int. Ed.*, 2002, **41**, 4513-4517.
189. P. Hamon, F. Justaud, O. Cador, P. Hapiot, S. Rigaut, L. Toupet, L. Ouahab, H. Stueger, J. R. Hamon and C. Lapinte, *J. Am. Chem. Soc.*, 2008, **130**, 17372-17383.
190. C. S. Lent, B. Isaksen and M. Lieberman, *J. Am. Chem. Soc.*, 2003, **125**, 1056-1063.
191. M. Lieberman, S. Chellamma, B. Varughese, Y. L. Wang, C. Lent, G. H. Bernstein, G. Snider and F. C. Peiris, *Ann. NY. Acad. Sci.*, 2002, **960**, 225-239.
192. A. O. Orlov, I. Amlani, G. H. Bernstein, C. S. Lent and G. L. Snider, *Science*, 1997, **277**, 928-930.
193. G. L. Snider, O. Orlov, I. Amlani, G. H. Bernstein, C. S. Lent, J. L. Merz and W. Porod, *Solid State Electron.*, 1998, **42**, 1355-1359.
194. C. S. Lent, *Science*, 2000, **288**, 1597-1599.
195. J. C. Ellenbogen and J. C. Love, *P. IEEE.*, 2000, **88**, 386-426.
196. A. P. de Silva and N. D. McClenaghan, *Chem. Eur. J.*, 2004, **10**, 574-586.
197. F. M. Raymo, *Adv. Mater.*, 2002, **14**, 401-414.
198. V. Balzani, A. Credi and M. Venturi, *Chemphyschem*, 2003, **4**, 49-59.
199. A. P. De Silva, *Nat. Mater.*, 2005, **4**, 15-16.
200. Z. H. Li, A. M. Beatty and T. P. Fehlner, *Inorg. Chem.*, 2003, **42**, 5707-5714.
201. Z. H. Li and T. P. Fehlner, *Inorg. Chem.*, 2003, **42**, 5715-5721.
202. J. Y. Jiao, G. J. Long, F. Grandjean, A. M. Beatty and T. P. Fehlner, *J. Am. Chem. Soc.*, 2003, **125**, 7522-7523.
203. J. Y. Jiao, G. J. Long, L. Rebbouh, F. Grandjean, A. M. Beatty and T. P. Fehlner, *J. Am. Chem. Soc.*, 2005, **127**, 17819-17831.
204. V. C. Lau, L. A. Berben and J. R. Long, *J. Am. Chem. Soc.*, 2002, **124**, 9042-9043.

205. M. I. Bruce, N. N. Zaitseva, P. J. Low, B. W. Skelton and A. H. White, *J. Organomet. Chem.*, 2006, **691**, 4273-4280.
206. M. Akita, Y. Tanaka, C. Naitoh, T. Ozawa, N. Hayashi, M. Takeshita, A. Inagaki and M. C. Chung, *Organometallics*, 2006, **25**, 5261-5275.
207. R. Packheiser, P. Ecorchard, T. Ruffer, M. Lohan, B. Brauer, F. Justaud, C. Lapinte and H. Lang, *Organometallics*, 2008, **27**, 3444-3457.
208. M. J. Irwin, L. ManojlovicMuir, K. W. Muir, R. J. Puddephatt and D. S. Yufit, *Chem. Commun.*, 1997, 219-220.
209. S. H. F. Chong, S. C. F. Lam, V. W. W. Yam, N. Y. Zhu, K. K. Cheung, S. Fathallah, K. Costuas and J. F. Halet, *Organometallics*, 2004, **23**, 4924-4933.
210. I. R. Whittall, M. G. Humphrey, S. Houbrechts, J. Maes, A. Persoons, S. Schmid and D. C. R. Hockless, *J. Organomet. Chem.*, 1997, **544**, 277-283.
211. C. E. Powell, M. P. Cifuentes, M. G. Humphrey, A. C. Willis, J. P. Morrall and M. Samoc, *Polyhedron.*, 2007, **26**, 284-289.
212. V. W. W. Yam, L. J. Zhang, C. H. Tao, K. M. C. Wong and K. K. Cheung, *J. Chem. Soc. Dalton Trans.*, 2001, 1111-1116.
213. N. J. Long, A. J. Martin, F. F. de Biani and P. Zanello, *J. Chem. Soc. Dalton Trans.*, 1998, 2017-2021.
214. N. J. Long, A. J. Martin, A. J. P. White, D. J. Williams, M. Fontani, F. Laschi and P. Zanello, *J. Chem. Soc. Dalton Trans.*, 2000, 3387-3392.
215. R. M. Medina, C. Moreno, M. L. Marcos, J. A. Castro, F. Benito, A. Arnanz, S. Delgado, J. Gonzalez-Velasco and M. J. Macazaga, *Inorg. Chim. Acta.*, 2004, **357**, 2069-2080.
216. C. Moreno, M. L. Marcos, G. Dominguez, A. Arnanz, D. H. Farrar, R. Teeple, A. Lough, J. Gonzalez-Velasco and S. Delgado, *J. Organomet. Chem.*, 2001, **631**, 19-28.
217. S. M. Draper, M. Delamesiere, E. Champeil, B. Twamley, J. J. Byrne and C. Long, *J. Organomet. Chem.*, 1999, **589**, 157-167.
218. S. K. Hurst and T. Ren, *J. Organomet. Chem.*, 2002, **660**, 1-5.
219. T. Weyland, C. Lapinte, G. Frapper, M. J. Calhorda, J. F. Halet and L. Toupet, *Organometallics*, 1997, **16**, 2024-2031.
220. D. Beljonne, M. C. B. Colbert, P. R. Raithby, R. H. Friend and J. L. Bredas, *Synthetic. Met.*, 1996, **81**, 179-183.
221. T. Weyland, K. Costuas, L. Toupet, J. F. Halet and C. Lapinte, *Organometallics*, 2000, **19**, 4228-4239.
222. T. Weyland, K. Costuas, A. Mari, J. F. Halet and C. Lapinte, *Organometallics*, 1998, **17**, 5569-5579.
223. M. C. B. Colbert, J. Lewis, N. J. Long, P. R. Raithby, M. Younus, A. J. P. White, D. J. Williams, N. N. Payne, L. Yellowlees, D. Beljonne, N. Chawdhury and R. H. Friend, *Organometallics*, 1998, **17**, 3034-3043.
224. F. Paul, B. G. Ellis, M. I. Bruce, L. Toupet, T. Roisnel, K. Costuas, J. F. Halet and C. Lapinte, *Organometallics*, 2006, **25**, 649-665.
225. R. Packheiser, P. Ecorchard, T. Ruffer and H. Lang, *Organometallics*, 2008, **27**, 3534-3546.
226. M. I. Bruce, K. Costuas, T. Davin, B. G. Ellis, J. F. Halet, C. Lapinte, P. J. Low, M. E. Smith, B. W. Skelton, L. Toupet and A. H. White, *Organometallics*, 2005, **24**, 3864-3881.
227. F. Paul, L. Toupet, J. Y. Thepot, K. Costuas, J. F. Halet and C. Lapinte, *Organometallics*, 2005, **24**, 5464-5478.

228. B. J. Lynch, P. L. Fast, M. Harris and D. G. Truhlar, *J. Phys. Chem. A*, 2000, **104**, 4811-4815.
229. N. J. Brown, P. K. Eckert, M. A. Fox, D. S. Yufit, J. A. K. Howard and P. J. Low, *Dalton Trans.*, 2008, 433-436.
230. D. E. Richardson and H. Taube, *Inorg. Chem.*, 1981, **20**, 1278-1285.
231. D. E. Richardson and H. Taube, *Coordin. Chem. Rev.*, 1984, **60**, 107-129.
232. M. E. Stoll, S. R. Lovelace, W. E. Geiger, H. Schimanke, I. Hyla-Kryspin and R. Gleiter, *J. Am. Chem. Soc.*, 1999, **121**, 9343-9351.
233. F. Paul, G. da Costa, A. Bondon, N. Gauthier, S. Sinbandhit, L. Toupet, K. Costuas, J. F. Halet and C. Lapinte, *Organometallics*, 2007, **26**, 874-896.
234. M. I. Bruce, B. G. Ellis, P. J. Low, B. W. Skelton and A. H. White, *Organometallics*, 2003, **22**, 3184-3198.
235. M. A. Fox, J. E. Harris, S. Heider, V. Perez-Gregorio, M. E. Zakrzewska, J. D. Farmer, D. S. Yufit, J. A. K. Howard and P. J. Low, *J. Organomet. Chem.*, 2009, **694**, 2350-2358.
236. D. L. Trumbo and C. S. Marvel, *J. Polym. Sci. A1.*, 1986, **24**, 2231-2238.
237. C. Bitcon and M. W. Whiteley, *J. Organomet. Chem.*, 1987, **336**, 385-392.
238. N. G. Connelly and W. E. Geiger, *Chem. Rev.*, 1996, **96**, 877-910.
239. M. Krejcik, M. Danek and F. Hartl, *J. Electroanal. Chem.*, 1991, **317**, 179-187.
240. M. L. Gou, M. Dai, X. Y. Li, L. Yang, M. J. Huang, Y. S. Wang, B. Kan, Y. Lu, Y. Wei and Z. Y. Qian, *Colloid. Surface. B.*, 2008, **64**, 135-139.
241. B. J. Lynch, Y. Zhao and D. G. Truhlar, *J. Phys. Chem. A*, 2003, **107**, 1384-1388.
242. G. A. Petersson and M. A. Allaham, *J. Chem. Phys.*, 1991, **94**, 6081-6090.
243. G. A. Petersson, A. Bennett, T. G. Tensfeldt, M. A. Allaham, W. A. Shirley and J. Mantzaris, *J. Chem. Phys.*, 1988, **89**, 2193-2218.
244. A. P. Scott and L. Radom, *J. Phys. Chem.*, 1996, **100**, 16502-16513.
245. J. C. Roder, F. Meyer, I. Hyla-Kryspin, R. F. Winter and E. Kaifer, *Chem. Eur. J.*, 2003, **9**, 2636-2648.
246. GaussView, version 4.0, R. Dennington II, T. Keith and J. Millam, Semichem, Inc., Shawnee Mission, KS, 2007
247. GaussSum, version 2.1.4, N. M. O'Boyle and J. G. Vos, Dublin City University, 2007
248. J. Maurer, B. Sarkar, W. Kaim, R. F. Winter and S. Zalis, *Chem. Eur. J.*, 2007, **13**, 10257-10272.
249. J. Maurer, M. Linseis, B. Sarkar, B. Schwederski, M. Niemeyer, W. Kaim, S. Zalis, C. Anson, M. Zabel and R. F. Winter, *J. Am. Chem. Soc.*, 2008, **130**, 259-268.
250. K. Kowalski, M. Linseis, R. F. Winter, M. Zabel, S. Zalis, H. Kelm, H. J. Kruger, B. Sarkar and W. Kaim, *Organometallics*, 2009, **28**, 4196-4209.
251. S. D. Glover, J. C. Goeltz, B. J. Lear and C. P. Kubiak, *Eur. J. Inorg. Chem.*, 2009, 585-594.
252. M. R. Torres, A. Vegas, A. Santos and J. Ros, *J. Organomet. Chem.*, 1986, **309**, 169-177.
253. M. R. Torres, A. Santos, J. Ros and X. Solans, *Organometallics*, 1987, **6**, 1091-1095.
254. A. Romero, A. Santos and A. Vegas, *Organometallics*, 1988, **7**, 1988-1993.
255. A. Romero, A. Santos, J. Lopez and A. M. Echavarren, *J. Organomet. Chem.*, 1990, **391**, 219-223.

256. M. R. Torres, A. Santos, A. Perales and J. Ros, *J. Organomet. Chem.*, 1988, **353**, 221-228.
257. A. F. Hill, eds. E. W. Abel, F. G. A. Stone and G. Wilkinson, Pergamon, Oxford, 1995, vol. 7, pp. 400-410.
258. M. R. Torres, A. Perales and J. Ros, *Organometallics*, 1988, **7**, 1223-1224.
259. M. R. Torres, A. Vegas, A. Santos and J. Ros, *J. Organomet. Chem.*, 1987, **326**, 413-421.
260. A. F. Hill and R. P. Melling, *J. Organomet. Chem.*, 1990, **396**, C22-C24.
261. D. S. Bohle, G. R. Clark, C. E. F. Rickard, W. R. Roper, W. E. B. Shepard and L. J. Wright, *J. Chem. Soc. Chem. Commun.*, 1987, 563-565.
262. M. Herberhold and A. F. Hill, *J. Organomet. Chem.*, 1990, **395**, 315-326.
263. A. Gieren, C. Ruizperez, T. Hubner, M. Herberhold and A. F. Hill, *J. Chem. Soc. Dalton Trans.*, 1988, 1693-1696.
264. W. R. Roper, G. E. Taylor, J. M. Waters and L. J. Wright, *J. Organomet. Chem.*, 1978, **157**, C27-C29.
265. W. R. Roper, G. E. Taylor, J. M. Waters and L. J. Wright, *J. Organomet. Chem.*, 1979, **182**, C46-C48.
266. N. W. Alcock, A. F. Hill and R. P. Melling, *Organometallics*, 1991, **10**, 3898-3903.
267. J. D. E. T. Wilton-Ely, S. J. Honarkhah, M. Wang, D. A. Tocher and A. M. Z. Slawin, *Dalton Trans.*, 2005, 1930-1939.
268. H. Werner, M. A. Esteruelas and H. Otto, *Organometallics*, 1986, **5**, 2295-2299.
269. H. Werner, W. Stuer, J. Wolf, M. Laubender, B. Weberndorfer, R. Herbst-Irmer and C. Lehmann, *Eur. J. Inorg. Chem.*, 1999, 1889-1897.
270. M. A. Esteruelas and H. Werner, *J. Organomet. Chem.*, 1986, **303**, 221-231.
271. C. S. Yi and D. W. Lee, *Organometallics*, 1999, **18**, 5152-5156.
272. A. V. Marchenko, H. Gerard, O. Eisenstein and K. G. Caulton, *New. J. Chem.*, 2001, **25**, 1244-1255.
273. J. T. Poulton, M. P. Sigalas, K. Folting, W. E. Streib, O. Eisenstein and K. G. Caulton, *Inorg. Chem.*, 1994, **33**, 1476-1485.
274. H. P. Xia, R. C. Y. Yeung and G. C. Jia, *Organometallics*, 1998, **17**, 4762-4768.
275. X. H. Wu, S. Jin, J. H. Liang, Z. Y. Li, G. A. Yu and S. H. Liu, *Organometallics*, 2009, **28**, 2450-2459.
276. A. M. McNair, D. C. Boyd and K. R. Mann, *Organometallics*, 1986, **5**, 303-310.
277. M. A. J. Tenorio, M. J. Tenorio, M. C. Puerta and P. Valerga, *Organometallics*, 1997, **16**, 5528-5535.
278. M. J. Tenorio, M. A. J. Tenorio, M. C. Puerta and P. Valerga, *Inorg. Chim. Acta.*, 1997, **259**, 77-84.
279. N. W. Alcock, I. D. Burns, K. S. Claire and A. F. Hill, *Inorg. Chem.*, 1992, **31**, 2906-2908.
280. C. Bohanna, M. A. Esteruelas, A. V. Gomez, A. M. Lopez and M. P. Martinez, *Organometallics*, 1997, **16**, 4464-4468.
281. I. D. Burns, A. F. Hill, A. J. P. White, D. J. Williams and J. D. E. T. Wilton-Ely, *Organometallics*, 1998, **17**, 1552-1557.
282. H. P. Xia, T. B. Wen, Q. Y. Hu, X. Wang, X. G. Chen, L. Y. Shek, I. D. Williams, K. S. Wong, G. K. L. Wong and G. C. Jia, *Organometallics*, 2005, **24**, 562-569.

283. P. Yuan, J. Yin, G. A. Yu, Q. Y. Hu and S. H. Liu, *Organometallics*, 2007, **26**, 196-200.
284. B. J. Coe and S. J. Glenwright, *Coordin. Chem. Rev.*, 2000, **203**, 5-80.
285. S. H. Choi, I. Bytheway, Z. Y. Lin and G. C. Jia, *Organometallics*, 1998, **17**, 3974-3980.
286. K. B. Wiberg and E. Martin, *J. Am. Chem. Soc.*, 1985, **107**, 5035-5041.
287. A. E. Dorigo, D. W. Pratt and K. N. Houk, *J. Am. Chem. Soc.*, 1987, **109**, 6591-6600.
288. J. Maurer, R. F. Winter, B. Sarkar and S. Zalis, *Journal of Solid State Electrochemistry*, 2005, **9**, 738-749.
289. F. de Montigny, G. Argouarch, K. Costuas, J. F. Halet, T. Roisnel, L. Toupet and C. Lapinte, *Organometallics*, 2005, **24**, 4558-4572.
290. M. Younus, N. J. Long, P. R. Raithby and J. Lewis, *J. Organomet. Chem.*, 1998, **570**, 55-62.
291. J. Otsuki, T. Akasaka and K. Araki, *Coordin. Chem. Rev.*, 2008, **252**, 32-56.
292. M. Fischer, G. Lieser, A. Rapp, I. Schnell, W. Mamdouh, S. De Feyter, F. C. De Schryver and S. Hoger, *J. Am. Chem. Soc.*, 2004, **126**, 214-222.
293. T. Weyland, K. Costuas, A. Mari, J. F. Halet and C. Lapinte, *Organometallics*, 1998, **17**, 5569-5579.
294. R. R. Tykwinski and P. J. Stang, *Organometallics*, 1994, **13**, 3203-3208.
295. T. J. J. Muller and H. J. Lindner, *Chem. Ber.*, 1996, **129**, 607-613.
296. J. Vicente, M. T. Chicote, M. M. Alvarez-Falcon and P. G. Jones, *Organometallics*, 2005, **24**, 2764-2772.
297. R. Packheiser, P. Ecorchard, T. Ruffer, B. Walforta and H. Lang, *Eur. J. Inorg. Chem.*, 2008, 4152-4165.
298. Q. Y. Hu, M. F. Lo, I. D. Williams, N. Koda, Y. Uchimaru and G. C. Jia, *J. Organomet. Chem.*, 2003, **670**, 243-247.
299. A. Ahmad, J. J. Levison, S. D. Robinson and M. F. Uttley, *Inorg. Syn.*, 1974, **15**, 45-64.
300. SAINT V6.45, Bruker, AXS, Madison, Wisconsin, USA, 2001
301. Gaussian 03, Revision C.02, M. J. Frisch, G. W. Trucks, H. B. Schlegel, G. E. Scuseria, M. A. Robb, J. R. Cheeseman, J. A. Montgomery, T. Vreven, K. N. Kudin, J. C. Burant, J. M. Millam, S. S. Iyengar, J. Tomasi, V. Barone, B. Mennucci, M. Cossi, G. Scalmani, N. Rega, G. A. Petersson, H. Nakatsuji, M. Hada, M. Ehara, K. Toyota, R. Fukuda, J. Hasegawa, M. Ishida, T. Nakajima, Y. Honda, O. Kitao, H. Nakai, M. Klene, X. Li, J. E. Knox, H. P. Hratchian, J. B. Cross, C. Adamo, J. Jaramillo, R. Gomperts, R. E. Stratmann, O. Yazyev, A. J. Austin, R. Cammi, C. Pomelli, J. W. Ochterski, P. Y. Ayala, K. Morokuma, G. A. Voth, P. Salvador, J. J. Dannenberg, V. G. Zakrzewski, S. Dapprich, A. D. Daniels, M. C. Strain, O. Farkas, D. K. Malick, A. D. Rabuck, K. Raghavachari, J. B. Foresman, J. V. Ortiz, Q. Cui, A. G. Baboul, S. Clifford, J. Cioslowski, B. B. Stefanov, G. Liu, A. Liashenko, P. Piskorz, I. Komaromi, R. L. Martin, D. J. Fox, T. Keith, M. A. Allaham, C. Y. Peng, A. Nanayakkara, M. Challacombe, P. M. W. Gill, B. Johnson, W. Chen, M. W. Wong, C. Gonzalez and J. A. Pople, Gaussian Inc., Wallingford, CT., 2004
302. M. Akita and T. Koike, *Dalton Trans.*, 2008, 3523-3530.
303. F. Diederich, *Chem. Commun.*, 2001, 219-227.
304. D. Touchard and P. H. Dixneuf, *Coordin. Chem. Rev.*, 1998, **178**, 409-429.
305. B. Xi and T. Ren, *C.R. Chim.*, 2009, **12**, 321-331.

306. D. J. Armitt, M. I. Bruce, M. Gaudio, N. N. Zaitseva, B. W. Skelton, A. H. White, B. Le Guennic, J. F. Halet, M. A. Fox, R. L. Roberts, F. Hartl and P. J. Low, *Dalton Trans.*, 2008, 6763-6775.
307. B. F. G. Johnson, A. K. Kakkar, M. S. Khan and J. Lewis, *J. Organomet. Chem.*, 1991, **409**, C12-C14.
308. S. J. Davies, B. F. G. Johnson, M. S. Khan and J. Lewis, *J. Chem. Soc. Chem. Commun.*, 1991, 187-188.
309. G. C. Jia, R. J. Puddephatt, J. D. Scott and J. J. Vittal, *Organometallics*, 1993, **12**, 3565-3574.
310. I. R. Whittall, A. M. McDonagh, M. G. Humphrey and M. Samoc, *Adv. Organomet. Chem.*, 1998, **42**, 291-362.
311. Y. Tanaka, J. A. Shaw-Taberlet, F. Justaud, O. Cador, T. Roisnel, M. Akita, J. R. Hamon and C. Lapinte, *Organometallics*, 2009, **28**, 4656-4669.
312. L. S. Devi, M. K. Al-Suti, N. Zhang, S. J. Teat, L. Male, H. A. Sparkes, P. R. Raithby, M. S. Khan and A. Kohler, *Macromolecules.*, 2009, **42**, 1131-1141.
313. L. B. Gao, J. Kan, Y. Fan, L. Y. Zhang, S. H. Liu and Z. N. Chen, *Inorg. Chem.*, 2007, **46**, 5651-5664.
314. L. Medei, L. Orian, O. V. Semeikin, M. G. Peterleitner, N. A. Ustynyuk, S. Santi, C. Durante, A. Ricci and C. Lo Sterzo, *Eur. J. Inorg. Chem.*, 2006, 2582-2597.
315. R. D'Amato, I. Fratoddi, A. Cappotto, P. Altamura, M. Delfini, C. Bianchetti, A. Bolasco, G. Polzonetti and M. V. Russo, *Organometallics*, 2004, **23**, 2860-2869.
316. A. Kohler and D. Beljonne, *Adv. Funct. Mater.*, 2004, **14**, 11-18.
317. S. Roue, S. Le Stang, L. Toupet and C. Lapinte, *C.R. Chim.*, 2003, **6**, 353-366.
318. A. Kohler, J. S. Wilson, R. H. Friend, M. K. Al-Suti, M. S. Khan, A. Gerhard and H. Bassler, *J. Chem. Phys.*, 2002, **116**, 9457-9463.
319. S. Le Stang, F. Paul and C. Lapinte, *Organometallics*, 2000, **19**, 1035-1043.
320. N. Chawdhury, A. Kohler, R. H. Friend, M. Younus, N. J. Long, P. R. Raithby and J. Lewis, *Macromolecules.*, 1998, **31**, 722-727.
321. J. Lewis, N. J. Long, P. R. Raithby, G. P. Shields, W. Y. Wong and M. Younus, *J. Chem. Soc. Dalton Trans.*, 1997, 4283-4288.
322. E. Viola, C. LoSterzo and F. Trezzi, *Organometallics*, 1996, **15**, 4352-4354.
323. E. Viola, C. LoSterzo, R. Crescenzi and G. Frachey, *J. Organomet. Chem.*, 1995, **493**, C9-C13.
324. M. C. Chung, X. H. Gu, B. A. Etzenhouser, A. M. Spuches, P. T. Rye, S. K. Seetharaman, D. J. Rose, J. Zubieta and M. B. Sponsler, *Organometallics*, 2003, **22**, 3485-3494.
325. K. Onitsuka, N. Ohara, F. Takei and S. Takahashi, *Organometallics*, 2008, **27**, 25-27.
326. M. S. Morton and J. P. Selegue, *J. Am. Chem. Soc.*, 1995, **117**, 7005-7006.
327. M. S. Morton, J. P. Selegue and A. Carrillo, *Organometallics*, 1996, **15**, 4664-4666.
328. N. Re, A. Sgamellotti and C. Floriani, *Organometallics*, 1996, **15**, 5330-5334.
329. M. Gruselle, H. Elhafa, M. Nikolski, G. Jaouen, J. Vaissermann, L. J. Li and M. J. McGlinchey, *Organometallics*, 1993, **12**, 4917-4925.
330. I. V. Barinov, O. A. Reutov, A. V. Polyakov, A. I. Yanovsky, Y. T. Struchkov and V. I. Sokolov, *J. Organomet. Chem.*, 1991, **418**, C24-C27.

331. S. F. T. Froom, M. Green, K. R. Nagle and D. J. Williams, *J. Chem. Soc. Chem. Commun.*, 1987, 1305-1307.
332. D. Osella, G. Dutto, G. Jaouen, A. Vessieres, P. R. Raithby, L. Debenedetto and M. J. McGlinchey, *Organometallics*, 1993, **12**, 4545-4552.
333. G. A. Olah, R. Krishnamurti and G. K. S. Prakash, *J. Org. Chem.*, 1990, **55**, 6061-6062.
334. C. K. Tseng, Migliore.Kg and S. I. Miller, *Tetrahedron*, 1974, **30**, 377-383.
335. H. G. Richey, L. E. Rennick, A. S. Kushner, J. M. Richey and J. C. Philips, *J. Am. Chem. Soc.*, 1965, **87**, 4017-4019.
336. T. J. J. Muller, *Eur. J. Org. Chem.*, 2001, 2021-2033.
337. G. G. Melikyan, S. Bright, T. Monroe, K. I. Hardcastle and J. Ciurash, *Angew. Chem. Int. Ed.*, 1998, **37**, 161-164.
338. S. Nakatsuji, K. Nakashima, K. Yamamura and S. Akiyama, *Tetrahedron Lett.*, 1984, **25**, 5143-5146.
339. J. P. Selegue, B. A. Young and S. L. Logan, *Organometallics*, 1991, **10**, 1972-1980.
340. J. P. Selegue, *Coordin. Chem. Rev.*, 2004, **248**, 1543-1563.
341. M. I. Bruce, *Chem. Rev.*, 1991, **91**, 197-257.
342. M. I. Bruce and A. G. Swincer, *Adv. Organomet. Chem.*, 1983, **22**, 59-128.
343. M. I. Bruce, *Chem. Rev.*, 1998, **98**, 2797-2858.
344. P. Manini, W. Amrein, V. Gramlich and F. Diederich, *Angew. Chem. Int. Ed.*, 2002, **41**, 4339-4343.
345. M. B. Nielsen and F. Diederich, *Synlett*, 2002, 544-552.
346. T. Lange, J. D. vanLoon, R. R. Tykwinski, M. Schreiber and F. Diederich, *Synthesis-Stuttgart*, 1996, 537-550.
347. A. H. Alberts and H. Wynberg, *J. Chem. Soc. Chem. Commun.*, 1988, 748-749.
348. Y. Rubin, C. B. Knobler and F. Diederich, *Angew. Chem. Int. Ed.*, 1991, **30**, 698-700.
349. H. Hauptmann, *Tetrahedron Lett.*, 1974, **15**, 3587-3588.
350. A. E. Gray and C. S. Marvel, *J. Am. Chem. Soc.*, 1925, **47**, 2796-2802.
351. M. I. Bruce, B. C. Hall, B. D. Kelly, P. J. Low, B. W. Skelton and A. H. White, *J. Chem. Soc. Dalton Trans.*, 1999, 3719-3728.
352. J. Anthony, A. M. Boldi, Y. Rubin, M. Hobi, V. Gramlich, C. B. Knobler, P. Seiler and F. Diederich, *Helv. Chim. Acta.*, 1995, **78**, 13-45.
353. P. Zuber and P. J. Low, unpublished work
354. T. S. Abram and W. E. Watts, *J. Chem. Soc. Perkin Trans. 1*, 1977, 1532-1536.
355. V. I. Boev and A. V. Dombrovskii, *J. Org. Chem. USSR (Eng. Transl.)*, 1985, **21**, 575-579.
356. C. Bilton, J. A. K. Howard, N. N. L. Madhavi, A. Nangia, G. R. Desiraju, F. H. Allen and C. C. Wilson, *Acta. Cryst.*, 2000, **B56**, 1071-1079.
357. V. R. Pedireddi, D. S. Reddy, B. S. Goud, D. C. Craig, A. D. Rae and G. R. Desiraju, *J. Chem. Soc. Perkin Trans. 2*, 1994, 2353-2360.
358. A. Bondi, *J. Phys. Chem.*, 1964, **68**, 441-451.
359. Y. Shirota, *J. Mater. Chem.*, 2000, **10**, 1-25.
360. W. E. Moerner and S. M. Silence, *Chem. Rev.*, 1994, **94**, 127-155.
361. Y. Nishikitani, M. Kobayashi, A. Uchida and T. Kubo, *Electrochimica Acta*, 2001, **46**, 2035-2040.
362. D. M. Pai and B. E. Springett, *Rev. Mod. Phys.*, 1993, **65**, 163-211.

363. M. Stolka, J. F. Yanus and D. M. Pai, *J. Phys. Chem.*, 1984, **88**, 4707-4714.
364. J. F. Hartwig, *Acc. Chem. Res.*, 2008, **41**, 1534-1544.
365. P. J. Low, R. Rousseau, P. Lam, K. A. Udachin, G. D. Enright, J. S. Tse, D. D. M. Wayner and A. J. Carty, *Organometallics*, 1999, **18**, 3885-3897.
366. H. J. Jiao, K. Costuas, J. A. Gladysz, J. F. Halet, M. Guillemot, L. Toupet, F. Paul and C. Lapinte, *J. Am. Chem. Soc.*, 2003, **125**, 9511-9522.
367. C. Lambert, G. Noll, E. Schmalzlin, K. Meerholz and C. Brauchle, *Chem.-Eur. J.*, 1998, **4**, 2129-2135.
368. V. W. W. Yam, K. M. C. Wong, L. L. Hung and N. Y. Zhu, *Angew. Chem. Int. Ed.*, 2005, **44**, 3107-3110.
369. K. M. C. Wong, X. L. Zhu, L. L. Hung, N. Y. Zhu, V. W. W. Yam and H. S. Kwok, *Chem. Commun.*, 2005, 2906-2908.
370. C. Lambert and G. Noll, *J. Am. Chem. Soc.*, 1999, **121**, 8434-8442.
371. S. C. Jones, V. Coropceanu, S. Barlow, T. Kinnibrugh, T. Timofeeva, J. L. Bredas and S. R. Marder, *J. Am. Chem. Soc.*, 2004, **126**, 11782-11783.
372. C. Lambert, W. Gaschler, G. Noll, M. Weber, E. Schmalzlin, C. Brauchle and K. Meerholz, *J. Chem. Soc. Perkin Trans. 2*, 2001, 964-974.
373. S. Ghosh and P. S. Mukherjee, *Organometallics*, 2008, **27**, 316-319.
374. K. R. J. Thomas and J. T. Lin, *J. Organomet. Chem.*, 2001, **637**, 139-144.
375. H. Fink, N. J. Long, A. J. Martin, G. Opromolla, A. J. P. White, D. J. Williams and P. Zanello, *Organometallics*, 1997, **16**, 2646-2650.
376. Nakashim.T and T. Kunitake, *B. Chem. Soc. Jpn.*, 1972, **45**, 2892-2895.
377. M. Iyoda, T. Kondo, T. Okabe, H. Matsuyama, S. Sasaki and Y. Kuwatani, *Chemistry Letters*, 1997, 35-36.
378. A. J. Fry, P. S. Jain and R. L. Krieger, *J. Organomet. Chem.*, 1981, **214**, 381-390.
379. P. J. Low, M. A. J. Paterson, A. E. Goeta, D. S. Yufit, J. A. K. Howard, J. C. Cherryman, D. R. Tackley and B. Brown, *J. Mater. Chem.*, 2004, **14**, 2516-2523.
380. K. Sreenath, C. V. Suneesh, V. K. R. Kumar and K. R. Gopidas, *J. Org. Chem.*, 2008, **73**, 3245-3251.
381. B. H. Yang and S. L. Buchwald, *J. Organomet. Chem.*, 1999, **576**, 125-146.
382. A. R. Muci and S. L. Buchwald, in *Cross-Coupling Reactions*, 2002, vol. 219, pp. 131-209.
383. J. F. Hartwig, *Acc. Chem. Res.*, 1998, **31**, 852-860.
384. L. M. Alcazar-Roman and J. F. Hartwig, *Organometallics*, 2002, **21**, 491-502.
385. J. Louie, M. S. Driver, B. C. Hamann and J. F. Hartwig, *J. Org. Chem.*, 1997, **62**, 1268-1273.
386. I. P. Beletskaya and A. V. Cheprakov, *Coordin. Chem. Rev.*, 2004, **248**, 2337-2364.
387. R. Chinchilla and C. Najera, *Chem. Rev.*, 2007, **107**, 874-922.
388. M. E. Smith, R. L. Cordiner, D. Albesa-Jove, D. S. Yufit, F. Hartl, J. A. K. Howard and P. J. Low, *Can. J. Chem.*, 2006, **84**, 154-163.
389. M. Malagoli and J. L. Bredas, *Chem. Phys. Lett.*, 2000, **327**, 13-17.
390. P. J. Low, M. A. J. Paterson, H. Puschmann, A. E. Goeta, J. A. K. Howard, C. Lambert, J. C. Cherryman, D. R. Tackley, S. Leeming and B. Brown, *Chem. Eur. J.*, 2004, **10**, 83-91.
391. A. N. Sobolev, V. K. Belsky, I. P. Romm, N. Y. Chernikova and E. N. Guryanova, *Acta. Cryst.*, 1985, **41**, 967-971.

392. R. Denis, L. Toupet, F. Paul and C. Lapinte, *Organometallics*, 2000, **19**, 4240-4251.
393. J. Courmarcel, G. Le Gland, L. Toupet, F. Paul and C. Lapinte, *J. Organomet. Chem.*, 2003, **670**, 108-122.
394. F. de Montigny, G. Argouarch, T. Roisnel, L. Toupet, C. Lapinte, S. C. F. Lam, C. H. Tao and V. W. W. Yam, *Organometallics*, 2008, **27**, 1912-1923.
395. F. H. Allen, O. Kennard, D. G. Watson, L. Brammer, A. G. Orpen and R. Taylor, *J. Chem. Soc. Perkin Trans. 2*, 1987, S1-S19.
396. M. I. Bruce, B. G. Ellis, P. J. Low, B. W. Skelton and A. H. White, *Organometallics*, 2003, **22**, 3184-3198.
397. M. I. Bruce, B. W. Skelton, A. H. White and N. N. Zaitseva, *J. Organomet. Chem.*, 2002, **650**, 141-150.
398. C. E. Powell, M. P. Cifuentes, A. M. McDonagh, S. K. Hurst, N. T. Lucas, C. D. Delfs, R. Stranger, M. G. Humphrey, S. Houbrechts, I. Asselberghs, A. Persoons and D. C. R. Hockless, *Inorg. Chim. Acta.*, 2003, **352**, 9-18.
399. I. R. Whittall, M. G. Humphrey and D. C. R. Hockless, *Organometallics*, 1995, **14**, 3970-3979.
400. M. I. Bruce, M. G. Humphrey, M. R. Snow and E. R. T. Tiekink, *J. Organomet. Chem.*, 1986, **314**, 213-225.
401. F. Paul, J. Y. Mevellec and C. Lapinte, *J. Chem. Soc. Dalton Trans.*, 2002, 1783-1790.
402. S. Amthor, B. Noller and C. Lambert, *Chem. Phys.*, 2005, **316**, 141-152.
403. S. Dapperheld, E. Steckhan, K. H. G. Brinkhaus and T. Esch, *Chem. Ber.*, 1991, **124**, 2557-2567.
404. S. Le Stang, D. Lenz, F. Paul and C. Lapinte, *J. Organomet. Chem.*, 1999, **572**, 189-192.
405. S. Le Stang, F. Paul and C. Lapinte, *Inorg. Chim. Acta.*, 1999, **291**, 403-425.
406. F. Paul, L. Toupet, T. Roisnel, P. Hamon and C. Lapinte, *C.R. Chim.*, 2005, **8**, 1174-1185.
407. R. Anemian, D. C. Cupertino, P. R. Mackie and S. G. Yeates, *Tetrahedron Lett.*, 2005, **46**, 6717-6721.
408. G. A. Petersson, T. G. Tensfeldt and J. A. Montgomery, *J. Chem. Phys.*, 1991, **94**, 6091-6101.